

Quantum coherence and -control in
mesoscopic systems

Habilitationsschrift

vorgelegt der Fakultät für Physik der
Ludwig-Maximilians-Universität München

Dr. Frank K. Wilhelm

München, im Oktober 2003

I think I can safely say that nobody understands quantum mechanics.
Richard P. Feynman, *The character of physical law*

Contents

1	Preface	1
2	Introduction	3
2.1	Quantum effects in solid-state systems	4
2.2	Small is different	5
2.3	Quantum computation	6
2.4	Solid-state quantum computation	8
2.5	Superconductivity, Josephson effect	9
2.5.1	Superconductivity	10
2.5.2	The Josephson effect	11
2.6	Superconducting quantum bits	14
2.7	Decoherence / classical physics	20
2.8	Quantum dot quantum bits	27
2.9	Nonequilibrium superconductivity	30
3	Original papers	49
3.1	Spectroscopy of superconducting qubits	49
3.2	Electromagnetic environment	71

3.3	Manipulation of superconducting qubits	102
3.4	Read-out of superconducting qubits	124
3.5	Active suppression of decoherence and errors	154
3.6	Elements for quantum computers	159
3.7	Decoherence in quantum dots	176
3.8	Junctions with conducting barriers	192
4	Acknowledgements	224

Chapter 1

Preface

This report has the main purpose to document the “Habilitationleistung”, for the partial fulfillment of the requirements for the Habilitation at the Ludwig-Maximilians-Universität in Munich. It summarizes a large part of the work I have done after my PhD-thesis.

The reported research is centered around quantum coherent manipulation of collective quantum states in small superconducting circuits, as they have been proposed as quantum bits. The main motivation for these theoretical investigations are the experiments on small superconducting loops performed in the Quantum Transport group at the TU Delft. They serve the purpose to understand and help improving these experiments and to assess whether, and if yes how, quantum computing can be implemented in such systems. As an intermediate step in the theoretical description, these circuits are reduced to abstract models which can also be physically implemented by other means, many results have a broader impact on diverse qubit realizations. This connection is spelled out in various places. On top of that, towards the end, the scientific neighborhood is explored: Concepts and methods similar to the results on superconductors are also applied to quantum dot quantum bits. To the end, the microscopic details of certain types of mesoscopic Josephson junctions are investigated.

The report consists of two parts: A physical introduction written with pedagogical intention in chapter 2. This part serves as an outline and should enable the reader to appreciate the main body of work: The collection of original, peer-reviewed publications in chapter 3. This chapter is split into sections which group papers on related issues, each section has its own introduction which summarizes the papers in the

form of extended abstracts, and comments on their interrelation.

All this work has been done after my PhD-thesis. In fact, papers which have appeared after my PhD which describe work done in my doctoral thesis have been excluded. The work in section 3.8, though, contains work on extensions and novel phenomena in a system I have already studied in my thesis.

Chapter 2

Introduction

Quantum mechanics makes predictions which are contrary to the experience of the everyday macroscopic world. It has been originally developed [1] as a description for experiments in atomic physics and light-matter interaction. Its consequences, however, reach much further and are one of the foundations of modern physics. The counterintuitive nature of quantum mechanics has led to controversial discussions on the foundation of physics [2, 3] which still persist [4] and have reached as far as influencing parts of modern philosophy. In fact, many of the original contributors to early quantum mechanics such as Max Planck and Albert Einstein have doubted its general validity. Nevertheless, quantum mechanics is nowadays a well-established theory which accurately describes the physics of systems with a small number of degrees of freedom such as atomic [5] and photonic systems [6] from ultra-cold gases in the Nanokelvin range [7] up to precision $(g - 2)$ -tests [8], neutrino [9] and $B\bar{B}$ -oscillations [10, 11], which occur at the range of $E = 237$ MeV. Quantum mechanics also lays the foundation of modern solid-state physics [12] in which it is responsible even for dramatic effects such as the band structure of semiconductors [13] and superconductivity [14, 15].

On the other hand, the predictions quantum mechanics is making for small systems do not seem to hold for the dynamics of the center-of-mass motion of macroscopic systems. For example, large objects such as chairs are usually not found to be in coherent superposition states of two positions which can be discriminated by the bare eye. This fact has already been recognized by Schrödinger and sharply cast in his famous cat paradox [16]. It opens the question to which extent quantum me-

chanical predictions do hold on a macroscopic scale, whether quantum mechanics breaks down at some system size or whether, given the rapid progress in experimentation, generic quantum effects can in principle be demonstrated on a macroscopic scale [15,17]. A method to approach this question theoretically is to carefully understand the emergence of the classical world within a generically quantum mechanical approach and to propose how the quantum-classical border can be overcome or at least stretched to larger and larger systems. In particular, such an analysis would show what “small” and “large” means in this context, i.e. provide measures related to the spatial extent or particle number of a system which allow to predict whether or not quantum-mechanical effects are visible [18].

One particularly important case of the transition between both worlds, which occurs within the formulation of quantum mechanics even for small systems, is the quantum measurement [15, 19–22]. Performing a measurement on a quantum-mechanical system transfers information from its quantum-mechanical state to a macroscopic object, the measuring device. According to the standard set of postulates of quantum mechanics, it is strongly invasive: It renders the system in a “classical” state of the measured observable. The details of this “collapse” of the wave function are seldom discussed and in particular it is not understood, how this postulate is compatible with the assumption that the degrees of freedom of the detector are also described by the laws of quantum-mechanics, such that e.g. the superposition principle should hold for the many-body states of the detector the same way as for the quantum object to be measured. The exploration of the measurement process, which narrows down but does not solve the quantum measurement problem [23–25], is hence a paradigmatic piece for understanding the connection between classical and quantum physics. Moreover, it is important for understanding whether or not the quantum measurement postulate is a necessary ingredient or whether quantum mechanics is complete without it.

2.1 Quantum effects in solid-state systems

The dualism of quantum and classical descriptions is prevalent in solid state system. Solids are composed of quantum mechanical degrees of freedom, electrons, protons and neutrons, in huge numbers. Crystalline solids are highly ordered through the laws of chemical bonding, which are generically quantum-mechanical [12, 26]. The deeper understanding

of the formation and stability of solids allows to create a wide range of materials with engineered properties and well-defined structures made from these [27]. The microscopic theory of solids is governed by the laws of quantum mechanics, which are e.g. responsible for the stability of the solid and its optical properties. The electronic and transport properties, which can be much easier accessed with macroscopic detectors, of many materials can be described by a semiclassical approach such as Bloch-Boltzmann dynamics or, in noble metals, the Drude-Sommerfeld model [26]. These descriptions are very close to classical theories treating electrons as classical point particles, supplemented with a number of quantum mechanical ingredients. They are very successful in describing transport at room temperature even though the underlying physics is fundamentally quantum. At low temperatures, quantum effects become more important and additional, generic quantum phenomena can be observed. In particular, most metallic elements undergo the transition to the superconducting state [14], which can be viewed as a macroscopic quantum state where the wave function of the superconducting electrons (Cooper pairs) serves as an order parameter. Still, although the order parameter is determined by quantum physics, it remains a formidable task to demonstrate generic quantum features [15] of this order parameter itself, e.g. to bring its phase in a superposition of two values. In this sense, the microscopic degrees of freedom of a solid are quantum-mechanical and do determine many of the macroscopic properties (such as the color or the conductivity) the *global collective* coordinates of large solids such as the usually follow the laws of classical physics: The order parameter is, besides small fluctuations, uniquely defined as a classical variable, so is the color and the conductivity or the position of the whole solid .

2.2 Small is different

As described in the previous section, the sheer size of a solid renders invisible many of the quantum effects that would be visible in atomic and molecular systems. Hence, as solid state setups get miniaturized more and more, they approach the sizes where additional quantum effects appear. This is the idea of mesoscopic solid-state physics [28, 29]: To study systems whose size is in-between macroscopic solids and large molecules. Depending on the quantum effect of interest, mesoscopic systems can still span a wide range of sizes from several microns (as for superconducting quantum interference devices, SQUIDS, in the quan-

tum regime) [30] down to about 10nm for molecules in contact with an electrical circuit [31]. Among the quantum coherent effects observed until the end of the 90s are signatures of the wave nature of electrons in transport properties (weak localization [32], Aharonov-Bohm effect [33], persistent normal currents [34], and universal conductance fluctuations [35]), quantization of the electron charge (as in Coulomb blockade devices [36]), transfer of superconductivity to normal metals (as in Andreev interferometers [37]), strong interaction in confined geometries (as in Luttinger Liquids [38,39]), quantum manybody physics of artificial controllable impurities (Kondo quantum dots [40]) and many more.

Although some aspects of quantum mechanics are revealed in the experiments described so far, the collective variables describing the state of matter are classical in nature: The conductance of a sample subject to weak localization takes, given identical parameters, a single value at a time. It has however already been proposed in the 80s (for SQUID systems) [15,41–44] and in the 90s (for Coulomb blockade devices) [36,45], that collective variables such as flux and charge can be brought into superposition of two notably distinct values. This enterprise has been pursued ever since, but it was only in the late 90s that it received the high degree of attention and interest it has now. The increase in interest was largely due to the perspective to realize a scalable solid-state quantum computer [46].

2.3 Quantum computation

The way of computing as performed in today’s information-processing devices is called *classical computing*. This implies, that the binary information stored and manipulated is purely classical in nature: Every bit is exclusively in one of its fundamental states 0 and 1. Computer programs are deterministic, such that (in principle) operating a program on a fixed set of data leads to the same output data every time. For most computer applications such as accounting or word processing, this is exactly what is intended. The enormous progress in computer technology has made huge computing power readily available which allows to solve many problems conveniently and in short time. The progress in hardware improvement follows the self-fulfilling Moore’s law [47], claiming that computer performance will double every 18 months. Although failures of Moore’s law are periodically predicted and *have* to occur at some time due to the laws of nature, it is by now expected to

still persist for a long time of a further 10–20 years [48, 49].

Quantum information, the type of information processed in a quantum computer, is radically different [50, 51]: The predictions of quantum mechanics open the option to realize different values of observables at the same time and to distribute the information non-locally using entangled states. These properties can be used as a computational resource. Using superpositions makes it possible to operate an algorithm on all possible input values at the same time (massive quantum parallelism), using entangled states and measurements allows to act on all qubits (quantum bits) simultaneously. This is in particular advantageous for problems which heavily rely on trying and comparing. As quantum mechanics is a probabilistic theory, it is not guaranteed that the outcome of a quantum computation can be extracted by a physical measurement with high fidelity. Nevertheless, the problem of finding an operational quantum algorithm which drastically speeds up the best classical solutions to the same problem has been solved in a number of cases, most notably fast database search [52] and factoring of huge numbers [53]. Whereas the former only uses quantum parallelism and leads to a square-root speedup, the latter uses entanglement and is exponentially faster than the classical solution. Cryptography in electronic communication as we know it today [54] essentially relies on factoring. It is immune against progress in classical computing, because when classical computers can solve the N -digit factoring problem in appreciable time T , one can go to $N + 1$ -digits and it will take time TN . Thus, by a mild extension of the length of the coding numbers, progress can always be beaten. This would not be true any more for quantum computers.

The requirements for building a universal quantum computer have been collected very early by DiVincenzo [55, 56]. These five criteria enjoy broad recognition and are, supplemented by two more on the conversion between stationary and flying qubits important for communication, the basis for most quantum computing research programs [57]. They will also be present in this report: Much of the research presented is devoted how its main subject, solid-state qubits, perform on these criteria. One has to be aware, that this standard paradigm is by no means exclusive, in fact, a whole subfield of basic quantum computing research is devoted to developing alternative criteria for quantum computing universality.

The DiVincenzo criteria in a modern formulation require:

1. A scalable physical system of well-characterized qubits

2. The ability to initialize the state of the qubits to a simple fiducial state
3. Long (relative) decoherence times, much longer than the gate-operation time
4. A universal set of quantum gates
5. A qubit-specific measurement capability
6. The ability to convert stationary to flying qubits and vice versa
7. The ability to faithfully transmit flying qubits between specified locations

So far, the physical implementation of quantum computing is most successful in nuclear magnetic resonance (NMR), where seven qubits have been implemented [58] and twelve have been recently announced [59]. Remarkably, in NMR there is no “strong” measurement capability nor the option to initialize a well-defined initial state [60]. Another successful line of implementations comes from optical and atomic physics, such as ion traps [61, 62], atoms in cavities [63, 64], linear optics [65], and neutral atoms [66]. All these realizations follow the general approach, that they start out from “generic” quantum systems, systems whose quantum-mechanical properties have been well-established a long time ago. Consequently, the phase coherence times are very long. The experimental progress towards today’s level has been the ability to externally control these systems better and better and to connect many of them to larger circuits. However, it is still not evident whether these systems are really scalable, although a number of theoretical proposals for scalable ion trap computing have been brought forward [67].

2.4 Solid-state quantum computation

Solid state circuits are readily scalable to huge size and complexity, as can be seen in the computers available today. In these computers, the information being processed is purely classical. However, the physics of the basic building blocks of classical computers is already fundamentally quantum: The physics of transistors relies on the band structure of semiconductor materials [68], a generic quantum-mechanical effect

¹. Remarkably, also the size of a single transistor (characterized by the gate length) is on the order of 100 nm or less [69] and thus even below the size scale of typical mesoscopic samples. Combined with the enormous clock speeds of several GHz, also the quantum limit of the electromagnetic communication between elements is within reach. Thus, it is justified to speculate that solid-state electronics would be able, by a radical design change, to process information quantum-mechanically and to pursue this as a goal of fundamental research.

The reason why the collective variables of solid state systems usually behave classically is decoherence and the lack of *quantum* fluctuations necessary for the preparation of generically non-classical states. As will be detailed in section 2.7, the mechanism underlying decoherence is the coupling to an environment with many degrees of freedom and low-lying excitations. Avoiding decoherence is *the* main issue in designing solid-state qubits. A number of proposals has been brought forward, which can be roughly classified in two classes: On the one hand, there is spin quantum computing using a controlled exchange interaction such as in phosphorus in silicon [70] and spin in quantum dots [71]. Pseudospin quantum computing, on the other hand, uses two-state systems other than spin such as charge states in quantum dots and superconducting quantum bits. The former promise very long coherence times but are difficult to fabricate and read-out. Thus the experimental realizations are on a rather pioneering stage [72, 73], but the possibilities are enormous [74, 75]. The status of the latter will be detailed in the following sections of this report.

2.5 Superconductivity and the Josephson effect

One specific class of promising qubit implementations is based on superconducting Josephson junctions. In this section, the necessary fundamentals of superconductors and the Josephson effect will be outlined, whereas in the following, in particular in section 2.6, specific quantum bits based on the Josephson effect will be detailed.

¹the fact that the information encoded is still purely classical is closely related to the classical behavior of global collective coordinates of large solids as described in the end of section 2.1

2.5.1 Superconductivity

Superconductivity has been discovered already in 1911 by Kammerlingh Onnes [76]. It manifests itself by vanishing electrical DC-resistance and by perfect diamagnetism. It has now been shown that most metallic elements become superconducting at low temperatures. A number of alloys becomes superconducting at somewhat higher temperatures, culminating at the recently discovered superconductivity of MgB_2 at 39 K [77]. Even higher transition temperatures can be found in the unconventional high-temperature superconductors [78]. These materials are typically cuprates and turn out to be antiferromagnetic insulators at high temperatures.

The theoretical understanding of superconductivity is now very mature and subject to a number of textbooks [14, 79, 80]. It has grown in different stages. Already the phenomenological London theory [81] of superconducting electrodynamics describes many superconducting phenomena rather well and, in its modern formulation, accounts for the fact that superconducting phenomena can be described by the dynamics of a single wave function that describes the collective properties of *all* superconducting electrons as if they were combined into a single quantum particle. The same type of model is behind the phenomenological Ginzburg-Landau-Theory [82] of the superconducting phase transition, in which this wave function serves as an order parameter: The modulus describes superconducting order and the symmetry with respect to the phase is spontaneously broken. This is similar to the modulus and the direction of the macroscopic magnetization in a Heisenberg ferromagnet. This picture is consistent with the microscopic BCS-theory [83]: In the presence of an attractive effective interaction, the conduction electrons form Cooper pairs, which condense in momentum space into a collective ground state. Thus, the “superconducting electrons” of the phenomenological theories are Cooper pairs whose charge is twice the elementary charge. The attractive interaction between electrons in metallic superconductors is phonon-mediated. In superconducting metals, this indirect interaction dominates over the Coulomb repulsion, which is screened and whose phase space is usually restricted by the Pauli principle.

Superconductivity is in itself a macroscopic quantum phenomenon: The simple manifestations of superconductivity such as flux quantization [84] and persistent currents can be straightforwardly connected to the uniquely defined phase of the condensate wave function. This

wave function is occupied by a macroscopic number of particles. In superconducting samples of macroscopic size the wave function itself is well-defined and the collective variables, number and phase, do not have quantum uncertainties. This is an example for the previous statement, that collective variables are usually not brought in superposition and behave classically. Thus it has been argued that these are not macroscopic quantum phenomena in the strict sense as in Schrödinger's cat paradox [15].

The elementary excitation of superconductors are quasiparticles. They are separated from the condensate by an energy gap $\Delta(\vec{k}_F)$, where \vec{k}_F points to an arbitrary point on the Fermi surface. Δ can be identified with the order-parameter of Ginzburg-Landau theory ². Elementary superconductors are conventional in the sense that the order parameter has the same symmetry as the crystal lattice, i.e. Δ is independent of \vec{k}_F . In high-temperature superconductors the mechanism mediating the attractive interaction is unknown. Still, it is confirmed that the Cooper pair charge is $2e$ and that the properties can be modeled by a BCS-model with an unconventional parameter with d -wave symmetry [85]. Other unconventional superconductors are also known, e.g. in heavy Fermion materials [86].

The gap of the elementary excitations is the reason why superconductors are so attractive for solid-state quantum computation: The elementary excitations are costly in energy and cannot be reached at low temperatures. At these low temperatures, also the lattice vibrations are frozen out. Consequently conventional superconductors promise to have very low intrinsic decoherence [87]. This argument does not hold for d -wave superconductors as $l = 2$ spherical harmonics have nodes, i.e. there are elementary excitations at arbitrarily low energies in specific directions of the Fermi wave vector.

2.5.2 The Josephson effect

The Josephson effect [88] is recognized as a hallmark of superconductivity. Its basic manifestation is that Cooper pairs can coherently tunnel between two superconductors connected by a weak link [89, 90]. This gives rise to a supercurrent which is controlled by the difference of the

²In some cases, such as superconductors with magnetic impurities or high-temperature-superconductors close to surfaces, one still keeps an order parameter Δ , although excitations below Δ exist

phases of the order parameter in the two superconductors $\phi = \phi_1 - \phi_2$. For weak coupling between the superconductors, which will be assumed henceforth unless stated otherwise, the current-phase-relation is sinusoidal,

$$I = I_c \sin \phi. \quad (2.1)$$

This is the first Josephson equation. At stronger coupling, the sine gets replaced by other 2π -periodic functions with odd parity ranging up to a sawtooth in the extreme case. Such strong coupling does usually not occur when the weak link is a tunnel junction formed by a thin oxide layer, but e.g. for microbridges, point contacts, and normal-metal or semiconductor barriers [90]. From basic consideration of gauge invariance, one can derive the second Josephson relation, which connects the time evolution of the phase difference ϕ with the difference in chemical potential of the Cooper pairs

$$\hbar \dot{\phi} = 2eV. \quad (2.2)$$

The Josephson effect has first been microscopically derived from the BCS theory and the tunneling Hamiltonian by Josephson. Later, a number of pedagogical derivations have appeared, which do *not* contain details of BCS theory and hence outline that the Josephson effect is a universal phenomenon whenever two spatially separated coherent wave functions are connected by a weak link [44, 91, 92]. In fact, Josephson effects have been observed in systems like superfluid He^3 and He^4 [93, 94], Bose-Einstein-Condensates [95], and molecular junctions [96].

Real Josephson junctions contain more possibilities to transport charge than the supercurrent:

1. The quasiparticle tunneling between superconductors gives rise to a resistive channel. The resulting effective shunt resistance R can have a strong dependence on temperature and voltage, e.g. it can show the famous gapped IV-characteristics in superconducting tunnel junctions. Specifically, the effective resistance is very high at low T and V . In real junctions, there is usually a subgap resistance due to defects. In junctions between high temperature superconductors, the V -dependence of the resistance is much smoother due to the smoothness of the d-wave gap [97]. In junctions with conducting interlayers, there is a pronounced subgap conductance due to Andreev reflection. These systems will be detailed in section 2.9, for the remainder we will concentrate on tunnel junctions.

2. Charge can also be transported as a displacement current through the effective capacitance of the junction. This capacitance is essentially the parallel plate capacitance between the superconductors. The capacitance can be rather big as tunnel junctions are typically fabricated in an overlap geometry.

Note, that one can combine the two Josephson equations into one and interpret the small-signal response of the superconducting channel as a nonlinear inductance: Following eq. (2.2) ϕ is proportional to the time-integral of a voltage and can hence be interpreted as dimensionless magnetic flux, $\phi = 2\pi\Phi/\Phi_0$, where $\Phi_0 = h/2e \simeq 2 \cdot 10^{-15}\text{Vs}$ is the superconducting flux quantum. We can linearize eq. (2.1) as $I(\Phi + \delta\Phi) = I_c \sin(2\pi\Phi/\Phi_0) + \delta\Phi/L_J$, or $\delta I = \delta\Phi/L_J(\Phi)$. This defines a kinetic inductance, $L_J(\Phi) = \Phi_0/(2\pi I_c \cos(2\pi\Phi/\Phi_0))$ [98, 99].

These ingredients can be put together into the famous resistively and capacitively shunted junction (RCSJ) model. It results from Kirchhoff's laws and results in a total current I

$$I_c \sin \phi + \frac{1}{R} \frac{\Phi_0}{2\pi} \dot{\phi} + C \frac{\Phi_0}{2\pi} \ddot{\phi} - I = \xi(t) \quad (2.3)$$

where $\xi(t)$ is current noise. This constitutes the classical equation of motion of a Josephson junction. The ratio of the coefficients in this model can be described by two parameters: The plasma frequency $\Omega_{\text{P0}} = (L_J(0)C)^{-1/2} = \sqrt{2\pi I_c/C\Phi_0}$ and the McCumber damping parameter $\beta_c = 2\pi RC/(L_J/R) = CR^2 I_c/\Phi_0$. The junction is underdamped if $\beta_c \gg 1$. This model has been extensively studied in the classical regime [90, 98, 99]. It has been derived, in a generalized form, from BCS theory [100]. We will in later sections study generalizations of the quantum version of this model.

Aside from these intrinsic elements one can of course fabricate an artificial shunting circuit on-chip in order to influence the dynamics of the junction.

Josephson junction circuits enjoy a huge variety of applications already on the classical level. Superconducting quantum interference devices, SQUIDS [101], are used as ultra-sensitive magnetometers and can be used e.g. for measuring brain activity, destruction-free material diagnosis, detection of astrophysical phenomena, high-sensitivity amplifiers, classical flux logic etc. As they are largely controlled by constants of nature such as e and \hbar and, using eq. (2.2) can convert frequency into

current, Josephson devices also have various applications in metrology [102].

2.6 Superconducting quantum bits

In this section, we will derive the macroscopic Hamilton operator of a Josephson junction and describe one specific realization of a Josephson quantum bit.

Without dissipation by a shunt conductance ($R = \infty$), we can rewrite eq. (2.3) as

$$\frac{\Phi_0}{2\pi} C \ddot{\phi} = I - I_c \sin \phi. \quad (2.4)$$

This is the equation of motion of a particle with coordinate ϕ and mass $C(\Phi_0/2\pi)^2$ in a tilted washboard potential $U(\phi) = -I\phi\frac{\Phi_0}{2\pi} - E_J \cos \phi$ where $E_J = I_c\Phi_0/2\pi$ is the Josephson energy. We can introduce a Lagrangian

$$\mathcal{L}(\phi, \dot{\phi}) = \frac{C}{2} \left(\frac{\Phi_0}{2\pi} \right)^2 \dot{\phi}^2 - U(\phi). \quad (2.5)$$

The first term, which plays the role of a kinetic energy, can be interpreted as charging energy, $E_{\text{ch}} = \frac{Q^2}{2C}$, where we have introduced the charge on a capacitor $Q = \frac{\Phi_0}{2\pi} C \dot{\phi} = CV$. It follows, that $\frac{\Phi_0}{2\pi} Q = \frac{\partial \mathcal{L}}{\partial \dot{\phi}}$, i.e. it is proportional to the canonical momentum to ϕ . The Hamilton function equivalent to eq. 2.5 reads

$$H(\phi, Q) = \frac{Q^2}{2C} + U(\phi). \quad (2.6)$$

So far, we have been treating Q and ϕ as classical variables. Following the canonical quantization procedure, we can readily quantize eq. (2.6) by identifying ϕ and Q with operators

$$\hat{H} = \frac{\hat{Q}^2}{2C} + U(\hat{\phi}) \quad \frac{\Phi_0}{2\pi} [\hat{\phi}, \hat{Q}] = i\hbar. \quad (2.7)$$

This is the basis of the macroscopic quantum theory of Josephson junctions. Eq. (2.7) specifically predicts that both ϕ and Q experience quantum fluctuations and cannot be both defined with arbitrary precision; instead, they are limited by a Heisenberg uncertainty relation [14, 103]. Typically, the energy scales E_J and E_{ch} determine the appropriate starting point for describing the junction. For $E_J \gg E_{\text{ch}}$

the phase fluctuations are weak, the elementary excitations are quantum vortices, and the charge wildly fluctuates. Junctions of this kind are often termed “classical”. In the opposite regime the charge is almost a good quantum number and the phase shows strong fluctuations, these are “quantum” junctions. Using the junction area A , one can estimate $E_J \propto I_c \propto A$ whereas $E_{\text{ch}} \propto 1/C \propto 1/A$, thus $E_J/E_{\text{ch}} \propto A^2$ and quantum junctions are typically much smaller in area than classical ones. One can show that the charge and the vortex side are dual and one can observe competing order and quantum phase transitions at $E_J \simeq E_{\text{ch}}$ [104].

In order to introduce damping in a Lagrangian / Hamiltonian formalism, one has to introduce extra degrees of freedom, typically a bath of harmonic oscillators coupling to the junction variables [105, 106]. (N.b.: One can also extend the Lagrange formalism by writing extra terms in the Euler-Lagrange equation [107], but this modification cannot be quantized). The Hamiltonian now contains extra, unobserved degrees of freedom which have to be integrated out when making physical predictions for the junction. This has been pioneered for a single Josephson junction by Caldeira and Leggett [108, 109]. We will now concentrate on junctions with very low intrinsic damping and will describe the remaining dissipation in a way which is compatible with quantum computing in section 2.7.

For building a quantum bit one has to make sure that single-qubit rotations are possible. This is ensured when the Hamiltonian has off-diagonal terms in the basis of externally controllable variables. Here this means that one has to make sure that *both* variables fluctuate sufficiently, i.e. if a charge-based device is used, one has to provide enough charge fluctuations and vice versa. Several realizations and proposals which accomplish this have been brought forward so far. These range from large single junctions [110–112], highly inductive loops (RF-SQUIDS) [30, 41] and small loops [113–116], which are flux-based devices to Cooper pair boxes [46, 117–120], which are charge-based. Other devices combine charge and phase fluctuations with comparable strength and operate in between [121]. Other proposals use the specific properties of unconventional superconductors [122, 123] or large arrays [124]. We will now describe one of these devices in more detail, namely the persistent current quantum bit, which is phase-based and uses a small loop. This device has been proposed at the TU Delft and MIT. As all approaches it has its specific strengths and weaknesses. Most of the theoretical work compiled in chapter 3 is motivated by this device, but the main ideas can be described in terms of universal Hamiltonians and

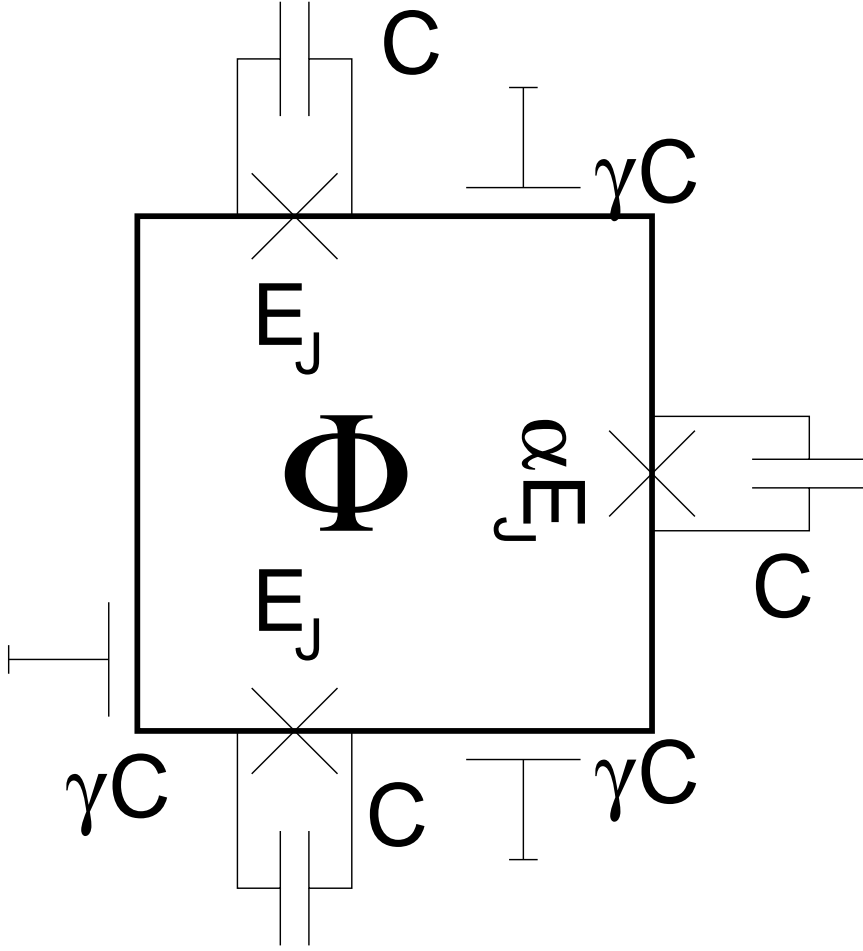
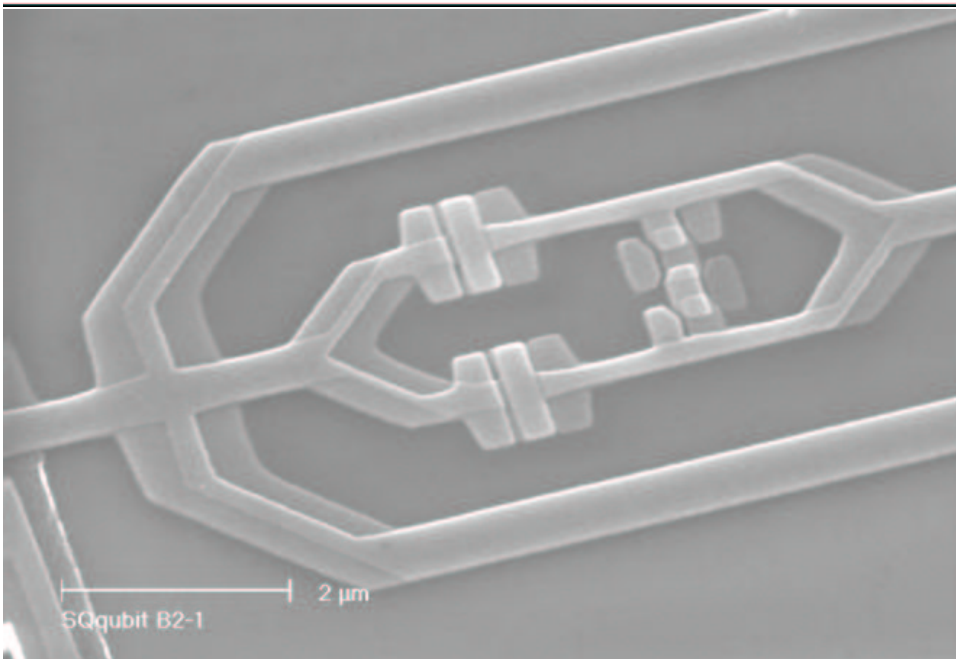
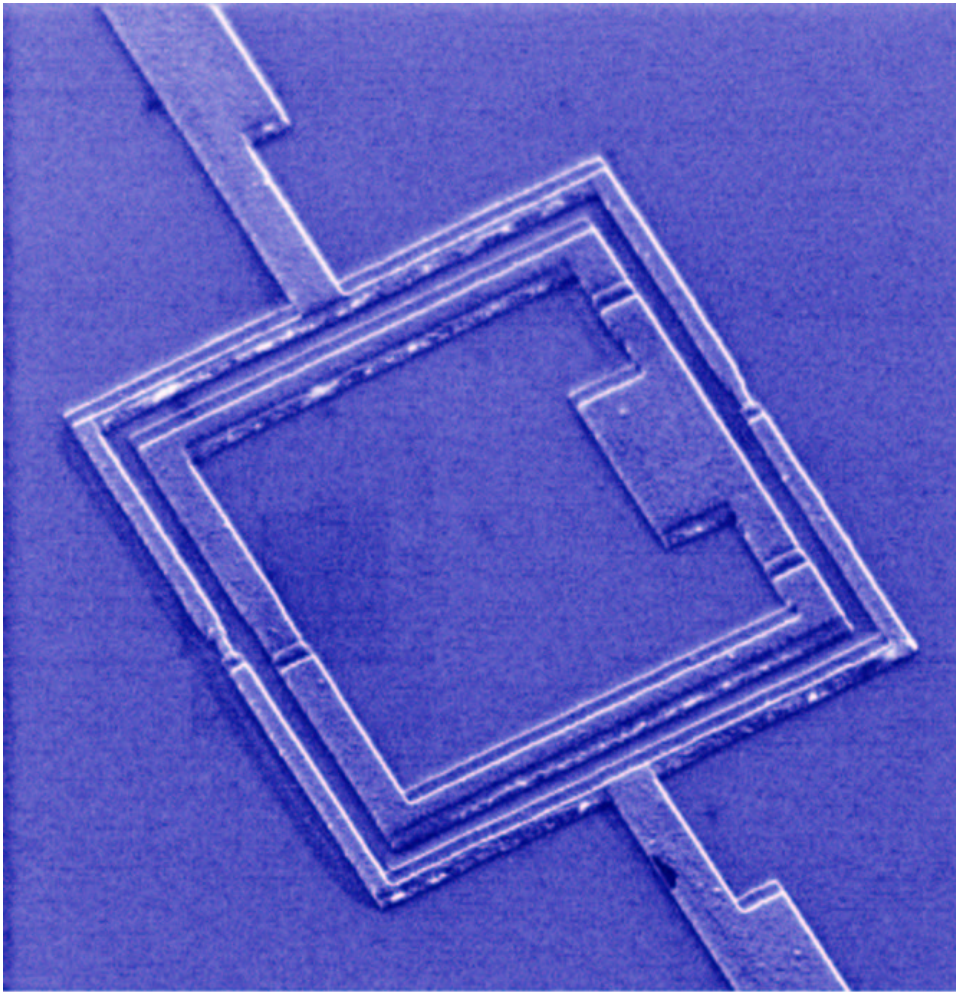


Figure 2.1: The circuit diagram of a flux qubit, including three Josephson junctions (crosses) and all geometric and stray capacitances .

can be applied to other setups as well.

The flux qubit, fig. 2.1, consists of a micrometer-sized superconducting loop, which is interrupted by three Josephson tunnel junctions made from the same, conventional technology: Two of equal size, one smaller by a factor $\alpha \simeq 0.8$. The loop dimensions are chosen such that the geometric self-inductance of the loop does not play any significant role. The loop is penetrated by a magnetic flux of size Φ_x , which imposes the quantization condition $\phi_1 + \phi_2 + \phi_3 = f$, where $f = (2\pi\Phi/\Phi_0) \bmod 2\pi$ is the magnetic frustration, for the phases across the three junctions. Thus we can eliminate ϕ_3 , the phase across the weaker junction, and obtain the potential energy

$$U = E_J (-\cos \phi_1 - \cos \phi_2 - \alpha \cos(2\pi f + \phi_1 - \phi_2)). \quad (2.8)$$



17

Figure 2.2: Top: First generation flux qubits with separate read-out device (outer loop); bottom: Second generation with integrated read-out-device. Picture a) taken by C.H. van der Wal and A.C.J. ter Haar, picture b) by I. Chiorescu and Y. Nakamura

This potential is plotted in figure 2.3. The potential is periodic and possesses a hexagonal pattern of minima separated by potential wells. The energy difference of adjacent minima can be tuned through the external flux: They are degenerate at $\Phi = \Phi_0/2$. From choosing one of the Josephson junctions smaller than the others, one direction is introduced in which the potential barrier is substantially smaller than in the other directions. The state in the minima correspond to clockwise and counterclockwise circulating current respectively.

The charging energy can be evaluated from Kirchhoff's laws. The result is written using vectors in the two dimensional $\{\phi_1, \phi_2\}$ and $\{Q_1, Q_2\}$ coordinate-space as

$$E_{\text{kin}} = 2e^2 \vec{Q}^T \mathbf{C}_M^{-1} \vec{Q}. \quad (2.9)$$

with a capacitance matrix

$$\mathbf{C}_M = C \begin{pmatrix} 1 + \alpha + \gamma & -\alpha \\ -\alpha & 1 + \alpha + \gamma \end{pmatrix}. \quad (2.10)$$

Here, γ is the ratio of the stray capacitances to ground over the junction capacitances, as seen in figure 2.1.

Carefully choosing appropriate parameters, one can reach a situation with exactly one bound state per minimum, where the tunneling along the easy direction is substantial and is strongly suppressed along the other directions. At low energies the dynamics of the system can be described in a two-state approximation in the basis of the states localized in the potential minima, the classical states,

$$\hat{H}_2 = \frac{1}{2} \begin{pmatrix} \epsilon & \Delta \\ \Delta & -\epsilon \end{pmatrix}. \quad (2.11)$$

The energy bias ϵ can be steered through the external flux following $\epsilon \simeq I_q(\Phi - \Phi_0/2)$, where I_q is the modulus of the circulating current in the classical states. Thus, the quantum dynamics of the device can be controlled by the external flux.

The tunnel splitting Δ can be made tunable by splitting the small junction into two parallel junctions, a DC-SQUID, which acts as an effective single junction whose Josephson coupling $E_J(\Phi_2) = 2E_{J,0} \cos(\pi\Phi_2/\Phi_0)$ can be tuned by the flux Φ_2 through this loop between the sum of the two couplings $2E_{J,0}$ and zero. Such a tunable Δ is necessary in a number of, but not in all, quantum computing protocols. The state of the system can be read out by measuring the extra magnetic flux produced by the circulating current through a very sensitive magnetometer: a

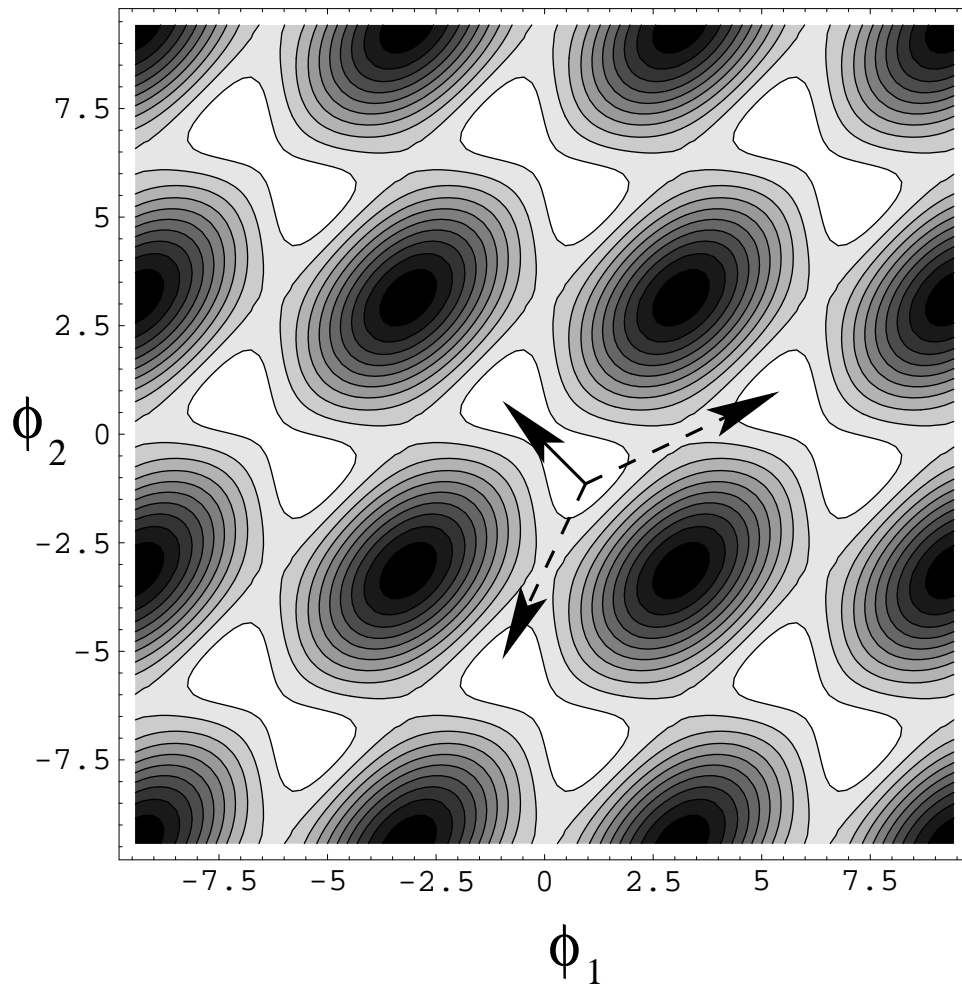


Figure 2.3: The potential landscape for a flux qubit as a function of the phases across the identical junctions, taking $\alpha = 0.8$. The solid arrow indicates an easy tunneling path whereas the dashed lines indicate hard directions.

SQUID [101]. Such a magnetometer works as a tunable junction as just described: E_J depends on the flux through the loop and can be measured electronically. The SQUID-readout corresponds to a measurement of $\hat{\sigma}_z$. Figure 2.2 shows micrographs of real devices together with their read-out apparatus.

The flux qubit is thus a well-defined quantum system that can perform single-qubit rotations. All other ingredients demanded by DiVincenzo's original five criteria can also be met, which will be detailed more in section 2 of this report. Note that eq. (2.11) predicts that superpositions of current states can be prepared close to $f = 1/2$. The current states involve up to 10^{10} electrons. Thus, these are superpositions of large objects. This does not yet imply that these states correspond to huge Schrödinger's cats: For analyzing this question one has to carefully evaluate the distance in Hilbert space between the two states, which is a by far more subtle issue [17, 18].

Structures of this kind are fabricated and studied in a number of laboratories in the world and a number of experimental demonstrations have been performed: Spectroscopy and level-repulsion [125], Rabi oscillations and Ramsey fringes [115], coupling of qubits [126], and single-shot readout [127]. Some of these goals have been declared to be physically impossible shortly before being demonstrated experimentally. This experimental progress gives rise to the hope that the program can be pursued further and more and more elaborate quantum-coherent manipulations can be performed.

2.7 Decoherence and the transition to classical physics

Coherence is the ability to interfere and is usually associated with the phase of a wave. In optics, light is called incoherent if its propagation can be described by geometrical optics alone [128]. The applicability of such a description clearly depends on the phenomenon being studied and on the scale of observation. The focusing of coherent laser light on large scales can, e.g., still be described by geometrical optics, the interference phenomena of the same laser beam in an interferometer require the use of a wave description. In quantum mechanics, the phase under consideration is usually the phase of the wave function and the incoherent limit of the theory is classical physics. Decoherence is the

loss of coherence, i.e. in quantum mechanics it describes the transition from generically quantum to classical behavior. When describing decoherence, one thus has to clearly specify which quantum interference phenomenon (and which classical counterpart) is being studied. E.g. in a two-state-system (TSS) one can specify the “decoherence of free quantum oscillations” instead of just “decoherence”. We will see that there are regimes when specific quantum phenomena, such as the formation of superpositions of classical states, are still observable, whereas others, such as real-time interference fringes, are already completely suppressed. In fact, this property of decoherence is important for the coexistence of classical and quantum description of matter e.g. in the large-scale classical description of molecules bound together by chemical bonds. The understanding of decoherence has huge impact on the general understanding of quantum mechanics [22, 129, 130].

Decoherence is an irreversible phenomenon and is in many cases closely related to thermodynamic irreversibility, i.e. the dissipation of energy and the generation of entropy. Consequently decoherence is not a generic part of elementary quantum mechanics based on the Schrödinger equation or its relativistic generalizations, which are all reversible at least in the sense of the CPT-theorem. This dilemma is easily solved in large systems with a thermodynamic number of degrees of freedom: Such a system has a high number of levels and from a general initial state its wave function will follow a complex beating of oscillations whose frequencies are set by all possible transition frequencies $\omega_{nm} = (E_n - E_m)/\hbar$ between all combinations of levels n, m . It will return to its initial state after a time T which satisfies $T = 2p_{nm}\pi/\omega_{nm}$ with a set of integers p_{nm} . This time is called Poincaré time and has very large values in thermodynamic systems with (quasi)continuous spectra. Thus, the reversibility cannot be observed in any reasonable experiment. On the other hand, there are always pairs of ω_{nm} and $\omega_{m'n'}$ very close together, such that coherent phenomena between states n and m are completely masked by those of states m', n' and can also not be observed on short time scales. Moreover, observing a system with this precision in a well-defined way requires the repeated preparation of the same microscopic initial state, which is not possible for such a high number of degrees of freedom. In other words: Even though microscopic physics may be reversible and coherent, we are very often not able to observe it.

From the above discussion we can readily understand how coherence and reversibility vanish for large systems. Here, we are however mostly interested in small arrays of qubits, systems with very few (effective)

degrees of freedom, and want to understand how they lose their coherence. The type of model invoked is closely related to the above example: The system is extended by coupling the quantum system to an environment (bath) containing a number of macroscopic degrees of freedom, whose detailed initial state is unknown except for its thermodynamical variables. Then one solves the dynamics of the full setup containing the quantum system and the bath. The solution will depend on the initial state of the bath and by tracing out the average over the ensemble of initial states of the bath, the effective reduced dynamics of the system under the influence of the bath is found. Baths of this kind always occur in nature: Generally, one has to be aware of the fact that the experimental machinery and the control and manipulation instruments can serve as a bath; in fact, even the electromagnetic vacuum is a bath to which energy can be emitted [5]. It is in particular easy to identify physical baths in solids: All the “unused” degrees of freedom, typically the lattice and electronic excitations, act as sources of decoherence for the qubit degrees of freedom. Recalling the preceding discussion of superconducting qubits, we note that superconductors are good candidates for building coherent structures, because the ubiquitous natural baths in a solid-state environment are suppressed: lattice vibrations are frozen out and the electronic excitations are gapped.

Due to the necessity to introduce an environment, quantum systems suffering from decoherence are often called “open quantum systems”. There has been speculation in the literature [131], that under certain circumstances decoherence can occur without a bath, which has lately been strongly challenged [132].

The transition to classical physics manifests itself in at least three ways, which are related but not equivalent. These situations will now be illustrated invoking a system described by a two-state Hamiltonian of the form eq. (2.11).

Firstly, a system can be by all means coherent and sufficiently isolated from the environment, but the coherent phenomenon manifests itself on an unobservable scale. E.g., we would not be able to observe coherence fringes in the propagation of a ping-pong ball, because the de Broglie wave length of the ball at any reasonable velocity is too small to be observed (at $v = 1\text{m/s}$ it is on the order of 10^{-30}m). In eq. (2.11), this would occur if the off-diagonal matrix element is so small that one cannot keep $\epsilon = 0$ with sufficient precision and hence cannot prepare superpositions, or if $\epsilon \gg \Delta$ such that coherent oscillations are too fast to be observed and/or too small in amplitude. This can be attributed

to the fact that the quantum fluctuations leading to the coherent coupling of the classical states (here, the eigenstates of $\hat{\sigma}_z$ are too small. For tunneling systems such as the flux qubit, Δ is proportional to the overlap of the basis states in some double-well potential [114]. We can thus associate a small Δ with the fact that the basis states are too strongly separated for coherent tunneling. They are hence too distinct - very similar to the fact that the wave functions “alive” and “dead” of Schrödinger’s cat [16] do not have overlap. This type of vanishing quantum effects is usually not referred to as decoherence but as macroscopic distinction [18] and has also been termed “false decoherence” [17].

Secondly, if the system has an appropriate effective Hamiltonian with a sufficiently large off-diagonal matrix element it would be able to show all kinds of quantum coherent interference phenomena leading to fringes or temporal oscillations, such as the coherent oscillations of a two-state system which is initially *not* prepared in an eigenstate of the Hamiltonian eq. (2.11). Due to the influence of the environment these oscillations lose their phase and are suppressed. This can be understood in an ensemble-average: The system plus the bath propagate together and display a complex beating pattern. As the bath is prepared in somewhat different states in each member of the ensemble, this propagation looks differently for each realization and the quantum subsystem, from a unique initial state, accumulates more and more differences between one realization of the other, until ensemble-averaged quantum properties die out. This phenomenon is called “dephasing”. It does not necessarily involve the exchange of energy with the environment. On the other hand, at long times we expect the system to go into a thermal state described by a diagonal Boltzmann-type density matrix. This process involves energy exchange with the environment and is called relaxation. It takes place if there are no special selection rules and *does* necessarily also lead to dephasing. The thermal state can still involve superpositions of the basis states, if the Hamiltonian has off-diagonal terms. All in all this type of dynamics is called (“generic”) decoherence.

Thirdly even if the system Hamiltonian eq. (2.11) has substantial off-diagonal elements, coherent tunneling between the classical states can be blocked on all time scales by interaction with the environment. In fact, the system gets dressed by fast degrees of freedom in the environment, i.e. the system states $|\psi_n\rangle$ have to be replaced by combined states $|\psi_n\rangle_{\text{eff}} = |\psi_n\rangle \otimes |ENV_n\rangle$, where $|ENV_n\rangle$ are the lowest-energy states of the bath under the condition that the quantum system is in state $|\psi_n\rangle$. This type of dressing leads to a renormalization of the system Hamiltonian. E.g., in eq. 2.11, Δ gets renormalized to Δ_{eff} when one couples

a bath of oscillators to $\hat{\sigma}_z$ [133, 134]. Such renormalization effects are known throughout physics as Lamb shift, Franck-Condon effect etc. , all of which describe the introduction of an effective Hamiltonian whose matrix elements are different from the original ones due to the interaction with some environment. If the bath is infinite and has sufficient spectral weight at all frequencies, the system can undergo a dissipative phase transition which leads to $\Delta_{\text{eff}} = 0$, making the system completely classical and localized, similar to Anderson's orthogonality catastrophe [135] in Fermionic systems. In fact, the dynamics described in the previous paragraph is always governed by H_{eff} . In particular, there are no superpositions of classical states left in a thermal mixture. Another way to interpret this is, that the system builds up entanglement with the environment, i.e. any superposition of different $|\psi_n\rangle_{\text{eff}}, |\psi_m\rangle_{\text{eff}}$ is entangled. If the entanglement is complete, such that the $|ENV_n\rangle$ are mutually orthogonal, the system cannot tunnel any more between the classical states ${}_{\text{eff}}\langle\psi_n|\psi_{m\neq n}\rangle_{\text{eff}} \rightarrow 0$. This is analogous to the first scenario: There the system states themselves are macroscopically distinct, here only the environment plus environment states are.

So far we have given a number of examples for baths which are physically quite different, but have not detailed how to model them. It turns out that many baths can be modelled using a few general models: In the thermodynamic limit at equilibrium, many systems are *Gaussian*, i.e. the distribution of values for collective variables X is of Gaussian form and can be fully described by the two-time correlation function $\langle X(t)X(0)\rangle$. All higher cumulants are zero. Such Gaussian models can be universally described as a bath of harmonic oscillators, and collective variables can be written as a linear combination of the oscillator coordinates [108, 133, 136]. In order to determine the appropriate couplings and distribution of the oscillators one introduces a spectral density $J(\omega)$ of the oscillators which is determined from the specific properties of the model under consideration. This matching to the physical model is usually done by comparing either the classical friction induced by the environment, or the noise correlation function, and will be detailed in chapter 3.2. Then the model of system plus bath with the appropriate $J(\omega)$ can be solved quantum-mechanically as described above. Oscillator bath models work well e.g. for phonon and photon baths such as electromagnetic noise.

Not all environments can be described this way. A prominent counterexample are localized modes with a bounded spectrum such as spins [137] and structural fluctuations generating classical telegraph noise [138, 139], which are inherently non-Gaussian. One expects from the

central limit theorem, that large ensembles of such fluctuators usually behave Gaussian again [140, 141], but details of this transition are only partially understood at present [139, 142].

The discussion in the previous section already indicates the importance of studying noise for understanding decoherence [143, 144]. In fact, parts of our results on decoherence can be understood from noise theory alone without a detour via an environmental Hamiltonian. This can be illustrated by the two-state system described by (2.11), where ϵ is noisy, $\epsilon = \epsilon_0 + \delta\epsilon(t)$. We can readily solve the associated Schrödinger equation. Even more intuitively we can describe the state of the system by the expectation values of the three components of the spin, and the Schrödinger equation becomes the classical equation of motion of magnetic moment in a fluctuating magnetic field. For each realization of the noise, the system behaves coherently, but the coherent evolution has a noisy component. Averaging over the noise then leads to incoherent evolution. Specifically, two key results can be derived on that level, assuming that $\delta\epsilon$ can be treated perturbatively [141, 145]: The relaxation rate is proportional to the noise spectral density S at a frequency corresponding to the level splitting $E = \sqrt{\epsilon^2 + \Delta^2}$

$$\Gamma_r = \frac{\Delta^2}{E^2} S(E). \quad (2.12)$$

Flip-less decoherence contains a zero energy exchange (zero frequency) contribution as well [46, 146, 147]

$$\Gamma_\phi = \Gamma_r/2 + \frac{\epsilon^2}{E^2} S(0). \quad (2.13)$$

Such methods for describing decoherence by averaging over semiclassical noise will generally fail whenever entanglement between system and bath is generated. This happens at large time scales, but also at stronger coupling beyond perturbation theory. This failure is due to the effect that under these conditions the system also has a pronounced influence on the bath, which changes the bath dynamics and from there acts back on the system. This is not captured if the noise is usually calculated for an a priori given (thermal) bath state as in the naive approach.

The more conventional methods for describing decoherence rely on studying the reduced density matrix of the quantum system. This density matrix is obtained from the full density matrix of system and environment by tracing out the environment as described above. The

reduced density matrix describes an ensemble of systems, i.e. the results obtained from it can be compared to results averaged over huge collections of quantum systems or a repeated experiment with identical initial conditions of the quantum system at each attempt (time-ensemble). The behavior of a *single* realization is *not* predicted, similar to the statistical description of quantum measurements [25], see above. In most cases the dynamics of the reduced density matrix can be described by a generalized master-equation with memory, i.e. by a linear integro-differential equation containing all the evolution in the past, which falls back onto the Liouville equation if the coupling to the bath is taken away [136, 148–150]. Even the path-integral descriptions for open quantum systems developed in the 80s have recently been cast in a master-equation form [136]. Master equations which are local in time are called *Markovian* [151–155]. Many approaches have been formulated within the Born approximation, which only contains the coupling to the bath in lowest, quadratic, order [156]. The simplest example for such a master equation is the Bloch equation from NMR [146, 157], which introduces longitudinal relaxation rates (relaxation of the spin component parallel to the magnetic field, corresponding to energy relaxation) and transversal rates corresponding to dephasing. These equations have first been phenomenologically introduced in the picture of classical spins without having decoherence in mind. They have been further developed in NMR and can be microscopically [146, 158] derived under suitable Markovian assumptions.

With very few exceptions, mainly such master equation methods are used in the papers compiled in this report. The technical aspects are highlighted in the papers.

There are other methods to describe open quantum systems, many of which are essentially numerical: The quantum jump or trajectory method [159, 160] and the Bayesian formalism [161] rely on additional assumptions and have the advantage that they stay within a wave function representation, which is advantageous for huge systems. Various renormalization group approaches [162–164] on the other hand are very precise and include the regime of large coupling, however, up to now they have difficulties in treating nonequilibrium or driven situations.

2.8 Quantum dot quantum bits

As already stated above superconducting systems are not the only candidates for solid-state quantum bits. Specifically quantum bits in semiconductor quantum dots are an active field of study [29, 71, 72, 74, 75, 165–167].

The fabrication of a lateral quantum dot starts from a two dimensional electron gas (2DEG) obtained in a band structure-engineered GaAs/AlGaAs multilayer heterostructure [27]. Such heterostructures have already been fabricated in the 80s and have been used e.g. in the discovery have been the quantum Hall effects [168]. Due to strong doping there are mobile conduction electrons even at low temperatures just as in a metal, however, the concentration is much lower. The motion perpendicular to the 2DEG is strongly confined by the engineered multilayer, such that the motion in that direction becomes quantized similar to a particle in a box, and at low temperatures only the lowest state in that direction is occupied.

To form a lateral quantum dot in the 2DEG, metallic gates are fabricated on top which are galvanically isolated from the 2DEG. By applying a high negative voltage the Coulomb repulsion depletes the 2DEG under the gate electrodes (Schottky effect). A potential landscape can be shaped this way that confines the electron motion inside the 2DEG. In particular one can define a small puddle of electrons which are connected to the remainder of the 2DEG only by quantum point contacts. Such a puddle is called a quantum dot. By making the dots small enough, on the order of hundreds of nanometers, and strongly depleting the 2DEG the dots develop a discrete energy level structure, i.e. they act as zero-dimensional quantum systems (artificial atoms) [169, 170]. N.b. that in real metals this only happens at much smaller dimensions [171], because there the Fermi wavelength is much smaller due to the high carrier density. Moreover in small quantum dots the Coulomb repulsion becomes significant and it costs lots of charging energy of the form eq. 2.9 to add another electron to the dot (Coulomb blockade). This makes quantum dots stable, controlled and tunable artificial atoms [169]. Figure 2.4 show a typical micrograph of a double quantum dot.

Many of the basic predictions for such Coulomb blockade physics, such as the the level structure, atomic and molecular states in multi-dot setups, spin and spin-orbit effects, and the Kondo effect, have been

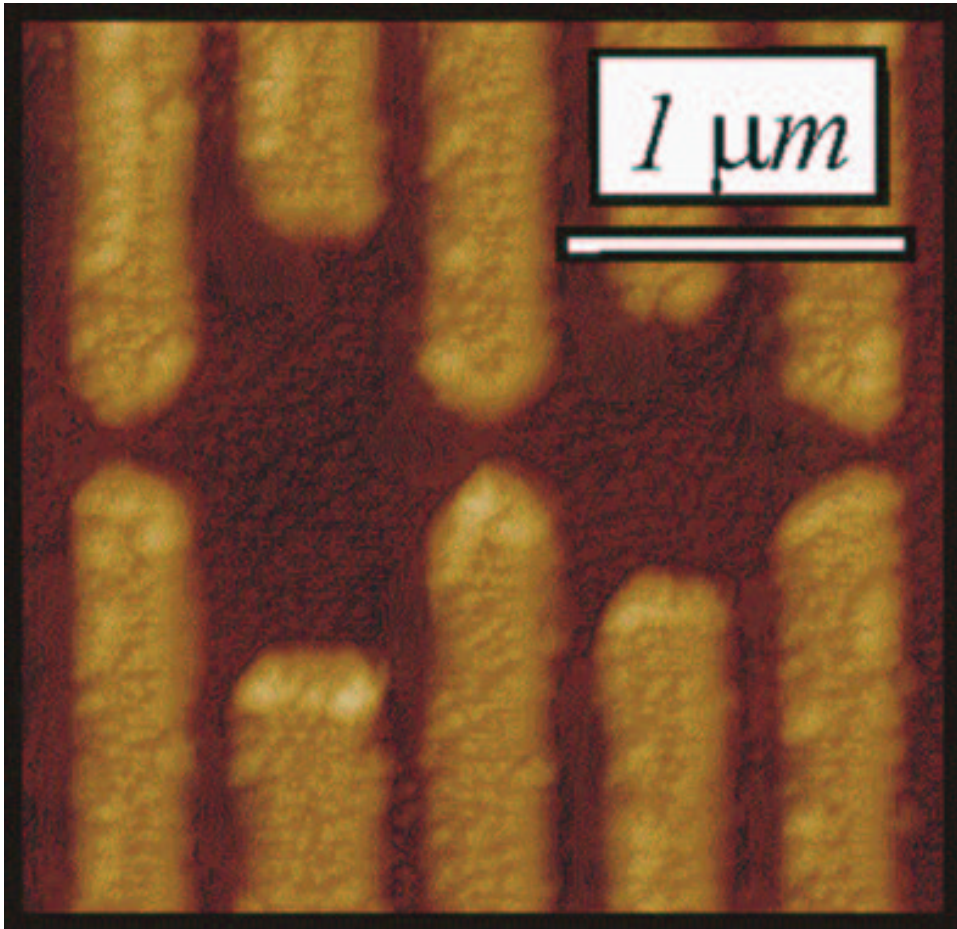


Figure 2.4: Micrograph of a double quantum dot system. The bright fingers are the electrostatic gates on top of the 2DEG, the dots are defined in the two disks. Picture taken by A.W. Holleitner

demonstrated experimentally in quantum dots. Some of these phenomena have counterparts in atomic physics [40, 166, 170, 172, 173].

This similarity to atoms makes quantum dots a natural candidate for solid-state qubits: The dot states offer various options for forming a two-state system. The states on the dot are isolated from the other conduction electrons by point contacts. The coupling to the lattice is, however, a serious problem, unlike in the case of superconductors. The phonon physics of GaAs, a piezoelectric material, in the heterostructure defining the 2DEG is less favorable — even at low temperatures, there is a substantial phase space for phonon emission [174]. This can potentially be overcome by fabricating dots on free-standing substrates which act as a phonon cavity [175, 176].

One natural approach to build a qubit is to use different charge states on a double quantum dot, such that the qubit states are defined through the position of a single mobile electron [165, 167, 177]. Such qubits can be coupled electrostatically and read out by single electron transistors or quantum point contacts. Due to the many gate controls of the dot charge states can be easily and quickly manipulated by pulses in the microwave range, they can be coupled using capacitors, and they can be read-out using single-electron electrometers [178] or quantum point contacts [72, 179]. However, their coherence is limited by phonons as described above, thus one has to operate on very short time scales.

Another option is to use spin states [71, 74, 75]. The spin in GaAs has long intrinsic coherence times [180, 181]. However although many generic spin effects have been observed it is still a major challenge to couple well to the spin, manipulate it coherently and read it out. Many of the promising proposals use the relation of position and spin e.g. through exchange interaction [70, 74]. It is consequently also important for spin qubits to understand the properties and the stability of charge states.

Next to this interest for quantum computing applications quantum dots also complement the knowledge of decoherence gained in superconducting qubits. Due to their electrostatic definition there is more freedom to change the Hamiltonian *in situ*. Moreover one can study nonequilibrium (and non-Gaussian) decoherence by studying the coupling to electronic leads and voltage-biased point-contact detectors.

2.9 Nonequilibrium superconductivity in mesoscopic systems

Similar to the work on quantum dots, section 2.8, this section on mesoscopic superconductivity mostly serves as an extension and complement of the main text on superconducting qubits.

So far, we have adopted a very simplistic view of the microscopic physics of Josephson junctions: Cooper pairs propagate through a weak link without losing coherence [88,91,92]. Indeed, Josephson *tunnel* junctions as they are mostly used in quantum computing usually do not show additional features—the physics is analogous to tunneling through a high potential barrier. There are, however, other types of weak links which have a rich internal structure, namely links with a conducting connector. These links are much longer than the few Ångstrom of the oxide layer of tunnel junctions, however, they are still shorter than the phase coherence length. The length makes direct tunneling across the structure almost impossible, so the Cooper pairs must make use of the finite conductance of the barrier [182,183]. Indeed, one can show that the collective wave function of the superconductor leaks into the normal metal and generates superconducting correlations there, which can support a (Josephson) supercurrent [184]. This is known as *proximity effect*. The microscopic mechanism leading to this effect is known as *Andreev reflection* [185]: Due to the energy gap in the superconductor, electrons from the normal metal cannot directly enter the superconductor. Nevertheless two electrons can enter the superconductor in a correlated way and form a Cooper pair. This means that an incoming electron above the Fermi edge is retroreflected into a hole. Due to momentum and energy conservation, the component of the momentum parallel to the interface is conserved whereas the perpendicular component is slightly different. Note that this is *retro* and not *mirror* reflection. This process is illustrated in Fig. 2.5 a). Thus the hole tends to trace back the path of the electron with a slightly different wave number. Electron and hole acquire a precisely defined phase relation at the interface due to the coupling to the Cooper pair condensate, see Fig. 2.5 b). If the conductor is bounded by two superconductors as it is the case in a weak link, the hole can Andreev-reflect at the other side into an electron and both can form a bound state. This bound state spectrum depends on the difference of the phases of the order parameters and carries the supercurrent.

Most of the metallic samples of this kind which can be studied exper-

imentally, contain lots of static disorder. Hence the paths forming the bound states are very complicated. They can be treated in an impurity-averaged way and lead to a gapped but otherwise smooth density of current-carrying states. This density has to be convoluted with the electron distribution function for predicting the macroscopic supercurrent. The options to artificially manufacture such structures, together with the possibility to control the distribution function through external leads and create far-from-equilibrium situations consequently make these setups powerful test-beds for studying the microscopic details of the supercurrent transport and nonequilibrium superconductivity.

One of the early striking features of this supercurrent has already been predicted and observed a while ago [186–188] namely the option to switch the junction into a state with a *negative* critical current, a so-called π -state, by an external voltage. In this report, section 3.8, a number of extensions of this idea is compiled, including a broad introduction to the basic physics.

π -junctions can be an interesting building block for superconducting electronics, both classical and quantum. Basic features of such applications have already been demonstrated, however, noise and high-frequency properties important for technology still need to be explored.

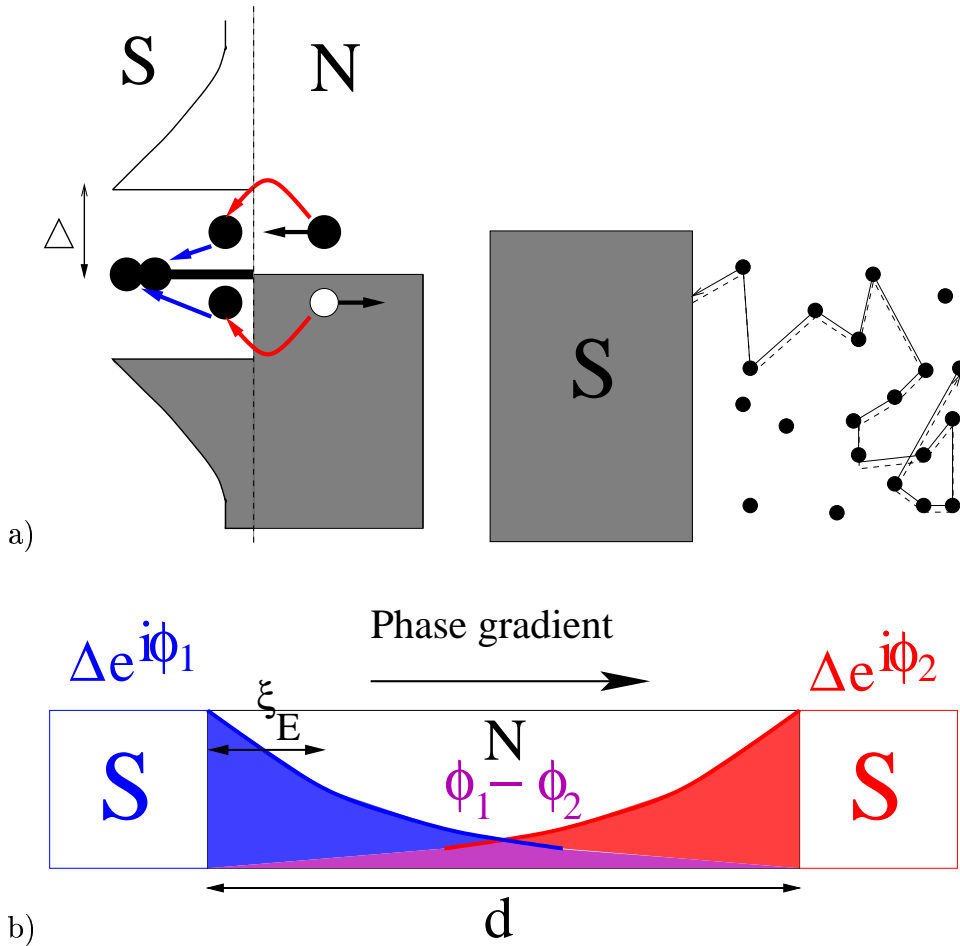


Figure 2.5: a) schematics of the Andreev reflection process. The left panel shows the density of states in a superconductor and a normal metal and indicates the energetics of the electron-hole conversion. The right panel shows the semiclassical paths of an incoming electron (solid line) and retro-reflected hole (dashed), which are nearly retro-reflected at the interface and are scattered off impurities. b) Density of superconducting correlations in an SNS-junction.

Bibliography

- [1] F. Hund. *Geschichte der Quantentheorie*. Bibliographisches Institut, Mannheim, 1967.
- [2] A. Einstein, B. Podolsky, and N. Rosen. Can quantum-mechanical description of physical reality be considered complete? *Phys. Rev.*, 41:777, 1935.
- [3] D. Bohm. *Quantum Theory*. Dover, N.Y., 1957.
- [4] H. Everett III. *The universal wavefunction*. PhD thesis, Princeton University, 1957.
- [5] C. Cohen-Tannoudji, J. Dupont-Roc, and G. Grynberg. *Atom-Photon Interactions*. Wiley Interscience, 1998.
- [6] D.F. Walls and G.J. Milburn. *Quantum Optics*. Springer, Berlin, 1994.
- [7] A.J. Leggett. Bose-einstein condensation in the alkali gases; some fundamental concepts. *Rev. Mod. Phys.*, 73:307, 2001.
- [8] A. Czarnecki and W.J. Marciano. The muon anomalous magnetic moment: A harbinger for "new physics". *Phys. Rev. D*, 64:013014, 2001.
- [9] R. Ahmad et al. The SNO Collaboration. Measurement of day and night neutrino energy spectra at SNO and constraints on neutrino mixing parameters. *Phys. Rev. Lett.*, 89:011302, 2002.
- [10] I.I. Bigi and A.I. Sanada. Notes on the observability of CP violations in B decays. *Nucl. Phys. B*, 193:85, 1981.
- [11] The Babar Collaboration: B. Aubert et al. Observation of CP violation in the B0 meson system. *Phys. Rev. Lett.*, 2001.
- [12] C. Kittel. *Quantum Theory of Solids*. Wiley, 1987.

- [13] P.Y. Yu and M. Cardona. *Fundamentals of Semiconductors*. Springer, Heidelberg, 2001.
- [14] M. Tinkham. *Introduction to Superconductivity*. McGraw-Hill, 1996.
- [15] A.J. Leggett. Macroscopic quantum systems and the quantum theory of measurement. *Progr. Theor. Phys.*, Suppl. 69:80, 1980.
- [16] E. Schrödinger. Die gegenwärtige Situation in der Quantenmechanik. *Naturwissenschaften*, 23:807, 823, 844, 1935.
- [17] A.J. Leggett. Testing the limits of quantum mechanics: Motivation, state of play, and prospects. *J. Phys. C*, 14:415, 2002.
- [18] W. Dür, C. Simon, and J.I. Cirac. On the effective size of certain macroscopic quantum superpositions. *Phys. Rev. Lett.*, 89:210402, 2002.
- [19] J. von Neumann. *Mathematical Foundations of Quantum Mechanics*. Princeton University Press, 1955.
- [20] W.H. Zurek. Pointer basis of quantum apparatus: Into what mixture does the wave packet collapse? *Phys. Rev. D*, 24:1516, 1981.
- [21] W.H. Zurek. Preferred states, predictability, classicality and the environment-induced decoherence. *Prog. Theor. Phys.*, 89:281, 1993.
- [22] A. Peres. *Quantum Theory: Concept and Methods*. Kluwer, Dordrecht, 1993.
- [23] P.W. Anderson. Science: A 'dappled world' or a 'seamless web'. *Studies in history and philosophy of modern physics*, 32:487, 2001.
- [24] P.W. Anderson. Reply to Cartwright. *Studies in history and philosophy of modern physics*, 32:499, 2001.
- [25] S.L. Adler. Why decoherence has not solved the measurement problem. *Studies in history and philosophy of modern physics*, 34:135, 2003.
- [26] N.W. Ashcroft and N.D. Mermin. *Solid state physics*. Holt-Saunders, 1976.
- [27] G. Bastard. *Wave mechanics applied to semiconductor heterostructures*. Edition de Physique, 1988.

- [28] Y. Imry. *Introduction to Mesoscopic Physics*. Oxford University Press, 1997.
- [29] L.P. Kouwenhoven, G. Schön, and L. Sohn, editors. *Mesoscopic electron transport*. Number E345 in Proceedings of the NATO Advanced Study Institute. Kluwer, Dordrecht, 1997.
- [30] J.R. Friedman, V. Patel, W. Chen, S.K. Tolpygo, and J.E. Lukens. Quantum superposition of distinct macroscopic states. *Nature*, 46:43, 2000.
- [31] A. Bachtold, P. Hadley, T. Nakanishi, and C. Dekker;. Carbon nanotube transistors. *Science*, 294:1317, 2001.
- [32] P.A. Lee and T.V. Ramakrishnan. Disordered electronic systems. *Rev. Mod. Phys.*, 57:287, 1985.
- [33] R.A. Webb, S. Washburn, C.P. Umbach, and R.B. Laibowitz. Observation of h/e Aharonov-Bohm oscillations in normal-metal rings. *Phys. Rev. Lett.*, 54:2696, 1985.
- [34] L.P. Levy, G. Dolan, J. Dunsmuir, and H. Bouchiat. Magnetization of mesoscopic copper rings: Evidence for persistent currents. *Phys. Rev. Lett.*, 64:2074, 1990.
- [35] A.D. Stone. Magnetoresistance fluctuations in mesoscopic wires and rings. *Phys. Rev. Lett.*, 54:2692, 1985.
- [36] H. Grabert and M.H. Devoret, editors. *Single Charge Tunneling*. Number B294 in NATO ASI Series. Plenum, New York, 1992.
- [37] W. Belzig, F.K. Wilhelm, G. Schön, C. Bruder, and A.D. Zaikin. Quasiclassical Green's function approach to mesoscopic superconductivity. *Superlattices and Microstructures*, 25:1251, 1999.
- [38] V.J. Emery. *Highly conducting one-dimensional solids*. Plenum, New York, 1979.
- [39] J. Voit. One-dimensional Fermi liquids. *Rep. Prog. Phys.*, 58:977, 1995.
- [40] L.P. Kouwenhoven and L.I. Glazman. Revival of the Kondo effect. *Physics World*, 14:33, 2001.
- [41] A.J. Leggett and A. Garg. Quantum mechanics versus macroscopic realism - is the flux there when nobody looks? *Phys. Rev. Lett.*, 54:857, 1985.

- [42] C.D. Tesche. Can a noninvasive measurement of magnetic flux be performed with superconducting circuits? *Phys. Rev. Lett.*, 64:2358, 1990.
- [43] K.K. Likharev. Really quantum-macroscopic effects in weak superconductivity. *Usp. Fiz. Nauk.*, 139:169, 1983.
- [44] P.W. Anderson. Special effects in superconductivity. In E.R. Caianiello, editor, *Lectures on the Many-Body Problem*, page 113. Academic Press, New York, 1964.
- [45] V. Bouchiat, D. Vion et P. Joyez, D. Esteve, and M.H. Devoret. Quantum coherence with a single Cooper pair. *Physica Scripta*, T76:165, 1998.
- [46] Yu. Makhlin, G. Schön, and A. Shnirman. Quantum-state engineering with Josephson-junction devices. *Rev. Mod. Phys.*, 73:357, 2001.
- [47] G.E. Moore. Cramming more components into integrated circuits. *Electronics*, 38:114, 1965.
- [48] G.E. Moore. No exponential is forever. Keynote Presentation International Solid State Circuits Conference, 2003.
- [49] Intel Co. Expanding Moore's law. Available at ftp://download.intel.com/labs/eml/download/EML_opportunity.pdf, 2002.
- [50] M.A. Nielsen and I.L. Chuang. *Quantum Computation and Quantum Information*. Cambridge University Press, 2000.
- [51] J. Preskill. Quantum computation lecture notes. Available at <http://www.theory.caltech.edu/people/preskill/ph219/>.
- [52] L.K. Grover. Quantum mechanics helps in searching for a needle in a haystack. *Proceedings of the 28'th Annual ACM Symposium on the Theory of Computing*, 79:325, 1997.
- [53] P. Shor. Algorithms for quantum computation: Discrete logarithms and factoring. *Proceedings 35th Annual Symposium on Foundations of Computer Science*, page 124, 1994.
- [54] H. Delfs and H. Knebl. *Introduction to Cryptography*. Springer Heidelberg, 2002.
- [55] D.P. DiVincenzo. Quantum computation. *Science*, 270:255, 1995.

- [56] D.P. DiVincenzo. The physical implementation of quantum computation. *Fortschr. Phys.*, 48:771, 2000.
- [57] R. Hughes, the ARDA Quantum Information Science, and Technology Panel. A quantum information science and technology roadmap. available at <http://qist.lanl.gov>.
- [58] L.M.K. Vandersypen, Matthias Steffen, Gregory Breyta, Costantino S. Yannoni, Mark H. Sherwood, and Isaac L. Chuang. Experimental realization of Shor's quantum factoring algorithm using nuclear magnetic resonance. *Nature*, 414:883, 2001.
- [59] *Workshop Theory in Quantum Computing (THINQC)*, 2003.
- [60] N.A. Gershenfeld and I.L. Chuang. Bulk spin-resonance quantum computing. *Science*, 275:350, 1997.
- [61] C. Monroe, D.M. Meekhof, B.E. King, W.M. Itano, and D.J. Wineland. Demonstration of a fundamental quantum logic gate. *Phys. Rev. Lett.*, 75:4714, 1995.
- [62] J.I. Cirac and P. Zoller. Quantum computations with cold trapped ions. *Phys. Rev. Lett.*, 74:4091, 1995.
- [63] Q.A. Turchette, C.J. Hood, W. Lange, H. Mabuchi, and H.J. Kimble. Measurement of conditional phase shifts for quantum logic. *Phys. Rev. Lett.*, 75:4710, 1995.
- [64] T. Pellizzari, S.A. Gardiner, J.I. Cirac, and P. Zoller. Decoherence, continuous observation, and quantum computing: A cavity QED model. *Phys. Rev. Lett.*, 75:3788, 1995.
- [65] E. Knill, R. Laflamme, and G.J. Milburn. A scheme for efficient quantum computing with linear optics. *Nature*, 409:46, 2001.
- [66] H.-J. Briegel, T. Calarco, D. Jaksch, J. I. Cirac, and P. Zoller. Quantum computing with neutral atoms. *Journal of modern optics*, 47:415, 2000.
- [67] D. Kielpinski, C. Monroe, and D. J. Wineland. Architecture for a large-scale ion-trap quantum computer. *Nature*, 417:709, 2002.
- [68] S.M. Sze. *Semiconductor devices, physics and technology*. Wiley-VCH, 2001.

- [69] Scott Thompson, Mohsen Alavi, Makarem Hussein, Pauline Jacob, Chris Kenyon, Peter Moon, Matthew Prince, Sam Sivakumar, Sunit Tyagi, and Mark Bohr. 130nm logic technology featuring 60nm transistors, low-k dielectrics, and Cu interconnects. *Intel Technology Journal*, 6, 2002.
- [70] B.E. Kane. A silicon-based nuclear spin quantum computer. *Nature*, 393:133, 1998.
- [71] D. Loss and D.P. DiVincenzo. Quantum computation with quantum dots. *Phys. Rev. A*, 57:120, 1998.
- [72] J.M. Elzerman, R. Hanson, J.S. Greidanus, L.H. Willems van Beveren, S. De Franceschi, L.M.K. Vandersypen, S. Tarucha, and L. P. Kouwenhoven. Few-electron quantum dot circuit with integrated charge read-out. *Phys. Rev. B*, 67:161308, 2003.
- [73] R.G. Clark, P.C. Hammel, A.S. Dzurak, A.R. Hamilton, L.C.L. Hollenberg, D.N. Jamieson, and C.I. Pakes. Toward a silicon-based nuclear-spin quantum computer. *Los Alamos Science*, 27:284, 2002.
- [74] L.M.K. Vandersypen, R. Hanson, L.H. Willems van Beveren, J.M. Elzerman, J.S. Greidanus, S. De Franceschi, and L.P. Kouwenhoven. *Quantum Computing and Quantum Bits in Mesoscopic Systems*, chapter 22. Kluwer, 2002.
- [75] G. Burkhard, H.A. Engel, and D. Loss. Spintronics and quantum dots for quantum computing and quantum communication. *Fortschr. Physik*, 48:965, 2000.
- [76] H. Kammerlingh Onnes. The superconductivity of mercury. *Leiden Comm.*, 122b:124, 1911.
- [77] J. Nagamatsu, N. Nakagawa, T. Muranaka, Y. Zenitani, and J. Akimitsu. Superconductivity of MgB_2 at 39K. *Nature*, 410:63, 2001.
- [78] J.G. Bednorz and K.A. Müller. Possible high T superconductivity in the Ba-La-Cu-O system. *Z. Phys. B*, 64:189, 1986.
- [79] P.G. de Gennes. *Superconductivity of metals and alloys*. Benjamin, N.Y., 1966.
- [80] J.R. Schrieffer. *Theory of Superconductivity*. Cummings, N.Y., 1988.

- [81] F. London. *Superfluids*. Wiley and Sons, N.Y., 1954.
- [82] V.L. Ginzburg and L.D. Landau. On the theory of superconductivity. *Zh. Eksp. Teor. Fiz.*, 20:1064, 1950.
- [83] J. Bardeen, L.N. Cooper, and J.R. Schrieffer. Theory of superconductivity. *Phys. Rev.*, 108:1175, 1957.
- [84] R. Doll and M. Näbauer. Experimental proof of magnetic flux quantization in a superconducting ring. *Phys. Rev. Lett.*, 7:51, 1961.
- [85] D.J. van Harlingen. Phase-sensitive tests of the symmetry of the pairing state in the high temperature superconductors — evidence for dx²-y² symmetry. *Rev. Mod. Phys.*, 67:515, 1995.
- [86] Y. Maeno, H. Hashimoto, K. Yoshida, S. Nishizaki, T. Fuijta, J.G. Bednorz, and F. Lichtenberg. Superconductivity in a layered perovskite without copper. *Nature*, 372:532, 1994.
- [87] L. Tian, L. Levitov, C.H. van der Wal, J.E. Mooij, T.P. Orlando, C.J.P.M. Harmans S. Lloyd, and J. J. Mazo. *Quantum Mesoscopic Phenomena and Mesoscopic Devices in Microelectronics*, chapter Decoherence of the superconducting persistent current qubit. Kluwer, 2000. edited by I. O. Kulik and R. Ellialogulu.
- [88] B.D. Josephson. Possible new effects in superconductive tunnelling. *Phys. Lett.*, 1:251, 1962.
- [89] A. Barone and G. Paterno. *Physics and applications of the Josephson effect*. Wiley, N.Y., 1982.
- [90] K.K. Likharev. *Dynamics of Josephson junctions and circuits*. Gordon and Breach, 1986.
- [91] R.P. Feynman. *Lectures in Physics*, volume 3. Addison Wesley, 1970.
- [92] L.D. Landau and E.M. Lifshitz. *Statistical Physics 2*. Akademie-Verlag, 1979.
- [93] S.V. Pereverzev, A. Loshak, S. Backhaus, J.C. Davis, and R.E. Packard. Quantum oscillations between two weakly coupled reservoirs of superfluid ³He. *Nature*, 388:449, 1997.
- [94] K. Sukhatme, Y. Mukharsky, T. Chui, and D. Pearson. Observation of the ideal Josephson effect in superfluid ⁴He. *Nature*, 411(280), 2001.

- [95] B. P. Anderson and M. A. Kasevich. Macroscopic quantum interference from atomic tunnel arrays. *Science*, 282:1686, 1998.
- [96] P. Hadley. private communication.
- [97] K.A. Delin and A.W. Kleinsasser. Stationary properties of high-critical-temperature proximity effect Josephson junctions. *Supercond. Sci. Technol.*, 9:227, 1996.
- [98] T.P. Orlando and K. Delin. *Foundations of applied superconductivity*. Prentice Hall, 1991.
- [99] T. van Duzer and C.W. Turner. *Principles of superconductive devices and circuits*. Elsevier, 1999.
- [100] V. Ambegaokar, U. Eckern, and G. Schön. Quantum dynamics of tunneling between superconductors. *Phys. Rev. Lett.*, 1982.
- [101] J. Clarke. *Applications of Superconductivity*, chapter Low- and High-Tc SQUIDS and Some Applications, page 1. Kluwer, 2000. edited by H. Weinstock.
- [102] J. Niemeyer. Josephson arrays for DC and AC metrology. *Supercond. Sci. and Technology*, 13:546, 2000.
- [103] A.D. Zaikin and G. Schön. Quantum coherent effects, phase transitions and the dissipative dynamics of ultra small tunnel junctions. *Phys. Rep.*, 198(237), 1990.
- [104] H.S.J. van der Zant and R. Fazio. Quantum phase transitions and vortex dynamics in superconducting networks. *Phys. Rep.*, 355:236, 2001.
- [105] R.P. Feynman and F.L. Vernon. The theory of a general quantum system interacting with a linear dissipative system. *Ann. Phys. (N.Y.)*, 24:118, 1963.
- [106] G.L. Ingold. *Quantum transport and dissipation*, chapter Dissipative quantum systems. Wiley-VCH, 1998.
- [107] L.D. Landau and E.M. Lifshitz. *Klassische Mechanik*, volume 1 of *Lehrbuch der theoretischen Physik*. Akademie Verlag, 1976.
- [108] A.O. Caldeira and A.J. Leggett. Influence of dissipation on quantum tunneling in macroscopic systems. *Phys. Rev. Lett.*, 46:211, 1981.

- [109] A.O. Caldeira and A.J. Leggett. Quantum tunneling in a dissipative system. *Ann. Phys. (NY)*, 149:374, 1983.
- [110] J.M. Martinis, S.W. Nam, J. Aumentado, and C. Urbina. Rabi oscillations in a large Josephson junction qubit. *Phys. Rev. Lett.*, 89:117907, 2002.
- [111] Y. Yu, S. Han, X. Chu, S-I. Chu, and Z/ Wang. Coherent temporal oscillations of macroscopic quantum states in a Josephson junction. *Science*, 286:889, 2002.
- [112] A.J. Berkley, H. Xu, R.C. Ramos, M.A. Gubrud, F.W. Strauch, P.R. Johnson, J.R. Anderson, A.J. Dragt, C.J. Lobb, and F.C. Wellstood. Entangled macroscopic quantum states in two superconducting qubits. *Science*, 300:1548, 2003.
- [113] J.E. Mooij, T.P. Orlando, L. Levitov, L. Tian, C.H. van der Wal, and S. Lloyd. Josephson persistent current qubit. *Science*, 285:1036, 1999.
- [114] T. P. Orlando, J. E. Mooij, L. Tian, C.H. van der Wal, L. S. Levitov, S. Lloyd, and J. J. Mazo. Superconducting persistent-current qubit. *Phys. Rev. B*, 60:15398, 1999.
- [115] I. Chiorescu, Y. Nakamura, C.J.P.M. Harmans, and J.E. Mooij. Coherent quantum dynamics of a superconducting flux qubit. *Science*, 299:1869, 2003.
- [116] E. Il'ichev, N. Oukhanski, A. Izmalkov, Th. Wagner, M. Grajcar, H.-G. Meyer, A.Yu. Smirnov, Alec Maassen van den Brink, M.H.S. Amin, and A.M. Zagoskin. Continuous observation of Rabi oscillations in a Josephson flux qubit. *Phys. Rev. Lett.*, 91:097906, 2003.
- [117] Y. Nakamura, Y.A. Pashkin, and J.S. Tsai. Coherent control of macroscopic quantum states in a single-Cooper-pair box. *Nature*, 398:786, 1999.
- [118] Y. Nakamura, Yu. A. Pashkin, T. Yamamoto, and J. S. Tsai. Charge echo in a Cooper-pair box. *Phys. Rev. Lett.*, 88:047901, 2002.
- [119] Y.A. Pashkin, T. Yamamoto, O. Astafiev, Y. Nakamura, D.V. Averin, and J.S. Tsai. Quantum oscillations in two coupled charge qubits. *Nature*, 421:823, 2003.

- [120] K.W. Lehnert, K. Bladh, L.F. Spietz, D. Gunnarsson, D.I. Schuster, P. Delsing, and R.J. Schoelkopf. Measurement of the excited-state lifetime of a microelectronic circuit. *Phys. Rev. Lett.*, 90:027002, 2003.
- [121] D. Vion, A. Aassime, A. Cottet, P. Joyez, H. Pothier, C. Urbina, D. Esteve, and M.H. Devoret. Manipulating the quantum state of an electrical circuit. *Science*, 296:286, 2002.
- [122] L. B. Ioffe, V. B. Geshkenbein, M. V. Feigel'man, A. L. Fauchere, and G. Blatter. Environmentally decoupled sds-wave Josephson junctions for quantum computing. *Nature*, 398:679, 1999.
- [123] A. Blais and A.M. Zagoskin. Operation of universal gates in a solid-state quantum computer based on clean Josephson junctions between d-wave superconductors. *Phys. Rev. A*, 61:042308, 2000.
- [124] L. B. Ioffe, M. V. Feigel'man, A. Ioselevich, D. Ivanov, M. Troyer, and G. Blatter. Topologically protected quantum bits using Josephson junction arrays. *Nature*, 398:678, 2002.
- [125] C.H. van der Wal, A.C.J. ter Haar, F.K. Wilhelm, R.N. Schouten, C.J.P.M.Harmans, T.P. Orlando, S. Lloyd, and J.E.Mooij. Quantum superposition of macroscopic persistent-current states. *Science*, 290:773, 2000.
- [126] J.B. Majer, F.G. Paauw, A.C.J. ter Haar, C.J.P.M. Harmans, and J.E. Mooij. Spectroscopy of coupled flux qubits. [cond-mat/0308192](https://arxiv.org/abs/cond-mat/0308192).
- [127] H. Tanaka, Y. Sekine, S. Saito, and H. Takayanagi. DC-SQUID readout for qubit. *Physica C*, 368:300, 2002.
- [128] E. Hecht. *Optics*. Addison-Wesley, Reading, Mass., 1987.
- [129] D. Giulini, E. Joos, C. Kiefer, J. Kupsch, I.-O. Stamatescu, and H. D. Zeh. *Decoherence and the Appearance of a Classical World in Quantum Theory*. Springer, 1996.
- [130] W.G. Unruh. Quantum coherence, wormholes, and the cosmological constant. *Phys. Rev. D*, 40:1053, 1989.
- [131] G. Ford, J. Lewis, and R. O'Connell. Quantum measurement and decoherence. *Phys. Rev. A*, 64:032101, 2001.
- [132] D. Gobert, J. von Delft, and V. Ambegaokar. Decoherence without dissipation? [quant-ph/0306019](https://arxiv.org/abs/quant-ph/0306019).

- [133] A.J. Leggett, S. Chakravarty, A.T. Dorsey, M.P.A. Fisher, A. Garg, and W. Zwerger. Dynamics of the dissipative two-state system. *Rev. Mod. Phys.*, 59:1, 1987.
- [134] V.J. Emery and A. Luther. Low- temperature properties of the Kondo hamiltonian. *Phys. Rev. B*, 9:215, 1974.
- [135] P.W. Anderson. Infrared catastrophe in Fermi gases with local scattering potentials. *Phys. Rev. Lett.*, 18:1049, 67.
- [136] U. Weiss. *Quantum Dissipative Systems*. Number 10 in Series in modern condensed matter physics. World Scientific, 2 edition, 1999.
- [137] N.V. Prokovev and P.C.E. Stamp. Theory of the spin bath. *Rep. Prog. Phys.*, 63:669, 2000.
- [138] H. Gassmann, F. Marquardt, and C. Bruder. Non-Markoffian effects of a simple nonlinear bath. *Phys. Rev. E*, 66:041111, 02.
- [139] E. Paladino, L. Faoro, G. Falci, and R. Fazio. Decoherence and 1/f noise in Josephson qubits. *Phys. Rev. Lett.*, 88:228304, 2002.
- [140] A. Shnirman, Yu. Makhlin, and G. Schön. Noise and decoherence in quantum two-level systems. *Phys. Scr.*, T102:147, 2002.
- [141] J.M. Martinis, S. Nam S, J. Aumentado, K.M. Lang, and C. Urbina. Decoherence of a superconducting qubit due to bias noise. *Phys. Rev. B*, 67:094510, 2003.
- [142] P. Dutta and P.M. Horn. Low-frequency fluctuations in solids: 1/f-noise. *Rev. Mod. Phys.*, 53:497, 1981.
- [143] R. J. Schoelkopf, A. A. Clerk, S. M. Girvin, K. W. Lehnert, and M. H. Devoret. *Quantum Noise*, chapter Qubits as spectrometers of quantum noise. Nato ASI. Kluwer, 2002. edited by Yu.V. Nazarov and Ya.M. Blanter.
- [144] R. Aguado and L.P. Kouwenhoven. Double quantum dots as detectors of high-frequency quantum noise in mesoscopic conductors. *Phys. Rev. Lett.*, 84:1986, 2000.
- [145] A. Cottet. *Implementation of a quantum bit in a superconducting circuit*. PhD thesis, Universite Paris 6, 2002.
- [146] C.P. Slichter. *Principles of magnetic resonance*. Number 1 in Springer Series in Solid-State Sciences. Springer, Berlin, 1996.

- [147] M. Grifoni, E. Paladino, and U. Weiss. Dissipation, decoherence and preparation effects in the spin-boson system. *Eur. Phys. J B*, 10:719, 1999.
- [148] S. Nakajima. On quantum theory of transport phenomena. *Progr. Theor. Phys.*, 20:948, 1958.
- [149] R. Zwanzig. Memory effects in irreversible thermodynamics. *Phys. Rev.*, 124:983, 1961.
- [150] P.N. Argyres and P.N. Kelley. Theory of spin resonance and relaxation. *Phys. Rev.*, 134:A98, 1964.
- [151] H. Spohn. Kinetic equations from Hamiltonian dynamics: Markovian limits. *Rev. Mod. Phys.*, 52:569, 1980.
- [152] G. Lindblad. On the generators of quantum dynamical semigroups. *Commun. Math. Phys.*, 48:119, 1976.
- [153] R. Alicki and K. Lendi. *Quantum dynamical semigroups and applications*. Number 286 in Lecture notes in physics. Springer, 1976.
- [154] H.J. Charmichael. *An open systems approach to quantum optics*. Springer, Berlin, 1993.
- [155] C.W. Gardiner and P. Zoller. *Quantum Noise. A Handbook of Markovian and Non-Markovian Quantum Stochastic Methods with Applications to Quantum Optics*. Springer series in synergetics. Springer, 1999.
- [156] D. Loss and D.P. DiVincenzo. Exact Born approximation for the spin-boson model. cond-mat/0304118.
- [157] F. Bloch. Generalized theory of relaxation. *Phys. Rev.*, 105:1206, 1957.
- [158] A.G. Redfield. On the theory of relaxation processes. *IBM J Res. Develop.*, 1:19, 1957.
- [159] M.B. Plenio and P. Knight. The quantum-jump approach to dissipative dynamics in quantum optics. *Rev. Mod. Phys.*, 70:101, 1998.
- [160] J. Dalibard, Y. Castin, and K. Molmer. Wave-function approach to dissipative processes in quantum optics. *Phys. Rev. Lett.*, 68:580, 1992.

- [161] A.N. Korotkov. Nonideal quantum detectors in Bayesian formalism. *Phys. Rev. B*, 67:235408, 2003.
- [162] T.A. Costi. Scaling and universality in the anisotropic Kondo model and the dissipative two-state system. *Phys. Rev. Lett.*, 80:1038, 1998.
- [163] S.K. Kehrein and A. Mielke. Diagonalization of system plus environment Hamiltonians. *J. Stat. Phys.*, 90:889, 1998.
- [164] M. Keil and H. Schoeller. Real-time renormalization-group analysis of the dynamics of the spin-boson model. *Phys. Rev. B*, 63:180302, 2001.
- [165] T.H. Oosterkamp, T. Fujisawa, W.G. van der Wiel, K. Ishibashi, R.V. Hijman, S. Tarucha, and L.P. Kouwenhoven. Microwave spectroscopy on a quantum-dot molecule. *Nature*, 395:873, 1998.
- [166] W.G. van der Wiel, S. De Franceschi, J.M. Elzerman, T. Fujisawa, S. Tarucha, and L.P. Kouwenhoven. Electron transport through double quantum dots. *Rev. Mod. Phys.*, 75:1, 2003.
- [167] R.H. Blick and H. Lorenz. Possible definition of quantum bits in coupled quantum dots. In *Proceedings IEEE International Symposium on Circuits and Systems*, volume II, page 245, 2000.
- [168] R.E. Prange and S.M. Girvin. *The quantum Hall effect*. Springer, New York, 1990.
- [169] M.A. Kastner. Artificial atoms. *Phys. Today*, 46(1):24, 1993.
- [170] M.A. Kastner. The single electron transistor and artificial atoms. *Ann. Phys. (Leipzig)*, 9:885, 2000.
- [171] J. von Delft and D.C. Ralph. Spectroscopy of discrete energy levels in ultrasmall metallic grains. *Phys. Rep.*, 345:61, 2001.
- [172] L.P. Kouwenhoven, D.G. Austing, and S. Tarucha. Few-electron quantum dots. *Rep. Prog. Phys.*, 64:710, 2001.
- [173] L.P. Kouwenhoven and C.M. Marcus. Quantum dots. *Phys. World*, 11(6):35, 1998.
- [174] T. Brandes and B. Kramer. Spontaneous emission of phonons by coupled quantum dots. *Phys. Rev. Lett.*, 83:3021, 1999.
- [175] T. Brandes and N. Lambert. Steering of a bosonic mode with a double quantum dot. *Phys. Rev. B*, 67:125323, 2003.

- [176] J. Kirschbaum, E. M. Höhberger, R. H. Blick, W. Wegscheider, and M. Bichler. Integrating suspended quantum dot circuits for applications in nanomechanics. *Appl. Phys. Lett.*, 81:280, 2002.
- [177] T. Fujisawa, D.G. Austing, Y. Tokura, Y. Hirayama, and S. Tarucha. Electrical pulse measurement, inelastic relaxation, and non-equilibrium transport in a quantum dot. *cond-mat/0308362*.
- [178] W. Lu, Z.W. Ji, L. Pfeiffer, K.W. West, and A.J. Rimberg. Real-time detection of electron tunnelling in a quantum dot. *Nature*, 423:422, 2003.
- [179] S.A. Gurvitz, L. Fedichkin, D. Mozyrsky, and G.P. Berman. Relaxation and Zeno effect in qubit measurements. *Phys. Rev. Lett.*, 91:066801, 2003.
- [180] A.V. Khaetskii and Yu. V. Nazarov. Spin-flip transitions between zeeman sublevels in semiconductor quantum dots. *Phys. Rev. B*, 64:125316, 2001.
- [181] R. de Sousa and S. Das Sarma. Electron spin coherence in semiconductors: Considerations for a spin-based solid-state quantum computer architecture. *Phys. Rev. B*, 67:033301, 2003.
- [182] C.J. Lambert and R. Raimondi. Phase-coherent transport in hybrid superconducting nanostructures. *J. Phys. Cond. Mat.*, 10:901, 1998.
- [183] B. Pannetier and H. Courtois. Andreev reflection and proximity effect. *J. Low Temp. Phys.*, 118:599, 1999.
- [184] P.G. de Gennes. Boundary effects in superconductors. *Rev. Mod. Phys.*, 36:225, 1964.
- [185] A.F. Andreev. The thermal conductivity of the intermediate state in superconductors. *Sov. Phys. JETP*, 19:1228, 1964.
- [186] F.K. Wilhelm, G. Schön, and A.D. Zaikin. The mesoscopic SNS transistor. *Phys. Rev. Lett.*, 81:1682, 1998.
- [187] J.J.A. Baselmans, A.F. Morpurgo, B.J. van Wees, and T.M. Klapwijk. Reversing the direction of the supercurrent in a controllable josephson junction. *Nature*, 397:43, 1999.

- [188] F.K. Wilhelm. *Ladungstransport in supraleitenden Nanostrukturen*. PhD thesis, Universität Karlsruhe (TH), Aachen, 1999. Shaker Verlag.
- [189] C.H. van der Wal, A.C.J. ter Haar, F.K. Wilhelm, R.N. Schouten, C.J.P.M. Harmans, T.P. Orlando, S. Lloyd, and J.E. Mooij. Quantum superposition of macroscopic persistent-current states. *Science*, 290:773, 2000.
- [190] F.K. Wilhelm, C.H. van der Wal, A.C.J. ter Haar, R.N. Schouten, C.J.P.M. Harmans, J.E. Mooij, T.P. Orlando, and S. Lloyd. Macroscopic quantum superposition of current states in a Josephson junction loop. *Phys. Usp. (Suppl.)*, 171:117, 2001.
- [191] C.H. van der Wal, A.C.J. ter Haar, F.K. Wilhelm, Schouten R.N, C.J.P.M. Harmans, T.P. Orlando, S. Lloyd, and J.E. Mooij. Macroscopic quantum superpositions in a three-Josephson-junction loop. In Istituto italiano per gli studi filosofici, editor, *Proceedings of the MQC2 workshop*, pages 25–34, 2000.
- [192] C.H. van der Wal, F.K. Wilhelm, C.J.P.M. Harmans, and J.E. Mooij. Engineering decoherence in Josephson persistent-current qubits. *Eur. Phys. J. B*, 31:111, 2003.
- [193] F.K. Wilhelm, M.J. Storcz, C.H. van der Wal, C.J.P.M. Harmans, and J.E. Mooij. Decoherence of flux qubits coupled to electronic circuits. *Adv. Sol. St. Phys.*, 43:763, 2003.
- [194] M.C. Goorden and F.K. Wilhelm. Theoretical analysis of continuously driven solid-state qubits. *Phys. Rev. B*, 68:012508, 2003.
- [195] M.J. Storcz and F.K. Wilhelm. Decoherence and gate performance of coupled solid-state qubits. *Phys. Rev. A*, 67:042319, 2003.
- [196] Frank K. Wilhelm. An asymptotic von-Neumann measurement strategy for solid-state qubits. *Phys. Rev. B*, 68:060503(R), 2003.
- [197] T.P. Orlando, L. Tian, D.S. Crankshaw, S. Lloyd, C.H. van der Wal, J.E. Mooij, and F.K. Wilhelm. Engineering the quantum-measurement process for the persistent current qubit. *Physica C*, 368:294, 2003.
- [198] F.K. Wilhelm, S. Kleff, and J. van Delft. The spin-boson model with a structured environment: A comparison of approaches. *Chem. Phys.*, in press.

- [199] H. Gutmann, F.K. Wilhelm, W.M. Kaminsky, and S. Lloyd. Compensation of decoherence from telgraph noise using bang-bang quantum control. *cond-mat/0308107*.
- [200] M.J. Storcz and F.K. Wilhelm. Design of realistic switches for coupling superconducting solid-state qubits. *Appl. Phys. Lett.*, 83:2389, 2003.
- [201] F.K. Wilhelm and J.E. Mooij. Large berry phase in superconducting flux qubits. submitted to *Europhys. Lett.*
- [202] U. Hartmann and F.K. Wilhelm. Decoherence of charge states in double quantum dots due to cotunneling. *phys. stat. sol.*, 233:385, 2002.
- [203] U. Hartmann and F.K. Wilhelm. Nonlinear cotunneling through an artificial molecule. *Phys. Rev. B*, 67:161307(R), 2003.
- [204] U. Hartmann and F.K. Wilhelm. Control of decoherence through nonequilibrium between two baths. *cond-mat/0302572*.
- [205] T.T. Heikkilä, J. Särkkä, and F.K. Wilhelm. Supercurrent-carrying density of states in diffusive mesoscopic Josephson weak links. *Phys. Rev. B*, 66:184513, 2002.
- [206] T.T. Heikkilä, F.K. Wilhelm, and G. Schön. Nonequilibrium supercurrent through mesoscopic ferromagnetic weak links. *Europhys. Lett.*, 51:434, 2000.
- [207] P. Dubos, H. Courtois, B. Pannetier, F.K. Wilhelm, A.D. Zaikin, and G. Schön. Josephson critical current in a long mesoscopic SNS Josephson junction. *Phys. Rev. B*, 63:064502, 2001.
- [208] J. Huang, F. Pierre, T.T. Heikkilä, F.K. Wilhelm, and N.O. Birge. Observation of a tunable π -junction in a 3-terminal Josephson device. *Phys. Rev. B*, 66:020507(R), 2002.
- [209] T.T. Heikkilä, T. Vänskä, and F.K. Wilhelm. Supercurrent-induced Peltier-like effect in superconductor/normal-metal weak links. *Phys. Rev. B*, 67:100502(R), 2003.

Chapter 3

Original papers

This chapter comprises my research papers and forms the main body of this report. The papers are grouped in sections on related subjects and each section has an introduction outlining the subjects and inter-relations of the papers. The papers are listed in the bibliography as references [189–209]. The work presented in these papers has been done exclusively after the completion of my PhD thesis.

3.1 Spectroscopy of superconducting qubits

In paper [189], macroscopic superpositions of persistent current states in superconducting loops are demonstrated. The loops are interrupted by three Josephson junctions in order to generate sufficient quantum fluctuations between the states, as described in section 2.6. The qubits are of appreciable size of about 450 nA, which involve the collective motion of at least 10^9 Cooper pairs. The measurement of the state is performed by a weakly coupled SQUID and involves averaging over about 5000 experiments in order to achieve enough resolution. The levels of the qubit are studied using microwave spectroscopy. At $f = 1/2$, when the classical current states are degenerate, level repulsion is clearly identified, which shows that the eigenstates are superpositions of the classical states. At strong microwave power, the absorption lines broaden as expected from Rabi's formula. At low power, the width saturates, indicating an ensemble dephasing time of $T_2^* = 10$ ns. However, this line width can also be fully explained by the classical back-action of the meter and is not necessarily intrinsic.

Paper [190] presents a new perspective on these data. Specifically, the step of the magnetization in thermal equilibrium is investigated in the vicinity of $f = 1/2$. If the temperature is lowered, the step in the ground state gets sharper, however, a finite rounding due to quantum fluctuations persist even at temperatures below the anticipated tunnel matrix elements. In fact, from analyzing the half-width of the step, this matrix element can be extracted. Its value is far above the value from the spectroscopy data. This can be explained by the relatively long timescale of the equilibrium experiment, in which slow fluctuations of the bias flux lead to an additional broadening of the step.

In paper [191], the aspects of the classical back-action in the read-out process in this experiment are emphasized and the relation to other experiments on macroscopic quantum coherence such as in Ref. [30] is detailed.

$\mu\text{g/ml}$ pepstatin, 4 mM PMSF, and 0.5% NP-40) was then added. The tubes were shaken for 2 hours in the The supernatant was collected for ELISA and protein measurements. The ELISA reaction was completed in 96-well plate (Dynatech, Chantilly, VA) according to the ELISA manufacturer's instructions (GDNF E_{max} ImmunoAssay Systems Kit G3520, Promega, Madison, WI). The optical densities were recorded in ELISA plate reader (at 450 nm wave length; Dynatech). Some lysates were diluted to ensure all the optical densities were within the standard curve. The con-

centrations or GDNF were calculated against six-point standard curve and then adjusted to picograms of GDNF per milligram of total protein. The total protein in each tissue lysate was measured using Bio-Rad protein assay kit (Bio-Rad, Richmond, CA).
 28. D. A. Kozlowski *et al.*, *ASNTR*, Abstr. 7, 25 (2000).
 29. J. L. Eberling *et al.*, *Brain Res.* **832**, 184 (1999).
 30. B. Connor *et al.*, *Gene Ther.* **6**, 1936 (1999).
 31. C. Rosenblad, D. Kirik, A. Björklund, *Exp. Neurol.* **16**, 503 (2000).
 32. This research was supported by a grant from the

Department of Defense, The Charles Shapiro Foundation, NS40578, and by the Swiss National Science Foundation and the Swiss National Program in Neurological Diseases. We thank T. Collier for comments on this manuscript, T. Kladis and J. Stansell for expert histological assistance, F. Pidoux and M. Rey for the technical assistance in the production of the lentiviral vectors, K. Gibbons for assistance with PET scans, and J. Sladek Jr. for photographic assistance.

9 December 1999; accepted 17 August 2000

Quantum Superposition of Macroscopic Persistent-Current States

Caspar H. van der Wal,^{1*} A. C. J. ter Haar,¹ F. K. Wilhelm,¹
 R. N. Schouten,¹ C. J. P. M. Harmans,¹ T. P. Orlando,²
 Seth Lloyd,³ J. E. Mooij^{1,2}

Microwave spectroscopy experiments have been performed on two quantum levels of a macroscopic superconducting loop with three Josephson junctions. Level repulsion of the ground state and first excited state is found where two classical persistent-current states with opposite polarity are degenerate, indicating symmetric and antisymmetric quantum superpositions of macroscopic states. The two classical states have persistent currents of 0.5 microampere and correspond to the center-of-mass motion of millions of Cooper pairs.

When a small magnetic field is applied to a superconducting loop, a persistent current is induced. Such a persistent supercurrent also occurs when the loop contains Josephson tunnel junctions. The current is clockwise or counterclockwise, thereby either reducing or enhancing the applied flux to approach an integer number of superconducting flux quanta Φ_0 (I). In particular when the enclosed magnetic flux is close to half-integer values of Φ_0 , the loop may have multiple stable persistent-current states, with at least two of opposite polarity. The weak coupling of the Josephson junctions then allows for transitions between the states. Previous theoretical work (2–4) proposed that a persistent current in a loop with Josephson junctions corresponds to the center-of-mass motion of all the Cooper pairs in the system and that quantum mechanical behavior of such persistent-current states would be a manifestation of quantum mechanical behavior of a macroscopic object. In a micrometer-sized loop, millions of Cooper pairs are involved. At very low temperatures, excitations of individual charge carriers around the center of mass

of the Cooper-pair condensate are prohibited by the superconducting gap. As a result, the coupling between the dynamics of persistent supercurrents and many-body quasi-particle states is very weak. Josephson junction loops therefore rank among the best objects for experimental tests of the validity of quantum mechanics for systems containing a macroscopic number of particles (3, 5, 6) [loss of quantum coherence results from coupling to an environment with many degrees of freedom (7)] and for research on the border between classical and quantum physics. The potential for quantum coherent dynamics has stimulated research aimed at applying Josephson junction loops as basic building blocks for quantum computation (qubits) (8–11).

We present microwave spectroscopy experiments that demonstrate quantum superpositions of two macroscopic persistent-current states in a small loop with three Josephson junctions (Fig. 1A). At an applied magnetic flux of $\frac{1}{2}\Phi_0$, the system behaves as a particle in a double-well potential, where the classical states in each well correspond to persistent currents of opposite sign. The two classical states are coupled via quantum tunneling through the barrier between the wells, and the loop is a macroscopic quantum two-level system (Fig. 1B) (12). The energy levels vary with the applied flux as shown (Fig. 1C). Classically, the levels cross at $\frac{1}{2}\Phi_0$. Tunneling between the wells leads to quantum mechanical eigenstates that at $\frac{1}{2}\Phi_0$ are symmet-

ric and antisymmetric superpositions of the two classical persistent-current states. The symmetric superposition state is the quantum mechanical ground state with an energy lower than the classical states; the antisymmetric superposition state is the loop's first excited state with an energy higher than the classical states. Thus, the superposition states manifest themselves as an anticrossing of the loop's energy levels near $\frac{1}{2}\Phi_0$. We performed spectroscopy on the loop's two quantum levels (Fig. 2) and our results show the expected anticrossing at $\frac{1}{2}\Phi_0$ (Fig. 3) (13). We also studied the resonance-line shapes and found behavior similar to microscopic quantum two-level systems (14, 15) (Fig. 4).

Detecting quantum superposition. In our experiments, the magnetic flux generated by the loop's persistent current was measured with an inductively coupled direct-current superconducting quantum interference device (DC-SQUID) (Figs. 1 and 2), while low-amplitude microwaves were applied to induce transitions between the levels. We observed narrow resonance lines at magnetic field values where the level separation ΔE was resonant with the microwave frequency. The DC-SQUID performs a measurement on a single quantum system. Thus, we should expect that the measurement process limits the coherence of our system. While the system is pumped by the microwaves, the SQUID actively measures the flux produced by the persistent currents of the two states. Detecting the quantum levels of the loop is still possible because the meter is only weakly coupled to the loop. The flux signal needs to be built up by averaging over many repeated measurements on the same system (Fig. 2B), such that an ensemble average is effectively determined. We measure the level separation, i.e., energy rather than flux, as we perform spectroscopy, and we observe a change in averaged flux when the microwaves are resonant with the level separation (the peaks and dips in Figs. 2B and 3A). We also chose to work with an extremely underdamped DC-SQUID with unshunted junctions to minimize damping of the quantum system via the inductive coupling to the SQUID.

Similar observations were recently made by Friedman *et al.* (16) who performed spectroscopy on excited states in a loop with a

¹Department of Applied Physics and Delft Institute for Micro Electronics and Submicron Technology (DIMES), Delft University of Technology, Post Office Box 5046, 2600 GA Delft, Netherlands. ²Department of Electrical Engineering and Computer Science and ³Department of Mechanical Engineering, Massachusetts Institute of Technology, Cambridge, MA 02139, USA.

*To whom correspondence should be addressed. E-mail: caspar@qt.tn.tudelft.nl

single Josephson junction (radio frequency SQUID). Previous experiments with single-junction loops have demonstrated resonant tunneling between discrete quantum states in two wells (17, 18) and microwave-induced transitions between the wells (19, 20). Other observations related to macroscopic superposition states are tunnel splittings observed with magnetic molecular clusters (21, 22) and quantum interference of C_{60} molecules (23). In quantum dots (24) and superconducting circuits where charge effects dominate over the Josephson effect (25–27), superpositions of charge states have been observed, as well as quantum coherent charge oscillations (28).

Macroscopic quantum system. Our quantum system is a low-inductance loop intersected by three Josephson tunnel junctions (Fig. 1A) (10, 11). The Josephson junctions are extremely underdamped and are characterized by their Josephson coupling E_J and charging energy $E_C = e^2/2C$, where C is the junction capacitance and e is the electron charge. The critical current of a junction is $I_{C0} = \frac{2e}{\hbar} E_J$, where $\hbar = \frac{h}{2\pi}$ is the reduced Planck constant. One of the junctions in the loop has E_J and C smaller by a factor $\beta \approx 0.8$. At an applied flux Φ_{ext} close to $\frac{1}{2}\Phi_0$, the total Josephson energy forms a double-well potential. The classical states at the bottom of

each well have persistent currents of opposite sign, with a magnitude I_p very close to I_{C0} of the weakest junction and with energies $E = \pm I_p(\Phi_{\text{ext}} - \frac{1}{2}\Phi_0)$ (dashed lines in Fig. 1C) (29). The system can be pictured as a particle with a mass proportional to C in the Josephson potential; the electrostatic energy is the particle's kinetic energy. The charging effects are conjugate to the Josephson effect. For low-capacitance junctions (small mass) quantum tunneling of the particle through the barrier gives a tunnel coupling t between the persistent-current states. In the presence of quantum tunneling and for E_J/E_C values between 10 and 100, the system should have two low-energy quantum levels E_0 and E_1 , which can be described using a simple quantum two-level picture (10, 11),

$$E_{0(1)} = -(\pm) \sqrt{t^2 + [I_p(\Phi_{\text{ext}} - \frac{1}{2}\Phi_0)]^2}$$

The loop's level separation $\Delta E = E_1 - E_0$ is then

$$\Delta E = \sqrt{(2t)^2 + [2I_p(\Phi_{\text{ext}} - \frac{1}{2}\Phi_0)]^2} \quad (1)$$

The system was realized by microfabricating an aluminum micrometer-sized loop with unshunted Josephson junctions (30). Around the loop, we fabricated the DC-SQUID magnetometer (Fig. 1A), which contains smaller Josephson junctions that were as under-

damped as the junctions of the inner loop. Loop parameters estimated from test junctions fabricated on the same chip and electron microscope inspection of the measured device give $I_{C0} = 570 \pm 60$ nA and $C = 2.6 \pm 0.4$ fF for the largest junctions in the loop and $\beta = 0.82 \pm 0.1$, giving $E_J/E_C = 38 \pm 8$ and $I_p = 450 \pm 50$ nA. Due to the exponential dependence of the tunnel coupling t on the mass (i.e., the capacitance C) and the size of the tunnel barrier, these parameters allow for a value for t/\hbar between 0.2 and 5 GHz. The parameters of the DC-SQUID junctions were $I_{C0} = 109 \pm 5$ nA and $C = 0.6 \pm 0.1$ fF. The self inductance of the inner loop and the DC-SQUID loop were estimated to be 11 ± 1 picoHenry (pH) and 16 ± 1 pH, respectively, and the mutual inductance M between the loop and the SQUID was 7 ± 1 pH (31). The flux in the DC-SQUID is measured by ramping a bias current through the DC-SQUID and recording the current level I_{SW} where the SQUID switches from the supercurrent branch to a finite voltage (Fig. 2A). Traces of the loop's flux signal were recorded by continuously repeating switching-current measurements while slowly sweeping the flux Φ_{ext} (Fig. 2B). The measured flux signal from the inner loop will be presented as \bar{I}_{SW} , which is an averaged value directly deduced from the raw switching-current data (32).

Results. Figure 3A shows the flux signal of the inner loop, measured in the presence of low-amplitude continuous-wave microwaves at different frequencies f . The rounded step in each trace at $\frac{1}{2}\Phi_0$ is due to the change in direction of the persistent current of the loop's ground state (see also Fig. 1C). Symmetrically around $\Phi_{\text{ext}} = \frac{1}{2}\Phi_0$ each trace shows a peak and a dip, which were absent when no microwaves were applied. The positions of the peaks and dips in Φ_{ext} depend on microwave frequency but not on amplitude. The peaks and dips result from microwave-induced transitions to the state with a persistent current of opposite sign. These occur when the level separation is resonant with the microwave frequency, $\Delta E = hf$.

In Fig. 3B, half the distance in Φ_{ext} between the resonant peak and dip $\Delta\Phi_{\text{res}}$ is plotted for all the frequencies f . The relation between ΔE and Φ_{ext} is linear for the high-frequency data. This gives $I_p = 484 \pm 2$ nA, in good agreement with the predicted value. At lower frequencies, $\Delta\Phi_{\text{res}}$ significantly deviates from this linear relation, demonstrating the presence of a finite tunnel splitting at $\Phi_{\text{ext}} = \frac{1}{2}\Phi_0$. A fit to Eq. 1 yields $t/\hbar = 0.33 \pm 0.03$ GHz, in agreement with the estimate from fabrication parameters. The level separation very close to $\frac{1}{2}\Phi_0$ could not be measured directly because at this point the expectation value for the persistent current is zero for both the ground state and the excited state (Fig. 1C). Nevertheless, the narrow res-

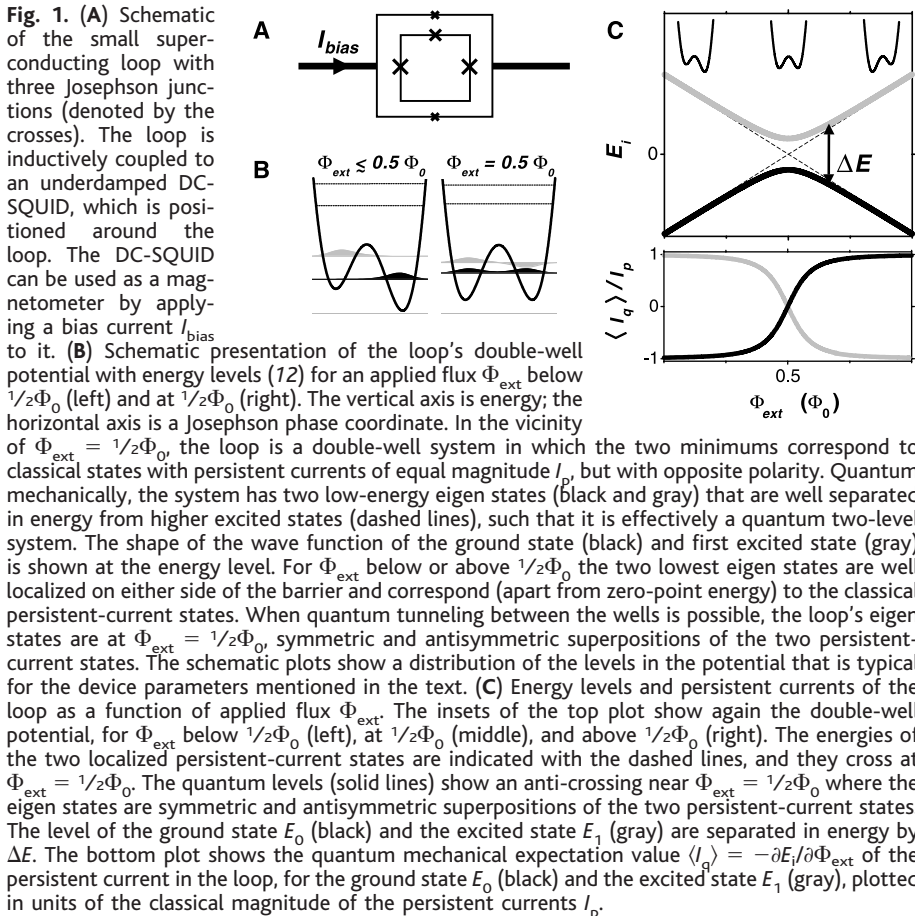


Fig. 1. (A) Schematic of the small superconducting loop with three Josephson junctions (denoted by the crosses). The loop is inductively coupled to an underdamped DC-SQUID, which is positioned around the loop. The DC-SQUID can be used as a magnetometer by applying a bias current I_{bias} to it. (B) Schematic presentation of the loop's double-well potential with energy levels (12) for an applied flux Φ_{ext} below $\frac{1}{2}\Phi_0$ (left) and at $\frac{1}{2}\Phi_0$ (right). The vertical axis is energy; the horizontal axis is a Josephson phase coordinate. In the vicinity of $\Phi_{\text{ext}} = \frac{1}{2}\Phi_0$, the loop is a double-well system in which the two minima correspond to classical states with persistent currents of equal magnitude I_p , but with opposite polarity. Quantum mechanically, the system has two low-energy eigen states (black and gray) that are well separated in energy from higher excited states (dashed lines), such that it is effectively a quantum two-level system. The shape of the wave function of the ground state (black) and first excited state (gray) is shown at the energy level. For Φ_{ext} below or above $\frac{1}{2}\Phi_0$ the two lowest eigen states are well localized on either side of the barrier and correspond (apart from zero-point energy) to the classical persistent-current states. When quantum tunneling between the wells is possible, the loop's eigen states are at $\Phi_{\text{ext}} = \frac{1}{2}\Phi_0$, symmetric and antisymmetric superpositions of the two persistent-current states. The schematic plots show a distribution of the levels in the potential that is typical for the device parameters mentioned in the text. (C) Energy levels and persistent currents of the loop as a function of applied flux Φ_{ext} . The insets of the top plot show again the double-well potential, for Φ_{ext} below $\frac{1}{2}\Phi_0$ (left), at $\frac{1}{2}\Phi_0$ (middle), and above $\frac{1}{2}\Phi_0$ (right). The energies of the two localized persistent-current states are indicated with the dashed lines, and they cross at $\Phi_{\text{ext}} = \frac{1}{2}\Phi_0$. The quantum levels (solid lines) show an anti-crossing near $\Phi_{\text{ext}} = \frac{1}{2}\Phi_0$ where the eigen states are symmetric and antisymmetric superpositions of the two persistent-current states. The level of the ground state E_0 (black) and the excited state E_1 (gray) are separated in energy by ΔE . The bottom plot shows the quantum mechanical expectation value $\langle I_p \rangle = -\partial E_i / \partial \Phi_{\text{ext}}$ of the persistent current in the loop, for the ground state E_0 (black) and the excited state E_1 (gray), plotted in units of the classical magnitude of the persistent currents I_p .

onance lines allow for an accurate mapping of the level separation near $\frac{1}{2}\Phi_0$, and the observed tunnel splitting gives clear evidence for quantum superpositions of the persistent-current states. The large uncertainty in the predicted t value does not allow for a quantitative analysis of a possible suppression of t due to a coupling between our two-level system and a bosonic environment (33) or a spin-bath environment (34, 35). However, the fact that we see a finite tunnel splitting indicates that the damping of our quantum system, which is caused by environmental degrees of freedom, is weak. The dimensionless dissipation parameter α introduced by Leggett *et al.* (33) must be $\alpha < 1$.

In Fig. 4, we show the dependence of the dip shape at 5.895 GHz on applied microwave amplitude. The dip amplitude and the full width at half the maximum amplitude (FWHM) were estimated for different microwave amplitudes by fitting a Lorentzian peak shape to the data. Figure 4B shows that the dip amplitude increases rapidly for microwave amplitudes up to $V_{AC} \approx 2$ arbitrary units (a.u.), followed by a saturation for larger microwave amplitudes. The saturated dip amplitude is ≈ 0.25 nA, which is close to half the full step height of the rounded step at $\frac{1}{2}\Phi_0$ (≈ 0.4 nA) in Fig. 3A. This indicates that on resonance the energy levels are close to being equally populated, as expected for pumping with continuous-wave microwaves.

Figure 4C shows a linear dependence between the FWHM and the microwave amplitude. Qualitatively, this dependence of the line shape on microwave amplitude agrees with spectroscopy results on microscopic quantum two-level systems. For negligible decoherence, spectroscopy on quantum two-level systems yields a Lorentzian line shape and transitions between the levels occur by coherent Rabi oscillations. The FWHM of the Lorentzian resonance line is two times the Rabi frequency and is proportional to the amplitude of the monochromatic perturbation (14). The linear dependence of the FWHM on microwave amplitude in Fig. 4C suggests that the line width for $V_{AC} > 2$ a.u. is dominated by the frequency of microwave-induced Rabi transitions. Transitions occur then by a few quantum coherent Rabi cycles. Using the linear relation between ΔE and Φ_{ext} for Φ_{ext} values away from $\frac{1}{2}\Phi_0$, the observed FWHM in Φ_{ext} units can be expressed in frequency units. This indicates a Rabi frequency of, for example, 150 MHz at $V_{AC} = 4$ a.u. However, we do not consider these results as proof for coherent quantum dynamics because other scenarios with weak decoherence give similar results (36).

Dephasing due to measuring SQUID.

The loss of dip amplitude and the apparent saturation of the FWHM at low V_{AC} is caused either by variations in the flux bias Φ_{ext}

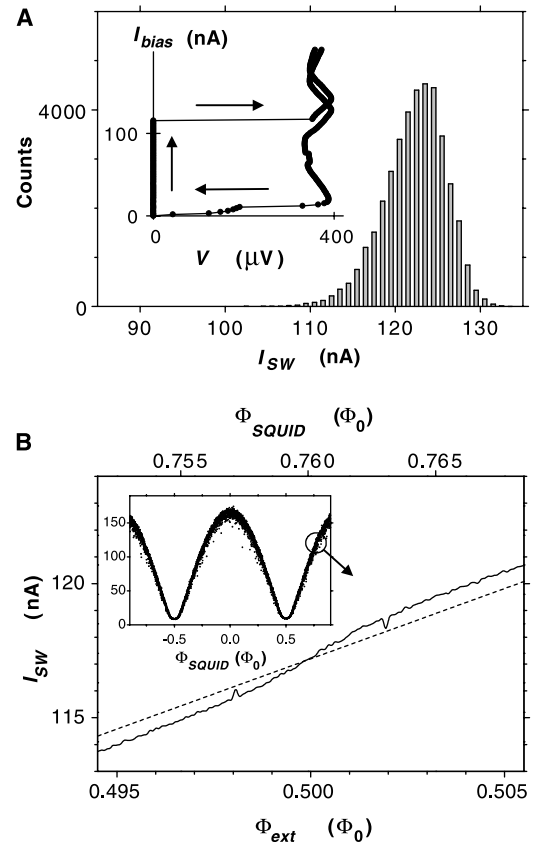
[corresponding to inhomogeneous broadening for the ensemble average (15)] or by an intrinsic dephasing mechanism. The effective dephasing time T_2^* (15) can be deduced from the FWHM at low V_{AC} . The FWHM (expressed in energy units) of a resonance line shape that is dominated by a finite dephasing time corresponds to $\frac{2h}{T_2^*}$ (15, 14). Using, once more, the linear relation between ΔE and Φ_{ext} for Φ_{ext} values away from $\frac{1}{2}\Phi_0$ to express the FWHM at $V_{AC} = \lesssim 2$ a.u. in energy units, gives $T_2^* \approx 15$ ns. As discussed below, this can be fully explained by variations in the applied magnetic flux that originate from the measuring DC-SQUID.

The DC-SQUID performs a weak measurement on the loop. It has two macroscopic phase degrees of freedom. One is associated with the circulating current in the SQUID's loop (internal degree of freedom), the other is associated with the bias current through the SQUID (external degree of freedom). As the bias current is ramped up, the coupling between these two degrees of freedom increases strongly due to the nonlinearity of the SQUID's current-phase relations (I). The external variable is coupled to a dissipative environment, and the associated effective mass (i.e., the capacitance across the SQUID) is very large. The internal degree of freedom

has negligible intrinsic damping and the associated mass (i.e., the capacitance of the junctions of the SQUID) is very small. Consequently, this variable exhibits quantum behavior. The classical external degree of freedom of the SQUID performs a measurement on the SQUID's inner quantum variable, which in turn is weakly coupled to our quantum loop. We therefore expect that the SQUID contributes dominantly to the loop's dephasing and damping with the present setup. The choice for an underdamped DC-SQUID resulted in very wide switching-current histograms. The width of the histogram corresponds to a standard deviation in the flux readout of $11 \cdot 10^{-3} \Phi_0$. The uncertainty in flux readout is much larger than the flux signal from the inner loop $2MI_p \approx 3 \cdot 10^{-3} \Phi_0$. Therefore, we can only detect the loop's signal by averaging over many switching events (Fig. 2).

The loss of dip amplitude in Fig. 4 is probably due to a small contribution to the effective Φ_{ext} from the circulating current in the DC-SQUID. The SQUID is operated at $0.76 \Phi_0$ in its loop, where its circulating current depends on the bias current due to its nonlinear behavior (I). This means that data recorded by switching events on the low I_{bias} side of the FWHM of the I_{sw} histogram in Fig. 2A differs in flux bias on the inner loop from that of the high side by $20 \cdot 10^{-6} \Phi_0$.

Fig. 2. (A) Current-voltage characteristic (inset) and switching-current histogram of the underdamped DC-SQUID. The plot with bias current I_{bias} versus voltage V is strongly hysteretic. The I_{bias} level where the SQUID switches from the supercurrent branch to a finite voltage state—the switching current I_{sw} —is a measure for the flux in the loop of the DC-SQUID. Switching to the voltage state is a stochastic process. The histogram in the main plot shows that the variance in I_{sw} is much larger than the flux signal of the inner loop's persistent current, which gives a shift in the averaged I_{sw} of about 1 nA (see Fig. 2B). **(B)** Switching-current levels of the DC-SQUID versus applied flux. The inset shows the modulation of I_{sw} versus the flux Φ_{SQUID} applied to the DC-SQUID loop (data not averaged, one point per switching event). The main figure shows the averaged level of I_{sw} (solid line) near $\Phi_{SQUID} = 0.76 \Phi_0$. At this point, the flux in the inner loop $\Phi_{ext} \approx \frac{1}{2}\Phi_0$. The rounded step at $\Phi_{ext} = \frac{1}{2}\Phi_0$ indicates the change of sign in the persistent current of the loop's ground state. Symmetrically around $\frac{1}{2}\Phi_0$ the signal shows a peak and a dip, which are only observed with measurements in the presence of continuous-wave microwaves (here 5.895 GHz). The peak and dip are due to resonant transitions between the loop's two quantum levels (Fig. 3). The background signal of the DC-SQUID that results from flux directly applied to its loop (dashed line) is subtracted from the data presented in Figs. 3A and 4A.



Resonance lines at low V_{AC} (i.e., with a $\text{FWHM} < 20 \cdot 10^{-6} \Phi_0$) cannot be observed as the peaks and dips smear out when averaging over many switching events. The loss of dip amplitude and the apparent saturation of the FWHM at low V_{AC} is probably dominated by this mechanism for inhomogeneous line broadening.

The width of the rounded steps in the measured flux in Fig. 3A is much broader

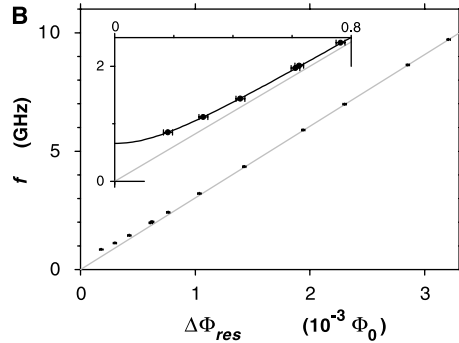
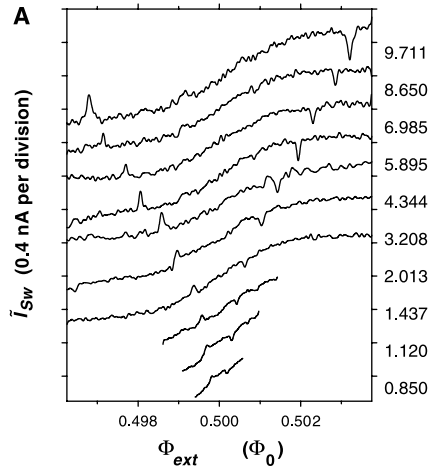
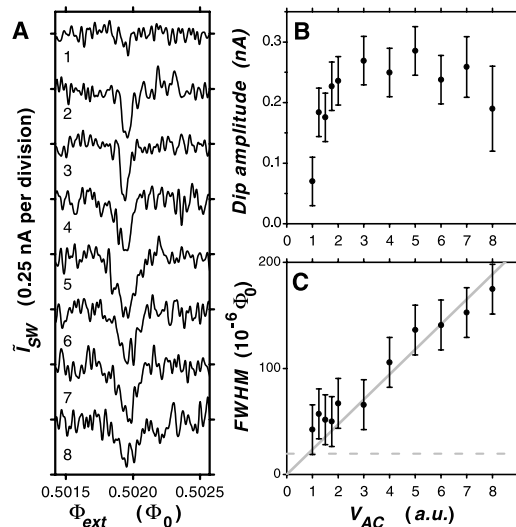


Fig. 3. (A) Switching-current levels \bar{I}_{SW} of the DC-SQUID as a function of Φ_{ext} , measured at different microwave frequencies f [labels on the right give f in GHz, \bar{I}_{SW} is deduced from the raw switching-current data I_{SW} by averaging and subtracting a background signal (32)]. Each trace clearly shows the rounded step at $\Phi_{ext} = 1/2\Phi_0$ where the persistent current of the loop's ground state changes sign. In the presence of continuous-wave microwaves a peak and a dip appear in the signal, symmetrically around $1/2\Phi_0$. The positions of the peak and dip depend on f . The peak and dip appear at values of Φ_{ext} where the level separation between the lowest quantum states of the loop is resonant with the microwave frequency, and the microwaves induce transitions to the state that has a persistent current of opposite sign. (B) Half the distance in Φ_{ext} between the resonant peak and dip $\Delta\Phi_{res}$ at different microwave frequencies f (f is plotted on the vertical axis for compatibility with Fig. 1C). Peak and dip positions are determined from traces as in (A). At high frequencies, the $\Delta\Phi_{res}$ values are proportional to the microwave frequency. The gray line is a linear fit through the high-frequency data points and zero. The slope is used to determine $I_p = 484$ nA. At low microwave frequencies the measured $\Delta\Phi_{res}$ values deviate significantly from this linear relation, demonstrating that the loop's lowest two energy levels repel each other near $\Phi_{ext} = 1/2\Phi_0$. The inset zooms in on the low-frequency data points. The black line is a fit of Eq. 1 with only the tunnel coupling t as a fitting parameter, yielding $t/h = 0.33 \pm 0.03$ GHz.

Fig. 4. (A) The influence of the microwave amplitude on the shape of the resonance dip in the scaled switching current \bar{I}_{SW} , measured at 5.895 GHz [the labels on the left give the amplitude V_{AC} in a.u.]. (B) The dip amplitude first increases with microwave amplitude V_{AC} , but saturates at $V_{AC} > 2$ a.u. (C) The FWHM of the dips increases with V_{AC} . The linear fit through the highest data points and zero (gray) is a guide to the eye. The horizontal dashed line indicates a flux value that corresponds to the shift in effective flux bias Φ_{ext} which is induced when the bias current is ramped through the DC-SQUID. This acts as a flux instability with an amplitude of $\approx 20 \cdot 10^{-6} \Phi_0$. Resonance lines with a FWHM below this value cannot be observed. The loss of dip amplitude in Fig. 4B when lowering $V_{AC} < 2$ a.u. sets in where the FWHM $\approx 20 \cdot 10^{-6} \Phi_0$. The flux shift from the SQUID is calculated using the I_{bias} interval (the FWHM of the switching-current histogram is used) where the SQUID typically switches.



than expected from quantum rounding on the scale of the value of t that was found with spectroscopy (see also Fig. 1C). We checked the temperature dependence of the step width, measured in the absence of microwaves. We found that at temperatures above 100 mK, the step width is in agreement with the thermally averaged expectation value for the persistent current $\langle I_{th} \rangle = I_p \tanh \left(\frac{\Delta E}{2k_B T} \right)$

(k_B is Boltzmann's constant), where we use the level separation ΔE and I_p found with spectroscopy. However, at low temperatures the observed step width saturates at an effective temperature of about 100 mK. We checked that the effective temperature for the SQUID's switching events did not saturate at the lowest temperatures. The high effective temperature of the loop is a result of the loop being in a nonequilibrium state. The population of the excited state could be caused by the measuring SQUID or other weakly coupled external processes.

Concluding remarks and future prospects. The data presented here provide clear evidence that a small Josephson junction loop can behave as a macroscopic quantum two-level system. The application of an underdamped DC-SQUID for measuring the loop's magnetization is a useful tool for future work on quantum coherent experiments with Josephson junction loops. The present results also demonstrate the potential of three-junction persistent-current loops for research on macroscopic quantum coherence and for use as qubits in a quantum computer. This requires quantum-state control with pulsed microwaves and development of measurement schemes that are less invasive. Circuits that contain multiple qubits with controlled inductive coupling are within reach using present-day technology.

References and Notes

1. M. Tinkham, *Introduction to Superconductivity* (McGraw-Hill, New York, ed. 2, 1996), pp. 196–234.
2. P. W. Anderson, in *Lectures on the Many-Body Problem*, E. R. Caianiello, Ed. (Academic Press, New York, 1964), vol. 2, pp. 113–135.
3. A. J. Leggett, *Prog. Theor. Phys. Suppl.* **69**, 80 (1980).
4. K. K. Likharev, *Sov. Phys. Usp.* **26**, 87 (1983).
5. A. J. Leggett, A. Garg, *Phys. Rev. Lett.* **54**, 857 (1985).
6. A. J. Leggett, *J. Supercond.* **12**, 683 (1999).
7. W. H. Zurek, *Phys. Today* **44**, 36 (October 1991).
8. M. F. Bocko, A. M. Herr, M. J. Feldman, *IEEE Trans. Appl. Supercond.* **7**, 3638 (1997).
9. L. B. Ioffe, V. B. Geshkenbein, M. V. Feigel'man, A. L. Fauchère, G. Blatter, *Nature* **398**, 679 (1999).
10. J. E. Mooij *et al.*, *Science* **285**, 1036 (1999).
11. T. P. Orlando *et al.*, *Phys. Rev. B* **60**, 15398 (1999).
12. The double-well potential shown in Fig. 1B is the relevant potential for the tunnel transitions between the system's two persistent-current states. The potential is the sum of the Josephson energies of all the junctions and the zero-point energy of a Josephson phase degree of freedom that is perpendicular to the tunnel direction between the two wells (10, 11). This zero-point energy is nearly constant along the tunnel trajectory between the wells, and it has a plasma frequency much higher than the level separation between the lowest two quantum levels. It should therefore be included in the effective potential for transitions between the two wells. For the sample parameters mentioned in the text the lowest two quantum levels are well below the top of the effective tunnel barrier.
13. The results presented here do not exclude alternative theories for quantum mechanics [e.g., macro-realistic theories (37)]. This would require a type of experiment as proposed by Leggett *et al.* (5).
14. C. Cohen-Tannoudji, B. Diu, F. Laloë, *Quantum Mechanics* (Wiley, New York, 1977), vol. 1, pp. 443–454.
15. A. Abragam, *Principles of Nuclear Magnetism* (Oxford Univ. Press, Oxford, 1961), pp. 39–57.
16. J. R. Friedman, V. Patel, W. Chen, S. K. Tolpygo, J. E. Lukens, *Nature* **406**, 43 (2000).

17. R. Rouse, S. Han, J. E. Lukens, *Phys. Rev. Lett.* **75**, 1614 (1995).
18. C. Cosmelli *et al.*, *Phys. Rev. Lett.* **82**, 5357 (1999).
19. S. Han, R. Rouse, J. E. Lukens, *Phys. Rev. Lett.* **76**, 3404 (1996).
20. ———, *Phys. Rev. Lett.* **84**, 1300 (2000).
21. W. Wernsdorfer, R. Sessoli, *Science* **284**, 133 (1999).
22. E. del Barco *et al.*, *Europhys. Lett.* **47**, 722 (1999).
23. M. Arndt *et al.*, *Nature* **401**, 680 (1999).
24. T. H. Oosterkamp *et al.*, *Nature* **395**, 873 (1998).
25. Y. Nakamura, C. D. Chen, J. S. Tsai, *Phys. Rev. Lett.* **79**, 2328 (1997).
26. V. Bouchiat, D. Vion, P. Joyez, D. Esteve, M. H. Devoret, *Phys. Scr.* **T76**, 165 (1998).
27. D. J. Flees, S. Han, J. E. Lukens, *J. Supercond.* **12**, 813 (1999).
28. Y. Nakamura, Yu. A. Pashkin, J. S. Tsai, *Nature* **398**, 786 (1999).
29. The small self-generated flux due to the persistent currents leads to a constant lowering of the energies. The crossing remains at $1/2\Phi_0$. In the discussion we take Φ_{ext} to be the total flux in the loop.
30. The sample consisted of a 5 μm by 5 μm aluminum loop with aluminum oxide tunnel junctions, micro-fabricated with e-beam lithography and shadow-evaporation techniques on a SiO_2 substrate. The lines of the loop were 450-nm wide and 80-nm thick. A DC-SQUID with a 7 μm by 7 μm loop was fabricated in the same layer around the inner loop. The DC-SQUID had an on-chip superconducting shunt capacitance of 2 pF and superconducting leads in a four-point configuration. The sample was mounted in a dilution refrigerator, inside a microwave-tight copper measurement box, magnetically shielded by two

high-permeability metal shields and one superconducting shield. All spectroscopy measurements were taken with the temperature stabilized at 30 ± 0.05 mK. Microwaves were applied to the sample by a coaxial line, which was shorted at the end by a small loop of 5-mm diameter. This loop was positioned parallel to the sample plane at about 1 mm distance. Switching currents were measured with dedicated electronics, with repetition rates up to 9 kHz and bias currents ramped at typically 1 $\mu\text{A}/\text{ms}$. A detailed description of the fabrication and experimental techniques can be found in [C. H. van der Wal, J. E. Mooij, *J. Supercond.* **12**, 807 (1999)].

31. The inductances were estimated numerically from the geometry with a finite-element method. The value for M is in agreement with the flux signal from the inner loop (estimated from the step height in flux units in Fig. 2B) divided by I_p .

32. Deducing I_{SW} from the raw switching-current data I_{SW} concerned the following three points: (i) Because the variance in I_{SW} was much larger than the signature from the loop's flux (Fig. 2), we applied low-pass FFT-filtering in Φ_{ext} space (over 10^7 switching events for the highest trace, and $2 \cdot 10^8$ events for the lowest trace in Fig. 3A). We checked that the cutoff frequency was chosen high enough not to influence any parameters deduced from the data. (ii) By applying Φ_{ext} , we also apply flux directly to the DC-SQUID. The resulting background signal was subtracted (Fig. 2B). We checked that the estimated dip and peak positions in Fig. 3B did not depend significantly on subtracting a background signal. (iii) Applying microwaves and changing the sample temperature influenced the switching-current levels substantially. To

make the flux signal of all data sets comparable, we scaled all data sets to $I_{\text{SW}} = 100$ nA at $\Phi_{\text{ext}} = 1/2\Phi_0$. Any uncertainty coming from this scaling is accounted for in the error bars in Figs. 3 and 4. Data taken in the presence of microwaves could only be obtained at specific frequencies where I_{SW} was not strongly suppressed by the microwaves. At temperatures above 300 mK, drift in the I_{SW} level due to thermal instabilities of the refrigerator obscured the signal.

33. A. J. Leggett *et al.*, *Rev. Mod. Phys.* **59**, 1 (1987).

34. N. Prokof'ev, P. Stamp, *Rep. Prog. Phys.* **63**, 669 (2000) (e-Print available at <http://xxx.lanl.gov/abs/cond-mat/0001080>).

35. L. Tian *et al.*, in *Quantum Mesoscopic Phenomena and Mesoscopic Devices in Microelectronics, Proceedings of a NATO-ASI Workshop*, in press (e-Print available at <http://xxx.lanl.gov/abs/cond-mat/9910062>).

36. M. Grifoni, P. Hänggi, *Phys. Rep.* **304**, 229 (1998).

37. For an in-depth discussion on macro-realism, see the essays of A. J. Leggett and A. Shimony in *Quantum Measurement: Beyond Paradox*, R. A. Healey, G. Hellman, Eds. (Univ. of Minnesota Press, Minneapolis, 1998), pp. 1–31.

38. We thank J. B. Majer, A. C. Wallast, L. Tian, D. S. Crankshaw, J. Schmidt, A. Wallraff, L. Levitov, and D. Esteve for help and for stimulating discussions. This work was financially supported by the Dutch Foundation for Fundamental Research on Matter (FOM), the European TMR research network on superconducting nanocircuits (SUPNAN), the U.S. Army Research Office (grant DAAG55-98-1-0369), and the NEDO joint research program (NTDP-98).

11 July 2000; accepted 8 September 2000

REPORTS

Triple Vortex Ring Structure in Superfluid Helium II

Demosthenes Kivotides, Carlo F. Barenghi,* David C. Samuels

Superfluids such as helium II consist of two interpenetrating fluids: the normal fluid and the superfluid. The helium II vortex ring has generally been considered merely as a superfluid object, neglecting any associated motion of the normal fluid. We report a three-dimensional calculation of the coupled motion of the normal-fluid and superfluid components, which shows that the helium II vortex ring consists of a superfluid vortex ring accompanied by two coaxial normal-fluid vortex rings of opposite polarity. The three vortex rings form a coherent, dissipative structure.

Vortex rings (I) have long been studied as ideal examples of organized flow structures. A large body of literature has been concerned with vortex rings in a zero-viscosity (inviscid) fluid in which the vortex core thickness is much smaller than the ring's radius. This mathematical idealization is realized in a quantum fluid (2, 3), helium II, which is a superposition of two fluid components: the normal fluid (which is a fluid with nonzero viscosity) and the superfluid (an inviscid fluid). The concept of the superfluid vortex ring (4) or loop has contributed to many advances

in superfluidity, ranging from vortex creation (5, 6) to turbulence (7–10). An example of this is the fundamental issue of quantum mechanical phase coherence and the onset of dissipation. Ions injected into superfluid helium II move without friction, provided that the speed does not exceed a critical value (11) above which superfluid vortex rings are created (5). Vortex creation (12, 13) and motion (14, 15) have been studied theoretically using various models and are also being investigated by atomic physicists in the context of Bose-Einstein condensation in clouds of alkaline atoms (15, 16). The concept of the vortex ring has been applied to interpretations of the nature of the roton (17–19) and the superfluid transition itself (20). Finally, vortex rings are important in the study of super-

fluid turbulence, which manifests itself as a disordered tangle of superfluid vortex loops (distorted vortex rings). Superfluid vortex lines may also end at walls, or at free surfaces, without forming closed loops. For simplicity, we will consider here a circular superfluid vortex ring, but our results should also apply to all superfluid vortex lines.

Recent experiments, such as the observation of decay rates of superfluid vorticity (21, 22) consistent with the decay rates of Navier-Stokes turbulence, motivate our study of the dynamical coupling between the superfluid vorticity and the normal-fluid component. Superfluid vorticity scatters (23) the thermal excitations that make up the normal fluid, producing a mutual friction acting on the velocity fields \mathbf{V}_s and \mathbf{V}_n of the two fluid components of helium II. Although the superfluid vorticity can be detected directly by the second sound technique (21), very little is actually known about the normal-fluid flow because we have no practical flow visualization techniques near absolute zero. We present results of a three-dimensional calculation in which \mathbf{V}_n and \mathbf{V}_s are determined self-consistently. The calculation reveals the surprising triple structure of the helium II vortex ring. We also discuss the implications of this finding for the interpretation of current turbulence experiments.

Our method is based on an improvement over the vortex dynamics approach of Schwarz (24, 25), who modeled a superfluid vortex line as a curve $\mathbf{S}(\xi, t)$ that obeys the

Mathematics Department, University of Newcastle, Newcastle upon Tyne NE1 7RU, UK.

*To whom correspondence should be addressed. E-mail: c.f.barenghi@ncl.ac.uk

Chernogolovka 2000: Mesoscopic and strongly correlated electron systems

6. Quantum computing

Macroscopic quantum superposition of current states in a Josephson-junction loop

F K Wilhelm, C H van der Wal, A C J ter Haar,
R N Schouten, C J P M Harmans, J E Mooij,
T P Orlando, S Lloyd

Abstract. Superconducting circuits with Josephson tunnel junctions are interesting systems for research on quantum-mechanical behavior of macroscopic degrees of freedom. A particular realization is a small superconducting loop containing three Josephson junctions. Close to magnetic frustration $1/2$, the physics of this system corresponds to a double well, whose minima correspond to persistent currents of opposite sign. We present DC measurements of the flux indicating a smooth transition close to the degeneracy point even at very low temperatures. Furthermore, microwave-spectroscopy experiments allow for the excitation to the next excited state. The dependence of the energy of the resonance on the applied flux clearly indicates the nature of these states as tunneling-split superpositions of flux states. We theoretically analyze the system using a generalized master-equation formulation of the spin-boson model. We address the nature of the measuring process by a switching DC SQUID and the possible interpretation of the spectroscopy data in terms of quantum coherence. We discuss these aspects in the context of further applications as a quantum bit.

1. Introduction: qubits and MQC

Since the formulation of quantum mechanics, its concepts have been heavily disputed. They can now be directly verified in the microscopic world of systems with very few degrees of freedom such as NMR, ion traps, or cavity QED. With present-day technology, such microscopic systems can be controlled externally. This has led to the proposal of a quantum computer, which makes explicit use of the possibility to create superpositions and allows to solve certain computational problems with a qualitatively reduced number of steps (see [1] for a recent review). The

aforementioned quantum systems have been used to demonstrate few-bit quantum computation, however, it appears to be very difficult if at all possible to integrate them into larger circuits.

Solid state electronics, on the other hand, can be very easily integrated. Moreover, in the field of mesoscopic physics, and in particular in mesoscopic superconductivity, genuine quantum-mechanical phenomena have already been demonstrated. This makes mesoscopic superconductors a candidate for the realization of quantum computation [2–5]. More specifically, we propose to utilize persistent-current states of small superconducting loops containing at least three Josephson junctions [4]. These states correspond to the collective motion of all superconducting electrons in the loop, hence they are macroscopic [6].

In this contribution, we are going to briefly outline the idea of our device [4] and present experimental results tracing the ground state as well as results of microwave spectroscopy [7]. The data show clear evidence of anti-crossing of energy levels, hence proving that around degeneracy, the system's eigenstates are superpositions of the two basis current states. The results will be further discussed in terms of macroscopic quantum superpositions and coherence. By creating a superposition of these states, which is necessary for quantum computation, we also address a fundamental issue in quantum mechanics: a Schrödinger's cat state. We acknowledge that the mere superposition does not exclude alternative theories for quantum mechanics (e.g. macrorealistic theories [8]). This would require a type of experiment as proposed by Leggett et al. [9].

2. The device

A single small Josephson tunnel junction with a capacitance C and a coupling energy E_J can be represented as a particle of mass C in a periodic potential, where the phase ϕ represents the coordinate, and the number of Cooper pairs is the conjugate momentum. Our system (Fig. 1a), consists of a micrometer-sized loop of negligible geometric inductance penetrated by a magnetic flux Φ_{ext} close to half a

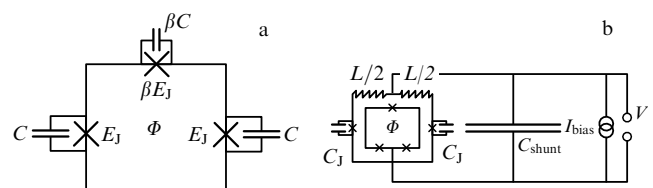


Figure 1. Schematic drawing of the qubit (a) and the measuring circuit (b). Crosses indicate Josephson junctions.

F K Wilhelm, C H van der Wal, A C J ter Haar, R N Schouten,
C J P M Harmans, J E Mooij Department of Applied Physics and
DIMES, Delft University of Technology, Lorentzweg 1, 2628 CJ Delft,
The Netherlands

J E Mooij, T P Orlando Department of Electrical Engineering and
Computer Science, Massachusetts Institute of Technology, Cambridge
MA, USA

S Lloyd Department of Mechanical Engineering, Massachusetts Institute
of Technology, Cambridge MA, USA

superconducting flux quantum Φ_0 . The loop contains three such junctions, whose phases are locked together by the applied flux due to the phase quantization condition, hence leading to a two-dimensional coordinate space. It has been demonstrated [4, 5], that by proper choice of the junction parameters, this effective potential is a periodic pattern of local double wells, whose minimums correspond to clock- and counter-clockwise supercurrent, respectively. The double wells are separated by strong potential barriers such that they are mutually very well uncoupled, whereas the barrier within a double well is sufficiently weak such that it can be overcome by quantum tunneling. The energy of the two minima can be controlled by tuning the applied external flux away from $\Phi_0/2$. The system parameters can be chosen such that there is only one bound state in each well. This renders the low-temperature (less than 100 mK) physics of the system equivalent to a two-level system. It has been predicted [10], that the intrinsic sources of noise and decoherence (quasi-particles, nuclear spins ...) allow for quantum-coherent behavior up to a decoherence time of $\tau_\phi = 1$ ms.

This setup invokes some key ideas of the ‘conventional’ MQC-proposal using an RF-SQUID [9, 11], with the key difference that no self-inductance is needed in order to form the double-well potential. This allows for much smaller loop sizes and hence facilitates the decoupling from environmental noise. Nevertheless, results similar to ours have recently been obtained in an RF-SQUID [12]. Other observations that have been related to macroscopic superposition states are tunnel splittings observed with magnetic molecular clusters [13] and quantum interference of C_{60} molecules [14]. In quantum dots [15] and superconducting circuits where charge effects dominate over the Josephson effect [16, 17] superpositions of charge states as well as quantum-coherent charge oscillations [18] have been observed.

The state of the qubit can be read out by a DC-SQUID magnetometer which detects the flux produced by the circulating current. Due to the small inductance of the system, this signal is only a small fraction of Φ_0 . Moreover, according to first principles of quantum mechanics, any measuring device (or ‘meter’) tends to decohere the quantum state. As we expect the quantum coherence to be very fragile, this property deserves special attention. In order to ensure sufficient coherence we have to guarantee that (i) the meter does not decohere the system while not measuring and (ii) the meter registers the result before the relaxation time, i.e. after the macroscopic environment constituted by the meter has put the qubit into a thermal mixture of states, wiping out the signatures of the initial state.

This decoherence is realized through the coupling to the external impedance. The measuring SQUID has two macroscopic phase degrees of freedom, which we choose as follows: one is associated with the circulating current in the SQUID’s loop (internal degree of freedom), the other is associated with the bias current through the SQUID (external degree of freedom). As the bias current is ramped up, the coupling between these two degrees of freedom increases strongly, due to the nonlinearity of the SQUID’s current-phase relations [19]. The external variable is coupled to a dissipative environment. The internal degree of freedom has negligible intrinsic damping and the associated mass (i.e. the capacitance of the junctions of the SQUID) is very small. This means that the circulating current is non-dissipative and does not disturb the system, i.e. there is little dephasing as long as we do not apply a measuring current.

In order to further minimize the unwanted decoherence in our device, we use a setup which uses only very few dissipative elements: an undamped SQUID with unshunted junctions with low critical current and no extra resistors. In order to still reduce fluctuations of the SQUID, it was made ‘heavy’ by shunting with a large superconducting capacitor.

This SQUID has a highly hysteretic $I-V$ characteristic [19]. The flux is determined through the switching current which provides a measure for the effective Josephson coupling across the SQUID. The escape to a voltage state is a stochastic process, which leads to a wide spread of those switching currents (see, e.g. [20] for an overview). The width of the switching current histogram in our experiments corresponds to a standard deviation in the flux readout of $11 \times 10^{-3} \Phi_0$, so the uncertainty in flux readout is much larger than the flux signal from the qubit $2MI_p \approx 3 \times 10^{-3} \Phi_0$. This width is much bigger than expected from simple theoretical models [20]. This may be due to quantum fluctuations of the circulating current (and consequently the total flux through the SQUID) and is subject of enduring investigation. In order to obtain the results presented in this paper, substantial statistical averaging over repeated measurements was necessary in order to get sufficient resolution. Consequently only ensemble-averaged quantities can be measured.

3. Experiments

The system was realized by microfabricating a micrometer-sized aluminum loop with unshunted Josephson junctions, using the technology described in Ref. [21]. Around the loop we fabricated the DC-SQUID magnetometer (Fig. 1b), with smaller Josephson junctions that were as underdamped as the junctions of the inner loop. Loop parameters estimated from test junctions fabricated on the same chip and electron-microscope inspection of the measured device give a critical current amplitude $I_{C0} = 570 \pm 60$ nA and $C = 2.6 \pm 0.4$ fF for the largest junctions in the loop. The size of the small junction is reduced by a factor $\beta = 0.82 \pm 0.1$, giving $E_J/E_{Ch} = 38 \pm 8$ and a circulating current in one of the potential minima of $I_p = 450 \pm 50$ nA. These parameters allow for a tunnel matrix element t/h between 0.2 and 5 GHz. The parameters of the DC-SQUID junctions were $I_{C0} = 109 \pm 5$ nA and $C_S = 0.6 \pm 0.1$ fF. The self-inductance of the inner loop and the DC-SQUID loop were estimated to be 11 ± 1 pH and 16 ± 1 pH respectively, and the mutual inductance M between the loop and the SQUID was 7 ± 1 pH.

4. Ground state measurements

In a first series of experiments, we have detected the flux produced by the qubit as a function of the static bias flux. We compare it to the expectation value for a quantum-mechanical two-level system coupled to a bath at temperature T ,

$$\langle \Phi_q \rangle = \Phi_a \frac{\epsilon}{\Delta E} \tanh\left(\frac{\Delta E}{2k_B T}\right), \quad (1)$$

where Φ_a is the flux produced when the system is purely in one of the classical states, $\Delta E = (\epsilon^2 + 4t_{\text{eff}}^2)^{1/2}$ is the energy splitting of the quantum-mechanical levels and $\epsilon = \epsilon(\Phi_{\text{ext}}) \propto \Phi - \Phi_0/2$ is the energy difference of the classical states. In general, this function shows a step around $\epsilon = 0$, which is

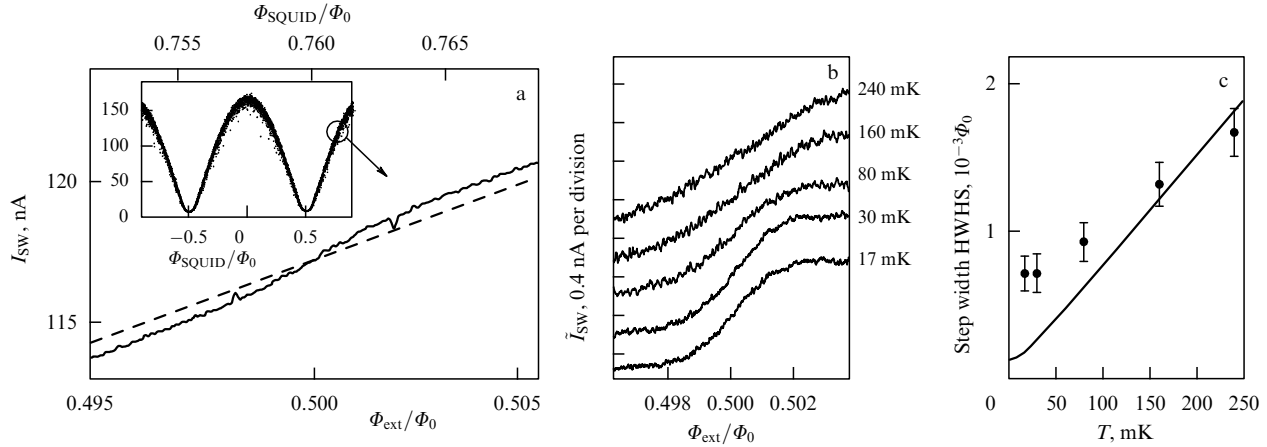


Figure 2. Switching-current levels of the DC-SQUID versus applied flux. (a) The main figure shows the averaged level of I_{SW} (solid line) near $\Phi_{ext} \approx \Phi_0/2$ which happens to be $\Phi_{SQUID} = 0.76 \Phi_0$ and the rounded step at $\Phi_{ext} = \Phi_0/2$ indicates the change of sign in the persistent current. The spikes are due to additionally applied microwaves. The inset shows the modulation of I_{SW} versus the flux Φ_{SQUID} applied to the DC-SQUID loop (data not averaged, one point per switching event). (b) Measured qubit flux from the qubit for different temperatures. The background signal resulting from flux directly applied to the SQUID-loop is subtracted. (c) Analysis of the step width (half-width at half-step, HWHS). The solid line corresponds to the extrapolation of equation (1), assuming the spectroscopically measured t_{eff} .

rounded due to thermal and quantum fluctuations. As $T \rightarrow 0$, the system is in its ground state and quantum fluctuations dominate. Any residual rounding is controlled by a finite tunneling matrix element t_{eff} and indicates that the ground state close to the degeneracy point is a superposition.

Experimentally, the step occurs on top of the bias flux through the SQUID (see Fig. 2a). The step width decreases with temperature (see Fig. 2b) but stays finite. The observed step width is even much broader than expected from quantum rounding on the scale of the value of t that was found with spectroscopy (see Fig. 2c). The width saturates at an effective temperature of about 100 mK. The high effective temperature of the loop can be the result of heating induced by the DC-SQUID after the switching. As the qubit is well isolated from the environment, this heat only relaxes very slowly.

5. Spectroscopy

On top of the DC-flux, which fixes the energy bias ϵ of our two-level system, we periodically modulate ϵ using continuous microwaves. Figure 3a shows the flux signal of the inner loop. On top of the step described in the previous section, each trace shows a peak and a dip symmetrically around $\Phi_{ext} = \Phi_0/2$, which were absent when no microwaves were applied. The positions of the peaks and dips in Φ_{ext} depend on microwave frequency f but not on amplitude. They reflect microwave-induced transitions to the state with a persistent current of opposite sign, they occur when the microwave frequency is resonant with the energy splitting $\Delta E = hf$. As the frequency is lowered, the resonances are moving towards the center, Fig. 3a.

In Figure 3b half the distance in Φ_{ext} between the resonant peak and dip is plotted for all frequencies f , which represents $\Delta E(\epsilon)$. The relation between ΔE and Φ_{ext} is linear at high frequencies. The slope of this part translates into $I_p = 484 \pm 2$ nA, in good agreement with the predicted value. At lower frequencies the energy splitting levels off, hence indicating a finite tunnel splitting of $t_{eff}/h \approx 0.33 \pm 0.03$ GHz. The level separation very close to $\Phi_0/2$ could not be measured directly since at this point the

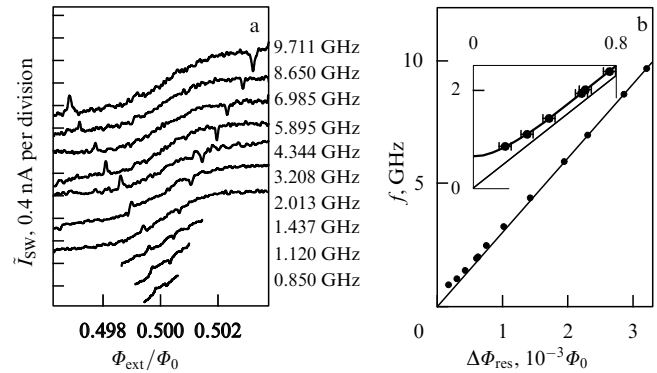


Figure 3. Results of cw-microwave spectroscopy. (a) Traces at fixed frequency showing resonances corresponding to pumping to the respective excited state. Symmetrically around $\Phi_0/2$ the signal shows a peak and a dip, which are only observed with measurements in the presence of the microwaves. They are due to resonant transitions between the loop's two quantum levels (see Fig. 2). Different curves represent different values of Φ_{ext} , measured at different microwave frequencies f (labels on the right). (b) Resonance positions are a clear indication of an anti-crossing. Half the distance in Φ_{ext} between the resonant peak and dip $\Delta\Phi_{res}$ at different microwave frequencies f (f is plotted on the vertical axis). Peak and dip positions are determined from traces as in Fig. 2a. At high frequencies the $\Delta\Phi_{res}$ values are proportional to the microwave frequency. The inset: the thin line is a linear fit through the high frequency data points and zero. The thick line is a fit of the energy eigenvalues with only the tunnel coupling t as a fitting parameter, yielding $t_{eff}/h = 0.33 \pm 0.03$ GHz.

expectation value for the persistent current is zero for both the ground state and the excited state. The measured value of t is compatible with the predicted value of t . As the predicted value depends exponentially on sample parameters and hence has a substantial uncertainty, a quantitative analysis of a possible suppression of t_{eff} due to a bosonic [22] or spin-bath [23] environment is not possible. The fact that we see a finite tunnel splitting indicates that the damping of our quantum system by environmental degrees of freedom is weak. The dimensionless dissipation parameter α [22] must be $\alpha < 1$.

This level repulsion close to the degeneracy point clearly indicates that the eigenstates, between which the transitions

occur, are superpositions of the localized basis states. At $\Phi_{\text{ext}} = \Phi_0/2$, these are symmetric and antisymmetric superpositions of the two classical persistent-current states which have respectively lower and higher energies than the localized classical states.

6. Nonlinear regime

In Figure 4a we show the dip at a fixed frequency of 5.895 GHz for different microwave amplitudes. The dip amplitude and the full width at half the maximum amplitude (FWHM) were extracted by fitting a Lorentzian peak shape to the data. Figure 4b shows that the dip amplitude increases rapidly for microwave amplitudes up to $V_{\text{AC}} \approx 2$ a. u., followed by a saturation for larger microwave amplitudes. The saturated dip amplitude is ≈ 0.25 nA, which is close to half the full step height of the rounded step at $\Phi_0/2$ (≈ 0.4 nA) in Fig. 2b. This indicates that on resonance the energy levels are close to being equally populated, as expected for continuous pumping.

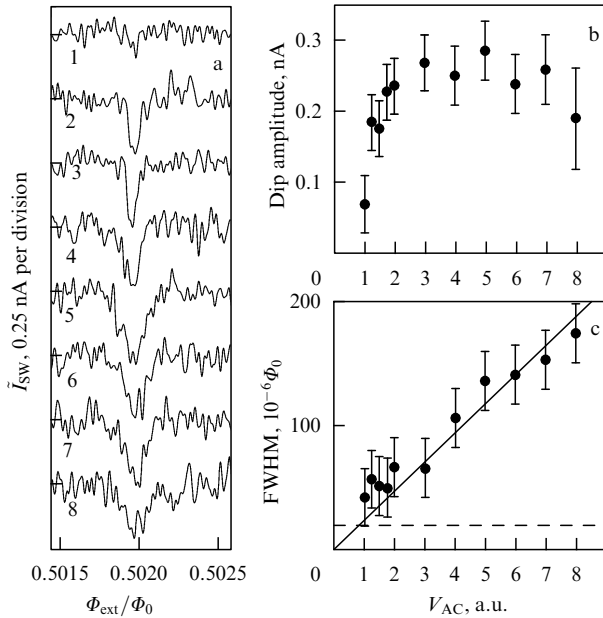


Figure 4. Results of cw-microwave spectroscopy at fixed frequency but different power. (a) The influence of the microwave amplitude on the shape of the resonance dip in the scaled switching current I_{SW} , measured at 5.895 GHz (the labels on the left give the amplitude V_{AC} in a.u.). (b) Resonance amplitude first increases with microwave amplitude V_{AC} , but saturates at $V_{\text{AC}} > 2$ a.u. (c) Resonance width as a function of the microwave power. The full-width-half-maximum (FWHM) of the dips increases with V_{AC} . The linear fit through the highest data points and zero is a guide to the eye. The horizontal dashed line is at a flux value that corresponds to the shift in effective flux bias Φ_{ext} that is induced when the bias current is ramped through the DC-SQUID. This acts as a flux instability with an amplitude of $\approx 20 \times 10^{-6}\Phi_0$. Resonance lines with a FWHM below this value cannot be observed.

Figure 4c shows a linear dependence between the FWHM and the microwave amplitude, as we would expect it for the Rabi resonance of a strongly and coherently driven two-level system [24]: the linear dependence of the FWHM on microwave amplitude in Fig. 4c suggests that the linewidth is indeed dominated by the frequency of microwave-induced Rabi transitions. In the presence of weak decoherence, the

Rabi oscillations decay over a time T_2 into a stationary mixture of ‘eigenstates’ of the driven system known as Floquet states. After T_2 , transitions between those states only occur due to incoherent processes. Even in this case, the peaks remain narrow Lorentzians [25, 26] which depend on the external parameters analogously to Rabi peaks: the FWHM of the Lorentzian resonance line is proportional to the amplitude of the monochromatic driving [24]. This allows to observe narrow resonances even after T_2 . Using the linear relation between ΔE and Φ_{ext} for Φ_{ext} values away from $\Phi_0/2$, the observed FWHM in Φ_{ext} units can be expressed in frequency units. This indicates a Rabi frequency of, for example, 150 MHz at $V_{\text{AC}} = 4$ a.u.

The loss of dip amplitude and the apparent saturation of the FWHM at low V_{AC} is either caused by variations in the flux bias Φ_{ext} (corresponding to inhomogeneous broadening for the ensemble average [27]) or by an intrinsic dephasing mechanism. The effective dephasing time T_2^* [27] can be deduced from the FWHM at low V_{AC} . The FWHM (expressed in energy units) of a resonance-line shape that is dominated by a finite dephasing time corresponds to $2\hbar/T_2^*$ [24, 27]. From our data, we find $T_2^* \approx 5$ ns, which allows for a few Rabi cycles. This is another hint on the presence of coherent Rabi dynamics, however, only time-resolved measurements would be fully conclusive. Possible sources for the relatively short value of T_2^* will be discussed in the following Section.

7. Discussion

The DC-SQUID performs a measurement on a single quantum system. As described above, our setup in principle still allows for reasonable dephasing and mixing times. The external electronics limits the ramping speed, so the SQUID is coupled to the qubit longer than theoretically required and is consequently strongly dephasing the qubit prior to the actual measurement. This can be avoided in future experiments by the use of more efficient measuring schemes.

The loss of dip amplitude in Fig. 4 is probably not due to the noise, but due to a small deterministic contribution to the effective Φ_{ext} from the circulating current in the DC-SQUID. The SQUID is operated at $0.76\Phi_0$ in its loop, where its circulating current depends on the bias current due to its nonlinear behavior [19], so the readout happens at a bias flux slightly altered due the SQUID. This bias flux depends on the switching current level, which in turn has a broad spread due to the large histograms described in the beginning of this paper. This means that data recorded by switching events for low bias side of I_{bias} differ in flux bias on the inner loop from that of the high current levels by $20 \times 10^{-6}\Phi_0$. Resonance lines at low V_{AC} (i. e. with a FWHM $< 20 \times 10^{-6}\Phi_0$) cannot be observed as the peaks and dips smear out when averaging over many switching events. The loss of dip amplitude and the apparent saturation of the FWHM at low V_{AC} is probably dominated by this mechanism for inhomogeneous line broadening and *not* by dephasing.

8. Concluding remarks and future prospects

We show clear experimental evidence of level repulsion in a small superconducting loop containing three Josephson junctions, which can behave as a macroscopic quantum two-level system. We demonstrate a useful readout for the magnetization of the loop scheme by an underdamped DC-SQUID.

This demonstrates the potential of these loops for further work on macroscopic quantum coherence and solid-state quantum computing. This requires quantum state control with pulsed microwaves and development of measurement schemes that are less invasive. Multiple qubit circuits with controlled coupling are within reach using present-day technology.

We thank J B Majer, A C Wallast, L Tian, D S Crankshaw, J Schmidt, A Wallraff, L S Levitov, M Grifoni, and D Esteve for help and stimulating discussions. This work was financially supported by the Dutch Foundation for Fundamental Research on Matter (FOM), the European TMR Research Network on Superconducting Nanocircuits (SUPNAN), the USA Army Research Office (Grant DAAG55-98-1-0369) and the NEDO Joint Research Program (NTDP-98).

References

1. Bennet C H, DiVincenzo D *Nature* **404** 247 (2000)
2. Makhlin Yu, Schön G, Shnirman A *Nature* **398** 305 (1999)
3. Ioffe L B et al. *Nature* **398** 679 (1999)
4. Mooij J E et al. *Science* **285** 1036 (1999)
5. Orlando T P et al. *Phys. Rev. B* **60** 15398 (1999)
6. Anderson P W, in *Lectures on the Many-Body Problem* Vol. 2 (Ed. E R Caianiello) (New York: Academic Press, 1964) p. 113; Leggett A J *Prog. Theor. Phys. Suppl.* **69** 80 (1980); Likharev K K *Usp. Fiz. Nauk* **139** 169 (1983) [*Sov. Phys. Usp.* **26** 87 (1983)]
7. Van der Wal C H et al. *Science* **290** 773 (2000)
8. For an in-depth discussion on macrorealism see the essays of Leggett A J, Shimony A, in *Quantum Measurement: Beyond Paradox* (Eds R A Healey, G Hellman) (Minneapolis: Univ. Minnesota Press, 1998) p. 1
9. Leggett A J, Garg A *Phys. Rev. Lett.* **54** 857 (1985)
10. Tian L et al., in *Quantum Mesoscopic Phenomena and Mesoscopic Devices in Microelectronics* (Dordrecht: Kluwer, 2000) p. 429
11. Leggett A J *J. Supercond.* **12** 683 (1999)
12. Friedman J R et al. *Nature* **406** 43 (2000)
13. Wernsdorfer W, Sessoli R *Science* **284** 133 (1999)
14. Arndt M et al. *Nature* **401** 680 (1999)
15. Oosterkamp T H et al. *Nature* **395** 873 (1998)
16. Nakamura Y, Chen C D, Tsai J S *Phys. Rev. Lett.* **79** 2328 (1997)
17. Bouchiat V et al. *Phys. Scripta T* **76** 165 (1998)
18. Nakamura Y, Pashkin Yu A, Tsai J S *Nature* **398** 786 (1999)
19. Tinkham M *Introduction to Superconductivity* (New York: McGraw-Hill, 1996)
20. Martinis J M, Devoret M H, Clarke J *Phys. Rev. B* **35** 4682 (1987)
21. Van der Wal C H, Mooij J E *J. Supercond.* **12** 807 (1999)
22. Leggett A J et al. *Rev. Mod. Phys.* **59** 1 (1987)
23. Prokof'ev N, Stamp P *Rep. Prog. Phys.* **63** 669 (2000); cond-mat/0001080
24. Cohen-Tannoudji C, Diu B, Laloë F *Quantum Mechanics* Vol. 1 (New York: Wiley, 1977) p. 443
25. Wilhelm F K, Grifoni M (in preparation)
26. Grifoni M, Hänggi P *Phys. Rep.* **304** 229 (1998)
27. Abragam A *Principles of Nuclear Magnetism* (Oxford: Oxford Univ. Press, 1961) p. 39

Quantum Andreev interferometer in an environment

Y M Gal'perin, L Y Gorelik, N I Lundin, V S Shumeiko, R I Shekhter, M Jonson

Abstract. The influence of a noisy environment on coherent transport in Andreev states through a point contact between two superconductors is considered. The amount of dephasing is estimated for a microwave-activated quantum interferometer. Possibilities of experimentally investigating the coupling between a superconducting quantum point contact and its electromagnetic environment are discussed.

1. Introduction

The assumption of coherent transport in Andreev states in a superconducting quantum point contact (SQPC) is widely used in theoretical work, see, e.g., the items of Ref. [1]. However, in realistic systems, interactions with a dynamical environment will always introduce some amount of dephasing, see the items of Ref. [2] for a review.

The so-called microwave-activated quantum interferometer (MAQI) [3] is a device proposed as a tool to study the dynamics of Andreev levels (ALs), present in a superconducting point contact. It is based on a short, single-mode, weakly biased SQPC which is subject to microwave irradiation. Confined to the contact area there are current-carrying Andreev states. The corresponding energy levels — Andreev levels — are found in pairs within the superconductor energy gap Δ , one below and one above the Fermi level. If an SQPC is short ($L \ll \xi_0$ where L is the length of the junction while ξ_0 is the superconductor coherence length), there is only one pair of Andreev levels and their positions depend on the order parameter phase difference, ϕ , across the contact as

$$E_{\pm} = \pm E(\phi) = \pm \Delta \sqrt{1 - D \sin^2\left(\frac{\phi}{2}\right)}. \quad (1)$$

The two states carry current in opposite directions and in equilibrium at low temperature only the lower state is populated. The applied bias, V , through the Josephson relation $\dot{\phi} = 2eV/\hbar$, forces the Andreev levels to move adiabatically within the energy gap with a period of $T_p = \hbar\pi/eV$, see Fig. 1.

The microwave field induces Landau – Zener (LZ) transitions between the Andreev levels (indicated by wavy lines in Fig. 1). If the upper level is populated after the second transition, a delocalized quasi-particle excitation will be created when this Andreev level merges with the continuum. The result will be a dc contribution to the current. Further, this current exhibits an interference pattern since there are two paths with different phase gains available to the upper

Y M Gal'perin University of Oslo, P. O. Box 1048 Blindern, N-0316 Oslo Norway

A F Ioffe Institute of the Russian Academy of Sciences, 194021 St. Petersburg, Russian Federation

L Y Gorelik, N I Lundin, V S Shumeiko, R I Shekhter, M Jonson Chalmers University of Technology, Department of Applied Physics, and Göteborg University, 412 96 Göteborg, Sweden

MACROSCOPIC QUANTUM SUPERPOSITION IN A THREE-JOSEPHSON-JUNCTION LOOP

Caspar H. van der Wal¹, A. C. J. ter Haar¹, F. K. Wilhelm¹,
R. N. Schouten¹, C. J. P. M. Harmans¹, T. P. Orlando²,
Seth Lloyd³, J. E. Mooij^{1,2}

¹*Department of Applied Physics and*

Delft Institute for Micro Electronics and Submicron Technology (DIMES)

Delft University of Technology, P. O. Box 5046, 2600 GA Delft, the Netherlands

²*Department of Electrical Engineering and Computer Science and*

³*Department of Mechanical Engineering, MIT, Cambridge, MA 02139, USA*

Corresponding author, e-mail: caspar@qt.tn.tudelft.nl

Submitted for the proceedings of the MQC² workshop, Naples, June 14-17, 2000.

Abstract We present microwave-spectroscopy experiments on two quantum levels of a superconducting loop with three Josephson junctions. The level separation between the ground state and first excited state shows an anti-crossing where two classical persistent-current states with opposite polarity are degenerate. This is evidence for symmetric and anti-symmetric quantum superpositions of two macroscopic states; the classical states have persistent currents of $0.5 \mu\text{A}$ and correspond to the center-of-mass motion of millions of Cooper pairs. A study of the thermal occupancies of the two quantum levels shows that the loop is at low temperatures in a non-equilibrium state.

1. INTRODUCTION

A Josephson supercurrent is a macroscopic degree of freedom in the sense that it corresponds to the center-of-mass motion of a condensate with a very large number of Cooper pairs [1]. Even though the Josephson effect itself (with classical current and voltage variables) is often called a macroscopic quantum phenomena, Anderson [1], Leggett [2] and Likharev [3] discussed that a quantum superposition of Josephson currents would be a "true" [3] manifestation of quantum mechanics at a macroscopic scale. A simple system in which such a superposition can be studied is a superconducting loop containing one or more Josephson

tunnel junctions, where an external magnetic field is used to induce a persistent current in the loop. When the enclosed magnetic flux is close to half a superconducting flux quantum Φ_0 , the loop may have multiple stable persistent-current states. The weak coupling of the Josephson junctions then allows for transitions between the states. At very low temperatures, the persistent-current states are very well decoupled from environmental degrees of freedom; excitations of individual charge carriers around the center of mass of the Cooper-pair condensate are prohibited by the superconducting gap. As a result, the transitions between the states can be a quantum coherent process, and superpositions of the macroscopic persistent-current states should be possible (loss of quantum coherence results from coupling to an environment with many degrees of freedom [4]). Josephson junction loops therefore rank among the best systems for experimental tests of the validity of quantum mechanics for systems containing a macroscopic number of particles [2, 5]. The potential for quantum coherent dynamics has stimulated research aimed at applying Josephson junction loops as basic building blocks for quantum computation (qubits) [6, 7, 8, 9].

We report in this chapter on microwave-spectroscopy experiments that demonstrate quantum superpositions of two macroscopic persistent-current states in a small loop with three Josephson junctions (Fig. 1, this is the qubit system discussed in [8, 9]). At an applied magnetic flux of $\frac{1}{2}\Phi_0$ this system behaves as a particle in a double-well potential, where the classical states in each well correspond to persistent currents of opposite sign (Fig. 1c). The two classical states are coupled via quantum tunneling through the barrier between the wells, and the loop is a macroscopic quantum two-level system. The energy levels vary with the applied flux as shown. While classically the levels should cross at $\frac{1}{2}\Phi_0$, quantum tunneling leads to an avoided crossing with symmetric and anti-symmetric superpositions of the two macroscopic persistent-current states. An inductively coupled DC-SQUID magnetometer was used to measure the flux generated by the loop's persistent current, while at the same time low-amplitude microwaves were applied to induce transitions between the levels (Fig. 2). We observed narrow resonance lines at magnetic field values where the level separation ΔE was resonant with the microwave frequency. The level separation shows the expected anti-crossing at $\frac{1}{2}\Phi_0$ (Fig. 3), which is interpreted as evidence for macroscopic superposition states [10, 11]. A study of the thermal broadening of the transition between the two states at $\frac{1}{2}\Phi_0$ shows that the loop is at low temperatures in a non-equilibrium state (Fig. 4).

Note that we have a scheme in which the meter (the DC-SQUID) is performing a measurement on a single quantum system. We should

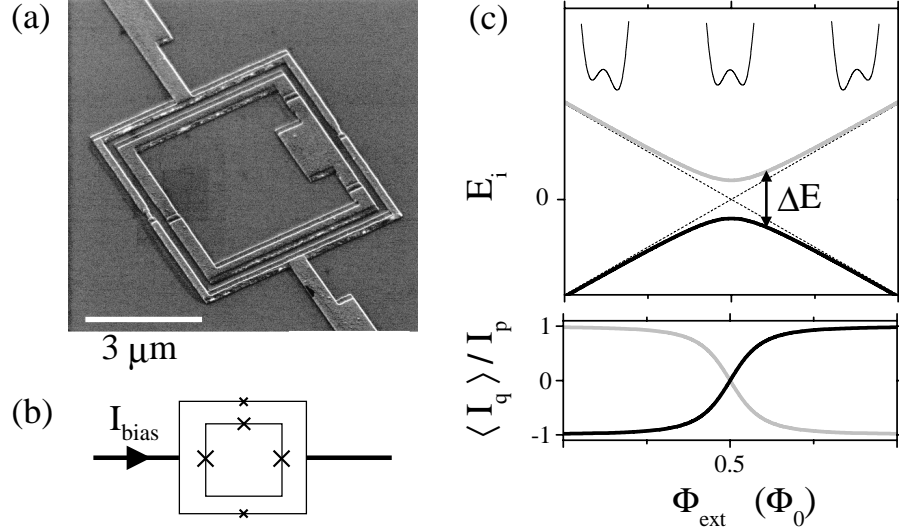


Figure 1 SEM-image (a) and schematic (b) of the small superconducting loop with three Josephson junctions (denoted by the crosses). The loop is inductively coupled to an underdamped DC-SQUID which is positioned around the loop. (c) Energy levels and persistent currents of the loop as a function of applied flux Φ_{ext} . The insets of the top plot show the double-well potential that is formed by the loop's total Josephson energy, plotted for a Φ_{ext} -value below $\frac{1}{2}\Phi_0$ (left), at $\frac{1}{2}\Phi_0$ (middle), and above $\frac{1}{2}\Phi_0$ (right). The horizontal axis for these potentials is a Josephson phase coordinate. The loop's two classical persistent-current states are degenerate at $\Phi_{\text{ext}} = \frac{1}{2}\Phi_0$ (dashed lines). The quantum levels (solid lines) show level repulsion at this point, and are separated in energy by ΔE . The bottom plot shows the quantum mechanical expectation value $\langle I_q \rangle = -\partial E_i / \partial \Phi_{\text{ext}}$ of the persistent current in the loop, for the ground state (black) and the excited state (grey), plotted in units of I_p .

therefore expect that the measuring process is limiting the coherence of our system. While the system is pumped by the microwaves, the SQUID is actively measuring the flux produced by the persistent currents of the two states. Detecting the quantum levels of the loop is still possible since the meter is only weakly coupled to the loop. The flux signal needs to be built up by averaging over many repeated measurements on the same system, such that effectively an ensemble average is determined (time-ensemble). We measure the level separation, i. e. energy, rather than flux, since we perform spectroscopy; we observe a shift in averaged flux when the microwaves are resonant with the level separation. In our experiment we also chose to work with an extremely underdamped DC-

SQUID with unshunted junctions to minimize damping of the quantum system via the inductive coupling to the SQUID.

A recent paper by Friedman *et al.* [12] reports on similar results obtained from spectroscopy on excited states in a loop with a single junction (RF-SQUID). Previous experiments on RF-SQUIDs have demonstrated resonant tunneling between discrete quantum states in two wells [13, 14] and microwave-induced transitions between the wells [15]. Other observations that have been related to macroscopic superposition states are tunnel splittings observed with magnetic molecular clusters [16] and quantum interference of C_{60} molecules [17]. In quantum dots [18] and superconducting circuits where charge effects dominate over the Josephson effect [19, 20, 21] superpositions of charge states have been observed, as well as quantum coherent charge oscillations [22].

A quantum description of our system was reported in Refs. [8, 9]. It is a low-inductance loop intersected by three extremely underdamped Josephson junctions (Fig. 1), which are characterized by their Josephson coupling E_J and charging energy $E_C = e^2/2C$. Here C is the junction capacitance and e the electron charge. The critical current of a junction is $I_{C0} = \frac{2e}{\hbar}E_J$, where $\hbar = \frac{h}{2\pi}$ is Planck's reduced constant. One of the junctions in the loop has E_J and C smaller by a factor $\beta \approx 0.8$. At an applied flux Φ_{ext} close to $\frac{1}{2}\Phi_0$ the total Josephson energy forms a double well potential. The classical states at the bottom of each well have persistent currents of opposite sign, with a magnitude I_p very close to I_{C0} of the weakest junction, and with energies $E = \pm I_p(\Phi_{\text{ext}} - \frac{1}{2}\Phi_0)$ (dashed lines in Fig. 1c). We assume here Φ_{ext} to be the total flux in the loop (the small self-generated flux due to the persistent currents leads to a constant lowering of the energies, but the crossing remains at $\frac{1}{2}\Phi_0$). The system can be pictured as a particle with a mass proportional to C in the Josephson potential; the electrostatic energy is the particle's kinetic energy. The charging effects are conjugate to the Josephson effect. For low-capacitance junctions (small mass) quantum tunneling of the particle through the barrier gives a tunnel coupling t between the persistent-current states. In the presence of quantum tunneling and for E_J/E_C -values between 10 and 100, the system should have two low-energy quantum levels E_0 and E_1 , which can be described using a simple quantum two-level picture [8, 9], $E_{0(1)} = -(+)\sqrt{t^2 + \left(I_p(\Phi_{\text{ext}} - \frac{1}{2}\Phi_0)\right)^2}$. The loop's level separation $\Delta E = E_1 - E_0$ is then

$$\Delta E = \sqrt{(2t)^2 + \left(2I_p(\Phi_{\text{ext}} - \frac{1}{2}\Phi_0)\right)^2}. \quad (1.1)$$

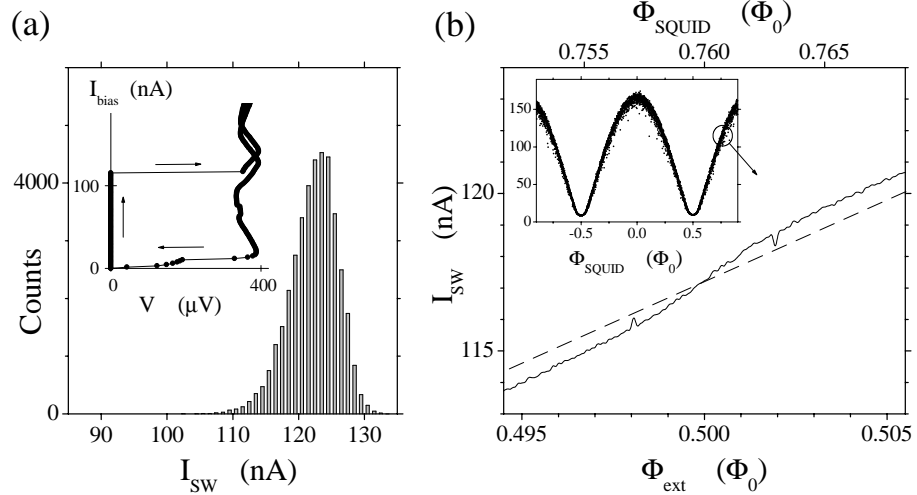


Figure 2 (a) Current-voltage characteristic (inset) and switching-current histogram of the underdamped DC-SQUID. The I_{bias} -level where the SQUID switches from the supercurrent branch to a finite voltage state –the switching current I_{SW} – is a measure for the flux in the loop of the DC-SQUID. The histogram in the main plot shows that the variance in I_{SW} is much larger than the flux signal of the inner loop’s persistent current, which gives a shift in I_{SW} of about 1 nA. (b) The inset shows the modulation of I_{SW} versus the flux Φ_{SQUID} applied to the DC-SQUID loop (data not averaged, one point per switching event). The main figure shows the averaged level of I_{SW} (solid line) near $\Phi_{\text{SQUID}} = 0.76 \Phi_0$. At this point the flux in the inner loop $\Phi_{\text{ext}} \approx \frac{1}{2} \Phi_0$. The rounded step at $\Phi_{\text{ext}} = \frac{1}{2} \Phi_0$ indicates the change of sign in the persistent current of the loop’s ground state. In the presence of continuous-wave microwaves (here 5.895 GHz) a peak and a dip appear in the signal, symmetrically around $\frac{1}{2} \Phi_0$. The background signal of the DC-SQUID that results from flux directly applied to its loop (dashed line) is subtracted from the data presented in Figs. 3a and 4a.

2. EXPERIMENTAL REALIZATION

The system was realized by microfabricating an aluminum micrometer-sized loop with unshunted Josephson junctions (Fig. 1a). The sample consisted of a $5 \times 5 \mu\text{m}^2$ aluminum loop with aluminum-oxide tunnel junctions, microfabricated with e-beam lithography and shadow-evaporation techniques on a SiO_2 substrate. The electrodes of the loop were 450 nm wide and 80 nm thick. The DC-SQUID magnetometer was fabricated in the same layer around the inner loop, with a $7 \times 7 \mu\text{m}^2$ loop and smaller Josephson junctions that were as underdamped as the junctions of the inner loop. The DC-SQUID had an on-chip superconducting shunt capacitance of 2 pF and superconducting leads in four-point con-

figuration. The sample was mounted in a dilution refrigerator, inside a microwave-tight copper measurement box, magnetically shielded by two mu-metal and one superconducting shield. All spectroscopy measurements were taken with the temperature stabilized at 30 ± 0.05 mK. Microwaves were applied to the sample by a coaxial line, which was shorted at the end by a small loop of 5 mm diameter. This loop was positioned parallel to the sample plane at about 1 mm distance. Switching currents were measured with dedicated electronics, with repetition rates up to 9 kHz and bias currents ramped at typically $1 \mu\text{A}/\text{ms}$ (further details of the fabrication and experimental techniques can be found in Ref. [23]). Loop parameters estimated from test junctions fabricated on the same chip and electron-microscope inspection of the measured device give $I_p = 450 \pm 50$ nA, $\beta = 0.82 \pm 0.1$, $C = 2.6 \pm 0.4$ fF for the largest junctions in the loop, giving $E_J/E_C = 38 \pm 8$. Due to the exponential dependence of the tunnel coupling t on the mass (C) and the size of the tunnel barrier, these parameters allow for a value for t/h between 0.2 and 5 GHz. The parameters of the DC-SQUID junctions were $I_{C0} = 109 \pm 5$ nA and $C = 0.6 \pm 0.1$ fF. The self inductance of the inner loop and the DC-SQUID loop were numerically estimated to be 11 ± 1 pH and 16 ± 1 pH respectively, and the mutual inductance between the loop and the SQUID was 7 ± 1 pH.

The flux in the DC-SQUID was measured by ramping a bias current through the DC-SQUID and recording the current level I_{SW} where the SQUID switches from the supercurrent branch to a finite voltage (Fig. 2a). Traces of the loop's flux signal were recorded by continuously repeating switching-current measurements while slowly sweeping the flux Φ_{ext} (Fig. 2b). The measured flux signal from the inner loop will be presented as \tilde{I}_{SW} , which is directly deduced from the raw switching-current data, as described in the following three points:

- 1) Because the variance in I_{SW} was much larger than the signature from the loop's flux (Fig. 2a) we applied low-pass FFT-filtering in Φ_{ext} -space (over 10^7 switching events for the highest trace, and $2 \cdot 10^8$ events for the lowest trace in Fig. 3a).
- 2) By applying Φ_{ext} we also apply flux directly to the DC-SQUID. The resulting background signal (dashed line in Fig. 2b) was subtracted.
- 3) Applying microwaves and changing the sample temperature influenced the switching current levels significantly. To make the flux signal of all data sets comparable we scaled all data sets to $I_{\text{SW}} = 100$ nA at $\Phi_{\text{ext}} = \frac{1}{2}\Phi_0$. Data taken in the presence of microwaves could only be obtained at specific frequencies where I_{SW} was not strongly suppressed by the microwaves. At temperatures above 300 mK drift in the I_{SW} -level due to thermal instabilities of the refrigerator obscured the signal.

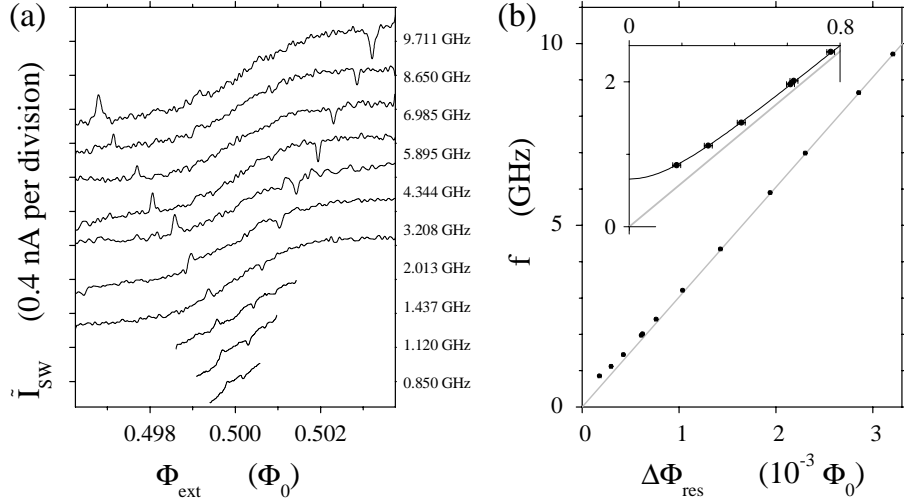


Figure 3 (a) Resonance lines in traces of the scaled switching current \tilde{I}_{SW} versus Φ_{ext} , measured at different microwave frequencies f (labels on the right). (b) Half the distance in Φ_{ext} between the resonant peak and dip $\Delta\Phi_{res}$ at different microwave frequencies f . Peak and dip positions are determined from traces as in Fig. 3a. The inset zooms in on the low frequency data points. The grey line is a linear fit through the high frequency data and zero. The black line is a fit of (1).

3. RESULTS

Figs. 2b and 3a show the flux signal of the inner loop, measured in the presence of low-amplitude continuous-wave microwaves at different frequencies f . The rounded step in each trace at $\frac{1}{2}\Phi_0$ is due to the change in direction of the persistent current of the loop's ground state (see also Fig. 1c). Symmetrically around $\Phi_{ext} = \frac{1}{2}\Phi_0$ each trace shows a peak and a dip, which were absent when no microwaves were applied. The positions of the peaks and dips in Φ_{ext} depend on microwave frequency but not on amplitude. The peaks and dips result from microwave-induced transitions to the state with a persistent current of opposite sign. These occur when the level separation is resonant with the microwave frequency, $\Delta E = hf$.

In Fig. 3b half the distance in Φ_{ext} between the resonant peak and dip $\Delta\Phi_{res}$ is plotted for all the frequencies f . The relation between ΔE and Φ_{ext} is linear for the high-frequency data. This gives $I_p = 484 \pm 2$ nA, in good agreement with the predicted value. At lower frequencies $\Delta\Phi_{res}$ significantly deviates from this linear relation, demonstrating the

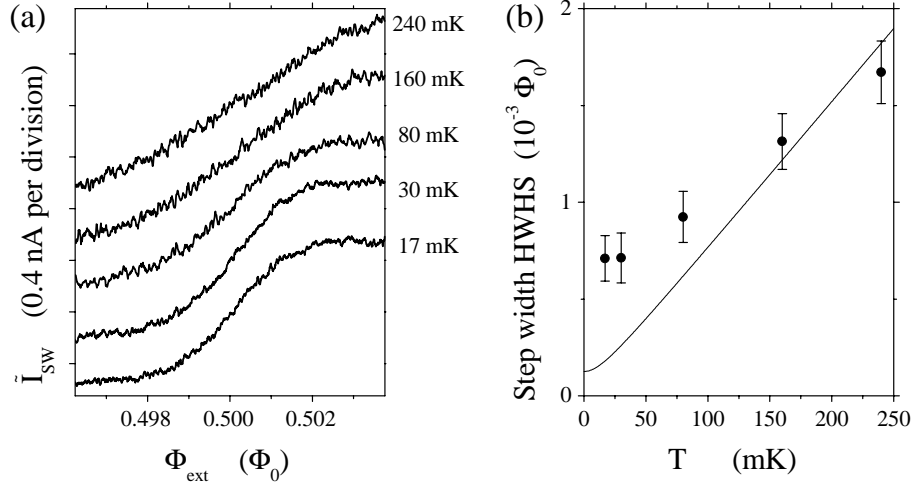


Figure 4 (a) \tilde{I}_{SW} versus Φ_{ext} , measured at different temperatures T (labels on the right). No microwaves were applied. The step in \tilde{I}_{SW} broadens with temperature. (b) The width of the step as a function of temperature. The half-width-half-step (HWHS) is defined as the distance in Φ_{ext} from $\frac{1}{2}\Phi_0$ to the point where the amplitude of the step is half completed. The solid line is the calculated HWHS for thermally mixed levels, using (1) and the I_p and t -value from the spectroscopy results, with a saturating width on the scale of t at low temperatures.

presence of a finite tunnel splitting at $\Phi_{\text{ext}} = \frac{1}{2}\Phi_0$. A fit to Eq. (1) yields $t/h = 0.33 \pm 0.03$ GHz, in agreement with the estimate from fabrication parameters. The level separation very close to $\frac{1}{2}\Phi_0$ could not be measured directly since at this point the expectation value for the persistent current is zero for both the ground state and the excited state (Fig. 1c). Nevertheless, the narrow resonance lines allow for an accurate mapping of the level separation near $\frac{1}{2}\Phi_0$, and the observed tunnel splitting gives clear evidence for quantum superpositions of the persistent-current states. The large uncertainty in the predicted t -value does not allow for a quantitative analysis of a possible suppression of t due to a coupling between our two-level system and a bosonic environment [24] or a spin-bath environment [25, 26]. However, the fact that we see a finite tunnel splitting indicates that the damping of our quantum system by environmental degrees of freedom is weak. The dimensionless dissipation parameter α introduced by Leggett *et al.* [24] must be $\alpha < 1$.

The width of the rounded steps in the measured flux in Figs. 2b and 3a is much broader than expected from quantum rounding on the scale

of the value of t that was found with spectroscopy (see also Fig. 1c). The temperature dependence of the step width presented in Fig. 4 confirms that the step width HWHS (defined in the caption of Fig. 4b) is too wide at low temperatures T . At temperatures above 100 mK the step width is in agreement with the thermally averaged expectation value for the persistent current $\langle I_{\text{th}} \rangle = I_p \tanh\left(\frac{\Delta E}{2k_B T}\right)$ (k_B is Boltzmann's constant), where we use the level separation ΔE and I_p found with spectroscopy. However, when lowering the temperature the observed step width saturates at an effective temperature of about 100 mK. We checked that the effective temperature for the SQUID's switching events did not saturate at the lowest temperatures. The high effective temperature of the loop is a result of the loop being in a non-equilibrium state. Cooling the sample longer after the dissipative switching events did not make the step narrower. The step width at $T = 30$ mK was measured with 100 μs and 50 ms dead time between switching events, but no significant differences were found. This indicates that the out-of-equilibrium population of the excited state is caused by the measurement process with the SQUID or other weakly coupled external processes, in combination with a long time scale for cooling the system to equilibrium (as can be expected since it is very well isolated from the environment). Note that the observed line width and the level separation near $\frac{1}{2}\Phi_0$ are small compared to the effective temperature of 100 mK. Silvestrini *et al.* [27] showed that this can be the case in a Josephson junction system when the transitions between the levels occur much faster than the thermal mixing time, a phenomena that is also well known from e. g. room-temperature NMR on liquids.

4. CONCLUSION

We have presented clear evidence that a quantum superposition of two macroscopic persistent currents can occur in a small Josephson junction loop. Even though the measuring DC-SQUID is contributing significantly to the decoherence of our system (see also Ref. [11]), it was possible to detect the superposition states since the SQUID was only weakly coupled to the loop. The present results demonstrate the potential of three-junction persistent-current loops for research on macroscopic quantum coherence and quantum computation.

Acknowledgments

We thank J. B. Majer, A. C. Wallast, L. Tian, D. S. Crankshaw, J. Schmidt, A. Wallraff and L. Levitov for help and stimulating discussions. This work was financially supported by the Dutch Foundation for Fundamental Research on Matter

(FOM), the European TMR research network on superconducting nanocircuits (SUP-NAN), the USA Army Research Office (grant DAAG55-98-1-0369) and the NEDO joint research program (NTDP-98).

References

- [1] P. W. Anderson, in *Lectures on the Many-Body Problem*, E. R. Caianiello, Ed. (Academic Press, New York, 1964), vol. 2, pp. 113-135.
- [2] A. J. Leggett, *Prog. Theor. Phys. Suppl.* **69**, 80 (1980).
- [3] K. K. Likharev, *Sov. Phys. Usp.* **26**, 87 (1983).
- [4] W. H. Zurek, *Phys. Today* **44**, 36 (October 1991).
- [5] A. J. Leggett, A. Garg, *Phys. Rev. Lett.* **54**, 857 (1985).
- [6] M. F. Bocko *et al.*, *IEEE Trans. Appl. Supercond.* **7**, 3638 (1997).
- [7] L. B. Ioffe *et al.*, *Nature* **398**, 679 (1999).
- [8] J. E. Mooij *et al.*, *Science* **285**, 1036 (1999).
- [9] T. P. Orlando *et al.*, *Phys. Rev. B.* **60**, 15398 (1999).
- [10] We acknowledge that the results presented here do not exclude alternative theories for quantum mechanics (e. g. macro-realistic theories). This would require a type of experiment as proposed by Leggett *et al.* [5].
- [11] C. H. van der Wal *et al.*, submitted to *Science*.
- [12] J. R. Friedman *et al.*, *Nature* **406**, 43 (2000).
- [13] R. Rouse, S. Han, J. E. Lukens, *Phys. Rev. Lett.* **75**, 1614 (1995).
- [14] C. Cosmelli *et al.*, *Phys. Rev. Lett.* **82**, 5357 (1999).
- [15] S. Han, R. Rouse, J. E. Lukens, *Phys. Rev. Lett.* **84**, 1300 (2000).
- [16] W. Wernsdorfer, R. Sessoli, *Science* **284**, 133 (1999).
- [17] M. Arndt *et al.*, *Nature* **401**, 680 (1999).
- [18] T. H. Oosterkamp *et al.*, *Nature* **395**, 873 (1998).
- [19] Y. Nakamura *et al.*, *Phys. Rev. Lett.* **79**, 2328 (1997).
- [20] V. Bouchiat *et al.*, *Phys. Scr.* **T76**, 165 (1998).
- [21] D. J. Flees, S. Han, J. E. Lukens, *J. Supercond.* **12**, 813 (1999).
- [22] Y. Nakamura, Yu. A. Pashkin, J. S. Tsai, *Nature* **398**, 786 (1999).
- [23] C. H. van der Wal, J. E. Mooij, *J. Supercond.* **12**, 807 (1999).
- [24] A. J. Leggett *et al.*, *Rev. Mod. Phys.* **59**, 1 (1987).
- [25] N. Prokof'ev, P. Stamp, *Rep. Prog. Phys.* **63**, 669 (2000).
- [26] L. Tian *et al.*, to be published; cond-mat/9910062.
- [27] P. Silvestrini *et al.*, *Phys. Rev. Lett.* **79**, 3046 (1997).

3.2 Decoherence from the electromagnetic environment

A central issue in engineering solid state qubits is to avoid decoherence. As explained above, the intrinsic decoherence of the solid-state environment is already well suppressed in superconducting systems. However, due to their relatively large size and good electric properties, superconducting quantum bits very sensitively couple to the *electromagnetic* environment formed by circuitry, control electronics, and the electromagnetic noise ubiquitous in the modern world. One cannot simply design the system to decouple from these environments as well as possible, because at least good coupling to parts of the electronic circuitry is important in order to control the qubit. One thus has to carefully understand the decoherence induced by the circuitry in order to carefully avoid this unwanted *backaction* on the qubit while still keeping the desired action.

In paper [192], a basic model for the decoherence due to circuitry coupling inductively to the flux qubit is developed. It is shown, that the coherence properties are essentially controlled by the flux noise affecting the qubit, which is set by the real part of the effective, linearized impedance of the external circuit. This type of modeling is extended to *nonlinear* electric circuits containing Josephson junctions and SQUIDs in the stable regime where they can be linearized. It is shown, that underdamped circuitry leads to a rich structure in the spectral density that is ultimately responsible for decoherence, and that in nonlinear circuits which are linearized around a fixed working point, the effective spectral density can be strongly influenced by setting the working point through an external current. In particular, the underdamped read-out SQUID can be (in linear order) decoupled from the qubit when no bias is applied.

In ref. [193], the same system is analyzed from a different point of view: Instead of studying the noise of the external circuit, the friction of the continuous particle-in-a-potential representation of the qubit is examined. It is shown that for the linear and the nonlinear circuit this leads to the same results as above. When analyzing even more complex nonlinear setups, it is usually easier to determine the friction, which only involves the classical equations of motion without the noise, than studying the noise. Thus, this approach may have practical advantages as circuitry grows more complex.

Engineering decoherence in Josephson persistent-current qubits

Measurement apparatus and other electromagnetic environments

C.H. van der Wal^a, F.K. Wilhelm^b, C.J.P.M. Harmans, and J.E. Mooij

Department of Applied Physics and Delft Institute for Micro Electronics and Submicron Technology (DIMES), Delft University of Technology, PO Box 5046, 2600 GA Delft, The Netherlands

Received 4 September 2002

Published online 27 January 2003 – © EDP Sciences, Società Italiana di Fisica, Springer-Verlag 2003

Abstract. We discuss the relaxation and dephasing rates that result from the control and the measurement setup itself in experiments on Josephson persistent-current qubits. For control and measurement of the qubit state, the qubit is inductively coupled to electromagnetic circuitry. We show how this system can be mapped on the spin-boson model, and how the spectral density of the bosonic bath can be derived from the electromagnetic impedance that is coupled to the qubit. Part of the electromagnetic environment is a measurement apparatus (DC-SQUID), that is permanently coupled to the single quantum system that is studied. Since there is an obvious conflict between long coherence times and an efficient measurement scheme, the measurement process is analyzed in detail for different measurement schemes. We show, that the coupling of the measurement apparatus to the qubit can be controlled *in situ*. Parameters that can be realized in experiments today are used for a quantitative evaluation, and it is shown that the relaxation and dephasing rates that are induced by the measurement setup can be made low enough for a time-resolved study of the quantum dynamics of Josephson persistent-current qubits. Our results can be generalized as engineering rules for the read-out of related qubit systems.

PACS. 03.67.Lx Quantum computation – 05.40.-a Fluctuation phenomena, random processes, noise, and Brownian motion – 74.50.+r Proximity effects, weak links, tunneling phenomena, and Josephson effects – 85.25.Dq Superconducting quantum interference devices (SQUIDS)

1 Introduction

The dynamics of electromagnetic circuits and other macroscopic objects is usually well described by classical laws; quantum coherent phenomena like superposition states are usually not observed in macroscopic systems. The founders of the quantum mechanical theory already recognized that there is in fact a conflict between a straight forward extrapolation of quantum mechanics to a macroscopic scale, and the laws of classical physics that govern the macroscopic world. In particular, this concerns the possibility of quantum superpositions of collective coordinates (*i.e.* center-of-mass-like coordinates) of objects that are much bigger than the atomic scale. These difficulties were first presented by Schrödinger [1], and are now known as Schrödinger's cat paradox. Schrödinger's discussion of the cat in the box was clearly meant as a *gedanken* experiment. Only several decades later, after the discovery of the Josephson effect, it was recognized that the validity

of quantum mechanics for a macroscopic degree of freedom could be tested in *real* experiments [2].

In 1980, Leggett pointed out that cryogenic and microfabrication technologies had advanced to a level where macroscopic Schrödinger's cat states could possibly be realized in small superconducting loops that contain Josephson tunnel junctions [3, 4]. In such systems, the Josephson phase (or equivalently, the persistent supercurrent in the loop) is a collective coordinate for the Cooper-pair condensate, and it is conjugate to a variable which describes the charge difference across the Josephson tunnel junction. However, while the analysis of the isolated quantum system shows that superpositions of the macroscopic coordinates might very well occur in these loops, it is by no means obvious that such behavior can also be demonstrated experimentally. Such superposition states are extremely fragile, reflecting the tendency of macroscopic systems towards classical behavior. Besides decoherence from a weak coupling to the environmental degrees of freedom inside the solid-state device (which is believed to be very much suppressed at low temperatures due to the energy gap for quasiparticle excitations in superconductors), also the fact that the loop is not isolated but permanently placed in an experimental setup may hinder attempts to study macroscopic quantum coherence. Nevertheless,

^a *Present address:* Department of Physics, Harvard University, 17 Oxford Street, Cambridge, MA 02138, USA

^b *Present address:* Sektion Physik and CeNS, Ludwig-Maximilians Universität, Theresienstr. 37, 80333 Munich, Germany

e-mail: wilhelm@theorie.physik.uni-muenchen.de

interesting results with evidence for macroscopic quantum tunneling, energy level quantization and coherent dynamics between quantum levels were obtained with systems where the Josephson phase coordinate is trapped in a metastable well (for an overview see [5–10]). Also with systems where the energy scale for single-charge effects is higher than, or comparable to the energy scale for the Josephson effect, quantum coherent dynamics has recently been demonstrated [11,12]. In Josephson junction loops, quantum superposition states of persistent currents have been demonstrated spectroscopically [13,14]. However, time-resolved experiments that prove quantum-coherent oscillations between macroscopically-distinct persistent-currents states in the sense of reference [4] have not been reported yet.

Whether such experiments can be realized at all has been intensively discussed in the literature [15], without consensus being reached. However, a detailed analysis with estimates based on measurement techniques that can be realized in experiments *today*, has been discussed very little. The quantum coherent dynamics observed with the other Josephson junction systems (such as Cooper pair boxes [11,12] or single junctions [9,10]), indicates that it might be possible to obtain similar experimental results with Josephson persistent-current loops. Efforts in this direction were stimulated by the prospect that it might be possible to realize a quantum computer with superconducting Josephson devices [16–21]. An important advantage of a Josephson quantum computer would be that, if accurate quantum coherent control of elementary units would be possible, it would be a system that can be extended to one containing a very large number of quantum bits (qubits). The large size of the qubits allows for individual (local) control and readout of the qubits and qubit-qubit couplings.

In this article we analyze the feasibility of demonstrating quantum coherent dynamics of Josephson persistent currents with experimental techniques for manipulating and reading qubit states that can be realized in the laboratories *today* (*i.e.* assuming the available techniques for device fabrication, cryogenics, microwave applications and electronic filtering). Such mesoscopic solid-state experiments suffer from the fundamental difficulty that one cannot avoid that an electronic measuring device is permanently coupled to the *single* quantum system that is studied [22]. We will not consider future measurement techniques which may couple less directly to the qubit. A meter must be present in any useful experiment, and, unlike experiments with for instance photons, this means that a measuring device must be permanently located very close to the solid-state quantum bit (*e.g.* fabricated on the same chip). With such a setup, there is obviously a conflict between an efficient measurement scheme with a strong measurement, and long decoherence times in the quantum system that is studied. For successful experiments in this direction, a detailed understanding of the measurement scheme is therefore needed such that the decoherence that is induced by the setup itself can be reduced to an acceptable level.

Obviously, there exist many other sources of decoherence for Josephson qubits that one should worry about as well. The critical current of the junctions may show telegraph noise [23], which would give rise to decoherence similar to what is described in reference [24]. Moreover, it has been stressed that a very high number of spin degrees of freedom is usually present in the solid state environment that may decohere Josephson qubits (see the work by Prokof'ev and Stamp [25,26] on the spin-bath, and reference [27] for estimates for persistent-current qubits). Another example is decoherence from quasiparticles that effectively shunt the junction [28]. These effects themselves are very interesting for further study. However, a study of for example the dephasing due to spin impurities remains impossible as long a reliable and well-understood measurement scheme for the loop's quantum dynamics is not available. Therefore, we will concentrate here on dephasing and mixing due to the experimental wiring and the measurement scheme itself.

Our analysis mainly focuses on experiments with the three-junction persistent-current qubit proposed by Mooij *et al.*, [14,19,20], in a setup where they are measured by underdamped DC-SQUID magnetometers (in this article we will reserve the word SQUID for the measuring DC-SQUID (Fig. 1a), and not use it for the three-junction qubit (Fig. 1, center)). The decohering influence of the inductively coupled DC-SQUID is analyzed as well as decoherence that results from inductive coupling to on-chip control lines for applying microwave signals and local magnetic fields. Model descriptions of the experimental setup will be mapped on the spin-boson model, such that we can use expressions for the relaxation and dephasing rates from the spin-boson literature. The typical experimental situations will be described quite extensively to justify the models and the approximations used. The results will be worked out quantitatively, and we will evaluate whether we can realize mixing and dephasing rates that are compatible with measurement schemes based on DC-SQUIDs. The design criteria developed in this work are more general and should also be of interest for experiments on loops with a single Josephson junction [13], and quantum circuits where the charge degree of freedom is measured, as Josephson charge quantum bits [18,21] and quantum dots [29]. In a more general context the value of this work is that it presents in detail an example of a measurement process on a single quantum system in which the decoherence enhances with increasing measurement strength. The issues discussed here are an example of experimental difficulties that will unavoidably play a role in many realizations of quantum computers.

1.1 Outline

In Section 2 we will summarize a theoretical description of the Josephson persistent-current qubit, and the spin-boson theory that will be applied in our analysis. Section 3 presents a description of the measurement process with the DC-SQUIDs, and a typical scheme for coupling the qubit to the on-chip control lines. In Section 4 we work out

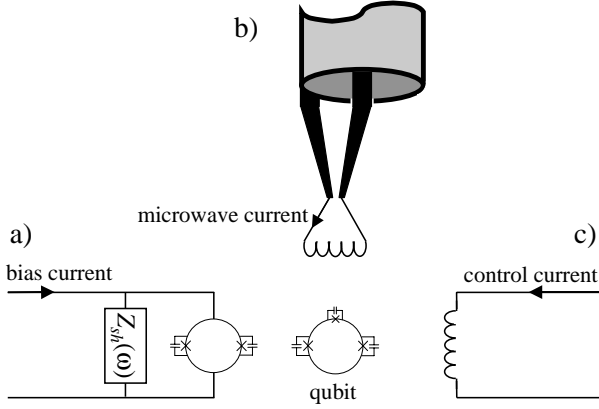


Fig. 1. Experimental setup for measurements on a Josephson persistent-current qubit. The qubit (center) is a superconducting loop that contains three Josephson junctions. It is inductively coupled to a DC-SQUID (a), and superconducting control lines for applying magnetic fields at microwave frequencies (b) and static magnetic fields (c). The DC-SQUID is realized with an on-chip shunt circuit with impedance Z_{sh} . The circuits a)–c) are connected to filtering and electronics (not drawn).

the qubit’s relaxation and dephasing rate that result from the coupling to a switching DC-SQUID. This is worked out quite extensively and the definitions presented in this section are also used in Section 5. Two measurement scenarios with different types of electromagnetic shunt circuits for the DC-SQUID will be compared. A short analysis of the decoherence due to the coupling to on-chip control lines is presented in Section 5. Section 6 presents a few control techniques that can improve decoherence rates.

2 Qubit Hamiltonian and theory for relaxation and dephasing

This work aims at calculating relaxation (mixing) rates and dephasing (decoherence) rates for a Josephson persistent-current qubit which result from its inductive coupling to the measurement setup. The measurement setup is formed by a DC-SQUID and control lines, which are attached to leads and coupled to filters and electronics (Fig. 1). This setup will be modeled as a macroscopic quantum two-level system (central spin) that is coupled to a linear electromagnetic impedance $Z_t(\omega)$, where ω the angular frequency. The impedance $Z_t(\omega)$ forms an oscillator bath and can be described by a set of LC oscillators. This allows for mapping the problem on the spin-boson model: a central spin- $\frac{1}{2}$ system that is coupled to a bosonic bath [30,31]. The parameters of the bath will be derived from the Johnson-Nyquist noise from $Z_t(\omega)$. In this section we will first introduce the qubit Hamiltonian and physical properties of the qubit, and then summarize the spin-boson expressions for relaxation and dephasing.

2.1 Qubit properties and Hamiltonian

The three-Josephson junction qubit [19,20,14] is a low-inductance superconducting loop which contains three Josephson tunnel junctions (Fig. 1). By applying an external flux Φ_q a persistent supercurrent can be induced in the loop. For values where Φ_q is close to a half-integer number of superconducting flux quanta Φ_0 , two states with persistent currents of opposite sign are nearly degenerate but separated by an energy barrier. We will assume here that the system is operated near $\Phi_q = \frac{1}{2}\Phi_0$. Classically, the persistent currents have here a magnitude I_p . Tunneling through the barrier causes a weak coupling between the two states, and at low energies the loop can be described by a Hamiltonian in the form of a two-level system [19,20,14],

$$\hat{H}_q = \frac{\varepsilon}{2}\hat{\sigma}_z + \frac{\Delta}{2}\hat{\sigma}_x, \quad (1)$$

where $\hat{\sigma}_z$ and $\hat{\sigma}_x$ are Pauli spin operators. The two eigen vectors of $\hat{\sigma}_z$ correspond to states that have a left or a right circulating current and will be denoted as $|L\rangle$ and $|R\rangle$. The energy bias $\varepsilon = 2I_p(\Phi_q - \frac{1}{2}\Phi_0)$ is controlled by the externally applied field Φ_q . We follow [32] and define Δ as the tunnel splitting at $\Phi_q = \frac{1}{2}\Phi_0$, such that $\Delta = 2W$ with W the tunnel coupling between the persistent-current states. This system has two energy eigen values $\pm\frac{1}{2}\sqrt{\Delta^2 + \varepsilon^2}$, such that the level separation ν gives

$$\nu = \sqrt{\Delta^2 + \varepsilon^2}. \quad (2)$$

In general Δ is a function of ε . However, it varies on the scale of the single junction plasma frequency, which is much above the typical energy range at which the qubit is operated, such that we can assume Δ to be constant for the purpose of this paper.

In the experiments Φ_q can be controlled by applying a magnetic field with a large superconducting coil at a large distance from the qubit, but for local control one can apply currents to superconducting control lines, fabricated on-chip in the direct vicinity of the qubit. The qubit’s quantum dynamics will be controlled with resonant microwave pulses (*i.e.* by Rabi oscillations). The proposed operation point is at $\varepsilon \approx 5\Delta$, which was analyzed to be a good trade-off between a system with significant tunneling, and a system with σ_z -like eigen states that can be used for qubit-qubit couplings and measuring qubit states [19,20]. For optimal microwave control the qubit will be placed in a small off-resonant cavity, and the microwave signals will be applied through on-chip superconducting control lines (*i.e.* the magnetic component of the fields from microwave currents will be used). The qubit has a magnetic dipole moment as a result of the clockwise or counter-clockwise persistent current. The corresponding flux in the loop is much smaller than the applied flux Φ_q , but large enough to be detected with a SQUID. This will be used for measuring the qubit states. For our two-level system equation (1), this means that both manipulation and readout

couple to $\hat{\sigma}_z$. Consequently, the noise produced by the necessary circuitry will couple in as flux noise and hence couple to $\hat{\sigma}_z$, giving ϵ a small, stochastically time-dependent part $\delta\epsilon(t)$. Our system also has electric dipole moments, represented by $\hat{\sigma}_x$. These couple much less to the circuitry and will hence not be discussed here.

2.2 Spin-boson theory for relaxation and dephasing

For defining the relaxation and dephasing rates, the state of the qubit is described with a reduced density matrix $\bar{\rho}$, in the basis which is spanned by the eigen vectors of $\hat{\sigma}_z$ in (1), *i.e.* by the semiclassical states with well-defined left (L) or right (R) circulating current

$$\bar{\rho} = \begin{pmatrix} \rho_{L,L} & \rho_{R,L} \\ \rho_{L,R} & \rho_{R,R} \end{pmatrix}. \quad (3)$$

We will concentrate our discussion on the undriven case. The qubit dynamics consists of quantum-coherent oscillations, which decay on a time-scale $\tau_\phi = \Gamma_\phi^{-1}$, the dephasing time. This dephasing is superimposed on an energy relaxation mechanism on a larger timescale $\tau_r = \Gamma_r^{-1}$, the relaxation time. This combined decoherence process brings the system into an incoherent thermal mixture of its energy eigen states. Expressed in the basis of these eigen states, the off-diagonal terms (coherences) of the density matrix $\bar{\rho}$ go to zero on the time scale of τ_ϕ , whereas the diagonal terms (populations) decay in τ_r to the Boltzmann factors. For estimating Γ_r and Γ_ϕ we will work from the systematic weak-damping approximation (SWDA) developed by Grifoni *et al.* [32], which covers recent theoretical progress for the spin-boson theory. Grifoni *et al.* calculated expressions for Γ_r and Γ_ϕ for a spin-boson system in which the coupling to the environment is dominated by bilinear coupling terms between $\hat{\sigma}_z$ and the bath coordinates. This is a good approximation for a quantum two-level system that is only weakly damped by the environment.

In our case the bath is formed by the impedance $Z_t(\omega)$, and can be described by a set of LC oscillators with flux coordinates $\hat{\Phi}_i$, conjugate charge coordinates \hat{Q}_i , and Hamiltonian

$$\hat{H}_{bath} = \sum_i \left(\hat{\Phi}_i^2 / 2L_i + \hat{Q}_i^2 / 2C_i \right). \quad (4)$$

The flux produced by the qubit will shift the flux $\hat{\Phi}_i$ in each LC oscillator. The coupling Hamiltonian is

$$\hat{H}_{q-bath} = \frac{\hat{\sigma}_z}{2} \sum_i c_i \hat{\Phi}_i, \quad (5)$$

where c_i is the coupling strength to the i th oscillator. In this model the influence of the oscillator bath on the qubit can be captured in the environmental spectral density function

$$J(\omega) = \frac{\pi}{2\hbar} \sum_i (c_i^2 / C_i \omega_i) \delta(\omega - \omega_i), \quad (6)$$

where ω_i the resonance frequency of the i th oscillator. The dense spectrum of the degrees of freedom in the electromagnetic environment allows for treating $J(\omega)$ as a continuous function.

From now on, we focus on the low-damping limit, $J(\omega) \ll \omega$. Thus, the energy-eigenstates of the qubit Hamiltonian, equation (1), are the appropriate starting point of our discussion. In this case, the relaxation rate Γ_r (and relaxation time τ_r) are determined by the environmental spectral density $J(\omega)$ at the frequency of the level separation ν of the qubit

$$\Gamma_r = \tau_r^{-1} = \frac{1}{2} \left(\frac{\Delta}{\nu} \right)^2 J(\nu/\hbar) \coth \left(\frac{\nu}{2k_B T} \right), \quad (7)$$

where T is the temperature of the bath. The dephasing rate Γ_ϕ (and dephasing time τ_ϕ) is

$$\Gamma_\phi = \tau_\phi^{-1} = \frac{\Gamma_r}{2} + \left(\frac{\epsilon}{\nu} \right)^2 \alpha 2\pi \frac{k_B T}{\hbar}. \quad (8)$$

These expressions have been derived in the context of NMR [33] using a Markov approximation and recently been confirmed by a full path-integral analysis [32].

The second term only contributes for an environment which is Ohmic at low frequencies (*i.e.* for $J(\omega) \propto \omega$). Here α is a dimensionless dissipation parameter. It is determined by the slope of $J(\omega)$ at low frequencies

$$\alpha = \lim_{\omega \rightarrow 0} \frac{J(\omega)}{2\pi\omega}, \quad (9)$$

which, if $J(\omega)$ is a sufficiently smooth function of ω can usually be taken as $\alpha = \frac{1}{2\pi} \frac{\partial J(\omega)}{\partial \omega}$ at $\omega \approx 0$. These results can be intuitively interpreted: The system can relax by dissipating all its energy ν into an environmental boson. Due to the weakness of the coupling, there are no multi-boson processes. The relaxation also dephases the state. Moreover, dephasing can occur due to the coupling to low-frequency modes which do not change the energy of the system. These expressions for relaxation and dephasing have also been found by studying the Hamiltonian of our qubit coupled to a damped oscillator, using a Markovian master equation approach by Tian *et al.* [34] (based on work by Garg *et al.* [35]).

The expressions (7) and (8) have prefactors $\left(\frac{\Delta}{\nu}\right)^2$ and $\left(\frac{\epsilon}{\nu}\right)^2$ that depend on the tunnel splitting Δ and the energy bias ϵ . These factors correspond to the angles between noise and eigen states usually introduced in NMR [33] and account for the effect that the qubit's magnetic dipole radiation is strongest where the flux in the qubit $\Phi_q = \frac{1}{2}\Phi_0$ (*i.e.* $\left(\frac{\Delta}{\nu}\right)$ maximal), and that the level separation ν is insensitive to flux noise at this point (*i.e.* $\frac{\partial \nu}{\partial \epsilon} = \left(\frac{\epsilon}{\nu}\right) \approx 0$). One should know and control $J(\omega)$ at the frequency ν/\hbar for controlling the relaxation, and at low frequencies for controlling the dephasing. In this article we will calculate the noise properties of a few typical experimental environments, and calculate how the noise couples to the qubit. This can be used to define $J(\omega)$ for our specific environments.

3 Measurement setup

This section describes a typical experimental setup for measurements on Josephson persistent-current qubits. Only the parts that are most strongly coupled to the qubit will be worked out (Fig. 1). The first part describes a DC-SQUID magnetometer that is used by measuring its switching current, the second part addresses the use of on-chip superconducting lines for applying magnetic fields to the qubit.

3.1 Switching DC-SQUID

SQUIDS are the most sensitive magnetometers, and they can be operated at very low power consumption [36]. We will consider here the use of a DC-SQUID with a hysteretic current-voltage characteristic (IV) and unshunted junctions that are extremely underdamped. It is used by ramping a current through it and recording the switching current: the bias current at which it switches from the supercurrent branch to a nonzero voltage in its IV (Fig. 2). The switching current is a measure for the magnetic flux in the loop of the SQUID. An important advantage of this scheme is that the SQUID produces before readout very little noise. As long as the SQUID is on the supercurrent branch, it does not produce any shot noise or Josephson oscillations. If the external noise and interference can be suppressed by filtering, there is only Johnson-Nyquist noise from the low-temperature leads and filtering that the SQUID is connected to. At low frequencies this residual noise has little power since the device is superconducting. Moreover, we will show in Section 4 that at low bias currents the effective coupling between this meter and the quantum system is very weak. In comparison, damped non-hysteretic SQUIDS have the problem that the shunt resistors at the junctions also provide a damping mechanism for the qubit. In a hysteretic SQUID there is more freedom to engineer the effective impedance seen by the qubit, and it also has the advantage that the voltage jump at the switching current is much larger [37]. Recently, a similar scheme with a superconducting single-charge device, that can be operated as a switching electrometer has been reported [12, 38]. Voltage biased single-electron transistors for quantum measurements have been analyzed in references [39–42].

For qualitative insight in the measurement process we will present here a simplified description of the SQUIDS noise and dynamics (valid for a DC-SQUID with symmetric junctions and a loop with negligible self inductance). In Section 4 it will be worked out in more detail. The supercurrent through the SQUID with a flux Φ in its loop is

$$I_{sq} = 2I_{co} \cos f \sin \varphi_{ext}, \quad (10)$$

where $f = \pi\Phi/\Phi_0$, I_{co} the critical current of the junctions, and φ_{ext} a Josephson phase coordinate. I_{sq} will be distinguished from the applied bias current I_{bias} , as part of the bias current may go into circuitry shunting the SQUID. Insight in the SQUID's response to a bias current

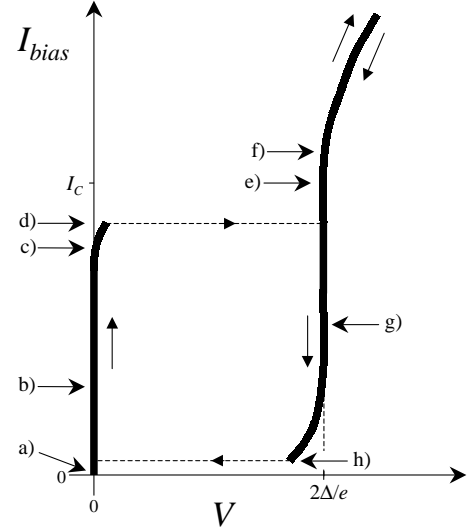


Fig. 2. Sketch of a typical hysteretic current-voltage characteristic (IV) for a current-biased Josephson junction or small DC-SQUID. The IV is hysteretic; arrows indicate which of the two branches is followed at an increase or decrease of the bias current. When the bias current I_{bias} is ramped up from zero (a), the voltage V first remains zero. The circuit is here on the supercurrent branch of the IV (b). When I_{bias} approaches the critical current I_C , a slow diffusive motion of the phase φ_{ext} leads to a very small voltage across the system (c). At slightly higher current (d), but always below I_C (e), the system switches to a running mode for φ_{ext} , and the voltage jumps to a value set by quasiparticle tunneling over the superconducting gap, $V = 2\Delta/e$ (this current level (d) is the switching current I_{SW}). At further increase of the current (f) the IV approaches an Ohmic branch, where transport is dominated by quasiparticle tunneling through the normal tunnel resistance of the junctions. When lowering the bias current the system follows the running mode (g) down to a low bias current where it retraps on the supercurrent branch (at the level I_{retrap} , indicated by (h)). See also the corresponding washboard potential model, in Figure 3.

is achieved by recognizing that (10) gives steady state solutions ($\partial U/\partial \varphi_{ext} = 0$) for a particle with coordinate φ_{ext} , trapped on a tilted washboard potential (Fig. 3)

$$U = -\frac{\hbar}{2e} (2I_{co} \cos f \cos \varphi_{ext} + I_{sq} \varphi_{ext}). \quad (11)$$

In this picture, the average slope of the potential is proportional to the bias current, and the supercurrent branch of the SQUID's IV corresponds to the particle being trapped in a well. The Josephson voltage across the SQUID $V = \frac{\hbar}{2e} \frac{d\varphi_{ext}}{dt}$ is nonzero for the particle in a running mode. In absence of noise and fluctuations, the SQUID will switch to the running mode at the critical current I_C

$$I_C = 2I_{co} |\cos f|. \quad (12)$$

A DC-SQUID can thus be regarded as a single Josephson junction with a flux-tunable critical current. In practice, noise and fluctuations of φ_{ext} will cause the SQUID

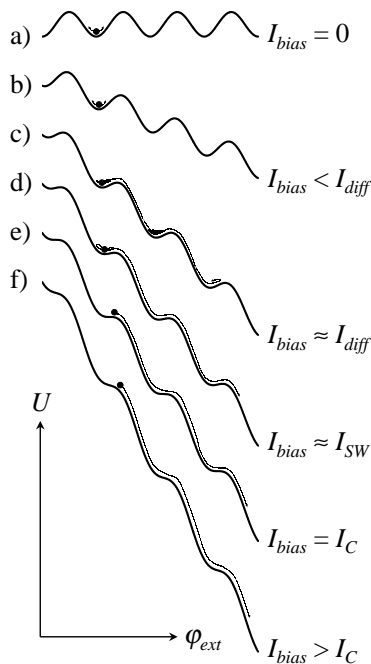


Fig. 3. The dynamics of a current-biased DC-SQUID, modeled as a particle with coordinate φ_{ext} in a one-dimensional tilted washboard potential U . The labeling (a)–(f) corresponds to that of Figure 2. At zero (a) and small bias currents (b), the particle is trapped in a well of the washboard. Apart from the small plasma oscillations at the bottom of the well, the particle’s coordinate φ_{ext} is fixed. When increasing the slope of the washboard, the particle will start to have a slow, on average downwards, diffusive dynamics, with rare excursions to one of the neighboring wells (c). At the switching current I_{SW} there is a high probability that the trapped particle will escape to a running mode (d), with effectively zero probability for retrapping. Here the loss of potential energy exceeds the dissipation when the particle moves one period down the washboard, and the particle builds up a high kinetic energy. Due to thermal fluctuations, external noise, and in certain cases quantum fluctuations, this occurs below the critical current I_C : the slope where all local minimums in the washboard potential disappear (e). At currents higher than this slope (f), the particle will always be in a running mode. The retrapping process when lowering the bias current follows similar dynamics.

to switch before the bias current reaches I_C . This current level will be denoted as the switching current I_{SW} to distinguish it from I_C . It is a stochastic variable, but averaging over repeated recordings of I_{SW} allows for determining f with great accuracy. This naive description can be used to illustrate three important properties of the measurement process with the SQUID.

In the experiment, the electronics for recording the SQUID’s IV obtains information about f when the SQUID switches. However, rewriting (10) as

$$\varphi_{ext} = \sin^{-1} \left(\frac{I_{sq}}{2I_{co} \cos f} \right) \quad (13)$$

shows that the SQUID’s coordinate φ_{ext} is already correlated (*i.e.* entangled) with the flux f at current val-

ues below I_{SW} . Small voltage fluctuations that result from small plasma oscillations and translations of φ_{ext} will cause dissipation in the electromagnetic environment of the SQUID, which damps the dynamics of φ_{ext} . This means, that in a quantum mechanical sense, the position of φ_{ext} , and thereby f , is measured by the degrees of freedom that form the electromagnetic impedance that is shunting the SQUID (*i.e.* the leads and filtering between the SQUID and the readout electronics), and that the measurement may in fact take place before it is recorded by a switching event.

Secondly, (13) shows that the SQUID’s coordinate φ_{ext} is independent of the flux in the loop ($\partial\varphi_{ext}/\partial f = 0$) for $I_{sq} = 0$. Therefore, in absence of fluctuations of φ_{ext} and current noise, the meter is at zero current effectively “off”. In practice this can not be perfectly realized, but it illustrates that the decoherence from the SQUID may be reduced by a large extent at low bias currents.

Thirdly, for bias currents well below I_C , the coordinate φ_{ext} is trapped in a potential that is for small oscillations close to harmonic. The SQUID can in this case be regarded as an inductance

$$L_J = \frac{\hbar}{2e} \frac{1}{\sqrt{4I_{co}^2 \cos^2 f - I_{sq}^2}} \quad (14)$$

(see also (26) below). The noise from the SQUID can here be described by the Johnson-Nyquist noise from the SQUID’s Josephson inductance (14) in parallel with the SQUID’s environmental impedance (Figs. 3a, b). For high bias currents very close to I_C , the spectrum will have more power and calculating the noise properties will be more complicated. Here non-harmonic terms in the trapping potential become important, and there maybe additional noise from a diffusive motion of φ_{ext} to neighboring wells (Fig. 3c). For hysteretic SQUIDS this regime with diffusive motion of φ_{ext} and switching currents very close to I_C will only occur in SQUIDS with a very specific electromagnetic shunt [37,43]. In many realizations of hysteretic DC-SQUIDS φ_{ext} will escape to a running mode without retrapping in lower wells (Fig. 3d), and I_{SW} can be much lower than I_C . In this case the approximation using (14) should be valid for description of the noise before a switching event.

The statistics of I_{SW} readouts depend strongly on the damping of the dynamics of φ_{ext} by the impedance that is shunting the SQUID. Experimental control over the damping, requires the fabrication of a shunt circuit in the direct vicinity of the SQUID, such that its impedance is well defined up to the frequency of the SQUID’s plasma oscillations (microwave frequencies). The shunt circuit is therefore preferably realized on-chip (Z_{sh} in Fig. 1a). The escape from the well may be thermally activated, but for underdamped systems with low-capacitance junctions quantum tunneling through the barrier can dominate the escape rate at low temperatures. The influence of the damping circuitry on the I_{SW} statistics [6,37,43] is now well understood. A SQUID with very underdamped dynamics usually has I_{SW} values much below I_C , and histograms of a set of I_{SW} recordings will be very wide.

This means that one needs to average over many repeated measurements to achieve the required resolution in readout. Thereby, averaging also needs to take place over many repeated experiments on the qubit, such that only a time-ensemble average can be measured. With a shunt that provides high damping at the plasma frequency very narrow switching current histograms can be realized [12,37,43–45], that in principle allow for single-shot readout in qubit experiments. While in such a scheme the SQUID's noise will also be enhanced, it is possible to engineer (for realistic fabrication parameters) a shunt impedance that is at the same time compatible with coherent dynamics of the qubit and single-shot readout [38]. The engineering of single-shot readout will not be addressed in detail in this paper.

The main disadvantage of the switching SQUID is that it is not very efficient. During each cycle through the hysteretic IV it is only measuring for a short time. Moreover, the IV is very nonlinear, such that the repetition frequency must be an order lower than the bandwidth of the filters. The filtering that is required for realizing low effective temperatures and the SQUID's shunt circuit have typically a bandwidth well below 1GHz, and the accurate readout electronics set a similar limit to the bandwidth. In practice this limits the repetition frequency to values in the range of 10 kHz [14,46] to 1 MHz [8,38]. More efficient readout may be realized with AC readout techniques (see *e.g.* Ref. [47]).

The slow operation of the switching DC-SQUID sets requirements for the mixing rate I_r of the qubit. It needs to be longer than the time required to perform a switching current measurement, which requires a time in the range 1 μ s to 100 μ s. One could go to shorter times by setting the SQUID ready at a high bias current when an experiment on the qubit is started, but it is also needed to have the mixing time longer than the time it takes to ramp the bias current through the range of the switching current histogram. At the same time we should realize that the quantum system is prepared by waiting for it to relax to the ground state, so relaxation times very much longer than 100 μ s will prohibit a high repetition frequency. A high repetition frequency is needed if the signal can only be built up by averaging over many switching events.

The experiments aim at working with many coherent Rabi oscillations with a period of about 10 ns [19]. We therefore aim at engineering SQUIDs that cause a dephasing time that is much longer than 10 ns. The dephasing and relaxation times turn out to be shortest at high bias currents through the SQUID. Unless mentioned otherwise, we will make in this article worst case estimates for the dephasing and relaxation times using bias current values near the switching current.

3.2 On-chip control lines

An attractive feature of macroscopic qubits is that one can address individual qubits with control signals from microfabricated lines (see also Fig. 1b, c). For persistent-current qubits, for example, a supercurrent through a line

that is mainly coupled to one specific qubit can be used for tuning this qubit's energy bias ε . Also, it is convenient to provide the microwave signals for control of the qubit's quantum dynamics using local superconducting lines. If this is realized in a microwave cavity with its first resonance well above the applied microwave frequency, one can apply microwave bursts with fast switch times without being hindered by high- Q electromagnetic modes in the volume that is formed by the cold metallic shielding that surrounds the sample.

Microwave signals can be applied using external microwave sources at room temperature. Alternatively, on-chip oscillators for example based on Josephson junction circuits [48,49] can be applied. High microwave currents in the control lines are achieved by shorting the microwave coax or wave guide close to the qubit with an inductance that has an impedance much lower than the source's output impedance (Fig. 1b). For external microwave sources, the typical level for the output impedance will be that of the available coax technology, typically 50 Ω . With on-chip Josephson oscillators the typical output impedance is one order lower. In both cases, it is in practice very tedious to engineer these impedance levels and our analysis below will show that this forms a constraint for qubit experiments: long decoherence times are in conflict with the wish for local qubit control and low power levels of the applied microwave signals.

If one uses external microwave sources at room temperature it is harder than for the quasi DC signals to filter out the high temperature noise. Low effective temperatures can be achieved by a combination of narrow-band microwave filters and strong attenuators at low temperatures.

4 Relaxation and dephasing from a switching DC-SQUID

4.1 Current-phase relations for the DC-SQUID

The DC-SQUID has two phase degrees of freedom, the gauge-invariant phases γ_r and γ_l of the junctions [36]. They are related to the supercurrents through the left and the right junction,

$$\begin{aligned} I_l &= (I_{co} + \frac{\Delta I_{co}}{2}) \sin \gamma_l, \\ I_r &= (I_{co} - \frac{\Delta I_{co}}{2}) \sin \gamma_r. \end{aligned} \quad (15)$$

Here I_{co} is the average of the critical current of the two junctions. A small asymmetry in the junctions' critical currents is accounted for by $\Delta I_{co} \ll I_{co}$ (typically a few percent). We will work here with the sum and difference phase coordinates φ_{int} and φ_{ext} , which are related by a linear transformation

$$\begin{aligned} \varphi_{ext} &= \frac{\gamma_l + \gamma_r}{2} \\ \varphi_{int} &= \frac{\gamma_l - \gamma_r}{2} \end{aligned} \quad \Leftrightarrow \quad \begin{aligned} \gamma_l &= \varphi_{ext} + \varphi_{int} \\ \gamma_r &= \varphi_{ext} - \varphi_{int} \end{aligned} \quad (16)$$

The new phase coordinates are related with the current passing through the SQUID I_{sq} and the circulating current

in the SQUID I_{cir}

$$\begin{aligned} I_{sq} &= I_l + I_r \\ I_{cir} &= \frac{I_l - I_r}{2} \end{aligned} \Leftrightarrow \begin{aligned} I_l &= \frac{1}{2} I_{sq} + I_{cir} \\ I_r &= \frac{1}{2} I_{sq} - I_{cir} \end{aligned}, \quad (17)$$

yielding the following current-phase relation for I_{sq} and I_{cir}

$$I_{sq} = 2I_{co} \cos \varphi_{int} \sin \varphi_{ext} + \Delta I_{co} \sin \varphi_{int} \cos \varphi_{ext}, \quad (18)$$

$$I_{cir} = I_{co} \sin \varphi_{int} \cos \varphi_{ext} + \frac{1}{2} \Delta I_{co} \cos \varphi_{int} \sin \varphi_{ext}. \quad (19)$$

We will assume that the DC-SQUID has junctions with a critical current and capacitance that are lower than that of the qubit junctions. In this case, the internal phase φ_{int} follows the flux adiabatically up to time scales much faster than $\frac{\hbar}{\nu}$. We will therefore use

$$\varphi_{int} = \pi \frac{\Phi}{\Phi_0} \stackrel{def}{=} f. \quad (20)$$

4.2 Noise on the qubit from the DC-SQUID resulting in $J(\omega)$

The noise that is induced by the measuring SQUID results from Johnson-Nyquist noise of the total impedance $Z_t(\omega)$ between the leads that are attached to the SQUID. The impedance $Z_t(\omega)$ is formed the SQUID's impedance in parallel with the impedance of the wiring and circuitry that the SQUID is connected to (see the circuit models in Fig. 4). At bias currents well below the critical current I_C , the phase dynamics can be linearized and the SQUID can be modeled as an inductor L_J . The coupling of φ_{ext} to the SQUID's inner degree of freedom φ_{int} and thereby to the qubit slightly alter the effective value for L_J , but the correction it is so small that it can be neglected. The Fourier-transformed power spectrum $\langle \delta V(t) \delta V(0) \rangle_\omega$ of the Johnson-Nyquist voltage fluctuations δV across the SQUID is [31,50]

$$\langle \delta V \delta V \rangle_\omega = \hbar \omega \text{Re}\{Z_t(\omega)\} \coth \left(\frac{\hbar \omega}{2k_B T} \right). \quad (21)$$

We will now calculate how this voltage noise leads to fluctuations $\delta \varepsilon$ of the energy bias on the qubit. As a rule, the spectral density $J(\omega)$ in (6) can then be derived by dividing the expression for $\langle \delta \varepsilon \delta \varepsilon \rangle_\omega$ by $\hbar^2 \coth \left(\frac{\hbar \omega}{2k_B T} \right)$.

The current-phase relations for I_{sq} and I_{cir} can be used for expressing the current fluctuations. The first term of (18) gives

$$\begin{aligned} \frac{dI_{sq}}{dt} &= i\omega I_{sq} \approx 2I_{co} \cos f \cos \bar{\varphi}_{ext} \frac{d\varphi_{ext}}{dt} \\ &= 2I_{co} \cos f \cos \bar{\varphi}_{ext} \frac{2e}{\hbar} V, \end{aligned} \quad (22)$$

where we used $\bar{\varphi}_{ext}$ for the time average of φ_{ext} . With a similar expression for the second term of (18) the current fluctuations in I_{sq} are

$$\delta I_{sq} \approx (2I_{co} \cos f \cos \bar{\varphi}_{ext} - \Delta I_{co} \sin f \sin \bar{\varphi}_{ext}) \delta \varphi_{ext}. \quad (23)$$

The SQUID is usually operated in regions where the average external flux in its loop is between an integer and half-integer number of Φ_0 . At these points $|\cos f| \approx |\sin f|$. Therefore, the second term in (23) can be neglected unless $|I_{co} \cos \bar{\varphi}_{ext}| \lesssim |\Delta I_{co} \sin \bar{\varphi}_{ext}|$. That is, it can be neglected unless the bias current is very high, for which $\sin \bar{\varphi}_{ext}$ approaches 1. For most purposes we can thus use

$$\delta I_{sq} \approx 2I_{co} \cos f \cos \bar{\varphi}_{ext} \delta \varphi_{ext}. \quad (24)$$

This is also used to define L_J by expressing

$$V = L_J \frac{dI_{sq}}{dt}, \quad (25)$$

such that with (22, 20) and (18) L_J should be defined as

$$L_J = \frac{\hbar}{2e} \frac{1}{2I_{co} \cos f \cos \bar{\varphi}_{ext}} = \frac{\hbar}{2e} \frac{1}{\sqrt{4I_{co}^2 \cos^2 f - I_{sq}^2}}. \quad (26)$$

For I_{cir} we get a similar expression as (23)

$$\delta I_{cir} \approx \left(-I_{co} \sin f \sin \bar{\varphi}_{ext} + \frac{1}{2} \Delta I_{co} \cos f \cos \bar{\varphi}_{ext} \right) \delta \varphi_{ext}. \quad (27)$$

Using again that the SQUID is operated where $|\cos f| \approx |\sin f|$ shows that the second term in (27) can be neglected unless $|I_{co} \sin \bar{\varphi}_{ext}| \lesssim |\Delta I_{co} \cos \bar{\varphi}_{ext}|$. For δI_{cir} the second term only plays a role at low bias currents in the SQUID for which $\bar{\varphi}_{ext} \approx 0$, and for most purposes we can use

$$\delta I_{cir} \approx -I_{co} \sin f \sin \bar{\varphi}_{ext} \delta \varphi_{ext}. \quad (28)$$

In the above we used $\bar{\varphi}_{ext}$ for the time average of φ_{ext} , but at places where it is not confusing it will be simply denoted as φ_{ext} .

Both noise in I_{sq} and I_{cir} can couple to the qubit, but we will assume that the qubit is mainly sensitive to noise in I_{cir} (as in the experiments in [14], where the qubit was placed symmetrically inside the SQUID's loop) and neglect an inductive coupling to noise in I_{sq} . For a more general approach, coupling to noise in I_{sq} can be treated on a similar footing as noise in I_{cir} , but for all useful sample geometries it should give a contribution to relaxation and dephasing rates that is at most on the same order as that of I_{cir} .

With $i\omega \delta I_{cir} = -\frac{2e}{\hbar} I_{co} \sin f \sin \varphi_{ext} \delta V$ follows for the fluctuations δI_{cir}

$$\langle \delta I_{cir} \delta I_{cir} \rangle_\omega = \left(\frac{2e}{\hbar} \right)^2 \frac{1}{\omega^2} I_{co}^2 \sin^2 f \sin^2 \varphi_{ext} \langle \delta V \delta V \rangle_\omega. \quad (29)$$

The fluctuations in the imposed qubit flux are $\delta \Phi_q = M \delta I_{cir}$, where M the mutual inductance between the SQUID loop and the qubit loop. This then yields the fluctuations in the energy bias with $\delta \varepsilon = 2I_p \delta \Phi_q$,

$$\langle \delta \varepsilon \delta \varepsilon \rangle_\omega = \left(\frac{2e}{\hbar} \right)^2 \frac{4}{\omega^2} M^2 I_p^2 I_{co}^2 \sin^2 f \sin^2 \varphi_{ext} \langle \delta V \delta V \rangle_\omega \quad (30)$$

where I_p is the amplitude of the circulating current in the qubit in the semiclassical states. Using (18) and (21) and filling in $\frac{\hbar}{2e} = \Phi_0$ this can be written as

$$\langle \delta\varepsilon \delta\varepsilon \rangle_\omega = \hbar (2\pi)^2 \frac{1}{\omega} \left(\frac{MI_p}{\Phi_0} \right)^2 I_{sq}^2 \tan^2 f \times \text{Re}\{Z_t(\omega)\} \coth\left(\frac{\hbar\omega}{2k_B T}\right). \quad (31)$$

The fluctuations $\langle \delta\varepsilon \delta\varepsilon \rangle_\omega$ are the result of the coupling to the oscillator bath, as in (6). This can be used to define $J(\omega)$ for our specific environment,

$$J(\omega) = \frac{(2\pi)^2}{\hbar} \frac{1}{\omega} \left(\frac{MI_p}{\Phi_0} \right)^2 I_{sq}^2 \tan^2 f \text{Re}\{Z_t(\omega)\}. \quad (32)$$

These results show, that although the SQUID is permanently close to the qubit, it may be effectively decoupled if there is no net bias current I_{sq} flowing through the device. The physical reason for this becomes apparent in equations (18) and (19): The SQUID remains mirror symmetric in that case and consequently the fluctuations of the bias current are diverted symmetrically around the arms of the SQUID and do not produce flux noise [51].

4.3 Relaxation times

With (7) and (32) follows the SQUID's contribution to the relaxation rate. It is here expressed as a function of the resonance frequency $\omega_{res} = \nu/\hbar$ at which the qubit is operated,

$$\Gamma_r = \left(\frac{\Delta/\hbar}{\omega_{res}} \right)^2 \frac{(2\pi)^2}{2\hbar} \frac{1}{\omega_{res}} \left(\frac{MI_p}{\Phi_0} \right)^2 I_{sq}^2 \tan^2 f \times \text{Re}\{Z_t(\omega_{res})\} \coth\left(\frac{\hbar\omega_{res}}{2k_B T}\right). \quad (33)$$

In this formula one can recognize a dimensionless factor $\left(\frac{MI_p}{\Phi_0}\right)^2$ which is a scale for how strongly the qubit is coupled to the measuring SQUID. A dissipation factor in the form $I^2 R$ can be recognized in $I_{sq}^2 \tan^2 f \text{Re}\{Z_t(\omega)\}$. The dissipation scales with the absolute value of the current fluctuations, so with I_{sq} , and the expression is independent of the critical current of the SQUID junctions I_{co} (unless $\text{Re}\{Z_t(\omega)\}$ depends on I_{co}). A weak measurement scheme in which the inductive coupling to a DC-SQUID $(MI_p/\Phi_0)^2 \ll 1$ can yield relaxation rates that are very low when compared to a scheme in which leads are directly attached to the loop [52]. A measurement of such a scheme's switching current could also be used for probing the qubit, but the influence of the voltage noise would be dramatically worse.

With the result (33) the relaxation rate for typical sample parameters will be calculated. Sample parameters similar to our recent experiment [14] are $\omega_{res} = 10$ GHz, $\Delta = 2$ GHz, $\frac{MI_p}{\Phi_0} = 0.002$. It is assumed that a SQUID

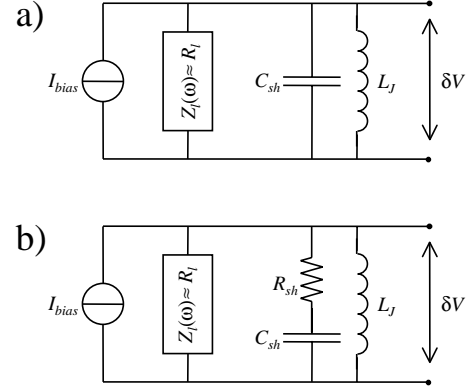


Fig. 4. Circuit models for the C -shunted DC-SQUID (a) and the RC -shunted DC-SQUID (b). The SQUID is modeled as an inductance L_J . A shunt circuit, the superconducting capacitor C_{sh} or the R_{sh} - C_{sh} series, is fabricated on chip very close to the SQUID. The noise that couples to the qubit results from Johnson-Nyquist voltage noise δV from the circuit's total impedance Z_t . Z_t is formed by a parallel combination of the impedances of the leads Z_l , the shunt and the SQUID, such that $Z_t = (1/Z_l + 1/(R_{sh} + 1/i\omega C_{sh}) + 1/i\omega L_J)^{-1}$, with $R_{sh} = 0$ for (a).

with $2I_{co} = 200$ nA is operated at $f = 0.75 \pi$ and biased near the switching current, at $I_{sq} = 120$ nA. For $T = 30$ mK the relaxation rate per Ohm environmental impedance is then

$$\tau_r = \Gamma_r^{-1} \approx \frac{150 \mu\text{s} \Omega}{\text{Re}\{Z_t(\omega_{res})\}}. \quad (34)$$

4.4 Engineering $\text{Re}\{Z_t(\omega)\}$ for slow relaxation

In practice the SQUID's resolution is improved by building an on-chip electromagnetic environment. We will consider here a large superconducting capacitive shunt (Fig. 4a, as in our recent experiment [14]). This scheme will be denoted as the C -shunted SQUID. As an alternative we will consider a shunt that is a series combination of a large capacitor and a resistor (Fig. 4b). This will be denoted as the RC -shunted SQUID. The C shunt only makes the effective mass of the SQUID's external phase φ_{ext} very heavy. The RC shunt also adds damping at the plasma frequency of the SQUID, which is needed for realizing a high resolution of the SQUID readout (*i.e.* for narrow switching-current histograms) [37]. The total impedance $Z_t(\omega)$ of the two measurement circuits are modeled as in Figure 4. We assume a perfect current source I_{bias} that ramps the current through the SQUID. The fact that the current source is non-ideal, and that the wiring to the SQUID chip has an impedance is all modeled by the impedance Z_l . The wiring can be engineered such that for a very wide frequency range the impedance Z_l is on the order of the vacuum impedance, and can be modeled by its real part R_l . It typically has a value of 100Ω . On chip, the impedance is formed by the Josephson inductance L_J in parallel with

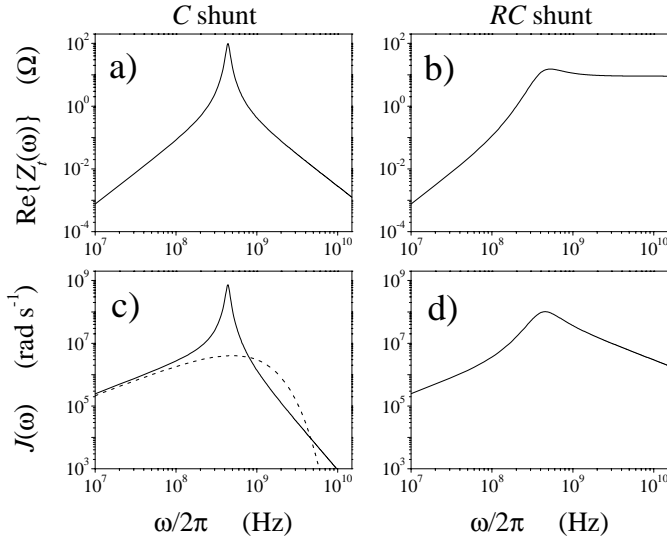


Fig. 5. A typical $\text{Re}\{Z_t(\omega)\}$ for the C -shunted SQUID (a) and the RC -shunted SQUID (b), and corresponding $J(\omega)$ in (c) and (d) respectively. For comparison, the dashed line in (c) shows a simple Ohmic spectrum (43) with exponential cut off $\omega_c/2\pi = 0.5$ GHz and $\alpha = 0.00062$. The parameters used here are $I_p = 500$ nA and $T = 30$ mK. The SQUID with $2I_{co} = 200$ nA is operated at $f = 0.75\pi$ and current biased at 120 nA, a typical value for switching of the C -shunted circuit (the RC -shunted circuit switches at higher current values). The mutual inductance $M = 8$ pH (*i.e.* $\frac{MI_p}{\Phi_0} = 0.002$). The shunt is $C_{sh} = 30$ pF and for the RC shunt $R_{sh} = 10 \Omega$. The leads are modeled by $R_l = 100 \Omega$.

the shunt circuit (C_{sh} , or the series combination of R_{sh} and C_{sh}). We thus assume that the total impedance $Z_t(\omega)$ can be described as

$$Z_t(\omega) = \left(\frac{1}{i\omega L_J} + \frac{1}{\frac{1}{i\omega C_{sh}} + R_{sh}} + \frac{1}{R_l} \right)^{-1}, \quad (35)$$

where R_{sh} should be taken zero for the C -shunt scenario.

The circuits in Figure 4 are damped LC resonators. It is clear from (7) and (32) that one should keep the LC -resonance frequency $\omega_{LC} = 1/\sqrt{L_J C_{sh}}$, where $\text{Re}\{Z_t(\omega)\}$ has a maximum, away from the qubit's resonance $\omega_{res} = \nu/\hbar$. For practical values this requires $\omega_{LC} \ll \omega_{res}$ for Aluminum technology (with Niobium-based technology, the regime $\omega_{LC} \gg \omega_{res}$ may be realized [44]). This then gives the circuits a $\text{Re}\{Z_t(\omega)\}$ and $J(\omega)$ as plotted in Figure 5. For the circuit with the C shunt

$$\text{Re}\{Z_t(\omega)\} \approx \begin{cases} \frac{\omega^2 L_J^2}{R_l}, & \text{for } \omega \ll \omega_{LC} \\ R_l, & \text{for } \omega = \omega_{LC} \\ \frac{1}{\omega^2 C_{sh}^2 R_l}, & \text{for } \omega \gg \omega_{LC}. \end{cases} \quad (36)$$

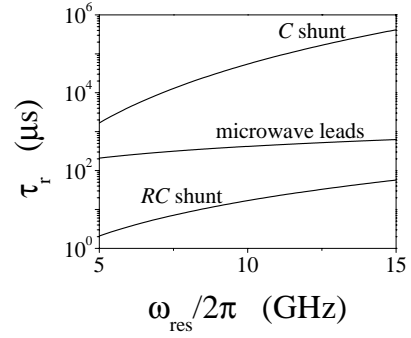


Fig. 6. Typical relaxation times due to the C -shunted SQUID, the RC -shunted SQUID, and coupling the microwave leads as a function of the resonance frequency at which the qubit is operated. The example of the microwave leads contribution is for a mutual inductance M_{mw} to the coaxial line of $M_{mw} = 0.1$ pH. Parameters are further as described in the caption of Figure 5.

For the circuit with the RC shunt

$$\text{Re}\{Z_t(\omega)\} \approx \begin{cases} \frac{\omega^2 L_J^2}{R_l}, & \text{for } \omega \ll \omega_{LC} \\ \lesssim R_l, & \text{for } \omega = \omega_{LC} \ll \frac{1}{R_{sh} C_{sh}} \\ R_l // R_{sh}, & \text{for } \omega = \omega_{LC} \gg \frac{1}{R_{sh} C_{sh}} \\ R_l // R_{sh}, & \text{for } \omega \gg \omega_{LC}. \end{cases} \quad (37)$$

The difference mainly concerns frequencies $\omega > \omega_{LC}$, where the C -shunted circuit has a $\text{Re}\{Z_t(\omega)\}$, and thereby a relaxation rate, that is several orders lower than for the RC -shunted circuit.

For a C -shunted circuit with $\omega_{LC} \ll \omega_{res}$ the $\text{Re}\{Z_t(\omega_{res})\} \approx \frac{1}{\omega_{res}^2 C_{sh}^2 R_l}$. This yields for $J(\omega)$ at $\omega > \omega_{LC}$

$$J(\omega) \approx \frac{(2\pi)^2}{\hbar} \frac{1}{\omega^3} \left(\frac{MI_p}{\Phi_0} \right)^2 I_{sq}^2 \tan^2 f \frac{1}{C_{sh}^2 R_l}. \quad (38)$$

The factor $1/\omega^3$ indicates a natural cut-off for $J(\omega)$, which prevents the ultraviolet divergence [30,32] and which in much of the theoretical literature is introduced by hand. The RC -shunted circuit has softer cut off $1/\omega$. The mixing rate for the C -shunted circuit is then

$$\Gamma_r \approx \frac{(\Delta/\hbar)^2 (2\pi)^2}{\omega_{res}^5} \frac{1}{2\hbar} \left(\frac{MI_p}{\Phi_0} \right)^2 I_{sq}^2 \tan^2 f \times \frac{1}{C_{sh}^2 R_l} \coth \left(\frac{\hbar\omega_{res}}{2k_B T} \right). \quad (39)$$

Figure 6 presents mixing times τ_r vs ω_{res} for typical sample parameters (here calculated with the non-approximated version of $\text{Re}\{Z_t(\omega)\}$). With the C -shunted circuit it seems possible to get τ_r values that are very long. They are compatible with the ramp times of the SQUID, but too slow for fast repetition rates. In Figure 5 one can directly see from the values of $J(\omega)$ that an RC -shunted circuit with otherwise similar parameters yields at $\omega_{res}/2\pi = 10$ GHz relaxation times that are about four

orders shorter. For the parameters used here they are in the range of 15 μs . While this value is close to the desired order of magnitude, one has to be aware of the fact at these high switching current values the linearization equation (26) may underestimate the actual noise. In that regime, phase diffusion between different minima of the washboard potential also becomes relevant and changes the noise properties [37, 53].

4.5 Dephasing times

At low frequencies $\omega < \omega_{LC}$ the C -shunted and RC -shunted scheme have $\text{Re}\{Z_t(\omega)\} \approx \frac{\omega^2 L_J^2}{R_l}$ such that with (32) and (9)

$$J(\omega) \approx \frac{(2\pi)^2}{\hbar} \omega \left(\frac{M I_p}{\Phi_0} \right)^2 I_{sq}^2 \tan^2 f \frac{L_J^2}{R_l}, \quad (40)$$

$$\alpha \approx \frac{2\pi}{\hbar} \left(\frac{M I_p}{\Phi_0} \right)^2 I_{sq}^2 \tan^2 f \frac{L_J^2}{R_l}. \quad (41)$$

The environment is Ohmic at low frequencies since we have $J(\omega) \propto \omega$. For our sample parameters the second term in (8) dominates, such that with (41) and for the qubit operated where $\varepsilon \approx \nu$

$$\Gamma_\phi \approx \frac{(2\pi)^2}{\hbar^2} \left(\frac{M I_p}{\Phi_0} \right)^2 I_{sq}^2 \tan^2 f \frac{L_J^2}{R_l} k_B T. \quad (42)$$

Note in (26) that $L_J \propto 1/I_c$, such that the dephasing rate (42) does not depend on the absolute value of the current, but on the ratio I_{sq}/I_c . For the typical sample parameters as used in Figure 5 the dephasing time is about 10 ns, which is too short. However, we can gain a few orders (if Γ_r is low enough) by the fact that we can do the quantum coherent control at low I_{sq} (the previous estimate was calculated for $I_{sq} = 120$ nA, in the switching region). At $I_{sq} = 0$ we find $\Gamma_\phi = 0$ in this linear approximation for the SQUID inductance. At $I_{sq} = 0$ we should therefore estimate the dephasing due to second order terms. However, in practice the dephasing is probably dominated by the second term in (27), which is due to a small asymmetry in the fabricated SQUID junctions of a few percent. This influence can be mapped on a small bias current (a few percent of the critical current, say 5 nA) through the SQUID. Therefore, at $I_{sq} \approx 0$ the dephasing times can be $(\frac{120}{5})^2$ times longer. Furthermore, the factor L_J^2 , as defined in (26), is at 5 nA about a factor 2 lower than at 120 nA. For our parameters this allows for $\tau_\phi \approx 20 \mu\text{s}$, see also Figure 7. Further improvement is feasible by making *e.g.* $R_l = 1$ k Ω , working with a lower mutual inductance M or tuning the qubit close to the degeneracy point, as in [12].

Finally, we would like to mention that in the literature on dissipative two-level systems one often assumes Ohmic dissipation, corresponding to a purely resistive shunt across the junctions of the qubit. For a description

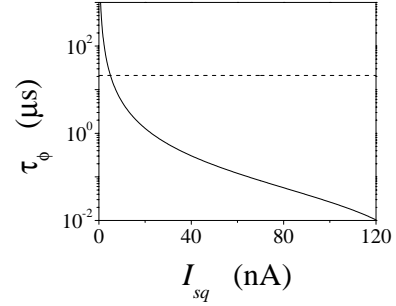


Fig. 7. The dephasing time (42) as a function of the bias current I_{sq} through the SQUID (solid line). The dashed line shows τ_ϕ for $I_{sq} = 5$ nA, a typical minimum value for the effective bias current for a SQUID with a few percent asymmetry between its junctions. At this point $\tau_\phi = 131 \mu\text{s}$, and $\alpha = 1 \times 10^{-7}$. Parameters are further as described in the caption of Figure 5.

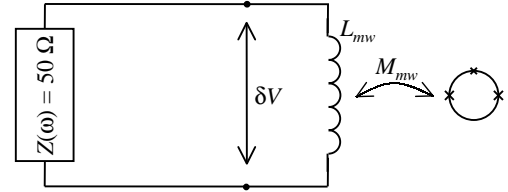


Fig. 8. Circuit model for coaxial line that is inductively coupled to the qubit. The coaxial line is modeled as a 50 Ω impedance that is shorted near the qubit with an inductance L_{mw} . The qubit is coupled to this short with a mutual inductance M_{mw} . The noise that couples to the qubit results from Johnson-Nyquist voltage noise δV from the circuit's total impedance Z_t , formed by a parallel combination of the 50 Ω impedance and L_{mw} .

of such a system one usually introduces an artificial exponential cut off at frequency ω_c , yielding $J(\omega)$ of the form

$$J(\omega) = \alpha \omega \exp\left(-\frac{\omega}{\omega_c}\right). \quad (43)$$

In our case, $J(\omega)$ has substantial internal structure originating from the frequency-dependence of $\text{Re}\{Z_t(\omega)\}$. In order to compare our results to the Ohmic case, we plot in Figure 5 an Ohmic fit to the actual $J(\omega)$ of the DC SQUID. For the parameters as in Figure 5 the resemblance is reasonable for a resistive shunt corresponding to $\alpha = 0.00062$, and a cut off $\omega_c = 0.5$ GHz. For low currents, as for the dashed line in Figure 7 $\alpha = 1 \times 10^{-7}$. This corresponds to an extremely underdamped system, with a long dephasing time.

5 Relaxation and dephasing from on-chip control circuits

We will treat here the influence of noise from the microwave leads in a similar way as worked out for the SQUID. Here the total environmental impedance $Z_t(\omega)$ is formed by a 50 Ω coax, that is shorted at the end by a small inductance L_{mw} , see the circuit model in Figure 8. This inductance L_{mw} has a mutual inductance M_{mw} to

the qubit. The voltage noise is given by (21). The noise leads to fluctuations $\delta\varepsilon$ of the energy bias separation ε as follows. The current noise in L_{mw} is $\delta I_L = \frac{1}{i\omega L_{mw}}\delta V$. The fluctuations in the flux Φ_q are then $\delta\Phi_q = M_{mw}\delta I_L$, and the fluctuations in the energy bias are $\delta\varepsilon = 2I_p\delta\Phi_q$. This gives for the fluctuations $\langle\delta\varepsilon\delta\varepsilon\rangle_\omega$

$$\langle\delta\varepsilon\delta\varepsilon\rangle_\omega = \frac{4\hbar}{\omega} \left(\frac{M_{mw}I_p}{L_{mw}}\right)^2 \text{Re}\{Z_t(\omega)\} \coth\left(\frac{\hbar\omega}{2k_B T}\right) \quad (44)$$

and for the environmental spectral density (6)

$$J(\omega) = \frac{4}{\hbar\omega} \left(\frac{M_{mw}I_p}{L_{mw}}\right)^2 \text{Re}\{Z_t(\omega)\}. \quad (45)$$

The $\text{Re}\{Z_t(\omega)\}$ is that of a first order low-pass LR filter with a -3 dB frequency $\omega_{LR} = R/L$. For the L_{mw} to be effectively a short its impedance ωL_{mw} should be small compared to 50Ω at the frequency of the applied microwave radiation (typically 10 GHz), giving $L_{mw} \ll 1$ nH. This can be realized by making the length of the short line less than about $100 \mu\text{m}$. This means that all relevant frequencies are below the -3 dB frequency ω_{LR} , and that for both relaxation and dephasing we can approximate

$$\text{Re}\{Z_t(\omega)\} \approx \frac{\omega^2 L_{mw}^2}{R_{mw}} \quad (46)$$

with $R_{mw} = 50 \Omega$. For $\omega < \omega_{LR}$, $J(\omega)$ is again Ohmic,

$$J(\omega) = \frac{4\omega}{\hbar} \frac{(M_{mw}I_p)^2}{R_{mw}}, \quad (47)$$

and with (9) we find for α

$$\alpha \approx \frac{4}{2\pi\hbar} \frac{(M_{mw}I_p)^2}{R_{mw}}. \quad (48)$$

Note that these results are independent of L_{mw} . A larger L_{mw} leads to enhanced voltage noise, but the resulting current noise is reduced by the same factor. For frequencies below ω_{LR} the current noise is just that of a shorted 50Ω resistor. For frequencies higher than ω_{LR} , $\text{Re}\{Z_t(\omega)\} \approx R_{mw}$, such that $J(\omega)$ has a very soft intrinsic $1/\omega$ cut off.

For the relaxation rate (7) as a function of the qubit's resonance frequency ω_{res} we now have

$$\Gamma_r \approx \frac{2\Delta^2}{\hbar^3\omega_{res}} \frac{(M_{mw}I_p)^2}{R_{mw}} \coth\left(\frac{\hbar\omega_{res}}{2k_B T}\right). \quad (49)$$

This has a much weaker dependence on ω_{res} than for the SQUID, results are plotted in Figure 6. The results are plotted for $M_{mw} = 0.1$ pH (further parameters are as used for the SQUID calculations) and for this M_{mw} value the relaxation times are in the required range of about $100 \mu\text{s}$. The value $M_{mw} \approx 0.1$ pH corresponds to a $5 \mu\text{m}$ loop at about $25 \mu\text{m}$ distance from the microwave line, and is compatible with the fabrication possibilities and

the microwave requirements. With this geometry it is still possible to apply sufficient microwave power for pumping the qubit's Rabi dynamics at 100 MHz (*i.e.* pumping with an oscillating Φ_q of about $0.001 \Phi_0$ [19], which needs an oscillating current of $\frac{0.001\Phi_0}{M_{mw}} \approx 20 \mu\text{A}$, corresponding to 20 nW, *i.e.* -47 dBm microwave power), while the dissipated microwave power in the attenuators at the refrigerator's base temperature remains well below the typical cooling power of $1 \mu\text{W}$.

For the second term of the dephasing rate (8) we thus find for the qubit operated where $\varepsilon \approx \nu$

$$\Gamma_\phi \approx \frac{4}{\hbar^2} \frac{(M_{mw}I_p)^2}{R_{mw}} k_B T. \quad (50)$$

Using the same parameters as in the above calculation of the relaxation time we find $\alpha \approx 1 \times 10^{-7}$ and for $T = 30$ mK the dephasing time is $\tau_\phi \approx 130 \mu\text{s}$. While this dephasing rate is sufficient for demonstration experiments and promising for applications, we like to note that it is much harder to engineer this dephasing rate as compared to the DC-SQUID dephasing. It is in practice quite tedious to apply microwave technology with impedance levels R_{mw} much higher than 50Ω , both for externally generated microwaves and on chip generators (it could for instance be increased using a planar impedance transformer [54]). Making M_{mw} smaller requires higher microwave currents, and thereby more microwave dissipation on the mixing chamber. The cooling power per qubit will quite likely remain below $1 \mu\text{W}$, so much stronger microwave signals from a larger distance is not an option. Moreover, making M_{mw} very small means that the control line is $100 \mu\text{m}$ or further away from the qubit. In this case, applying microwaves locally to one specific qubit on a chip with several coupled qubits is much harder.

6 Suppressing rates by freezing states and idle states

With additional control techniques the decoherence rates can be made better than the estimates made in the previous sections. These are based on the pre-factors in equations (7) and (8). Bringing the qubit in a so-called idle state ($\varepsilon = 0$) [18] can reduce the dephasing, but not beyond $\Gamma_r/2$ (which is enhanced at $\varepsilon = 0$).

Another useful technique is freezing. Here, the tunnel coupling Δ between the two qubit states is strongly reduced before the measurement process starts with a fast but adiabatic control current [19]. This allows for much slower measurements, thus for weaker coupling to a damped SQUID with very high resolution. Moreover, it has the advantage that the tunnel coupling becomes so weak that the Hamiltonian almost commutes with $\hat{\sigma}_z$. This can improve the correlation between the outcome of $\hat{\sigma}_z$ measurements, and energy states in the case that the calculation states are energy eigen states. However, freezing requires that the qubit junctions are realized as small DC-SQUIDS. This means that $\hat{\sigma}_x$ noise will be strongly enhanced. The influence of this additional noise source can

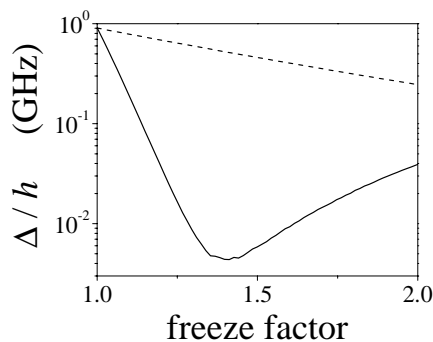


Fig. 9. Numerically simulated suppression of Δ in qubits where one (solid) or three (dashed) of the junctions are realized as small DC-SQUIDS, using typical qubit parameters as mentioned in the text. The horizontal axis is the factor by which the Josephson energy of the relevant junctions is increased. For the solid line, one can observe a non-monotonic dependence of Δ on the freeze factor, which results from the fact that if the Josephson coupling of the weak junction is strongly increased, alternative tunneling paths between the current states open up, see also reference [19].

be calculated along the same lines as in [32] and, assuming that it is not correlated with the other noise sources, add up to the rates we have calculated in this paper. See Figure 9 for numerical estimates on the possible adiabatic suppression of Δ .

7 Discussion and conclusion

We have developed a scheme for modeling the decoherence of a persistent-current qubit due to its electromagnetic environment. Examples for both control and read-out electronics are worked out quantitatively. We discussed how the dephasing and relaxation rates of the qubit can be derived from the impedance of the electronic circuitry, and provided design criteria for such electronics. In particular, we have shown that even though the readout SQUID is always close to the qubit, it can be effectively decoupled. Our examples show that the present status of experimental technology should allow for the observation of quantum coherent oscillations between macroscopic persistent-current states.

In this final section, we like to point out that the theory that is used is still in development. In particular, an environment with a strongly structured spectrum may violate the weak-coupling Born approximation at its resonance frequencies, but it may also induce weak additional decoherence off-resonance. This situation is hardly accessible with traditional theoretical methods for this problem and alternative approaches such as the flow-equation scheme in [55] may be needed. Furthermore, it is not clear whether the impedance can be described by a single temperature. At low frequencies, noise from parts in the system with a higher temperature can reach the sample. However, the experimental results reported in reference [12] indicate,

that an analysis of the decoherence of the type we give here gives good predictions of the experimental decoherence time scales in a superconducting qubit.

The authors thank D. Esteve, M. Grifoni, Y. Nakamura, P.C. E. Stamp, A.C. J. ter Haar, L. Levitov, T.P. Orlando, L. Tian, and S. Lloyd for help and stimulating discussions. Financial support by the Dutch Foundation for Fundamental Research on Matter (FOM), the European TMR research network on superconducting nanocircuits (SUPNAN), the USA National Security Agency (NSA) and Advanced Research and Development Activity (ARDA) under Army Research Office (ARO) contract numbers DAAG55-98-1-0369 and P-43385-PH-QC, and the NEDO joint research program (NTDP-98) is acknowledged.

Note added in proof

During the referral of this manuscript, Rabi oscillations have been observed in a setup of this type.

References

1. E. Schrödinger, *Naturwissenschaften* **23**, 807–812, 823–828, 844–849 (1935)
2. P.W. Anderson, in *Lectures on the Many-Body Problem*, edited by E.R. Caianiello (Academic Press, New York, 1964), Vol. 2, pp. 113–135
3. A.J. Leggett, *Prog. Theor. Phys. Suppl.* **69**, 80 (1980)
4. A.J. Leggett, A. Garg, *Phys. Rev. Lett.* **54**, 857 (1985)
5. K.K. Likharev, *Sov. Phys. Usp.* **26**, 87 (1983)
6. J. Clarke, A.N. Cleland, M.H. Devoret, D. Esteve, J.M. Martinis, *Science* **239**, 992 (1988)
7. S. Han, R. Rouse, J.E. Lukens, *Phys. Rev. Lett.* **76**, 3404 (1996)
8. P. Silvestrini, V.G. Palmieri, B. Ruggiero, M. Russo, *Phys. Rev. Lett.* **79**, 3046 (1997)
9. Y. Yu, S.Y. Han, X. Chu, S.I. Chu, Z. Wang, *Science* **296**, 889 (2002)
10. J.M. Martinis, S. Nam, J. Aumentado, C. Urbina, *Phys. Rev. Lett.* **89**, 117901 (2002)
11. Y. Nakamura, Yu. A. Pashkin, J.S. Tsai, *Nature* **398**, 786 (1999)
12. D. Vion, A. Aassime, A. Cottet, P. Joyez, H. Pothier, C. Urbina, D. Esteve, M.H. Devoret, *Science* **296**, 886 (2002)
13. J.R. Friedman, V. Patel, W. Chen, S.K. Tolpygo, J.E. Lukens, *Nature* **406**, 43 (2000)
14. C.H. van der Wal *et al.*, *Science* **290**, 773 (2000)
15. C.D. Tesche, *Phys. Rev. Lett.* **64**, 2358 (1990)
16. M.F. Bocko, A.M. Herr, M.J. Feldman, *IEEE Trans. Appl. Supercond.* **7**, 3638 (1997)
17. L.B. Ioffe, V.B. Geshkenbein, M.V. Feigel'man, A.L. Fauchère, G. Blatter, *Nature* **398**, 679 (1999)
18. Yu. Makhlin, G. Schön, A. Shnirman, *Nature* **398**, 305 (1999)
19. J.E. Mooij *et al.*, *Science* **285**, 1036 (1999)
20. T.P. Orlando *et al.*, *Phys. Rev. B* **60**, 15398 (1999)
21. Yu. Makhlin, G. Schön, A. Shnirman, *Rev. Mod. Phys.* **73**, 357 (2001)

22. Alternatively, one could also take an NMR-like approach and measure on an ensemble of loops. This is not discussed in this article
23. R.T. Wakai, D.J. van Harlingen, Phys. Rev. Lett. **58** 1687 (1987)
24. E. Paladino, L. Faoro, G. Falci, R. Fazio, Phys. Rev. Lett. **88**, 228304 (2002)
25. N. Prokof'ev, P. Stamp, Rep. Prog. Phys. **63**, 669 (2000); `cond-mat/0001080`
26. N.V. Prokof'ev, P.C.E. Stamp, *Spin-bath mediated decoherence in superconductors*, submitted to Phys. Rev. Lett., (2000); `cond-mat/0006054`
27. L. Tian *et al.*, in *Quantum Mesoscopic Phenomena and Mesoscopic Devices in Microelectronics*, edited by I.O. Kulik, R. Ellialtıođlu (Kluwer Academic Publishers, Dordrecht, 2000), pp. 429–438; `cond-mat/9910062`
28. U. Eckern, G. Schön, V. Ambegaokar Phys. Rev. B **30**, 6419 (1984)
29. T.H. Oosterkamp *et al.*, Nature **395**, 873 (1998)
30. A.J. Leggett *et al.*, Rev. Mod. Phys. **59**, 1 (1987); Rev. Mod. Phys. **67**, 725(E) (1995)
31. U. Weiss, *Quantum Dissipative Systems*, 2nd edn. (World Scientific, Singapore, 1999)
32. M. Grifoni, E. Paladino, U. Weiss, Eur. Phys. J. B **10**, 719 (1999)
33. A. Abragam, *Principles of Nuclear Magnetism* (Oxford University Press, Oxford, 1961)
34. L. Tian, S. Lloyd, T.P. Orlando, Phys. Rev. B **65**, 144516 (2002)
35. A. Garg, J.N. Onuchic, V. Ambegaokar, J. Chem. Phys. **83**, 3391 (1985).
36. M. Tinkham, *Introduction to Superconductivity*, 2nd edn. (McGraw-Hill, Inc., New York, 1996)
37. P. Joyez, D. Vion, M. Götz, M.H. Devoret, D. Esteve, J. Supercond. **12**, 757 (1999)
38. A. Cottet, D. Vion, A. Aassime, P. Joyez, D. Esteve, M.H. Devoret, Physica C **367**, 197 (2002)
39. A. Shnirman, G. Schön, Phys. Rev. B **57**, 15400 (1998)
40. M.H. Devoret, R.J. Schoelkopf, Nature **406**, 1039 (2000)
41. A.B. Zorin, Physica C **368**, 284 (2002)
42. A.N. Korotkov, D.V. Averin, Phys. Rev. B **64**, 165310 (2001)
43. D. Vion, M. Götz, P. Joyez, D. Esteve, M.H. Devoret, Phys. Rev. Lett. **77**, 3435 (1996)
44. T.P. Orlando *et al.*, private communication
45. H. Tanaka, Y. Sekine, S. Saito, H. Takayanagi, Physica C **368**, 300 (2002)
46. W. Wernsdorfer, D. Mailly, A. Benoit, J. Appl. Phys. **87**, 5094 (2000)
47. M. Mück, J.B. Kycia, J. Clarke, Appl. Phys. Lett. **78**, 967 (2001)
48. A.K. Jain. K.K. Likahrev, J.E. Lukens, J.E. Sauvageau, Phys. Rep. **109**, 309 (1998)
49. D.S. Crankshaw, E. Trías, T.P. Orlando, IEEE Trans. on Appl. Superconductivity **11**, 1223 (2001)
50. M.H. Devoret, in *Quantum Fluctuations*, edited by S. Reynaud, E. Giacobino, J. Zinn-Justin (Elsevier Science, Amsterdam, 1997), pp. 351–386
51. A similar decoupling to the measuring DC-SQUID based on symmetry can be realized with a additional flux-controlled coupling loop, see J. Clarke *et al.*, Phys. Scr. **102**, 173 (2002)
52. U. Geigenmüller, J. Appl. Phys. **80**, 3934 (1996)
53. W.T. Coffey, Y.P. Kalmykov, J.T. Waldron, *The Langevin Equation; with Applications in Chemistry and Electrical Engineering* (World Scientific, Singapore, 1996)
54. M. Feldman, private communications
55. S. Kleff, S. Kehrein, J. von Delft, to appear in Physica E

Decoherence of Flux Qubits Coupled to Electronic Circuits

F. K. Wilhelm¹, M. J. Storcz¹, C. H. van der Wal²,
C. J. P. M. Harmans³, and J. E. Mooij³

¹ Sektion Physik and CeNS, Ludwig-Maximilians-Universität
80333 München, Germany

² Dpt. of Physics, Harvard University
Cambridge, MA 02138, USA

³ Dpt. of Nanoscience, Delft University of Technology
2600 GA Delft, Netherlands

Abstract. On the way to solid-state quantum computing, overcoming decoherence is the central issue. In this contribution, we discuss the modeling of decoherence of a superconducting flux qubit coupled to dissipative electronic circuitry. We discuss its impact on single qubit decoherence rates and on the performance of two-qubit gates. These results can be used for designing decoherence-optimal setups.

1 Introduction

Quantum computation is one of the central interdisciplinary research themes in present-day physics [1]. It promises a detailed understanding of the often counterintuitive predictions of basic quantum mechanics as well as a qualitative speedup of certain hard computational problems. A generic, although not necessarily exclusive, set of criteria for building quantum computers has been put forward by DiVincenzo [2]. The experimental realization of quantum bits has been pioneered in atomic physics, optics and NMR. There, the approach is taken to use microscopic degrees of freedom which are well isolated and can be kept quantum coherent over long times. Efficient controls are attached to these degrees of freedom. Even though these approaches are immensely successful demonstrating elementary operations, it is not evident how they can be scaled up to macroscopic computers.

Solid-state systems on the other hand have proven to be scalable in present-day classical computers. Several proposals for solid-state based *quantum* computers have been put forward, many of them in the context of superconductors [3]. As solid-state systems contain a macroscopic number of degrees of freedom, they are very sensitive to decoherence. Mastering and optimizing this decoherence is a formidable task and requires deep understanding of the physical system under investigation. Recent experimental success [4,5] suggests that this task can in principle be performed.

In this contribution, we are going to study decoherence of superconducting qubits coupled to an electromagnetic environment which produces Johnson-Nyquist noise. We show, how the decoherence properties can be engineered

by carefully designing the environmental impedance. We will discuss how the decoherence affects the performance of a CNOT operation.

2 Superconducting Flux Qubits

Superconducting qubits [3,4,5,6] are very well suited for the task of solid-state quantum computation, because two of the most obvious decoherence sources in solid-state systems are suppressed: Quasiparticle excitations experience an energy gap and phonons are frozen out at low temperatures [7]. The computational Hilbert space is engineered using Josephson tunnel junctions that are characterized by two competing energy scales: The Josephson coupling of a junction with critical current I_c , $E_J = I_c \Phi_0 / 2\pi$, and the charging energy $E_{\text{ch}} = 2e^2 / C_J$ of a single Cooper pair on the geometric capacitance C_J of the junction. Here $\Phi_0 = h/2e$ is the superconducting flux quantum. There is a variety of qubit proposals classified by the ratio of these energies. Whereas another contribution in this volume [8] focuses on the case of charge qubits, $E_{\text{ch}} > E_J$, this contribution is motivated by flux qubit physics, $E_J > E_{\text{ch}}$. However, most of the discussion has its counterpart in other superconducting setups as well. Specifically, we discuss a three junction qubit [6,9], a micrometer-sized low-inductance superconducting loop containing three Josephson tunnel junctions (Fig. 1). By applying an external flux Φ_q a persistent supercurrent can be induced in the loop. For values where Φ_q is close to a half-integer number of flux quanta, two states with persistent currents of opposite sign are nearly degenerate but separated by an energy barrier. We will assume here that the system is operated near $\Phi_q = \frac{1}{2}\Phi_0$. The

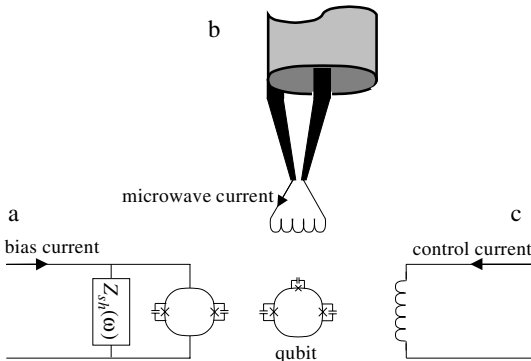


Fig. 1. Experimental setup for measurements on a flux qubit. The qubit (*center*) is a superconducting loop that contains three Josephson junctions. It is inductively coupled to a DC-SQUID (a), and superconducting control lines for applying magnetic fields at microwave frequencies (b) and static magnetic fields (c). The DC-SQUID is realized with an on-chip shunt circuit with impedance $Z(\omega)$. The circuits a)-c) are connected to filtering and electronics (not drawn)

persistent currents in the classically stable states have here a magnitude I_p . Tunneling through the barrier causes a coupling between the two states, and at low energies the loop can be described by a Hamiltonian of a two state system [6,9],

$$\hat{H}_q = \frac{\varepsilon}{2}\hat{\sigma}_z + \frac{\Delta}{2}\hat{\sigma}_x, \quad (1)$$

where $\hat{\sigma}_z$ and $\hat{\sigma}_x$ are Pauli matrices. The two eigenvectors of $\hat{\sigma}_z$ correspond to states that have a left or a right circulating current and will be denoted as $|L\rangle$ and $|R\rangle$. The energy bias $\varepsilon = 2I_p(\Phi_q - \frac{1}{2}\Phi_0)$ is controlled by the externally applied field Φ_q . We follow [10] and define Δ as the tunnel splitting at $\Phi_q = \frac{1}{2}\Phi_0$, such that $\Delta = 2W$ with W the tunnel coupling between the persistent-current states. This system has two energy eigen values $\pm\frac{1}{2}\sqrt{\Delta^2 + \varepsilon^2}$, such that the level separation ν gives $\nu = \sqrt{\Delta^2 + \varepsilon^2}$. In general Δ is a function of ε . However, it varies on the scale of the single junction plasma frequency, which is much above the typical energy range at which the qubit is operated, such that we can assume Δ to be constant for the purpose of this paper.

In the experiments Φ_q can be controlled by applying a magnetic field with a superconducting coil at a distance from the qubit and for local control one can apply currents to superconducting lines, fabricated on-chip in the vicinity of the qubit. The qubit's quantum dynamics will be controlled with resonant microwave pulses (i. e. by Rabi oscillations). In recent experiments the qubits were operated at $\varepsilon \approx 5\Delta$ or $\varepsilon \approx 0$ [4,9]. The numerical values given in this paper will concentrate on the former case. At this point, there is a good trade-off between a system with significant tunneling, and a system with $\hat{\sigma}_z$ -like eigenstates that can be used for qubit-qubit couplings and measuring qubit states [6]. The qubit has a magnetic dipole moment as a result of the clockwise or counter-clockwise persistent current. The corresponding flux in the loop is much smaller than the applied flux Φ_q , but large enough to be detected with a SQUID. This will be used for measuring the qubit states. For our two-level system Eq. (1), this means that both manipulation and readout couple to $\hat{\sigma}_z$. Consequently, the Nyquist noise produced by the necessary external circuitry will couple in as flux noise and hence couple to $\hat{\sigma}_z$, giving ε a small, stochastically time-dependent part $\delta\varepsilon(t)$.

Operation at $\varepsilon \approx 0$ has the advantage that the flux noise leads to less variation of ν . In the first experiments [4] this has turned out to be crucial for observing time-resolved quantum dynamics. Here, the qubit states can be measured by incorporating the qubit inside the DC-SQUID loop. While not working that out in detail, the methods that we present can also be applied for the analysis of this approach. This also applies to the analysis of the impact of electric dipole moments, represented by $\hat{\sigma}_x$. With $E_{ch} \ll E_J$, these couple much less to the circuitry and will hence not be discussed here.

As the internal baths are well suppressed, the coupling to the electromagnetic environment (circuitry, radiation noise) becomes a dominant source of decoherence. This is a subtle issue: It is not possible to couple the circuitry

arbitrarily weakly or seal the experimental setup, because it has to remain possible to control the system. One rather has to engineer the electromagnetic environment to combine good control with low unwanted back-action.

Any linear electromagnetic environment can be described by an effective impedance Z_{eff} . If the circuit contains Josephson junctions below their critical current, they can be included through their kinetic inductance $L_{\text{kin}} = \Phi_0 / (2\pi I_c \cos \bar{\phi})$, where $\bar{\phi}$ is the average phase drop across the junction. The circuitry disturbs the qubit through its Johnson-Nyquist noise, which has Gaussian statistics and can thus be described by an effective Spin-Boson model [11]. In this model, the properties of the oscillator bath which forms the environment are characterized through a spectral function $J(\omega)$, which can be derived from the external impedance. Note, that other nonlinear elements such as tunnel junctions which can produce non-Gaussian shot noise are generically *not* covered by oscillator bath models.

As explained above, the flux noise from an external circuit leads to $\epsilon = \epsilon_0 + \delta\epsilon(t)$ in Eq. (1). We parametrize the noise $\delta\epsilon(t)$ by its power spectrum

$$\langle \{\delta\epsilon(t), \delta\epsilon(0)\} \rangle_\omega = \hbar^2 J(\omega) \coth(\hbar\omega/2k_B T). \quad (2)$$

Thus, from the noise properties calculated by other means one can find $J(\omega)$ as was explained in Detail in [12]. In this contribution, we would like to outline an alternative approach pioneered by Leggett [13], where $J(\omega)$ is derived from the classical friction induced by the environment. In reality, the combined system of SQUID and qubit will experience fluctuations arising from additional circuit elements at different temperatures, which can be treated in a rather straightforward manner.

3 Decoherence from the Electromagnetic Environment

3.1 Characterizing the Environment from Classical Friction

We study a DC-SQUID in an electrical circuit as shown in Fig. 1. It contains two Josephson junctions with phase drops denoted by $\gamma_{1/2}$. We start by looking at the average phase $\gamma_{\text{ex}} = (\gamma_1 + \gamma_2)/2$ across the read-out SQUID. Analyzing the circuit with Kirchhoff rules, we find the equation of motion

$$2C_J \frac{\Phi_0}{2\pi} \ddot{\gamma}_{\text{ex}} = -2I_{c,0} \cos(\gamma_i) \sin \gamma_{\text{ex}} + I_{\text{bias}} - \frac{\Phi_0}{2\pi} \int dt' \dot{\gamma}_{\text{ex}}(t') Y(t-t'). \quad (3)$$

Here, $\gamma_{\text{in}} = (\gamma_1 - \gamma_2)/2$ is the dynamical variable describing the circulating current in the loop which is controlled by the flux, I_{bias} is the bias current imposed by the source, $Y(\omega) = Z^{-1}(\omega)$ is the admittance in parallel to the whole SQUID and $Y(\tau)$ its Fourier transform. The SQUID is described by the junction critical currents $I_{c,0}$ which are assumed to be equal, and their capacitances C_J . We now proceed by finding a static solution which sets the operation point $\gamma_{\text{in/ex},0}$ and small fluctuations around them, $\delta\gamma_{\text{in/ex}}$. The

static solution reads $I_{\text{bias}} = I_{c,\text{eff}} \sin \gamma_{\text{ex},0}$ where $I_{c,\text{eff}} = 2I_{c,0} \cos \gamma_{\text{in},0}$ is the effective critical current of the SQUID. Linearizing Eq. 3 around this solution and Fourier-transforming, we find that

$$\delta\gamma_{\text{ex}}(\omega) = \frac{2\pi I_b \tan \gamma_{\text{in},0} Z_{\text{eff}}(\omega)}{i\omega\Phi_0} \delta\gamma_i(\omega) \quad (4)$$

where $Z_{\text{eff}}(\omega) = (Z(\omega)^{-1} + 2i\omega C_J + (i\omega L_{\text{kin}})^{-1})^{-1}$ is the effective impedance of the parallel circuit consisting of the $Z(\omega)$, the kinetic inductance of the SQUID and the capacitance of its junctions. Neglecting self-inductance of the SQUID and the (high-frequency) internal plasma mode, we can straightforwardly substitute $\gamma_{\text{in}} = \pi\Phi/\Phi_0$ and split it into $\gamma_{\text{in},0} = \pi\Phi_{x,\text{S}}/\Phi_0$ set by the externally applied flux $\Phi_{x,\text{S}}$ through the SQUID loop and $\delta\gamma_i = \pi M_{\text{SQ}} I_Q/\Phi_0$ where M_{SQ} is the mutual inductance between qubit and the SQUID and $I_Q(\varphi)$ is the circulating current in the qubit as a function of the junction phases, which assumes values $\pm I_p$ in the classically stable states.

In order to analyze the backaction of the SQUID onto the qubit in the two-state approximation, Eq. (1), we have to get back to its full, continuous description, starting from the classical dynamics. These are equivalent to a particle, whose coordinates are the two independent junction phases in the three-junction loop, in a two-dimensional potential

$$\mathcal{C}(\Phi_0/2\pi)^2 \ddot{\varphi} = -\nabla U(\varphi, \Phi_{x,q} + I_S M_{\text{SQ}}). \quad (5)$$

The details of this equation are explained in [6]. \mathcal{C} is the capacitance matrix describing the charging of the Josephson junctions in the loop, $U(\varphi)$ contains the Josephson energies of the junctions as a function of the junction phases and I_S is the circulating current in the SQUID loop. The applied flux through the qubit Φ_q is split into the flux from the external coil $\Phi_{x,q}$ and the contribution from the SQUID. Using the above relations we find

$$I_S M_{\text{SQ}} = \delta\Phi_{\text{cl}} - 2\pi^2 M_{\text{SQ}}^2 I_B^2 \tan^2 \gamma_{\text{in},0} \frac{Z_{\text{eff}}}{i\omega\Phi_0^2} I_Q \quad (6)$$

where $\delta\Phi_{\text{cl}} \simeq M_{\text{SQ}} I_{c,0} \cos \gamma_{\text{ex},0} \sin \gamma_{\text{in},0}$ is the non-fluctuating back-action from the SQUID.

From the two-dimensional problem, we can now restrict ourselves to the one-dimensional subspace defined by the preferred tunneling direction [6], which is described by an effective phase φ . The potential restricted on this direction, $U_{1\text{D}}(\varphi)$ has the form of a double well [11,14] with stable minima situated at $\pm\varphi_0$. In this way, we can expand $U_{1\text{D}}(\varphi, \Phi_q) \simeq U(\varphi, \Phi_q, x) + I_Q(\varphi) I_Q M_{\text{SQ}}$. Approximating the phase-dependence of the circulating current as $I_Q(\varphi) \approx I_p \varphi/\varphi_0$ where I_p the circulating current in one of the stable minima of φ , we end up with the classical equation of motion of the qubit including the backaction and the friction induced from the SQUID

$$\left[-C_{\text{eff}} \left(\frac{\Phi_0}{2\pi} \right)^2 \omega^2 + 2\pi^2 M_{\text{SQ}}^2 I_{\text{bias}}^2 \tan^2 \gamma_{\text{in},0} \frac{Z_{\text{eff}} I_{\text{p}}^2}{i\varphi_0 \omega \Phi_0^2} \right] \varphi = -\partial_\varphi U_{1\text{D}}(\varphi, \Phi_{x,q} + \delta\Phi_{\text{cl}}). \tag{7}$$

From this form, encoded as $D(\omega)\varphi(\omega) = -\partial U/\partial\varphi$ we can use the prescription given in [13] and identify the spectral function for the continuous, classical model as $J_{\text{cont}} = \text{Im}D(\omega)$. From there, we can do the two-state approximation for the particle in a double well [14] and find $J(\omega)$ in analogy to [12]

$$J(\omega) = \frac{(2\pi)^2}{\hbar\omega} \left(\frac{M_{\text{SQ}} I_{\text{p}}}{\Phi_0} \right)^2 I_{\text{bias}}^2 \tan^2 \left(\frac{\pi\Phi}{\Phi_0} \right) \text{Re}\{Z_{\text{eff}}(\omega)\}. \tag{8}$$

3.2 Qubit Dynamics under the Influence of Decoherence

From $J(\omega)$, we can analyze the dynamics of the system by studying the reduced density matrix, i.e. the density matrix of the full system where the details of the environment have been integrated out, by a number of different methods. The low damping limit, $J(\omega)/\omega \ll 1$ for all frequencies, is most desirable for quantum computation. Thus, the energy-eigenstates of the qubit Hamiltonian, Eq. (1), are the appropriate starting point of our discussion. In this case, the relaxation rate Γ_r (and relaxation time τ_r) are determined by the environmental spectral function $J(\omega)$ at the frequency of the level separation ν of the qubit

$$\Gamma_r = \tau_r^{-1} = \frac{1}{2} \left(\frac{\Delta}{\nu} \right)^2 J \left(\frac{\nu}{\hbar} \right) \coth \left(\frac{\nu}{2k_B T} \right), \tag{9}$$

where T is the temperature of the bath. The dephasing rate Γ_ϕ (and dephasing time τ_ϕ) is

$$\Gamma_\phi = \tau_\phi^{-1} = \frac{\Gamma_r}{2} + 2\pi\alpha \left(\frac{\varepsilon}{\nu} \right)^2 \frac{k_B T}{\hbar} \tag{10}$$

with $\alpha = \lim_{\omega \rightarrow 0} J(\omega)/(2\pi\omega)$. These expressions have been derived in the context of NMR [15] and recently been confirmed by a full path-integral analysis [10]. In this paper, all rates are calculated for this regime.

For performing efficient measurement, one can afford to go to the strong damping regime. A well-known approach to this problem, the noninteracting blip approximation (NIBA) has been derived in [13]. This approximation gives good predictions at degeneracy, $\epsilon = 0$. At low $|\epsilon| > 0$ it contains an artifact predicting incoherent dynamics even at weak damping. At high bias, $\epsilon \gg \Delta$ and at strong damping, it becomes asymptotically correct again. We will not detail this approach here more, as it has been extensively covered in [11,14].

If $J(\omega)$ is not smooth but contains strong peaks the situation becomes more involved: At some frequencies, $J(\omega)$ may fall in the weak and at others in the strong damping limit. In some cases, when $J(\omega) \ll \omega$ holds at least for $\omega \leq \Omega$ with some $\Omega \gg \nu/\hbar$, this can be treated approximately: one can first renormalize Δ_{eff} through the high-frequency contributions [11] and then perform a weak-damping approximation from the fixed-point Hamiltonian. This is detailed in [16]. In the general case, more involved methods such as flow equation renormalization [17] have to be used.

4 Engineering the Measurement Apparatus

From Eq. (8) we see that engineering the decoherence induced by the measurement apparatus essentially means engineering Z_{eff} . This includes also the contributions due to the measurement apparatus. In this section, we are going to outline and compare several options suggested in literature. We assume a perfect current source that ramps the bias current I_{bias} through the SQUID. The fact that the current source is non-ideal, and that the wiring to the SQUID chip has an impedance is all modeled by the impedance $Z(\omega)$. The wiring can be engineered such that for a very wide frequency range the impedance $Z(\omega)$ is on the order of the vacuum impedance, and can be modeled by its real part R_l . It typically has a value of 100 Ω .

4.1 R-Shunt

It has been suggested [18] to overdamp the SQUID by making the shunt circuit a simple resistor $Z(\omega) = R_S$ with $R_S \ll \sqrt{L_{\text{kin}}/2C_J}$. This is inspired by an analogous setup for charge qubits, [3]. Following the parameters given in [12], a SQUID with $I_{c,0} = 200\text{nA}$ at $\Phi/\Phi_0 \simeq 0.75$ biased at $I_{\text{bias}} = 120\text{nA}$, we find $L_{\text{kin}} \simeq 2 \cdot 10^{-9}H$. Together with $C_J \simeq 1\text{fF}$, this means that the SQUID is overdamped if $R \ll R_{\text{max}} = 1.4\text{k}\Omega$. Using Eq. 8, we find that this provides an Ohmic environment with Drude-cutoff, $J(\omega) = \alpha\omega/(1 + \omega^2/\omega_{LR}^2)$ where $\omega_{LR} = R/L_{\text{kin}}$ and $\alpha = (2\pi)^2/\hbar (M_{SQ}I_q/\Phi_0)^2 I_{\text{bias}}^2 \tan^2(\pi\Phi/\Phi_0)L_{\text{kin}}^2/R_S$. Using the parameters from [12], $M_{SQ}I_q/\Phi_0 = 0.002$, we find $\alpha R = 0.08\Omega$ and $\omega_{LR}/R = 8.3\text{GHz}/\Omega$. Thus, for our range of parameters (which essentially correspond to weak coupling between SQUID and qubit), one still has *low* damping of the qubit from the (internally overdamped) environment at reasonable shunt resistances down to tens of Ohms. For such a setup, one can apply the continuous weak measurement theory as it is outlined e.g. in [18]. This way, one can readily describe the readout through measurement of Z_{eff} which leaves the system on the superconducting branch. If one desires to read out the state by monitoring the voltage at bias currents *above* the $I_{c,\text{eff}}$, our analysis only describes the pre-measurement phase and at least shows that the system is hardly disturbed when the current is ramped.

4.2 Capacitive Shunt

Next, we consider a large superconducting capacitive shunt (Fig. 2a, as implemented in [4,9]). The C shunt only makes the effective mass of the SQUID's external phase γ_{ex} very heavy. The total impedance $Z_{\text{eff}}(\omega)$ and $J(\omega)$ are modeled as before, see Fig. 3. As limiting values, we find

$$\text{Re}\{Z_{\text{eff}}(\omega)\} \approx \begin{cases} \frac{\omega^2 L_J^2}{R_l}, & \text{for } \omega \ll \omega_{LC} \\ R_l, & \text{for } \omega = \omega_{LC} \\ \frac{1}{\omega^2 C_{sh}^2 R_l}, & \text{for } \omega \gg \omega_{LC} \end{cases} \quad (11)$$

We can observe that this circuit is a weakly damped LC -oscillator and it is clear from (9) and (8) that one should keep its resonance frequency $\omega_{LC} = 1/\sqrt{L_J C_{sh}}$, where $\text{Re}\{Z_{\text{eff}}(\omega)\}$ has a maximum, away from the qubit's resonance $\omega_{\text{res}} = \nu/\hbar$. This is usually done by choosing $\omega_{LC} \ll \omega_{\text{res}}$. For a C -shunted circuit with $\omega_{LC} \ll \omega_{\text{res}}$, this yields for $J(\omega \approx \omega_{LC})$

$$J(\omega) \approx \frac{(2\pi)^2}{\hbar\omega^3} \left(\frac{M I_P}{\Phi_0} \right)^2 I_{\text{bias}}^2 \tan^2 \left(\frac{\pi\Phi}{\Phi_0} \right) \frac{1}{C_{sh}^2 R_l} \quad (12)$$

The factor $1/\omega^3$ indicates a natural cut-off for $J(\omega)$, which prevents the ultraviolet divergence [11,10] and which in much of the theoretical literature is introduced by hand. Using Eq. (9), we can directly analyze mixing times τ_r vs ω_{res} for typical sample parameters (here calculated with the

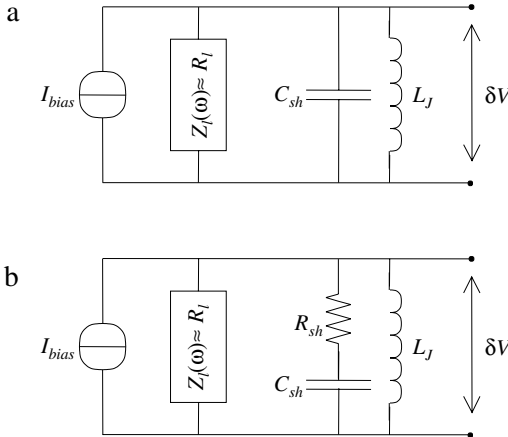


Fig. 2. Circuit models for the C -shunted DC-SQUID (a) and the RC -shunted DC-SQUID (b). The SQUID is modeled as an inductance L_J . A shunt circuit, the superconducting capacitor C_{sh} or the R_{sh} - C_{sh} series, is fabricated on chip very close to the SQUID. The noise that couples to the qubit results from Johnson-Nyquist voltage noise δV from the circuit's total impedance Z_{eff} . Z_{eff} is formed by a parallel combination of the impedances of the leads Z_l , the shunt and the SQUID, such that $Z_{\text{eff}}^{-1} = 1/Z_l + 1/(R_{sh} + 1/i\omega C_{sh}) + 1/i\omega L_J$, with $R_{sh} = 0$ for circuit (a)

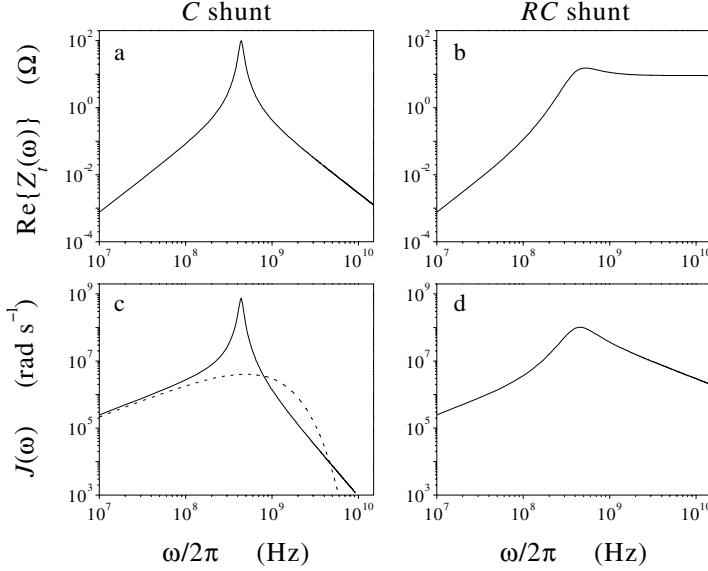


Fig. 3. A typical $\text{Re}\{Z_t(\omega)\}$ for the C -shunted SQUID (a) and the RC -shunted SQUID (b), and corresponding $J(\omega)$ in (c) and (d) respectively. For comparison, the dashed line in (c) shows a simple Ohmic spectrum, $J(\omega) = \alpha\omega$ with exponential cut off $\omega_c/2\pi = 0.5$ GHz and $\alpha = 0.00062$. The parameters used here are $I_p = 500$ nA and $T = 30$ mK. The SQUID with $2I_{co} = 200$ nA is operated at $f = 0.75\pi$ and current biased at 120 nA, a typical value for switching of the C -shunted circuit (the RC -shunted circuit switches at higher current values). The mutual inductance $M = 8$ pH (i. e. $MI_p/\Phi_0 = 0.002$). The shunt is $C_{sh} = 30$ pF and for the RC shunt $R_{sh} = 10 \Omega$. The leads are modeled by $R_l = 100 \Omega$

non-approximated version of $\text{Re}\{Z_t(\omega)\}$, see [12] for details. The mixing rate is then $\Gamma_r \approx (2\pi\Delta/\hbar)^2 \omega_{res}^{-5} (MI_p/\Phi_0)^2 I_{bias}^2 \tan^2(\pi\Phi/\Phi_0) (2\hbar C_{sh}^2 R_l)^{-1} \coth(\hbar\omega_{res}/2k_B T)$. With the C -shunted circuit it seems possible to get τ_r values that are very long. They are compatible with the ramp times of the SQUID, but too slow for fast repetition rates. For the parameters used here they are in the range of 15 μs . While this value is close to the desired order of magnitude, one has to be aware of the fact that at these high switching current values the linearization of the junction as a kinetic inductor may underestimate the actual noise. In that regime, phase diffusion between different minima of the washboard potential also becomes relevant and changes the noise properties [19,20].

4.3 RC-Shunt

As an alternative we will consider a shunt that is a series combination of a capacitor and a resistor (Fig. 2b) (RC -shunted SQUID). The RC shunt also adds damping at the plasma frequency of the SQUID, which is needed for

realizing a high resolution of the SQUID readout (i. e. for narrow switching-current histograms) [19]. The total impedance $Z_t(\omega)$ of the two measurement circuits are modeled as in Fig. 2. For the circuit with the RC shunt

$$\text{Re}\{Z_t(\omega)\} \approx \begin{cases} \frac{\omega^2 L^2}{R_l}, & \text{for } \omega \ll \omega_{LC} \\ \leq R_l, & \text{for } \omega = \omega_{LC} \ll \frac{1}{R_{sh} C_{sh}} \\ R_l // R_{sh}, & \text{for } \omega = \omega_{LC} \gg \frac{1}{R_{sh} C_{sh}} \\ R_l // R_{sh}, & \text{for } \omega \gg \omega_{LC} \end{cases}. \quad (13)$$

The difference mainly concerns frequencies $\omega > \omega_{LC}$, where the C -shunted circuit has a stronger cutoff in $\text{Re}\{Z_{\text{eff}}(\omega)\}$, and thereby a relaxation rate, that is several orders lower than for the RC -shunted circuit. Given the values of $J(\omega)$ from Fig. 3 one can directly see from the values of that an RC -shunted circuit with otherwise similar parameters yields at $\omega_{res}/2\pi = 10$ GHz relaxation times that are about four orders of magnitude shorter.

5 Coupled Qubits

So far, we have applied our modeling only to single qubits. In order to study entanglement in a controlled way and to eventually perform quantum algorithms, this has to be extended to coupled qubits.

5.1 Hamiltonian

There is a number of ways how to couple two solid-state qubits in a way which permits universal quantum computation. If the qubit states are given through real spins, one typically obtains a Heisenberg-type exchange coupling. For other qubits, the three components of the pseudo-spin typically correspond to physically completely distinct variables. In our case, $\hat{\sigma}_z$ corresponds to the flux through the loop whereas $\hat{\sigma}_{x/y}$ are charges. Consequently, one usually finds Ising-type couplings. The case of $\hat{\sigma}_y^{(1)} \otimes \hat{\sigma}_y^{(2)}$ coupling, i.e. coupling by a component which is orthogonal to all possible single-qubit Hamiltonians, has been extensively studied [21,22], because this type is straightforwardly realized as a *tunable* coupling of charge qubits [3]. We study the generic case of coupling the “natural” variables of the pseudospin to each other, which can be realized in flux qubits using a switchable superconducting transformer [6,23], but has also been experimentally utilized for coupling charge qubits by fixed capacitive interaction [24].

We model the Hamiltonian of a system of two qubits, coupled via Ising-type coupling. Each of the two qubits is described by the Hamiltonian Eq. (1). The coupling between the qubits is described by $\hat{H}_{\text{qq}} = -(K/2)\hat{\sigma}_z^{(1)} \otimes \hat{\sigma}_z^{(2)}$ that represents e.g. inductive interaction. Thus, the complete two-qubit Hamiltonian in the absence of a dissipative environment reads

$$\hat{H}_{2qb} = -\frac{1}{2} \sum_{i=1,2} \left(\epsilon_i \hat{\sigma}_z^{(i)} + \Delta_i \hat{\sigma}_x^{(i)} \right) - \frac{1}{2} K \hat{\sigma}_z^{(1)} \hat{\sigma}_z^{(2)}. \quad (14)$$

For two qubits, there are several ways to couple to the environment: Both qubits may couple to a common bath such as picked up by coupling elements [6]. Local readout and control electronics coupling to individual qubits [6] can be described as coupling to two uncorrelated baths. In analogy to the procedure described above, one can determine the spectral functions of these baths by investigating the corresponding impedances.

In the case of two uncorrelated baths, the full Hamiltonian reads

$$\hat{H}_{2qb}^{2b} = \hat{H}_{2qb} + \sum_{i=1,2} \frac{1}{2} \hat{\sigma}_z^{(i)} \hat{X}^{(i)} + \hat{H}_{B_1} + \hat{H}_{B_2}, \quad (15)$$

$\hat{X}^{(i)} = \zeta \sum_{\nu} \lambda_{\nu} x_{\nu}$ are collective coordinates of the bath. In the case of two qubits coupling to one common bath we model our two qubit system in a similar way with the Hamiltonian

$$\hat{H}_{2qb}^{1b} = \hat{H}_{2qb} + \frac{1}{2} \left(\hat{\sigma}_z^{(1)} + \hat{\sigma}_z^{(2)} \right) \hat{X} + \hat{H}_B, \quad (16)$$

where \hat{X} is a collective bath coordinate similar to above.

5.2 Rates

We can derive formulae for relaxation and dephasing rates similar to Eqs. (9) and (10). Our Hilbert space is now four-dimensional. We label the eigenstates as $|E1\rangle \dots |E4\rangle$. We chose $|E1\rangle$ to be the singlet state $(|\uparrow\downarrow\rangle - |\downarrow\uparrow\rangle) / \sqrt{2}$, which is always an eigenstate [25] whereas $|E2\rangle \dots |E4\rangle$ are the energy eigenstates in the triplet subspace, which are typically *not* the eigenstates of $\hat{\sigma}_z^{(1)} + \hat{\sigma}_z^{(2)}$. As we have 4 levels, we have 6 independent possible quantum coherent oscillations, each of which has its own dephasing rate, as well as 4 relaxation channels, one of which has a vanishing rate indicating the existence of a stable thermal equilibrium point. The expressions for the rates, although of similar form as in Eqs. (9) and (10) are rather involved and are shown in [25]. Figure 4 displays the dependence of typical dephasing rates and the sum of all relaxation rates Γ_R on temperature for the case $\Delta = \epsilon = K = h\nu_S$ with $\nu_S = 1\text{GHz}$. The rates are of the same magnitude for the case of one common bath and two distinct baths. If the temperature is increased above the roll off point set by the intrinsic energy scales, $T_s = (h/k_B)\nu_s = 4.8 \cdot 10^{-2} \text{K}$, where $E_s = 1\text{GHz}$, the increase of the dephasing and relaxation rates follows a linear dependence, indicating that the environmental fluctuations are predominantly thermal. As a notable exception, in the case of one common bath the dephasing rates $\Gamma_{\varphi_{21}} = \Gamma_{\varphi_{12}}$ go to zero when the temperature is decreased while all other rates saturate for $T \rightarrow 0$. This can be understood as follows: the singlet state $|E1\rangle$ is left invariant by the Hamiltonian of coupled qubits in a common bath, Eq. (16), i.e. it is an energy eigenstate left unaffected by the environment. Superpositions of the singlet with *another* eigenstate are usually still unstable, because the other eigenstate generally suffers from

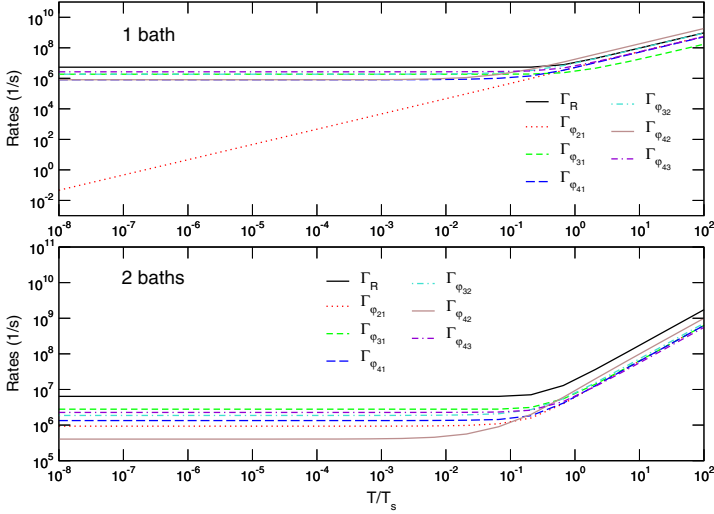


Fig. 4. Log-log plot of the temperature dependence of the sum of the four relaxation rates and selected dephasing rates. Qubit parameters K , ϵ and η are all set to E_s and the bath is assumed to be Ohmic $\alpha = 10^{-3}$. The *upper panel* shows the case of one common bath, the *lower panel* the case of two distinct baths. At the characteristic temperature of approximately $0.1 \cdot T_s$ the rates increase very steeply

decoherence. However, the lowest-energy state of the triplet subspace $|E2\rangle$ cannot decay by spontaneous emission and flip-less dephasing vanishes at $T = 0$, hence the dephasing rate between eigenstates $|E1\rangle$ and $|E2\rangle$ vanishes at low temperatures, see Fig. 4. As shown in [25], there can be more “protected” transitions of this kind if the qubit parameters are adjusted such that the symmetry between the unperturbed qubit and the coupling to the bath is even higher, e.g. at the working point for a CPHASE operation.

5.3 Gate Performance

The rates derived in the previous section are numerous and do strongly depend on the tunable parameters of the qubit. Thus, they do not yet allow a full assessment of the performance as a quantum logic element. A quantitative measure of how well a two-qubit setup performs a quantum logic gate operation are the gate quality factors introduced in [26]: the fidelity, purity, quantum degree and entanglement capability. These factors characterize the density matrices obtained after attempting to perform the gate operation in a hostile environment, starting from all possible initial conditions $\rho(0) = |\Psi_{in}^j\rangle \langle \Psi_{in}^j|$. To form all possible initial density matrices needed to calculate the gate quality factors, we use the 16 unentangled product states $|\Psi_{in}^j\rangle$, $j = 1, \dots, 16$ defined [22] according to $|\Psi_a\rangle_1 |\Psi_b\rangle_2$, ($a, b = 1, \dots, 4$), with $|\Psi_1\rangle = |0\rangle$, $|\Psi_2\rangle = |1\rangle$, $|\Psi_3\rangle = (1/\sqrt{2})(|0\rangle + |1\rangle)$, and $|\Psi_4\rangle = (1/\sqrt{2})(|0\rangle + i|1\rangle)$.

They form one possible basis set for the superoperator ν_G which describes the open system dynamics such that $\rho(t_G) = \nu_G \rho(0)$ [22,26]. The CNOT gate is implemented using rectangular DC pulses and describing dissipation through the Bloch-Redfield equation as described in [3,25].

The fidelity is defined as $F = (1/16) \sum_{j=1}^{16} \langle \Psi_{in}^j | U_G^\dagger \rho_G^j U_G | \Psi_{in}^j \rangle$. The fidelity is a measure of how well a quantum logic operation was performed. Clearly, the fidelity for the ideal quantum gate operation is equal to 1. The second quantifier is the purity $P = (1/16) \sum_{j=1}^{16} \text{tr} [(\rho_G^j)^2]$, which should be 1 in a pure and 1/4 in a fully mixed state. The purity characterizes the effects of decoherence. The quantum degree measures nonlocality. It is defined as the maximum overlap of the resulting density matrix after the quantum gate operation with the maximally entangled Bell-states $Q = \max_{j,k} \langle \Psi_{me}^k | \rho_G^j | \Psi_{me}^k \rangle$. For an ideal entangling operation, e.g. the CNOT gate, the quantum degree should be 1. It has been shown [27] that all density operators that have an overlap with a maximally entangled state that is larger than the value 0.78 [22] violate the Clauser-Horne-Shimony-Holt (CHSH) inequality and are thus non-local. The entanglement capability \mathcal{C} is the smallest eigenvalue of the partially transposed density matrix for all possible unentangled input states $|\Psi_{in}^j\rangle$. (see below). It has been shown [28] to be negative for an entangled state. This quantifier should be -0.5, e.g. for the ideal CNOT, thus characterizing a maximally entangled final state.

In Fig. 5, the deviations due to decoherence of the gate quality factors from their ideal values are shown. Similar to most of the rates, all gate quality factors saturate at temperatures below a threshold set by the qubit energy scales. The deviations grow linearly at higher temperatures until they reach their theoretical maximum. Comparing the different coupling scenarios, we see that at low temperatures, the purity and fidelity are higher for the case of one common bath, but if temperature is increased above this threshold, fidelity and purity are approximately equal for both the case of one common and two distinct baths. This is related to the fact that in the case of one common bath all relaxation and dephasing rates vanish during the two-qubit-step of the CNOT (see [25] for details), due to the special symmetries of the Hamiltonian, when temperature goes to zero as discussed above. Still, the quantum degree and the entanglement capability tend towards the same value for both the case of one common and two distinct baths. This is due to the fact that both quantum degree and entanglement capability are, different than fidelity and purity, not defined as mean values but rather characterize the “best” possible case of all given input states.

In the recent work by Thorwart and Hänggi [22], the CNOT gate was investigated for a $\hat{\sigma}_y^{(i)} \otimes \hat{\sigma}_y^{(j)}$ coupling scheme and one common bath. They find a pronounced degradation of the gate performance with gate quality factors only weakly depending on temperature. If we set the dissipation and the intrinsic energy scale to the same values as in their work, we also observe only a weak decrease of the gate quality factors for both the case of one com-

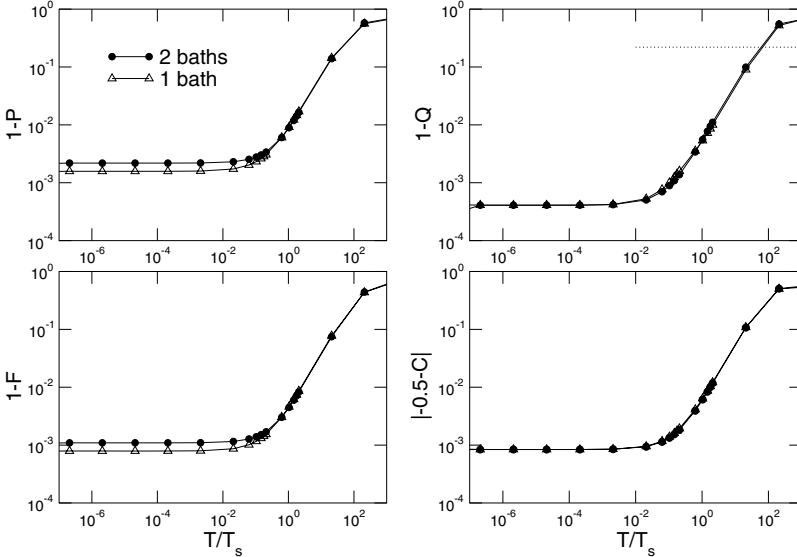


Fig. 5. Log-log plot of the temperature dependence of the deviations of the four gate quantifiers from their ideal values. Here the temperature is varied from ≈ 0 to $2 \cdot E_s$. In all cases $\alpha = \alpha_1 = \alpha_2 = 10^{-3}$. The dotted line indicates the upper bound set by the Clauser-Horne-Shimony-Holt inequality

mon bath and two distinct baths in the same temperature range discussed by Thorwart and Hänggi. However, see Fig. 5, overall we find substantially better values. This is due to the fact that for $\hat{\sigma}_y \otimes \hat{\sigma}_y$ coupling, the Hamiltonian does *not* commute with the coupling to the bath during the two-qubit steps of the pulse sequence, i.e. the symmetries of the coupling to the bath and the inter-qubit coupling are not compatible. The dotted line in Fig. 5 shows that already at comparably high temperature, about 20 qubit energies, a quantum degree larger than $Q \approx 0.78$ can be achieved. Only then, the Clauser-Horne-Shimony-Holt inequality is violated and non-local correlations between the qubits occur as described in [22]. Thus, even under rather modest requirements on the experimental setup which seem to be feasible with present day technology, it appears to be possible to demonstrate nonlocality and entanglement between superconducting flux qubits.

6 Summary

It has been outlined, how one can model the decoherence of an electromagnetic environment inductively coupled to a superconducting flux qubit. We have exemplified a procedure based on analyzing the classical friction induced by the environment for the specific case of the read-out SQUID. It is shown that the SQUID can be effectively decoupled from the qubit if no bias cur-

rent is applied. The effect of the decoherence on relaxation and dephasing rates of single qubits has been discussed as well as the gate performance of coupled qubits. We have shown that by carefully engineering the impedance and the symmetry of the coupling, one can reach excellent gate quality which complies with the demands of quantum computation.

Acknowledgements

We would like to thank M. Governale, T. Robinson, and M. Thorwart for discussions. FKW and MJS acknowledge support from ARO under contract-No. P-43385-PH-QC.

References

1. see e.g. D. Bouwmeester, A.K. Ekert, and A. Zeilinger, *The Physics of Quantum Information* (Springer, Berlin, Heidelberg, 2000). 763
2. D. DiVincenzo, *Science* **270**, 255 (1995). 763
3. Yu. Makhlin, G. Schön, and A. Shnirman, *Rev. Mod. Phys.* **73**, 357 (2001). 763, 764, 769, 772, 775
4. I. Chiorescu, Y. Nakamura, C.J.P.M. Harmans, and J.E. Mooij, *Science* **299**, 1869 (2003). 763, 764, 765, 770
5. Yu.A. Pashkin, T. Yamamoto, O. Astafiev, Y. Nakamura, D.V. Averin, and J.S. Tsai, *Nature* **421**, 823 (2003). 763, 764
6. J.E. Mooij, T.P. Orlando, L. Levitov, L. Tian, C.H. van der Wal, and S. Lloyd, *Science* **285**, 1036 (1999); T.P. Orlando, J.E. Mooij, L. Tian, C.H. van der Wal, L.S. Levitov, S. Lloyd, and J.J. Mazo, *Phys. Rev. B* **60**, 15398 (1999). 764, 765, 767, 772, 773
7. L. Tian, L.S. Levitov, C.H. van der Wal, J.E. Mooij, T.P. Orlando, S. Lloyd, C.J.P.M. Harmans, and J.J. Mazo in I. Kulik and R. Elliatogly, *Quantum Mesoscopic Phenomena and Mesoscopic Devices in Microelectronics* (Kluwer, Dordrecht, 2000), 429. 764
8. Yu. Makhlin *et al.*, this volume. 764
9. C.H. van der Wal, A.C.J. ter Haar, F.K. Wilhelm, R.N. Schouten, C.J.P.M. Harmans, T.P. Orlando, S. Lloyd, and J.E. Mooij, *Science* **290**, 773 (2000). 764, 765, 770
10. M. Grifoni, E. Paladino, U. Weiss, *Eur. Phys. J. B* **10**, 719 (1999). 765, 768, 770
11. A.J. Leggett, S. Chakravarty, A.T. Dorsey, M.P.A. Fisher, A. Garg, and W. Zwerger, *Rev. Mod. Phys.* **59**, 1 (1987). 766, 767, 768, 769, 770
12. C.H. van der Wal, F.K. Wilhelm, C.J.P.M. Harmans, and J.E. Mooij, *Eur. Phys. J. B* **31**, 111 (2003). 766, 768, 769, 771
13. A.J. Leggett, *Phys. Rev. B* **30**, 1208 (1984). 766, 768
14. U. Weiss, *Quantum Dissipative Systems*, (World Scientific, Singapore, ed. 2, 1999). 767, 768
15. A. Abragam, *Principles of Nuclear Magnetism* (Oxford University Press, Oxford, 1961). 768
16. F.K. Wilhelm, submitted to *Phys. Rev. B*. 769

17. S. Kleff, S. Kehrein, and J. von Delft, to appear in *Physica E*. [769](#)
18. Yu. Makhlin, G. Schön, and A. Shnirman, *Physica C* **368**, 276 (2002). [769](#)
19. P. Joyez, D. Vion, M. Götz, M.H. Devoret, D. Esteve, *J. Supercond.* **12**, 757 (1999). [771](#), [772](#)
20. W.T. Coffey, Y.P. Kalmykov, J.T. Waldron, *The Langevin Equation; with Applications in Chemistry and Electrical Engineering*, (World Scientific, Singapore, 1996). [771](#)
21. M. Governale, M. Grifoni, G. Schön, *Chem. Phys.* **268**, 273 (2001). [772](#)
22. M. Thorwart, P. Hänggi, *Phys. Rev. A* **65**, 012309 (2002). [772](#), [774](#), [775](#), [776](#)
23. J.B. Majer, priv. comm. (2002). [772](#)
24. Yu.A. Pashkin, T. Yamamoto, O. Astafiev, Y. Nakamura, D.V. Averin, J.S. Tsai, *Nature* **421**, 823 (2003). [772](#)
25. M.J. Storcz and F.K. Wilhelm, *Phys. Rev. A* **67**, 042319 (2003). [773](#), [774](#), [775](#)
26. J.F. Poyatos, J.I. Cirac, P. Zoller, *Phys. Rev. Lett.* **78**, 390 (1997). [774](#), [775](#)
27. C.H. Bennett, G. Brassard, S. Popescu, B. Schumacher, J.A. Smolin, and W.K. Wootters, *Phys. Rev. Lett.* **76**, 722 (1996). [775](#)
28. A. Peres, *Phys. Rev. Lett.* **77**, 1413 (1996). [775](#)

3.3 Manipulation of superconducting qubits

In the previous works, we have focused on finding the appropriate parameters for mapping a superconducting qubit coupled to an electric circuit by a system-plus-bath Hamiltonian. From this, we have straightforwardly predicted the dynamics of a qubit with a time-independent system Hamiltonian. In Ref. [194], we study the interplay of driving and dissipation on a single qubit. We focus on continuous driving, reflecting the status of experiments [189] which had already been completed while this work was done. In contrast to models in quantum optics and NMR, the driving of the flux qubit cannot be reduced to a simple, integrable rotating-wave Hamiltonian: the symmetry is lower than in atomic systems and driving fields can - and (given the strong decoherence) have to - be stronger. Thus, nonlinear driving effects are likely to occur and can be used in order to experimentally characterize all relevant properties of the sample.

In paper [195], a system of two coupled qubits in given environments is studied. The model of the qubits and environments is motivated by what can be done in superconducting flux qubits. In particular, since in these systems the decoherence is predominantly due to flux noise and the inter-qubit coupling is due to flux, the coupling to the noise commutes with the coupling Hamiltonian, but not with the single-qubit Hamiltonians. The dynamics of this setups is far more complex than in the single qubit case, in particular, it has six distinct nonzero eigenfrequencies, corresponding to $n(n - 1)/2$ level splittings in the case of $n = 2^q$ levels and $q = 2$ qubits. We give the distinct dephasing rates of these transitions and illustrate the dynamics. However, these data do not provide too clear information on the performance on the device. Specifically, the rates depend on the parameter settings of the Hamiltonian in subtle and diverse ways. Thus, we also simulate controlled phase-shift (CPHASE) and controlled not (CNOT) quantum gates using rectangular DC pulses, and characterize our results in terms of the gate-quality factors from quantum information theory. We show that on the level of coherence of present day devices, it may be well within reach to demonstrate entanglement between coupled qubits. At low temperatures, the performance of the CPHASE becomes ideal, because the Hamilton operator commutes with the bath coupling at all times. The CNOT is by far more limited, because the single-qubit operations which are necessary on top of the CPHASE do not have this symmetry property.

Theoretical analysis of continuously driven dissipative solid-state qubits

M. C. Goorden^{1,2} and F. K. Wilhelm^{1,3}¹*Quantum Transport Group, Department of Applied Physics and DIMES, Delft University of Technology, Lorentzweg 1, 2628 CJ Delft, The Netherlands*²*Lorentz Institute, University of Leiden, P.O. Box 9506, NL-2300 RA Leiden, The Netherlands*³*Sektion Physik and CeNS, Ludwig-Maximilians-Universität, Theresienstrasse 37, 80333 München, Germany*

(Received 4 April 2003; published 28 July 2003)

We study a realistic model for driven qubits using the numerical solution of the Bloch-Redfield equation as well as analytical approximations using a high-frequency scheme. Unlike in idealized rotating-wave models suitable for NMR or quantum optics, we study a driving term which neither is orthogonal to the static term nor leaves the adiabatic energy value constant. We investigate the underlying dynamics and analyze the spectroscopy peaks obtained in recent experiments. We show, that unlike in the rotating-wave case, this system exhibits nonlinear driving effects. We study the width of spectroscopy peaks and show, how a full analysis of the parameters of the system can be performed by comparing the first and second resonance. We outline the limitations of the NMR linewidth formula at low temperature and show, that spectroscopic peaks experience a strong shift which goes much beyond the Bloch-Siegert shift of the eigenfrequency.

DOI: 10.1103/PhysRevB.68.012508

PACS number(s): 74.50.+r, 05.40.-a, 85.25.Dq, 03.67.Lx

Coherent manipulation of quantum states is a well established technique in atomic and molecular physics. In these fields, one works with “clean” generic quantum systems which can be very well decoupled from their environments. Moreover, it is possible to apply external fields in a way such that strong symmetry relations between the static and the time-dependent part of the Hamiltonian apply and the resulting dynamics is very simple and can be treated analytically. In solid-state systems, the situation is different. Not only do they contain a macroscopic number of degrees of freedom which form a heat bath decohering the quantum states to be controlled, but also is the choice of controllable parameters much more restricted. A quantum-mechanical two state system (TSS) realized in a mesoscopic circuit can be identified with a (pseudo)spin, however, in that case the different components of the spin may correspond to physically distinct observables such as, e.g., magnetic flux and electric charge.¹ This naturally limits the possibilities of controlling arbitrary parameters of the pseudospin. Hence, in order to describe the direct control of quantum states in mesoscopic devices, concepts from NMR or quantum optics cannot be *directly* applied but have to be carefully adapted. In particular, as decoherence is usually rather strong in condensed matter systems, one can attempt to drive the system rather strongly in order to have the operation time for a quantum gate, usually set by the Rabi frequency, as short as possible.

We concentrate on the case of a persistent current quantum bit²⁻⁴ driven through the magnetic flux through the loop and damped predominantly by flux noise⁵ with Gaussian statistics. This setup is accurately described by the driven^{6,7} spin-boson model⁸

$$H = \frac{\epsilon(t)}{2} \hat{\sigma}_z - \frac{\Delta}{2} \hat{\sigma}_x + \hat{\sigma}_z \sum_i c_i \hat{x}_i + \sum_i \left(\frac{\hat{p}_i^2}{2m_i} + \frac{1}{2} m_i \omega_i^2 \hat{x}_i^2 \right), \quad (1)$$

where $\epsilon(t) = \epsilon_0 + s \cos \Omega t$ and the oscillator bath is assumed to be ohmic with a spectral density $J(\omega) = (\pi/2) \sum_i (c_i^2/m_i \omega_i) \delta(\omega - \omega_i) = 2\pi \alpha \omega e^{-\omega/\omega_c}$. The connec-

tion of $J(\omega)$ to the setup parameters is detailed in Ref. 5. The static energy splitting of the pseudospin is $\nu = \sqrt{\epsilon_0^2 + \Delta^2}$. This model is also applicable to other Josephson qubits and other realizations.^{8,9} In particular, the strong driving regime we are going to elaborate on has recently been realized in several setups.¹⁰⁻¹² We study the effective dynamics of the pseudospin having traced out the bath in the limit of weak damping $\alpha \ll 1$ which is appropriate for quantum computation. This is done using the Bloch-Redfield equation.¹³ The resulting equation is of Markovian form in the sense that it only contains the density matrix at a single time, however, it is derived in such a way, that the free coherent evolution during the interaction with the bath is fully taken into account such that the resulting equation is numerically equivalent to a fully non-Markovian path-integral scheme^{7,9} and only memory terms beyond the Born approximation are dropped. The explicit form of the equations for this situation as well as the formulas for the rates correspond to those given in Ref. 7. We compare our numerical results to analytical formulas derived in the framework of a high-frequency approximation¹⁴ which involves averaging over the driving field and has nonetheless shown to give a good estimate for the system dynamics even close to resonances.⁷

Initial experiments on quantum bits such as Ref. 3 do not monitor the real-time dynamics of the system as in Ref. 4, because the read-out is much slower than the decoherence, i.e., the dephasing time τ_ϕ is too short. In order to optimize the experimental setup, it is important to measure both τ_ϕ and the relaxation time τ_R , even and in particular if they are insufficient. In the standard NMR-case, this is done by studying the width of the resonance.¹⁵ We will detail that a somewhat modified analysis can be performed for solid-state qubits and what are its limitations. We discuss both situations.^{3,4} Our results thus help to analyze the decoherence as observed in Refs. 3,4, and outline the possibilities and limitations of driving the system in the nonlinear regime.

We have numerically solved the driven Bloch-Redfield equation. The real-time dynamics is illustrated in Fig. 1.

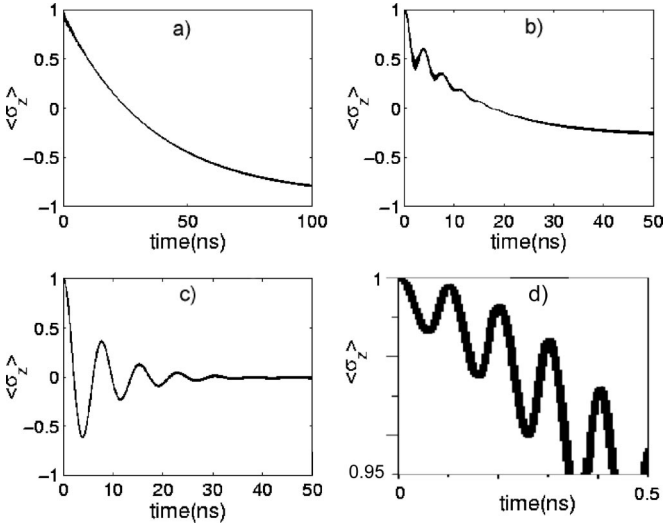


FIG. 1. $\langle \sigma_z \rangle(t)$ at fixed frequency $\Omega/2\pi = 6.6$ GHz for different bias points. (a) Off resonance, $\nu/2\pi = 2.9$ GHz, incoherent decay towards thermal equilibrium, (c) on resonance, $\nu/2\pi = 6.6$ GHz, Rabi oscillations decaying on the scale of a dephasing time τ_ϕ towards a dynamical equilibrium state, (b) close to the resonance, $\nu/2\pi = 6.4$ GHz, combination of decoherence and relaxation, and (d) short-time dynamics highlighting the fast oscillating component, see text.

The dynamics shows distinct features on different time scales. As expected, there are clear Rabi oscillations on the scale of the effective driving strength (see below). In quantum computing applications, these would be used for the implementation of a Hadamard gate. On top of this, there are fast components: The dominating one oscillates with the driving frequency, which originates in the fact that the driving is not perpendicular to the static field. A weaker one, which oscillates at twice the driving frequency, comes from the counter-rotating term perpendicular to the static field.

These oscillations can lead to errors of the Hadamard gate. On a longer time scale, the Rabi oscillations decay. The time scales will be discussed later on. In general, if one is not exactly on resonance, these oscillations are combined with nonoscillatory decay, see Figs. 1(a) and 1(b). At very long times, the system assumes a quasistationary value P_∞ .

Corresponding to the situation of a spectroscopy experiment, we now turn to the analysis of the quasistationary state which is established after a long time $t \gg \tau_\phi, \tau_R, \omega_R^{-1}$. We compare our full numerical solutions with analytical expressions we have obtained from the high-frequency approximation of Refs. 7,14. As a result of this approach, the TSS is mapped onto a coupled ensemble of TSSs corresponding to the original system emitting or absorbing n photons from the driving field during the tunneling. The energy bias of these individual systems is $\epsilon_n = \epsilon_0 - n\Omega$ and the tunnel matrix element

$$\Delta_n = \Delta J_n(s/\Omega), \quad (2)$$

where the J_n are Bessel functions. At low driving fields, we can approximate $\Delta_n = (\Delta/n!)(s/2\Omega)^n$ as we would expect from the expansion of a perturbation series in the driving strength. The Δ_n can hence be viewed as n -photon Rabi frequencies. This implies, that the usual single-photon frequency gets replaced by $\Delta_1 \approx s\Delta/\nu$, which can be interpreted as only the projection of the driving field onto the direction in pseudospin space orthogonal to the static Hamiltonian. In order to obtain the solid curves in Fig. 2 the secular equations for the eigenfrequencies have been solved, taking into account an appropriate number of terms.¹⁶ The dynamical two state systems are characterized by individual dynamical dephasing rates $\Gamma_{\phi,n}$ and a common relaxation rate Γ_r .⁷ On the n th resonance, $\Gamma_{\phi,n}$ can be very low, much lower than off resonance, as can be seen in Fig. 1, and largely exceed the intrinsic dephasing time. This has been observed in Refs. 1,4.

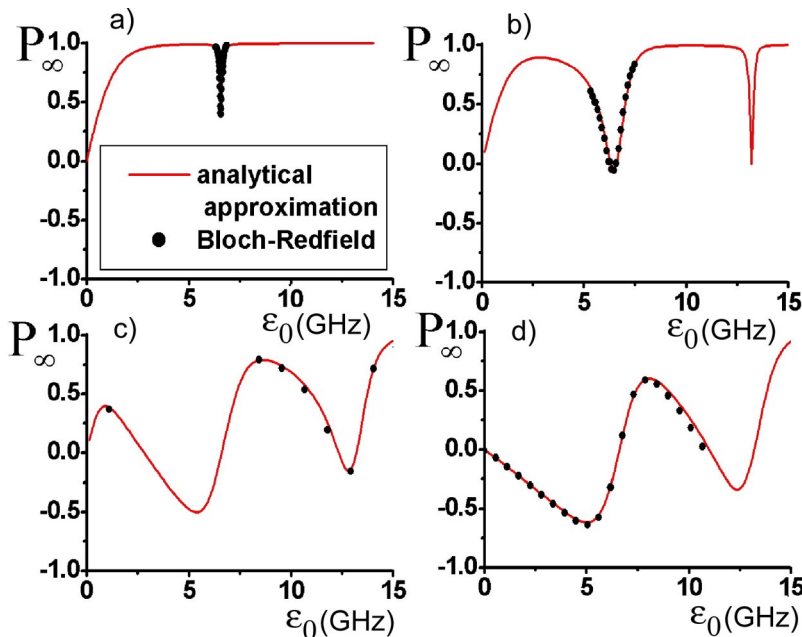


FIG. 2. $\langle \sigma_z \rangle$ in the long-time limit at fixed frequency $\Omega/2\pi = 6.6$ GHz as a function of the energy bias ϵ_0 for different values of the driving strength $s/\Omega = 0.034, 0.43, 1.7, 2.4$ [(a)–(d)]. From (b)–(d), nonlinear resonances can be identified. (d) already shows negative values at *small positive* ϵ_0 , which can be identified as the coherent destruction of zero-photon tunneling. Further peaks occur at even higher bias.

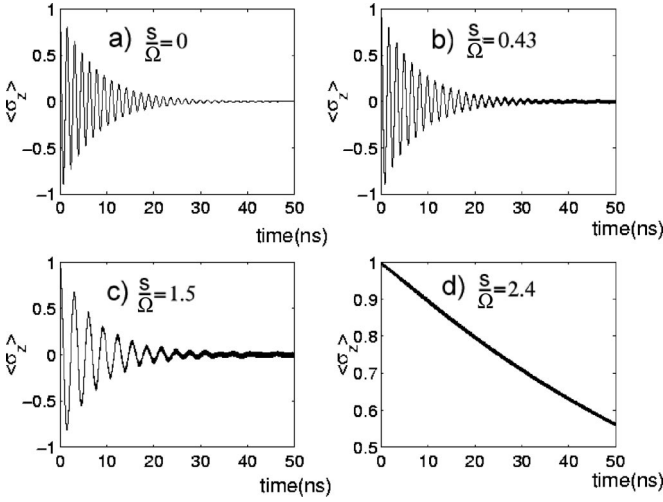


FIG. 3. $\langle \sigma_z \rangle$ at strong driving with high frequency $\Omega/2\pi = 6.6$ GHz (where $\Delta/2\pi = 660$ MHz). By increasing the driving strength, the tunneling is slowed down and brought to a standstill.

Figure 2 shows numerical and analytical results for $P_\infty = \lim_{t \rightarrow \infty} \langle \sigma_z \rangle$ at a fixed frequency $\Omega/2\pi = 6.6$ GHz as a function of the energy bias ϵ_0 . This corresponds to a realistic experimental situation.³ In Fig. 2(a), taken at weak driving field, only the regular resonance corresponding to the transition between the two eigenstates driven by absorbing a single photon can be seen. At somewhat stronger driving, Fig. 2(b), this peak grows wider and a second resonance appears, corresponding to the simultaneous absorption of two photons. At higher fields, Fig. 2(c), these peaks grow and start to dominate over the background. They also turn asymmetric. This trend culminates in the situation shown in Fig. 2(d). In that case, P_∞ does *not* grow to positive values at small positive ϵ_0 , but it gets negative and then directly approaches the first resonance. The reason for this behavior can be identified within the high-frequency approximation: The lowest order-tunnel frequency $\Delta_0 = \Delta J_0(s/\Omega)$ vanishes at this particular driving strength. Indeed, comparing Figs. 2(a) and 2(d) one

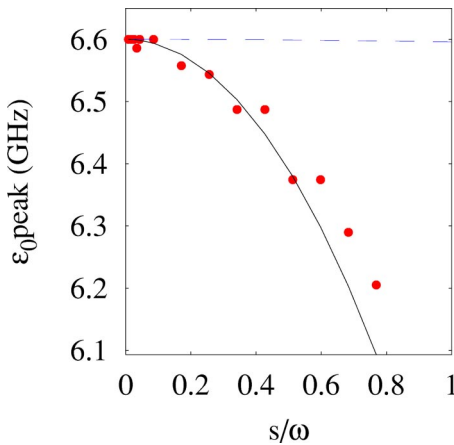


FIG. 4. Shift of the spectroscopy peak as a function of the driving strength for $\omega/2\pi = 6.6$ GHz and $\Delta/2\pi = 660$ MHz. We compare to the usual Bloch-Siegert shift formula (dashed) and the formula derived in the text (solid).

can see, that the step which is at $\epsilon_0 = 0$ in case (a) is shifted to $\epsilon_0 \approx \Omega$ in case (d). This phenomenon, the coherent destruction of tunneling⁶ relies on destructive interference of the dressed state¹⁷ formed by the TSS and a cloud of photons from the driving field. This interpretation is supported by the dynamics of $\langle \sigma_z \rangle(t)$. As seen in Fig. 3, which shows the dynamics at the degeneracy point for different driving strengths, the zero-photon tunneling is slowed down and brought to a standstill. If that strong driving can be applied to solid-state qubits, it would provide an alternative for controlling Δ_0 by a cw microwave field instead of an additional magnetic flux as proposed in Ref. 2.

At very weak driving, the peak position corresponds to the qubit eigenfrequency $\Omega = \nu$. This is not reliably predicted by the high-frequency approximation. At stronger driving, the peak gets shifted. Closer inspection as in Fig. 4 shows, that this shift goes much beyond the usual Bloch-Siegert shift⁶ of the dynamical eigenfrequency, in fact, one can show that the position of the *peak* in steady state and the eigenfrequency do not coincide. The former is given by balancing of rates and it can be shown that in lowest order gets shifted by¹⁶ $\delta\epsilon_{\text{peak}} \approx s^2/8\Omega$ whereas the Bloch-Siegert shift for our case is $\delta\epsilon_{\text{BS}} \approx \Delta^2 s^2/(16\Omega^3)$. As a more general conclusion, already at modest not-too-weak driving, the resonance positions do not necessarily reflect the eigenfrequencies of the system.

In Fig. 5, the height of the two lowest order peaks is shown. It can be seen, that, from the low-driving side, they saturate as soon as their effective Rabi frequency Δ_n exceeds $1/\sqrt{\tau_r \tau_\phi}$. At very high driving, the peaks show an inversion of population.

For the optimization of qubit setups on the way to coherent dynamics, it is important to characterize its coherence properties from the spectroscopic data. In NMR, this is done from the linewidth given by

$$\delta\Omega = 2\sqrt{\tau_\phi^{-2} + \omega_R^2 \tau_R / \tau_\phi}, \quad (3)$$

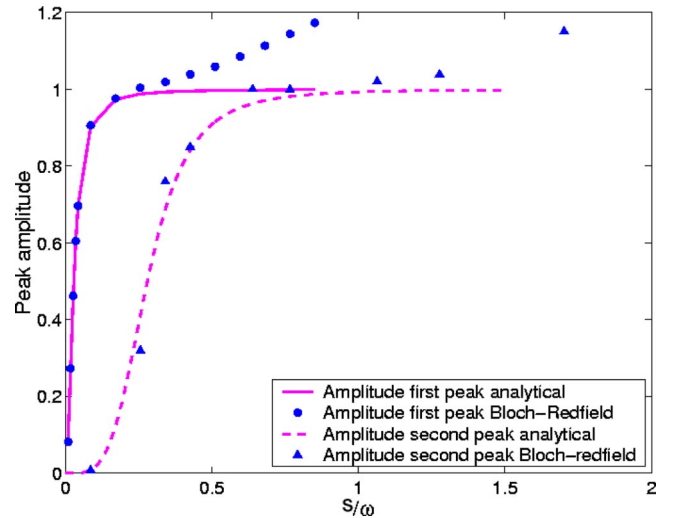


FIG. 5. Heights of the two lowest resonances as a function of the driving strength s at $\nu/2\pi = 6.6$ GHz, $\Delta/2\pi = 660$ MHz, $\Omega/2\pi = 6.6$ GHz. The solid and dashed lines are extrapolated NMR formulas.

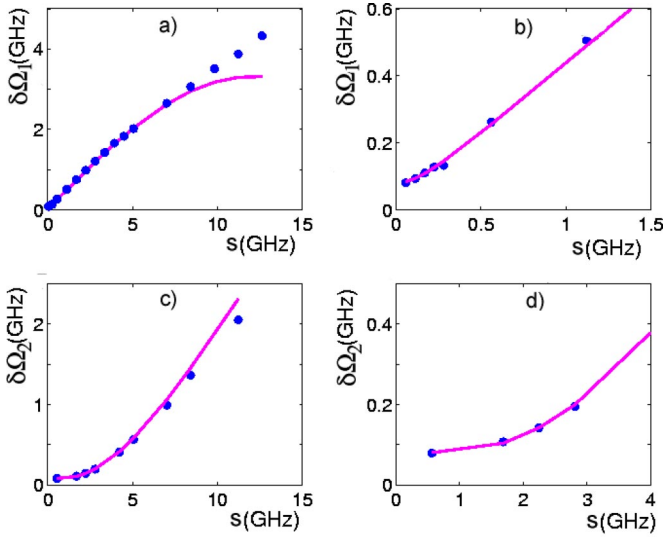


FIG. 6. Widths of the two lowest resonances as a function of the driving strength s at $\Delta/2\pi = 660$ MHz and $\Omega/2\pi = 6.6$ GHz. The solid line corresponds to the extrapolated NMR formula discussed in the text.

where ω_R is the Rabi frequency at resonance, which coincides with the strength of the driving field. A generalization of this formula to our case has to take into account low temperatures and the different driving situation. Moreover, ω_R is usually not directly known to sufficient precision, because the driving strength depends on the attenuation of the applied fields on their way to the sample and the efficiency of the coupling.^{3,5}

Our analysis suggests the generalization of Eq. (3) is given by

$$\delta\Omega_n = 2\sqrt{\tau_\phi^{-2} + \Delta_n^2 \tau_R / \tau_\phi}, \quad n = \pm 1, \pm 2 \dots, \quad (4)$$

where $\delta\Omega_n$ is the width (in frequency) of the n -photon resonance and Δ_n is the effective Rabi frequency defined above. At low powers $s < \Omega$, they are given by the rates from the undriven Ohmic case

$$\tau_R^{-1} = \alpha \frac{\Delta^2}{2\nu} \coth\left(\frac{\hbar\nu}{2k_B T}\right), \quad \tau_\phi^{-1} = (2\tau_R)^{-1} + 2\pi\alpha \frac{k_B T}{\hbar} \frac{\epsilon_0^2}{\nu^2}. \quad (5)$$

This result is confirmed by our numerical simulations Fig. 6.

We can essentially identify three regimes: A saturation broadening regime at low powers, where $\delta\Omega_n \approx 2\tau_\phi^{-1}$, a saturated regime, $\delta\Omega_n \approx 2\Delta_n \sqrt{\tau_R / \tau_\phi}$ and a nonlinear regime, where the numerical curve deviates from Eq. (4) due to the fact, that the high Rabi frequency shifts the relevant energy scales and modifies the time scales given in Eq. (5). Note, that in this regime, the general curve of P_∞ is greatly deformed (see Fig. 2) and the width of a peak becomes ambiguous.

This result allows to measure essentially all interesting parameters of the system experimentally. By extrapolating the level separation at the degeneracy point [as it was done in Eq. (3)], one obtains Δ . By tracking the resonance positions at weak driving, one can evaluate ϵ_0 as a function of the external control parameter [in Eq. (3) this would be the magnetic flux]. By driving in the saturated regime, the widths of the first and second peak become, according to Eq. (4) $\delta\Omega_{1/2} = 2\Delta_{1/2} \sqrt{\tau_R / \tau_\phi}$, hence by taking their ratio we find the effective driving strength from $\Delta_2 / \Delta_1 = J_1(s/\Omega) / J_0(s/\Omega) \approx s/2$ and by tracking the slope of the first resonance we find the ratio τ_r / τ_ϕ . Finally, examining the saturation broadening regime of the first resonance gives the absolute value of τ_ϕ .

In conclusion, we have numerically and analytically analyzed the spin-boson system, which, e.g., represents a SQUID qubit, in the weak damping regime, driven by continuous fields. As compared to the more familiar situation in NMR, this system is both different in the character of the driving and the low temperature governing the dissipation. We have shown, that the key features of this system, Rabi oscillations, and saturation of the linewidth, persist qualitatively as has been experimentally confirmed.⁴ They are, however, altered on a quantitative level, such as an unanticipated strong shift of the position of the resonance peak, and also supplemented by new phenomena such as higher-harmonics generation, oscillations of $\langle \sigma_z \rangle$ on the scale of the driving field, and coherent destruction of tunneling. We have finally outlined a scheme how to determine all relevant parameters (tunnel splitting, energy dispersion, driving strength, dephasing and relaxation time) of a quantum bit solely through spectroscopy.

We thank M. Grifoni, C.H. van der Wal, A.C.J. ter Haar, C.J.P.M. Harmans, J. von Delft, and I. Goychuk for discussions. Work supported by the EU through TMR ‘‘Supnan’’ and IST ‘‘Squibit.’’ F.K.W. acknowledges support by the ARO under Contract No. P-43385-PH-QC.

¹D. Vion *et al.*, Science **296**, 886 (2002).

²J.E. Mooij *et al.*, Science **285**, 1036 (1999).

³C.H. van der Wal *et al.*, Science **290**, 773 (2000).

⁴I. Chiorescu *et al.*, Science **299**, 1869 (2003).

⁵C.H. van der Wal *et al.*, Eur. Phys. J. B **31**, 111 (2003); T.P. Orlando *et al.*, Physica C **368**, 294 (2002).

⁶P. Hänggi and M. Grifoni, Phys. Rep. **304**, 229 (1998).

⁷L. Hartmann *et al.*, Phys. Rev. E **61**, 4687 (2000).

⁸A.J. Leggett *et al.*, Rev. Mod. Phys. **59**, 1 (1987).

⁹U. Weiss, *Quantum Dissipative Systems*, 2nd ed. (World Scientific, Singapore, 1999).

¹⁰A.C.J. ter Haar *et al.* (private communication).

¹¹A. Wallraff *et al.*, Phys. Rev. Lett. **90**, 037003 (2003).

¹²Y. Nakamura *et al.*, Phys. Rev. Lett. **87**, 246601 (2001).

¹³P.N. Argyres and P.L. Kelley, Phys. Rev. **134**, A98 (1964).

¹⁴M. Grifoni *et al.*, Phys. Rev. E **53**, R2033 (1996).

¹⁵A. Abragam, *The Principles of Nuclear Magnetism* (Oxford University Press, Glasgow, 1961).

¹⁶For details see M.C. Goorden, Master’s thesis, TU Delft, 2002; available on qt.tn.tudelft.nl

¹⁷M. Thorwart *et al.*, J. Mod. Opt. **47**, 2905 (2000).

Decoherence and gate performance of coupled solid-state qubits

Markus J. Storcz* and Frank K. Wilhelm

Sektion Physik and CeNS, Ludwig-Maximilians-Universität, Theresienstrasse 37, 80333 München, Germany

(Received 16 December 2002; published 23 April 2003; publisher error corrected 28 April 2003)

Solid-state quantum bits are promising candidates for the realization of a *scalable* quantum computer. However, they are usually strongly limited by decoherence due to the many extra degrees of freedom of a solid-state system. We investigate a system of two solid-state qubits that are coupled via $\sigma_z^{(i)} \otimes \sigma_z^{(j)}$ type of coupling. This kind of setup is typical for *pseudospin* solid-state quantum bits such as charge or flux systems. We evaluate decoherence properties and gate quality factors in the presence of a common and two uncorrelated baths coupling to σ_z , respectively. We show that at low temperatures, uncorrelated baths do degrade the gate quality more severely. In particular, we show that in the case of a common bath, optimum gate performance of a controlled-PHASE gate can be reached at very low temperatures, because our type of coupling commutes with the coupling to the decoherence, which makes this type of coupling interesting as compared to previously studied proposals with $\sigma_y^{(i)} \otimes \sigma_y^{(j)}$ coupling. Although less pronounced, this advantage also applies to the controlled-NOT gate.

DOI: 10.1103/PhysRevA.67.042319

PACS number(s): 03.67.Lx, 03.65.Yz, 05.40.-a, 85.25.-j

I. INTRODUCTION

Quantum computation has been shown to perform certain tasks much faster than classical computers [1–3]. Presently, very mature physical realizations of this idea originate in atomic physics, optics, and nuclear magnetic resonance. These systems are phase coherent in abundance, however, scaling up the existing few-qubit systems is not straightforward. Solid-state quantum computers have the potential advantage of being arbitrarily scalable to large systems of many qubits [4–6]. Their most important drawback is the coupling to the many degrees of freedom of a solid-state system. Even though recently, there has been fast progress in improving the decoherence properties of experimentally realized solid-state quantum bits [7–11], this remains a formidable task.

Quite a lot is known about decoherence properties of single solid-state qubits, see, e.g., Refs. [12–14], but much less is known about systems of two or more coupled qubits [15–17]. However, only for systems of at least two qubits, the central issue of entanglement can be studied. The physically available types of qubit coupling can be classified as Heisenberg-type exchange that is typical for real spin-1/2 systems, and Ising-type coupling, which is characteristic for *pseudospin* setups, where the computational degrees of freedom are not real spins. In the latter, the different spin components typically correspond to distinct variables, such as charge and flux [10,18] whose couplings can and have to be engineered on completely different footing. Previous work [16,17] presented the properties of a system of two coupled solid-state qubits that are coupled via $\sigma_y^{(i)} \otimes \sigma_y^{(j)}$ type coupling as proposed in Ref. [14] as the current-current coupling of superconducting charge quantum bits.

On the other hand, many systems such as inductively coupled flux qubits [6], capacitively coupled charge qubits [7,8], and other pseudospin systems [19] are described by a

$\sigma_z^{(i)} \otimes \sigma_z^{(j)}$ Ising-type coupling. This indicates that the computational basis states are coupled, which, i.e., in the case of flux qubits are magnetic fluxes, whereas $\sigma_{x/y}$ are electric charges. The σ_z observable is a natural way of coupling, because it is typically easy to couple to. We will study a two qubit-system coupled this way that is exposed to Gaussian noise coupling to σ_z , the “natural” observable. This example accounts for the crucial effect of electromagnetic noise in superconducting qubits. We will compare both the cases of noise that affects both qubits in a correlated way and the case of uncorrelated single-qubit errors. We determine the decoherence properties of the system by application of the well-known Bloch-Redfield formalism and determine quality factors of a controlled-NOT (CNOT) gate for both types of errors and feasible parameters of the system.

II. MODEL HAMILTONIAN

We model the Hamiltonian of a system of two qubits, coupled via Ising-type coupling. Each of the two qubits is a two-state system that is described in pseudospin notation by the single-qubit Hamiltonian [13]

$$\mathbf{H}_{sq} = -\frac{1}{2}\epsilon\hat{\sigma}_z - \frac{1}{2}\Delta\hat{\sigma}_x, \quad (1)$$

where ϵ is the energy bias and Δ the tunnel matrix element. The coupling between the qubits is determined by an extra term in the Hamiltonian $\mathbf{H}_{qq} = -(K/2)\hat{\sigma}_z^{(1)} \otimes \hat{\sigma}_z^{(2)}$ that represents e.g., inductive interaction (directly or via flux transformer) in the case of flux qubits [6,20]. Thus, the complete two-qubit Hamiltonian in the absence of a dissipative environment reads

$$\mathbf{H}_{2qb} = \sum_{i=1,2} \left(-\frac{1}{2}\epsilon_i\hat{\sigma}_z^{(i)} - \frac{1}{2}\Delta_i\hat{\sigma}_x^{(i)} \right) - \frac{1}{2}K\hat{\sigma}_z^{(1)}\hat{\sigma}_z^{(2)}. \quad (2)$$

The dissipative (bosonic) environment is conveniently modeled as either a common bath or two distinct baths of har-

*Electronic address: storcz@theorie.physik.uni-muenchen.de

monic oscillators, coupling to the σ_z components of the two qubits. This approach universally models baths which produce *Gaussian* fluctuations, such as the noise from linear electrical circuits. An example for a situation described by a common bath is long correlation length electromagnetic noise from the experimental environment or noise generated or picked up by coupling elements such as flux transformers [6]. Short correlation length radiation or local readout and control electronics coupling to individual qubits [13] might be described as coupling to two uncorrelated baths of harmonic oscillators.

One should note that if the number of qubits is increased to more than two, there might also occur dissipative effects that neither affect all qubits nor only a single qubit, but rather a cluster of qubits, thus, enhancing the complexity of our considerations [21].

In the case of two uncorrelated baths, the full Hamiltonian reads

$$\mathbf{H}_{2qb}^{2b} = \sum_{i=1,2} \left(-\frac{1}{2} \epsilon_i \hat{\sigma}_z^{(i)} - \frac{1}{2} \Delta_i \hat{\sigma}_x^{(i)} + \frac{1}{2} \hat{\sigma}_z^{(i)} \hat{X}^{(i)} \right) - \frac{1}{2} K \hat{\sigma}_z^{(1)} \hat{\sigma}_z^{(2)} + \mathbf{H}_{B_1} + \mathbf{H}_{B_2}, \quad (3)$$

where each qubit couples to its own, distinct harmonic oscillator bath \mathbf{H}_{B_i} , $i=1,2$, via the coupling term $\hat{\sigma}_z^{(i)} \hat{X}^{(i)}$, $i=1,2$, that bilinearly couples a qubit to the collective bath coordinate $\hat{X}^{(i)} = \zeta \sum_{\nu} \lambda_{\nu} x_{\nu}$. We again sum over the two qubits. In the case of two qubits coupled to one common bath, we model our two-qubit system with the Hamiltonian

$$\mathbf{H}_{2qb}^{1b} = -\frac{1}{2} \sum_{i=1,2} (\epsilon_i \hat{\sigma}_z^{(i)} + \Delta_i \hat{\sigma}_x^{(i)}) - \frac{1}{2} K \hat{\sigma}_z^{(1)} \hat{\sigma}_z^{(2)} + \frac{1}{2} (\hat{\sigma}_z^{(1)} + \hat{\sigma}_z^{(2)}) \hat{X} + \mathbf{H}_B, \quad (4)$$

where \mathbf{H}_B denotes one common bath of harmonic oscillators.

The appropriate starting point for our further analysis is the singlet/triplet basis, consisting of $|\uparrow\uparrow\rangle := (1,0,0,0)^T$, $(1/\sqrt{2})(|\uparrow\downarrow\rangle + |\downarrow\uparrow\rangle) := (0,1,0,0)^T$, $|\downarrow\downarrow\rangle := (0,0,1,0)^T$, and the singlet state $(1/\sqrt{2})(|\uparrow\downarrow\rangle - |\downarrow\uparrow\rangle) := (0,0,0,1)^T$. In the case of flux qubits, the \uparrow and \downarrow states correspond to clockwise and counterclockwise currents respectively.

In this basis, the undamped Hamiltonian \mathbf{H}_{2qb} , Eq. (2), of the two-qubit system assumes the matrix form

$$\mathbf{H}_{2qb} = -\frac{1}{2} \begin{pmatrix} \epsilon + K & \eta & 0 & -\Delta\eta \\ \eta & -K & \eta & \Delta\epsilon \\ 0 & \eta & K - \epsilon & \Delta\eta \\ -\Delta\eta & \Delta\epsilon & \Delta\eta & -K \end{pmatrix}, \quad (5)$$

with $\epsilon = \epsilon_1 + \epsilon_2$, $\eta = (\Delta_1 + \Delta_2)/\sqrt{2}$, $\Delta\eta = (\Delta_1 - \Delta_2)/\sqrt{2}$, and $\Delta\epsilon = \epsilon_1 - \epsilon_2$. From now on, for simplicity, we concentrate on the case of equal parameter settings, $\Delta_1 = \Delta_2$ and $\epsilon_1 = \epsilon_2$.

If we now also express the coupling to the dissipative environment in this basis, we find in the case of coupling to two uncorrelated distinct baths that

$$\mathbf{H}_{2qb}^{2b} = -\frac{1}{2} \begin{pmatrix} \epsilon - s + K & \eta & 0 & 0 \\ \eta & -K & \eta & -\Delta s \\ 0 & \eta & K - \epsilon + s & 0 \\ 0 & -\Delta s & 0 & -K \end{pmatrix}, \quad (6)$$

with $s = X_1 + X_2$ and $\Delta s = X_1 - X_2$. Here, the bath mediates transitions between the singlet and triplet states, the singlet is not a protected subspace.

In the case of two qubits with equal parameters that are coupled to one common bath, we obtain the matrix

$$\mathbf{H}_{2qb}^{1b} = -\frac{1}{2} \begin{pmatrix} \epsilon - s + K & \eta & 0 & 0 \\ \eta & -K & \eta & 0 \\ 0 & \eta & K - \epsilon + s & 0 \\ 0 & 0 & 0 & -K \end{pmatrix}, \quad (7)$$

where $s = 2X$ and $\Delta s = 0$. One directly recognizes that compared to Eq. (6) in this case, thermalization to the singlet state is impeded, because Eq. (7) is block diagonal in the singlet and triplet subspaces. The singlet and triplet are completely decoupled from each other, and in the case of one common bath the singlet is also completely decoupled from the bath and thus, protected from dissipative effects. Therefore, a system in contact with one common bath that is prepared in the singlet state will never experience any decoherence effects. The singlet state is a decoherence free subspace (DFS) [22], although a trivial, one-dimensional one.

III. EIGENENERGIES AND EIGENSTATES OF THE TWO-QUBIT HAMILTONIAN

We calculate exact analytical eigenvalues and eigenvectors of the unperturbed two-qubit system Hamiltonian in the aforementioned symmetric case of Eq. (5), which reads

$$\mathbf{H}_{2qb} = -\frac{1}{2} \begin{pmatrix} \epsilon + K & \eta & 0 & 0 \\ \eta & -K & \eta & 0 \\ 0 & \eta & K - \epsilon & 0 \\ 0 & 0 & 0 & -K \end{pmatrix}. \quad (8)$$

This Hamiltonian is block diagonal and the largest block, the triplet, is three dimensional, i.e., it can be diagonalized using Cardano's formula. Details of that calculation are given in Ref. [23]. The case of nonidentical qubits is more easily handled numerically.

In the following, $|E1\rangle$, $|E2\rangle$, $|E3\rangle$, and $|E4\rangle$ denote the eigenstates of the two-qubit system. The eigenenergies of the unperturbed Hamiltonian (8) depend on the three parameters K , ϵ , and η . Fig. 1 displays the eigenenergies in more detail for typical experimentally accessible values. The values that are chosen for the parameters ϵ , η , and K in Fig. 1 correspond to what can be reached in flux qubits. They typically assume values of a few GHz resembling the parameters

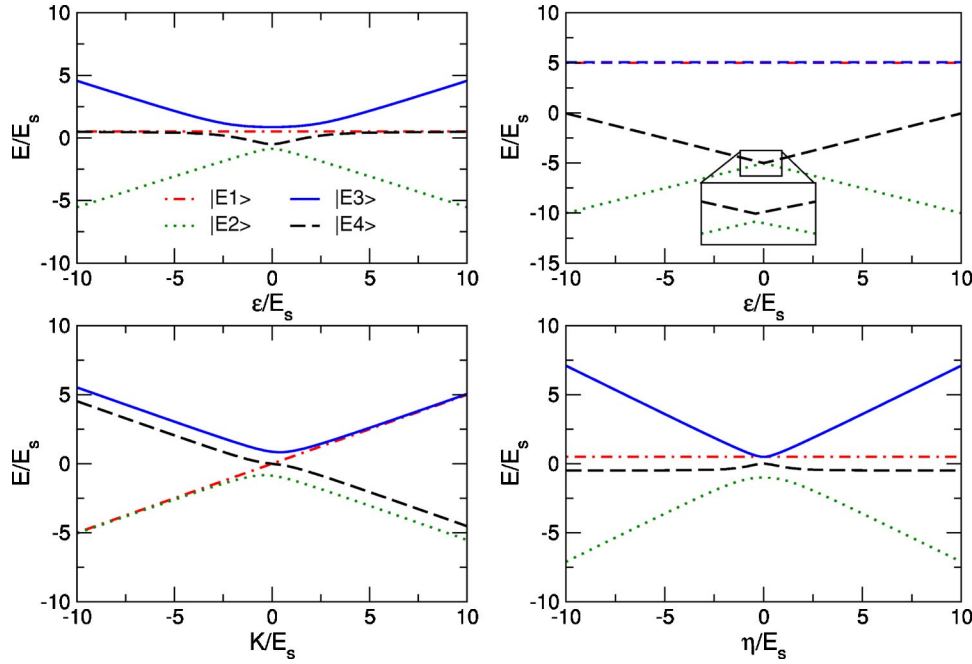


FIG. 1. Plot of the eigenenergies of the eigenstates $|E1\rangle$, $|E2\rangle$, $|E3\rangle$, and $|E4\rangle$. From upper left to lower right: (1) $K = \eta = E_s$ and ϵ is varied, (2) $K = 10E_s$, $\eta = E_s$, and ϵ is varied; the inset resolves the avoided level crossing due to the finite transmission amplitude η ; (3) $\eta = \epsilon = E_s$ and K is varied; (4) $K = \epsilon = E_s$ and η is varied.

of known single- and two-qubit experiments in Delft [13] and at MIT [24]. Therefore, we will use a characteristic energy scale E_s , which is typically $E_s = 1$ GHz. The corresponding scales are $t_s = 1$ ns, $\omega_s = 2\pi \times 1$ GHz, and $T_s = \nu_s (h/k_B) = 4.8 \times 10^{-2}$ K. Panel (1) shows that for large values of ϵ , two of the eigenenergies are degenerate (namely, for $\epsilon \gg \eta, K$ the states $|E1\rangle$ and $|E4\rangle$ equal the states $(1/\sqrt{2})(|\uparrow\downarrow\rangle - |\downarrow\uparrow\rangle)$ and $(1/\sqrt{2})(|\uparrow\downarrow\rangle + |\downarrow\uparrow\rangle)$, hence the eigenenergies are degenerate) while near zero energy bias (magnetic frustration $f = 1/2$) all four eigenenergies might be distinguished. Note also that, therefore, at zero energy bias, the transition frequency $\omega_{14} = -\omega_{41}$ has a local *maximum*, which, as will be shown below, can only be accessed via nonsymmetric driving.

If K is set to a big positive value corresponding to large ferromagnetic coupling [Fig. 1, panel (2), $K = 10E_s$], the Hamiltonian (8) is nearly diagonal and, hence, the eigenstates in good approximation are equal to the singlet/triplet basis states. In this case, $|E3\rangle$ equals the triplet state $(1/\sqrt{2})(|\uparrow\downarrow\rangle + |\downarrow\uparrow\rangle)$, $|E2\rangle$ and $|E4\rangle$ equal $|\uparrow\uparrow\rangle$ and $|\downarrow\downarrow\rangle$, respectively, for positive values of ϵ . For large negative values of ϵ , the two states $|E2\rangle$ and $|E4\rangle$ become equal $|\downarrow\downarrow\rangle$ and $|\uparrow\uparrow\rangle$ with a pseudo-spin-flip between clockwise and counterclockwise rotating currents at $\epsilon = 0$ when going from positive to negative ϵ . In the case of large ferromagnetic coupling, the ground state tends towards the superposition $(1/\sqrt{2})(|\uparrow\uparrow\rangle + |\downarrow\downarrow\rangle)$. Panel (2) shows that only for ϵ equal to zero, both $|E2\rangle = |\uparrow\uparrow\rangle$ ($|E2\rangle = |\downarrow\downarrow\rangle$, for negative ϵ) and $|E4\rangle = |\downarrow\downarrow\rangle$ ($|E4\rangle = |\uparrow\uparrow\rangle$, for negative ϵ) have the same energies (which one would expect if the $-(1/2)K\sigma_z^{(1)}\sigma_z^{(2)}$ term in the Hamiltonian dominates), because if ϵ is increased, the $\epsilon_i \hat{\sigma}_z^{(i)}$ ($i = 1, 2$) terms in the Hamiltonian change the energy.

For large antiferromagnetic coupling, $|-K| \gg \epsilon, \Delta$ the states $|\uparrow\downarrow\rangle$ and $|\downarrow\uparrow\rangle$ are favorable. In this limit, the ground state tends towards $(1/\sqrt{2})(|\uparrow\downarrow\rangle + |\downarrow\uparrow\rangle)$ and the energy splitting between $(1/\sqrt{2})(|\uparrow\downarrow\rangle + |\downarrow\uparrow\rangle)$ and $(1/\sqrt{2})(|\uparrow\downarrow\rangle - |\downarrow\uparrow\rangle)$ vanishes asymptotically, leaving the ground state nearly degenerate.

From Fig. 1, panel (3), one directly recognizes that the singlet eigenenergy crosses the triplet spectrum, which is a consequence of the fact that the singlet does not interact with any triplet states. At zero energy bias (magnetic frustration $f = 1/2$, for a flux qubit), none of the eigenstates equal one of the triplet basis states (e.g., as observed for a large energy bias ϵ), they are rather nontrivial superpositions. This is elucidated further in the following paragraph. The inset of panel (2) depicts the level anticrossing between the eigenenergies of the two states $|E2\rangle$ and $|E4\rangle$ due to quantum tunneling.

In general, the eigenstates are a superposition of singlet/triplet states. Figure 2 shows how singlet/triplet states combine into eigenstates for different qubit parameters. The first eigenstate $|E1\rangle$ equals $(1/\sqrt{2})(|\uparrow\downarrow\rangle - |\downarrow\uparrow\rangle)$ for all times while the other eigenstates $|E2\rangle$, $|E3\rangle$, and $|E4\rangle$ are in general superpositions of the singlet/triplet basis states. For large values of $|\epsilon|$, the eigenstates approach the singlet/triplet basis states. In particular, at typical working points, where $\epsilon \approx 5\Delta$ [13], the eigenstates already nearly equal the singlet/triplet basis states. Hence, although the anticrossing described above corresponds to the anticrossing used in Refs. [9,25] to demonstrate Schrödinger's cat states, *entanglement* is prevalent away from the degeneracy point. For an experimental proof, one still would have to show that one has successfully prepared coherent couplings by spectroscopically tracing the energy spectrum. Note that, for clarity, in

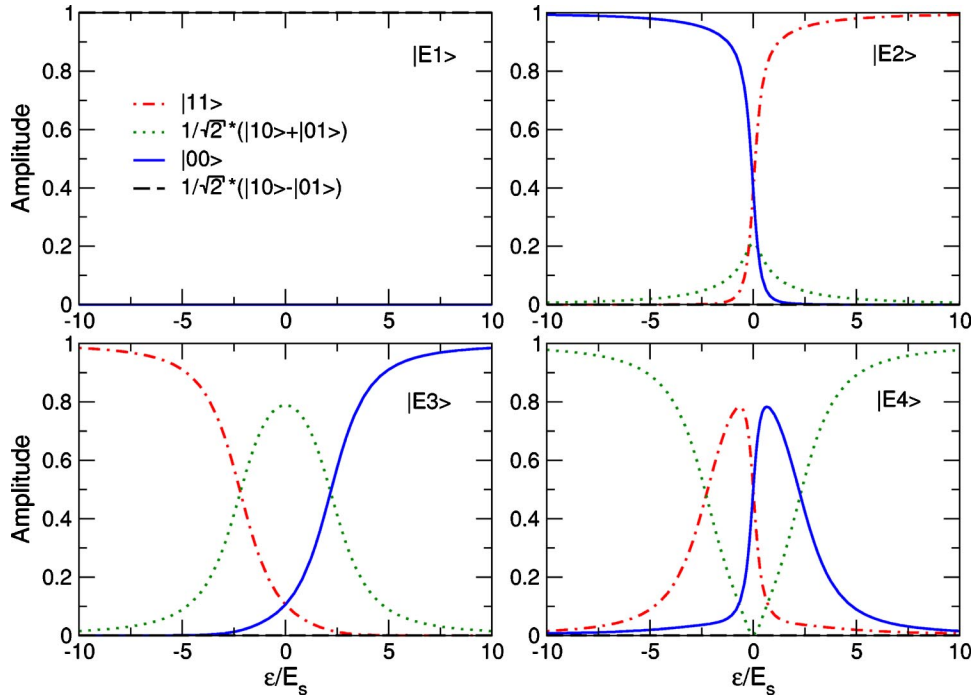


FIG. 2. Plot of the amplitude of the different singlet (triplet) states of which the eigenstates denoted by $|E1\rangle$, $|E2\rangle$, $|E3\rangle$, and $|E4\rangle$ are composed for the four eigenstates. In all plots ϵ is varied, and K and η are fixed to E_s .

Fig. 2, the interqubit coupling strength K is fixed to a rather large value of E_s that also sets the width of the anticrossing, which potentially can be very narrow.

Spectroscopy

As a first technological step towards demonstrating coherent manipulation of qubits, usually the transition frequencies between certain energy levels are probed [9,25], i.e., the energy *differences* between the levels. Figures 3 and 4 depict the transition frequencies between the four eigenstates. The transition frequencies are defined as $\omega_{nm} = (E_n - E_m)/\hbar$ and

$\omega_{nm} = -\omega_{mn}$. The transitions between the singlet state $|E1\rangle$ and the triplet states are forbidden in the case of one common bath, due to the special symmetries of the Hamiltonian (4), if the system is driven collectively through a time-dependent energy bias $\epsilon_1(t) = \epsilon_2(t)$. However, in the case of two distinct baths, the environment can mediate transitions between the singlet and the triplet states.

Not all transition frequencies have local minima at $\epsilon = 0$. The frequencies ω_{41} and ω_{34} have local maxima at zero energy bias ϵ . This can already be inferred from Fig. 1, panel (1), the energy of the eigenstate $|E4\rangle$ has a local minimum at $\epsilon = 0$. Similarly, the substructure of ω_{34} can be understood from Fig. 1: the frequency ω_{34} has a local maximum at ϵ

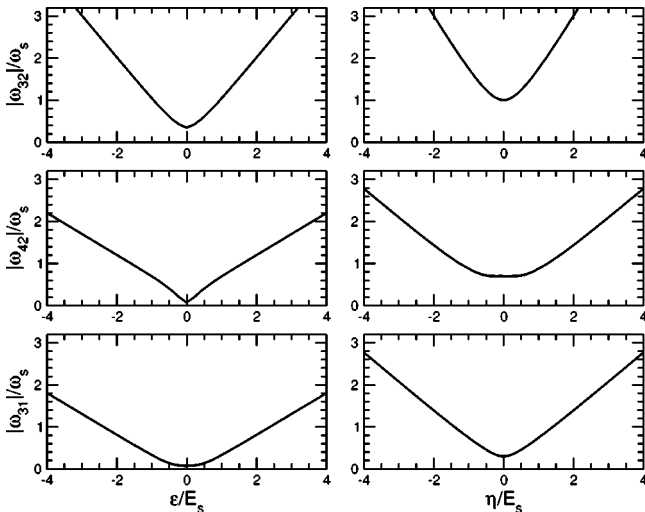


FIG. 3. Plot of the absolute value of the transition frequencies ω_{32} , ω_{42} , and ω_{31} . In the left column $K = \eta = 0.2E_s$ and ϵ is varied. In the right column, $K = 0.2E_s$, $\epsilon = E_s$, and η is varied.

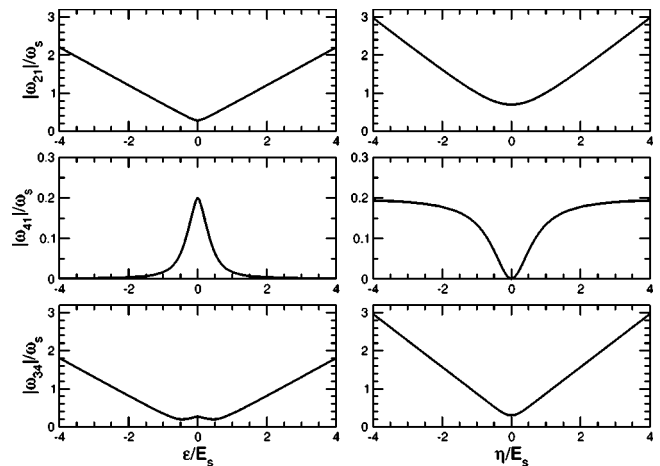


FIG. 4. Plot of the transition frequencies ω_{21} , ω_{41} , and ω_{34} . In the left column, $K = \eta = 0.2E_s$ and ϵ is varied. In the right column, $K = 0.2E_s$, $\epsilon = E_s$, and η is varied.

$=0$, because of the local minimum of the eigenenergy of the state $|E4\rangle$. First, if ϵ is increased, the level spacing of $|E4\rangle$ and $|E3\rangle$ decreases. Then, for larger values of ϵ , the level spacing of $|E4\rangle$ and $|E3\rangle$ increases again. Thus, the structure observed for ω_{34} around $\epsilon=0$ emerges in Fig. 4.

IV. BLOCH-REDFIELD FORMALISM

In order to describe decoherence in the weak damping limit, we use the Bloch-Redfield Formalism [26]. It provides a systematic way of finding a set of coupled master equations which describes the dynamics of the reduced (i.e., the reservoir coordinates are traced out) density matrix for a given system in contact with a dissipative environment and has recently been shown to be numerically equivalent to the more elaborate path-integral scheme [27]. The Hamiltonian of our two-qubit system in contact with a dissipative environment, Eqs. (3) and (4), has the generic ‘‘system+bath’’ form

$$\mathbf{H}_{op}(t) = \mathbf{H}_{2qb} + \mathbf{H}_B + \mathbf{H}_{int}, \quad (9)$$

where \mathbf{H}_B is a bath of harmonic oscillators and \mathbf{H}_{int} inherits the coupling to a dissipative environment. In our case, the effects of driving are not investigated. In Born approximation and when the system is only weakly coupled to the environment, Bloch-Redfield theory provides the following set of equations for the reduced density matrix ρ describing the dynamics of the system [28,29]:

$$\dot{\rho}_{nm}(t) = -i\omega_{nm}\rho_{nm}(t) - \sum_{kl} R_{nmk\ell}\rho_{k\ell}(t), \quad (10)$$

where $\omega_{nm} = (E_n - E_m)/\hbar$, and $\max_{n,m,k,\ell} |\text{Re}(R_{nmk\ell})| < \min_{n \neq m} |\omega_{nm}|$ must hold. The Redfield relaxation tensor $R_{nmk\ell}$ comprises the dissipative effects of the coupling of the system to the environment. The elements of the Redfield relaxation tensor are given through golden rule rates [28]

$$R_{nmk\ell} = \delta_{\ell m} \sum_r \Gamma_{nrrk}^{(+)} + \delta_{nk} \sum_r \Gamma_{\ell rrm}^{(-)} - \Gamma_{\ell mnk}^{(+)} - \Gamma_{\ell mnk}^{(-)}. \quad (11)$$

A. Two qubits coupled to two distinct baths

We now evaluate the Golden rule expressions in Eq. (11) in the case of two qubits, each coupled to a distinct harmonic oscillator bath. Here, $\tilde{H}_I(t) = \exp(iH_B t/\hbar) H_I \exp(-iH_B t/\hbar)$ denotes the coupling between system and bath in the interaction picture, and the bracket denotes thermal average of the bath degrees of freedom. Writing down all contributions gives

$$\begin{aligned} \Gamma_{\ell mnk}^{(+)} &= \hbar^{-2} \int_0^\infty dt e^{-i\omega_{nk}t} \langle e^{[i(H_{B_1} + H_{B_2})t/\hbar]} \\ &\times (\sigma_{z,\ell m}^{(1)} \otimes \hat{X}^{(1)} + \sigma_{z,\ell m}^{(2)} \otimes \hat{X}^{(2)}) e^{-[i(H_{B_1} + H_{B_2})t/\hbar]} \\ &\times (\sigma_{z,nk}^{(1)} \otimes \hat{X}^{(1)} + \sigma_{z,nk}^{(2)} \otimes \hat{X}^{(2)}) \rangle, \end{aligned} \quad (12)$$

where $\sigma_{z, nm}^{(i)}$ ($i=1,2$) are the matrix elements of $\hat{\sigma}_z^{(i)}$ with respect to the eigenbasis of the unperturbed Hamiltonian (8) and likewise for $\Gamma_{\ell mnk}^{(-)}$.

We assume Ohmic spectral densities with a Drude cutoff. This is a realistic assumption, i.e., for electromagnetic noise [13] and leads to integrals in the rates which are tractable by the residue theorem. The cutoff frequency ω_c for the spectral functions of the two qubits is typically assumed to be the largest frequency in the problem, this is discussed further in Sec. IV E,

$$J_1(\omega) = \frac{\alpha_1 \hbar \omega}{\omega^2 + \frac{\omega_c^2}{2}} \quad \text{and} \quad J_2(\omega) = \frac{\alpha_2 \hbar \omega}{\omega^2 + \frac{\omega_c^2}{2}}. \quad (13)$$

The dimensionless parameter α describes the strength of the dissipative effects that enter the Hamiltonian via the coupling to the environment, described by s and Δs . In order for the Bloch-Redfield formalism, which involves a Born approximation in the system-bath coupling, to be valid, we have to assume $\alpha_{1/2} \ll 1$. After tracing out over the bath degrees of freedom, the rates read

$$\begin{aligned} \Gamma_{\ell mnk}^{(+)} &= \frac{1}{8\hbar} [\Lambda^1 J_1(\omega_{nk}) + \Lambda^2 J_2(\omega_{nk})] [\coth(\beta \hbar \omega_{nk}/2) - 1] \\ &+ \frac{i}{4\pi\hbar} [\Lambda^2 M^-(\omega_{nk}, 2) + \Lambda^1 M^-(\omega_{nk}, 1)] \end{aligned} \quad (14)$$

with $\Lambda^1 = \Lambda_{\ell mnk}^1 = \sigma_{z,\ell m}^{(1)} \sigma_{z,nk}^{(1)}$, $\Lambda^2 = \Lambda_{\ell mnk}^2 = \sigma_{z,\ell m}^{(2)} \sigma_{z,nk}^{(2)}$, and

$$M^\pm(\Omega, i) = \mathcal{P} \int_0^\infty d\omega \frac{J_i(\omega)}{\omega^2 - \Omega^2} [\coth(\beta \hbar \omega/2) \Omega \pm \omega], \quad (15)$$

here \mathcal{P} denotes the principal value. Likewise,

$$\begin{aligned} \Gamma_{\ell mnk}^{(-)} &= \frac{1}{8\hbar} [\Lambda^1 J_1(\omega_{\ell m}) + \Lambda^2 J_2(\omega_{\ell m})] [\coth(\beta \hbar \omega_{\ell m}/2) + 1] \\ &+ \frac{i}{4\pi\hbar} [\Lambda^2 M^+(\omega_{\ell m}, 2) + \Lambda^1 M^+(\omega_{\ell m}, 1)]. \end{aligned} \quad (16)$$

The rates $\Gamma_{\ell mnk}^{(+)}$ and $\Gamma_{\ell mnk}^{(-)}$ might be inserted into Eq. (11) to build the Redfield tensor. Note, here, that for $\omega_{nk} \rightarrow 0$, and $\omega_{\ell m} \rightarrow 0$ respectively, the real part of the rates (which is responsible for relaxation and dephasing) is of value $\Gamma_{\ell mnk}^{(+)} = \Gamma_{\ell mnk}^{(-)} = (1/4\beta\hbar) [\sigma_{z,\ell m}^{(1)} \sigma_{z,nk}^{(1)} \alpha_1 + \sigma_{z,\ell m}^{(2)} \sigma_{z,nk}^{(2)} \alpha_2]$.

To solve the set of differential equations (10), it is convenient to collapse ρ into a vector. In general, the Redfield equations (10) without driving are solved by an ansatz of the type $\rho(t) = B \exp(\tilde{R}t) B^{-1} \rho(0)$, where \tilde{R} is a diagonal matrix. The entries of this diagonal matrix are the eigenvalues of the Redfield tensor (11), written in matrix form, including the dominating term $i\omega_{nm}$ [cf. Eq. (10)]. Here, the reduced density matrix $\rho = (\rho_{11}, \dots, \rho_{44})^T$ is written as a vector. The

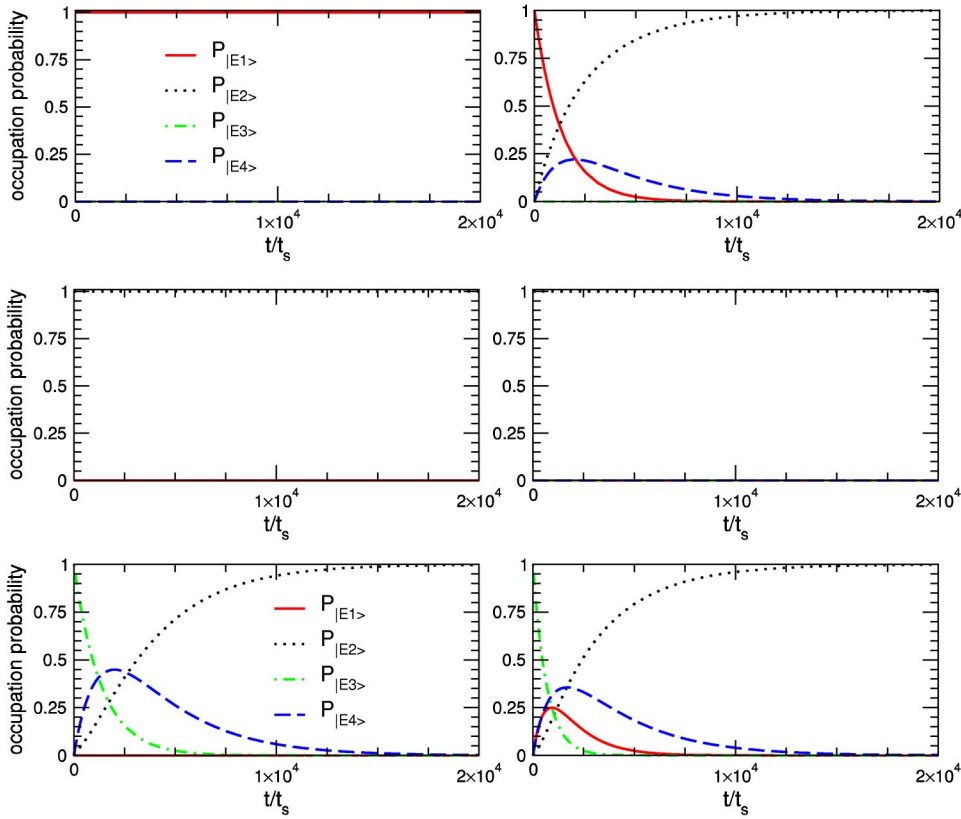


FIG. 5. Plot of the occupation probability of the four eigenstates $|E1\rangle$, $|E2\rangle$, $|E3\rangle$, and $|E4\rangle$ for initially starting in one of the eigenstates $|E1\rangle$ (first row), $|E2\rangle$ (second row), or $|E3\rangle$ (third row) at $T=0$. The left column illustrates the case of two qubits coupling to one common bath and the right column the case of two qubits coupling to two distinct baths. The energies K , ϵ , and η are all fixed to E_s . The characteristic time scale t_s is $t_s = 1/\nu_s$.

matrix B describes the basis change to the eigenbasis of \tilde{R} , in which \tilde{R} has diagonal form.

B. Two qubits coupled to one common bath

For the case of two qubits coupled to one common bath, we perform the same calculation as in the preceding section, which leads to expressions for the rates analogous to Eqs. (16)

$$\Gamma_{\ell mnk}^{(+)} = \frac{1}{8\hbar} \Lambda J(\omega_{nk}) [\coth(\beta\hbar\omega_{nk}/2) - 1] + \frac{i\Lambda}{4\pi\hbar} \times \mathcal{P} \int_0^\infty d\omega \frac{J(\omega)}{\omega^2 - \omega_{nk}^2} [\coth(\beta\hbar\omega/2)\omega_{nk} - \omega], \quad (17)$$

with $\Lambda = \Lambda_{\ell mnk} = \sigma_{z,\ell m}^{(1)} \sigma_{z,nk}^{(1)} + \sigma_{z,\ell m}^{(1)} \sigma_{z,nk}^{(2)} + \sigma_{z,\ell m}^{(2)} \sigma_{z,nk}^{(1)} + \sigma_{z,\ell m}^{(2)} \sigma_{z,nk}^{(2)}$ and

$$\Gamma_{\ell mnk}^{(-)} = \frac{1}{8\hbar} \Lambda J(\omega_{\ell m}) [\coth(\beta\hbar\omega_{\ell m}/2) + 1] + \frac{i\Lambda}{4\pi\hbar} \times \mathcal{P} \int_0^\infty d\omega \frac{J(\omega)}{\omega^2 - \omega_{\ell m}^2} [\coth(\beta\hbar\omega/2)\omega_{\ell m} + \omega]. \quad (18)$$

The difference between the rates for the case of two distinct baths (14) and (16) are the two extra terms $\sigma_{z,\ell m}^{(1)} \sigma_{z,nk}^{(2)}$ and

$\sigma_{z,\ell m}^{(2)} \sigma_{z,nk}^{(1)}$. They originate when tracing out the bath degrees of freedom. In the case of one common bath, there is only one spectral function, which we also assume to be Ohmic $J(\omega) = (\alpha\hbar\omega)/(1 + \omega^2/\omega_c^2)$. For $\omega_{nk} \rightarrow 0$, and $\omega_{\ell m} \rightarrow 0$, respectively, the real part of the rates is of the value $\Gamma_{\ell mnk}^{(+)} = \Gamma_{\ell mnk}^{(-)} = (\alpha/4\beta\hbar)\Lambda$, for $\omega_{\ell m}, \omega_{nk} \rightarrow 0$.

C. Dynamics of coupled flux qubits with dissipation

The dissipative effects affecting the two-qubit system lead to decoherence, which manifests itself in two ways. The system experiences energy relaxation on a time scale $\tau_R = \Gamma_R^{-1}$ (Γ_R is the sum of the relaxation rates of the four diagonal elements of the reduced density matrix; $\Gamma_R = -\sum_n \Theta_n$ and Θ_n are the eigenvalues of the matrix that consists of the tensor elements $R_{n,m,n,m}$, $n, m = 1, \dots, 4$), called relaxation time, into a thermal mixture of the system's energy eigenstates. Therefore, the diagonal elements of the reduced density matrix decay to the value given by the Boltzmann factors. The quantum coherent dynamics of the system are superimposed on the relaxation and decay on a usually shorter time scale $\tau_{\varphi_{ij}} = \Gamma_{\varphi_{ij}}^{-1}$ ($i, j = 1, \dots, 4; i \neq j$ and $\Gamma_{\varphi_{nm}} = -\text{Re}R_{n,m,n,m}^{1b,2b}$) termed dephasing time. Thus, dephasing causes the off-diagonal terms (coherences) of the reduced density matrix to tend towards zero.

First, we investigate the incoherent relaxation of the two-qubit system out of an eigenstate. At long times, the system is expected to reach thermal equilibrium, $\rho_{eq} = (1/Z)e^{-\beta H}$. Special cases are $T=0$, where ρ_{eq} equals the projector on

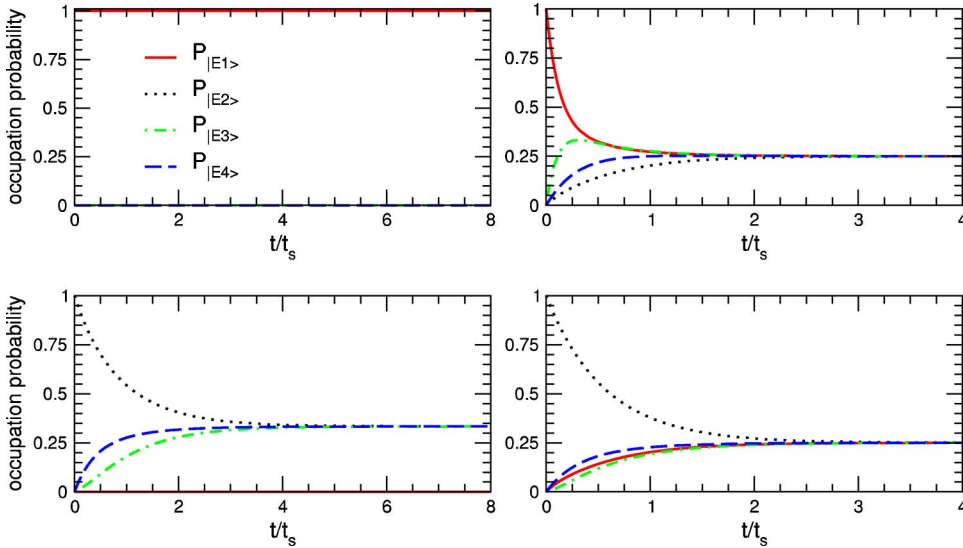


FIG. 6. Plot of the occupation probability of the four eigenstates $|E1\rangle$, $|E2\rangle$, $|E3\rangle$, and $|E4\rangle$ for initially starting in one of the eigenstates $|E1\rangle$ (upper row) or $|E2\rangle$ (lower row) at $T=21T_s$. The left column illustrates the case of two qubits coupling to one common bath and the right column the case of two qubits coupling to two distinct baths. The energies K , ϵ , and η are all fixed to E_s . The characteristic time scale t_s is $t_s = 1/\nu_s$.

the ground state and $T \rightarrow \infty$, where all eigenstates are occupied with the same probability, i.e., $\rho_{\text{eq}} = (1/4)\hat{1}$. Figures 5 and 6 illustrate the relaxation of the system prepared in one of the four eigenstates for temperatures $T=0$ and $T=21T_s$, respectively. The qubit energies K , ϵ , and η are all set to E_s and α is set to $\alpha = 10^{-3}$. From Fig. 1, one recognizes relaxation into the eigenstate $|E2\rangle$, the ground state for this set of parameters.

At low temperatures ($T=0$), we observe that for the case of two distinct uncorrelated baths, a system prepared in one of the four eigenstates always relaxes into the ground state. In the case of two qubits coupling to one common bath, this is not always the case, as can be seen in the upper left panels of Figs. 5 and 6. This can be explained through our previous observation, that the singlet is a protected subspace: Neither the free nor, unlike in the case of distinct baths, the bath-mediated dynamics couple the singlet to the triplet space. Moreover, we can observe that relaxation to the ground state happens by populating intermediate eigenstates with a lower energy than the initial state the system was prepared in at $t=0$ (cf. Fig. 1).

For high temperatures ($T \approx 21T_s$), the system thermalizes into thermal equilibrium, where all eigenstates have equal occupation probabilities. Again, in the case of one common bath, thermalization of the singlet state is impeded and the three eigenstates $|E2\rangle$, $|E3\rangle$ and $|E4\rangle$ have equal occupation probabilities of $1/3$ after the relaxation time.

If the system is prepared in a superposition of eigenstates, e.g., $|E3\rangle$ and $|E4\rangle$ as in Fig. 7, which are not in a protected subspace, we observe coherent oscillations between the eigenstates that are damped due to dephasing and after the decoherence time, the occupation probability of the eigenstates is given by the Boltzmann factors. This behavior is depicted in Fig. 7. Here, for $\alpha = 10^{-3}$, the cases of $T=0$ and $T=2.1T_s$ are compared. When the temperature is low enough, the system will relax into the ground state $|E2\rangle$, as illustrated by the right column of Fig. 7. Thus, the occupation probability of the state $(1/\sqrt{2})(|E3\rangle + |E4\rangle)$ goes to zero. Here, in the case of zero temperature, the decoherence

times for the case of one common or two distinct baths are of the same order of magnitude. The left column illustrates the behavior when the temperature is increased. At $T=2.1T_s$, the system relaxes into an equally populated state on times much shorter than for $T=0$. For low temperatures, the characteristic time scale for dephasing and relaxation is somewhat shorter for the case of one common bath ($\tau^{1b}/\tau^{2b} \approx 0.9$, for $\alpha = 10^{-3}$). This can be explained by observing the temperature dependence of the rates shown in Fig. 8. Though for the case of one common bath, two of the dephasing rates are zero at $T=0$, the remaining rates are always slightly bigger for the case of one common bath compared to the case of two distinct baths. If the system is prepared in a general superposition, here $|E3\rangle$ and $|E4\rangle$, nearly all rates become important thus compensating the effect of the two rates that are approximately zero at zero temperature and leading to faster decoherence.

If α and, therefore, the strength of the dissipative effects is increased from $\alpha = 10^{-3}$ to $\alpha = 10^{-2}$, the observed coherent motion is significantly damped. Variation of α leads to a phase shift of the coherent oscillations, due to renormalization of the frequencies [16]. However, in our case, the effects of renormalization are very small, as discussed in Sec. IV E, and cannot be observed in our plots.

D. Temperature dependence of the rates

Figure 8 displays the dependence of typical dephasing rates and the relaxation rate Γ_R on temperature. These decoherence rates are the inverse decoherence times. The rates are of the same magnitude for the cases of one common bath and two distinct baths. As a notable exception, in the case of one common bath, the dephasing rates $\Gamma_{\varphi_{21}} = \Gamma_{\varphi_{12}}$ go to zero when the temperature is decreased, while all other rates saturate for $T \rightarrow 0$. This phenomenon is explained later on. If the temperature is increased from $T_s = (h/k_B)\nu_s = 4.8 \times 10^{-2}$ K, the increase of the dephasing and relaxation rates follows a power-law dependence. It is linear in temperature T with a slope given by the prefactors of the expression in the Red-

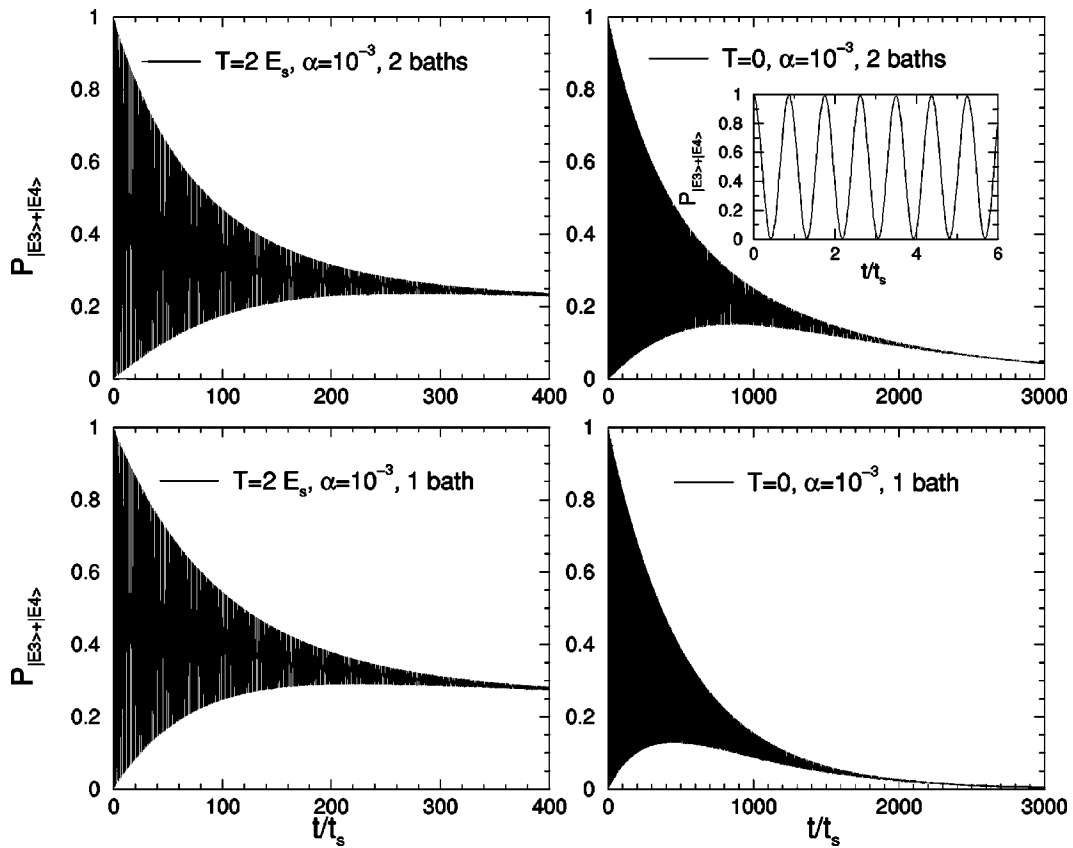


FIG. 7. Plot of the occupation probability $P_{(1/\sqrt{2})(|E3\rangle+|E4\rangle)}(t)$ when starting in the initial state $(1/\sqrt{2})(|E3\rangle+|E4\rangle)$, which is a superposition of eigenstates $|E3\rangle$ and $|E4\rangle$. The first row shows the behavior for two qubits coupling to two uncorrelated baths. The lower row shows the behavior for two qubits coupled to one common bath. The qubit parameters ϵ , η , and K are set to E_s and α is set to $\alpha = 10^{-3}$. The inset resolves the time scale of the coherent oscillations.

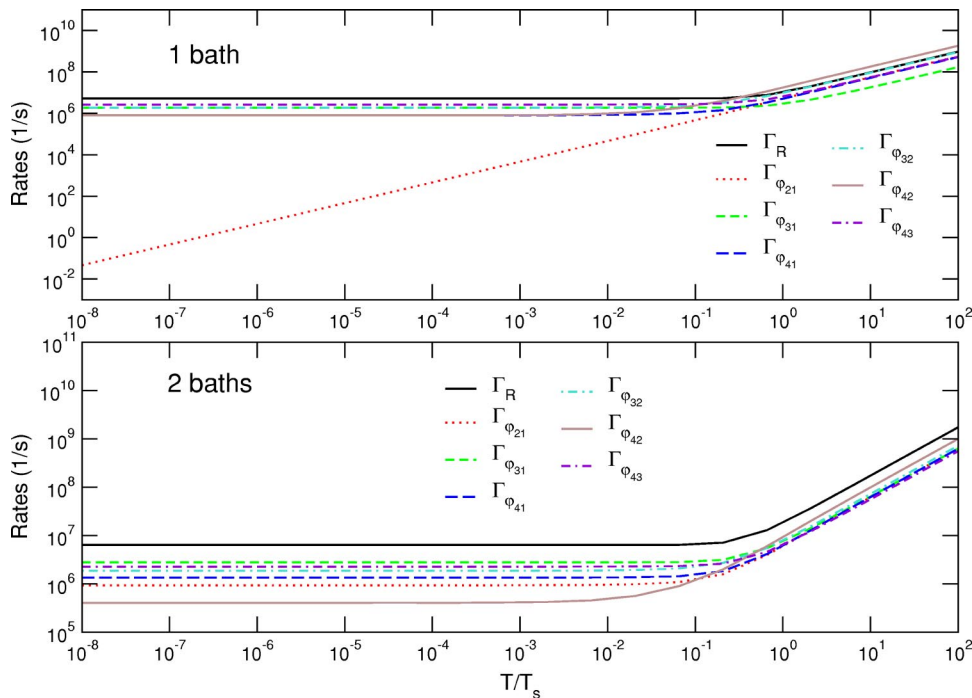


FIG. 8. Log-log plot of the temperature dependence of the sum of the four relaxation rates and selected dephasing rates. Qubit parameters K , ϵ , and η are all set to E_s and $\alpha = 10^{-3}$. The upper panel shows the case of one common bath and the lower panel the case of two distinct baths. At the characteristic temperature of approximately $0.1T_s$, the rates increase very steeply.

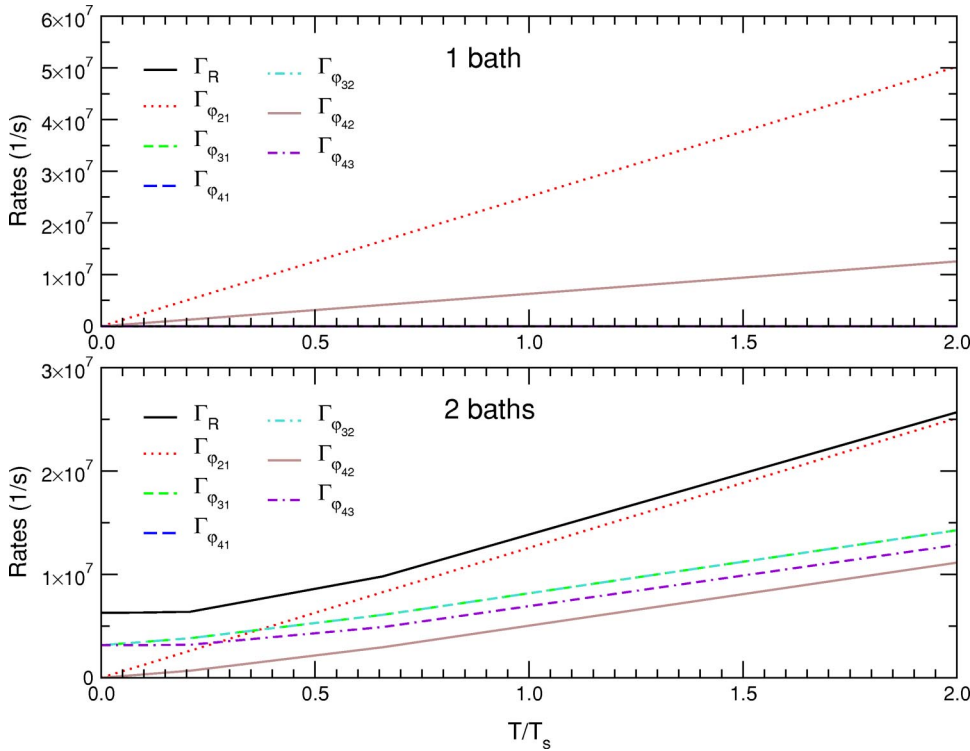


FIG. 9. Plot of the temperature dependence of the sum of the four relaxation rates and selected dephasing rates. Qubit parameters ϵ and η are set to 0, K is set to E_s , and $\alpha = 10^{-3}$ corresponding to the choice of parameters used for the U_{XOR} operation. The upper panel shows the case of one common bath and the lower panel the case of two distinct baths. In the case of one common bath the system will experience no dissipative effects at $T=0$.

field rates that depends on temperature. At temperature $T \approx 0.1T_s$, the rates show a sharp increase for both cases. This roll-off point is set by the characteristic energy scale of the problem, which in turn is set by the energy bias ϵ , the transmission matrix element η , and the coupling strength K . For the choice of parameters in Fig. 8, the characteristic energy scale expressed in temperature is $T \approx 0.1T_s$.

Note that there is also dephasing between the singlet and the triplet states. When the system is prepared (by application of a suitable interaction) in a coherent superposition of singlet and triplet states, the phase evolves coherently. Then two possible decoherence mechanisms can destroy phase coherence. First, “flipless” dephasing processes, where $\langle E \rangle$ remains unchanged. These flipless dephasing processes are described by the terms for $\omega_{\ell m}, \omega_{nk} \rightarrow 0$ in the rates, Eqs. (16) and (18). Obviously, these terms vanish for $T \rightarrow 0$, as the low-frequency component of Ohmic Gaussian noise is strictly thermal. Second, relaxation due to emission of a boson to the bath is also accompanied by a loss of phase coherence. This process in general has a *finite* rate at $T=0$. This explains the T dependence of the rates in the single-bath case: $|E1\rangle$ alone is protected from the environment. As there are incoherent transitions between the triplet eigenstates even at $T=0$, the relative phase of a coherent oscillation between $|E1\rangle$ and any of those is randomized, and the decoherence rates $\Gamma_{\varphi_{3/4,1}}$ are finite even at $T=0$. As a notable exception, $|E2\rangle$, the lowest-energy state in the triplet subspace, can only be flipped through absorption of energy, which implies that the dephasing rate $\Gamma_{\varphi_{21}}$ also vanishes at low temperature. The described behavior can be observed in Fig. 8.

If the parameters ϵ and η are tuned to zero, thus K being the only nonvanishing parameter in the Hamiltonian, all dephasing and relaxation rates will vanish for $T=0$ in the

case of one common bath. This behavior is depicted in Fig. 9. It originates from the special symmetries of the Hamiltonian in this case and the fact that for this particular two-qubit operation, the system Hamiltonian and the coupling to the bath are diagonal in the same basis. This special case is of crucial importance for the quantum gate operation as described in Sec. V and affects the gate quality factors.

E. Renormalization effects

Next to causing decoherence, the interaction with the bath also renormalizes the qubit frequencies. This is mostly due to the fast bath modes, and can be understood analogous to the Franck-Condon effect, the Lamb shift, or the adiabatic renormalization [30]. Renormalization of the oscillation frequencies ω_{nm} is controlled by the imaginary part of the Redfield tensor [16]

$$\omega_{nm} \rightarrow \tilde{\omega}_{nm} := \omega_{nm} - \text{Im}R_{nmnm}. \quad (19)$$

Note that $\text{Im}R_{nmnm} = -\text{Im}R_{mnmn}$ due to the fact that the correlators in the Golden Rule expressions have the same parity. The imaginary part of the Redfield tensor is given by

$$\text{Im}\Gamma_{\ell mnk}^{(+)} = C_{\ell mnk}^{\text{1b,2b}} \frac{1}{\pi\hbar} \mathcal{P} \int_0^\infty d\omega J(\omega) \left(\frac{1}{\omega^2 - \omega_{nk}^2} \right) \times [\coth(\beta\hbar\omega/2)\omega_{nk} - \omega] \quad (20)$$

and

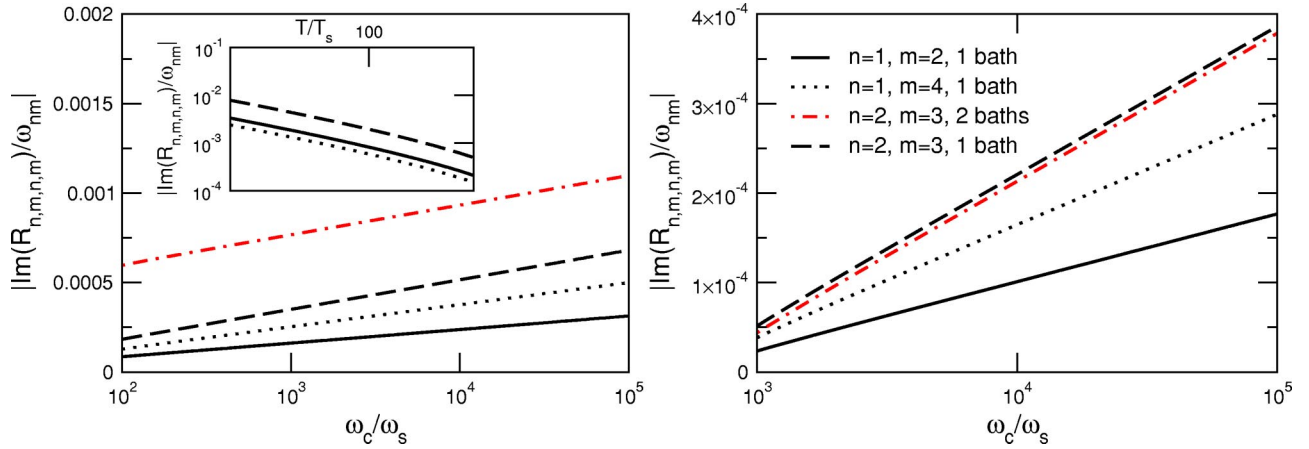


FIG. 10. The left plot depicts the ratio of the renormalization effects and the corresponding transition frequencies. Parameters: $\alpha = 10^{-3}$, $T=0$, and ω_c/ω_s is varied between 10^2 and 10^5 for several frequencies (ω_{12} , ω_{14} , and ω_{23}) for the case of two baths and in the case of ω_{23} also for the case of one common bath. The parameters for the right plot are $\alpha = 10^{-3}$, $T=2.1T_s$, and ω_c/ω_s is varied between 10^3 and 10^5 . The inset of the left plot shows a log-log plot of the temperature dependence of the renormalization effects. Here $\alpha = 10^{-3}$ and $\omega_c = 10^{13}$. Note that for small temperatures the renormalization effects do *not* depend on temperature. (This is elucidated further in Sec. IV E.) The plots are scaled logarithmically to emphasize the logarithmic divergence of the renormalization effects with ω_c .

$$\text{Im}\Gamma_{\ell mnk}^{(-)} = C_{\ell mnk}^{1b,2b} \frac{1}{\pi\hbar} \mathcal{P} \int_0^\infty d\omega J(\omega) \left(\frac{1}{\omega^2 - \omega_{\ell m}^2} \right) \times [\coth(\beta\hbar\omega/2)\omega_{\ell m} + \omega], \quad (21)$$

where \mathcal{P} denotes the principal value, and $C_{\ell mnk}^{1b,2b}$ are prefactors defined, in the case of two distinct baths, according to $C_{\ell mnk}^{2b} = \frac{1}{4} [\sigma_{z,\ell m}^{(1)} \sigma_{z,nk}^{(1)} + \sigma_{z,\ell m}^{(2)} \sigma_{z,nk}^{(2)}]$ and in the case of one common bath $C_{\ell mnk}^{1b} = \frac{1}{4} \Lambda$. Here, for simplicity, we assumed $\alpha_1 = \alpha_2 = \alpha$ and thus, $J_1(\omega) = J_2(\omega) = J(\omega)$. Evaluation of the integral leads to the following expression for $\Gamma_{\ell mnk}^{(+)}$:

$$\text{Im}\Gamma_{\ell mnk}^{(+)} = C_{\ell mnk}^{1b,2b} \frac{\alpha\omega_c^2\omega_{nk}}{2\pi(\omega_c^2 + \omega_{nk}^2)} \left[\psi(1+c_2) + \psi(c_2) - 2\text{Re}[\psi(ic_1)] - \pi \frac{\omega_c}{\omega_{nk}} \right], \quad (22)$$

with $c_1 := (\beta\hbar\omega_{nk})/(2\pi)$ and $c_2 := (\beta\hbar\omega_c)/(2\pi)$. In the case of $\Gamma_{\ell mnk}^{(-)}$, the expression is

$$\text{Im}\Gamma_{\ell mnk}^{(-)} = C_{\ell mnk}^{1b,2b} \frac{\alpha\omega_c^2\omega_{\ell m}}{2\pi(\omega_c^2 + \omega_{\ell m}^2)} \left[\psi(1+c_2) + \psi(c_2) - 2\text{Re}[\psi(ic_1)] + \pi \frac{\omega_c}{\omega_{\ell m}} \right], \quad (23)$$

with $c_1 := (\omega_{\ell m}\beta\hbar)/(2\pi)$. The terms in Eqs. (22) and (23) which are linear in ω_c give no net contribution to the imaginary part of the Redfield tensor [16]. To illustrate the size of the renormalization effects, the ratio of the renormalization effects to the frequencies which are renormalized is depicted in Fig. 10.

If c_1 and c_2 are large, and the digamma functions can be approximated by a logarithm, the resulting expression for the renormalization effects will be independent of temperature.

The temperature dependence of Eqs. (22) and (23) at higher temperatures, where c_1 and c_2 are small and the renormalization effects are very weak, is shown in Fig. 10. The rates (22) and (23) diverge logarithmically with ω_c in analogy to the well-known ultraviolet-divergence of the spin boson model [30]. When comparing the left ($T=0$) and right ($T=2.1T_s$) panel, one recognizes that for the first case, one common bath gives somewhat smaller renormalization effects than two distinct baths, while in the second case for $T=2.1T_s$, the renormalization effects deviate only slightly (see the behavior for ω_{23}) and the renormalization effects are smaller for the case of two distinct baths. The effects of renormalization are always very small [$|\text{Im}(R_{n,m,n,m})/\omega_{nm}|$ below 1% for our choice of parameters] and are therefore, neglected in our calculations. However, having calculated Eqs. (22) and (23), these are easily incorporated in our numerical calculations. The case of large renormalization effects is discussed in Ref. [31].

We only plotted the size of the renormalization effects for ω_{12} , ω_{14} , and ω_{34} , because in general, all values of ω_{nk} are of the same magnitude and give similar plots. The size of the renormalization effects diverges linearly with α , the dimensionless parameter that describes the strength of the dissipative effects.

For flux qubits, the cutoff frequency ω_c is given by the circuit properties. For a typical first order low-pass LR filter [32] in a qubit circuit [13], one can insert $R = 50 \Omega$ (typical impedance of coaxial cables) and $L \approx 1$ nH (depends on the length of the circuit lines) into $\omega_{LR} = R/L$, and gets that $\omega_{LR} \approx 5 \times 10^{10}$ Hz. ω_{LR} is the largest frequency in the problem (see again Ref. [13], Chap. 4.5) and $\omega_c \gg \omega_{LR}$ should hold. Then $\omega_c \approx 10^{13}$ Hz ($= 10^4 E_s$) as cutoff frequency is a reasonable assumption.

V. GATE QUALITY FACTORS

In Sec. IV, we evaluated the dephasing and relaxation rates of the two-qubit system that is affected by a dissipative

environment. Furthermore, we visualized the dynamics of the two-qubit system. This does not yet allow a full assessment of the performance as a quantum logic element. These should perform unitary gate operations and based on the rates alone, one can not judge how well quantum gate operations might be performed with the two-qubit system. Therefore, to get a quantitative measure of how our setup behaves when performing a quantum logic gate operation, one can evaluate gate quality factors [33]. The performance of a two-qubit gate is characterized by four quantities: the fidelity, purity, quantum degree, and entanglement capability. The fidelity is defined as

$$\mathcal{F} = \frac{1}{16} \sum_{j=1}^{16} \langle \Psi_{in}^j | U_G^\dagger \rho_G^j U_G | \Psi_{in}^j \rangle, \quad (24)$$

where U_G is the unitary matrix describing the desired ideal gate and the density matrix obtained from attempting a quantum gate operation in a hostile environment is $\rho_G^j = \rho(t_G)$, which is evaluated for all initial conditions $\rho(0) = |\Psi_{in}^j\rangle\langle\Psi_{in}^j|$. The fidelity is a measure of how well a quantum logic operation was performed. Without dissipation, the reduced density matrix ρ_G^j after performing the quantum gate operation, applying U_G and the inverse U_G^\dagger would equal $\rho(0)$. Therefore, the fidelity for the ideal quantum gate operation should be 1.

The second quantifier is the purity

$$\mathcal{P} = \frac{1}{16} \sum_{j=1}^{16} \text{tr}((\rho_G^j)^2), \quad (25)$$

which should be 1 without dissipation and 1/4 in a fully mixed state. The purity characterizes the effects of decoherence.

The third quantifier, the quantum degree, is defined as the maximum overlap of the resulting density matrix after the quantum gate operation with the maximally entangled states, the Bell states

$$\mathcal{Q} = \max_{j,k} \langle \Psi_{me}^k | \rho_G^j | \Psi_{me}^k \rangle, \quad (26)$$

where the Bell states Ψ_{me}^k are defined according to

$$|\Psi_{me}^{00}\rangle = \frac{|\downarrow\downarrow\rangle + |\uparrow\uparrow\rangle}{\sqrt{2}}, \quad |\Psi_{me}^{01}\rangle = \frac{|\downarrow\uparrow\rangle + |\uparrow\downarrow\rangle}{\sqrt{2}}, \quad (27)$$

$$|\Psi_{me}^{10}\rangle = \frac{|\downarrow\downarrow\rangle - |\uparrow\uparrow\rangle}{\sqrt{2}}, \quad |\Psi_{me}^{11}\rangle = \frac{|\downarrow\uparrow\rangle - |\uparrow\downarrow\rangle}{\sqrt{2}}. \quad (28)$$

For an ideal entangling operation, e.g., the controlled-NOT gate, the quantum degree should be one. The quantum degree characterizes nonlocality. It has been shown [34] that all density operators that have an overlap with a maximally entangled state that is larger than the value 0.78 [17] violate the Clauser-Horne-Shimony-Holt inequality and are thus nonlocal.

The fourth quantifier, the entanglement capability \mathcal{C} , is the smallest eigenvalue of the partially transposed density matrix for all possible unentangled input states $|\Psi_{in}^j\rangle$. (see below). It has been shown [35] to be negative for an entangled state. This quantifier should be -0.5 , e.g., for the ideal U_{XOR} , thus characterizing a maximally entangled final state. Two of the gate quality factors, namely, the fidelity and purity might also be calculated for single-qubit gates [12]. However, entanglement can only be observed in a system of at least two qubits. Therefore, the quantum degree and entanglement capability cannot be evaluated for single-qubit gates.

To form all possible initial density matrices, needed to calculate the gate quality factors, we use the 16 unentangled product states $|\Psi_{in}^j\rangle$, $j=1, \dots, 16$ defined [17] according to $|\Psi_a\rangle_1 |\Psi_b\rangle_2$ ($a, b=1, \dots, 4$), with $|\Psi_1\rangle = |\downarrow\rangle$, $|\Psi_2\rangle = |\uparrow\rangle$, $|\Psi_3\rangle = (1/\sqrt{2})(|\downarrow\rangle + |\uparrow\rangle)$, and $|\Psi_4\rangle = (1/\sqrt{2})(|\downarrow\rangle + i|\uparrow\rangle)$. They form one possible basis set for the superoperator ν_G with $\rho(t_G) = \nu_G \rho(0)$ [17,33]. The states are chosen to be unentangled for being compatible with the definition of \mathcal{C} .

A. Implementation of two-qubit operations

1. Controlled phase-shift gate

To perform the controlled-NOT operation, it is necessary to be able to apply the controlled phase-shift operation together with arbitrary single-qubit gates. In the computational basis ($|00\rangle, |01\rangle, |10\rangle, |11\rangle$), the controlled phase-shift operation is given by

$$U_{CZ}(\varphi) = \begin{pmatrix} 1 & 0 & 0 & 0 \\ 0 & 1 & 0 & 0 \\ 0 & 0 & 1 & 0 \\ 0 & 0 & 0 & e^{i\varphi} \end{pmatrix}, \quad (29)$$

and for $\varphi = \pi$, up to a global phase factor,

$$U_{CZ} = \exp\left(i\frac{\pi}{4}\sigma_z^{(1)}\right) \exp\left(i\frac{\pi}{4}\sigma_z^{(2)}\right) \exp\left(i\frac{\pi}{4}\sigma_z^{(1)}\sigma_z^{(2)}\right). \quad (30)$$

Note that in Eq. (30) only σ_z operations, which commute with the coupling to the bath, are needed. The controlled phase-shift operation together with two Hadamard gates and a single-qubit phase-shift operation then gives the controlled-NOT gate.

2. Controlled-NOT gate

Due to the fact that the set consisting of the U_{XOR} (or controlled-NOT) gate and the one-qubit rotations, is complete for quantum computation [36], the U_{XOR} gate is a highly important two-qubit gate operation. Therefore we further investigate the behavior of the four gate quality factors in this case. The U_{XOR} operation switches the second bit, depending on the value of the first bit of a two bit system. In the computational basis, this operation has the following matrix form:

TABLE I. Parameters of the Hamiltonians which are needed to perform the U_{XOR} gate operation; only the nonzero parameters are listed: $\xi = E_s$ in our case.

No.	Operation	Parameters (E_s)	Time (s)
1	$\exp\left[-i\frac{\pi}{2}\left(\frac{\sigma_x^2 + \sigma_z^2}{\sqrt{2}}\right)\right]$	$\epsilon_2 = -\xi, \Delta_2 = -\xi$	$\tau_1 = \frac{\sqrt{2}}{2\xi}$
2	$\exp\left(i\frac{\pi}{2}\sigma_z^1\right)$	$\epsilon_1 = \xi$	$\tau_2 = \frac{1}{2\xi}$
3	$\exp\left(i\frac{\pi}{4}\sigma_z^1\sigma_z^2\right)$	$K = \xi$	$\tau_3 = \frac{1}{4\xi}$
4	$\exp\left(i\frac{\pi}{4}\sigma_z^2\right)$	$\epsilon_2 = \xi$	$\tau_4 = \frac{1}{4\xi}$
5	$\exp\left(i\frac{\pi}{4}\sigma_z^1\right)$	$\epsilon_1 = \xi$	$\tau_5 = \frac{1}{4\xi}$
6	$\exp\left[-i\frac{\pi}{2}\left(\frac{\sigma_x^2 + \sigma_z^2}{\sqrt{2}}\right)\right]$	$\epsilon_2 = -\xi, \Delta_2 = -\xi$	$\tau_6 = \frac{\sqrt{2}}{2\xi}$

$$U_{\text{XOR}} = \begin{pmatrix} 1 & 0 & 0 & 0 \\ 0 & 1 & 0 & 0 \\ 0 & 0 & 0 & 1 \\ 0 & 0 & 1 & 0 \end{pmatrix}. \quad (31)$$

Up to a phase factor, the two-qubit U_{XOR} (or CNOT) operation can be realized by a sequence of five single-qubit and one two-qubit quantum logic operations. Each of these six operations corresponds to an appropriate Hamiltonian undergoing free unitary time evolution $\exp[-(i/\hbar)\mathbf{H}_{op}t]$. The single-qubit operations are handled with Bloch-Redfield formalism, like the two-qubit operations. We assume dc pulses (instantaneous on and off switching of the Hamiltonian with zero rise time of the signal) or rectangular pulses

$$U_{\text{XOR}} = \exp\left[-i\frac{\pi}{2}\left(\frac{\sigma_x^{(2)} + \sigma_z^{(2)}}{\sqrt{2}}\right)\right] U_{CZ}(\pi) \\ \times \exp\left(i\frac{\pi}{2}\sigma_z^{(1)}\right) \exp\left[-i\frac{\pi}{2}\left(\frac{\sigma_x^{(2)} + \sigma_z^{(2)}}{\sqrt{2}}\right)\right], \quad (32)$$

where $U_{CZ}(\pi)$ is given by Eq. (30). This generic implementation has been chosen in order to demonstrate the comparison to other coupling schemes [17] as well as for computational convenience, it is not necessarily the optimum scheme for application under cryogenic conditions, where slow rise-time ac pulses are preferred. Table I shows the parameters we inserted into the one- and two-qubit Hamiltonian to receive the U_{XOR} operation. In our case, we assumed $\xi = E_s$. However, there is no restriction in the use of other values for ξ . For a typical energy scale of 1 GHz, the resulting times from Table I are in the nanosecond range.

To better visualize the pulse sequence needed to perform the quantum U_{XOR} operation, which was already given in

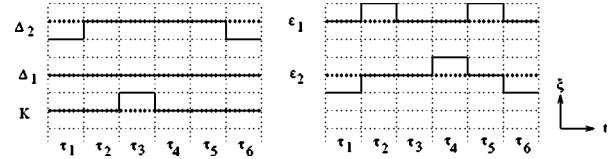


FIG. 11. Pulse sequence needed to perform the quantum U_{XOR} operation. Here, the elements of the unperturbed single- and two-qubit Hamiltonian needed to perform a certain operation undergoing free unitary time evolution are shown. The dotted horizontal lines denote $\xi = 0$, and the horizontal lines are spaced by $|\xi| = E_s$. The durations of each pulse are not equal in general $\tau_j \neq \tau_i$, $i, j = 1, \dots, 6$ (cf. Table I).

Table I, Fig. 11 depicts the values of the elements of the Hamiltonians. Interestingly enough, we find that for the only two-qubit operation included in the U_{XOR} operation, ϵ and η are zero. Thus, K is the only nonzero parameter and \mathbf{H}_{2qb} assumes diagonal form. For flux qubits, implementing the pulse sequence Fig. 11 involves negative and positive values tuning the magnetic frustration through the qubit loop below or above $f = 1/2$. Note that, e.g., for realistic models of inductively coupled flux qubits, it is very difficult to turn on the interaction Hamiltonian between the two qubits without the individual σ_z terms in the Hamiltonian. However, for the pulse sequence given in Eq. (32), we might simply perform the third, fourth, and fifth operations of Eq. (32) at once using only the Hamiltonian with both the individual σ_z terms and the interqubit coupling.

To obtain the final reduced density matrix after performing the six unitary operations (32), we iteratively determine the density matrix after each operation with Bloch-Redfield theory and insert the attained resulting density matrix as initial density matrix into the next operation. This procedure is repeated for all possible unentangled initial states given in the preceding section. We inserted no additional time intervals between the operations. This is usually needed, if one applies Bloch-Redfield formalism, because it is known to violate complete positivity on short time scales. However, we circumvent this problem in our calculations by dropping the memory after each operation, when we iteratively calculate the reduced density matrix. This procedure may lead to small inaccuracies as compared to using QUAPPI [17], which, however, should not affect our main conclusions.

B. Temperature dependence

1. Controlled phase-shift gate

We have analyzed the gate quality factors in the cases of a common and of two distinct baths, respectively. In Fig. 12, the temperature dependence of the deviations of the four gate quality factors from their ideal values are depicted as a log-log plot. At temperatures below $T = 2.5 \times 10^{-2} \text{ K} \approx 0.5T_s$, the purity and fidelity are clearly higher for the case of one common bath, but if temperature is increased above this characteristic threshold, fidelity and purity are slightly higher for the case of two baths.

In the case of one common bath the fidelity, purity, and entanglement capability are approaching their ideal value 1,

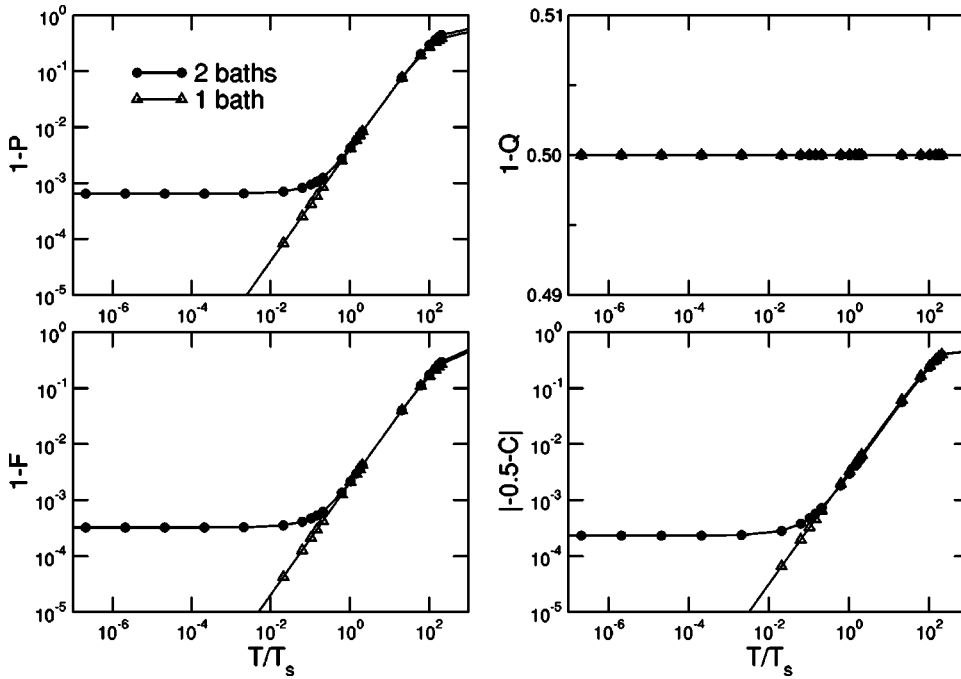


FIG. 12. Log-log plot of the temperature dependence of the deviations of the four gate quantifiers from their ideal values after performing the controlled phase-shift (CPHASE) gate operation. In all cases, $\alpha = \alpha_1 = \alpha_2 = 10^{-3}$. The full curves are provided as guides to the eye.

when temperature goes to zero. This is related to the fact that in the case of one common bath all relaxation and dephasing rates vanish during the two-qubit step of the controlled phase-shift gate due to the special symmetries of the Hamiltonian, when temperature goes to zero as depicted in Fig. 9.

The controlled phase-shift operation creates entanglement. The creation of entanglement is impeded by decoherence effects that vanish when temperature approaches zero. Therefore, the entanglement capability exhibits the same behavior as the fidelity and purity. For zero dissipation ($\alpha = 0$), the quantum degree has the value 0.5 but the entanglement capability is -0.5 thus, characterizing a maximum entangled state. The reason is that the Bell-states, which are generated by the controlled phase-shift gate from the input states, result in a basis that is different from the used basis, but can be transformed using only local transformations.

Furthermore, for finite dissipation, Fig. 9 shows that also for the case of two distinct baths, there are only three non-vanishing rates for $T \rightarrow 0$. The system, being prepared in one of the 16 initial states, might relax into one of the eigenstates that is an entangled state.

We observe the saturation of the deviation for the case of two baths and can directly recognize the effects of the symmetries of the controlled phase-shift operation. For given α , the fidelity and purity cannot be increased anymore by lowering the temperature in the case of two distinct baths. Interestingly enough, we find that for two qubits coupling to one common bath, the situation is different for temperatures below $0.5T_s$. Above a temperature of $T_s = 4.8 \times 10^{-2}$ K, the decrease of the gate quality factors shows a linear dependence on temperature for both cases of one common or two distinct heat baths before it again saturates at about 10^2 K $\approx 2 \times 10^3 T_s$. Finite decoherence effects in the fidelity, purity and entanglement capability at $T=0$ for the case of two distinct baths are resulting from the coupling of the system to the environment of harmonic oscillators, which (at $T=0$) are

all in their ground states and can be excited through spontaneous emission. But for the case of one common bath, the deviation from the ideal fidelity goes to zero, when temperature goes to zero. This is due to the special symmetries (K is the only *nonvanishing* parameter in the two-qubit operation) of the Hamiltonian, which rules out spontaneous emission. These symmetries are also reflected in the temperature dependence of the rates, Fig. 9. There, for one common bath, all rates vanish for $T \rightarrow 0$. Note that these rates only describe the two-qubit part of the operation. However, the single-qubit part behaves similarly, because the terms in the single-qubit Hamiltonian are also $\propto \sigma_z$.

2. Controlled-NOT gate

Different to the preceding section, we now add two single-qubit operations (Hadamard gates) to the controlled phase-shift operation that do *not* commute with the coupling to the bath. In Fig. 13, the deviations of the gate quality factors from their ideal values are depicted as a log-log plot. Again, at temperatures below $T = 2.5 \times 10^{-2}$ K $\approx 0.5T_s$, the purity and fidelity are higher for the case of one common bath, but if temperature is increased above this characteristic threshold, fidelity and purity are higher for the case of two baths. Note that, we have chosen a rather large α , this value can substantially be improved by means of engineering [13]. The fidelity and purity are clearly higher for the case of one common bath, when temperature is decreased below $0.5T_s$. This is related to the fact that in the case of one common bath, all relaxation and dephasing rates vanish during the two-qubit-step of the U_{XOR} , due to the special symmetries of the Hamiltonian, when temperature goes to zero as discussed in the preceding paragraph. However, the quantum degree and the entanglement capability tend towards the same value for both the case of one common and two distinct baths. This is due to the fact that both quantum degree and entanglement capability are, different than fidelity and purity, not defined

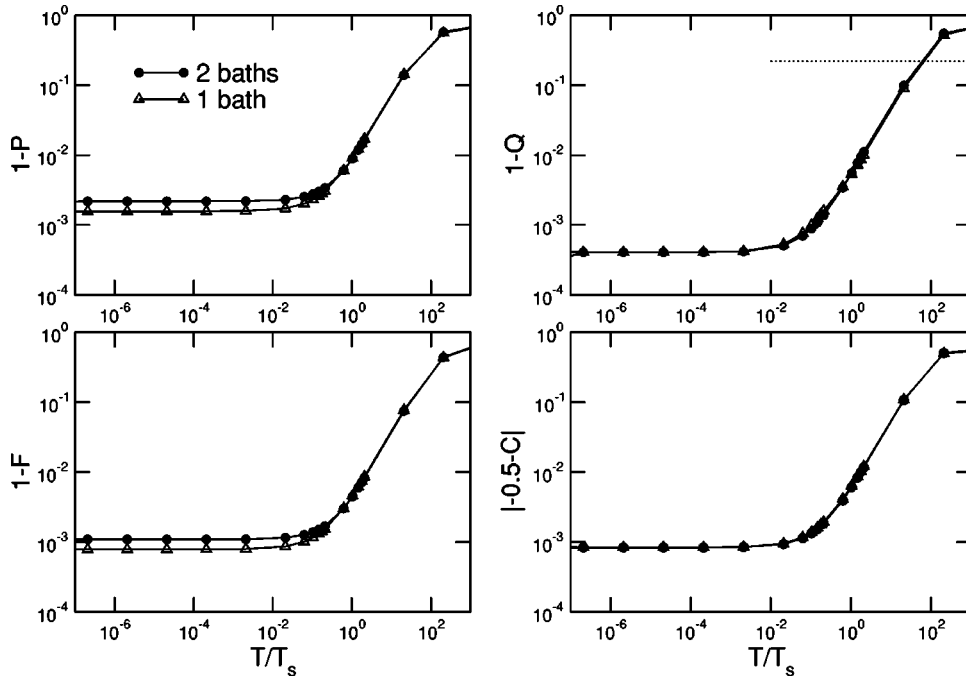


FIG. 13. Log-log plot of the temperature dependence of the deviations of the four gate quantifiers from their ideal values after performing the U_{XOR} gate operation. In all cases, $\alpha = \alpha_1 = \alpha_2 = 10^{-3}$. The dotted line indicates the upper bound set by the Clauser-Horne-Shimony-Holt inequality. The full curves are provided as guides to the eye.

as mean values but rather characterize the “best” possible case of all given input states. This results in the same value for both cases.

In the recent work by Thorwart and Hänggi [17], the U_{XOR} gate was investigated for a $\sigma_y^{(i)} \otimes \sigma_y^{(j)}$ coupling scheme and one common bath. They find a pronounced degradation of the gate performance, in particular, the gate quality factors only weakly depend on temperature. They set the strength of the dissipative effects to $\alpha = 10^{-4}$. Their choice of parameters was $\epsilon \approx 10E_s$, $\Delta \approx 1E_s$, and $K \approx 0.5E_s$ which is on the same order of magnitude as the values given in Table I. As can be seen in Fig. 13, we also observe only a weak decrease of the gate quality factors for both the cases of one common bath and two distinct baths in the same temperature range discussed by Thorwart and Hänggi, both for $\alpha = 10^{-3}$ and $\alpha = 10^{-4}$ and overall substantially better values. This is due to the fact that for $\sigma_y^{(i)} \otimes \sigma_y^{(j)}$ coupling, the Hamiltonian does *not* commute with the coupling to the bath during the two-qubit steps of the U_{XOR} pulse sequence.

We observe the saturation of the deviation for both the cases of two baths and one common bath. For given α , the fidelity and purity can not be increased anymore by lowering the temperature, different from the behavior for the controlled phase-shift gate that was discussed in the preceding section. This is due to the application of the Hadamard gate whose Hamiltonian does not commute with the coupling to the bath. Above a temperature of T_s , the decrease of the gate quality factors shows a linear dependence on temperature for both cases. Here, different from the controlled phase-shift gate, we observe finite decoherence effects in all four gate quantifiers also at $T=0$, both for the case of one common or two distinct heat baths. These decoherence effects are resulting from the coupling of the system to the environment of harmonic oscillators, which (at $T=0$) are all in their ground states and can be excited through spontaneous emission as already described above.

The dotted line in Fig. 13 shows that the temperature has to be less than about $T = 21T_s = 1$ K in order to obtain values of the quantum degree being larger than $Q \approx 0.78$. Only then, the Clauser-Horne-Shimony-Holt inequality is violated and nonlocal correlations between the qubits occur as described in Ref. [17].

C. Dependence on the dissipation strength

The deviations from the ideal values of the gate quantifiers possess a linear dependence on α as expected. Generally (if no special symmetries of the Hamiltonian are present), there are always finite decoherence effects also at $T=0$. Therefore, we can not improve the gate quality factors below a certain saturation value, when lowering the temperature [17], as was also discussed in the preceding section. By better isolating the system from the environment and by carefully engineering the environment [13], one can decrease the strength of the dissipative effects characterized by α . In order to obtain the desired value of 0.99999 for \mathcal{F} , \mathcal{P} , and Q [17], α needs to be below 10^{-6} at $T = 0.21T_s = 10$ mK.

D. Time resolved controlled-NOT operation

To investigate the anatomy of the U_{XOR} quantum logic operation, we calculated the occupation probabilities of the singlet/triplet states after each of the six operations, of which the U_{XOR} consists. This time resolved picture of the dynamics of the two-qubit system, when performing a gate operation, gives insight into details of our implementation of the U_{XOR} operation and the dissipative effects that occur during the operation. Thus, we are able to characterize the physical process, which maps the input density matrix ρ_0 to ρ_{out} in an open quantum system [33]. When the system is prepared in the state $|\downarrow\downarrow\rangle = |00\rangle$, the U_{XOR} operation (31) does not alter the initial state and after performing the U_{XOR} operation, the final state should equal the initial state $|\downarrow\downarrow\rangle = |00\rangle$. This can

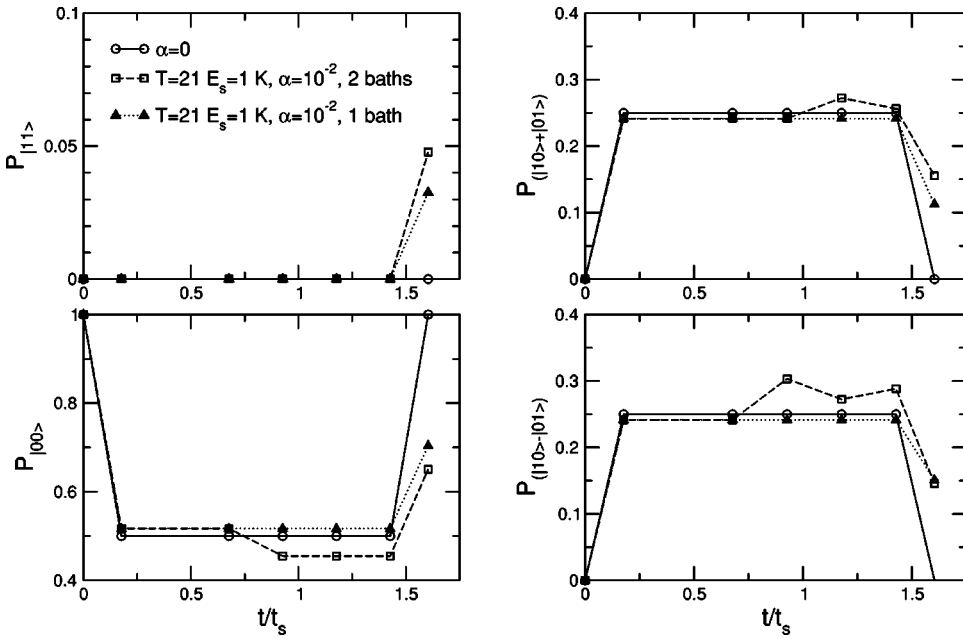


FIG. 14. Time resolved U_{XOR} operation. The system is initially prepared in the state $|00\rangle$. Occupation probabilities of the singlet/triplet states are shown after completion of a time step τ_i ($i = 1, \dots, 6$). For $\alpha = \alpha_1 = \alpha_2 = 10^{-2}$ and $T = 21T_s = 1$ K clear deviations from the ideal case can be observed. Qubit parameters are set according to Table I. The lines are provided as guides to the eye.

clearly be observed in Fig. 14. During the U_{XOR} operation, occupation probabilities of the four states change according to the individual operations given in Eq. (32). At $T = 21T_s$, the case of two baths differs significantly from the case of one common bath. After the third operation (the two-qubit operation; only there the distinction between one common or two distinct baths makes sense), occupation probabilities are different for both environments resulting in a less ideal result for the case of two baths.

In Fig. 14, the resulting state after performing the U_{XOR} operation always deviates more from the ideal value (for $\alpha = 0$, i.e., no dissipation) for the case of two distinct baths, if all other parameters are fixed and set to the same values for both cases. The state $P_{|00\rangle}$ is less close to the ideal occupation probability one and the other singlet/triplet states are

also less close to their ideal value for the case of two distinct baths. The case of two distinct baths also shows bigger deviations from the ideal case ($\alpha = 0$) during the U_{XOR} operation (see Fig. 14). But, if the system is initially prepared in the state $|\uparrow\uparrow\rangle = |11\rangle$, the case of two distinct baths shows bigger deviations from the ideal case during the U_{XOR} operation, while the resulting state is closer to the ideal case for two distinct baths compared to one common bath.

In Figs. 14 and 15, it looks like there would be no decoherence effects (or at least much weaker decoherence effects) after performing the (first two) single-qubit operations. However, not all input states are affected by the decoherence effects the same way. And when we regard all possible input states, there are finite decoherence effects. This can be explained with Fig. 16. Figure 16 depicts the time resolved

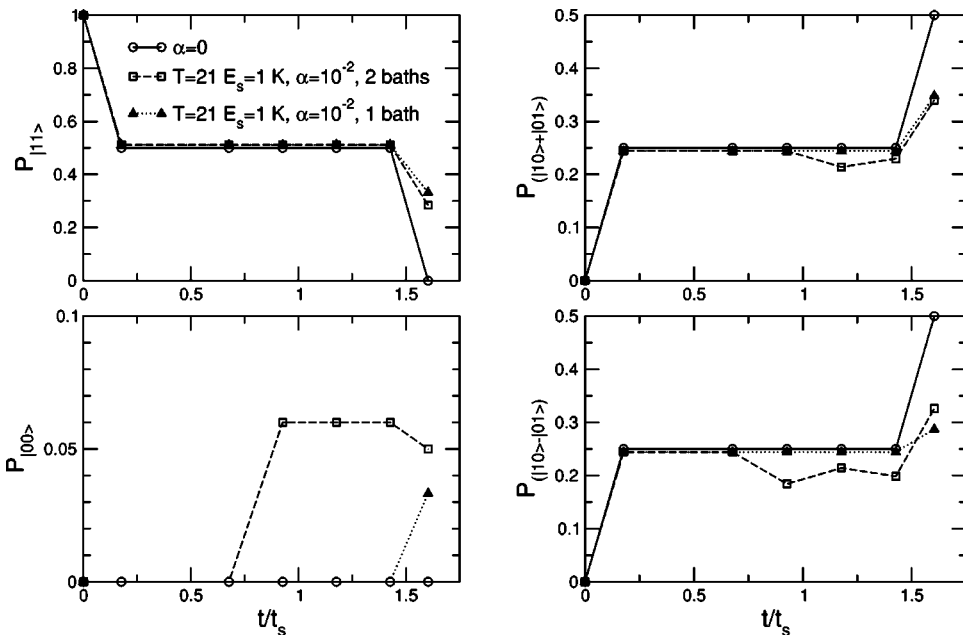


FIG. 15. Time resolved U_{XOR} operation. The system is initially prepared in the state $|11\rangle$. Occupation probabilities of the singlet/triplet states are shown after completion of a time step τ_i ($i = 1, \dots, 6$). For $\alpha = \alpha_1 = \alpha_2 = 10^{-2}$ and $T = 21T_s = 1$ K, deviations from the ideal case can be observed. Qubit parameters are set according to Table I. The lines are provided as guides to the eye.

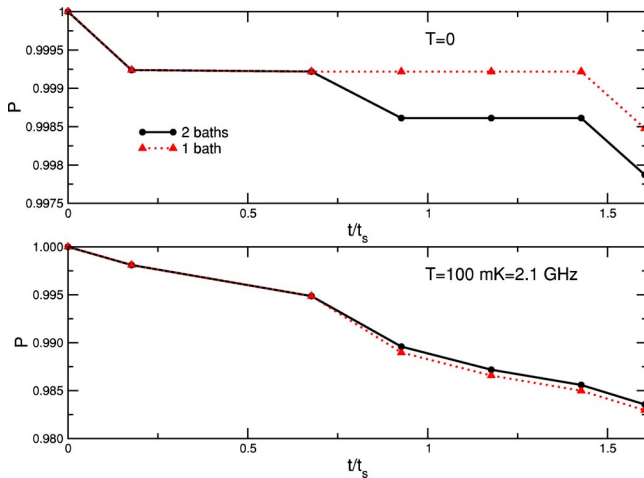


FIG. 16. Time resolved purity for the U_{XOR} operation. The value of the purity after each time step τ_i ($i=1, \dots, 6$) is shown. Here $\alpha = \alpha_1 = \alpha_2 = 10^{-2}$, and $T = 2.1T_s = 100$ mK (lower panel) or $T = 0$ (upper panel). Qubit parameters are set according to Table I. The lines are provided as guides to the eye.

purity when performing the U_{XOR} operation. We clearly observe that there are finite decoherence effects for the first single-qubit operations in Eq. (32) as well. The difference between the single-qubit and two-qubit operations is the steeper decrease of the purity due to stronger decoherence in the case of the two-qubit operation. The upper panel in Fig. 16 depicts the behavior of the purity for $T \rightarrow 0$. Decoherence due to the σ_z terms in the Hamiltonian will vanish for $T \rightarrow 0$ in the case of one common bath.

VI. CONCLUSION

We presented a full analysis of the dynamics and decoherence properties of two solid-state qubits coupled to each other via a generic type of Ising coupling and coupled, moreover, either to a common bath, or two independent baths.

We calculated the dynamics of the system and evaluated decoherence times. From the temperature dependence of the decoherence rates (Fig. 8), we conclude that both types of environments show a similar behavior; however, in the case of one common bath, two of the decoherence rates are zero, and the remaining ones are slightly larger than in the case of two distinct baths. This temperature dependence is also reflected in the characteristics of the gate quality factors from quantum information theory, which are introduced as robust

measures of the quality of a quantum logic operation. We illustrate that the gate quality factors depend linearly on α , as expected. The time resolved U_{XOR} operation (Figs. 14 and 15) again illustrates the difference between one common and two distinct baths, and moreover, we observe that single-qubit decoherence effects $\propto \sigma_z$ during the U_{XOR} operation are weak. The time scales of the dynamics of the coupled two qubit system are comparable to the time scales, which were already observed in experiments and discussed in the literature [13].

The question, whether one common bath or two distinct baths are less destructive regarding quantum coherence can not be clearly answered. For low enough temperatures, coupling to one common bath yields better results. However, when the temperature is increased, two distinct baths do better; in both temperature regimes, though, the gate quantifiers are only slightly different for both cases.

Compared to the work of Thorwart [17], the interaction part of our model Hamiltonian possesses symmetries (the Hamiltonian of the two-qubit operation and the errors commute) that lead to better gate quality factors. Furthermore, analysis of the symmetries and error sources of our model system can lead to improved coupling schemes for solid-state qubits. Milburn and co-workers on the other hand focused on comparison of classical and quantum mechanical dynamics [15] and estimated the decoherence properties of two coupled two-state systems.

Governale [16] determined the decoherence properties of two coupled charge qubits whose Hamiltonian differs from Eq. (2) by the type of interqubit coupling, namely, $\sigma_y^{(1)} \otimes \sigma_y^{(2)}$ coupling. However, introducing the quality factors gives a measure to judge how certain qubit designs perform quantum gate operations.

As a next step, one should consider driving, to be able to observe and discuss Rabi oscillations in systems of two coupled qubits. It should be investigated, how the decoherence properties are modified, if one adds more qubits to the system.

ACKNOWLEDGMENTS

We thank B. Singh, L. Tian, C. H. van der Wal, M. Governale, M. C. Goorden, A. C. J. ter Haar, H. Aschauer, R. Raussendorf, A. J. Leggett, P. Hänggi, C. J. P. M. Harmans, H. Gutmann, U. Hartmann and J. von Delft for fruitful discussions. We acknowledge financial support from ARO, under Contract No. P-43385-PH-QC, and from DAAD under Contract No. DAAD/NSF D/0104619.

[1] P. Shor, in *Proceedings of 35th Annual Symposium on the Foundations of Computer Science*, edited by S. Goldwasser (IEEE Computer Society Press, Los Alamitos, 1994), pp. 124–134.
 [2] L.K. Grover, *Phys. Rev. Lett.* **79**, 325 (1997).
 [3] D. Deutsch, *Proc. R. Soc. London, Ser. A* **400**, 97 (1985).
 [4] D.P. DiVincenzo, *Science* **269**, 225 (1995).
 [5] B.E. Kane, *Nature (London)* **393**, 133 (1998).

[6] T.P. Orlando *et al.*, *Phys. Rev. B* **60**, 15 398 (2000); J.E. Mooij *et al.*, *Science* **285**, 1036 (1999).
 [7] Yu.A. Pashkin, T. Yamamoto, O. Astafiev, Y. Nakamura, D.V. Averin, and J.S. Tsai, *Nature (London)* **421**, 823 (2003).
 [8] Y. Nakamura, Yu.A. Pashkin, and J.S. Tsai, *Nature (London)* **398**, 786 (2002).
 [9] J.R. Friedman, V. Patel, W. Chen, S.K. Tolpygo, and J.E. Lukens, *Nature (London)* **406**, 43 (2000).

- [10] D. Vion, A. Aassime, A. Cottet, P. Joyez, H. Pothier, C. Urbina, D. Esteve, and M.H. Devoret, *Science* **296**, 886 (2002).
- [11] Y. Nakamura (private communication).
- [12] M.C. Goorden, Masters thesis, Delft University of Technology, 2002 (unpublished); M.C. Goorden and F.K. Wilhelm (unpublished).
- [13] C.H. van der Wal, *Quantum Superpositions of Persistent Josephson Currents* (Delft University Press, Delft, 2001); C.H. van der Wal, F.K. Wilhelm, C.J.P.M. Harmans, and J.E. Mooij, *Eur. Phys. J. B* **31**, 111 (2003).
- [14] Y. Makhlin, G. Schön, and A. Shnirman, *Rev. Mod. Phys.* **73**, 357 (2001).
- [15] G.J. Milburn, R. Laflamme, B.C. Sanders, and E. Knill, *Phys. Rev. A* **65**, 032316 (2002).
- [16] M. Governale, M. Grifoni, and G. Schön, *Chem. Phys.* **268**, 273 (2001).
- [17] M. Thorwart and P. Hänggi, *Phys. Rev. A* **65**, 012309 (2002).
- [18] F.K. Wilhelm and J.E. Mooij (unpublished).
- [19] R.H. Blick and H. Lorenz, in *ISCAS 2000 Proceedings* (unpublished), pp. II245-II248.
- [20] J.B. Majer (private communication).
- [21] D.A. Lidar, I.L. Chuang, and K.B. Whaley, *Phys. Rev. Lett.* **81**, 2594 (1998).
- [22] J. Kempe, D. Bacon, D.A. Lidar, and K.B. Whaley, *Phys. Rev. A* **63**, 042307 (2001).
- [23] M.J. Storcz, Masters thesis, University of Bonn, 2002 (unpublished).
- [24] K. Segall *et al.*, *IEEE Trans. Appl. Supercond.* (to be published).
- [25] C.H. van der Wal *et al.*, *Science* **290**, 773 (2000).
- [26] P.N. Argyres and P.L. Kelley, *Phys. Rev.* **134**, A98 (1964).
- [27] L. Hartmann, I. Goychuk, M. Grifoni, and P. Hänggi, *Phys. Rev. E* **61**, R4687 (2000); L. Hartmann, *Driven Tunneling Dynamics of Dissipative Two-State Quantum Systems* (Shaker Verlag, Aachen, 2000).
- [28] U. Weiss, *Quantum Dissipative Systems*, 2nd ed. (World Scientific, Singapore, 1999).
- [29] K. Blum, *Density Matrix Theory and Applications*, 1st ed. (Plenum, New York, 1981).
- [30] A.J. Leggett *et al.*, *Rev. Mod. Phys.* **59**, 1 (1987).
- [31] S. Kehrein and M. Vojta, e-print cond-mat/0208390.
- [32] P. Horowitz and W. Hill, *The Art of Electronics*, 2nd ed. (Cambridge University Press, Cambridge, 1989).
- [33] J.F. Poyatos, J.I. Cirac, and P. Zoller, *Phys. Rev. Lett.* **78**, 390 (1997).
- [34] C.H. Bennett, G. Brassard, S. Popescu, B. Schumacher, J.A. Smolin, and W.K. Wootters, *Phys. Rev. Lett.* **76**, 722 (1996); J.F. Clauser, M.A. Horne, A. Shimony, and R.A. Holt, *ibid.* **23**, 880 (1969).
- [35] A. Peres, *Phys. Rev. Lett.* **77**, 1413 (1996).
- [36] A. Barenco, C.H. Bennett, R. Cleve, D.P. DiVincenzo, N. Margolus, P. Shor, T. Sleator, J.A. Smolin, and H. Weinfurter, *Phys. Rev. A* **52**, 3457 (1995).

3.4 Read-out of superconducting qubits

After quantum manipulations have been performed, the result has to be read out. This very obvious requirement is connected to the fundamental physical problem of the quantum measurement process, which is discussed in the introduction. Our enterprise is more modest: Within the range of useful detectors which can be built and modeled, the properties of the specific read-out process have to be deduced and understood. The modeling of the meter has already been described in the papers compiled in section 3.2. In paper [196], this model is taken to an extreme limit: The peak in the environmental spectral density is moved to high frequencies and is strongly emphasized. In that limit, the system entangles strongly with that resonance, tunneling becomes suppressed i.e. it becomes localized in the classically preferred states. Thus, we meet the condition for a detector-dominated projective measurement.

In ref. [197], the equivalence between the peaked spectral resonance and the model of a qubit coupled to a damped harmonic oscillator is worked out in more detail.

The analysis of the peaked spin boson model in Refs. [196, 197] was based on a physically motivated mapping on a low-temperature Hilbert space. In Ref. [198], the same model is mathematically analyzed with a number of state-of-the-art methods such as NIBA, Bloch-Redfield, and flow equation renormalization. Next to confirming the results of [196], a number of other features are found: The renormalization of the energy splitting of the spin due to the environment changes sign depending on the ratio of the environmental and the qubit resonance energy, following the usual quantum-mechanical level repulsion. The weak-coupling results taken to stronger coupling generally tend to overestimate the decoherence, in particular close to resonance. This has a clear physical interpretation: The resonance reflects strong coupling to a *single* quantum system, which changes the system dynamics strongly, but changes it in a coherent way, because decoherence would require an *infinite* environment.

Asymptotic von Neumann measurement strategy for solid-state qubits

F. K. Wilhelm

Quantum Transport Group, Technische Natuurkunde, TU Delft, P.O. Box 5046, 2600 GA Delft, The Netherlands and Sektion Physik and CeNS, Ludwig-Maximilians-Universität, Theresienstrasse 37, 80333 München, Germany

(Received 19 May 2003; published 19 August 2003)

A measurement on a macroscopic quantum system does not, in general, lead to a projection of the wave function in the basis of the detector as predicted by von Neumann's postulate. Hence, it is a question of fundamental interest, how the preferred basis onto which the state is projected is selected out of the macroscopic Hilbert space of the system. Detector-dominated von Neumann measurements are also desirable for both quantum computation and verification of quantum mechanics on a macroscopic scale. The connection of these questions to the predictions of the spin-boson model is outlined. I propose a measurement strategy, which uses the entanglement of the qubit with a weakly damped harmonic oscillator. It is shown that the degree of entanglement controls the degree of renormalization of the qubit and identify that this is equivalent to the degree to which the measurement is detector dominated. This measurement very rapidly decoheres the initial state, but the thermalization is slow. The implementation in Josephson quantum bits is described and it is shown that this strategy also has practical advantages for the experimental realization.

DOI: 10.1103/PhysRevB.68.060503

PACS number(s): 03.67.Lx, 03.65.Ta, 03.65.Yz, 74.50.+r

The field of quantum computation¹ has been experimentally pioneered in quantum optics, atomic physics, and nuclear magnetic resonance (NMR). In these quantum-mechanical systems with few degrees of freedom and strong quantum coherence, the measurement devices ("meters") are well described and can be classified into two types. In atomic physics, e.g., "strong" measurements can be performed, which satisfy von Neumann's measurement postulate,² i.e., the state of the system is projected onto the eigenstate of the *meter* corresponding to the measurement result. In NMR, on the other hand, the meter couples weakly to each individual spin and decoheres it only weakly. In order to still obtain enough signal and information, the measurement is performed on an ensemble of qubits.

These qubits cannot be easily integrated to large-scale circuits. Thus, solid-state qubits, which can be lithographically manufactured, are a promising alternative. Solid-state systems consist of many degrees of freedom, hence quantum coherence can so far only be maintained over very short times.^{3,4} It was proposed that superconducting Josephson circuits in the charge^{3,5} or flux^{4,6} regime could act as solid-state qubits with appreciable coherence times. In these cases, the measurement apparatus is permanently close to the qubit, although the interaction may effectively be switched off.^{7,8} The measurement process in this system can be described within the spin-boson^{9,10} or related models.^{7,11,12}

From a density-matrix description, we can obtain detailed (although incomplete) information about the dynamics of the measurement: After a dephasing time τ_ϕ , the density matrix is brought into an incoherent mixture, and after the relaxation time τ_r it thermalizes and the information about the initial state is lost.⁷ In order to render τ_r long enough, usually³⁻⁵ the meter is only weakly coupled to the qubit. This makes it necessary to ensemble average by repeating the measurement. Theoretical research^{7,11,12} shows that an optimization of these weak measurements allows for single-shot measurements without averaging, by waiting longer than the dephasing time. These are *optimized weak measurements* or *qubit dominated* measurements: They completely decohere

the state of the qubit, however, the final state is *not* an eigenstate of the measured observable, but of the qubit. Qubit and apparatus do *not* get strongly entangled. It has also been shown theoretically,⁷ that detector-dominated *strong* measurements of superconducting qubits are possible, on the expense of τ_R being very short, which sets a strong experimental challenge. It is a fundamental question, under which conditions a measurement performed on a potentially macroscopic object follows the postulates of quantum mechanics and how, in general, the preferred observable basis is selected out of the large Hilbert space of the system and the detector.¹³ This question should be addressed using specific models which describe actual detectors. Moreover, there are practical issues: (i) The theoretical signal-to-noise ratio of a weak measurement is limited to 4 (Ref. 12), (ii) and Efficient quantum algorithms such as error correction¹⁴ or the test of Bell-type inequalities¹⁵ rely on strong measurements.

In this paper, I am going to connect the abstract notions of quantum measurement theory to the concepts of the spin-boson model, in particular, the issue of entanglement will be connected to scaling of the tunnel matrix element. I will outline a method how to perform genuine detector-dominated measurements in this context.

For definiteness, it is assumed that the variable of the quantum bit which is measured is described by the pseudospin operator $\hat{\sigma}_z$. When the measurement apparatus is coupled to the qubit, the same term experiences a fluctuating force, which is assumed to be Gaussian and be modeled by a bath of harmonic oscillators. Consequently, we end up with the spin-boson Hamiltonian.^{9,16} After integrating out high frequencies, its pseudospin part reads

$$\hat{H}_{\text{eff}} = \hbar \left(\frac{\epsilon}{2} \hat{\sigma}_z + \frac{\Delta_{\text{eff}}}{2} \hat{\sigma}_x \right), \quad (1)$$

where the off-diagonal term Δ_{eff} is in general rescaled due to the environment as compared to the original splitting Δ of an isolated qubit. The spin-boson model generally predicts¹⁶ the dynamics described in the preceding section. In particular,

after the dephasing time, the density matrix is projected onto a mixture of *eigenstates of H_{eff}* . Usually, in the weak-coupling regime,⁹ Δ_{eff} is close to the bare Δ of the qubit and consequently the eigenstates of H_{eff} are far from being eigenstates of $\hat{\sigma}_z$. Consequently, the state of the qubit will not be projected onto the measured variable, i.e., the measurement is qubit dominated. A detector-dominated measurement would be realized for $\Delta_{\text{eff}}=0$,¹⁷ i.e., when $\hat{H}_{\text{eff}}=(\epsilon/2)\hat{\sigma}_z$ and hence commutes with the coupling to the meter. A number of schemes allow to directly suppress Δ using an external control parameter.^{5,6,18} In what follows, I want to describe, using a generic model, how this is accomplished by the measurement apparatus itself, in agreement with the usual understanding of quantum measurements.

Consider a qubit coupled to a single (big) harmonic oscillator, which experiences linear friction, which is in turn described quantum mechanically through a bath of oscillators. The Hamiltonian of this system then reads

$$\hat{H} = \hbar \left(\frac{\epsilon}{2} \hat{\sigma}_z + \frac{\Delta}{2} \hat{\sigma}_x \right) + \frac{\hat{P}^2}{2M} + \frac{M}{2} \Omega^2 (\hat{X} - q \hat{\sigma}_z)^2 + \sum_i \left(\frac{\hat{p}_i^2}{2m_i} + \frac{m_i}{2} \omega_i^2 (\hat{x}_i - (c_i/m_i \omega_i^2) \hat{X})^2 \right), \quad (2)$$

where the displacement q characterizes the coupling of the qubit to the big oscillator. The oscillator bath is characterized through an ohmic spectral density $J(\omega) = \sum (\pi c_i^2 / (2m_i \omega_i)) \delta(\omega - \omega_i) = M\Gamma\omega$, where $\Gamma/2$ is the friction coefficient of the damped big oscillator. It was shown¹⁹ that this system is equivalent to the spin-boson model, with an effective spectral density

$$J_{\text{eff}}(\omega) = 2\pi\alpha\omega \frac{\Omega^4}{(\omega^2 - \Omega^2)^2 + 4\Gamma^2\omega^2}, \quad (3)$$

where $\alpha = 2Mq^2\Gamma/h$ is a dimensionless dissipation coefficient, which here is assumed to be small, $\alpha \ll 1$. From now on, we want to concentrate on the case $\epsilon, \Delta \ll \Omega$.

At $\Gamma=0$, the low-energy Hilbert space is spanned by $|\pm\rangle_{\text{eff}} = |\pm\rangle|L/R\rangle$ where $|\pm\rangle$ are the basis states of the qubit, $\sigma_z|\pm\rangle = \pm|\pm\rangle$, and $|L/R\rangle$ are coherent states of the harmonic oscillator centered around $X = \pm q$, see Fig. 1 (left). So in a general low-energy state $|\psi\rangle = a|+\rangle_{\text{eff}} + b|-\rangle_{\text{eff}}$, $|a|^2 + |b|^2 = 1$, qubit and oscillator are entangled²⁰ and the oscillator states are pointers onto the qubit states.¹³ In this low-energy basis, the Hamiltonian acquires form (1), with $\Delta_{\text{eff}} = \Delta\langle L|R\rangle = \Delta e^{-\eta}$ where $\eta = M\Omega q^2/\hbar$. Under an appropriate choice of parameters, we can achieve $\eta > 1$ and $\Delta_{\text{eff}} \ll \Delta$. This choice corresponds to the condition of almost [meaning here and henceforth “up to an error of $O(e^{-\eta})$ ”] *orthogonal* states in the environment, which has been identified as the condition for an ideal von Neumann measurement.^{13,21}

For finite Γ , this system can be analyzed using adiabatic renormalization.^{9,22} One finds²³ $\Delta_{\text{eff,damp}}(\alpha) = \Delta e^{-\eta/(1-\alpha)} (\Delta/\Omega)^{\alpha/(1-\alpha)}$. Thus, finite dissipation $0 < \alpha \ll 1$ scales Δ down even slightly further.

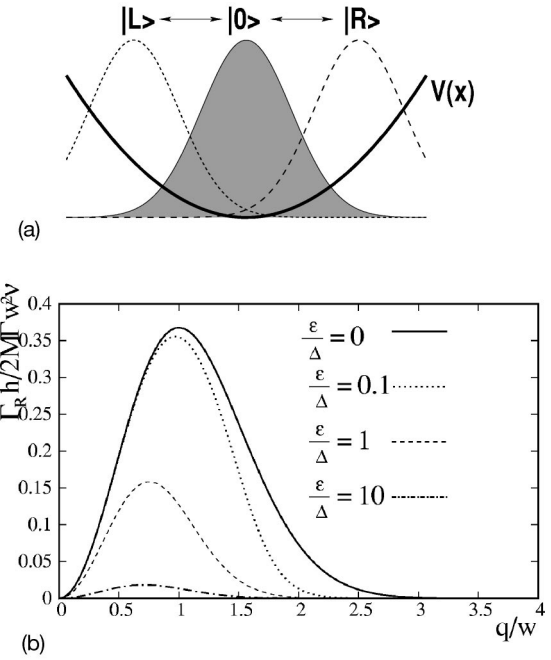


FIG. 1. Left: Visualization of the ground state $|0\rangle$ and the coherent pointer states $|L\rangle$ and $|R\rangle$ of the oscillator in the potential $V(x)$; right: Relaxation rates as a function of the coupling q/w for different energy biases. w is the width of the ground-state wave function of the pointer, $w = \sqrt{\hbar/M\Omega}$.

The coherence properties of our system can at $\epsilon, \Delta, T \ll \Omega$ be studied using a systematic weak damping approximation¹⁶ of the spin-boson model. The relaxation and dephasing rates $\Gamma_{r/\phi} = \tau_{r/\phi}^{-1}$ are given by

$$\Gamma_r = \pi\alpha \frac{\Delta_{\text{eff}}^2}{\nu_{\text{eff}}} \coth\left(\frac{\nu}{2T}\right), \quad \Gamma_\phi = \frac{\Gamma_r}{2} + 2\pi\alpha k_B \frac{\epsilon^2}{\nu_{\text{eff}}} T/\hbar, \quad (4)$$

where $\nu_{\text{eff}} = \sqrt{\Delta_{\text{eff}}^2 + \epsilon^2}$. In our case, if $\eta > 1$, Δ_{eff} is exponentially reduced compared to Δ , transitions between the basis states are suppressed leaving relaxation very slow, i.e., the state becomes almost localized or “frozen,” see Fig. 1 (right). The second contribution to Γ_ϕ in Eq. (4) reflects dephasing processes which do not change the qubit energy and are consequently not frozen.

The use of a weak damping approximation for $\Gamma_{r,\phi}$ is appropriate, although $J(\omega)$ can be large at the peak and in fact the down scaling of Δ_{eff} is essentially a nonperturbative effect. However, decoherence is mostly probing the $J_{\text{eff}}(\omega)$ around $\omega = \nu_{\text{eff}} \ll \Omega$, where the weak damping condition holds. This is supported by two observations: i) if we project the full Hamiltonian onto its low-energy Hilbert space spanned by $|\pm\rangle_{\text{eff}}$, we find an effective ohmic model leading to Eq. 4; (ii) a full nonperturbative calculation²³ based on the noninteracting blip approximation (NIBA)⁹ reproduces both the scaling and Γ_r within the known¹⁶ limitations of NIBA.

The measurement can now be performed as follows: As a first step, q is adiabatically ramped from $q=0$ to a finite q_0 where $\eta > 1$ and $\Delta \rightarrow \Delta_{\text{eff}} \ll \Delta$. The adiabatic theorem pre-

dicts, that the state of the system evolves as $(\alpha|+\rangle + \beta|-\rangle) \otimes |0\rangle \rightarrow (\alpha^{\text{eff}}|+\rangle|L\rangle + \beta^{\text{eff}}|-\rangle|R\rangle)$, where

$$\begin{pmatrix} \alpha^{\text{eff}} \\ \beta^{\text{eff}} \end{pmatrix} = \begin{pmatrix} \cos\left(\frac{\theta^{\text{eff}} - \theta}{2}\right) & \sin\left(\frac{\theta^{\text{eff}} - \theta}{2}\right) \\ -\sin\left(\frac{\theta^{\text{eff}} - \theta}{2}\right) & \cos\left(\frac{\theta^{\text{eff}} - \theta}{2}\right) \end{pmatrix} \begin{pmatrix} \alpha \\ \beta \end{pmatrix} \quad (5)$$

and $\tan \theta^{\text{(eff)}} = \epsilon / \Delta^{\text{(eff)}}$. The condition for adiabaticity is $dq/dt \ll v_{\text{eff}}^2 / 2qM\Omega\Delta_{\text{eff}}$, i.e., for small q the ramping can be very fast.

When $\eta > 1$, the matrix element is scaled down and the state is ‘‘premeasured’’ by entanglement with well-separated pointer states L and R .¹³ Only now, we start the measurement, by coupling the oscillator to the meter and decohering the state is projected onto the eigenstates of \hat{H}_{eff} , which are close to the ones of $\hat{\sigma}_z$. We can then read off the position of the big oscillator serving as a pointer and switch off the meter (or q) again way before τ_r without destroying information by relaxation.

In practice, it will usually not be possible to switch the coupling between oscillator and meter separately. Thus, before the entanglement is established, the relaxation rate (4) does *not* profit from the reduction of Δ_{eff} , see Fig. 1 (right). In order not to lose the information to be measured, the *maximum* relaxation rate $\Gamma_{r,\text{max}}$ reached at $\eta = 1/2$ (i.e., $q = q_c = \sqrt{\hbar/2M\Omega}$) should be slow enough, such that by the time τ_{ent} it takes to ramp above q_c , the information is not lost. In practice, this can be achieved by switching q very fast, at a time $\tau_{\text{ent}} \ll \Gamma_{r,\text{max}}^{-1}$, to q_c and slower afterwards, when the actual measurement occurs.

In the ohmic spin-boson model,^{9,16} i.e., for $J_{\text{eff}} = 2\pi\alpha\omega e^{-\omega/\omega_c}$, a scaling of Δ_{eff} to zero can be achieved through a dissipative phase transition at strong coupling to the bath ($\alpha > 1$).^{9,17,24,25} This transition is driven by the entanglement with a *collective* state involving the whole oscillator bath. Ramping α to large values increases $J_{\text{eff}}(\omega)$ at all frequencies, which leads to rapid relaxation *before* the scaling is established. Moreover, it is not known, how long it will take for the system to go through this phase transition. Here, according to the adiabatic theorem, this time is set through the inverse level spacing of the coupled system, which is infinite for the dense Ohmic spectrum. On the contrary, the model studied in the present paper provides strong scaling of Δ_{eff} with predictably *slow* relaxation and gives a clear prediction for the time scale of the entanglement set by the finite level spacing.

This model does not generally predict the efficiency of the detection. In order to do so, I chose a specific realization of the model, a superconducting quantum bit.^{5,6} In this case, the readout device is a Josephson junction, whose critical current I_0 is influenced by the state of the qubit, either a superconducting single-electron transistor⁵ or a dc superconducting quantum interference device (SQUID),⁶ see Fig. 2. We study the junction on the superconducting branch at low bias current I_B . We assume the tunable junction to be shunted only by a very large resistor R and an external capacitance C_x and consequently underdamped. This system has been studied in

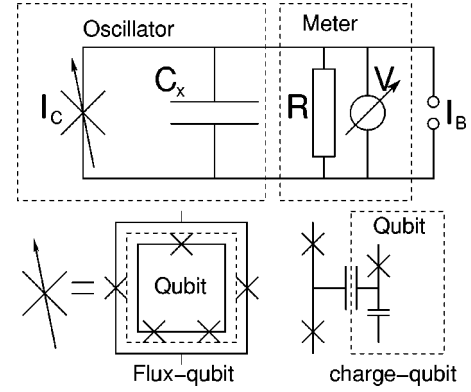


FIG. 2. Underdamped readout devices for superconducting flux (left) and charge (right) quantum bits.

the weak damping regime in Ref. 8 and resembles the one experimentally used in (Ref. 4). The oscillator in our model represents the plasma resonance²⁶ of the tunable junction at $\Omega = \sqrt{2eI_0/\hbar C_x}(1 - I_B^2/I_0^2)^{1/4}$. We can identify $M = C_x(\hbar/2e)^2$, $X = \phi$ (the Josephson phase), and $q = (\delta I_c/I_c)(I_B/\sqrt{I_0^2 - I_B^2})$, where $\delta I_c/I_c$ is the difference in critical current induced by the two fundamental states of the qubit. The damping is provided by the resistor and leads to $\alpha = \hbar q^2/2e^2 R = q^2 11.8k\Omega/R$, and the scaling exponent reads $\eta = q^2 \sqrt{C_x I_c \hbar}/8e^3$.

When ramping I_B , the junction switches to a finite voltage at $I_{\text{sw}} < I_0$, which provides a measure for I_0 . This switching is a stochastic process, so, if the measurement is repeated, one finds a histogram of switching currents^{27,28} centered around $I_{\text{sw},0}$, whose width δI_{sw} limits the resolution of this detector. In our case, the switching is predominantly due to thermal activation, where we can express $I_{\text{sw},0}/I_0 = 1 - [\ln(\omega_T/\Gamma_s)/u_0]^{2/3}$ and $\delta I/I_0 = [u_0^2 \ln(\omega_T/\Gamma_s)]^{-1/3}$ through the dimensionless height of the barrier at zero bias $u_0 = (4\sqrt{2}/3)(\hbar I_c/2ekT)$, the activation frequency $\omega_T = 2\Omega/\pi$, and the ramp rate $\Gamma_s = d(q/q_{\text{max}})/dt$. The current can be switched within a time $\tau_{\text{sw}} = \Omega^{-1}$, i.e., the ramp rate is limited by $\Gamma_{s,\text{max}} = \Omega$.

In a flux qubit, one can realize⁴ $I_c = 1 \mu\text{A}$, shunt with $C_x = 100 \text{ pF}$ and $R = 10 \text{ k}\Omega$, and $q_{\text{max}} = 0.05$ at a typical switching current level. We will assume $\Delta_0 = 1 \text{ GHz}$ and $\epsilon = 1 \text{ GHz}$ for the qubit. These parameters are accessible by doubling the size of the sample studied in (Ref. 4). This leads to $\Omega = 2 \text{ GHz}$, $\alpha = 0.003$, and $\eta_{\text{max}} = 3.5$, i.e., $\Delta_{\text{eff}} = 0.03\Delta_0$. Entanglement sets in at $q_c = 0.015$, where the relaxation time is $\tau_{r,\text{min}} = \Gamma_{r,\text{max}}^{-1} = 5 \mu\text{s}$. For 1% error, the first switch over this point has to be done at 700 ns, which is way above $\Gamma_{s,\text{max}} = 500 \text{ ps}$ and the adiabatic condition $qdq/dt < (500 \text{ ns})^{-1}$. Close to the measuring point $I_{\text{sw},0}$, we find $\tau_r = 120 \mu\text{s}$ and $\tau_\phi = 100 \text{ ns}$, which leaves a huge measurement window.

For definiteness, we set the temperature to $T = 200 \text{ mK}$ and find, using $\Gamma_s = (15 \mu\text{s})^{-1}$, that $I_{\text{sw},0}/I_0 = 0.96$ and $\delta I/I_0 = 0.35\%$, so, because $q = 5\%$, we have a signal-to-noise ratio of about 14. Hence, a single-shot von Neumann measurement appears to be feasible within a gradual improvement of technology.

For the readout for a charge qubit³ by a superconducting single electron transistor (S-SET), one can achieve values of $q=0.5$ within a charging energy $E_{C,SET}=2K$, corresponding to a capacitance scale of $C=1$ fF. We take the critical current of the SET to be $I_c=10$ nA and a shunt of $R=10$ k Ω and $C_x=1$ pF shunt capacitance. This leads to $\eta=3.5$, $\Omega=2$ GHz, and damping $\alpha=0.25$. Assuming $\Delta=1$ GHz, and $\epsilon=1$ GHz, we find $\tau_{R,min}=60$ ns, so for 1% error we have to switch to q_c in about 10 ns, which is close to the limit of $\Gamma_{s,max}=500$ ps. However, this may pose some challenge for the limiting time scales which are *not* due to the on-chip circuitry. For the readout step, we find $\tau_R=25$ μ s and $\tau_\phi=15$ ns. Applying the histogram theory as above at $T=200$ mK and $\Gamma_S=(3 \mu\text{s})^{-1}$, we end up with $I_{sw,0}/I_0=40\%$ and $\delta I_{sw}/I_c=8\%$, which can resolve our large signal of $q=30\%$ at signal-to-noise ratio of 4. It has been shown^{29,30} that experimentally SET's *can* reach signal-to-noise figures comparable to the quantum limit, hence even though the resolution is slightly less favorable than above, von Neumann measurements appear to be possible. For qubits³¹ operating in the regime of $E_J/E_c \approx 1$, more favorable parameters should be accessible.

The readout of the detector by switching is only one, and not necessarily the optimum alternative. Measurements could also be performed by detecting the kinetic inductance using the same parameters.

A similar circuit, a *normal conducting* SET with *out* the shunt capacitor has been thoroughly studied in Refs. 5,7. In that case, the measurement is started by rapidly switching the gate and monitoring the current. It has been shown that in

this way weak as well as strong measurements can be performed. As a consequence of the direct coupling of a dense spectrum of normal electrons to the qubit, the entanglement and the decoherence are not as strongly separated as in our case. Typical⁵ mixing times during the whole measurement are of the order of 1 μ s, i.e., one has to be able to monitor the current through the SET on the scale of 100 ns. In our case, one has to make the first entanglement switch on a similar scale, but has to monitor the voltage only afterwards, when mixing times are on the scale of 10 μ s. These numbers clearly indicate an advantage of the entanglement with the intermediate oscillator.

I have proposed a strategy for performing detector-dominated von Neumann measurements on qubits, using entanglement with coherent states of an harmonic oscillator. This system has been quantitatively analyzed using the spin-boson model and it has been shown that it has very favorable coherence and relaxation properties. A connection between the familiar scaling of the tunnel matrix element and the degree of entanglement with the environment has been established. Realistic superconducting circuitry, which could perform such measurements within present-day technology, has been proposed.

I thank J. von Delft, M. Governale, M. Grifoni, A.C.J. ter Haar, P. Hadley, P. Hakonen, C.J.P.M. Harmans, S. Kleff, L. Levitov, S. Lloyd, A. Lupascu, J.E. Mooij, T.P. Orlando, A. Shnirman, and C.H. van der Wal for clarifying discussions, as well as acknowledge support by the EU through TMR Supnan and Quiprocone and through ARO under Contract No. P-43385-PH-QC.

¹See, e.g., M.A. Nielsen and I.L. Chuang, *Quantum Computation and Quantum Information* (Cambridge University Press, Cambridge, 2000).

²J. von Neumann, *Mathematical Foundations of Quantum Mechanics* (Princeton University Press, Princeton, NJ, 1955).

³Y. Nakamura, Yu.A. Pashkin, and J.S. Tsai, *Nature (London)* **398**, 786 (1999).

⁴C.H. van der Wal *et al.*, *Science* **290**, 773 (2000); I. Chiorescu *et al.*, *ibid.* **299**, 1869 (2003).

⁵Yu. Makhlin, G. Schön, and A. Shnirman, *Nature (London)* **386**, 305 (1999); *Rev. Mod. Phys.* **73**, 357 (2001).

⁶J.E. Mooij *et al.*, *Science* **285**, 1036 (1999).

⁷A. Shnirman and G. Schön, *Phys. Rev. B* **57**, 15 400 (1998).

⁸C.H. van der Wal *et al.*, *Eur. Phys. J. B* **31**, 111 (2003).

⁹A.J. Leggett *et al.*, *Rev. Mod. Phys.* **59**, 1 (1987).

¹⁰M. Grifoni, E. Paladino, and U. Weiss, *Eur. Phys. J. B* **10**, 719 (1999).

¹¹A.N. Korotkov and D.V. Averin, *Phys. Rev. B* **64**, 165310 (2001).

¹²D.V. Averin, *Exploring the Quantum/Classical Frontier*, edited by J.R. Friedman and S. Han (Nova, Commack, NY, 2002).

¹³W.H. Zurek, *Phys. Rev. D* **24**, 1516 (1981); *Prog. Theor. Phys.* **89**, 281 (1993).

¹⁴P.W. Shor, *Phys. Rev. A* **52**, R2493 (1995).

¹⁵A.J. Leggett and A. Garg, *Phys. Rev. Lett.* **54**, 857 (1985).

¹⁶See, e.g., U. Weiss, *Quantum Dissipative Systems*, 2nd ed. (World Scientific, Singapore, 1999).

¹⁷G.T. Zimanyi and K. Vladar, *Phys. Rev. A* **34**, 3496 (1986).

¹⁸T.P. Orlando *et al.*, *Phys. Rev. B* **60**, 15 398 (1999).

¹⁹A. Garg, J.N. Onuchic, and V. Ambegaokar, *J. Chem. Phys.* **83**, 4491 (1985).

²⁰This nonseparable state is not fully entangled, the degree of entanglement is $1 - e^{-\eta}$.

²¹A. Peres, *Quantum Theory: Concepts and Methods* (Kluwer, Dordrecht, 1993).

²²S. Chakravarty, *Phys. Rev. Lett.* **49**, 681 (1982).

²³F.K. Wilhelm, S. Kleff, and J. von Delft (unpublished).

²⁴A. Schmid, *Phys. Rev. Lett.* **51**, 1506 (1983); see also G. Schön and A.D. Zaikin, *Phys. Rep.* **198**, 237 (1990).

²⁵J.S. Penttilä *et al.*, *Phys. Rev. Lett.* **82**, 1004 (1999).

²⁶For an introduction to Josephson-junction physics, see, e.g., M. Tinkham, *Introduction to Superconductivity*, 2nd ed. (McGraw-Hill, New York, 1996).

²⁷R.F. Voss and R.A. Webb, *Phys. Rev. Lett.* **47**, 265 (1981).

²⁸A summary of this field is found in J.M. Martinis, M.H. Devoret, and J. Clarke, *Phys. Rev. B* **35**, 4682 (1987).

²⁹M.H. Devoret and R.J. Schoellkopf, *Nature (London)* **406**, 1039 (2000).

³⁰D. Vion *et al.*, *Phys. Rev. Lett.* **77**, 3435 (1996).

³¹D. Vion *et al.*, *Science* **296**, 886 (2002).



Engineering the quantum measurement process for the persistent current qubit

T.P. Orlando^{a,*}, Lin Tian^a, D.S. Crankshaw^a, S. Lloyd^a, C.H. van der Wal^b, J.E. Mooij^b, F. Wilhelm^c

^a *Massachusetts Institute of Technology, 77 Mass. Ave., Cambridge, MA 02139, USA*

^b *Delft University of Technology, P.O. Box 5046, 2628 CJ Delft, The Netherlands*

^c *Ludwig-Maximilians-Universitaet, Theresienstr. 37, 80333 Munich, Germany*

Abstract

The SQUID used to measure the flux state of a superconducting flux-based qubit interacts with the qubit and transmits its environmental noise to the qubit, thus causing the relaxation and dephasing of the qubit state. The SQUID–qubit system is analyzed and the effect of the transmittal of environmental noise is calculated. The method presented can also be applied to other quantum systems. © 2001 Elsevier Science B.V. All rights reserved.

PACS: 03.67.Lx; 74.90.+n; 85.25.Dq; 85.25.Cp J

Keywords: Quantum bit; Quantum computing; Superconductive devices

1. Introduction—the qubit

Present schemes for the measurement of a single flux-based superconducting qubit usually employ a SQUID as the measurement meter [1–6]. The meter, however, is permanently coupled to the single qubit and becomes entangled with it. This coupling also allows a channel for the environment to interact indirectly with the qubit to cause decoherence. Therefore, a detailed analysis of the particular measurement scheme is necessary for engineering the decoherence to an acceptable level. In this paper we will analyze a persistent current qubit surrounded by a DC SQUID as the meter.

The method outlined here is applicable to other flux-based qubits and other schemes of measurements.

The persistent current qubit is a macroscopic quantum system which consists of a superconducting ring interrupted by three Josephson junctions [2].

When the external flux bias $\Phi_{\text{ext}} = f_{\text{ext}} \Phi_0$ is near $f_{\text{ext}} = 1/2$, the periodic potential of the qubit has two wells. These two lowest energy states correspond to a persistent current I_{pc} circulating in opposite directions, and these are the $|0\rangle$ and $|1\rangle$ states of the qubit. The qubit is represented symbolically in Fig. 1 as a ring with an up-arrow denoting the magnetic moment of the $|0\rangle$ state. L_{pc} is the self-inductance of the qubit loop, L_{SQ} is the geometric inductance of the DC SQUID, M is the mutual inductance. I_s is the circulating current in

* Corresponding author.

E-mail address: orlando@mit.edu (T.P. Orlando).

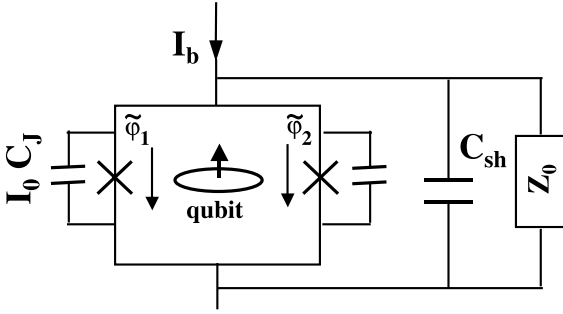


Fig. 1. The measuring circuit of the DC SQUID which surrounds the qubit. C_J and I_0 are the capacitance and critical current of each of the junctions, and $\tilde{\varphi}_i$ are the gauge-invariant phases of the junctions. The qubit is represented symbolically by a loop with an arrow indicating the magnetic moment of the $|0\rangle$ state. The SQUID is shunted by a capacitor C_{sh} and the environmental impedance $Z_0(\omega)$.

the DC SQUID and I_b is the bias current. For both loops, $L_i I_i \ll \Phi_0$.

A model Hamiltonian for these two states of the qubit is $H_q = (\epsilon_0)\sigma_z + (t_0/2)\sigma_x$. Here, $U_{\pm} = \pm \Phi_0 I_{pc}(f_{ext} - 1/2)$ is the potential energy of the upper (lower) state caused by the magnetic field for small self-inductance so that $\epsilon_0 = U_+ - U_- = 2\Phi_0 I_{pc}(f_{ext} - 1/2)$; and t_0 is the coupling energy due to tunneling. The corresponding energy difference ν between the two states is $\nu = (\epsilon_0^2 + t_0^2)^{1/2}$. Using an external oscillator, the energy level difference has been mapped out for the persistent current qubit [4] and also for the RF-SQUID qubit [5].

2. The meter

The state of the qubit adds or subtracts flux in the loop of the DC SQUID. Because the critical current I_c of the DC SQUID is modulated by the total flux in its loop, the state of the qubit can be inferred from the change ΔI_c .

To be more quantitative, we consider the Hamiltonian of the coupled systems. The DC SQUID has two Josephson junctions which have gauge-invariant phases $\tilde{\varphi}_1$ and $\tilde{\varphi}_2$ respectively. For convenience of discussion, we assume the two junctions are identical. When the self-inductance L_{SQ} and mutual inductance M of the SQUID are

considered, we have the flux quantization relation: $\tilde{\varphi}_1 - \tilde{\varphi}_2 = -2\pi(f_{ext} + L_{SQ}I_s/\Phi_0 + MI_{pc}/\Phi_0)$, where I_s is the circulating current in the DC SQUID. The Lagrangian of the SQUID is $L = T - U$, in terms of $\tilde{\varphi}_1$ and $\tilde{\varphi}_2$,

$$T = \frac{C_J}{2} \left(\frac{\Phi_0}{2\pi} \dot{\tilde{\varphi}}_1 \right)^2 + \frac{C_J}{2} \left(\frac{\Phi_0}{2\pi} \dot{\tilde{\varphi}}_2 \right)^2 + \frac{C_{sh}}{2} \left(\frac{\Phi_0}{4\pi} (\dot{\tilde{\varphi}}_1 + \dot{\tilde{\varphi}}_2) \right)^2, \quad (1)$$

$$U = -E_J^{SQ} \cos \tilde{\varphi}_1 - E_J^{SQ} \cos \tilde{\varphi}_2 + \frac{L_{SQ}}{2} I_s^2 - I_b \frac{\Phi_0}{4\pi} (\tilde{\varphi}_1 + \tilde{\varphi}_2)$$

where C_J is the junction capacitance, and C_{sh} is the shunt capacitance parallel to the SQUID. $E_J^{SQ} = I_0 \Phi_0 / (2\pi)$ is the Josephson energy of the junctions in the SQUID. The first three terms in the Lagrangian depend on the time derivatives of the phase variables and are the charging energies of the capacitances. U is the potential energy of the SQUID, including the Josephson energies of the junctions, the energy due to the self-inductance, and the work done by the bias current I_b .

The Hamiltonian of the qubit-SQUID system can be derived from the Lagrangian by adding the qubit Hamiltonian H_q to the total energy. We choose the independent variables of the SQUID to be: $\tilde{\varphi}_p = (\tilde{\varphi}_1 + \tilde{\varphi}_2)/2$ and $\tilde{\varphi}_m = (\tilde{\varphi}_1 - \tilde{\varphi}_2)/2$. $\tilde{\varphi}_p$ is the external variable that directly correlates with the ramping current I_b , and $\tilde{\varphi}_m$ is the inner variable that corresponds to the circulating current of the SQUID. $\tilde{\varphi}_m$ inductively couples with the qubit flux. The total Hamiltonian of the qubit-SQUID system is:

$$\begin{aligned} H_t &= H_q + H_{SQ} + H_{int}, \\ H_q &= \frac{\epsilon_0}{2} \sigma_z + \frac{t_0}{2} \sigma_x, \\ H_{SQ} &= \frac{P_p^2}{2m_p} + \frac{P_m^2}{2m_m} - 2E_J^{SQ} \cos \tilde{\varphi}_p \cos \tilde{\varphi}_m \\ &\quad + 2E_J^{SQ} \frac{(\tilde{\varphi}_m + \pi f_{ext})^2}{\beta_{SQ}} - I_b \frac{\Phi_0}{2\pi} \tilde{\varphi}_p, \\ H_{int} &= \frac{4\pi f_s E_J^{SQ}}{\beta_{SQ}} (\tilde{\varphi}_m + \pi f_{ext}) \sigma_z \end{aligned} \quad (2)$$

which includes the qubit Hamiltonian H_q , the SQUID Hamiltonian H_{SQ} under external flux f_{ext} ,

and the qubit–SQUID interaction H_{int} . P_p and P_m are the conjugate variables of the corresponding phases. $m_m = 2C_J(\Phi_0/2\pi)^2$ is the mass of the inner variable; $m_p = (C_{\text{sh}} + 2C_J)(\Phi_0/2\pi)^2$ is the mass of the external variable. For convenience we introduce $\beta_{\text{SQ}} = 2\pi L_{\text{SQ}}I_0/\Phi_0$ to represent the self-inductance.

Typical parameters of the experiments are: $E_J^{\text{SQ}} = 40$ GHz with $I_0 = 80$ nA, $C_J = 2$ fF, $C_{\text{sh}} = 5$ pF, $L_q = 10$, $L_{\text{SQ}} = 16$ pH and $M = 8$ pH. The circulating current of the qubit gives a flux of $f \approx 10^{-3}$ flux quanta, which is coupled to the SQUID by mutual inductance.

The mutual inductive coupling also changes the flux through the qubit. However, since the magnetic energy of the qubit states is linear near $f = 1/2$, the potential energies of the upper and lower states are $U_{\pm} = \pm\Phi_0 I_{\text{pc}}(f_{\text{ext}} + MI_s/\Phi_0 \pm L_q I_{\text{pc}}/\Phi_0 - 1/2)$ where L_q is the self-inductance of the qubit. Therefore, the energy difference is $\epsilon = U_+ - U_- = 2\Phi_0 I_{\text{pc}}(f_{\text{ext}} + MI_s/\Phi_0 - 1/2)$. However, $f_{\text{ext}} \gg MI_s/\Phi_0$ so that to lowest order, ϵ does not change; nevertheless, the mutual inductive coupling will be important when we consider it as the main channel through which environmental noise interacts with the qubit. Also to first order the tunneling does not change, so that H_q remains the same.

The current I_{sw} , at which the SQUID switches from the zero voltage state to the finite voltage state, is smaller than I_c due to thermal activation and quantum tunneling. What is measured experimentally then is a histogram of switching currents for a given applied flux as the bias current I_b is swept linearly in time. The circuitry which shunts the SQUID affects the statistics of I_{sw} [7–9]. An underdamped SQUID has $I_{\text{sw}} < I_c$ and the histograms are wide and require a number of repeated measurements for the needed resolution. A damped SQUID can give a narrow histogram at the expense of decoherence. Hence, a compromise is needed to damp the SQUID sufficiently to gain a fast, sensitive readout while maintaining a long coherence time. In this paper we will focus on underdamped SQUIDS as used in the recent experiments, but the method holds for damped SQUIDS also. The repetition frequency of the measurement of I_{sw} is limited by the bandwidth of

the low pass filters used for the measurements and by the read-out electronics. This limits the repetition frequency to the range of 10 kHz to 1 MHz. A more efficient readout may be realized by measuring the dynamical inductance of the SQUID [11].

3. Decoherence engineering

The relaxation and dephasing times may be found by solving the master equation for the reduced density in the spin–boson model [12,13]. The relaxation and dephasing times in terms of the spectral density of the effective environmental noise $J_{\text{eff}}(\omega)$ are

$$\frac{1}{\tau_r} = \frac{t_0^2}{2\omega_0^2} \left[J_{\text{eff}}(\omega) \coth \frac{\hbar\omega}{2k_B T} \right]_{\omega=\omega_0}, \quad (3)$$

$$\frac{1}{\tau_\phi} = \frac{1}{2\tau_r} + \frac{\epsilon_0^2}{\omega_0^2} \left[J_{\text{eff}}(\omega) \coth \frac{\hbar\omega}{2k_B T} \right]_{\omega \rightarrow 0}$$

where $\omega = \nu/\hbar$ is the frequency corresponding to the average energy difference of the qubit states.

The environmental spectral density function is calculated from the fluctuations in the energy levels of the qubit, $J_{\text{eff}} = \langle \delta\epsilon \delta\epsilon \rangle / \hbar^2$. Intuitively, the change in the energy level $\epsilon = 2\Phi_0 I_{\text{pc}}(f_{\text{ext}} + MI_s/\Phi_0 - 1/2)$ is $\delta\epsilon = 2I_{\text{pc}}M\delta I_s$, where we have assumed that the external bias field is constant and the main source of fluctuations is the Johnson noise acting through the circulating current in the SQUID. The bias current for the SQUID is $I_b = 2I_0 \cos \tilde{\varphi}_m \sin \tilde{\varphi}_p$ and the circulating current is $I_s = 2I_0 \sin \tilde{\varphi}_m \cos \tilde{\varphi}_p$. Let $\tilde{\varphi}_m \approx \pi f_{\text{ext}}$ so that

$$\frac{dI_s}{dt} = -2I_0 \sin(\pi f_{\text{ext}}) \sin \tilde{\varphi}_p \frac{2\pi}{\Phi_0} V \quad (4)$$

where $V = (\Phi_0/2\pi)d\tilde{\varphi}_p/dt$ is the voltage across the SQUID. Taking the Fourier transform of the above and using the definition of I_b , we have

$$\delta I_s(\omega) = i \frac{2\pi}{\omega\Phi_0} I_b \tan(\pi f_{\text{ext}}) \delta V(\omega). \quad (5)$$

The fluctuations in the voltage are given by the Johnson–Nyquist formula

$$\langle \delta V(\omega) \delta V(\omega) \rangle = \hbar\omega \text{Re}\{Z_t(\omega)\} \coth \frac{\hbar\omega}{2k_B T} \quad (6)$$

where $Z_t(\omega)$ is the total impedance seen by the SQUID, which in the case of Fig. 1 is a parallel combination of the environmental impedance and the capacitor C_{sh} . The spectral density function becomes

$$J_{\text{eff}}(\omega) = \frac{1}{\hbar\omega} \left(\frac{2\pi M I_{\text{pc}}}{\Phi_0} \right)^2 I_{\text{b}}^2 \times \tan^2(\pi f_{\text{ext}}) \text{Re}\{Z_t(\omega)\} \coth \frac{\hbar\omega}{2k_{\text{B}}T} \quad (7)$$

where $\tilde{\varphi}_{\text{m}} \approx \pi f_{\text{ext}}$.

A more detailed analysis [13] begins by linearizing the Hamiltonian, which was implicitly assumed in the more intuitive approach. After linearizing the potential energy near the energy minimum, the SQUID variables behave as harmonic oscillators interacting with each other, and the Hamiltonian becomes

$$H_t = H_{\text{q}} + \frac{P_{\text{m}}^2}{2m_{\text{m}}} + \frac{1}{2} m_{\text{m}} \omega_{\text{m}}^2 (\varphi_{\text{m}} + \delta\varphi_0 \sigma_z)^2 + \frac{P_{\text{p}}^2}{2m_{\text{p}}} + \frac{1}{2} m_{\text{p}} \omega_{\text{p}}^2 \varphi_{\text{p}}^2 + J_1 \varphi_{\text{m}} \varphi_{\text{p}}. \quad (8)$$

The phases $\varphi_{\text{m}} = \tilde{\varphi}_{\text{m}} - \tilde{\varphi}_{\text{m}}^0$ and $\varphi_{\text{p}} = \tilde{\varphi}_{\text{p}} - \tilde{\varphi}_{\text{p}}^0$ are the oscillator coordinates relative to the energy minimum ($\tilde{\varphi}_{\text{m}}^0, \tilde{\varphi}_{\text{p}}^0$). The inner oscillator frequency depends on the self-inductance of the SQUID, L_{SQ} , and the capacitance of the junctions C_{J} , as $\omega_{\text{m}} = \sqrt{2/L_{\text{SQ}}C_{\text{J}}}$. In the experiment, the self-inductance of the SQUID is weak with $\beta_L = 2\pi L_{\text{SQ}}I_0/\Phi_0 = 0.004$. Hence $\omega_{\text{m}} \approx 10^3$ GHz is higher than all the other relevant energies of the qubit–SQUID system. As a result, the inner oscillator is slaved to the qubit and follows the qubit’s dynamics even during qubit operation. The external oscillator frequency depends on the ramping current as $\omega_{\text{p}} = \omega_{\text{p}}^0 [1 - (I_{\text{b}}/I_{\text{c}})^2]^{1/4}$ where $\omega_{\text{p}}^0 = \sqrt{2\pi I_{\text{c}}/(C_{\text{sh}}\Phi_0)}$ is the oscillator frequency at zero current and I_{c} is the effective critical current of the SQUID under external frustration. Typical numbers are $\omega_{\text{p}}^0 = 1.3$ GHz and $\omega_{\text{p}} = 1.0$ GHz at $I_{\text{b}} = 0.8I_{\text{c}}$. As I_{b} increases the potential barrier decreases faster than ω_{p} , and the linearization will become invalid when I_{b} is close enough to the critical current. It can be shown that the harmonic oscillator approximation stays valid until $I_{\text{b}} \approx 0.95I_0$. However, in the present experiment with a linear ramp of I_{b} , the

SQUID usually switches to the finite voltage state before this current. In Eq. (8), the inner oscillator coordinate φ_{m} is offset by the qubit by $\pm\delta\varphi_0$ when $\sigma_z = \pm 1$. This offset originates from the inductive interaction between the qubit and the SQUID: $\delta\varphi_0 = \pi M I_{\text{pc}}/\Phi_0$. The J_1 term is the bilinear coupling between φ_{m} and φ_{p} at the potential energy minimum and is determined by the ramping current I_{b} . We have $J_1 = |\tan \tilde{\varphi}_{\text{m}}^0| I_{\text{b}} \Phi_0/2\pi$. When the ramping current is turned off, the J_1 coupling disappears, and φ_{m} and φ_{p} interact via a higher order term $\varphi_{\text{m}}\varphi_{\text{p}}^2$ which brings negligible entanglement with the qubit state.

Hence, we can divide the qubit–SQUID system into two parts: the measured system that includes the qubit and the inner oscillator of the SQUID; and the “meter” that is the external oscillator of the SQUID. The current ramping process is the system–meter entanglement process. When the SQUID switches, the meter variable escapes from the supercurrent branch to the finite voltage branch and a macroscopically distinguishable record is obtained; in the process, the coherence of the system is completely destroyed by quasiparticle excitations at the gap voltage. Note that the switching current in any given measurement is not perfectly correlated with the state of the qubit. In other words the measurement is not strictly speaking a von Neumann measurement, but rather a more general positive operator valued measurement [14].

The effect of the environmental noise is included by adding to the Hamiltonian a bath of oscillators which are coupled to the modes of the system. In this case we only include the coupling to the external φ_{p} modes of the SQUID as the major source of noise. The spectral density of the bath is described by the Johnson–Nyquist spectral density of $Z_t(\omega)$, the shunting impedance [15]. The problem can then be recast in terms of an effective bath that the qubit itself sees; that is, the inner and external SQUID oscillations are absorbed into an effective bath. The spectral density of this effective bath can be found from the generalized susceptibility of the qubit by writing the equations of motion for the linearized Hamiltonian and considering the variables as classical variables [16,17].

By treating the Hamiltonian classically, the resulting equations of motion describe the time

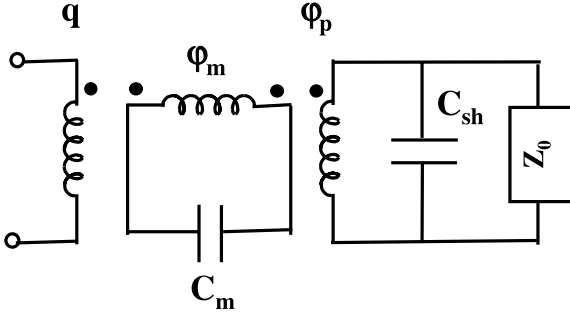


Fig. 2. Equivalent circuit of the linearized qubit-SQUID system. φ_m and φ_p are the two independent variables of a DC SQUID. φ_m corresponds to the circulating current of the SQUID, and φ_p couples with the ramping current of the SQUID. The capacitances of the inner oscillator loop and the external oscillator loop are $C_m = 2C_J$ and C_p , the shunt capacitance outside the SQUID. Flux of the three loops, $q = q_0\sigma_z$, φ_m , and φ_p , are chosen as independent variables in the calculation. Each of the inductances in the three loops interacts by mutual inductances as are indicated by the paired dots near the inductances.

evolution of the average of the quantum variables σ_z , φ_m , and φ_p . For the example in Fig. 1, the resulting linear equations can be represented by the equivalent circuit in Fig. 2 [13]. The reservoir of the SQUID has been modeled as an impedance $Z_0(\omega)$. The effective admittance Y_{eff} of this circuit is the inductance of qubit in parallel with a contribution from the outer circuits through the mutual inductive coupling with the inner oscillator. This contribution depends on the SQUID oscillator parameters and the impedance Z_0 . The current noise from this effective admittance is $J_{\text{eff}}(\omega) = (\hbar\omega/4e^2)\text{Re}[Y_{\text{eff}}]$. When $\omega_m \gg \omega_p, \omega$, we have:

$$J_{\text{eff}}(\omega) \approx \frac{(eI_b M I_{\text{pc}})^2}{C_{\text{sh}}^2 \hbar^3 R_{\text{sh}}} \frac{\omega}{(\omega^2 - \omega_p^2)^2 + (\omega/R_{\text{sh}} C_{\text{sh}})^2} \quad (9)$$

where C_{sh} is the SQUID shunt capacitance and the shunt impedance Z_0 is simplified as a resistor R_{sh} . At $\omega \approx \omega_0$, the noise is filtered by a factor of $(\omega_p/\omega)^4$. When $\omega \sim \omega_p$, a sharp Lorentzian peak appears in the spectrum that has a width of $(R_{\text{sh}} C_{\text{sh}})^{-1}$.

Once $J_{\text{eff}}(\omega)$ is known, the decoherence and relaxation times can be calculated from Eq. (3).

We use the experimental parameters of $C_{\text{sh}} = 5$ pF, $M = 8$ pH, $I_{\text{pc}} = 80$ nA and $I_b = 0.8I_c$, and we assume an environmental impedance of $R_{\text{sh}} = 100 \Omega$. At a temperature of 20 mK the derived decoherence time is then $\tau_\phi = 4 \mu\text{s}$ at $I_b = 0.8I_c$, and the relaxation time is $\tau_r = 0.3$ s. The decoherence time is shorter than the estimated intrinsic noise decoherence of 0.1 ms [18]; while the relaxation time is long enough so that it will not hinder the extraction of accurate information of the qubit states.

4. Summary

The DC SQUID decoheres the qubit during the measurement, when the bias current of the SQUID is ramped up to measure the qubit's state. This means that while the SQUID's bias current is zero, it does not contribute to the decoherence of the qubit, and thus it does not degrade the Q (the number of operations which can be performed prior to qubit decoherence). Assuming that the operations have been completed, the only consideration required is whether the SQUID's bias current can be ramped to the switching point before the qubit can relax to its ground state, $t_{\text{ramp}} < \tau_r$. In the recent qubit experiments [4], however, excitations are applied to the qubit simultaneous to the ramping of the SQUID's current. This results in the application of the SQUID's dephasing at the same time as the logical operation, resulting in the short dephasing time observed. Note that this technique for calculating the decoherence can be applied to other circuits, some of which continuously couple to the qubit.

Similar analyses have been done for a shunting circuit which includes a resistor [10,19] and the coupling of an external driving circuit to this qubit, both by an external oscillator [10,19] and an on-chip oscillator [20].

Acknowledgements

The work at MIT is supported by AFOSR grant F49620-01-1-0457 funded under the Department of Defense University Research Initia-

tive on Nanotechnology (DURINT) program and by the ARDA, the Dutch Foundation for Fundamental Research on Matter (FOM) and the European TMR Research network on superconducting nanocircuits (SUPNAN). Work on type-II quantum computing at MIT is supported by the AFOSR. The authors would like to thank M. Grifoni, Daniel Nakada, Alexander ter Haar, and C.J.P.M. Harmans for helpful discussions.

References

- [1] M.F. Bocko, A.M. Herr, M.F. Feldman, *IEEE Trans. Appl. Supercond.* 7 (1997) 3638.
- [2] J.E. Mooij, T.P. Orlando, L. Tian, C.H. van der Wal, L. Levitov, S. Lloyd, J.J. Mazo, *Science* 285 (1999) 1036.
- [3] T.P. Orlando, J.E. Mooij, L. Tian, C.H. van der Wal, L.S. Levitov, S. Lloyd, J.J. Mazo, *Phys. Rev. B* 60 (1999) 15398.
- [4] C.H. van der Wal, A.C.J. ter Haar, F.K. Wilhelm, R.N. Schouten, C.J.P.M. Harmans, T.P. Orlando, S. Lloyd, J.E. Mooij, *Science* 290 (2000) 773.
- [5] J.R. Friedman, V. Patel, W. Chen, S.K. Tolpygo, J.E. Lukens, *Nature* 406 (2000) 43.
- [6] P. Carelli, M.G. Castellano, F. Chiarello, C. Cosmelli, R. Leoni, G. Torrioli, *IEEE Trans. Appl. Supercond.* 11 (2001) 210.
- [7] J. Clarke, A.N. Cleland, M.H. Devoret, D. Esteve, J. Martinis, *Science* 239 (1988) 992.
- [8] D. Vion, M. Götze, P. Joyez, P.J.D. Esteve, M.H. Devoret, *Phys. Rev. Lett.* 77 (1997) 3435.
- [9] P. Joyez, D. Vion, M. Götze, M.H. Devoret, D. Esteve, *J. Supercond.* 12 (1999) 757.
- [10] C.H. van der Wal, Quantum superpositions of persistent current qubits, Ph.D. thesis, Technical University of Delft, The Netherlands, 2001.
- [11] C. Harmans, private communications.
- [12] M. Grifoni, E. Paladino, U. Weiss, *Euro. Phys. J. B* 10 (1999) 719.
- [13] L. Tian, S. Lloyd, T.P. Orlando, preprint, 2001.
- [14] A. Peres, *Quantum theory: Concepts and Methods*, Kluwer, The Netherlands, 1993.
- [15] M.H. Devoret, in: S. Reynaud, E. Giacobino, J. Zinn-Justin (Eds.), *Quantum Fluctuations*, Elsevier, Amsterdam, 1997.
- [16] A.J. Leggett, *Phys. Rev. Lett.* 30 (1984) 1208.
- [17] A. Garg, J.N. Onuchic, V. Ambegaokar, *J. Chem. Phys.* 83 (9) (1985) 4491.
- [18] L. Tian, L. Levitov, C.H. van der Wal, J.E. Mooij, T.P. Orlando, S. Lloyd, C.J.P.M. Harmans, J.J. Mazo, in: I.O. Kulik, R. Ellialoglu (Eds.), *Quantum Mesoscopic Phenomena and Mesoscopic Devices in Microelectronics*, Kluwer, The Netherlands, 2000.
- [19] C.H. van der Wal et al., preprint, 2001.
- [20] D.S. Crankshaw, E. Trías, T.P. Orlando, *IEEE Trans. Appl. Supercond.* 11 (2001) 1223.

The spin-boson model with a structured environment: A comparison of approaches[★]

F.K. Wilhelm^{a,*} S. Kleff^a J. von Delft^a

^a*Sektion Physik and CeNS, Ludwig-Maximilians-Universität, Theresienstr. 37, D-80333 München, Germany*

Abstract

In the spin-boson model, the properties of the oscillator bath are fully characterized by the spectral density of oscillators $J(\omega)$. We study the case when this function is of Breit-Wigner shape and has a sharp peak at a frequency Ω with width $\Gamma \ll \Omega$. We use a number of approaches such as the weak-coupling Bloch-Redfield equation, the non-interacting blip approximation (NIBA) and the flow-equation renormalization scheme. We show, that if Ω is much larger than the qubit energy scales, the dynamics corresponds to an Ohmic spin-boson model with a strongly reduced tunnel splitting. We also show that the direction of the scaling of the tunnel splitting changes sign when the bare splitting crosses Ω . We find good agreement between our analytical approximations and numerical results. We illuminate how and why different approaches to the model account for these features and discuss the interpretation of this model in the context of an application to quantum computation and read-out.

Key words: Spin-boson model, quantum computing, quantum measurement, cavity quantum electrodynamics

PACS: 03.65.Yz, 03.67.Lx, 05.40.-a, 85.25.Cp

1 Introduction

The subject of open-system quantum mechanics and the physics of the boundary between classical and quantum physics has been of strong interest since the early days of quantum theory. A paradigmatic standard model for the study of

[★] Dedicated to the 60th birthday of Ulrich Weiss

* Corresponding author

Email address: wilhelm@theorie.physik.uni-muenchen.de (F.K. Wilhelm).

open quantum systems is the spin-boson model [1,2]: A single two-state system coupled to a bath of harmonic oscillators described by the Hamiltonian

$$H = \frac{1}{2}(\epsilon\hat{\sigma}_z + \Delta\hat{\sigma}_z) + \frac{1}{2}\hat{\sigma}_z \sum_i c_i x_i + \frac{1}{2} \sum_i \left(\frac{p_i^2}{m} + m_i \omega_i^2 x_i^2 \right) + H_0. \quad (1)$$

Here, H_0 is a constant counter-term. The energy eigenvalues of the two state system alone are $\pm E/2$ with $E = \sqrt{\epsilon^2 + \Delta^2}$. The oscillator bath can model arbitrary *Gaussian* noise sources. It is fully characterized by a spectral function $J(\omega)$ which depends on the distribution of frequencies and couplings

$$J(\omega) = \sum_i \frac{c_i^2}{2m_i \omega_i^2} \delta(\omega - \omega_i). \quad (2)$$

For a given physical system, e.g. a superconducting quantum bit coupled to a noisy electronic circuit, $J(\omega)$ can be obtained by analyzing either the effective friction [3] or noise [4] originating from the environment. It is useful to also introduce the semiclassical noise power $S(\omega) = J(\omega) \coth(\omega/2T)$.

Next to its long tradition in chemical physics, the physics of open quantum systems and in particular the spin-boson model has gained recent practical importance in the field of quantum computation [5]. There, one is interested in obtaining long phase coherence times for the actual computation and long relaxation times for the readout. In a number of quantum computation realizations, the researcher has the option to engineer at least part of the properties of the quantum system and the dissipative environment under study [6], e.g. in the case of superconducting qubits coupled to their control and readout electronics [4]. In particular, environments with nontrivial internal dynamics, e.g. with resonances, can be realized and appear to be attractive [4,7,8]. Much is known about the physics of the spin-boson model whose spectral density is a power law with an exponential cutoff [1,2]. Such spectral densities only contain the cutoff as internal energy scale, which is typically assumed to be very high, leading to scale-free rates.

Much less is known about structured environments. We are interested in a generic realization of this physics described by a spectral density containing a Breit-Wigner resonance

$$J(\omega) = \alpha \omega \frac{\Omega^4}{(\omega^2 - \Omega^2)^2 + 4\omega^2 \Gamma^2} \quad (3)$$

in the underdamped case $\Gamma \ll \Omega$. In that case, we can expand

$$J(\omega) = \frac{\alpha\Omega^3}{8i\Gamma} \sum_{\sigma,\sigma'=\pm 1} \frac{\sigma\sigma'}{\omega - i\sigma'\tilde{\Omega} - i\sigma\Gamma} \quad \tilde{\Omega} = \Omega - 2\Gamma^2/\Omega. \quad (4)$$

Moreover, we will be able to profit from the analytical continuation of results with a Drude spectral density, noting that eq. 3 can be written as

$$J(\omega) = \frac{\alpha\Omega^3}{4i\Gamma} \sum_{\sigma=\pm 1} \frac{\sigma\omega}{\omega^2 - (\sigma\tilde{\Omega} + i\Gamma)^2}. \quad (5)$$

Note, that the shift of the real part of the resonance frequency from Ω towards $\tilde{\Omega}$ can be neglected in the underdamped case, except close to the resonance. We will henceforth only emphasize this shift in those cases, when it actually affects the results.

This type of spectral density is generically obtained by coupling the spin to a harmonic oscillator with eigenfrequency Ω which in turn is damped with a linear friction coefficient $\Gamma/2$. This friction is modeled quantum-mechanically by a bath of harmonic oscillators. Using a normal mode transformation, one can show that this is equivalent to our spin-boson Hamiltonian with a structured bath [9]. More details are given in section 5. This model is realized in various physical systems such as chemical reactions involving biomolecules [9], atoms in cavities [10] or superconducting qubits coupled to resonators [4,8,11–14]. It is related to the nonlinear dimer model of polaron physics [15]. The case of no dissipation with restriction to a rotating wave approximation is known in quantum optics as the Jaynes-Cummings model [16]. Our notation corresponds to the one adopted in Ref. [7] and is slightly different to the one of Ref. [17].

The spin-boson model cannot be solved exactly in closed form. It has been studied by a number of approaches. Some of them are largely numerical such as quantum Monte Carlo [18], real-time renormalization group [19], quasi-adiabatic path integrals [20] flow equation renormalization [21] and numerical renormalization group [22], others are mainly analytical such as the noninteracting blip approximation (NIBA), a systematic weak damping approximation or exact Born approximation [23,24] or Bloch-Redfield [25–27]. A spectral density of the type eq. 3 poses a challenge to most of these approaches, since the dimensionless coupling, the spectral density in units of the frequency, $J(\omega)/\omega$, can be either very small (off-resonance) or large (on-resonance). In order to explore the physics of this model and to obtain useful analytical information, these approximation schemes have to be applied within their range of validity and compared to numerical methods which are essentially nonperturbative in $J(\omega)/\omega$. Alternatively, one can treat the coupled TSS and oscillator system

as multilevel quantum system and only the friction to the oscillator as a bath [28].

The plan of this paper is to analyze this model using the weak-coupling Bloch-Redfield theory and the nonperturbative NIBA and to compare the results to a full numerical study obtained in the flow equation scheme. We will very briefly introduce these methods and compare the dynamics of the reduced density matrix [characterized through the expectation value $s_z(t) = \langle \hat{\sigma}_z \rangle (t)$ with, for definiteness, localized initial condition $s_z(0) = 1$], effective reduced Hamiltonians, dephasing and coherence rates. Interpretations of the results in terms of a superconducting quantum bit coupled to a resonant measurement circuit will be given.

2 Bloch-Redfield

The Bloch-Redfield-theory has originally been developed in the context of nuclear magnetic resonance (NMR) [25]. It offers a systematic way to obtain a generalized master equation within the weak coupling Born approximation between system and bath with $J(\omega)/\omega$ as small parameter. It contains a subtle Markov approximation such that the resulting master equation is local in time; however, the main bath correlations relevant within the Born approximation are kept and they do lead to time-dependent rates for a driven system [27,29]. Bloch-Redfield has been shown to be numerically equivalent to a full non-Markovian path integral technique for a rather generic choice of parameters [27]. Nevertheless, recent calculations at $T = 0$ seem to indicate [24] that there may under certain circumstances be additional terms in the Born approximation, that are neglected in the Bloch-Redfield approach.

The natural starting point for the Bloch Redfield theory in the undriven case are the energy eigenstates of the spin-part of the Hamiltonian 1. In that “energy basis”, the Bloch-Redfield equation can be written as (see e.g. ref. [2])

$$\dot{\rho}_n m = -i\omega_{nm}\rho_{nm} + \sum_{kl} R_{nmkl}\rho_{kl} \quad (6)$$

where all indices take the values $+$ and $-$ corresponding to the ground and excited state and $\omega_{nm} = (E_n - E_m)/\hbar$. The Redfield tensor has the form

$$R_{nmkl} = \delta_{lm} \sum_r \Gamma_{nrrk}^{(+)} + \delta_{nk} \sum_r \Gamma_{lrrm}^{(-)} - \Gamma_{lmnk}^{(+)} - \Gamma_{lmnk}^{(-)} \quad (7)$$

where we have introduced

$$\Gamma_{lmnk}^{(+)} = (\sigma_z)_{lm}(\sigma_z)_{nk}\Gamma(\omega_{nk}) \quad \text{and} \quad \Gamma_{lmnk}^{(-)} = (\sigma_z)_{lm}(\sigma_z)_{nk}\Gamma^*(-\omega_{lm}) \quad (8)$$

where $(\sigma_z)_{nk}$ are matrix elements of σ_z in the energy basis, the $*$ denotes complex conjugation. The basic building block of the rates in the Redfield tensor is the rate Γ which can be written as

$$\Gamma(\delta\omega) = \frac{1}{2\pi\hbar} \int_0^\infty dt e^{-i\delta\omega t} e^{-0^+t} \int_0^\infty d\omega J(\omega) \left[\cos \omega t \coth\left(\frac{\omega}{2T}\right) - i \sin \omega t \right]. \quad (9)$$

The resulting dynamics displays exponential decay and reads

$$s_z(t) = \frac{\epsilon^2}{E_{\text{eff}}^2} \left(e^{-\Gamma_r t} + \tanh\left(\frac{E_{\text{eff}}}{2T}\right) (1 - e^{-\Gamma_r t}) \right) + \frac{\Delta_{\text{eff}}^2}{E_{\text{eff}}^2} \cos(E_{\text{eff}} t) e^{-\Gamma_\phi t}. \quad (10)$$

The quantities Δ_{eff} and $E_{\text{eff}} = \sqrt{\epsilon^2 + \Delta_{\text{eff}}^2}$ can be associated with a renormalized Hamiltonian

$$H_{\text{eff}} = \frac{1}{2} (\epsilon \hat{\sigma}_z + \Delta_{\text{eff}} \hat{\sigma}_x). \quad (11)$$

The details of the shift of the tunnel splitting $\Delta \mapsto \Delta_{\text{eff}}$ will be discussed below.

The term in eq. 10 containing Γ_r describes incoherent energy relaxation. It leads the system into thermal occupation of the renormalized Hamiltonian described below. The relaxation rate can be deduced from the Bloch-Redfield rates eqs. 9, 7 and 8

$$\begin{aligned} \Gamma_r &= R_{----} + R_{++++} = (\sigma_z)_{-+} (\sigma_z)_{+-} (\Gamma(E) + \Gamma(-E) + c.c.) \\ &= \frac{\Delta^2}{2E^2} S(E). \end{aligned} \quad (12)$$

This result is easily understood in terms of the Born-approximation: In order to relax, the system has to exchange the energy corresponding to the energy splitting E with the environment at once, using a single photon.

The last term in eq. 10 describes quantum coherent oscillations analogous to Larmor precession of a spin [30]. These are the hallmark of (macroscopic) quantum coherence in the spin-boson system. Their decay rate can hence be identified with the dephasing rate and can, using eqs. 7, 8 and 9, be written as

$$\begin{aligned} \Gamma_\phi &= -\text{Re}\Gamma_{-+-+} = \text{Re} [2(\sigma_z)_{--} (\sigma_z)_{++} \Gamma(0) + (\sigma_z)_{-+} (\sigma_z)_{+-} (\Gamma(E) + \Gamma^*(-E))] \\ &= \frac{\Gamma_r}{2} + \alpha T \frac{\epsilon^2}{\Delta^2}. \end{aligned} \quad (13)$$

Note, that on very general grounds [30] we have $2\Gamma_\phi \geq \Gamma_r$. The extra factor of 1/2 originates from the fact that there are in principle *two* dephasing channels corresponding to clockwise and counterclockwise Larmor precession. We are following here the standard NMR-motivated notation [30]; one could equivalently define $2\Gamma_\phi$ as the true physical dephasing rate. The first term in eq. 13 is proportional to the relaxation rate eq. 12, which reflects that a relaxation process certainly also randomizes the phase information. The additional term involves $S(0)$, which in our case is $\propto T$. This contribution originates from “flips” dephasing processes which randomize the phases while keeping energy constant, i.e. transitions from a state into itself.

The form of both rates eqs. 12 and 13 resembles the case of unstructured environments [23], even though the spectral density eq. 4 has singularities close to the real axis. The high relaxation rate at $E \simeq \Omega$ corresponds to resonant interaction between the qubit and the central environmental oscillator. When interpreting this result, one has to be aware, that the Born approximation involved is only valid for $\Gamma_{r,\phi} \ll E$, which, bounding $J(\omega) \leq J(\Omega)$, means $\alpha\Omega^2 < \Gamma^2$. This a very rigorous constraint in the underdamped case, $\Gamma \ll \Omega$, which we are considering. Also physically, we do not expect this result to be consistent up to strong couplings, because the relatively weakly damped big oscillator is a highly coherent quantum system which mostly *reversibly* exchanges energy with the spin. Since the Golden-Rule approximation in Bloch-Redfield only takes the long time limit, this reversible exchange cannot be seen in the Bloch-Redfield result. This can be understood from the order of limits prescribed by Bloch-Redfield and shown in the appendix: The imaginary part of the energy is *first* sent to zero. Non-Markovian approximation schemes [23,24] would at least take a self-consistent value and thus shift the $S(E)$ in eq. 12 into $\text{Re}S(E + i\Gamma_r)$. Such shifts can be important in particular if $E \simeq \Omega$, when both predicted rates are very high. Results are summarized in figure 1. We clearly see the peaked behavior at resonance and notice that the influence of the self-consistent solution is rather small even at rather extreme parameters. On the other hand, the self-consistent solution predicts lower rates as compared to the non-self-consistent one, similar to the predictions of flow-equation studies [17].

As mentioned above, the environment not only causes dephasing and relaxation, it also renormalizes the tunnel splitting Δ (and with it the transition frequency), by dressing the two-state system with environmental degrees of freedom. This is similar to the physics of the Lamb shift or the Franck Condon effect and leads, in the nonperturbative regime, to the dissipative quantum phase transition [1,31,32]. In our case, the transition frequency is renormalized according to $E \rightarrow E - \text{Im}R_{+-+}$. If we look at the imaginary part of the generic rate, eq. A.2, $\Gamma'(E) = \frac{1}{4\pi\hbar} \int d\omega J(\omega) \mathcal{P} \frac{1}{\omega^2 - E^2} [\coth(\beta\omega/2)E - \omega]$ we observe a weight function $\mathcal{P}(\omega^2 - E^2)^{-1}$ which changes sign at $\omega \simeq E$. Thus we can expect an upward renormalization of E if most of the spectral weight

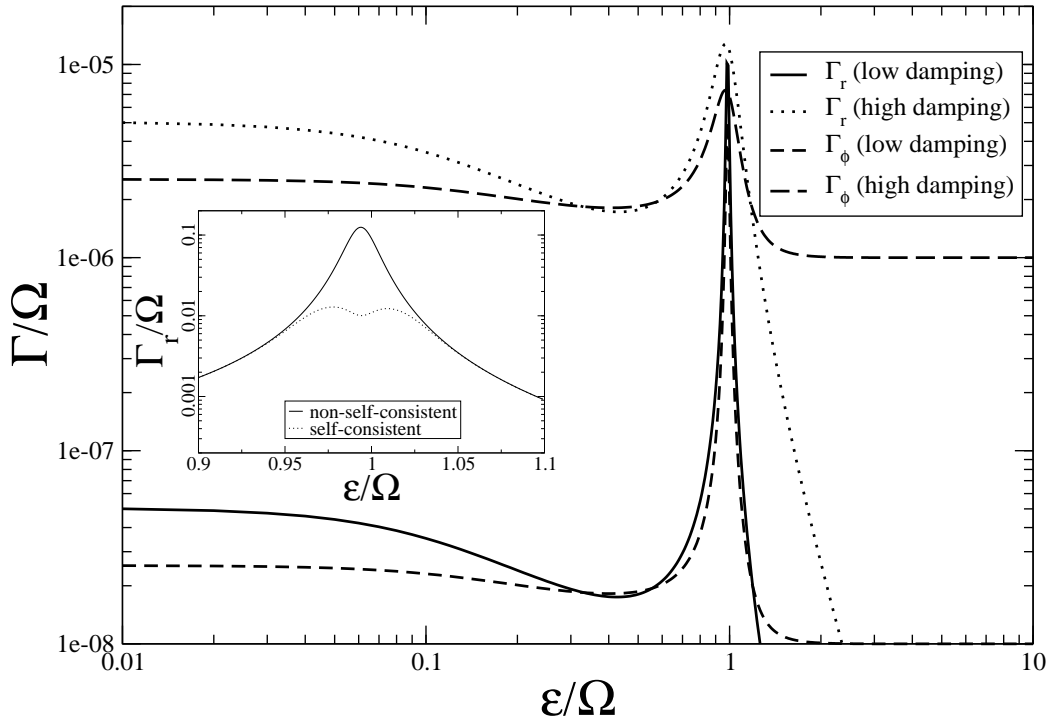


Fig. 1. Relaxation and dephasing rates as a function of energy bias predicted from Bloch-Redfield theory. Parameters are $\Delta = 0.1\Omega$, $T = 0.01\Omega$. For the low-damping plots we have chosen $\alpha = 10^{-6}$, $\Gamma = 10^{-2}\Omega$, for the high-damping plots we have chosen $\alpha = 10^{-4}$, $\Gamma = 10^{-4}\Omega$. The inset compares the self-consistent and non-self-consistent relaxation rate around the resonance for $\Delta = 0.1\Omega$, $T = 0$, $\alpha = 10^{-2}$ and $\Gamma = 10^{-2}\Omega$.

of $J(\omega)$ is above E (corresponding to $E < \Omega$) whereas E scales downward in the opposite case. Physically, this corresponds to level repulsion between the spin and the oscillators in the environment. The result also is consistent with usual second order perturbation theory for the energies. The sign change happens at $E \simeq \Omega$, the point where most of the spectral weight is concentrated, thus we expect a rather sharp structure of the splitting $E_{\text{eff}}(\Omega)$. Note, that this sign change is not predicted for the usual spin-boson in the scaling limit, which can be studied by the well-known adiabatic renormalization approach [1,31]. In that case, E_{eff} is always reduced. This is consistent with our findings, because in the scaling limit, the vast majority of the environmental oscillators have high frequency, much above the qubit splitting.

From the structure of the dephasing rate eq. 13 we can conclude that the last term in eq. A.3, which is even in energy, drops from the final result. Moreover, the remaining contribution to eq. A.3 vanishes as $E \rightarrow 0$. If we finally go to low temperatures, we can replace p in eq. A.3 by an appropriate logarithm and find for the shift of the transition frequency

$$\delta E = \frac{\Delta^2}{E^2} \frac{\alpha}{2\pi} \frac{i\Omega^2 E}{\Gamma} \sum_{\sigma} \frac{\sigma}{E^2 - (\sigma\tilde{\Omega}^2 + i\Gamma)^2} \log\left(\frac{\Gamma - i\sigma\tilde{\Omega}}{iE}\right). \quad (14)$$

In the underdamped limit we are working in, we can approximate the logarithm as $\log|\Omega/E| - i\sigma\pi/2$ and split the result as $E_{\text{eff}} = E + \delta E$, $\delta E = \delta E_{\Omega} + \delta E_{\text{res}}$. It contains a logarithmic contribution which resembles the scaling in the Ohmic case (with cutoff frequency Ω),

$$\delta E_{\Omega} = \frac{2}{\pi} \frac{\Delta^2}{E^2} J(E) \log \left| \frac{E}{\Omega} \right|. \quad (15)$$

This contribution changes sign from an upward shift at $\Omega < E$ to a downward shift at $\Omega > E$ as is expected from the general arguments above. The logarithmic divergence at low E can be indicated as a precursor of a dissipative phase transition. The other contribution takes into account the enormous spectral weight of the resonance,

$$\delta E_{\text{res}} = \frac{\Delta^2}{E^2} J(E) \frac{E^2 - \tilde{\Omega}^2}{\Omega\Gamma}. \quad (16)$$

This contribution is of the order α/Γ . It will be shown below, that terms of this kind persist even in the absence of damping of the external oscillator. It, too, undergoes the expected sign change. It is linear at low E and hence does not contribute to a dissipative phase transition. It instead represents a substantial but finite renormalization. This is due to the fact, that for a dissipative phase transition, the environment has to get entangled with the spin down to arbitrarily small frequencies. These results are summarized in figure 2. As expected, we find in fig. 2, that the energy shift has a sharp structure around the sign change at $E \simeq \Omega$. At this point, the spin becomes strongly entangled with the central oscillator, hence the concept of “qubit energy splitting” is of limited applicability. This observation is consistent with the usual dressed atom approach of cavity quantum electrodynamics.

3 NIBA

So far, we have restricted ourselves to the Born approximation, i.e. to the lowest order in $J(\omega)/\omega$ and have otherwise kept the system general. We now turn to the noninteracting blip approximation (NIBA), which is nonperturbative in that parameter. It can be derived from evaluating the influence functional in a path-integral approach by assuming that the off-diagonal excursions (“blips”) of the density matrix contributing to the path of the two state system are uncorrelated [1,2]. It is thus justified when $E \ll \Omega$, because then the bath is oscillating rapidly on the scale of the two-state system and the time-integrated bath correlation function quickly averages out, leading to weak damping on

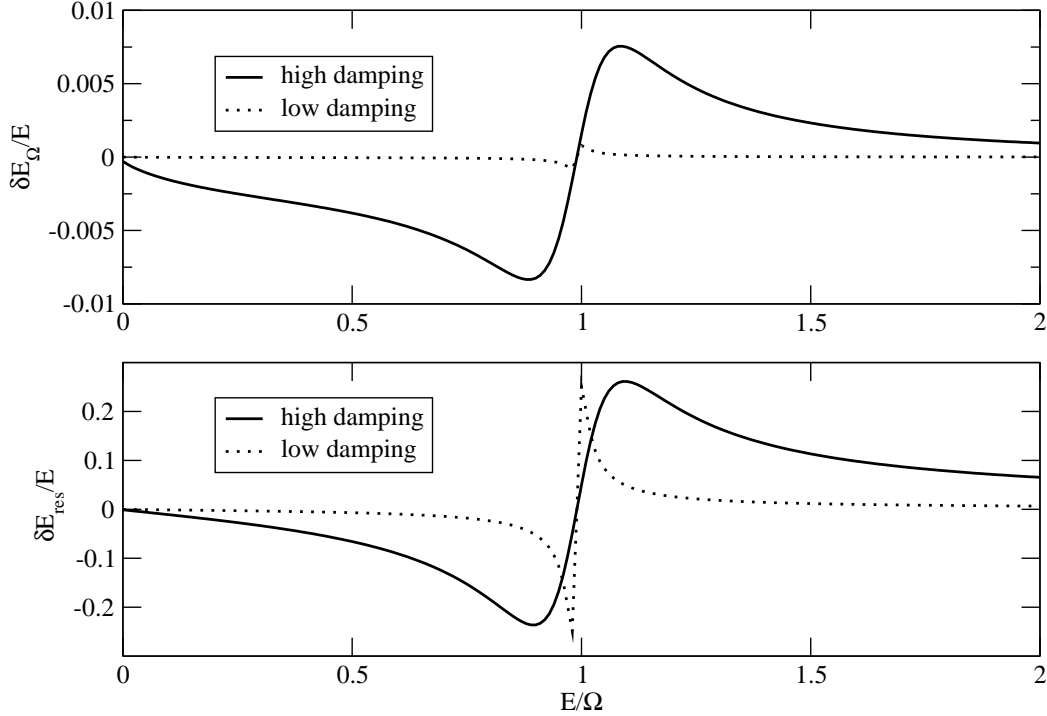


Fig. 2. Renormalization of the energy splitting at $T = 0$ taken at the degeneracy point $\epsilon = 0$, defined as *positive* if the splitting is decreased. Upper panel: Ohmic-like logarithmic contribution from eq. 15; lower panel: Contribution of the environmental resonance from eq. 16 (for discussion see text). Low damping: $\Gamma = 0.01\Omega$, $\alpha = 10^{-4}$, high damping: $\Gamma = 0.1\Omega$, $\alpha = 10^{-2}$.

longer time scales. Alternatively, the NIBA can be obtained by analyzing a the polaron-transformed version of the spin-boson Hamiltonian.

NIBA is known to work well under these conditions at the degeneracy point $\epsilon = 0$. At $\epsilon \neq 0$, the situation is more subtle. At $\epsilon \gg \Delta$ [1,2] the true dynamics is dominated by incoherent relaxation, which is again accurately predicted. This application of NIBA is closely related to the so-called $P(E)$ theory of Coulomb blockade [2,33–35].

In this approach, the dynamics turns out to be governed by the Laplace transformed exponentiated correlation function

$$P(\lambda) = \frac{\Delta^2}{2\pi} \int_0^\infty e^{-\lambda t} e^{K(t)} dt \quad (17)$$

where $K(t)$ is the twice integrated bath correlation function from eq. 9

$$K(t) = \frac{1}{2\pi} \int_0^\infty dt \frac{J(\omega)}{\omega^2} \left((\cos \omega t - 1) \coth \left(\frac{\omega}{2T} \right) + i \sin \omega t \right). \quad (18)$$

At the degeneracy point, the dynamics of the system in Laplace space is readily found from

$$s_z(\lambda) = \int_0^{\infty} e^{-\lambda t} s_z(t) dt = \frac{1}{\lambda + \text{Re}S(\lambda)} \quad (19)$$

where $S(\lambda) = (P(\lambda) + P^*(\lambda^*))/2$. Far from the degeneracy point, we find incoherent relaxation

$$s_z(t) = e^{-\Gamma_r t} \left[1 - \tanh\left(\frac{\epsilon}{2T}\right) \right] + \tanh\left(\frac{\epsilon}{2T}\right) \quad \Gamma_r = 2\text{Re}P(i\epsilon + 0). \quad (20)$$

At $T = 0$, we can use eq. 4 to evaluate $K(t)$ in closed form

$$K(t) = \frac{\alpha\Omega}{8\pi\Gamma i} \sum_{\sigma\sigma'} \frac{\sigma'\Omega - i\Gamma\sigma}{i\sigma'\Gamma + \sigma\Omega} \left[e^{(i\sigma\Omega - \sigma'\Gamma)t} \text{Ei}(-i(\sigma\Omega - \sigma'\Gamma)t) - \gamma - \log(-i(\sigma\Omega - \sigma'\Gamma)t) \right] \quad (21)$$

This is too complicated to allow a direct calculation of $P(\lambda)$ from eq. 17. At low energies, $E \ll \Omega$ we can concentrate on the long time limit of eq. 21 and find, keeping only lowest order terms in Γ/Ω

$$K_{\text{long}}(t) = -\frac{\alpha\Omega}{\Gamma} - 2\alpha [\log |\Omega t| + \gamma + i\pi/2] \quad (22)$$

where γ is the Euler-Mascheroni-constant. This is a combination of a constant term of the order α/Γ and a logarithmic term which resembles the findings in the Ohmic case [2,1]. This is similar to what we observed in our Bloch-Redfield result for the scaling in eqs. 15 and 16. From here, we find $P(\lambda)$ being

$$P(\lambda) = e^{-\alpha\Omega/\Gamma} e^{-2\gamma\alpha} e^{-i\alpha\pi} \frac{\Delta^2}{\lambda} \Gamma(1 - 2\alpha) \left(\frac{\lambda}{\Omega}\right)^{2\alpha}. \quad (23)$$

Off the degeneracy point, we can directly evaluate the relaxation rate from eq. 20 which reads

$$\Gamma_r = \frac{\Delta^2}{|\epsilon|} e^{-\frac{\alpha\Omega}{\Gamma}} \frac{e^{-2\gamma\alpha}}{\Gamma(2\alpha)} \left(\frac{|\epsilon|}{\Omega}\right)^{2\alpha}. \quad (24)$$

This rate resembles to the Ohmic case [33,2] but is reduced by an extra exponential prefactor $\exp(-\alpha\Omega/\Gamma)$, which again represents the contribution of the resonance and can be very small. Thus, we find the important result that

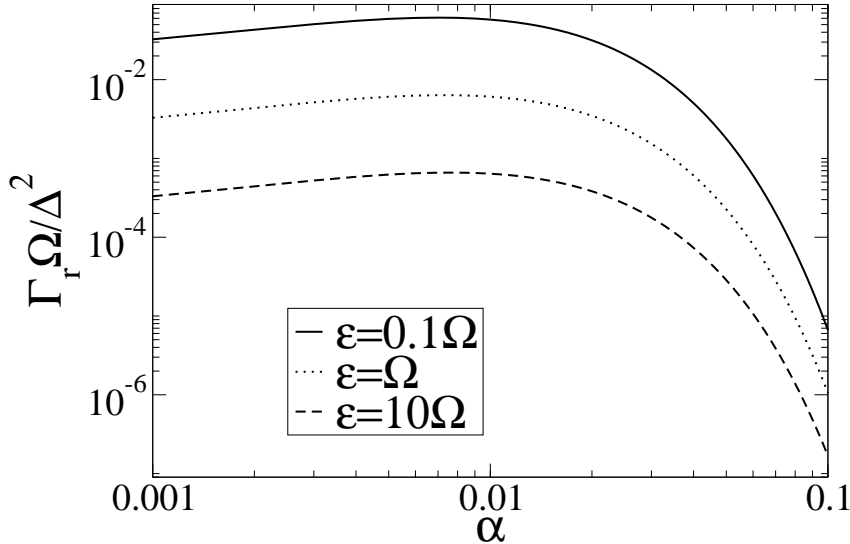


Fig. 3. Relaxation rates calculated from the NIBA eq. 24, in the long time approximation using $\Gamma = 0.01\Omega$. Note, that for small α values the rate first grows with growing α , until the localization due to the resonance takes over and relaxation rates drop dramatically.

by designing small α but appreciable $\alpha\Omega/\Gamma$, the incoherent relaxation rate of the spin can be reduced to extremely small values. A physical interpretation of this finding will be given later on. The predictions of equation 24 are shown in fig. 3. At the degeneracy point, at $\epsilon = 0$, we find the Laplace transform of s_z using eqs. 19 and 23. In analogy to the Ohmic case [2,1] we obtain for the back-transform that

$$s_z(t) = E_{2-2\alpha} \left(-(\Delta_{\text{eff}} t)^{2-2\alpha} \right) \quad (25)$$

where E is the Mittag-Leffler function [2,1,36] and

$$\Delta_{\text{eff}} = \Delta \left(\frac{\Delta}{\Omega} \right)^{\alpha/(1-\alpha)} \left(e^{-\alpha\Omega/\Gamma} e^{-2\gamma\alpha} \cos \pi\alpha\Gamma(1-2\alpha) \right)^{1/(2-2\alpha)} \quad (26)$$

is the renormalized tunnel splitting. Note that this is only valid at $\Delta \ll \Omega$ because we have taken the long time limit for $K(t)$. Consequently, it always predicts a downward renormalization. As in the Ohmic case, the dynamics show a crossover from decaying oscillations at low α to incoherent decay at $\alpha \geq 1/2$ at $\epsilon = 0$. The renormalized tunneling frequency Δ_{eff} shows a combination of the usual Ohmic scaling behavior governed by α , including a dissipative phase transition at $\alpha = 1$, plus a very effective down-scaling of $e^{-\alpha\Omega/2\Gamma(1-\alpha)}$ governed by α/Γ only, which also occurs for an undamped resonance and is not present for the Ohmic case. This again captures the contribution of the resonance and reflects the behavior we have observed in eqs. 16 and fig. 2 to lowest order in α/Γ . The dynamics is illustrated in figure 4. We can observe,

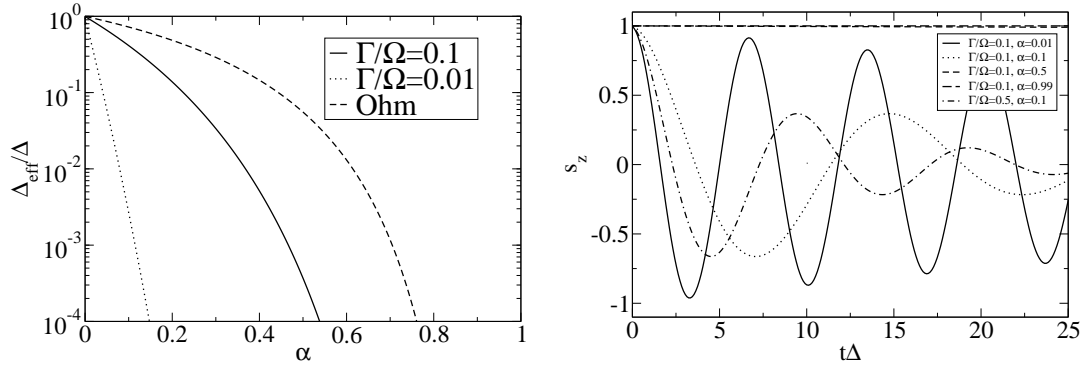


Fig. 4. Dynamical properties within the long time approximation of the NIBA at $\epsilon = 0$. Left panel: Effective tunnel matrix element eq. 26 for $\Omega/\Delta = 10$ for different values of the environment line width as a function of α . Lower Γ means more spectral weight of the resonance and stronger down-scaling of Δ_{eff} . Right panel: Expectation value of σ_z , eq. 25 for different values of the damping parameters and $\Delta/\Omega = 0.1$.

that the time evolution of the spin is almost brought to a standstill, in the sense of absence of *both* oscillations and decay, already at modest coupling constants.

4 Comparison to flow equation results

So far, we have studied our system using traditional methods for open quantum systems. In order to complement this work, we want to compare the above results with previous work [17], in which the same setup was studied with the flow-equation renormalization method [21], which originates from strongly correlated electron systems and very well suited for treating problems with several different energy scales. We will restrict ourselves to $\epsilon = 0$. This method typically can be used to calculate spin-spin correlation functions in equilibrium such as $C(t) = \langle \sigma_z(t)\sigma_z(0) \rangle_{\text{eq}}$. A typical example is shown in fig. 5. The Fourier-transformed correlation function $C(\omega)$ is peaked at several frequencies. The resonance around Δ_{eff} corresponds to coherent oscillations, its width can be identified with the dephasing rate. There can also be a resonance around Ω corresponding to oscillations of the oscillator leaving a trace on the qubit, but it hardly carries spectral weight. We have numerically solved the flow equations for small and moderate coupling strengths. More complete results are published elsewhere [17]. We see, that at $\Delta \ll \Omega$, Δ_{eff} is rescaled downwards similar to the NIBA, but with quantitative differences. The Bloch-Redfield result produces the correct slope at small α , see fig. 6. Around $\Delta = \Omega$, the rescaling changes sign. Remarkably, Bloch-Redfield also predicts the slope above the sign change with good accuracy, see inset of fig. 6, although this set of data is taken very close to resonance. Please note, that in the inset fig. 6 it is important to keep $\tilde{\Omega}$ in eq. 14.

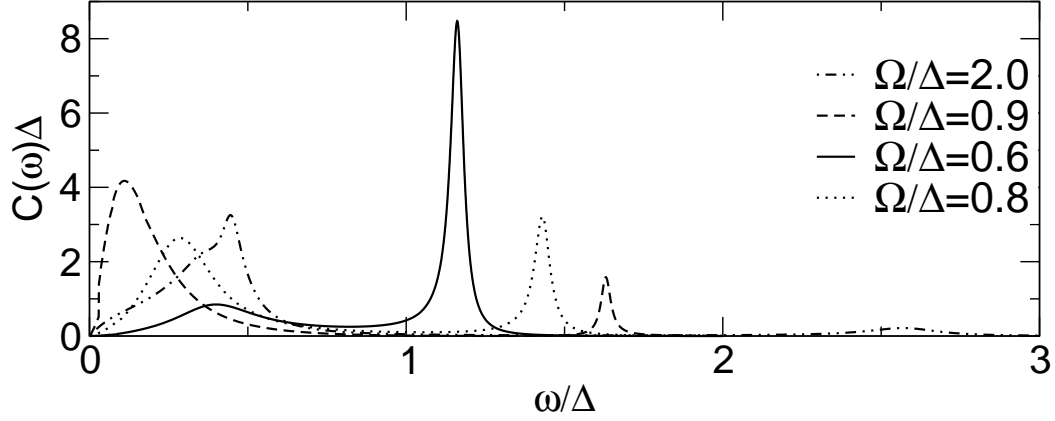


Fig. 5. Correlation function as evaluated from the flow-equation method using $\Omega/\Gamma = 0.06$ and $\alpha = 0.15$.

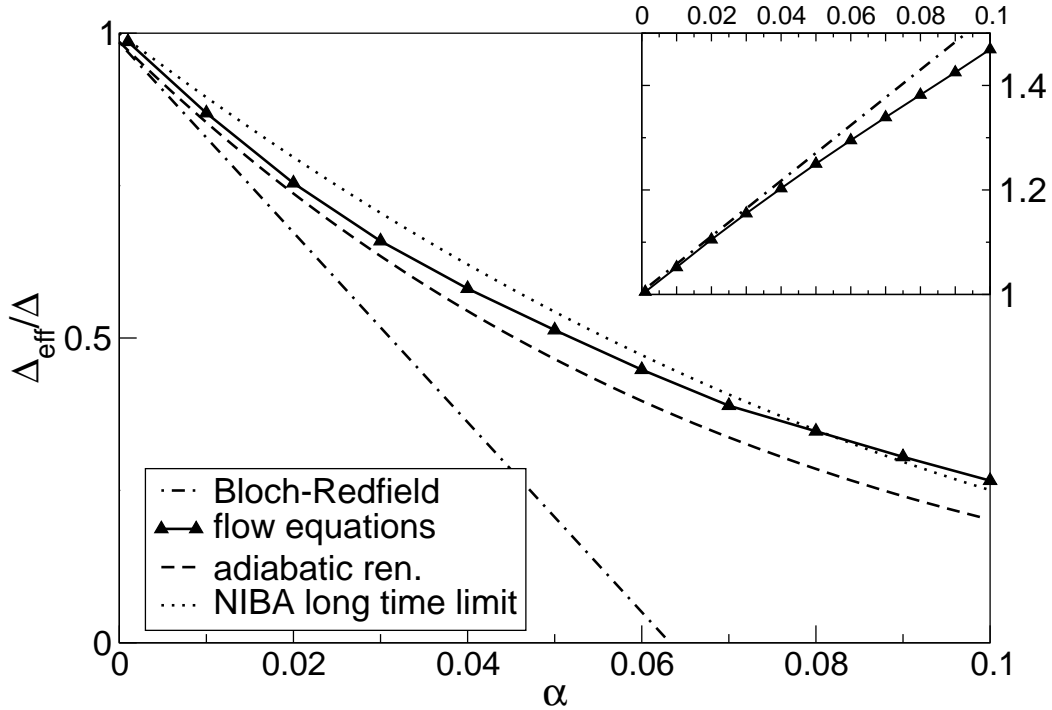


Fig. 6. Rescaling of the tunneling matrix element using different methods. Main plot: $\Gamma/\Omega = 0.02\pi$, $\Delta/\Omega = 0.1$; inset: $\Gamma/\Omega = 0.06\pi$, $\Delta/\Omega = 1.1$.

5 Relation to quantum measurement and entanglement

As already mentioned in the introduction, a straightforward way to implement this model with the spectral density eq. 3 is to couple the TSS to a single harmonic oscillator with resonance frequency Ω , which is in turn damped by additional oscillators. This model has the Hamiltonian

$$\hat{H} = \frac{\epsilon}{2}\hat{\sigma}_z + \frac{\Delta}{2}\hat{\sigma}_x + \frac{\hat{P}^2}{2M} + \frac{M}{2}\Omega^2(\hat{X} - q\hat{\sigma}_z)^2 + \sum_i \left(\frac{\hat{p}_i^2}{2m_i} + \frac{m_i}{2}\omega_i^2(\hat{x}_i - (\tilde{c}_i/m_i\omega_i^2)\hat{X})^2 \right). \quad (27)$$

The oscillator bath is characterized through an ohmic spectral density $\tilde{J}(\omega) = \sum \frac{\pi\tilde{c}_i^2}{2m_i\omega_i}\delta(\omega - \omega_i) = M\Gamma\omega$, where, $\Gamma/2$ is the friction coefficient of the damped big oscillator. It was shown in [9], using a normal-mode decomposition, that this system is equivalent to the spin-boson Hamiltonian eq. 1 with spectral density eq. 3, where $\alpha = 2Mq^2\Gamma/\hbar$.

There are a number of realizations of such models. We would like to concentrate on a specific implementation in superconducting quantum circuits: A flux quantum bit coupled to the plasma resonance of a DC-SQUID. This setup has been thoroughly analyzed in Refs. [3,4]. It has been shown that the spectral density of the flux noise indeed leads to eq. 3 and how the circuit parameters relate to the parameters of that function. Moreover, it has been shown that the coupling parameter q actually can be tuned by the bias current through the SQUID. A representative circuit is shown in fig. 7. It is also shown there and discussed in Ref. [7], that a similar though less favorable realization can be found for charge quantum bits. We are mentioning this model, because it describes a detector of a quantum variable. Thus, we are going to interpret the findings of this paper in terms of quantum measurement theory. Other applications of resonators coupled to superconducting qubits have been discussed in [12–14] As a key result, we have found above within Bloch-Redfield as well as within NIBA, that at $\epsilon, \Delta \ll \Omega$, the system dynamics can be interpreted as an Ohmic spin-boson model with a strongly down-scaled tunneling matrix element. This can be understood in terms of the following model, which was introduced and discussed already in Ref. [7]. We start from the undamped case, $\Gamma = 0$. the low-energy Hilbert space is spanned by $|\pm\rangle_{\text{eff}} = |\pm\rangle|L/R\rangle$ where $|\pm\rangle$ are the basis states of the qubit, $\sigma_z|\pm\rangle = \pm|\pm\rangle$ and $|L/R\rangle$ are coherent states of the harmonic oscillator centered around $X = \pm q$, see Fig. 8. So in a general low-energy state $|\psi\rangle = a|+\rangle_{\text{eff}} + b|-\rangle_{\text{eff}}$, $|a|^2 + |b|^2 = 1$, qubit and oscillator are entangled. In this low-energy basis, the Hamiltonian acquires the form of the renormalized spin part of the spin-boson Hamiltonian eq. (11), with $\Delta_{\text{eff}} = \Delta\langle L|R\rangle = \Delta e^{-\eta}$, where $\eta = M\Omega q^2/\hbar$. This coincides with the result of eq. 26 in the limit of $\alpha \rightarrow 0$ but $\alpha/\Gamma = \text{const}$. Under an appropriate choice of parameters, we can achieve $\eta > 1$ and $\Delta_{\text{eff}} \ll \Delta$. Following the notion of Ref. [37], the degree of entanglement is equal to $1 - e^{-2\eta} = 1 - |\Delta_{\text{eff}}/\Delta|^2$, i.e. we can interpret strong separation of the preferred states of the external oscillator and strong renormalization, i.e. $\Delta_{\text{eff}}/\Delta \ll 1$ with strong entanglement. In terms of quantum measurement theory, the oscillator states are pointers onto the qubit states [38]. Choosing $\eta \gg 1$ corresponds to the condition of almost *orthogonal* pointer states in the environment, which has been identified as the condition

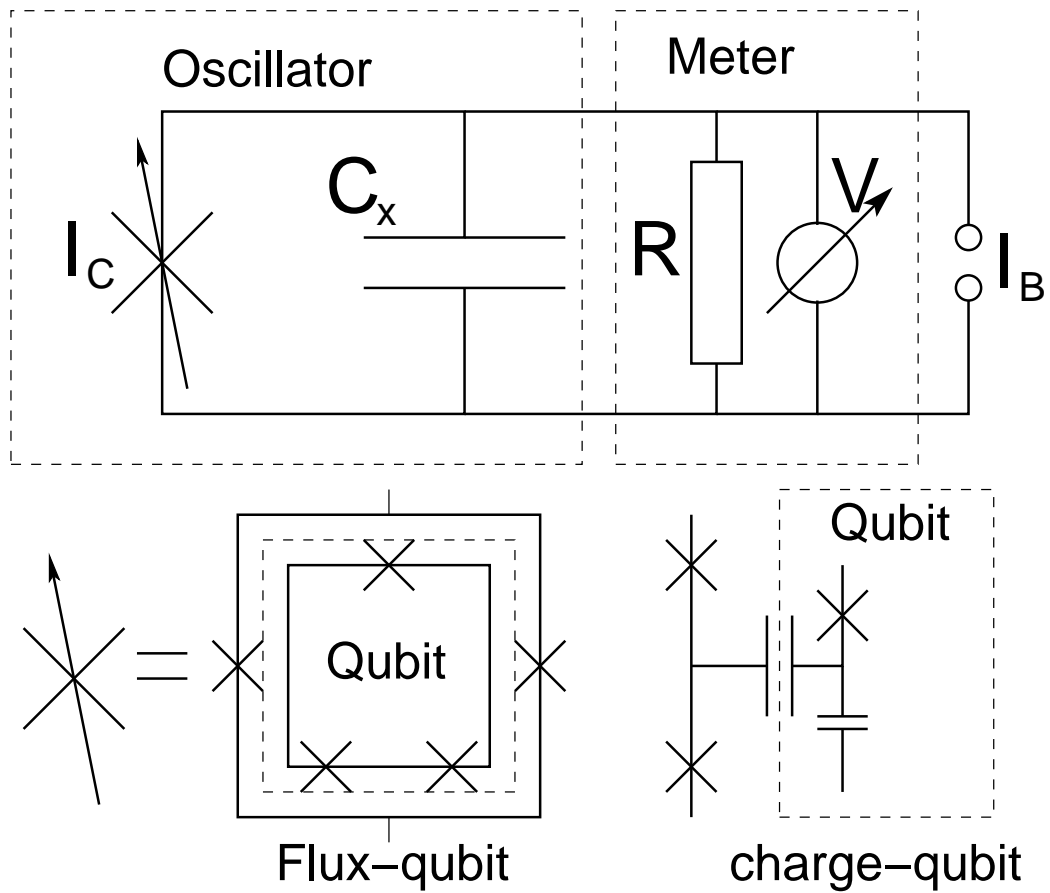


Fig. 7. Underdamped read-out devices for superconducting flux (left) and charge (right) quantum bits involving a tunable Josephson junction representing a SQUID or a superconducting SET.

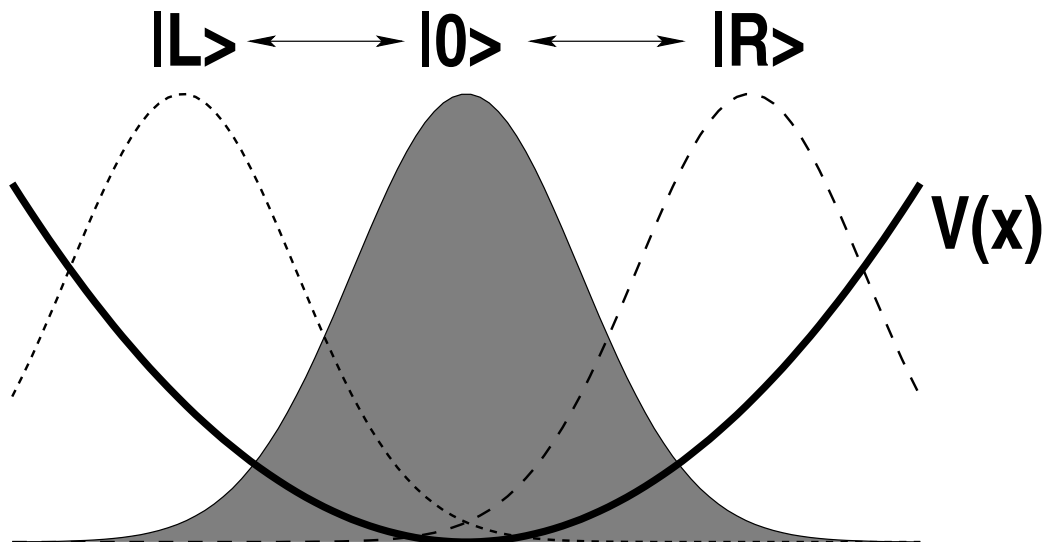


Fig. 8. Visualization of the ground state $|0\rangle$ and the coherent pointer-states $|L\rangle$ and $|R\rangle$ of the oscillator in the potential $V(x)$

for an ideal detector-dominated von-Neumann-measurement [38,39]. Such a measurement corresponds to the standard textbook quantum measurement: The preferred states into which superpositions are decohered are assumed to be Eigenstates of the measured observable regardless of the Hamiltonian of the qubit. In our case, eq. 27 describes coupling of the pointer degree of freedom to $\hat{\sigma}_z$ and hence measurement thereof. Rescaling Δ_{eff} asymptotically to zero means bringing the target states of the decoherence arbitrarily close to Eigenstates of $\hat{\sigma}_z$, thus realizing the aforementioned textbook assumption.

As it stands, the qubit just gets entangled with the pointers, but they are not read out. This can be done by coupling to the dissipative environment. As shown above, its influence corresponds to that of an Ohmic environment of strength α . Taking $\alpha \ll 1$, this leads to dephasing and relaxation rates analogous to the Bloch Redfield results eqs. 12 and 13

$$\Gamma_r = \pi\alpha \frac{\Delta_{\text{eff}}^2}{E_{\text{eff}}} \coth\left(\frac{E_{\text{eff}}}{2T}\right) \quad \Gamma_\phi = \frac{\Gamma_r}{2} + 2\pi\alpha k_B \frac{\epsilon^2}{E_{\text{eff}}} T/\hbar. \quad (28)$$

Note, that the result on Γ_r correspond, for $\epsilon = 0$ to the nonperturbative NIBA result, eq. 24. There may be non-exponential contributions to the dynamics as well [24].

It is important to notice that in the strongly entangled case, $\Delta_{\text{eff}} \ll \Delta$, the relaxation rate, which describes the thermalization of the system independent from the initial state, is strongly reduced, whereas the dephasing rate, which describes the projection of a superposition into a mixture of the eigenstates H_{eff} is hardly affected. This is a very favorable situation for a practical measurement: The information is quickly available, after $\tau_\phi = \Gamma_\phi^{-1}$ and is destroyed only after $\tau_R = \Gamma_R^{-1}$. This is not only convenient for experimental implementation but also guarantees high fidelity: The probability for reading out the correct result after the dephasing time is $P = e^{-\tau_\phi/\tau_R}$ and thus close to unity. For completing the description of the measurement, one has to evaluate the resolution of the detector and the typical measurement times. This depends on details of the physical realization of interest and has been done in Ref. [7] for the superconducting setup. In general, our scheme should permit very high resolution up to single shot, because the signal can be enhanced by strong coupling without reducing τ_r .

6 Summary and outlook

We have studied the spin-boson model with a structured bath using three different approaches: Bloch-Redfield, NIBA, and flow equation renormalization. We have arrived at a number of common features: If the peak in the spectral

density is at frequencies much above the environmental resonance, the system is equivalent to a renormalized Ohmic spin-boson model. This has been interpreted in terms of quantum measurement and the usefulness of this result for modeling quantum detectors has been outlined. We have furthermore shown that the tunneling matrix element of the spin part is renormalized downward if its initial value Δ is below the environmental resonance Ω and renormalized upward if it is above. We have compared this renormalization from all approaches and shown that they are in reasonable agreement within the scope of their applicability. In particular, our analytical results from NIBA and Bloch-Redfield reliably approximate the numerical results from flow equations.

We would like to thank M. Grifoni and S. Kehrein for useful discussions. Work supported in part by the National Security Agency (NSA) and Advanced Research and Development Activity (ARDA) under Army Research Office (ARO) contract Nr. P-43385-PH-QC, and by the Deutsche Forschungsgemeinschaft through SFB 631.

A Calculation of rates including poles of the spectral density

We now want to outline how to calculate the rates eq. 9 We can interchange the order of integration and evaluate the time integral, which can be expanded into a delta function contribution and a Cauchy principal value. We can split $\Gamma(E)$ into real and imaginary part, $\Gamma'(E)$ and $\Gamma''(E)$ and find

$$\Gamma'(E) = \frac{1}{8\hbar} J(E) [\coth(\beta E/2) - 1] \quad (\text{A.1})$$

for the real part, which determines the decoherence and

$$\Gamma''(E) = \frac{1}{4\pi\hbar} \int d\omega J(\omega) \mathcal{P} \frac{1}{\omega^2 - E^2} [\coth(\beta\omega/2)E - \omega] \quad (\text{A.2})$$

for the imaginary part, which controls the frequency shifts. The latter can be calculated by extending the integration contour to the complete real axis, applying the residue theorem and resumming the resulting Matsubara series. We end up with

$$\Gamma = \frac{\alpha}{2\pi} \frac{\Omega^2 E}{2i\Gamma} \sum \frac{\sigma}{E^2 - (\sigma\Omega + i\Gamma)^2} \left[p(\Gamma - i\sigma) - \text{Re}p(iE) - \pi \frac{\Gamma - i\sigma\Omega}{E} \right] \quad (\text{A.3})$$

where $p(x) = \psi(1 + \beta x/2\pi) + \psi(\beta x/2\pi)$ involves the digamma function ψ .

References

- [1] A.J. Leggett *et al.*, Rev. Mod. Phys. **59**, 1 (1987).
- [2] U. Weiss, *Quantum dissipative systems*, 2nd ed., (World Scientific, Singapore, 1999).
- [3] F.K. Wilhelm, M.J. Storcz, C.H. van der Wal, C.J.P.M. Harmans, and J.E. Mooij, to appear in Adv. Sol. St. Phys. Vol. 43; A.J. Leggett, Phys. Rev. B **30**, 1208 (1984).
- [4] C.H. van der Wal, F.K. Wilhelm, C.J.P.M. Harmans, and J.E. Mooij, Eur. Phys. J. B **31**, 111-124 (2003).
- [5] see e.g. M.A. Nielsen and I.L. Chuang, *Quantum Computation and Quantum Information*, (CUP, Cambridge, 2000).
- [6] C.J. Myatt, B.E. King, Q.A. Turchette, C.A. Sackett, D. Kielpinski, W.M. Itano, C. Monroe and D.J. Wineland, Nature **403**, 269 (2000).
- [7] F.K. Wilhelm, Phys. Rev. B **68**, 060503(R) (2003).
- [8] J.M. Martinis, S. Nam, J. Aumentado, K.M. Lang and C. Urbina, Phys. Rev. B **67** 094510 (2003).
- [9] A. Garg, J.N. Onuchic, and V. Ambegaokar, J. Chem. Phys. **83**, 4491 (1985).
- [10] M. Thorwart, L. Hartmann, I. Goychuk and P. Hänggi, J. Mod. Opt., **47**, 2905 (2000).
- [11] A.B. Zorin, Phys. Rev. Lett. **86**, 3388 (2001).
- [12] A. Blais, A. Maassen van der Brink, and A.M. Zagoskin, Phys. Rev. Lett. **90**, 127901 (2003).
- [13] F. Marquardt and C. Bruder, Phys. Rev. B **63**, 054514 (2001).
- [14] F. Plastina and G. Falci, Phys. Rev. B **67**, 224514 (2003).
- [15] A.S. Davydov, Sov. Phys. Usp. **25**, 898 (1982).
- [16] E.T. Jaynes and F.W. Cummings, IEEE Proc. **51**, 90 (1963).
- [17] S. Kleff, S. Kehrein, and J. von Delft, submitted; cond-mat/0304177.
- [18] R. Egger and U. Weiss, Z. Phys. B **89**, 97 (1992).
- [19] M. Keil and H. Schoeller, Phys. Rev. B **63**, 180302(R) (2001).
- [20] M. Thorwart, M. Grifoni, and P. Hänggi, Annals of Physics (New York) **293**, 15 (2001)
- [21] S.K. Kehrein and A. Mielke, Ann. Phys. (Leipzig) **6**, 90 (1997).
- [22] T.A. Costi and C. Kieffer, Phys. Rev. Lett. **76**, 1683 (1996).

- [23] M. Grifoni, E. Paladino, and U. Weiss, *Eur. Phys. J. B* **10**, 719 (1999).
- [24] D. Loss and D.P DiVincenzo, unpublished cond-mat/0304118.
- [25] A.G. Redfield, *Adv. Magn. Reson.* **1**, 1 (1965).
- [26] P.N. Agyres and P.L. Kelley, *Phys. Rev.* **134**, A 98 (1964).
- [27] L. Hartmann, I. Goychuk, M. Grifoni and P. Hänggi, *Phys. Rev. E* **61**, R4687 (2000).
- [28] M. Thorwart *et al.*, this volume.
- [29] M.C. Goorden and F.K. Wilhelm, *Phys. Rev. B* **68**, 012508 (2003).
- [30] C.P. Slichter, “Principles of nuclear magnetic resonancs”, 3rd ed., (Springer, New York, 1992).
- [31] S. Chakravaty, *Phys. Rev. Lett.* **49**, 681 (1982).
- [32] A. Schmid, *Phys. Rev. Lett.* **51**, 1506 (1983).
- [33] G.-L. Ingold and Yu. V. Nazarov in H. Grabert and M. Devoret, eds., “Single charge tunneling” (NATO ASI Series, Plenum, 1992).
- [34] G. Schön in T. Dittrich et al., “Quantum transport and dissipation” (Wiley-VCH, Weinheim, 1998).
- [35] F.K. Wilhelm, G.T. Zimanyi, and G. Schön, *Phys. Rev. Lett.* **87**, 136802 (2001).
- [36] A. Erdelyi *et al.*, *Higher transcendental functions* (McGraw Hill, N.Y., 1955).
- [37] W. Dür, C. Simon, and J.I. Cirac, *Phys. Rev. Lett.* **89**, 210402 (2002).
- [38] W.H. Zurek, *Phys. Rev. D* **24**, 1516 (1981); *Prog. Theor. Phys.* **89**, 281 (1993).
- [39] A. Peres *Quantum Theory: Concepts and Methods*, (Kluwer, Dordrecht, 1993).

3.5 Active suppression of decoherence and errors

So far, we have taken the approach to carefully analyze the decoherence from a dissipative environment acting on a qubit which is controlled as if it was fully coherent. Understanding this allows to engineer the decoherence properties by carefully engineering the selection rules of the coupling and the spectrum of the environment. This is particularly suitable for noise from the electromagnetic environment. In Ref. [199], a radically different approach is pursued: For a *given* coupling to the environment, the system is controlled in such a way that decoherence has less impact. This approach is particularly suited for noise intrinsic to the material, which cannot be arbitrarily engineered. The paper concentrates on the compensation of slow telegraph noise which is typical for disordered materials. The impact of this noise is suppressed by application of the quantum bang-bang protocol, which essentially averages out the noise by applying a rapid train of short spin-flips. We show that this train of control pulses very efficiently refocuses the dynamics and suppresses the deviation from the mean by a factor proportional to the ratio of the separation of bang-bang pulses over the typical flipping time of the telegraph noise. The approach employed for modeling the system is based on analyzing the resulting random walk on the Bloch sphere and averaging over noise realizations. This is different from the generalized master equation approaches used in the other sections. The reason for this is, that those approaches typically rely on the assumption of weak coupling to the environment and on the mapping onto a harmonic oscillator bath model and in many cases also on a Markov approximation. Both requirements are not satisfied in the case of telegraph noise: The spectral density grows to large values at low frequencies (in fact, few telegraph sources lead to $1/f$ -noise) and the statistics of the noise is Poissonian with a relatively long characteristic time scale which also displays the memory.

Compensation of decoherence from telegraph noise by means of bang-bang control

Henryk Gutmann and Frank K. Wilhelm

Sektion Physik and CeNS, Ludwig-Maximilians-Universität, 80333 München, Germany

William M. Kaminsky

Department of Physics, Massachusetts Institute of Technology, Cambridge, Massachusetts 02139

Seth Lloyd

Department of Mechanical Engineering, Massachusetts Institute of Technology, Cambridge, Massachusetts 02139

With the growing efforts in isolating solid-state qubits from external decoherence sources, the origins of noise inherent to the material start to play a relevant role. One representative example are charged impurities in the device material or substrate, which typically produce telegraph noise and can hence be modelled as bistable fluctuators. In order to demonstrate the possibility of the active suppression of the disturbance from a *single* fluctuator, we theoretically implement an elementary bang-bang control protocol. We numerically simulate the random walk of the qubit state on the Bloch sphere with and without bang-bang compensation by means of the stochastic Schrödinger equation and compare it with an analytical saddle point solution of the corresponding Langevin equation in the long-time limit. We find that the deviation with respect to the noiseless case is significantly reduced when bang-bang pulses are applied, being scaled down approximately by the ratio of the bang-bang period and the typical flipping time of the bistable fluctuation. Our analysis gives not only the effect of bang-bang control on the variance of these deviations, but also their entire distribution. As a result, we expect that bang-bang control works as a high-pass filter on the spectrum of noise sources. This indicates how the influence of $1/f$ -noise ubiquitous to the solid state world can be reduced.

PACS numbers: 03.65.Yz, 03.67.Lx, 05.40.-a

In order to implement solid-state quantum information processing devices, the decoherence acting on the quantum states has to be carefully understood, controlled and eliminated. So far, research has concentrated on decoupling from external noise sources (like thermal heat baths and electromagnetic noise). With the success of this effort, noise sources intrinsic to the material such as defect states increase in importance and have to be controlled in order to improve coherence even further.

Most external noise sources are composed of extended modes in the thermodynamic limit close to equilibrium such that their fluctuations are purely Gaussian. Thus, their influence can be modelled by an oscillator bath, see e.g., [1]. However, there are physical situations when this assumption fails [2, 3]. In particular, this is true for localized noise sources with bounded spectra as they occur in disordered systems for hopping defect states [4]. Physical examples for this situation are background charges in charge qubits [5, 6, 7] or traps in the oxide layers of Josephson tunnel junctions [8]. Such localized noise sources are more realistically represented by a collection of bistable fluctuators [9] (henceforth abbreviated bfls), as their noise spectrum is considerably non-Gaussian. If many of these noise sources with different flipping times are appropriately superimposed, they lead to $1/f$ noise [4, 10]. With the progress of fabrication technology and miniaturization of qubits, we expect however that there might only be a few fluctuators in a qubit [8].

We analyze the impact of a single fluctuator in the

semiclassical limit, where it acts as a source of telegraph noise. We apply an open loop quantum control technique, namely quantum bang-bang [11, 12, 13], which is designed suitably for slowly fluctuating noise sources. We simulate the noise-influenced qubit dynamics with and without bang-bang correction by integrating the time-dependent Schrödinger equation for each specific realization of the noise. We present the resulting random walks around the unperturbed signal on the Bloch sphere and analyze the quality of this suppression by an comparison of the ensemble averaged deviations of these random walks with and without bang-bang correction.

We describe our system by the effective Hamiltonian

$$H_q^{\text{eff}}(t) = H_q + H_{q,\text{bfl}}^{\text{noise}}(t) \quad (1)$$

$$H_q = \hbar\epsilon_q\hat{\sigma}_z^q + \hbar\Delta_q\hat{\sigma}_x^q \quad H_{q,\text{bfl}}^{\text{noise}}(t) = \hbar\alpha\xi_{\text{bfl}}(t)\hat{\sigma}_z^q \quad (2)$$

where α denotes the coupling strength between the fluctuator and the qubit and $\xi_{\text{bfl}}(t)$ represents a symmetric telegraph process that is flipping between ± 1 , whose switching events are Poisson distributed with a mean separation τ_{bfl} between two flips.

On a microscopic level, such noise is typically generated coupling the qubit to a two-state impurity, which is in turn coupled to a heat bath causing the two-state system to flip randomly and incoherently. Our model corresponds to the semiclassical limit and should be accurate whenever the coupling of the impurity to the bath is much stronger than its coupling to the qubit [2, 5] such that the qubit does not act back on the noise source.

The assumption of a *symmetrical* telegraph process corresponds to a high bath temperature compared to the impurity level spacing. This restriction is not essential for the following investigations, for an asymmetric noise signal would only produce an additional constant drift.

We describe the resulting evolution of the noise influenced qubit by a stochastic Schrödinger equation [14, 15] with the time-dependent Hamiltonian (2). For any initial state of the qubit, we numerically integrate

$$\psi(t) = \mathbb{T} \exp \left(-i/\hbar \int_0^t H_q^{\text{eff}}(t') dt' \right) \psi(0) \quad (3)$$

with \mathbb{T} the time-ordering operator and ψ the state vector of the two-state system. The result is a random walk on the sphere, which is centered around the free precession on the Bloch sphere corresponding to ϵ_q and Δ_q .

We implement the following idealized open quantum control scheme: apply an infinite train of π -pulses on the qubit with negligibly short pulse durations and a constant separation time τ_{bb} between neighboring pulses. In doing so, we intend to average out the $\hat{\sigma}_z$ parts of the effective Hamiltonian (and thereby in particular the noise term) on time scales large compared to τ_{bb} . This is accomplished by iteratively spin-flipping the qubit and thus effectively switching the sign of the noisy part of the Hamiltonian. This mechanism thus works analogously to the well-known spin-echo procedure, specifically the Carr-Purcell procedure of NMR [16]. We expect to compensate a fraction of the telegraph noise effects: the size of the random walk induced by the noise is determined by the typical time separation of the fluctuators influence between two flips τ_{bff} and its coupling strength α and scales roughly with $\alpha\tau_{\text{bff}}$. Using bang-bang, the bffs influence remains uncompensated for at most a single bang-bang period. Thus, we reduce the influence of the bff randomly by an average factor of $\tau_{\text{bff}}/\tau_{\text{bb}}$.

As generic conditions of the system dynamics we consider for the numerical simulations $\epsilon_q = \Delta_q \equiv \Omega_0$. Without loss of generality, we assume $\langle \hat{\sigma}_z^q \rangle = +1$ as an initial state. If there were no noise, the spin would precess on the Bloch sphere around the rotation axis $\hat{\sigma}_x^q + \hat{\sigma}_z^q$. So we expect for not too large an interaction strength ($\alpha \ll 1$) a slight deviation of the individual quantum trajectory from the free evolution case. We take $\alpha = 0.1$ for our coupling strength. All the following time and energy measures are given in units of the unperturbed system Hamiltonian: our time unit is $\tau_{\text{Sys}} = 2/\Omega_0$ and our energy unit is $\Delta E = \sqrt{\epsilon_q^2 + \Delta_q^2} = \sqrt{2}\Omega_0$. Note that in these units, a period lasts $\pi\tau_{\text{Sys}}/\sqrt{2}$. We have integrated Equ. (3) and averaged over $N = 1000$ realizations. The time scale ratio $\tau_{\text{bff}}/\tau_{\text{bb}} = 10$ if not denoted otherwise. We characterize our results by the root-mean-square de-

viation from the unperturbed signal

$$\Delta\bar{\sigma}_{\text{rms}}(t) = \sqrt{\frac{1}{N} \sum_j \left(\bar{\sigma}_j^q(t) - \bar{\sigma}_{\text{noisy},j}^q(t) \right)^2} \quad (4)$$

In order to characterize the degree of noise suppression by means of bang-bang control, we define the suppression factors for a given time t_0

$$\mathcal{S}_{t_0}(\tau_{\text{bff}}/\tau_{\text{bb}}) = \frac{\Delta\bar{\sigma}_{\text{rms}}^{\text{bff}}(t_0)}{\Delta\bar{\sigma}_{\text{rms}}^{\text{bb}}(t_0)}. \quad (5)$$

The deviation as a function of time is plotted in Fig. (1). We recognize that the total deviations on intermediate time scales are suppressed by a ratio of $\simeq 10$. Detailed analysis shows that the tangential and the orthogonal deviation, corresponding respectively to dephasing and relaxation, are of the same size for the uncompensated case. In contrast, the bang-bang modulation mostly compensates the dephasing-type deviation, as shown in the

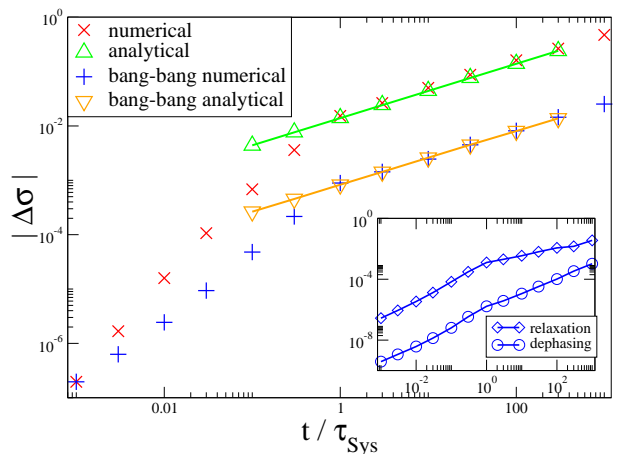


FIG. 1: Time evolution of the mean deviations for bff-induced random walks with and without bang-bang. The straight lines are square-root fits of the analytical derived random walk model variances (plotted as triangles). Inset: Transverse and perpendicular components of bang-bang suppressed noise.

We now develop analytical random walk models for our system. Although the random walk on the Bloch sphere is in general two-dimensional, bang-bang control effectively reduces it to a one-dimensional model, representing the relevant perpendicular part. We restrict ourselves to the long-time limit.

For simplicity, we replace the fluctuating number of random walk steps for a given time Δt of noisy evolution by its expectation value $\Delta t/\tau_{\text{bff}}$ [17]. This allows to use the number of random walk steps as time parameter. We encounter different one-step-distributions, depending on whether the number of steps is odd or even, corresponding to an “up” or “down” state of the bff [21]. The

step-size distribution of the bfl model in our small deviation regime is given from Poisson statistics

$$\Phi_{\text{odd/even}}^{\text{bfl}}(x) = \frac{e^{\mp x/\beta} \theta(\pm x)}{\beta} \quad (6)$$

with $\beta = \alpha \tau_{\text{bfl}}$ as a typical random walk one-step deviation. τ_{unit} is a time unit, corresponding to a discrete step length $x_{\text{unit}} = \alpha \tau_{\text{unit}}$ of the random walk. $\theta(x)$ denotes the Heaviside step function. We neglect the correlations between transverse and perpendicular deviations as they average out in the long-time limit.

For the bang-bang suppressed random walk, the flipping positions of the bfl-noise sign in the bang-bang time-slots are essentially randomly distributed as long as $\tau_{\text{bb}} \ll \tau_{\text{bfl}}$. We find a homogenous step-size distribution between zero deviation and a maximum $\gamma = \frac{\alpha 2 \tau_{\text{bb}}}{\sqrt{2}}$,

$$\Phi_{\text{odd/even}}^{\text{bb}}(x) = \frac{\theta(\pm x) \theta(\pm[\gamma - x])}{\gamma}. \quad (7)$$

The ubiquitous $\frac{1}{\sqrt{2}}$ occurs, because the bang-bang sequence also averages over the static ϵ_q -term and hence slows down the free evolution.

By means of these one-step probability distributions, we are able to calculate via convolution the distributions for $2N$ -step random walks. Specifically, they are the inverse Fourier transforms of the N -fold products of the Fourier transforms of the two-step distribution [17]. For the uncompensated case, we find

$$\Phi_{2N}^{\text{bfl}}(x) = \int_{-\pi}^{\pi} \frac{dk}{2\pi\beta^{2N}} e^{-ikx} \left(\frac{1}{1 - 2 \cos(k) e^{-1/\beta} + e^{-2/\beta}} \right)^N \quad (8)$$

whereas for the compensated case

$$\Phi_{2N}^{\text{bb}}(x) = \int_{-\pi}^{\pi} \frac{dk}{2\pi\gamma^{2N}} e^{-ikx} \left(\frac{[1 - \cos((\gamma + 1)k)]^2}{[1 - \cos(k)]^2} \right)^N \quad (9)$$

Already for random walk step-numbers in the order of ten, the resulting distributions are almost Gaussian. Their standard deviations give the rms deviations of the random walk models plotted in Fig. (1). As expected, they grow as a square-root of the number of steps.

The above integrals can be evaluated analytically using the saddle point approximation. We find variances of

$$\sigma_{\text{bfl}}(N) = \sqrt{2N} \alpha \tau_{\text{bfl}} \quad (10)$$

for the pure bfl random walk and

$$\sigma_{\text{bb}}(N) = \sqrt{\frac{2N}{3}} \alpha \tau_{\text{bb}} \quad (11)$$

for the compensated one. In the large- N limit, this model shows excellent agreement with the simulation.

Beyond predicting the variance, our analysis also allows evaluation of the full distribution. We compared

evolution with and without bang-bang compensation via simulations with 10^4 realizations and calculated the full distribution function for a evolution time $t_0 = \tau_{\text{Sys}}$. The numerical histograms of the deviation with their respective one- and two-dimensional Gaussian fits are shown in Fig.(2). We observe that not only the bang-bang com-

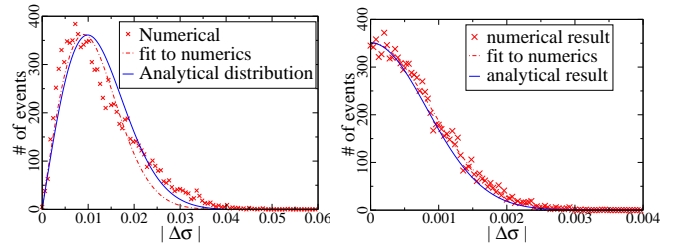


FIG. 2: Histograms of the deviation from free evolution with and without bang-bang and fits to the expected two- (pure bfl case), respectively one-dimensional (bang-bang corrected evolution) random walk statistics. Numerical data collect over 10000 realizations at a fixed time $t_0 = \tau_{\text{Sys}}$. With $\tau_{\text{bfl}} = 0.01 \tau_{\text{Sys}}$ the random walk distributions are calculated for $N = \tau_{\text{Sys}}/\tau_{\text{bfl}} = 100$ steps. (NB: The x -axis scale of the right graph is 15 times smaller than that of the left graph.)

pensated distribution is much narrower than the uncompensated distribution, but also that its shape is qualitatively different: its maximum is at zero error whereas the uncompensated distribution has its maximum at a finite error $|\Delta\sigma| \approx 0.01$ and zero probability of zero error.

We have systematically studied suppression factors for different ratios of the switching time $\tau_{\text{bfl}}/\tau_{\text{bb}}$ at a constant fluctuator flipping rate $\tau_{\text{bfl}} = 10^{-2} \tau_{\text{Sys}}$ and evolution time $t_0 = \tau_{\text{Sys}}$. The numerical data in Fig. (3) show that the suppression efficiency is linear in the bang-bang repetition rate, $S = \mu \tau_{\text{bfl}}/\tau_{\text{bb}}$. The numerically derived value of the coefficient, $\mu_{\text{numerical}} \approx 1.679$, is in excellent agreement with our analytical result $\mu_{\text{analytical}} = \sqrt{3} \approx 1.732$ from the saddle point approximation, Eqs. (10) and (11). This small discrepancy reflects the correlations between the transverse and longitudinal random walk in the uncompensated case, see Fig. (2).

We have demonstrated the ability of a bang-bang protocol to compensate environmental fluctuations with frequency $\omega \ll 1/\tau_{\text{bb}}$. Thus, bang-bang is acting as a “high pass filter” for noise with a roll-off frequency of $1/\tau_{\text{bb}}$. Evidently, the bang-bang correction is suitable for suppressing the impact of telegraph noise on qubits and can enhance the coherence by orders of magnitude. The application of the scheme which we outlined requires a relatively strict separation of time scales: One has to be able to flip the spin very rapidly, typically two orders of magnitude faster than τ_{bfl} . It remains to be investigated how this scheme works with pulse durations that are finite rather than infinitesimal. Moreover, we have assumed that the environment produces symmetric telegraph noise regardless of the qubit dynamics. Clearly,

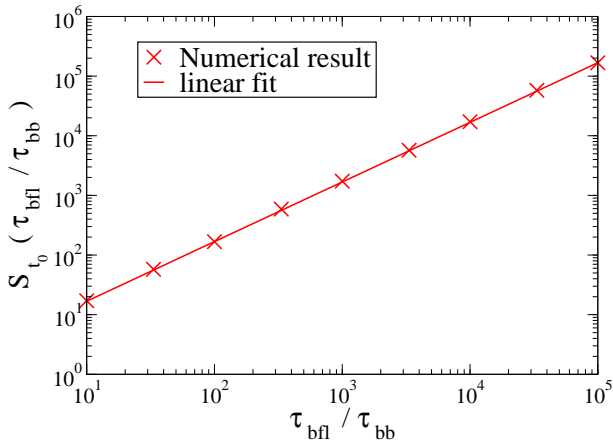


FIG. 3: The suppression factor $S_{t_0}(\tau_{\text{bfl}}/\tau_{\text{bb}}) = \frac{\Delta\sigma_{\text{rms}}^{\text{bfl}}(t_0)}{\Delta\sigma_{\text{rms}}^{\text{bb}}(t_0)}$ evaluated for $t_0 = \tau_{\text{Sys}}$ as a function of the ratio of the flipping time τ_{bfl} and the bang-bang pulse separation τ_{bb} .

the issue of when one may neglect feedback effects between the qubit and bfl must be critically revisited in the low-temperature limit. We speculate that the setup is promising for $1/f$ -noise, as in particular the most harmful and predominantly low-frequency fraction of a corresponding ensemble of fluctuators would be compensated most strongly. Finally, one has to be aware that also the static term of the Hamiltonian is averaged out, and this generally reduces the degree of control on the qubit. This is only a technical constraint, however, as one could imagine interchanging two different types of bang-bang pulses to admit corresponding quantum gate operations.

Another approach for decoupling from slow noise is to choose an appropriate working point with a dominant term $\Omega\sigma_x$ in the static Hamiltonian. The action of this term can be understood as a rapid flipping of the spin, similar to our bang-bang protocol. Using a Gaussian approximation the noise from the bfl with standard rate expressions (e.g., [18]), it can be shown that the dephasing rate reads $\Gamma_\phi = \alpha/\tau_{\text{bfl}}\Omega^2$ instead of $\Gamma_\phi = \alpha\tau_{\text{bfl}}$, which corresponds to the same amount of reduction as in our case. This scheme has been implemented in superconducting qubits [19]. In that case, it turned out that because the σ_x term was limited by fabrication, this consideration led to a major redesign. Our compensation scheme purely relies on external control and thus keeps the hardware design flexible.

A related problem has been addressed in Ref. [20], which deals with bang-bang suppression of *Gaussian* $1/f$ -noise, i.e., a bosonic bath with an appropriate sub-Ohmic spectrum. That system is treated in the weak-coupling approximation, i.e. it assumes $S(\omega)/\omega \ll 1$ at low frequencies where $S(\omega)$ is the noise spectral function. Both assumptions are serious constraints in the $1/f$ -case [4, 5]. Our work is not constrained to weak coupling, takes the full non-Gaussian statistics of telegraph noise into ac-

count, and gives the full resulting distribution of errors.

In summary, we examined the decoherence of a single qubit from a single symmetric telegraph noise source and proposed an adequate open quantum control compensation protocol for suppressing its impact. We simulated the qubits dynamics using a stochastic Schrödinger equation and analyzed its deviation from free evolution. We formulated analytically solvable one- and two-dimensional random walk models, which are in excellent agreement with the simulations in the long time limit. Specifically, we show quantitatively, how the degree of noise compensation is controlled by the ratio between bfl flipping time scale and bang-bang pulse length. We give the full statistics of deviations in both cases.

We thank T.P. Orlando, I. Goychuk, J. von Delft and especially A. Käck for helpful and insights deepening discussions. HG and FKW are also indebted to T.P. Orlando for his great hospitality at MIT. WMK gratefully acknowledges fellowship support from the Fannie and John Hertz Foundation. This work was supported by a DAAD NSF travel grant, by ARO project P-43385-PH-QC and the DFG through SFB 631.

-
- [1] U. Weiss, *Quantum Dissipative Systems* (World Scientific, Singapore, 2001).
 - [2] H. Gassmann, F. Marquardt, and C. Bruder, *Phys. Rev. E* **66**, 041111 (2002).
 - [3] N. Prokof'ev and P. Stamp, *Rep. Prog. Phys.* **63**, 669 (2000).
 - [4] P. Dutta and P. M. Horn, *Rev. Mod. Phys.* **53**, 497 (1981).
 - [5] E. Paladino, L. Faoro, G. Falci, and R. Fazio, *Phys. Rev. Lett.* **88**, 228304 (2002).
 - [6] H. Muller, M. Fularn, T. Heinzl, and K. Ensslin, *Europhys. Lett.* **55**, 253 (2001).
 - [7] A. Zorin *et al.*, *Phys. Rev. B* **53**, 13682 (1996).
 - [8] R. Wakai and D. van Harlingen, *Phys. Rev. Lett.* **58**, 1687 (1987).
 - [9] T. Ytakura and Y. Tokura, *cond-mat*, 0303412 (2003).
 - [10] J. M. Martinis *et al.*, *Phys. Rev. B* **67**, 094510 (2003).
 - [11] S. Lloyd, *Phys. Rev. Lett.* **75**, 346 (1995).
 - [12] S. Lloyd, *Phys. Rev. A* **62**, 022108 (2000).
 - [13] S. Lloyd and L. Viola, *Phys. Rev. A* **65**, 010101 (2001).
 - [14] N. G. van Kampen, *Stochastic processes in physics and chemistry* (Elsevier, Amsterdam, 1997).
 - [15] L. Arnold, *stochastische Differentialgleichungen* (Oldenbourg, München, 1973).
 - [16] H. Carr and E. Purcell, *Phys. Rev.* **94**, 630 (1954).
 - [17] G. H. Weiss, *Aspects and Applications of the Random Walk* (North-Holland, Amsterdam, 1994).
 - [18] C. van der Wal, F. Wilhelm, C. Harmans, and J. Mooij, *Eur. Phys. J. B* **31**, 111 (2003).
 - [19] D. Vion *et al.*, *Science* **296**, 886 (2002).
 - [20] K. Shiokava and D. Lidar, *quant-ph/0211081* (unpublished).
 - [21] We assume the bfl being initially in its “upper” state. This restriction is of no relevance for the long time limit.

3.6 Elements for superconducting quantum computers

So far, a number of designs for superconducting quantum bits have been brought forward. The experiments have so far mostly focused on the single-qubit level and on qubits with a fixed coupling. Although there are workarounds, it is most desirable to have tunable couplings. Most straightforwardly, flux qubits can be mutually coupled by a flux-transformer interrupted by a superconducting switch. In ref. [200] we examine such a coupler interrupted by different types of *dissipative* switches. We give general criteria for the use of dissipative switches in terms of subgap conductance and critical current density. In particular, we show that a voltage-controlled Josephson field effect transistor (JoFET) can, assuming a modest improvement of present-day device parameters be used in superconducting qubit architectures: Due to its operation principle, it is only noisy in the “on” state but noiseless in the “off” state. Other dissipative elements such as π -junctions are less favorable. Compared to the proposal to use a DC-SQUID as a switch, the JoFET has the advantage of a very well-defined off-state. Moreover, since it is voltage-operated, it avoids cross-talk with the qubit flux.

The use of charge control in flux qubit architectures is further investigated in Ref. [201]. It is shown that in a single flux qubits with an electrostatic gate, the Aharonov-Casher effect can be used in order to control the phase of the tunnel matrix element, such that full control over all components of the effective spin representation of the qubit Hamiltonian can be achieved. This can be used, e.g., to demonstrate the Berry phase and implement geometric quantum computation, which in many cases is more fault-tolerant than usual, pulsed quantum computing. As a byproduct, the paper also describes the contribution of background charge noise to the decoherence of flux qubits.

Design of realistic switches for coupling superconducting solid-state qubits

Markus J. Storz^{a)} and Frank K. Wilhelm

Sektion Physik and CeNS, Ludwig-Maximilians-Universität, Theresienstr. 37, 80333 München, Germany

(Received 16 June 2003; accepted 31 July 2003)

Superconducting flux qubits are a promising candidate for solid-state quantum computation. One of the reasons is that implementing a controlled coupling between the qubits appears to be relatively easy, if one uses tunable Josephson junctions. We evaluate possible coupling strengths and show how much extra decoherence is induced by the subgap conductance of a tunable junction. In light of these results, we evaluate several options of using intrinsically shunted junctions and show that based on available technology, Josephson field effect transistors and high- T_c junctions used as π shifters would be a good option, whereas the use of magnetic junctions as π shifters severely limits quantum coherence. © 2003 American Institute of Physics. [DOI: 10.1063/1.1612901]

Quantum computation promises qualitative improvement of computational power as compared to today's classical computers. An important candidate for the implementation of a scalable quantum computer are superconducting qubits.^{1,2} After experimental demonstration of basic features, e.g., in flux qubits,^{3,4} the improvement of the properties of such setups involves engineering of couplings and decoherence, see, e.g., Ref. 5.

To perform universal quantum computation with a system of coupled qubits it is very desirable to be able to switch the couplings (although there are in principle workarounds).⁶ It has already been described that for flux qubits, this can be achieved by using a superconducting flux transformer interrupted by a tunable Josephson junction,² i.e., a superconducting switch, as shown in Fig. 1. The primary and most straightforward proposal for the implementation of this switch is to use an unshunted dc-superconducting quantum interference device (SQUID) based on tunnel junctions utilizing the same technology as for the qubit junctions. Although this holds the promise of inducing very little extra decoherence, it suffers from two practical restrictions: (i) the SQUID loop has to be biased by exactly half a flux quantum in the off state and (ii) the external control parameter is a magnetic flux, which introduces the possibility of flux crosstalk between the qubits and the switch. The combination of (i) and (ii) implies that even small flux crosstalk will severely perturb the off state of the switch.

This can be avoided by using different switches: A voltage-controlled device such as a Josephson field effect transistor (JoFET)⁷ or a super-normal-metal-conductor (SNS)-transistor completely avoids the cross-talk problem. As an intermediate step,⁸ one can improve the SQUID by using a large π junction, in order to fix the off-state at zero field. Such π junctions can be found in high- T_c systems⁹ or in systems with a magnetic barrier.¹⁰ All these junctions are damped by a large subgap conductance because they contain a large number of low-energy quasiparticles.

In this letter, we quantitatively evaluate the coupling

strength between two qubits coupled by a switchable flux transformer. We evaluate the strength of the decoherence induced by the subgap current modeled in terms of the resistively shunted junction (RSJ) model. Based on this result, we assess available technologies for the implementation of the switch.

We start by calculating the strength K of the coupling between the two qubits without a switch and then show how it is modified by the presence of the switch. From Fig. 1 and the law of magnetic induction we find the following equations for the flux through qubit 1 and 2 induced by currents in the qubits and the flux transformer

$$\delta \begin{pmatrix} \Phi_S \\ \Phi_1 \\ \Phi_2 \end{pmatrix} = \begin{pmatrix} M_{TT} & M_{TQ} & M_{TQ} \\ M_{TQ} & M_{QQ} & 0 \\ M_{TQ} & 0 & M_{QQ} \end{pmatrix} \begin{pmatrix} I_S \\ I_1 \\ I_2 \end{pmatrix}, \quad (1)$$

where M_{QQ} is the self-inductance of the qubits (assumed to be identical), M_{TQ} is the mutual inductance between the transformer and the qubits and the mutual inductance between the qubits is assumed to be negligible. The fluxes $\delta\Phi$ in Eq. (1) are the screening fluxes in the transformer and the two qubits, i.e., the deviations from the externally applied values. Henceforth, we abbreviate Eq. (1) as $\delta\Phi = \mathbf{M}\mathbf{I}$. These formulas are general and can be applied for any flux through

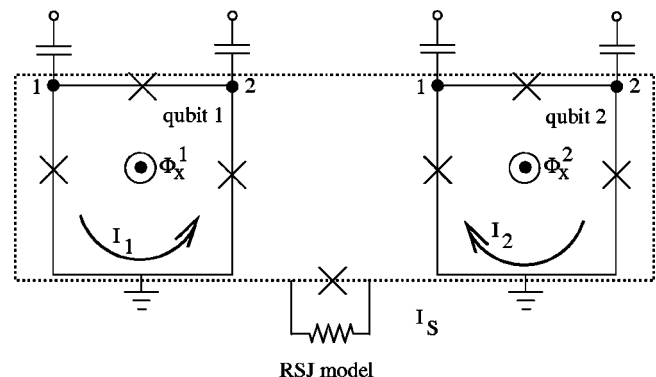


FIG. 1. The flux transformer inductively couples two flux qubits (see Ref. 2). It can be switched, e.g., by a dc-SQUID or by a tunable shunted Josephson junction.

^{a)}Electronic mail: storcz@theorie.physik.uni-muenchen.de

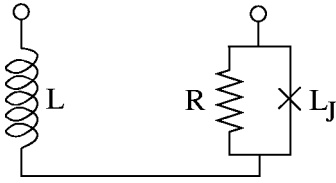


FIG. 2. Equivalent circuit diagram of the flux transformer circuit. The JoFET is modeled by a resistively shunted Josephson junction.

the transformer loop. It is most desirable to couple zero net flux through the device, which can be achieved by using a gradiometer configuration.¹¹ For this gradiometer case, we get $I_S = -(M_{TQ}/M_{TT})(I_1 + I_2)$, which we might insert into Eq. (1) and find for the inductive energy

$$E_{\text{ind}} = \left(M_{QQ} - \frac{M_{TQ}^2}{M_{TT}} \right) (I_1^2 + I_2^2) - 2 \frac{M_{TQ}^2}{M_{TT}} I_1 I_2. \quad (2)$$

The terms resulting from the off-diagonal elements of Eq. (1) can directly be identified as the interqubit coupling strength $K = -2(M_{TQ}^2/M_{TT})I_1 I_2$ which enters the $\hat{\sigma}_z \otimes \hat{\sigma}_z$ Ising-coupling described in Refs. 2 and 12. Note, that the dynamics of the qubit flux is dominated by the Josephson energies,² to which the diagonal term is only a minor correction.

We now introduce the tunable Josephson junction into the loop. Using fluxoid quantization, we rewrite the Josephson relation¹¹ $I_S = I_c \sin[-2\pi(\Phi_S/\Phi_0)]$ and insert it into Eq. (1). The resulting nonlinear equation can be solved in the following cases: (i) If $|I_S/I_c| \ll 1$ (“on” state of the switch) we find $K = -2(M_{TQ}^2/M_{TT}^*)I_1 I_2$ with $M_{TT}^* := M_{TT} + (\Phi_0/2\pi I_c) = M_{TT} + L_{\text{kin}}(0)$. This can be understood as an effective increase of the self-inductance of the loop by the kinetic inductance of the Josephson junction at zero bias. (ii) In the case $|I_S/I_c| \approx 1$, “off” state, the circulating current is close to the critical current of the switch, hence the phase drop is $\pm\pi/2$ and we find an analogous form $K = -2(M_{TQ}^2/M_{TT}')I_1 I_2$ with $M_{TT}' = M_{TT} + (\Phi_0/4|I_c|)$, i.e., at low I_c the coupling can be arbitrarily weak due to the enormous kinetic inductance of the junction close to the critical current.

We now turn to the discussion of the decoherence induced by the subgap conductance of the tunable junction. The decoherence occurs due to the flux noise generated through the current noise from the quasiparticle shunt. Hence, both qubits experience the same level of noise. The decoherence of such a setup has been extensively studied in Ref. 12 as a function of the environment parameters. In this letter, we evaluate these environment parameters for our specific setup.

We model the junction by the RSJ-model for a sound quantitative estimate of the time scales even though the physics of the subgap conductance is usually by far more subtle than that. We evaluate the fluctuations of the current between two points of the flux transformer loop sketched in Fig. 1. L is the geometric inductance of the loop, L_J is the Josephson inductance characterizing the Josephson contact and R is the shunt resistance. The correlation is given by the fluctuation-dissipation theorem $\langle \delta I \delta I \rangle_\omega = \coth(\beta \hbar \omega / 2) \hbar \omega \text{Re} Y(\omega)$, where $Y(\omega)$ is the admittance of the effective circuit depicted in Fig. 2. Following the lines of Ref. 5, this translates into a spectral function of the energy

fluctuations of the qubit of the shape $\langle \delta \epsilon(t) \delta \epsilon(0) \rangle_\omega = J(\omega) \coth(\hbar \omega / 2k_B T)$ with $J(\omega) = \alpha \omega^2 / (\omega^2 + \omega_c^2)$ with the important result that the dimensionless dissipation parameter here reads

$$\alpha = \frac{4I_{\text{circ}}^2 M_{TQ}^2 L_J^2}{\hbar R (L + L_J)^2} \quad (3)$$

and an intrinsic cutoff $\omega_c = R(L + L_J)/LL_J$. Here, $L_J = \Phi_0/2\pi I_c$ is the kinetic inductance of the junction. From Eq. (3) we receive in the limit $L \gg L_J$ the expression $\alpha \propto 1/R I_c^2$ and for $L \approx L_J$, $L \ll L_J$ it follows that $\alpha \propto 1/R$. From the results of Ref. 12, we can conclude that $\alpha \approx 10^{-6}$ poses an upper bound for gate operations to be compatible with quantum error correction. In the following sections we will evaluate α for different types of junctions in the switch, a JoFET, a superconductor-ferromagnet-superconductor (SFS) junction and a high- T_c junction by inserting typical parameters. We use the normal resistance R_N to estimate the shunt resistance in the RSJ model. Here, it is important to note that the parameters I_c and R_N of the junction determine the suitability of the device as a (low-noise) switch, which are given by a combination of material and geometry properties. In the following we exemplify the calculation of the dissipative effects with several experimental parameter sets.

For present day qubit technology¹³ we can assume $L \approx 1$ nH, $I_{\text{circ}} \approx 100$ nA $M_{TQ} \approx 100$ pH. In the following, we estimate α for a number of junction realizations, adjusting the junction area for sufficient critical current.

A JoFET can be understood as a SNS junction where the role of the normal metal is played by a doped semiconductor. By applying a gate voltage, it is possible to tune the electron density of the semiconductor.

The critical current of such a junction containing N_{ch} channels can be found using the formula of Kulik and Omel'yanchuk $I_c = (\pi \Delta) / (R_N e)$.^{11,14} $R_N = h / (2e^2 N_{\text{ch}})$ is the point-contact resistance. In a JoFET, the back gate essentially controls N_{ch} . The typical normal resistance is around $R_N \approx 10 \Omega$. For a JoFET the critical current of the Josephson junction is $I_c \approx 30 \mu\text{A}$ and the Josephson inductance is $L_J \approx 11$ pH.⁷

Inserting the earlier estimates we get $\alpha \approx 7 \times 10^{-6}$. This means that the dissipative effects are weak and a JoFET should be a reasonable switch that poses no new constraints. Besides the obvious technological challenge,⁷ one drawback of JoFETs is that due to wide junctions with dimensions of around $w = 500$ nm they are likely to trap vortices, which can cause $1/f$ noise by hopping between different pinning sites. However, this can be reduced by pinning, e.g., by perforating the junction.

If we go away from the on state with the JoFET, we reduce both I_c and G_N linearly by depleting the density of states. Figure 3 shows that we find that the dissipative effects are strongest during the switching process when $L_J(\rho_e/\rho_e^{\text{on}}) \approx L$, and *not* in the on state of the switch. In the off state of the switch (for $\rho_e(0) \rightarrow 0$) also α goes to zero. If the switch is tuned from the off state to the on state, α reaches a local maximum and then decreases again. This makes the JoFET a very attractive switch: It induces an acceptably low level decoherence in the on state and can be made completely silent in the off state.

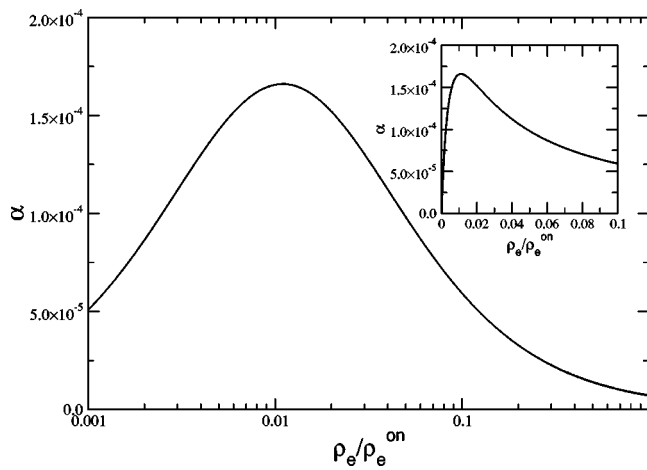


FIG. 3. The dimensionless dissipation parameter α as a function of the electron density in the two-dimensional electron gas for a JoFET. The inset shows a linear plot of the region with the largest α .

A SFS junction in the π state is based on a metallic material, thus the estimate of the shunt resistance in the RSJ model yields a much smaller result than in the case of the JoFET, $R \approx 10^{-5} \Omega$.¹⁰ The critical current of the SFS junction is $I_c \approx 0.2$ mA. Thus, leaving the transformer properties unchanged, we find $L_J \approx 1.7$ pH. Using these estimates the strength of the dissipative effects is of the order of $\alpha \approx 0.16$. This makes such a device unsuitable at the present level of technology, however, it appears that superconductor-insulator-ferromagnet superconductor (SIFS) junctions¹⁵ are

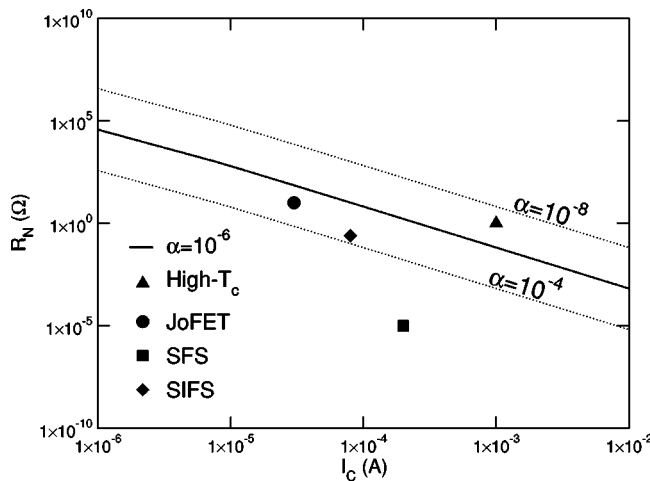


FIG. 4. Log-log plot of the normal state resistance vs the critical current of the junction. Here R_N is taken as an estimate for the shunt resistance of the junction. The solid line denotes $\alpha = 10^{-6}$ and the two dotted lines are for $\alpha = 10^{-4}$ (lower line) and $\alpha = 10^{-8}$ (upper line). Parameters for the SIFS junction are $I_c \approx 8.5 \times 10^{-5}$ A and $R_N \approx 250$ m Ω (see Ref. 15).

by far closer to the desired values, see Fig. 4.

High- T_c junctions can be realized in different ways. Here, we take from Ref. 9 parameters for a typical noble metal (Au)-bridge junction with a film thickness of about $w \approx 100$ nm. The product $I_c R_N \approx 1$ mV and $\rho_N = 8.3 \Omega \text{ nm}$. We assume that in principle I_c for the π state and the 0 state are the same. For a contact area of around 900 nm^2 , $I_c \approx 1$ mA and $R_N \approx 1 \Omega$. Now the strength of the dissipative effects is easily evaluated to be $\alpha \approx 6.5 \times 10^{-8}$, which is much better than SFS π junctions and even better than the JoFET.

We estimated the strength of the dissipative effects that will occur due to the switch for several possible switches. These results are summarized in Fig. 4 for typical parameters of the analyzed systems. We find that the noise properties of a JoFET and π shifters based on high- T_c materials introduce no important noise source. On the other hand, the parameters found from π shifters based on magnetic materials are much less encouraging.

The authors would like to thank T. P. Orlando, P. Baars, and A. Marx for useful discussions. This work was supported in part by the National Security Agency (NSA) and Advanced Research and Development Activity (ARDA) under Army Research Office (ARO) contract No. P-43385-PH-QC.

- ¹Yu. Makhlin, G. Schön, and A. Shnirman, *Rev. Mod. Phys.* **73**, 357 (2001).
- ²T. P. Orlando, J. E. Mooij, C. H. van der Wal, L. Levitov, S. Lloyd, and J. J. Mazo, *Phys. Rev. B* **60**, 15398 (1999); J. E. Mooij, T. P. Orlando, L. Levitov, L. Tian, C. H. van der Wal, and S. Lloyd, *Science* (Washington, DC, U.S.) **285**, 1036 (1999).
- ³C. H. van der Wal, A. C. J. ter Haar, F. K. Wilhelm, R. N. Schouten, C. J. P. M. Harmans, T. P. Orlando, S. Lloyd, and J. E. Mooij, *Science* (Washington, DC, U.S.) **290**, 773 (2000).
- ⁴I. Chiorescu, Y. Nakamura, C. J. P. M. Harmans, and J. E. Mooij, *Science* (Washington, DC, U.S.) **299**, 1869 (2003).
- ⁵C. H. van der Wal, F. K. Wilhelm, C. J. P. M. Harmans, and J. E. Mooij, *Eur. Phys. J. B* **31**, 111 (2003).
- ⁶X. Zhou, Z.-W. Zhou, G.-C. Guo, and M. J. Feldman, *Phys. Rev. Lett.* **89**, 197903 (2002).
- ⁷A. Richter, *Adv. Solid State Phys.* **40**, 321 (2000).
- ⁸G. Blatter, V. B. Geshkenbein, and L. B. Ioffe, *Phys. Rev. B* **63**, 174511 (2001).
- ⁹K. A. Delin and A. W. Kleinsasser, *Supercond. Sci. Technol.* **9**, 227 (1996).
- ¹⁰V. V. Ryazanov, V. A. Oboznov, A. Yu. Rusanov, A. V. Veretennikov, A. A. Golubov, and J. Aarts, *Phys. Rev. Lett.* **86**, 2427 (2001).
- ¹¹M. Tinkham, *Introduction to Superconductivity*, 2nd ed. (McGraw-Hill, New York, 1996).
- ¹²M. J. Storz and F. K. Wilhelm, *Phys. Rev. A* **67**, 042319 (2003).
- ¹³B. Singh and T. P. Orlando (private communication).
- ¹⁴I. O. Kulik and A. N. Omelyanchuk, *Sov. J. Low Temp. Phys.* **3**, 459 (1977).
- ¹⁵T. Kontos, M. Aprili, J. Lesueur, F. Genêt, B. Stephanidis, and R. Boursier, *Phys. Rev. Lett.* **89**, 137007 (2002).

Berry phase in gated persistent current quantum bits

F.K. WILHELM^{1,2} AND J.E. MOOIJ¹

¹ *Quantum Transport Group, Technische Natuurkunde, TU Delft, P.O. Box 5046, 2600 GA Delft, The Netherlands*

² *Sektion Physik and CENS, Ludwig-Maximilians-Universität, 80333 München, Germany*

PACS. 85.25.Dq – Superconducting quantum interference devices (SQUIDS).

PACS. 03.65.Vf – Phases: geometric; dynamic or topological.

PACS. 03.67.Lx – Quantum Computation.

Abstract. – We outline a method to generate a Berry phase in a small superconducting loop interrupted by Josephson tunnel junctions, to which an electrostatic gate is coupled. We quantify the achievable phase and show how it can reach large values, if the junctions are made tunable. We show, that this system can be used for geometric quantum computation. We furthermore propose a direct test of a quantum mechanical prediction on the macroscopic scale, namely of the Bloch-character of a wave function in a periodic potential. Our results can be used to estimate the effect of offset charges onto a regular persistent current qubit.

Small Josephson circuits are a model system for quantum mechanics on a macroscopic scale [1]. In particular, it has been recently demonstrated that small superconducting loops interrupted by one [2] or three [3] Josephson junctions can be brought into a superposition of macroscopically distinct flux states. They show quantum-coherent dynamics in the time domain [4] and are hence a possible candidate for the realization of a quantum computer [5–7].

Quantum computing schemes are usually based on the application of fast pulses, i.e. the switching of a term in a Hamiltonian in a well-defined time. This can be understood as interference of *dynamic* phase factors, which are proportional to the time-integral over the difference of energy levels. The quantum evolution generally can also exhibit *geometric* phase factors [8]. In particular, if the Hamiltonian of a quantum system is adiabatically varied such that there are no transitions between the respective energy eigenstates, a geometric phase called the Berry phase [9] occurs. The adiabatic condition is satisfied as long as the rate of change of energy level splittings $\delta\epsilon_{ij} = \epsilon_i - \epsilon_j$ is much smaller than the level splittings themselves, $\hbar|d\delta\epsilon/dt| \ll |\delta\epsilon|^2$. The Berry phase occurs even if the variation is taken around a closed loop back to the initial Hamiltonian. It hence *does* explicitly depend on the path in parameter space describing the variation, not only on the initial and final points. In this sense, it is non-Abelian. It has been pointed out [10] that this phase can be used for implementing a universal quantum computer. The Berry phase does *not* depend on the timing of the variation, as long as it remains adiabatic. It has so far been observed in microscopic systems such as NMR [10, 11], photons [12] or microscopic spins in semiconductor nanostructures [13]. Recently, a Berry phase experiment in a superconducting circuit in the charging regime,

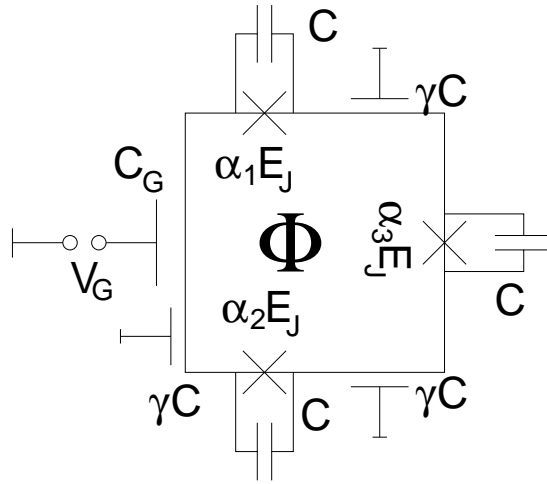


Fig. 1 – Proposed experimental setup. The Josephson junctions may all be of different coupling strength, e.g. realized as SQUIDS. The capacitances of the junctions are assumed to be identical.

has been proposed [14]. We are going to show, how the wave function of a macroscopic magnetic flux in a small superconducting loop can acquire such a geometric phase. Quantum computation in the flux regime has the potential advantage over the charge regime, that the fundamental states are less sensitive to $1/f$ noise from offset charge fluctuations, which are expected to limit both phase coherence and large-scale integrability [5, 7]. Moreover, as the fundamental flux states involve a macroscopic number of Cooper pairs, whereas in the charging regime only a single Cooper pair is controlled, it has been argued that flux-based experiments are suitable for probing quantum mechanics on a truly macroscopic scale.

We first discuss a simple circuit containing three junctions, which allows to demonstrate the phenomenon. Then, we turn a six-junction design, which allows the generation of Berry phases of arbitrary size, profiting from the periodicity of the system's wavefunction.

The device is sketched in Fig. 1. It consists of a small, micrometer-sized superconducting loop interrupted by three Josephson tunnel junctions with capacitances C_i and Josephson couplings with capacitances $\alpha_i E_J$. The α_i are supposed to be close to unity and can be made tunable by replacing them with DC-SQUIDS, i.e. by two junctions in parallel [15]. One of the three islands connecting the junctions is coupled to an electrostatic gate with capacitance C_G , which is held at a voltage V_G and induces a gate charge $Q_G = V_G C_G = 2en_G$ carried by n_G induced Cooper pairs. Inevitably, all three islands do also electrostatically couple to ground by a geometric capacitance C_g . Here and henceforth, we assume the junction capacitances and the ground capacitances among themselves to be identical $C_i = C$, $C_{g,i} = \gamma C$. Without the external gate, this system has already been discussed in Refs. [3, 5, 6]. A similar setup, a Josephson *array* with a gate, has been used to study the Aharonov-Casher effect of quantum vortices in junction arrays [16]. General symmetry properties of a bigger class of related devices including gates have been discussed in Ref. [17].

Using current conservation and fluxoid quantization, we can proceed along the lines of Refs. [5, 6] and describe the dynamics of the device by two independent variables, the phases across junctions 1 and 2. The Hamiltonian corresponds to that of a particle in two dimensional $\{\phi_1, \phi_2\}$ coordinate-space

$$H = 2e^2 \vec{\pi}^T \mathbf{C}_M^{-1} \vec{\pi} + U(\vec{\phi}).$$

The capacitance matrix is

$$\mathbf{C}_M = C \begin{pmatrix} 2 + \gamma & -1 \\ -1 & 2 + \gamma \end{pmatrix},$$

the scalar potential reads

$$U = E_J (-\alpha_1 \cos \phi_1 - \alpha_2 \cos \phi_2 - \alpha_3 \cos(2\pi f + \phi_1 - \phi_2))$$

and a pseudo vector-potential set by the gate charge $\vec{Q}_G = V_G C_G \begin{pmatrix} 1 \\ -1 \end{pmatrix}$ so the kinematic momentum operator is $\vec{\pi} = \vec{p} + \vec{Q}_G/2e$, where $\vec{p} = -i\hbar\nabla_{\vec{r}}$ is the canonical momentum. Note that without the gate, at $n_G = 0$, there is no pseudo vector potential, hence the Hamiltonian is a completely real differential operator and the Berry phase vanishes.

From now on, we will discuss the properties of the system close to frustration, i.e. when the magnetic flux through the system is close to half a superconducting flux quantum $\Phi/\Phi_0 \simeq 1/2$. Then, the potential shows a periodic pattern of minima, which form a hexagonal lattice. This symmetry reflects the *three* junctions of the loop [17]. The minima are separated by potential barriers, whose strength is determined for each of the three unit lattice vectors through the corresponding α_i , see fig. 2 (a-c).

It can be shown [6], that under an appropriate choice of parameters of $E_J C/2e^2 \simeq 80$ and $\alpha_i \simeq 1$, there is exactly one bound state per minimum. These states correspond to either clock-or counterclockwise supercurrents and span the low-energy Hilbert space of the system. The eigenstates of the system can be expressed as Bloch functions, whose quasi-momentum $Q_G/2e$ is set by the gate charge.

From now on, we will tacitly assume that one of the three junctions, labeled i_0 , is weaker, $\alpha_{i_0} \simeq 0.8$, than the other ones with $\alpha_i = 1$. In this case, drawn in Fig. 2, the minima form a periodic pattern of strongly coupled double well potentials, whereas tunneling into other directions, between the wells, is strongly suppressed [5].

Simple Berry phase. In a system, where the α_i are fixed by the lithography, i.e. where the junctions in Fig. 1 are single junctions, a finite Berry phase can be demonstrated. We choose the third junction to be the weak one, $i_0 = 3$, Fig. 2 c). Following the discussion in the preceding paragraph and in Refs. [5,6], the low-energy properties of this system are described by the two-level Hamiltonian

$$H^{\text{TLS}} = \frac{1}{2} \begin{pmatrix} \epsilon(\Phi) & \Delta \\ \Delta^* & -\epsilon(\Phi) \end{pmatrix} \quad \epsilon = I_{\text{circ}} (\Phi - \Phi_0/2) \quad (1)$$

where I_{circ} is the amplitude of the circulating current in the basis states.

The tunneling matrix element $\Delta = |\Delta|e^{i\phi}$ can be calculated within the WKB approximation. In Ref. [6] $|\Delta|$ has already been calculated and shown to be of appreciable size. The phase ϕ is due to the pseudo-vector potential \vec{Q}_G . The minima of the potential are located at $\phi = \pm \text{Arcos}(-1/2\alpha_3)(\text{mod}2\pi)$, so we find as a phase factor $\phi = n_G \text{Arccos}(-1/2\alpha_3) \simeq 0.72\pi n_G$. As \vec{Q}_G plays the role of quasi-momentum, it is only defined within the first Brillouin zone, and hence we are restricted to $0 \leq |n_G| < 1/2$ and a phase $|\phi| < \phi_{\text{max}} = (1/2)\text{Arccos}(-1/2\alpha)$. In principle, higher values of $|n_G| > 1/2$ would lead to even higher phases, however such states are outside the first Brillouin zone and correspond to a higher energy band. This means, that they can only be achieved by non-adiabatic pulses and possess a finite lifetime.

Using the gate and the bias flux Φ we have control over the two-level Hamiltonian eq. 1. and can, within the limits set by ϕ_{max} perform arbitrary cycles on the Bloch sphere. As an example, we can perform the cycle described in Table I. This cycle allows a Berry phase as

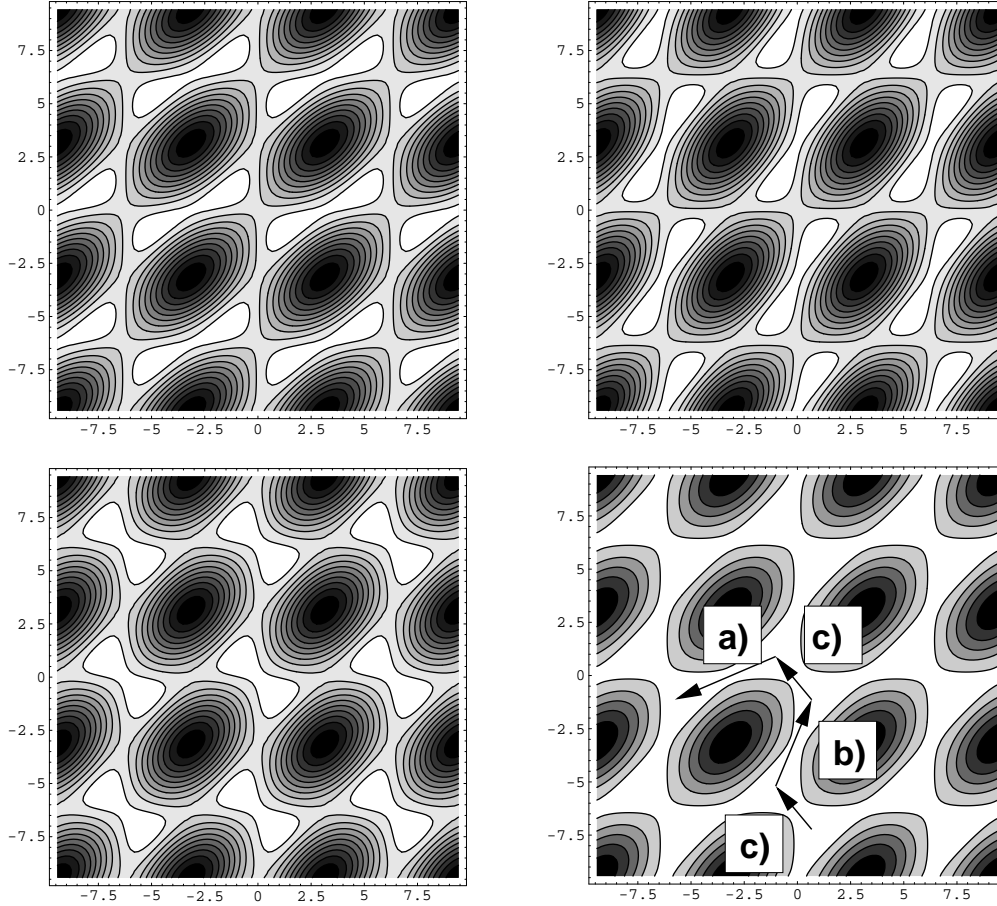


Fig. 2 – Contour plots of the potential U/E_J as a function of the junction phases ϕ_1 and ϕ_2 at half frustration for $\alpha_1 = 0.8, \alpha_2 = \alpha_3 = 1$ (upper left), $\alpha_2 = 0.8, \alpha_1 = \alpha_3 = 1$ (upper right) and $\alpha_3 = 0.8, \alpha_1 = \alpha_2 = 1$ (lower left); dark color indicates high potential; d) shows a schematic plot of the minima taken at $\alpha_1 = \alpha_2 = \alpha_3 = 1$ with an exemplary pattern connecting two equivalent minima. The letters indicate, which of the three potential realizations has to be chosen in order to achieve the desired transport of the ground state.

large as $\phi_{B,\max} = 2\phi_{\max}$. This theoretical limit may not be achievable in practice, because when exploring the limits of n_G the system becomes more sensitive to decoherence due to random fluctuations of the gate charge, which can induce single-charge tunneling events even before the edge of the Brillouin zone is reached. Although insufficient for geometric quantum computing, this setup allows for demonstrating a clearly detectable Berry phase.

Arbitrarily large Berry phase. We now want to turn to a six-junction circuit, where all of the “junctions” in Fig. 1 are made tunable by replacing them by DC-SQUIDS. We will still focus on the situation when not more than *one* junction is weakened ($\alpha_{i_0} = 0.8$) with respect to the others ($\alpha_i = 1$) at the same time fig. 2 a)–c).

The strategy to achieve large Berry phases is to adiabatically shift the wavefunction by a full unit cell, using an appropriate sequence of settings for i_0 . This is done with a fixed setting

of the gate \vec{Q}_G using the pattern indicated in Fig. 2 (d): Similar to above, we start with positive flux $\delta f = f_0$ and $i_0 = 3$, hence we are in the initial state, see Fig. 2 (d). By tuning to $\delta f = -f_0$, we transport the state into the second point and acquire a piece of geometric phase. Now we interchange the role of the weak junction to $i_0 = 2$. The state is still localized in the second point, but now the preferred tunneling direction is to the third point. By tuning $\delta f = f_0$, we transport the ground state to the third point. Repeating the procedure using $i_0 = 1$ for the last step, we complete the pattern. Note, that through the lowering the barriers this experiments only takes about twice as long as the one explained previously.

After these moves, the initial ground-state wavefunction, which is a Bloch function, is readily mapped onto itself with an extra geometrical phase $\phi_B = \theta_0 n_G$ in the end point, where θ_0 has been defined in Table I. It is hence not necessary to move the state back in order to close the loop. An experiment would search for an interference fringe between ground and excited state as explained in [14] and below. Note, that it has been argued that wave functions of Josephson-systems cannot have Bloch-form because the shift of all junction phases by 2π leaves a trace in the environment [18]. If that would be true, nothing can be detected because the path has not been traced back, if an interference fringe from the opposite geometric phases of ground and excited state can be detected, the Bloch-character of the wave function would be verified in a more direct way than e.g. Bloch-oscillation experiments [19].

Possibility of geometrical quantum computation. The experimental detection of the Berry phase in both cases can be performed by embedding the cycles into a spin-echo-type scheme [10, 14]. Starting from the ground state $|\psi\rangle = |\downarrow\rangle$ obtained after relaxation at $\epsilon = \epsilon_0$, the system is brought into superposition $|\psi\rangle = (|\uparrow\rangle + |\downarrow\rangle)/\sqrt{2}$ by a $\pi/2$ -pulse. Then, the appropriate contour is performed, e.g. the one sketched in table I, and both states acquire dynamical and Berry phases of the same amplitude but opposite signs. In order to compensate the additional dynamical phase, the states have to be interchanged by a π -pulse and then the contour has to be traced a second time in the opposite direction. Un-splitting the superposition by another $\pi/2$ -pulse translates the phase into weights of clock- and counterclockwise current states, i.e. we find $\langle\sigma_z\rangle \propto \cos(4\phi_B)$.

Although this detection method still requires the fast pulses and precision in time, it allows for a demonstration experiment of Berry's phase based on available technology [4].

Noise and inaccuracies in the applied field may lead to an additional, unwanted flux δf on top of the applied one. For clarity, we discuss its influence specifically for the first contour, see table I. An additional flux changes the limits of ϵ from $\pm\epsilon_0$ to $\pm\epsilon_0 + \delta\epsilon$, The Berry phase hence changes following $\phi_B = \phi_F(\theta(\epsilon_0 + \delta\epsilon) - \theta(-\epsilon_0 + \delta\epsilon))$, where ϕ_F is the gate-dependent prefactor evaluated above for both cases. We find a change

$$\frac{\delta\phi_B}{\phi_F} = \left[\frac{\epsilon_0 + \delta\epsilon}{\sqrt{\Delta^2 + (\epsilon_0 + \delta\epsilon)^2}} + \frac{\epsilon_0 - \delta\epsilon}{\sqrt{\Delta^2 + (\epsilon_0 - \delta\epsilon)^2}} - 2 \frac{\epsilon}{\sqrt{\Delta^2 + \epsilon_0^2}} \right]. \quad (2)$$

If $\delta\epsilon \ll \Delta$ is a small error, we find $\delta\phi_B \propto (\delta\epsilon/\Delta)^2$, manifesting the celebrated fault-tolerance of geometric quantum computation. On the other hand, in order to perform geometric quantum computation, it must be possible to couple Berry phases to each other, i.e. to make the Berry phase of one qubit depend on the state of the other one. It has already been discussed [5, 6], that qubits of the type discussed here can be coupled by a switchable flux transformer, providing a coupling of the type $H_{qq} = \epsilon_c \sigma_{z,1} \otimes \sigma_{z,2}$, i.e. the state of qubit 2 influences qubit 1 by changing its energy bias ϵ by $\delta\epsilon$. In the light of the above discussion, this coupling consequently affects the Berry phase only in the nonlinear regime $\delta\epsilon > \Delta$ of eq. 2. It has been shown theoretically [6], that such large couplings can be achieved by properly designing the flux transformer. Further research in this direction should make non-Abelian geometric factors

beyond the Berry phase possible, which would lead to holonomic quantum computation [20].

Discussion. Geometric quantum computing is supposed to have two principal advantages: There are only very few short pulses needed and the system shows stronger fault-tolerance, i.e. small errors in the setting of parameters only affect the phase quadratically. Both of these features can be particularly important for Josephson qubits: The application of microwave pulses under cryogenic conditions is generally very difficult and small variations in fabrication parameters may lead to inaccuracies in the applied transformations.

On the other hand, maintaining the Berry phase requires all manipulations to be carried out within the coherence time τ_ϕ [21]. As the manipulations have to be carried out on an adiabatic time scale τ_{ad} , we have the double inequality $1/\Delta < \tau_{\text{ad}} < \tau_\phi$, whereas for pulsed schemes only a single inequality is imposed, i.e. the demand for a long phase coherence time is less restrictive. Moreover, the need to control a gate charge implies that the main advantage of the flux qubit with respect to the charge qubit, the independence of offset charge noise, is reduced and the system is more sensitive to decoherence. This sensitivity is different for both scenarios: In the first one, only differences of gate charges play a role (see Table I), so a static offset charge has no effect. In the second proposal, the absolute value of the gate charge is important. Nevertheless, also this setup permits to trace back the same path with a different gate setting, which makes $\phi_B = 2\pi(n_{G,1} - n_{G,2})$ again independent of static offset charges.

Our results finally allow to estimate the effect of offset charge noise onto the standard pulsed persistent current qubit [3–5] without extra gates operated in the time-domain. As long as these charges are static, they act like a fixed gate setting and do only induce a constant phase shift $\delta\phi$. This shift does not affect the computation. If a charge *jumps* during a gate pulse, there is an additional, random geometrical phase next to the controlled dynamical phase, which potentially leads to an error.

This background charge noise has typically a $1/f$ power spectrum. For definiteness, we follow the approach taken in [22] to treat this noise as a limiting case of the Sub-Ohmic Oscillator bath, i.e. we assume a bath oscillator spectral density $J_\phi(\omega)$ as

$$\frac{1}{2} \langle \{\phi(t), \phi(0)\} \rangle_\omega = J_\phi(\omega) \coth(\omega/2T) \quad J_\phi(\omega) = \frac{\pi}{2} \hbar \alpha \omega_s^{1-s} \omega^s \quad (3)$$

and take the limit $s \rightarrow 0$. Using a standard unitary transformation with $U = \exp(-i\hat{\sigma}_z \delta\phi(t)/2)$, we find from $H = \frac{1}{2} \begin{pmatrix} \epsilon & \Delta e^{-i\delta\phi} \\ \Delta e^{i\delta\phi} & -\epsilon \end{pmatrix}$ the transformed Hamiltonian

$$H' = U^\dagger H U - iU^\dagger \partial_t U = \frac{1}{2} \begin{pmatrix} \epsilon + \delta\dot{\phi} & \Delta \\ \Delta & -\epsilon - \delta\dot{\phi} \end{pmatrix} \quad (4)$$

i.e. the Spin-Boson Hamiltonian with a super-Ohmic spectral density $J_{\text{SB}}(\omega) = \omega^2 J_\phi(\omega)$. In the weak damping limit, this problem is readily solved [23] and the dynamics of the reduced density matrix is described by a combination of incoherent relaxation on a time scale T_1 given through the rate $T_1^{-1} = (\Delta^2/2E^2) J_{\text{SB}}(E) \coth(E/2T)$ where $E = \sqrt{\Delta^2 + \epsilon^2}$ is the energy splitting of the qubit states, and $T_2 = 2T_1$. Thus, the decoherence is rather regular and the coherence time can be very long because the destructive low-frequency noise only has very little spectral weight. Transforming the reduced density matrix back using $\rho = U^\dagger \rho U$ and performing the ensemble average, we find that this dynamics is also recovered in the original basis with the slight difference that the effective size of the off-diagonal matrix elements is reduced by an effective time-independent prefactor. Thus, we have confirmed the claimed [5,6] relative insensitivity of flux qubits to the noise of offset charges and quantified their effect.

In conclusion, we have shown how Berry phases up to a limited size can be realized in gated superconducting three-junction loops. We have discussed the preparation of arbitrary large

TABLE I – A cycle in flux-gate voltage parameter space given by its corner points and the corresponding Hamiltonians and directions on the Bloch sphere. $\delta f = 2\pi\Phi/\Phi_0 - 1/2$, $\epsilon_0 = \frac{\hbar}{2e}I_q\delta f$, I_q is the circulating current in the qubit, $\phi_0 = n_0\alpha\cos(-1/2\alpha_3)$ and $\theta_0 = \text{atan}\epsilon_0/\Delta$. From the solid spanned by this contour, we find a Berry phase of $\phi_B = 2\sin\theta_0\phi_0 = 2\phi_0\epsilon_0/\sqrt{\Delta^2 + \epsilon_0^2}$

	1	2	3	4	$\bar{5}=1$
n_G	$-n_0$	$-n_0$	n_0	n_0	
δf	f_0	$-f_0$	$-f_0$	f_0	
\hat{H}	$\frac{1}{2} \begin{pmatrix} \epsilon_0 & \Delta e^{-i\phi_0} \\ \Delta e^{i\phi_0} & -\epsilon_0 \end{pmatrix}$	$\frac{1}{2} \begin{pmatrix} -\epsilon_0 & \Delta e^{-i\phi_0} \\ \Delta e^{i\phi_0} & \epsilon_0 \end{pmatrix}$	$\frac{1}{2} \begin{pmatrix} -\epsilon_0 & \Delta e^{i\phi_0} \\ \Delta e^{-i\phi_0} & \epsilon_0 \end{pmatrix}$	$\frac{1}{2} \begin{pmatrix} \epsilon_0 & \Delta e^{i\phi_0} \\ \Delta e^{-i\phi_0} & -\epsilon_0 \end{pmatrix}$	
\hat{n}	$\begin{pmatrix} \sin\theta_0 \cos\phi_0 \\ -\sin\theta_0 \sin\phi_0 \\ \cos\theta_0 \end{pmatrix}$	$\begin{pmatrix} \sin\theta_0 \cos\phi_0 \\ -\sin\theta_0 \sin\phi_0 \\ -\cos\theta_0 \end{pmatrix}$	$\begin{pmatrix} \sin\theta_0 \cos\phi_0 \\ \sin\theta_0 \sin\phi_0 \\ -\cos\theta_0 \end{pmatrix}$	$\begin{pmatrix} \sin\theta_0 \cos\phi_0 \\ \sin\theta_0 \sin\phi_0 \\ \cos\theta_0 \end{pmatrix}$	

Berry phases in six-junction devices and outlined the application of this device to quantum computing. Finally, we have quantified the impact of offset charge noise to flux qubits.

Work supported by the EU through TMR Supnan and IST ‘‘Squbit’’. FKW is supported by ARO under contract P-43385-PH-QC. We acknowledge useful discussions with P. Hadley, Y. Gefen, L. Levitov, S. Lloyd, J.B. Majer, Yu. Nazarov, C.H. van der Wal, and R. Whitney.

REFERENCES

- [1] For a recent review see e.g. R. Fazio and H.S.J. van der Zant, Phys. Rep. **355**, 235 (2001); Yu. Makhlin, G. Schön and A. Shnirman, Rev. Mod. Phys. **73**, 357 (2001).
- [2] J.R. Friedman *et al.*, Nature **406**, 43 (2000).
- [3] C.H. van der Wal *et al.*, Science **290**, 773 (2000).
- [4] I. Chiorescu *et al.*, Science **299**, 1869 (2003).
- [5] J.E. Mooij *et al.*, Science **285**, 1036 (1999).
- [6] T.P. Orlando *et al.*, Phys. Rev. B **60**, 15398 (1999).
- [7] Yu. Makhlin, G. Schön, and A. Shnirman, Nature **398**, 306 (1998).
- [8] A. Shapere and F. Wilczek (eds.), *Geometric phases in physics* (World Scientific, 1989).
- [9] M.V. Berry, Proc. R. Soc. Lond. A **392**, 45 (1984).
- [10] J.A. Jones *et al.*, Nature **403**, 869 (2000).
- [11] D. Suter, G.C. Chingas, R.A. Harris, and A. Pines, Mol. Phys. **61**, 1327 (1987).
- [12] A. Tomita and R. Chiao, Phys. Rev. Lett. **57**, 937 (1986).
- [13] Jeng-Bang Yau, E.P. De Poortere and M. Shayegan, Phys. Rev. Lett. **84**, 4481 (2002).
- [14] G. Falci *et al.*, Nature **407**, 355 (2000).
- [15] for a discussion of DC-Squids see e.g. M. Tinkham *Introduction to superconductivity*, 2nd ed., (McGraw-Hill, New York, 1996).
- [16] Y. Aharonov and A. Casher, Phys. Rev. Lett. **53**, 319 (1984); W.J. Elion, J.J. Wachters, L.L. Sohn, and J.E. Mooij, Phys. Rev. Lett. **71**, 2311 (1993).
- [17] D.A. Ivanov, L.B. Ioffe, V.B. Geshkenbein, and G. Blatter, Phys. Rev. B **65**, 024509 (2002).
- [18] K.K. Likharev and A. Zorin, J Low Temp Phys **59**, 347 (1985).
- [19] L. Kuzmin and D.S. Haviland, Phys. Rev. Lett. **67**, 2890 (1991).
- [20] P. Zanardi and M. Rasetti, Phys. Lett. A **264**, 94 (1999).
- [21] R. Whitney and Yu. Gefen, cond-mat/0208141.
- [22] A. Shnirman, Yu. Makhlin, and G. Schön, Phys. Scr. **102**, 142 (2002).
- [23] M. Grifoni, E. Paladino, and U. Weiss, Eur. Phys. J B **10**, 719 (1999).

3.7 Decoherence of charge states in quantum dots

The papers reviewed in this section examine the decoherence of charge states in double quantum dot in Coulomb blockade due to cotunneling with the electronic leads. Cotunneling is a second order process, which dominates because the first order process, sequential tunneling, is suppressed in the blockade region. In order to capture it, the Hamiltonian is transferred using a generalized Schrieffer-Wolf transformation, such that the coupling term to the leads is of particle-hole scattering form. This method, together with first results, is explained in Ref. [202]. In particular, it is shown that even if the coupling to the leads is diagonal in the basis of qubit eigenstates, the state can relax through cotunneling, because the leads are assumed to keep their voltage constant, i.e. they have to be physically connected through the voltage source, which transfers the relaxing electron.

This system is studied further in Ref. [203], where the transport in the case of finite tunnel coupling and arbitrary asymmetry are studied. We concentrate on the crossover between elastic and inelastic cotunneling, i.e. the onset of transport processes which excite the qubit and which show up as an extra contribution in the cotunneling current. At fixed voltage, these processes are allowed at intermediate tunnel couplings, which are large enough to allow current flow but small enough such that the molecular level splitting is smaller than the applied voltage. Thus, the current is a nonmonotonic function of the inter-dot coupling strength.

In Ref. [204], the relaxation of excited states and the decoherence in the same system is studied. One would expect that the relaxation time is longest in the equilibrium state, when the transport voltage between the leads is zero. This is however misleading, because vanishing net current only means that the current contributions with opposite polarity have different modulus, whereas relaxation processes contribute to the total rate with equal sign. Moreover, if the eigenstates are spread out across the double dot, there are also relaxation processes which only involve one lead and do not carry current. Indeed, it turns out that the relaxation time is usually maximum at finite voltage, namely if the voltage equals the level splitting at a polarity blocking the most prominent relaxation channel. At this point, excitation due to inelastic cotunneling (i.e. absorption from the environment) is still suppressed and one of the two relaxation processes (i.e. emission to the environ-

ment) is blocked because the gain in energy from the relaxation does not compensate the electromagnetic energy of the voltage source which has to be overcome.

Decoherence of Charge States in Double Quantum Dots Due to Cotunneling

U. HARTMANN¹⁾ and F. K. WILHELM

*Sektion Physik and CeNS, Ludwig-Maximilians-Universität, Theresienstr. 37,
80333 München, Germany*

(Received July 22, 2002; accepted July 29, 2002)

PACS: 03.67.Lx; 72.10.-d; 73.23.Hk; 73.63.Kv

Solid state quantum bits are a promising candidate for the realization of a scalable quantum computer, however, they are usually strongly limited by decoherence. We consider a double quantum dot charge qubit, whose basis states are defined by the position of an additional electron in the system of two laterally coupled quantum dots. The coupling of these two states can be controlled externally by a quantum point contact between the two dots. We discuss the decoherence through coupling to the electronic leads due to cotunneling processes. We focus on a simple Gedanken experiment, where the system is initially brought into a superposition and then the interdot coupling is removed nonadiabatically. We treat the system by invoking the Schrieffer-Wolff transformation in order to obtain a transformed Hamiltonian describing the cotunneling, and then obtain the dynamics of the density matrix using the Bloch-Redfield theory. As a main result, we show that there is energy relaxation even in the absence of inter-dot coupling. This is in contrast to what would be expected from the Spin-Boson model and is due to the fact that a quantum dot is coupled to *two* distinct baths.

Quantum dots (“artificial atoms”) are prototype systems for studying the properties of discrete levels embedded in a solid-state environment [1]. In particular, various schemes for realizing quantum bits, fully controlled quantum coherent two-state systems, using quantum dots have been brought forward. Next to using optically excited charge states in quantum dots [2] and electronic quantum dots used for spin manipulation [3], it has been proposed [4] to use the charge states of a double quantum dot as a computational basis. The proposed setup is sketched in Fig. 1. In order to minimize the inevitable decoherence through coupling to the electronic leads, the system can be brought into the Coulomb blockade regime where sequential tunneling is suppressed. We are going to discuss in this article, how the inevitable cotunneling still decoheres the system in this regime. The calculation is carried out for one specific Gedanken experiment which should capture the most generic features, the decay of a superposition state when the coupling between the dots is switched off. A more complete treatment of this setup is in preparation [5].

We restrict our analysis on spin-polarized electrons. The relevant Hilbert space is characterized by four basis states, written as $|i, j\rangle$, which denotes i additional electrons on the left dot, j additional electrons on the right dot. The two states $|1, 0\rangle$ and $|0, 1\rangle$ define the computational basis, see e.g. [6]. In order to describe cotunneling, we use the closest energetically forbidden states as virtual intermediate states. These are $|v_0\rangle = |0, 0\rangle$ and $|v_2\rangle = |1, 1\rangle$. Zero- and two electron states with internal polarization are energetically even less favorable due to the high charging energy of the individual dots.

¹⁾ Corresponding author; e-mail: hartmann@theorie.physik.uni-muenchen.de

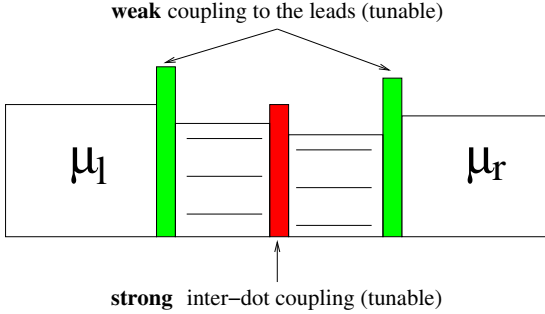


Fig. 1 (online colour). Sketch of the double dot system. The coupling of the double dot to the leads is assumed to be weak, whereas the coupling between the dots can be strong. The leads are biased such that sequential tunneling is suppressed

The Hamiltonian of this system can be written as

$$H = H_0 + H_1, \quad (1)$$

$$H_0 = \epsilon_{\text{as}}(\hat{n}_l - \hat{n}_r) - \epsilon_\alpha \hat{n}_{v_0} + \epsilon_\beta \hat{n}_{v_2} \\ + \gamma \sum_n (a_n^{L+} a_n^R + a_n^{R+} a_n^L) + \sum_{\mathbf{k}} c_{\mathbf{k}}^L b_{\mathbf{k}}^{L+} b_{\mathbf{k}}^L + \sum_{\mathbf{k}'} c_{\mathbf{k}'}^R b_{\mathbf{k}'}^{R+} b_{\mathbf{k}'}^R, \quad (2)$$

$$H_1 = t_c \sum_{\mathbf{k}, n} (a_n^{L+} b_{\mathbf{k}}^L + a_n^L b_{\mathbf{k}}^{L+}) + t_c \sum_{\mathbf{k}', m} (a_m^{R+} b_{\mathbf{k}'}^R + a_m^R b_{\mathbf{k}'}^{R+}). \quad (3)$$

Note, that the sum over dot states only runs over the restricted Hilbert space described above. H_0 describes the energy spectrum of the uncoupled system, whereas the tunneling part H_1 describes the coupling of each dot to its lead and will be treated as a perturbation. $\hat{n}_{l/r}$ are the number operators for the additional electrons on either dot. The asymmetry energy ϵ_{as} describes the difference between the energy level for the additional electron in left dot and the corresponding energy level in the right dot. It can be tuned through via the gate voltages which are applied at each dot. ϵ_β and ϵ_α are the energy differences towards the higher level $|v_2\rangle$ and the lower level $|v_0\rangle$, respectively. γ is the tunable inter-dot coupling. The $a^{(+)}$ s and $b^{(+)}$ s denote the creation/destruction operators in the dots and leads. In H_1 the symbol t_c represents the coupling constant concerning the coupling of the dots to the leads, which should be small compared to the asymmetry energy. Note, that we have chosen a slightly asymmetric notation in order to highlight the physical model: For the actual calculation, H_1 is also expressed in the eigenstate basis of the dot.

For our Gedanken experiment, we assume that first the inter-dot coupling γ is large ($\gamma \gg \epsilon_{\text{as}}, V$) such that the system relaxes into the ground state, which is a molecular superposition state of the form $|g\rangle = (|0, 1\rangle - |1, 0\rangle)/\sqrt{2}$. Then the gate voltage that controls the inter-dot coupling is switched to high values, so that the coupling is practically zero. After this, the system dephases and relaxes into a thermal mixture of the localized eigenstates of the new system.

Thus, in order to describe decoherence, we only have to consider the case $\gamma = 0$ K. This means, that H_0 is already diagonal, i.e. the states $|1, 1\rangle$, $|1, 0\rangle$, $|0, 1\rangle$ and $|0, 0\rangle$ are eigenstates of our system.

The decoherence is analyzed applying the well-established Bloch-Redfield theory, which is based on the Born approximation in the system-bath coupling. As we are in the Coulomb blockade regime, the rates evaluated from the original coupling Hamiltonian H_1 vanish in that order. In order to treat cotunneling with this formalism, we per-

form a generalized Schrieffer-Wolf transformation [7, 8]. This transformation maps our original Hamiltonian H_1 , which is zero in the computational basis but couples the computational states to the $|v_{0/2}\rangle$ onto a Hamiltonian which does *not* have this coupling to higher states but which has nonzero matrix elements in the computational basis. The new terms in the Hamiltonian describe the amplitude of transitions between the basis states via the intermediate states. We perform this transformation perturbatively up to second order, i.e. all processes involving at most *one* intermediate state are taken into account.

The new Hamiltonian H_1 in our special case then can be written as

$$H_{1,++} = A(R+, R, ++) b_m^{R+} b_n^R + A(L, L+, ++) b_l^L b_k^{L+}, \tag{4}$$

$$H_{1,--} = A(L+, L, --) b_k^{L+} b_l^L + A(R, R+, --) b_n^R b_m^{R+}, \tag{5}$$

$$H_{1,+ -} = A(R+, L, +-) b_m^{R+} b_l^L + A(L, R+, +-) b_l^L b_m^{R+}, \tag{6}$$

$$H_{1,- +} = A(L+, R, -+) b_k^{L+} b_n^R + A(R, L+, -+) b_n^R b_k^{L+}. \tag{7}$$

The + and - signs are indices for the states $|1, 0\rangle$ and $|0, 1\rangle$, respectively. We call A the Schrieffer-Wolff coefficients, they are calculated along the lines of [8] using mainly second order perturbation theory. For example, $A(R+, R, ++)$ is

$$A(R+, R, ++)= \frac{t_c^2}{2} \left[\frac{1}{\epsilon_m^R - (-\epsilon_{as} + \epsilon_\beta)} - \frac{1}{\epsilon_n^R - (\epsilon_{as} - \epsilon_\beta)} \right]. \tag{8}$$

We now use the Bloch-Redfield equations [9, 10]

$$\dot{Q}_{nm}(t) = -i\omega_{nm}Q_{nm} - \sum_{k,l} R_{nmkl}Q_{kl}(t), \tag{9}$$

where R_{nmkl} are the elements of the Redfield tensor. These equations of motion for the reduced density matrix are obtained within Born approximation in the effective system-bath coupling, so after the Schrieffer-Wolff transformation, R is of order t_c^4 . Let us remark that our perturbation theory naturally breaks down below the Kondo temperature, which can however be made arbitrarily small by lowering t_c through pinching off the contacts to the reservoirs.

The Bloch-Redfield equations are of Markovian form, however, by properly using the free time evolution of the system, they take into account all bath correlations which are relevant within the Born approximation [11].

The Redfield tensor has the form

$$R_{nmkl} = \delta_{lm} \sum_r \Gamma_{nrrk}^{(+)} + \delta_{nk} \sum_r \Gamma_{lrrm}^{(-)} - \Gamma_{lmnk}^{(+)} - \Gamma_{lmnk}^{(-)}. \tag{10}$$

The rates entering the Redfield tensor elements are given by the following Golden-Rule expressions

$$\Gamma_{lmnk}^{(+)} = \hbar^{-2} \int_0^\infty dt e^{-i\omega_{nk}t} \langle \tilde{H}_{1,lm}(t) \tilde{H}_{1,nk}(0) \rangle, \tag{11}$$

$$\Gamma_{lmnk}^{(-)} = \hbar^{-2} \int_0^\infty dt e^{-i\omega_{lm}t} \langle \tilde{H}_{1,lm}(0) \tilde{H}_{1,nk}(t) \rangle, \tag{12}$$

where H_I appears in the interaction representation (written as \tilde{H}_I). In our formalism, it is of crucial importance that the expectation values over H_I vanish, i.e. that the bath

produces only noise. As a number of expectation values of H_1 turns out to be finite, we tacitly replace H_1 by $H_1 - \langle H_1 \rangle$ in Eqs. (11) and (12) and use the finite expectation values to renormalize the diagonalized, unperturbed Hamiltonian $H_0 \rightarrow H_0 + \langle H_1 \rangle$. In our case, the effect of this renormalization is of the order of 0.1% of the original matrix elements of H_0 .

After a straightforward calculation of the above Golden-Rule rates, one gets in the general case a (large) sum over terms with the generic form

$$\Gamma^{(+)} = c \left\{ \frac{i\pi}{\epsilon_b - \epsilon_a \mp 2\epsilon_{as}} [f_1(\epsilon_b \mp 2\epsilon_{as}) (1 - f_2(\epsilon_b)) - f_1(\epsilon_a) (1 - f_2(\epsilon_a \pm 2\epsilon_{as}))] \right. \\ \left. + \frac{-n_1(\mu_2 \mp 2\epsilon_{as})}{\epsilon_b - \epsilon_a \mp 2\epsilon_{as}} \left[\psi \left(\frac{1}{2} + \frac{i\beta}{2\pi} (\epsilon_b \mp 2\epsilon_{as} - \mu_1) \right) \right. \right. \\ \left. \left. - \psi \left(\frac{1}{2} + \frac{i\beta}{2\pi} (\epsilon_a - \mu_1) \right) - \psi \left(\frac{1}{2} + \frac{i\beta}{2\pi} (\epsilon_b - \mu_2) \right) \right. \right. \\ \left. \left. + \psi \left(\frac{1}{2} + \frac{i\beta}{2\pi} (\epsilon_a \pm 2\epsilon_{as} - \mu_2) \right) \right] \right\}, \quad (13)$$

$$\Gamma^{(-)} = c \left\{ \frac{i\pi}{\epsilon_b - \epsilon_a \mp 2\epsilon_{as}} [f_2(\epsilon_b)(1 - f_1(\epsilon_b \mp 2\epsilon_{as})) - f_2(\epsilon_a \pm 2\epsilon_{as})(1 - f_1(\epsilon_a))] \right. \\ \left. + \frac{-n_2(\mu_1 \pm 2\epsilon_{as})}{\epsilon_b - \epsilon_a \mp 2\epsilon_{as}} \left[-\psi \left(\frac{1}{2} + \frac{i\beta}{2\pi} (\epsilon_b \mp 2\epsilon_{as} - \mu_1) \right) \right. \right. \\ \left. \left. + \psi \left(\frac{1}{2} + \frac{i\beta}{2\pi} (\epsilon_a - \mu_1) \right) + \psi \left(\frac{1}{2} + \frac{i\beta}{2\pi} (\epsilon_b - \mu_2) \right) \right. \right. \\ \left. \left. - \psi \left(\frac{1}{2} + \frac{i\beta}{2\pi} (\epsilon_a \pm 2\epsilon_{as} - \mu_2) \right) \right] \right\}, \quad (14)$$

where $c = \frac{t_c^4 \pi V^2 m_*^2}{4\hbar(2\pi\hbar^2)^2}$. One can express the coupling to the leads t_c by $t_c = \sqrt{\frac{g}{8\pi^2}} \frac{E_F}{n}$, where g is a conductance in terms of the quantum conductance, E_F is the Fermi energy of the leads and n is the number of electrons in the leads. Consequently, c is then changed to $c = \frac{t_c^2 g}{32\pi\hbar}$. The ϵ_a and ϵ_b are terms containing varying sums or differences of ϵ_β , ϵ_α and ϵ_{as} . Due to the multitude of possibilities for virtual transitions, each element of the Redfield tensor contains a number of terms of this generic structure.

In the above equations, the terms containing the Fermi function $f(\epsilon)$ only play a role close to resonance and can be neglected in the Coulomb blockade [12]. The $n_{l/r}$ represent Bose functions for the electron-hole pairs (excitons) that are generated during the virtual processes. The ψ denote Digamma functions and hence diverge logarithmically at low temperatures.

By solving Eq. (9), one finds that the off-diagonal elements decay towards zero on a time scale τ_ϕ (dephasing time) whereas the diagonal density matrix elements equilibrate on a time scale τ_r (relaxation time).

Using the above expressions, we find the rates as

$$\Gamma_r = 2(\Gamma_{+--+}^{(+)} + \Gamma_{-++-}^{(-)}), \quad (15)$$

$$\Gamma_\phi = \frac{\Gamma_r}{2} + (\Gamma_{++++}^{(+)} + \Gamma_{----}^{(-)} - 2\Gamma_{+--+}^{(+)}), \quad (16)$$

where

$$\Gamma_{+---+}^{(+)} = \Gamma_{+---+}^{(-)} = c(-n_r(\mu_l + 2\epsilon_{as})) Z, \tag{17}$$

$$\Gamma_{-++-}^{(+)} = \Gamma_{-++-}^{(-)} = c(-n_l(\mu_r - 2\epsilon_{as})) Z, \tag{18}$$

$$\Gamma_{++++}^{(+)} = \Gamma_{++++}^{(-)} = c \frac{1}{\beta} Y_1, \tag{19}$$

$$\Gamma_{-----}^{(+)} = \Gamma_{-----}^{(-)} = c \frac{1}{\beta} Y_{-1}, \tag{20}$$

$$\Gamma_{++--}^{(+)} = \Gamma_{++--}^{(-)} = c \frac{1}{\beta} Y_{1,-1}. \tag{21}$$

Z is a function containing several ψ -functions (or logarithms). Y_1 , Y_{-1} and $Y_{1,-1}$ are different functions of several ψ' -(Trigamma-) functions (or reciprocals), however, these functions only have a very weak temperature dependence. The most important part of the temperature dependence comes in through $1/\beta$ and in $n_{l/r}$ and is summarized in Fig. 2. We find in Fig. 2 that the temperature dependence is similar to the Spin-Boson case [13]. This can be confirmed by inspection of the formulas (17)–(21): For the relaxation rate, one has only Bose functions taken at the finite amount energy which is dissipated. In case of the dephasing rate, there are also terms that are proportional to T , which represent dephasing processes which do not change the energy of the qubit, i.e. cotunneling processes which originate and end in the same state. This explains the observed behaviour. Note, that in the Spin-Boson case, where there is only one lead, the situation corresponding to our Gedanken-experiment (no tunneling between the classical states) would correspond to pure dephasing, whereas in our system relaxation is always possible by extracting an electron on one side and adding one on the other side from the other lead.

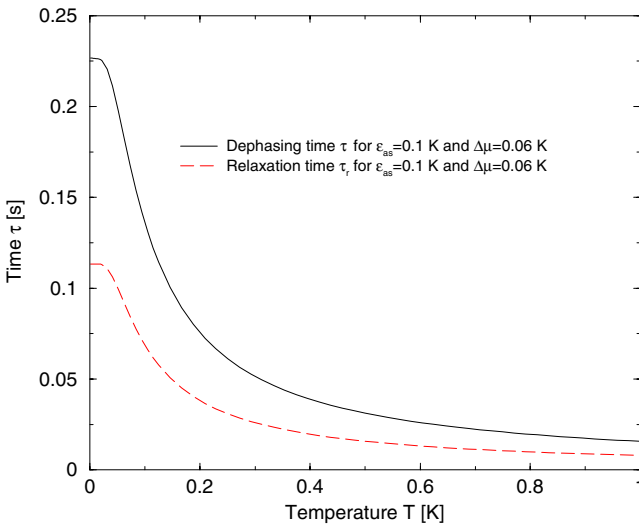


Fig. 2 (online colour). Relaxation and dephasing times (τ_r and τ_ϕ) as a function of temperature T , with $\mu_l = 0.85$ K, $\mu_r = 0.91$ K, $\epsilon_{as} = 0.1$ K, $\epsilon_\beta = 11$ K, $\epsilon_\alpha = 9$ K, $g = 0.1$, $V = 10^{-12}$ m², $E_F = 5$ meV and $n/V = 1.7 \times 10^{15}$ m⁻²

The numerical values for the relaxation and dephasing times are comparably huge, on the order of 100 milliseconds as compared to the experimentally measured times, which are in the order of nanoseconds. Other possibilities to explain the small decoherence time are phononic and/or photonic baths [14–16], or the influence of the whole electronic circuitry.

We analyzed relaxation and dephasing processes in a system of two laterally coupled quantum dots which is coupled to two electronic (i.e. fermionic) baths. We showed that even in the case of vanishing inter-dot coupling, the system's energy can relax, unlike in the Spin-Boson model. On top of that, the temperature dependence of the rates resembles that of the Spin-Boson model. We identify, that this originates in the fact that the cotunneling rates are mostly sensitive to the distribution function of excitons.

As a next step, the case where the inter-dot coupling γ has finite values will be considered [5].

Acknowledgement We thank J. von Delft, L. Borda, J. König, R. H. Blick, A.W. Holleitner, A. K. Hüttel and E. M. Höhberger for clarifying discussions. We acknowledge financial support from ARO, contract-No. P-43385-PH-QC.

References

- [1] R. C. ASHOORI, *Nature* **379**, 413 (1996).
- [2] P. ZANARDI and F. ROSSI, *Phys. Rev. Lett.* **81**, 4752 (1998).
F. ROSSI et al., 275th WE-Heraeus-Seminar. Hardware Concepts for Quantum Computing, 12.–15. 5. 2002; Bad Honnef, Germany; *phys. stat. sol. (b)* **233**, No. 3 (2002).
- [3] D. LOSS and D. DiVINCENZO, *Phys. Rev. A* **57**, 120 (1998).
- [4] R. BLICK and H. LORENZ, *Proc. ISCAS 2000* (pp. II245–II248).
- [5] U. HARTMANN and F. K. WILHELM, in preparation.
- [6] M. A. NIELSEN and I. L. CHUANG, *Quantum Computation and Quantum Information*, CUP, Cambridge 2000.
- [7] J. R. SCHRIEFFER and P. A. WOLFF, *Phys. Rev.* **149**, 491 (1966).
- [8] C. COHEN-TANNOUDJI, J. DUPONT-ROC, and G. GRYNBERG, *Atom–Photon Interactions*, Wiley, New York 1992.
- [9] U. WEISS, *Quantum Dissipative Systems*, 2nd ed., World Scientific Publ. Co., Singapore 1999.
- [10] K. BLUM, *Density Matrix Theory and Applications*, Plenum Press, New York 1981.
- [11] L. HARTMANN, I. GOYCHUK, M. GRIFONI, and P. HÄNGGI, *Phys. Rev. E* **61**, R4687 (2000).
- [12] J. KÖNIG, J. KÖNIG, H. SCHOELLER, and G. SCHÖN, *Phys. Rev. Lett.* **78**, 4482 (1997).
- [13] M. GRIFONI, E. PALADINO, and U. WEISS, *Eur. Phys. J. B* **10**, 719 (1999).
- [14] T. BRANDES and B. KRAMER, *Phys. Rev. Lett.* **83**, 3021 (1999).
- [15] S. DEBALD, T. BRANDES, and B. KRAMER, *Phys. Rev. B* **66**, R041301 (2002).
- [16] H. QIN, A. W. HOLLEITNER, K. EBERL, and R. H. BLICK, *Phys. Rev. B* **64**, R241302 (2001).

Nonlinear cotunneling through an artificial molecule

Udo Hartmann* and Frank K. Wilhelm

Sektion Physik and CeNS, Ludwig-Maximilians-Universität, Theresienstrasse 37, D-80333 München, Germany

(Received 3 December 2002; revised manuscript received 21 January 2003; published 30 April 2003)

We study electron transport through a system of two lateral quantum dots coupled in series. We consider the case of weak coupling to the leads and a bias point in the Coulomb blockade. After a generalized Schrieffer-Wolff transformation, cotunneling through this system is described using methods from lowest-order perturbation theory. We study the system for arbitrary bias voltages below the Coulomb energy. We observe a rich, non-monotonic behavior of the stationary current depending on the internal degrees of freedom. In particular, it turns out that at fixed transport voltage, the current through the system is largest at weak-to-intermediate interdot coupling.

DOI: 10.1103/PhysRevB.67.161307

PACS number(s): 73.63.Kv, 73.23.Hk, 72.10.-d, 03.67.Lx

Quantum dots are prototype systems for studying the properties of discrete levels embedded in a solid-state environment. Single dots (“artificial atoms”¹) can be coupled through quantum point contacts, leading to “artificial molecules.” Indeed it has been shown experimentally^{2–4} that the eigenstates of double-dot systems are coherent molecular superpositions of single dot (atomic) states. Unlike real molecules, these dots are readily contacted and tunable *in situ*, making them a natural test bed for molecular transport. Double dots have also been proposed as charge quantum bits.^{5,6}

This raises the question, which information on the energy spectrum and the wave functions of the dot can be probed by transport measurements. This is only possible if artifacts induced by the coupling to the leads can be sorted out and the double-dot is disturbed as little as possible. This is the case when the coupling to the outside leads is weak (see Fig. 1) and the gates are tuned to the Coulomb blockade regime.^{7,8} In that regime, only states with a fixed number of electrons are energetically permissible and hence sequential tunneling is suppressed. The leading transport mechanism in this case is cotunneling,¹¹ the coherent transfer of two electrons via virtual levels in the dots. Our work stands between studies focusing on sequential tunneling⁹ and work on *linear response* in the Kondo regime.¹⁰ The properties of cotunneling currents as a spectroscopic tool for the spectrum of quantum dot system have recently been studied in exquisitely controlled experiments on systems similar to ours.^{4,12}

In this paper, we analyze a serial configuration of lateral quantum dots in the cotunneling regime. We study finite voltages up to the order of the charging energy, i.e., do not restrict ourselves to linear response. We find a rich nonmonotonic structure in the current as a function of the dot parameters. In particular, we find a pronounced crossover indicating the opening of an inelastic transport channel, which leads to the surprising result, that a too strong interdot coupling actually inhibits charge transport. We analyze the influence of the asymmetry of the dots on the current.

In the Coulomb blockade regime,^{7,8} the relevant Hilbert space is spanned by four basis states $|i, j\rangle$, $i, j \in \{0, 1\}$, which denotes i and j additional electrons (as compared to an appropriate neutral state) on the left and right dots, respectively. We study the situation where the gate voltages of the

single dots are very close to each other and the interdot coupling is, although appreciable, much smaller than the single-dot addition energy. Thus, the subspace spanned by the two states $|1, 0\rangle$ and $|0, 1\rangle$ is energetically most favorable. The next closest states $|v_0\rangle = |0, 0\rangle$ and $|v_2\rangle = |1, 1\rangle$ are outside the transport window and serve as virtual states.¹¹ States with higher dipolar moment are energetically even less favorable due to the high charging energy of the individual dots.

The Hamiltonian of this system can be written as

$$H = H_0 + H_1, \quad (1)$$

$$H_0 = H_{\text{sys}} + H_{\text{res}}, \quad (2)$$

$$H_{\text{sys}} = \varepsilon_{\text{as}}(\hat{n}_l - \hat{n}_r) - \varepsilon_{\alpha} \hat{n}_{v_0} + \varepsilon_{\beta} \hat{n}_{v_2} + \gamma \sum_n (a_n^{L\dagger} a_n^R + a_n^{R\dagger} a_n^L), \quad (3)$$

$$H_{\text{res}} = \sum_k \varepsilon_k^L b_k^{L\dagger} b_k^L + \sum_{\vec{k}'} \varepsilon_{\vec{k}'}^R b_{\vec{k}'}^{R\dagger} b_{\vec{k}'}^R, \quad (4)$$

$$H_1 = t_c \sum_{k,n} (a_n^{L\dagger} b_k^L + a_n^L b_k^{L\dagger}) + t_c \sum_{\vec{k}',n} (a_n^{R\dagger} b_{\vec{k}'}^R + a_n^R b_{\vec{k}'}^{R\dagger}). \quad (5)$$

Note that the sum over dot states n only runs over the restricted Hilbert space described above. H_0 describes the isolated double-dot (H_{sys}) and the leads (H_{res}), whereas the tunneling part H_1 describes the coupling of each dot to its

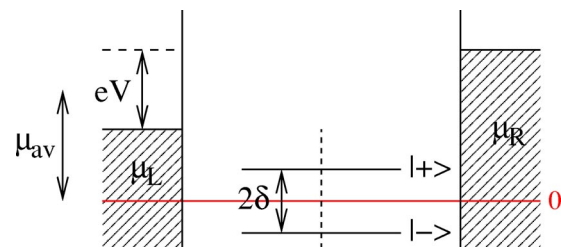


FIG. 1. Sketch of the considered artificial molecule, where 2δ is the level splitting and V is the bias voltage. The coupling to the outside leads (hatched areas) is assumed to be small whereas the interdot coupling (dotted line) can be strong.

lead and will be treated as a perturbation. $\hat{n}_{l/r}$ are the number operators counting additional electrons on either dot. The asymmetry energy $\varepsilon_{as} = (\varepsilon_l - \varepsilon_r)/2$ describes half of the difference between the energy level for the additional electron in left dot (ε_l) and the corresponding energy level in the right dot (ε_r), which can be tuned through the gate voltages. ε_β and ε_α are the charging energies towards the higher level $|v_2\rangle$ and the lower level $|v_0\rangle$, respectively. γ is the tunable interdot coupling strength. The $a^{(\dagger)}$ s and $b^{(\dagger)}$ s denote electron creation/annihilation operators in the dots and leads. In H_1 , the symbol t_c represents the tunnel matrix element between the dots and the leads. It is independent of the energies in the double-dot system and the corresponding sequential tunneling rate $\hbar\Gamma = 2\pi t_c^2 N(\varepsilon_F)$ should be small compared to the internal energies. $N(\varepsilon_F)$ is the density of states in the leads taken at the Fermi energy. We restrict our analysis to spin-polarized electrons, these can be polarized by an appropriate in-plane magnetic field. Figure 1 shows a sketch of the system. In Fig. 1, $V = \mu_R - \mu_L$ is the bias voltage between the two leads (hatched) and $2\delta = 2\sqrt{\varepsilon_{as}^2 + \gamma^2}$ is the level splitting in the molecular two-state system.

Pursuing our aforementioned objective, we take the interdot coupling γ into account to all orders by diagonalizing H_{sys} and transforming H_1 into the new basis. Already now, there is no simple selection rule or symmetry of the coupling of the states to the leads anymore. We want to use well-established tools of lowest-order perturbation theory for both finding the density matrix of the system and evaluating the current. In order to capture cotunneling by this approach, we perform a Schrieffer-Wolff transformation¹³ up to second order, i.e., we take into account all indirect transitions between arbitrary final and initial states of the dot which involve only a *single* intermediate state. This takes the transformed Hamiltonian into the generic form

$$\begin{aligned} \tilde{H}_I = \sum_{c,d} \alpha_c^\dagger \alpha_d \left[\sum_{Y,Y',\vec{k},\vec{k}'} H_{\vec{k},\vec{k}',c,d}^{Y,Y'} b_{\vec{k}}^{Y\dagger} b_{\vec{k}'}^{Y'} \right. \\ \left. + \sum_{Y,Y',\vec{k},\vec{k}'} H_{\vec{k},\vec{k}',c,d}^{Y,Y'} b_{\vec{k}}^Y b_{\vec{k}'}^{Y'\dagger} \right], \end{aligned} \quad (6)$$

where the $H_{\vec{k},\vec{k}',c,d}^{Y,Y'}$ are Schrieffer-Wolff amplitudes and $c, d = \pm$ denote the two molecular levels, $\alpha_{c/d}^{(\dagger)}$ the associated molecular operators, and Y, Y' the position of the electrons involved in these processes. Due to the molecular nature of the double-dot eigenstates, all the amplitudes are finite and composed of a huge number of contributions with no particular symmetry. The perturbation-theory formula for this general case can be found, e.g., in Ref. 14 and is worked out in more detail in Refs. 6 and 15. In Eq. (6), we have taken matrix elements in the double-dot eigenbasis only whereas we stick to second-quantized notation in the leads, because this notation readily connects to the formalism used later on.

The stationary density matrix is found using the well-established and controlled Bloch-Redfield theory.¹⁶ This is a systematic technique for deriving generalized master equations within Born approximation in \tilde{H}_I , Eq. (6), which in-

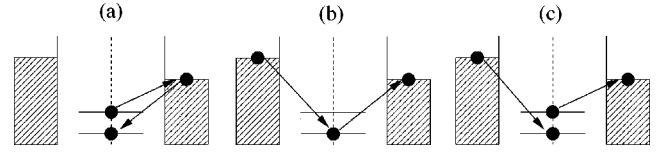


FIG. 2. Examples for relevant processes: (a) a relaxation process without current, (b) current without relaxation (only dephasing), and (c) a process that carries current and also relaxes the system.

cludes all relevant non-Markovian parts. This approach has been shown¹⁷ to be numerically equivalent to formally exact path-integral methods for the spin-boson model in the weak-coupling limit. The Redfield equations¹⁸ for the elements of the reduced density matrix ρ in the molecular basis read

$$\dot{\rho}_{nm}(t) = -i\omega_{nm}(t)\rho_{nm}(t) - \sum_{k,l} R_{nmkl}\rho_{kl}(t), \quad (7)$$

where $\omega_{nm} = (E_n - E_m)/\hbar$ are the appropriate energy splittings and R_{nmkl} are the elements of the Redfield tensor. They are composed of golden rule rates involving \tilde{H}_I from Eq. (6). n, m, k , and l can be either $+$ (molecular excited state) or $-$ (molecular ground state). The E 's are the eigenenergies of the two molecular states. Due to the lack of symmetry, this leads to a huge number of processes contributing to each term.¹⁵ We are only interested in stationary solutions here. A full treatment of the simple case with $\gamma=0$ can be found in Ref. 6.

The current is derived from the standard formula¹⁹

$$I(t) = -e \frac{i}{\hbar} \int_{-\infty}^t dt' \langle [\dot{N}_L(t), \tilde{H}_I(t')] \rangle, \quad (8)$$

where N_L is the particle number operator on the left dot in the interaction representation and the transformed interaction Hamiltonian \tilde{H}_I from Eq. (6) is also taken in the interaction picture. Carrying out the integration in Eq. (8) and rotating back to the Schrödinger picture, we get a time-independent expression for the current I . Using the stationary occupation probability of the molecular ground ($\rho_{--,st}$) or excited state ($\rho_{++,st}$), we obtain for the expectation value of the stationary current

$$I_{st} = \text{tr}(\rho_{st}I) = \rho_{++,st}I_{++} + \rho_{--,st}I_{--}, \quad (9)$$

where we find from balancing relaxation processes in the Bloch-Redfield equation, Eq. (7),

$$\rho_{++,st} = \frac{R_{++--}}{R_{++--} - R_{++++}}, \quad \rho_{--,st} = \frac{R_{--++}}{R_{--++} - R_{----}}. \quad (10)$$

The current amplitudes I_{++} and I_{--} in Eq. (9) are of the same form as the contributions to the Redfield tensor. We emphasize that the choice of processes from all possibilities is very distinct. As an example, Fig. 2 displays a variety of possible processes in such a double-dot system. Processes of the type displayed in Fig. 2(a) contribute to the relaxation but do not carry current, (b) shows a process which carries current but does not relax the state, and (c) relaxes and carries

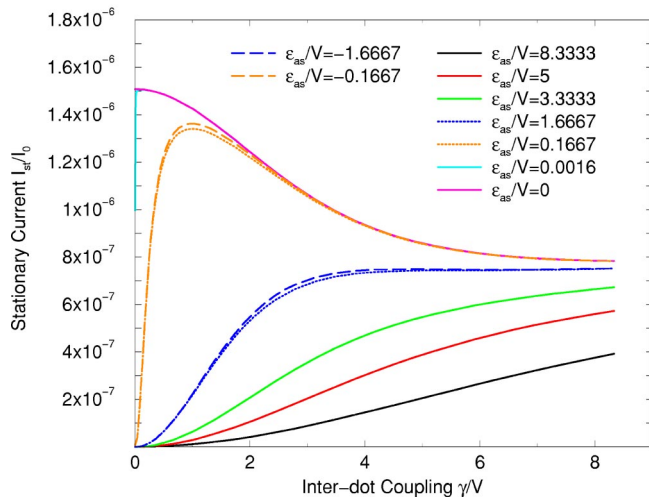


FIG. 3. Stationary current I_{st}/I_0 for different ϵ_{as}/V as a function of the coupling γ/V (with $T=140$ mK, $V=5.170$ μ V and $\mu_{av}=(\mu_R+\mu_L)/2=75.832$ μ eV and $\Gamma=1$ GHz).

current. The phase information of the quantum state is lost in all three pictures of Fig. 2. Consequently, one must not confuse cotunneling rates with relaxation rates.

We now turn to the discussion of the results. All internal energies ϵ_{as} and γ are normalized in units of the bias voltage V , the stationary current I_{st} in terms of $I_0=e\Gamma$.

In Fig. 3, the current at fixed bias voltage as a function of the interdot coupling is shown. The sign of ϵ_{as} plays a role, as one can see above, for an intermediate ϵ_{as} regime. This effect is more pronounced in $I(V)$, see Ref. 15. Close to $\gamma=0$, the curves all turn to zero because at that point the dots are disconnected and no current can flow. However, a number of curves, the ones with $\epsilon_{as}/V < 1$, exhibit an intermediate maximum at low γ next to a very sharp minimum at $\gamma=0$, which sometimes is hardly resolved. At high $\gamma \geq V$, the stationary current saturates into a value, which for our parameters turns out to be about $I_{0,st}/I_0=7.5 \times 10^{-7}$. Remarkably, this is half the value of the current at the aforementioned low- γ maximum. This is the central result of this paper.

These regimes can be classified in terms of the level splitting 2δ .²⁰ At $V < 2\delta$, the energy V supplied from the leads is only sufficient to use one of the molecular states for transport (elastic cotunneling) whereas at $V > 2\delta$, both states participate and also inelastic processes contribute, i.e., there is a second current channel, which carries the same contribution of I_0 . The crossover naturally occurs at $\gamma = \sqrt{V^2/4 - \epsilon_{as}^2}$, which can only be reached if $\epsilon_{as}/V < 1/2$. As long as γ is not too low, the coupling to the leads is the limiting element for the current flow. Only if $\gamma < \epsilon_{as}$, the double-dot eigenstates become localized and the interdot coupling becomes the current bottleneck. Consequently, associated dips have a half-width of ϵ_{as} for low temperatures and bias voltages and can thus be extremely narrow. We would like to remark that the notion of transport ‘‘channels’’ is appropriate here because cotunneling is a coherent transport process.

Figure 4 shows the dependence of the stationary current

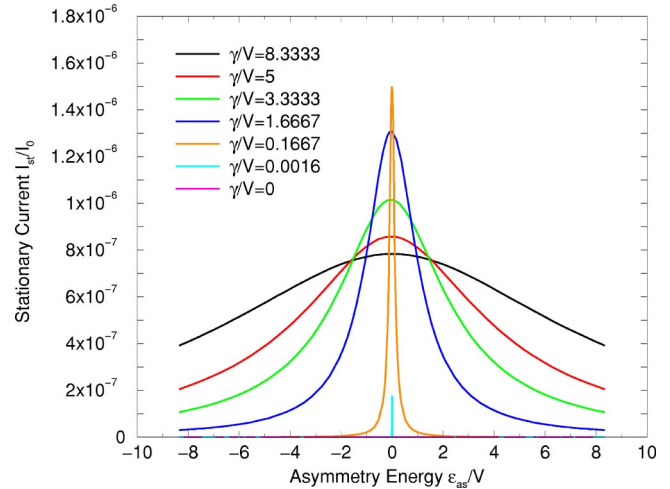


FIG. 4. Stationary current I_{st}/I_0 for different values of γ/V as a function of the asymmetry energy ϵ_{as}/V (with $T=140$ mK, $V=5.170$ μ V and $\mu_{av}=75.832$ μ eV and $\Gamma=1$ GHz).

on ϵ_{as}/V . It confirms the interpretation of Fig. 3. The plot is only weakly asymmetric to $\epsilon_{as}/V=0$. At zero asymmetry, $\epsilon_{as}/V=0$, the condition for charge transport is ideal, $\sqrt{V^2/4 - \epsilon_{as}^2}$ has its maximum and therefore the current is only governed by the interdot coupling γ/V , resulting in a zero-asymmetry maximum.

Still, all three transport regimes can be recognized in Fig. 4. The $\gamma/V=0$ curve shows that the stationary current I_{st}/I_0 is exactly zero as expected. For growing, but small values of γ/V , the maximum at $\epsilon_{as}/V=0$ reaches the highest value $I_{st}/I_0=2I_{0,st}/I_0$ at about 1.5×10^{-6} (like in Fig. 3), corresponding to two open transport channels (elastic and inelastic). If we raise γ/V further, the height of the peak goes down again and saturates at $I_{st}/I_0=I_{0,st}/I_0 \approx 7.5 \times 10^{-7}$, corresponding to only the elastic channel being open.

The three transport regimes are summarized in Fig. 5: (i)

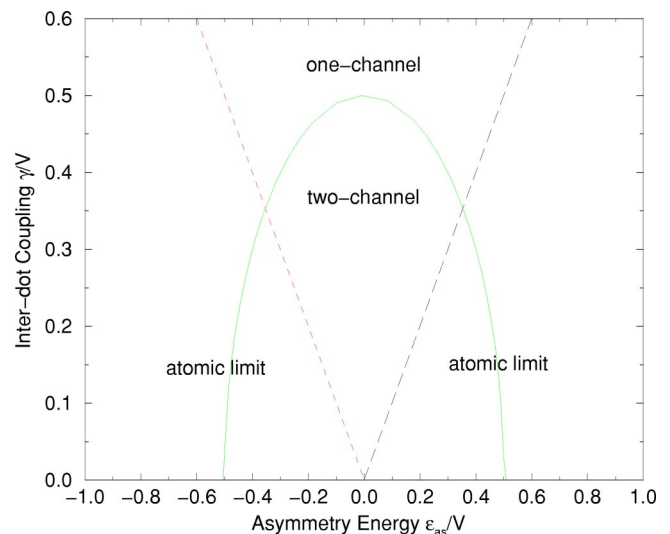


FIG. 5. Limits for the three transport regimes with $V=5.170$ μ V.

the atomic limit (no transport) $\gamma < \varepsilon_{\text{as}}$, (ii) the two-channel case (inelastic cotunneling) $\varepsilon_{\text{as}} < \gamma < \sqrt{V^2/4 - \varepsilon_{\text{as}}^2}$, and (iii) the one-channel case (elastic cotunneling) $\gamma > \sqrt{V^2/4 - \varepsilon_{\text{as}}^2}$.

These conditions show that indeed cotunneling can be used as a tool for investigating the energy spectrum of an undisturbed artificial molecule.⁴ The crossover between the elastic and the inelastic cotunneling in dependence of the applied bias voltage has recently been observed.¹² A similar conclusion was found in Ref. 20.

Although the notion of (elastic and inelastic) cotunneling was already introduced very early,¹¹ its consequences for realistic quantum dot systems have only been discussed very recently,²⁰ along with detailed and accurate experiments on small semiconductor quantum dots^{4,12} becoming available. The sharp crossover between elastic and inelastic cotunneling, which we discuss, has been identified in a vertical quantum dot¹² by changing the transport voltage. Reference 4 studies cotunneling in a parallel double-dot topology, using again cotunneling and the elastic-to-inelastic crossover as a spectroscopic tool and tuning the interdot coupling *in situ*. In both cases, the narrow regime of decoupled dots would not have been accessible through a conductance measurement. Some of the experimental issues have been theoretically addressed in Ref. 20. In that case, however, the behavior of a single multilevel dot system was modeled with phenomenological couplings to the leads, whereas we take a realistic model and only by this manage to predict effects which, e.g., depend on the serial dot topology of the sample. Note that

parts of the double-dot literature focus on phonon/photon assisted transport (see, e.g., Refs. 21 and 22 for experiments and Refs. 23 and 24 for theory). Unlike Ref. 25, we concentrate on the Coulomb blockade regime and do not consider cotunneling at resonance. In Ref. 26, a different approach to the problem was developed, in which the master equation is carried to second order instead of using a Schrieffer-Wolff transformation, and a few setups simpler than ours are studied. Our approach does not require the molecule to be artificial, in principle, it can be applied to “real” molecules.²⁷ In contrast to the approach in Ref. 28, it permits to take into account charging effects, however, the Schrieffer-Wolff transformation is clearly a laborious step for larger systems.

To conclude, we analyzed the stationary coherent cotunneling current I_{st} through a double quantum dot system or artificial molecule. As a function of the interdot coupling strength it displays a rich, nonmonotonic structure, which enables us to perform “molecular cotunneling spectroscopy.” Strikingly, we have shown that at fixed bias voltage, the current is highest, if the dots are weakly to intermediately connected, such that the interdot coupling is at least as strong as the coupling to the leads, but the splitting of the molecular wave functions is still smaller than the transport voltage.

We thank J. von Delft, J. König, L. Borda, M. Sindel, A.W. Holleitner, A.K. Hüttel, and E.M. Höhberger for clarifying discussions. We acknowledge financial support from ARO, Contract No. P-43385-PH-QC.

*Corresponding author. Email address: hartmann@theorie.physik.uni-muenchen.de.

¹R.C. Ashoori, *Nature* (London) **379**, 413 (1996).

²F.R. Waugh *et al.*, *Phys. Rev. Lett.* **75**, 705 (1995).

³R.H. Blick *et al.*, *Phys. Rev. Lett.* **80**, 4032 (1998).

⁴A.W. Holleitner *et al.*, *Science* **297**, 70 (2002).

⁵R.H. Blick and H. Lorenz, *Proc. ISCAS 2000*, II245 (2000).

⁶U. Hartmann and F.K. Wilhelm, *Phys. Status Solidi B* **233**, 385 (2002).

⁷L.P. Kouwenhoven *et al.*, in *Mesoscopic Electron Transport*, Vol. 345 of *NATO Advanced Studies Institute, Series E: Applied Sciences*, edited by L.L. Sohn, L.P. Kouwenhoven, and Gerd Schön (Kluwer Academic, Dordrecht, 1997), p. 105.

⁸W.G. van der Wiel *et al.*, *Rev. Mod. Phys.* **75**, 1 (2003).

⁹T.H. Stoof and Yu.V. Nazarov, *Phys. Rev. B* **53**, 1050 (1996).

¹⁰See e.g., L. Borda *et al.*, *Phys. Rev. Lett.* **90**, 026602 (2003).

¹¹D. V. Averin and Yu. V. Nazarov, in *Single Charge Tunneling*, Vol. 294 of *NATO Advanced Studies Institute, Series B: Physics*, edited by H. Grabert and M. H. Devoret (Plenum, New York, 1992), pp. 217–247.

¹²S. De Franceschi *et al.*, *Phys. Rev. Lett.* **86**, 878 (2001).

¹³J.R. Schrieffer and P.A. Wolff, *Phys. Rev.* **149**, 491 (1966).

¹⁴C. Cohen-Tannoudij, J. Dupont-Roc, and G. Grynberg, *Atom-Photon Interactions* (Wiley, New York, 1992).

¹⁵U. Hartmann, Master’s thesis, University of Bonn, 2002; U. Hartmann and F. K. Wilhelm (unpublished).

¹⁶P.N. Agyres and P.L. Kelley, *Phys. Rev.* **A134**, 98 (1964).

¹⁷L. Hartmann, I. Goychuk, M. Grifoni, and P. Hänggi, *Phys. Rev. E* **61**, R4687 (2000).

¹⁸U. Weiss, *Quantum Dissipative Systems*, 2nd ed. (World Scientific, Singapore, 1999).

¹⁹G. D. Mahan, *Many-Particle Physics*, 3rd ed. (Kluwer Academic, New York, 2000).

²⁰M.R. Wegewijs and Yu.V. Nazarov, cond-mat/0103579 (unpublished).

²¹H. Qin, A.W. Holleitner, K. Eberl, and R.H. Blick, *Phys. Rev. B* **64**, 241302 (2001).

²²T.H. Oosterkamp *et al.*, *Nature* (London) **395**, 873 (1998).

²³B.L. Hazelzet, M.R. Wegewijs, T.H. Stoof, and Yu.V. Nazarov, *Phys. Rev. B* **63**, 165313 (2001).

²⁴T. Brandes and B. Kramer, *Phys. Rev. Lett.* **83**, 3021 (1999).

²⁵J. König, H. Schoeller, and G. Schön, *Phys. Rev. Lett.* **78**, 4482 (1997).

²⁶E.V. Sukhorukov, G. Burkard, and D. Loss, *Phys. Rev. B* **63**, 125315 (2001).

²⁷H.B. Weber *et al.*, *Chem. Phys.* (to be published).

²⁸J. Heurich, J.C. Cuevas, W. Wenzel, and G. Schön, *Phys. Rev. Lett.* **88**, 256803 (2002).

Control of decoherence through disequilibrium between two baths

Udo Hartmann* and Frank K. Wilhelm

Sektion Physik and CeNS, Ludwig-Maximilians-Universität, Theresienstr. 37, D-80333 München, Germany

(Dated: February 28, 2003)

We analyze the decoherence of a two-state system (TSS) coupled to two baths being in mutual disequilibrium: a double quantum dot in the cotunneling regime at finite voltage. This system is treated using the Bloch-Redfield generalized master equation for the Schrieffer-Wolff transformed Hamiltonian. We show that the decoherence, characterized through a relaxation τ_r and a dephasing time τ_ϕ , can be controlled through the external voltage and that the optimum point where these times are maximum is not necessarily in equilibrium. We discuss the relevance of our results for recently proposed charge qubit realizations and show how they can be experimentally verified.

PACS numbers: 03.67.Lx, 05.40.-a, 73.21.La, 72.70.+m

The loss of quantum coherence is one of the central paradigms of modern physics. It not only governs the transition between the quantum-mechanical and the classical world, but has recently also gained practical importance in the context of engineering quantum computing devices. Decoherence naturally occurs in small quantum systems coupled to macroscopic heat baths. A huge class of such baths generates Gaussian noise and can hence be mapped on an ensemble of harmonic oscillators as in the Spin-Boson model [1]. This can even apply, if the fundamental degrees of freedom of the bath are Fermions [2], as it is e.g. the case if the bath is a linear electrical circuit [3, 4, 5], which is producing Gaussian Johnson-Nyquist noise. In the case of a quantum system simultaneously coupled to two distinct particle reservoirs, the situation is different: The leads can have different chemical potentials. Oscillator baths cannot straightforwardly account for this, as their quanta are not conserved particles. As a matter of fact, it is also known that at sufficiently large voltages, $V > k_B T/e$, the noise of two baths exchanging particles is shot-noise which is strongly non-Gaussian [6].

This setting introduces a new parameter for controlling the decoherence properties of the system, the voltage, and naturally raises the question, under which conditions the decoherence is minimal. One may naïvely assume, that this is the point of equilibrium, when there is no *net* exchange of particles which disturb the quantum system between the reservoirs. The central result of the paper will be that this is not true in general.

We study a well-defined realization of such a setup, a double quantum dot in the cotunneling regime. As in the Gaussian case, one has to distinguish between relaxation and dephasing: Dephasing is the loss of phase information of the quantum states, manifest through the decay of coherent oscillations. This corresponds to the time evolution of the off-diagonal elements of the reduced density matrix expressed in the energy eigenbasis. Relaxation is the process during which a TSS exchanges energy with the environment and ends up in a stationary state. This is described through the time evolution of the diagonal density matrix elements. We are going to show

that our system possesses two competing optimum working points: An out-of equilibrium one at a finite voltage, where energy relaxation is suppressed, and an equilibrium working point, where flipless dephasing processes can be suppressed. Depending on the choice of parameters, the former one may have least decoherence. Our work also provides a theory for the cotunneling contribution to the decoherence of quantum dot charge quantum bits [7].

As a prototype system for studying the properties of discrete quantum states in a macroscopic environment, we study serially coupled lateral quantum dots (i.e. an artificial molecule [8]). The existence of coherent molecular states in these systems has been demonstrated experimentally [9, 10] and they have been proposed as charge quantum bits [7, 11].

The computational basis is formed by the position eigenstates of an additional electron (either left or right dot). A superposition of these two states can be created by variation of the inter-dot coupling. In order to have a stable TSS, the coupling of the dots to the two leads is very weak and additionally the dot is tuned to the Coulomb Blockade regime [12], where sequential tunneling is suppressed through the addition energy. Even then, the system couples to the environment through the cotunneling mechanism [13], the coherent exchange of two electrons with the external leads which ends up in a state with the same charge as the initial one.

In our specific model, the relevant Hilbert space is spanned by four basis states, written as $|i, j\rangle$, which denotes i additional electrons on the left dot, j additional electrons on the right dot. The two states $|1, 0\rangle$ and $|0, 1\rangle$ define the computational basis [14] because they are energetically accessible, the closest virtual intermediate states for cotunneling are $|v_0\rangle = |0, 0\rangle$ and $|v_2\rangle = |1, 1\rangle$.

The Hamiltonian of this system can be written as $H = H_0 + H_1$ where $H_0 = H_{\text{sys}} + H_{\text{res}}$ describes the energy spectrum of the isolated double-dot through $H_{\text{sys}} = \varepsilon_{\text{as}}(a^{L\dagger}a^L - a^{R\dagger}a^R) - \varepsilon_\alpha \hat{n}_{v_0} + \varepsilon_\beta \hat{n}_{v_2} + \gamma(a^{L\dagger}a^R + a^{R\dagger}a^L)$ and the two electronic leads $H_{\text{res}} = \sum_{\vec{k}} \varepsilon_{\vec{k}}^L b_{\vec{k}}^{L\dagger} b_{\vec{k}}^L + \sum_{\vec{k}'} \varepsilon_{\vec{k}'}^R b_{\vec{k}'}^{R\dagger} b_{\vec{k}'}^R$. The sum over dot states only runs over the

restricted Hilbert space described above, the $a^{L/R}$ act on the lowest additional electron state on either dot. The double-dot is characterized by the asymmetry energy ε_{as} between the individual dots and the interdot tunnel coupling γ . The virtual states $|v_2\rangle$ and $|v_0\rangle$ are separated by energy differences ε_β and ε_α towards the higher level $|v_2\rangle$ and the lower level $|v_0\rangle$ respectively. The tunneling part $H_1 = t_c \sum_{\vec{k},n} (a_n^L \dagger b_{\vec{k}}^L + a_n^L b_{\vec{k}}^L \dagger) + t_c \sum_{\vec{k}',m} (a_m^R \dagger b_{\vec{k}'}^R + a_m^R b_{\vec{k}'}^R \dagger)$ describes the coupling of each dot to its lead and will be treated as a perturbation. For simplicity, the analysis is restricted to spin-polarized electrons. Fig. 1 shows a sketch of the system under consideration.

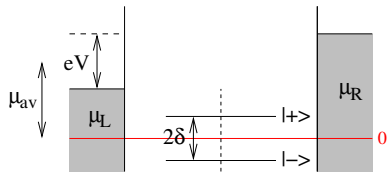


FIG. 1: Sketch of the considered artificial molecule, where 2δ is the level splitting and V the bias voltage, that is applied between the two leads (grey).

From now on, we use the molecular basis obtained by diagonalizing H_{sys} , the eigenstates of which are molecular wavefunctions with energy splitting $2\delta = 2\sqrt{\varepsilon_{\text{as}}^2 + \gamma^2}$. In order to capture cotunneling by leading-order perturbation theory in the density matrix, we rewrite H_1 using a Schrieffer-Wolff transformation [15], which removes the transitions to the virtual states and generates an effective Hamiltonian containing indirect transition terms between the molecular states. The basic formulae of this procedure are found in [16] and a more detailed description of our calculation is given in [11, 17]. The final coupling Hamiltonian is of the general form $H = H_0 + H'_1$ where $H'_1 = \sum_{i,j,n,m,\vec{k},\vec{k}'} A_{ij}(n,m,\vec{k},\vec{k}') \alpha_n^\dagger \alpha_m b_{\vec{k}}^{i\dagger} b_{\vec{k}'}^j + \text{h.c.}$ where i and j denote right or left lead, the α s are operators in the molecular basis and the coefficients A_{ij} are given through usual second order perturbation theory with energy denominators containing the energy cost of the intermediate state. Note that H'_1 conserves the particle number, because it acts upon the double-dot by injecting and extracting an electron in a single step. Hence, the terms with $i \neq j$ transfer charge between different reservoirs.

In order to describe the open system dynamics, we derive an effective master equation using the well-established and controlled Bloch-Redfield theory [18], which has been demonstrated to work well down to low temperature for certain models [19]. It involves a Born approximation in H'_1 , i.e. by virtue of the Schrieffer-Wolff transformation it captures all cotunneling processes in lowest nonvanishing order.

The Redfield equations [2] for the elements of the reduced density matrix ρ in the eigenstate basis of H_{sys}

(i.e. the molecular basis) read

$$\dot{\rho}_{nm}(t) = -i\omega_{nm}(t)\rho_{nm}(t) - \sum_{k,l} R_{nmkl}\rho_{kl}(t), \quad (1)$$

where $\omega_{nm} = (E_n - E_m)/\hbar$ and R_{nmkl} are the Redfield tensor elements, which are given by a large number of Golden Rule rates describing different cotunneling processes, which are essentially independent due to the low symmetry of the system. Each process contributes a typical cotunneling rate of the type outlined in Ref. [11, 17]. An overview of the most important processes is given below with the discussion of our results. n, m, k and l can be either $+$ (excited molecular state) or $-$ (molecular ground state). The E s are the eigenenergies of the two molecular states.

We restrict ourselves to the undriven case with a time-independent Hamiltonian, where the Bloch-Redfield equation eq. (1) is readily solved. From the solution, we can identify coherent dynamics as well as incoherent relaxation and up to lowest order in R the relaxation and dephasing rates read

$$\Gamma_r = \text{Re}(R_{++++} + R_{----}) = \frac{1}{\tau_r} \quad (2)$$

$$\Gamma_\phi = \text{Re}(R_{+--+}) = \text{Re}(R_{-++-}) = \frac{1}{\tau_\phi}, \quad (3)$$

where the R_{nmkl} are again the elements of the Redfield tensor. Note that there are also weak renormalization effects, which are discussed elsewhere [17].

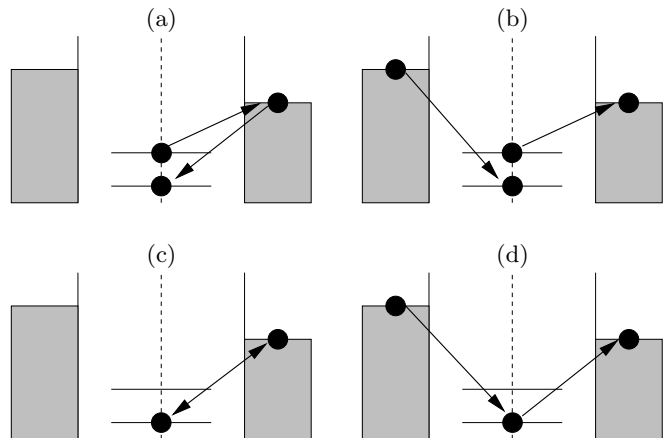


FIG. 2: Examples for relevant processes in the system: (a) a relaxation process that carries no current, (b) a relaxation process with current, (c) a pure dephasing process without current flow and (d) a current-carrying dephasing process.

Fig. 2 shows a choice of processes, which contribute to the Redfield tensor. All processes contribute to dephasing, because at least the phase information is always lost, if an electron is injected from the reservoirs. (a) and (b) illustrate relaxation processes. Note that only (b) carries

a current, i.e. in general the *relaxation* rate must not be confused with the cotunneling *current*. In (c) and (d) two pure dephasing processes are presented, only in (d) a cotunneling current flows through the TSS. In general, processes without current can emerge, if the cotunneling processes take place between a *single* lead and the TSS.

We have evaluated the rates entering eqs. (2)-(3) using the A_{ij} . Due to the high number of terms, details are not shown and will be given elsewhere [17].

We now turn to the discussion of our results. In the figures below, we normalized all times by $T_\delta = \frac{2\pi\hbar}{2\delta}$, which is the period of coherent oscillations between the two molecular states. We start with the discussion of the dependence of the relaxation time τ_r on the transport voltage $V = \mu_R - \mu_L$. We observe in Fig. 3 that for an asym-

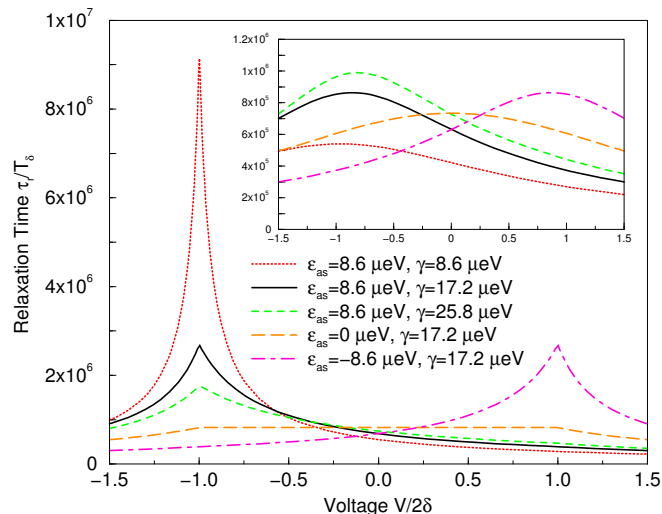


FIG. 3: Relaxation time τ_r for different values of ϵ_{as} and γ , when the bias voltage $V/2\delta$ is varied (with $T = 0.1$ mK and $\mu_{av} = (\mu_R + \mu_L)/2 = 75.832 \mu\text{eV}$); inset: $T = 140$ mK.

metric TSS, i.e. for $\epsilon_{as} \neq 0$, there is a pronounced peak of the relaxation time at $V = -\text{sgn}(\epsilon_{as})2\delta$, i.e. the sign has to be chosen with opposite polarity to the asymmetry energy. This means in particular, that the relaxation is minimal far away from equilibrium. For quantum computation, achieving a maximum relaxation time is e.g. appreciable during *read-out* [3, 4].

The appearance of the peaks in Fig. 3 can be understood by investigating the different classes of relaxation processes contributing to eq. (2), notably the current-carrying processes, [e.g. Fig. 2 (b) and (d)] as schematically shown in Fig. 5 for low temperatures. At low voltages, $|V| < 2\delta$, the system relaxes into a thermal state, which at low temperature is close to the ground state. Relaxation takes place by spontaneous emission of energy into the environment and creation of an electron-hole pair in the leads. This pair can recombine through the electrical circuit, which fixes the electrochemical potentials. This manifests itself as electrical current. As the

voltage is increased away from $V = 0$, emission processes which lead to a current *against* the polarity of the source are suppressed, the others are increased, see Figs. 5 (a) and (b). Depending on the asymmetry of the double dot, i.e. on the weight of the excited state on the left and the right dot, this leads to an enhancement or a suppression of the rate. At $|V| \geq 2\delta$, the emission processes against the source are completely blocked: The dot relaxation does not provide enough energy to overcome the electromotive force. The rate vanishes *linearly* as a function of voltage reflecting the size of the available phase space for cotunneling, see Fig. (5).

At higher voltages, $|V| \geq 2\delta$, inelastic cotunneling [20] sets in, see Figs. 5 (c) and (d): The source provides enough energy to even excite the double dot, creating a nonequilibrium steady-state population of the molecular levels. Hence, inelastic cotunneling provides a way for the dot to *absorb* energy from the environment even at low temperature. This process can be experimentally identified by a sharp increase of the current [11, 20].

Hence, at $V = \pm 2\delta$, three of the four processes depicted in Fig. 5 vanish at low temperatures, whereas at $V = 0$ only two vanish. The linear voltage-dependence of the rates leads to the rather sharp cusps seen in Fig. 3. This behavior is smeared at higher temperatures by Bose-function-type factors. The peak height is set by the remaining processes: Energy emission *with* the source and current-less relaxation, Fig. 2 (a). As explained above, the relative weight of the former strongly depends on the weight of the excited molecular state on the individual dots and thus is responsible for the strong asymmetry of the peaks in Fig. 3 for different asymmetry energies.

Next, we analyze the properties of the dephasing time τ_ϕ as a function of the bias voltage. The total dephasing

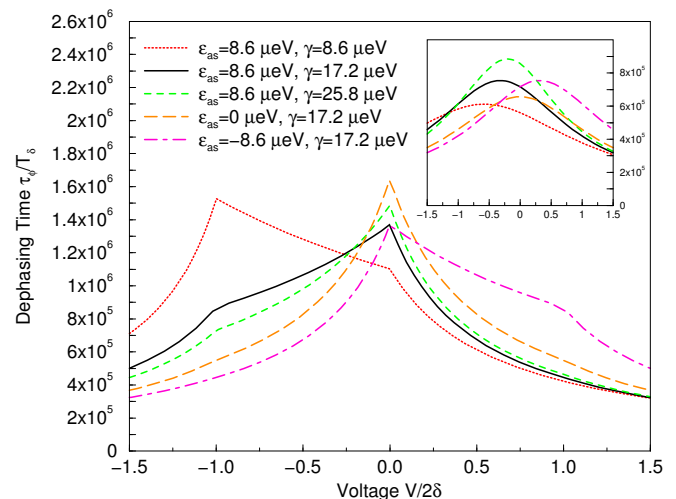


FIG. 4: Dephasing time τ_ϕ for different values of ϵ_{as} and γ , when the bias voltage $V/2\delta$ is varied (with $T = 0.1$ mK and $\mu_{av} = (\mu_R + \mu_L)/2 = 75.832 \mu\text{eV}$); inset: $T = 140$ mK.

rate contains relaxing as well as flipless (“elastic”) pro-

cesses. We hence observe in Fig. 4 a peak structure at $V = -\text{sgn}(\varepsilon_{\text{as}})2\delta$ as in the relaxation time, Fig. 3 and a similar structure at $V = 0$. The physics of the peak at $V = 0$ can be understood due to the suppression of flip-flop processes (energy exchange 0) in an analogous way to the peak in Fig. 3 (energy exchange 2δ). Depending on the degree of asymmetry, the one or the other peak is higher: at low asymmetry energy $\varepsilon_{\text{as}} < \gamma$, the dephasing time at $V = 0$ is longest and for higher asymmetry $\varepsilon_{\text{as}} \geq \gamma$, this is the case at $V = \pm 2\delta$. In general, this indicates the existence of two preferable working points for quantum computation: One *in* equilibrium, the other again *far from* equilibrium. $V = -2\text{sgn}(\varepsilon_{\text{as}})\delta$ is even longer. The curves for different signs of ε_{as} again reflect mirror symmetry. As also already seen in the inset of Fig. 3, the voltage dependence at higher temperature is smeared out and the characteristics of the two peaks is lost.

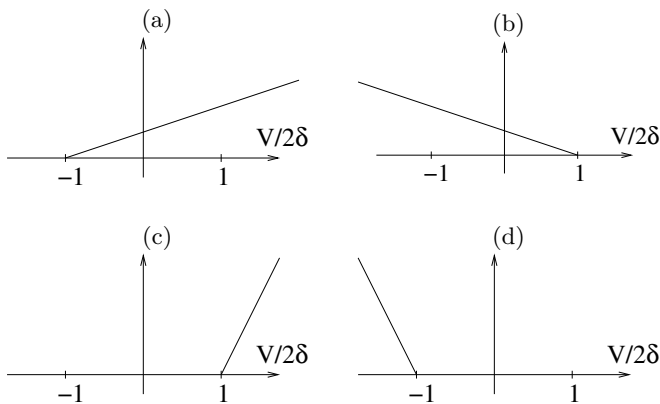


FIG. 5: Qualitative voltage dependence of the rates of “emission” [(a) and (b)] and “absorption” [(c) and (d)] processes, see text

A measurement of the relaxation and dephasing times should be feasible by the following methods: a time-resolved measurement of $\langle \sigma_z(t) \rangle$, e.g. through a single-electron transistor observing the charge on one of the dots [3], the saturation broadening method [21] or resonance schemes such as proposed in Ref. [22] for spins.

Note that parts of the double-dot literature focus on decoherence through phonons/photons (see Refs. 10, 23, 24, 25), whereas we focus on cotunneling. Our results indicate that, as long as phonons are not suppressed by an appropriate cavity [26], they give the main contribution, such that our results describe the next evolutionary step in the development of double quantum dot charge qubits.

To conclude, we have chosen a generic and realistic model system to describe decoherence through coupling to reservoirs in disequilibrium, a double quantum dot in the cotunneling regime. We have shown that decoherence can be controlled through a bias voltage V (and thus creating a non-equilibrium situation) between the two fermionic baths. In particular, the optimum working

point for read-out and potentially also for operation of the qubit can be in an out-of-equilibrium situation at a voltage $V = -\text{sgn}(\varepsilon_{\text{as}})2\delta$. We have given a consistent physical interpretation of our findings in terms of stability and phase space.

We thank J. von Delft, L. Borda, J. König, M.J. Storcz, A.W. Holleitner, A.K. Hüttel and E.M. Höhberger for clarifying discussions. We acknowledge financial support from ARO, Contract-No. P-43385-PH-QC.

* Correspondence to

hartmann@theorie.physik.uni-muenchen.de

- [1] A.J. Leggett et al., Rev. Mod. Phys. **59**, 1 (1987).
- [2] U. Weiss, *Quantum dissipative systems, 2nd ed.*, (World Scientific, Singapore, 1999).
- [3] Y. Makhlin, Gerd Schön and Alexander Shnirman, Rev. Mod. Phys. **73**, 357 (2001).
- [4] C.H. van der Wal, F.K. Wilhelm, C.J.P.M. Harmans, and J.E. Mooij, Eur. Phys. J. B **31**, 111 (2003).
- [5] see e.g. F.K. Wilhelm, G. Schön, and G.T. Zimanyi, Phys. Rev. Lett. **87**, 136802 (2001).
- [6] see e.g. Yu. V. Nazarov and D.A. Bagrets, Phys. Rev. Lett. **88**, 196801 (2002).
- [7] R.H. Blick and H. Lorenz, ISCAS 2000 proceedings, pp. II245-II248.
- [8] R.C. Ashoori, Nature **379**, 413 (1996).
- [9] F.R. Waugh et al., Phys. Rev. Lett. **75**, 705 (1995).
- [10] T.H. Oosterkamp et al., Nature **395**, 873 (1998).
- [11] U. Hartmann and F.K. Wilhelm, phys. stat. sol. (b) **233**, No. 3, pp. 385-390 (2002); U. Hartmann and F.K. Wilhelm, cond-mat/0212063 (2002).
- [12] W.G. van der Wiel et al., Rev. Mod. Phys. **75**, 1 (2003).
- [13] D.V. Averin and Y.V. Nazarov in *Single Charge Tunneling* (eds H. Grabert and M.H. Devoret), Proc. NATO ASI Ser. B 294, (Plenum, New York, 1992), pp. 217-247.
- [14] M.A. Nielsen and I.L. Chuang, *Quantum Computation and Quantum Information*, (CUP, Cambridge, 2000).
- [15] J.R. Schrieffer and P.A. Wolff, Phys. Rev. **149**, 491 (1966).
- [16] C. Cohen-Tannoudij, J. Dupont-Roc, and G. Grynberg, *Atom-Photon Interactions* (Wiley, N.Y., 1992).
- [17] U. Hartmann, master’s thesis and U. Hartmann and F.K. Wilhelm, in preparation.
- [18] P.N. Agyres and P.L. Kelley, Phys. Rev. **134**, A 98 (1964).
- [19] L. Hartmann, I. Goychuk, M. Grifoni and P. Hänggi, Phys. Rev. E **61**, R4687 (2000).
- [20] S. De Franceschi et al., Phys. Rev. Lett. **86**, 878 (2001).
- [21] M.C. Goorden and F.K. Wilhelm, submitted to Phys. Rev. B (2002).
- [22] H.-A. Engel and D. Loss, Phys. Rev. Lett. **86**, 4648 (2001); Phys. Rev. B **65**, 195321, (2002).
- [23] H. Qin, A.W. Holleitner, K. Eberl and R.H. Blick, Phys. Rev. B **64**, 241302 (2001).
- [24] B.L. Hazelzet, M.R. Wegewijs, T.H. Stoof and Yu.V. Nazarov, Phys. Rev. B **63**, 165313 (2001).
- [25] T. Brandes and B. Kramer, Phys. Rev. Lett. **83**, 3021 (1999).
- [26] J. Kirschbaum et al., Appl. Phys. Lett. **81**, 280 (2002).

3.8 Mesoscopic Josephson junctions with conducting barriers

This work is a continuation and generalization of an idea already presented in my PhD-thesis: the tunable π -junction effect previously studied in mesoscopic superconductor-normal metal-superconductor (SNS) junctions with a control line. Ref. [205] provides a detailed quantitative study of that effect, including the influence of imperfections, such as different geometries and nonideal interfaces. It is shown that this effect is relatively robust and, e.g., can also be found in short SNS-junctions, which can support much higher critical current than long ones.

Ref. [206] departs from previous work in the choice of materials. It is shown, that the tunable π -junction phenomenon bears some analogy to the π -junction effect predicted (and later observed) in ferromagnetic junctions: Essentially, the interference leading to the supercurrent is modified by changing the distribution of the available electrons: In the former case, these are electrons from two different leads, in the latter, the two different spins separated by exchange or Zeeman fields. It is shown that in a controlled SFS-junction, both effects can be defined and that one half of the supercurrent from the case of a nonmagnetic barrier can be recovered by compensating the exchange field through a control voltage of the same magnitude.

All the theoretical work compiled in this section has been done using the microscopic quasiclassical Green's function technique in the diffusive limit. This is a very efficient and well-established method which contains a number of systematic and controlled approximations. The accuracy of the approach is, together with the high level of present day experimentation, demonstrated in Ref. [207]. The Josephson critical current for a junction with good metallic contacts is calculated for different lengths d of the junction, parameterized by the Thouless energy, $E_{\text{Th}} = \mathcal{D}/d^2$, where \mathcal{D} is the diffusion constant. This energy is compared with the superconducting gap Δ . It is found that for short junctions, the critical current times the normal state resistance at zero temperature is given by the gap as predicted by the Ambegaokar-Baratoff formula. For long junctions, the Thouless energy limits the current to $I_c R_N/e = 10.8 E_{\text{Th}}$. Theory and experiment are compared at different temperatures and show excellent agreement over several decades of the current.

Ref. [208] considers a geometry with an important difference: Instead

of a control-line, only a single control-terminal is used, turning the setup into a transistor-like 3-terminal device. It is shown, that the π -junction effect persists and has, in the absence of inelastic scattering, the same magnitude as in four-terminal devices. On top of this, it is more immune to inelastic effects due to a subtle restriction of scattering phase space. The paper focuses on an experimental realization of the device which can be fitted quantitatively within our theoretical model.

As is shown in Ref. [209], the three terminal setup has a number of additional features due to the parallel and antiparallel flow of the dissipative current to the supercurrent in the arms. Injecting nonequilibrium quasiparticles into a supercurrent-carrying state leads to a superflow of heat. As the normal-superconductor interface is a perfect insulator, this total flow has to be compensated by a dissipative heat flow driven by a gradient of the effective temperature. Thus, the supercurrent leads to an effective temperature gradient, which can be interpreted as a generalized Peltier-effect. In contrast to usual thermoelectric effects, this effect does not depend on subtleties of the lattice or electron-hole symmetry breaking and is thus typically much larger.

Supercurrent-carrying density of states in diffusive mesoscopic Josephson weak linksTero T. Heikkilä^{1,2,*}, Jani Särkkä,¹ and Frank K. Wilhelm³¹*Materials Physics Laboratory, Helsinki University of Technology, P.O. Box 2200, FIN-02015 HUT, Finland*²*Institut für Theoretische Festkörperphysik, Universität Karlsruhe, D-76128 Karlsruhe, Germany*³*Sektion Physik and CeNS, Ludwig-Maximilians-Universität, Theresienstr. 37, D-80333 München, Germany*

(Received 3 May 2002; revised manuscript received 16 July 2002; published 26 November 2002)

Recent experiments have demonstrated the nonequilibrium control of the supercurrent through diffusive phase-coherent normal-metal weak links. The experimental results have been accurately described by the quasiclassical Green's-function technique in the Keldysh formalism. Taking into account the geometry of the structure, different energy scales, and the nonidealities at the interfaces allows us to obtain a quantitative agreement between the theory and the experimental results in both the amplitude and the phase dependence of the supercurrent, with no or very few fitting parameters. Here we discuss the most important factors involved with such comparisons: the ratio between the superconducting order parameter and the Thouless energy of the junction, the effect of additional wires on the weak link, and the effects due to imperfections, most notably due to the nonideal interfaces.

DOI: 10.1103/PhysRevB.66.184513

PACS number(s): 74.50.+r, 73.23.-b, 74.40.+k, 74.80.Fp

I. INTRODUCTION

Many quantum phenomena in many-body systems are based on probing the spectrum of states corresponding to the desired observable, the states being filled according to an appropriate distribution function. A similar viewpoint can be taken also on the Josephson effect: supercurrent is carried by states in the weak link and their occupation is determined by a distribution function antisymmetric between the electron and hole spaces. This aspect is directly reflected in the mathematical structure of the supercurrent formula derived from the Keldysh Green's-functions method.¹⁻³ Such an approach has been taken in some recent experiments⁴⁻⁹ controlling the Josephson effect in phase-coherent normal-metal wires through the control of the distribution function by an injection of normal quasiparticle current. One of the most remarkable results of these experiments is the inversion of the sign of the supercurrent for a given phase difference across the weak link when the junctions turn into a π state.

Quantitative fit to the experimentally obtained results has been very successful for the equilibrium supercurrent¹⁰ using the equilibrium quasiclassical theory. In the nonequilibrium case, detailed knowledge of the relaxation mechanisms controlling the shape of the interactions, but also the precise spectrum of supercurrent-carrying states, is required.^{6,8} Previously,¹ for the calculation of this spectrum, one has assumed a two-probe setup with some idealized conditions on the length scales and on the nature of the interfaces. In this paper, we systematically investigate the spectrum of this current-carrying density of states, or spectral supercurrent, show how it is calculated, and how it depends on the length of the weak link, presence of additional terminals, or on the nonidealities in the interfaces between the normal-metal weak link and the superconductors. We also discuss the current-phase relation of such a system: at low temperatures, it can be far from sinusoidal, and at certain conditions, its period can even be halved.¹¹ We focus on the diffusive limit where the dimensions d of the weak link are much greater than the elastic mean free path l . This is the typical limit for

most normal-metal weak links. The corresponding ballistic limit $d \ll l$ has been extensively described in the literature¹²⁻¹⁸ in terms of Andreev bound states (ABS). We show qualitatively a connection between the discrete ABS and the continuous diffusive-limit spectral supercurrent.

This paper is organized as follows. After this introduction, Sec. II introduces to the theoretical formalism which is based on the real-time Usadel equation for the quasiclassical Green's function in the diffusive limit.^{19,20} In the case of nonideal interfaces or in multiterminal geometries, the boundary conditions to these functions are also essential. Understanding the results of the following sections does not require a detailed reading of this part but it is enough to grasp the idea of the relation of the spectral supercurrent and the observable one. In Sec. III we look how the spectral supercurrent depends on the length of the weak link compared to the superconducting coherence length and separate two extreme cases. In the limit of a short junction where the coherence length is much longer than the weak link, one obtains an analytical solution for the spectral supercurrent without further approximations. The current-phase relation in diffusive normal-metal weak links is considered in Sec. IV. We show how, especially at low temperatures, higher harmonics appear in addition to the usual sinusoidal phase dependence and indicate how the period can be halved in a nonequilibrium situation. Section V considers the effect of additional normal-metal terminals on the current-carrying density of states, and in Sec. VI, we discuss how nonidealities in the normal metal – superconductor (NS) interface change its shape. Finally, in Sec. VII, we summarize the main results.

To be specific, we consider the structure shown in Fig. 1. The main wire with length L and cross section A_w between the superconductors forms the weak link whereas the additional wires with length L_c and integrated cross section A_c are used for the control of the distribution functions and therefore referred to as the control wires. We assume that the superconducting and normal reservoirs are much larger than

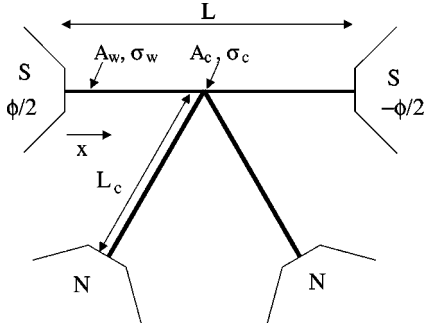


FIG. 1. Multiterminal SNS Josephson junction. The weak link consists of a phase coherent normal-metal wire of length L , cross section A_w , and normal-state conductivity σ_w , yielding a normal-state resistance $R_N = L/\sigma_w A_w$. Additional normal-metal wires of length L_c , total cross section A_c , and normal-state conductivity σ_c , i.e., with resistance $R_c = L_c/\sigma_w A_w$, called the control wires, are connected to the center of the weak link, and from their other end, to normal reservoirs.

the weak link and the control wire, such that the Green's functions describing them take their bulk values very close to the interfaces. Furthermore, we assume that the width of the control wires is much smaller than the length L of the weak links. This allows us to consider the wires as quasi-one-dimensional (1D) structures by assuming translational invariance in the transverse directions.

II. THEORETICAL BACKGROUND

Circuits composed of normal and superconducting metals in the diffusive limit (dimensions larger than the elastic mean free path l) are effectively described in terms of the quasi-classical Green's functions \check{G} satisfying the Usadel equations^{19,20}

$$D\nabla(\check{G}\nabla\check{G}) = [-i(E + i\Gamma)\check{\tau}_3 + \check{\Delta}, \check{G}], \quad (1)$$

where $D = \frac{1}{3}v_F l$ is the diffusion constant, E is energy relative to the chemical potential of the superconductors (which is assumed to be the same for all S terminals), Γ describes a small inelastic scattering rate, and $\check{\Delta}$ the superconducting pair potential (we set $\hbar = 1$ throughout). Since we aim to describe nonequilibrium effects, we adopt the Keldysh real-time formalism²¹ and hence

$$\check{G} = \begin{pmatrix} \hat{G}^R & \hat{G}^K \\ 0 & \hat{G}^A \end{pmatrix}, \quad \check{\Delta} = \begin{pmatrix} \hat{\Delta} & 0 \\ 0 & \hat{\Delta} \end{pmatrix}, \quad \check{\tau}_3 = \begin{pmatrix} \hat{\tau}_3 & 0 \\ 0 & \hat{\tau}_3 \end{pmatrix}. \quad (2)$$

All of the submatrices denoted by a hat (\hat{G}^R , etc.) are 2×2 matrices in Nambu particle-hole space, in particular, $\hat{\tau}_3$ is the third Pauli matrix and $\hat{\Delta}$ has the form

$$\hat{\Delta} = \begin{pmatrix} 0 & \Delta(x) \\ \Delta^*(x) & 0 \end{pmatrix}. \quad (3)$$

The pair potential $\Delta(x)$ can in principle be obtained from a self-consistency relation.^{20,22} However, since we consider

only superconducting reservoirs much wider than the weak link, we adopt the usual step-function form for $\Delta(x)$ (finite constant in the superconductors, zero in the normal-metal wires).

In addition to Eq. (1), Usadel Green's function satisfies a normalization condition $\check{G}^2 = \check{1}$. Therefore it can be parametrized with four scalar parameters as follows.²⁰ The Keldysh Green's function \hat{G}^K describing the occupation numbers of different quantum states, i.e., the (non)equilibrium state of the system can be expressed with two real distribution functions f_L and f_T as $\hat{G}^K = \hat{G}^R(f_L + f_T\hat{\tau}_3) - (f_L + f_T\hat{\tau}_3)\hat{G}^A$ whereas the retarded and advanced Green's functions, \hat{G}^R and \hat{G}^A , describing the spectral properties which do not directly depend on the distribution functions are

$$\hat{G}^R = \begin{pmatrix} \cosh(\theta) & \sinh(\theta)\exp(i\chi) \\ -\sinh(\theta)\exp(-i\chi) & -\cosh(\theta) \end{pmatrix} \quad (4)$$

and $\hat{G}^A = -\hat{\tau}_3(\hat{G}^R)^\dagger\hat{\tau}_3$. Here $\theta(x; E)$ and $\chi(x; E)$ are in general complex scalar functions.

In what follows, we describe a quasi-one-dimensional situation, where the functions are assumed to vary only in one dimension x . Expressing the coordinate x in terms of the separation L of the superconductors between which the supercurrent flows, $x \equiv x'L$, the spectral equations for $\hat{G}^{R(A)}$ read in a normal metal ($\Delta = 0$)

$$\partial_x^2 \theta = -2i(E' + i\Gamma')\sinh(\theta) + \frac{1}{2}(\partial_x \chi)^2 \sinh(2\theta), \quad (5)$$

$$j_E \equiv -\sinh^2(\theta)\partial_x \chi, \quad \partial_x j_E = 0. \quad (6)$$

Here, the prime over the (dimensionless) quantities denotes the fact that the energies are expressed in the units of the Thouless energy $E_T = D/L^2$ corresponding to the length L . Below, we tacitly assume all lengths and energies expressed in these natural units even if not marked by a prime. The kinetic equations satisfied by the distribution functions f_L and f_T are described, e.g., in Ref. 20, where the part of the distribution function which is symmetric about the chemical potential of the superconductors corresponds to f_T and the antisymmetric part to f_L . These two components acquire different space and energy dependent diffusion coefficients due to the superconducting proximity effect.

If the interfaces to the reservoirs are ideal metallic, the parameters are continuous at the boundaries to the reservoirs and can be identified with the bulk values, $\theta_S = \text{artanh}(\Delta/E)$ and $\theta_N = 0$ in the superconducting and normal-metal reservoirs, respectively. In general, e.g., if a supercurrent is driven through the system, there can be a phase difference, which we choose to be applied symmetrically between the superconductors, such that in the left superconductor $\chi = \phi/2$ and in the right $\chi = -\phi/2$. Below, if not mentioned otherwise, we choose $\phi = \pi/2$, which typically yields a supercurrent close to the critical current of the junction.

Nonideal interfaces with reduced transmissivities are not directly described by the Usadel equation, because they are

of microscopic, atomic-scale thickness. They can, however, be taken into account using boundary conditions derived by Zaitsev²³ for Eilenberger Green's functions (valid independent of the mean free path) and later simplified in the diffusive limit by Kuprianov and Lukichev for a tunnelling case²⁴ and Nazarov for a general interface,²⁵ described by a scattering matrix. For an interface characterized by the transmission eigenvalues T_n , the Green's functions \check{G}_1 on the right-hand side and \check{G}_2 on the left-hand side of the interface satisfy^{25,26}

$$\begin{aligned} \sigma_N^1 A_1 \check{G}_1 \partial_x \check{G}_1 &= \sigma_N^2 A_2 \check{G}_2 \partial_x \check{G}_2 \\ &= \frac{2e^2}{\pi} \sum_n \frac{T_n[\check{G}_1, \check{G}_2]}{4 + T_n(\{\check{G}_1, \check{G}_2\} - 2)}, \end{aligned} \quad (7)$$

evaluated at the position of the interface. In most cases, the individual transmission eigenvalues are not known, but since typical interfaces contain a huge number of channels, it is enough to integrate over the probability distribution of the eigenvalues to obtain the desired boundary condition.

In the case of a tunneling interface (where all the transmission eigenvalues of the interface are small) the boundary conditions between the parametrized functions in wires 1 and 2 reduce to^{20,24}

$$\partial_x \theta_1 = [\sinh(\theta_1) \cosh(\theta_2) - \sinh(\theta_2) \cosh(\theta_1) \cos(\Delta\chi)] / r_b, \quad (8)$$

$$\sinh^2(\theta_1) \partial_x \chi_1 = \sinh(\theta_1) \sinh(\theta_2) \sin(\Delta\chi) / r_b. \quad (9)$$

Here, $\Delta\chi \equiv \chi_1 - \chi_2$ and $\theta_{1(2)} \equiv \theta(x_b^{+(-)})$ and $\chi_{1(2)} \equiv \chi(x_b^{+(-)})$ are the parameters θ and χ at the interface, $x = x_b$, but on the side of the wire 1 (2). The nonideality of the interface is characterized by the ratio of its resistance R_I and of the weak-link resistance R_N , $r_b \equiv R_I / R_N$ and the derivatives point towards the wire 1. In the case of a dirty interface, where the boundary condition is evaluated using the distribution function of the transmission eigenvalues corresponding to an interface with a random array of scatterers in a 2D layer,²⁷ we get

$$\partial_x \theta_1 = \frac{\sqrt{2} [\sinh(\theta_1) \cosh(\theta_2) - \sinh(\theta_2) \cosh(\theta_1) \cos(\Delta\chi)]}{r_b \mathcal{D}}, \quad (10)$$

$$\sinh^2(\theta_1) \partial_x \chi_1 = \frac{\sqrt{2} \sinh(\theta_2) \sinh(\theta_1) \sin(\Delta\chi)}{r_b \mathcal{D}}. \quad (11)$$

Here we denoted the denominator $\mathcal{D} \equiv \sqrt{1 + \cosh(\theta_2) \cosh(\theta_1) - \sinh(\theta_2) \sinh(\theta_1) \cos(\Delta\chi)}$. This denominator reflects the contribution of open conduction channels which are not present in Eq. (9).

Note that both types of boundary conditions indicate a form of a conservation of a spectral current over the interface, the second equation being the conservation of the spectral supercurrent j_E .

In geometries with more than two terminals, we assume that narrow quasi-one-dimensional wires connect to each other at some point of the structure. Therefore we need to impose appropriate matching conditions.^{20,25,28,29} In this

case, they are the continuity of the functions θ and χ and the conservation of the spectral currents. Assuming that the derivatives in the N wires $i = 1, \dots, N$ with cross sections A_i and normal-state conductivities σ_N^i point towards the crossing point at x_c , we get

$$\theta_i(x_c) = \theta_j(x_c) \quad \forall i, j = 1, \dots, N, \quad (12)$$

$$\chi_i(x_c) = \chi_j(x_c) \quad \forall i, j = 1, \dots, N, \quad (13)$$

$$\sum_{i=1}^N A_i \sigma_N^i \partial_x \theta_i(x_c) = 0, \quad (14)$$

$$\sum_{i=1}^N A_i \sigma_N^i \partial_x \chi_i(x_c) = 0. \quad (15)$$

In the last condition we used the continuity of the parameters θ across the crossing point.

Below, we assume the system depicted in Fig. 1: two superconductors connected by "horizontal" mesoscopic normal wires to which we connect normal reservoirs by the "vertical" mesoscopic normal wires (labeling of the wires as in Fig. 1). When considering the supercurrent between the two superconductors, for the spectral equations it is enough to treat any number of "vertical" wires by a single wire for which the product of $\sigma_N A$ is simply the sum of these products in the individual wires. In the case that the dependence on the length L_c of these wires becomes important, the smallest of them characterizes the situation the best. In this case, since there can be no supercurrent flowing to the normal reservoirs, Eq. (15) reduces to $j_E^1 = -j_E^2$. Furthermore, for simplicity, we assume the system left-right symmetric, such that the part of the weak link in the left-hand side of the cross is similar to that in the right-hand side.

Finally, the observable supercurrent is obtained from the solutions to the spectral and kinetic equations by

$$I_S = \frac{E_T}{2eR_N} \int_{-\infty}^{\infty} dE' \text{Im}[j_E(E')] f_L(E'). \quad (16)$$

In the reservoirs with voltage V with respect to the potential of the superconductors (which are assumed equal for both superconductors in order to avoid the ac Josephson effect), f_L obtains the form

$$f_L(E; V, T) = \frac{1}{2} \left[\tanh\left(\frac{E + eV}{2k_B T}\right) + \tanh\left(\frac{E - eV}{2k_B T}\right) \right]. \quad (17)$$

It can be shown^{1,6} that, in the absence of inelastic interactions and for energies $E < \Delta$, f_L remains constant throughout the control wires, and hence the reservoir value can directly be used for the calculation of the supercurrent.

In this paper, we will consider two limits for f_L . These are the equilibrium finite-temperature limit, where $f_L = \tanh(E/2k_B T)$, and the zero-temperature nonequilibrium case when f_L is driven in a normal-metal wire,¹ $f_L = \vartheta(E - eV) - \vartheta(-eV - E)$, where $\vartheta(E)$ is the Heaviside step function.

The spectrum of supercurrent-carrying states typically consists of both the states carrying the supercurrent parallel to the phase gradient and those carrying it in the opposite direction,^{1,12} depending on their energy. Hence, by controlling the occupation of these states by the above steplike distribution function, one is able to vary the sign of the observable supercurrent and, e.g., obtain the π state.

The form of the spectrum can be qualitatively understood by considering a ballistic (scattering-free) weak link. There, the quasiparticles form bound states^{12–18} which contain an Andreev reflection³⁰ at both NS interfaces. Since the first reflection at the left is from hole- to particle (particle- to hole) -like states and the second at the right interface from particle- to hole (from a hole- to particle) -like states, the net result is a transfer of a Cooper pair from the left superconductor to the right (from right to left). Bound-state energies are found by requiring that the total phase the quasiparticles acquire within a single cycle is a multiple of 2π . This leads to (for $E_m \ll \Delta$)

$$E_m^\pm = \frac{1}{2\tau} \left[2\pi \left(m + \frac{1}{2} \right) \pm \phi \right], \quad (18)$$

the sign in front of the phase depending on the direction of the supercurrent flow. Here $\tau = v_F/L$ is the time of flight between two successive Andreev reflections and L is the corresponding length of the trajectory. The supercurrent-carrying density of states is then found from

$$j_S(E; \phi) \propto \sum_m \frac{\partial E_m^\pm}{\partial \phi} \delta(E - E_m), \quad (19)$$

resulting into a peaklike spectrum that contains states carrying both positive ($E = E_m^+$) and negative ($E = E_m^-$) supercurrent. In the presence of disorder, the distribution of the times of flight τ depends on the impurity potential and the spectral supercurrent is conveniently characterized by its impurity-averaged smooth density of states. However, the resulting spectrum still contains many properties similar to the clean limit, such as the varying sign of the supercurrent carried at different energies. This analogy holds, even though on a formal level, the calculation within our quasiclassical technique does not directly invoke these concepts.

III. SHORT- AND LONG-JUNCTION LIMITS

The spectrum of current-carrying states in the weak link depends very much on the ratio of the length L of the weak link and the superconducting coherence length $\xi_0 = \sqrt{D/2\Delta}$, or in other words, on the ratio between the superconducting order parameter Δ and the Thouless energy $E_T = D/L^2$ of the weak link. In the case of a long weak link,¹ $L \gg \xi_0$ (or, equivalently, $E_T \ll \Delta$), the spectrum is wide and many energy states contribute to the supercurrent with only a small phase-dependent gap of the order of a few E_T at low energies. In the opposite limit, only the states with energy $E \in [\Delta|\cos(\phi/2)|, \Delta]$ carry supercurrent and between these limits, Δ serves as a cutoff for the spectral supercurrent: there may exist some current-carrying states with $E > \Delta$, but

their contribution vanishes quickly with $E - \Delta$.

The energy ranges can be understood as follows: In the center of the junction, which is the bottleneck for the supercurrent, both superconductors provide sufficient correlations that a gap in the energy spectrum of a size E_g is induced at $\phi = 0$, where the size of E_g interpolates between E_T (long junction) and Δ (short junction).^{31,32} If now a finite phase difference is applied, the correlations from either side start to interfere more and more destructively leading to a closing of the gap at $\phi = \pi$.³³ Hence the lower energy bound, below which no bound states exist, is set by this phase-dependent gap. Above Δ , the states depend less and less on the superconducting properties, hence their phase dependence is rapidly lost and they also do not contribute to the supercurrent.

A. Short-junction limit $L \ll \xi_0$

In the limit when the superconducting order parameter Δ is much smaller than the Thouless energy, the supercurrent is carried by states with energies much below E_T and we may thus neglect the first term on the right side of Eq. (5). In this case, we get an analytical solution to the differential equations without further approximations,

$$\theta(x) = \operatorname{arccosh} \left(\frac{\sqrt{\alpha^2 + 1}}{\alpha} \cosh[j_E \alpha (x - x_0)] \right), \quad (20)$$

$$\chi(x) = \chi_0 - \arctan\{\alpha \tanh[j_E \alpha (x - x_0)]\}, \quad (21)$$

where α and x_0 are constants which along with the spectral supercurrent j_E are determined from the boundary conditions. In the two-probe case we can choose the origin in the center of the weak link, and assume the functions $\theta(x)$ and $\chi(x)$ take the bulk values at the NS boundary ($x = \pm L/2$). Thus we get $x_0 = 0$ and

$$\alpha = \frac{\sqrt{E^2 - \Delta^2 \cos^2(\phi/2)}}{\Delta \cos(\phi/2)}, \quad (22)$$

$$j_E = \frac{2\Delta \cos(\phi/2)}{\sqrt{E^2 - \Delta^2 \cos^2(\phi/2)}} \operatorname{arccosh} \left(\sqrt{\frac{E^2 - \Delta^2 \cos^2(\phi/2)}{E^2 - \Delta^2}} \right). \quad (23)$$

In the real-time calculation of the supercurrent, we are mostly interested in the imaginary part of the spectral supercurrent j_E . This is

$$\operatorname{Im}(j_E) = \begin{cases} 0, & E > \Delta \\ \frac{\pi \Delta \cos(\phi/2)}{\sqrt{E^2 - \Delta^2 \cos^2(\phi/2)}}, & E \in [\Delta|\cos(\phi/2)|, \Delta] \\ 0, & |E| < \Delta|\cos(\phi/2)|, \end{cases} \quad (24)$$

and $\operatorname{Im}[j_E(-E)] = -\operatorname{Im}[j_E(E)]$. At $T = 0$, we get the observable supercurrent by simply integrating $\operatorname{Im}(j_E)$ over the energy to obtain

$$I_S = \frac{\pi \Delta \cos(\phi/2)}{eR_N} \operatorname{artanh}[\sin(\phi/2)]. \quad (25)$$

For a finite temperature, we have to multiply this by the distribution function $\tanh(E/2k_B T)$ and integrate over the energy, which is conveniently done using the Matsubara technique [i.e., substituting $E = i\omega_n$, where $\omega_n = \pi T(2n+1)$ are the poles of $\tanh(E/2k_B T)$ and summing $\text{Re}(j_E)$ over $n = 0, 1, \dots$, see Refs. 10 and 20 for details], yielding

$$I_S = \frac{2\pi\Delta T}{eR_N} \cos(\phi/2) \sum_{n=0}^{\infty} \frac{1}{\sqrt{\Delta^2 \cos^2(\phi/2) + \omega_n^2}} \times \arctan\left(\frac{\Delta \sin(\phi/2)}{\sqrt{\Delta^2 \cos^2(\phi/2) + \omega_n^2}}\right). \quad (26)$$

As expected, Eqs. (25) and (26) are the same as obtained by Kulik and Omel'yanchuk³⁴ and in numerical studies¹⁰ for the same limit.

In a setup where the distribution function can be controlled by an additional probe coupled to the system via a narrow normal wire (such that the current-carrying states are not essentially deformed), the resulting supercurrent as a function of control voltage V at $T=0$ reads

$$I_S(V) = \frac{\pi\Delta \cos(\phi/2)}{2eR_N} \ln\left[\frac{\Delta[1 + \sin(\phi/2)]}{V + \sqrt{V^2 - \Delta^2 \cos^2(\phi/2)}}\right] \quad (27)$$

for $V \in [\Delta|\cos(\phi/2)|, \Delta]$. Above Δ , I_S vanishes, and for $V \leq \Delta|\cos(\phi/2)|$, the supercurrent has the form of Eq. (25), independent of V .

The spectral supercurrent of Eq. (24) can also be obtained from the diffusive limit of the corresponding quantity derived in Ref. 35. There, the supercurrent is written as a sum of the contributions from different bound states,

$$I_S = \frac{e\Delta}{2} \sin(\phi) \sum_{p=1}^N \frac{\tau_p}{E_p} \tanh\left(\frac{E_p}{2k_B T}\right), \quad (28)$$

where the bound-state energies E_p depend on the transmission eigenvalues τ_p by $E_p = \Delta[1 - \tau_p \sin^2(\phi/2)]^{1/2}$. Writing Eq. (28) in the form of an energy integral,

$$I_S = \frac{e\Delta}{2} \sin(\phi) \int dE \sum_{p=1}^N \frac{\tau_p}{E} \tanh\left(\frac{E}{2k_B T}\right) \delta(E - E_p), \quad (29)$$

and averaging the transmission eigenvalues over their diffusive-limit distribution,³⁶ $\rho(\tau) = (\pi/2e^2 R_N) \times (\tau\sqrt{1-\tau})^{-1}$, yields a spectral supercurrent given by Eq. (24) multiplying the distribution function $\tanh(E/2k_B T)$.

B. Long and intermediate-length junctions

If the length L of the weak link is much longer than ξ_0 , the supercurrent is carried by a wide spectrum of energies.^{1,2,37} At low E , however, the current-carrying density of states has a phase-dependent minigap reminiscent of the gap in the usual density of states of a SNS sample.²⁹ Above the gap, $\text{Im}(j_E)$ rises sharply, then starts to oscillate with an exponentially decaying envelope. This oscillatory

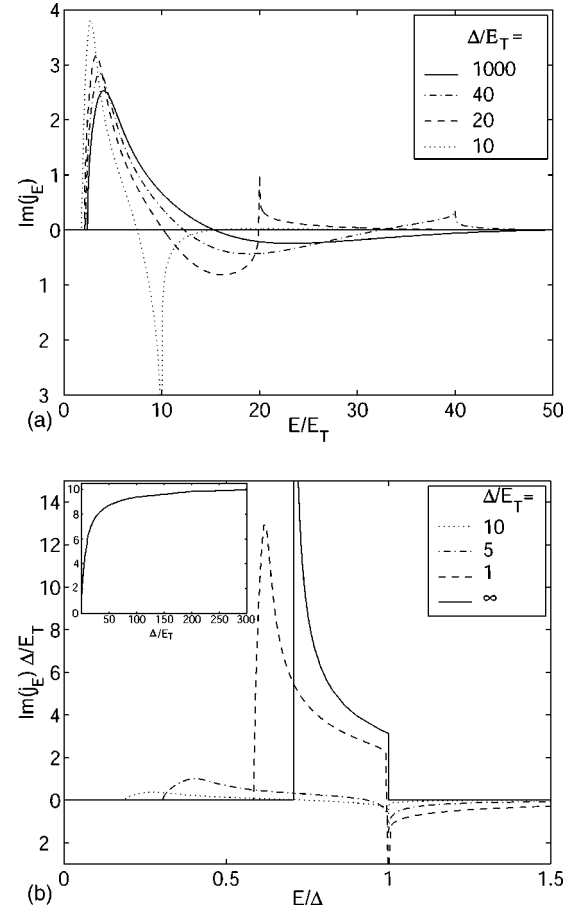


FIG. 2. Spectral supercurrent for a few values of Δ/E_T . (a) Junctions longer than the superconducting coherence length ξ_0 . A finite Δ/E_T shows up as a peak at $E = \Delta$. (b) Short junctions $L \sim \xi_0$: the peak at $E = \Delta$ persists, but another develops around $E = \Delta \cos(\phi/2)$. In (b), the spectral supercurrent is normalized by E_T/Δ to allow for the analytical solution at $E_T/\Delta \rightarrow \infty$. The inset shows how the zero-temperature, zero-voltage critical current behaves as a function of Δ/E_T , in accordance with Ref. 10.

behavior is responsible for the occurrence of the π state in nonequilibrium-controlled Josephson junctions^{5,6} and in ferromagnetic weak links.^{38,39}

The spectral supercurrent as a function of energy is plotted for a few values of Δ/E_T in Fig. 2, the upper figure showing the limit $E_T \ll \Delta$ and the lower the limit $E_T \approx \Delta$.

For a finite ratio Δ/E_T , the divergence of the density of states at the superconducting gap edge is reflected as a peak in the spectral supercurrent at $E = \Delta$. The direction of the peak, positive or negative, is determined by geometric considerations and hence depends on the precise value of Δ/E_T . For $E_T \approx \Delta$, the spectral supercurrent $\text{Im}(j_E)$ tends towards the short-junction result, Eq. (24), replacing the Thouless gap by the gap of width $\Delta \cos(\phi/2)$. Moreover, for $\Delta/E_T \rightarrow 0$, the width of the peak at $E = \Delta$ tends to zero.

In the limit $T \gg E_T$ for a long junction ($E_T \ll \Delta$), the temperature dependence of the obtained observable supercurrent tends to the limits considered by Likharev⁴⁰ for $\Delta \ll T$ and by Zaikin and Zharkov⁴¹ for a general Δ/T .

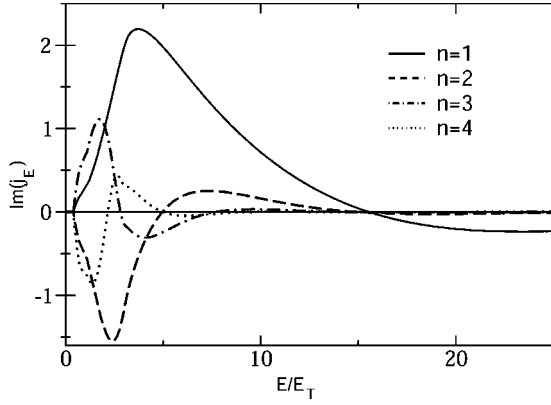


FIG. 3. Energy dependence of the Fourier sine transformed spectral supercurrent: four lowest harmonics $n=1,2,3,4$ corresponding to the phase dependencies $\sin(n\phi)$. The energy scales and magnitudes of the different harmonic constituents decay as $1/n$.

IV. PHASE DEPENDENCE

Originally, the Josephson effect was discovered for insulating weak links in the tunneling regime, i.e., in the limit of a very low tunneling probability. There, the supercurrent is due to an uncorrelated transfer of Cooper pairs through the weak link.⁴² As a result, one obtains the familiar dc Josephson relation $I_S = I_C \sin(\phi)$. However, it has been shown (see, e.g., Refs. 13 and 34) that other kinds of weak links, through which the transmission probability is much above zero, may have a different current-phase relation. Thus we may write in general

$$I_C(\phi) = \sum_{n=1}^{\infty} I_C^n \sin(n\phi), \quad (30)$$

where the amplitudes I_C^n are the coefficients of the Fourier sine series of $I_C(\phi)$. For example, in a ballistic weak link where the transmission probability for Cooper pairs is 1, $I_C^n \propto -(-1)^n/n$, yielding a sawtooth form for $I_C(\phi)$.^{13,16} The odd parity with respect to ϕ (appearance of only sine terms) of this representation reflects the fact that the supercurrent is driven by the spatial asymmetry introduced by the application of the phase: changing the phase to a negative value corresponds to mirroring the structure about the center and hence to a reversal of the current.

The occurrence of higher harmonics in Eq. (30) may be interpreted as a correlated transfer of n Cooper pairs through the weak link as a result of the pairing correlations extending through quasiparticle paths containing multiple Andreev reflections. For example, the flux quantum for the n th harmonic is $h/2ne$, i.e., corresponding to a charge $2ne$.

In a diffusive weak link considered in this paper, the transmission probabilities for the Cooper pairs are widely distributed between zero and 1.³⁶ As a result, one may get contributions from the higher harmonics to the phase dependence. This is shown in Fig. 3 where the amplitudes $\text{Im}(j_E^n)$ of the first four harmonics of the Fourier sine transformed spectral supercurrent through a long weak link ($L \gg \xi_0$) are plotted as a function of energy. Both the amplitude of $\text{Im}(j_E^n)$

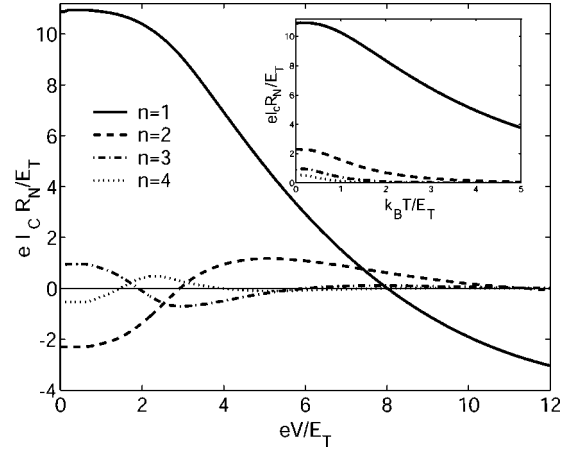


FIG. 4. Voltage dependence of the amplitudes of the first four harmonics of the observable supercurrent. Inset: Corresponding temperature dependence (even harmonics yield negative amplitudes, but here we plot the absolute values of the supercurrent).

and the effective energy scales decay with a power of n suggesting that the observation of the higher harmonics is easiest at low temperatures. The corresponding temperature and voltage dependencies of the critical currents I_C^n plotted in Fig. 4 behave analogously. A numerical fit to the obtained critical currents at $eV = k_B T = 0$ yields roughly $I_C^n \propto -(-1)^n/n^2$ and to the voltage V_n^* where $I_C^n(V)$ first changes sign suggests that the effective energy scales behave as $E_n^* = E_T(c_1 + c_2/n)$, with some constants $c_{1,2}$.

This behavior can be understood by identifying the higher harmonics with the correlated transfer of a cluster of n Cooper pairs. Now instead of the phase ϕ , the cluster has the phase $n\phi$ and since the cycle contains $2n$ Andreev reflections, the effective trajectory length is increased from L to nL . In Eq. (18), making these replacements yields the observed result, $E_n^* \propto (c_1 + c_2/n)$. In the diffusive limit, the effective trajectory length increases in the second power of the length of the weak link, $l_{\text{eff}} \propto L^2$, but since the phase is reset after each traversal through the weak link, we simply get $l_{\text{eff},n} \propto nL^2$. Hence, similarly to the alternating sign, the scaling of the effective energies with index n follows the behavior of the ballistic-limit spectral supercurrent.

Since the crossover voltages V_n^* , where $I_C^n(V_n^*) = 0$, depend on n , the actual critical current never vanishes at the crossover: it is rather that the current-phase relation changes its form near the crossover voltages. Such a change was observed in Ref. 11, where the current-phase relation of a controllable Josephson junction was measured in a superconducting quantum interference device (SQUID) geometry.

In the short-junction regime $L \ll \xi_0$ the contributions of the different harmonics can be derived analytically. A general form for $\text{Im}(j_E^n)$ would be complicated, but as an example, the first two amplitudes are

$$\text{Im}(j_E^1) = \left(\frac{E}{\Delta}\right)^2, \quad (31)$$

$$\text{Im}(j_E^2) = -\frac{E^2(2\Delta^2 - 3E^2)}{\Delta^4}. \quad (32)$$

Clearly all the harmonics share the same energy scale, Δ , but as for the case of a long weak link, the amplitude decays also here roughly as $1/n^2$. Namely, integrating $\text{Im}(j_E^n)$ over the energy, we get for a short weak link

$$I_C^n = -\frac{(-1)^n e \Delta}{R_N(2n+1)(2n-1)}. \quad (33)$$

Replacing Δ by E_T and scaling by a numerical factor close to 33, this form fits the amplitudes of the long-junction harmonics as well but a rigorous proof does not exist.

V. EXTRA TERMINALS

In order to relate our results to physical observables, we have to evaluate statistical expectation values. In two-probe SNS weak links in equilibrium, most of the experimental observations have been accurately described with the equilibrium Matsubara technique.¹⁰ However, one of the recent advances in the research of the Josephson effect has been done in nonequilibrium situations where the distribution function in the weak link has been controlled by coupling one or more normal-metal reservoirs to the weak link by phase-coherent wires.^{5,6} While making it possible to control the occupation of the current-carrying states, these extra wires also affect the form of $\text{Im}(j_E)$.² In the discussion of these effects, we concentrate on the regime of a long junction, $L \gg \xi_0$. There, most notably, the control probes allow for the existence of states with low energies, and therefore the Thouless gap is lifted. Moreover, the existence of the normal reservoirs brings some extra depairing by imposing a vanishing boundary condition for the pairing amplitude $f = \sinh(\theta)$ inside the reservoirs. As a result, the amplitude of the spectral supercurrent decreases due to the extra probes. In what follows, we consider the effects of the integrated cross-sectional area A_c of the control wires attached to the center of the weak link with cross section A_w (note: a similar effect would be present if the control wires and the weak link were made of different materials with normal-state conductivities $\sigma_{N,c}$ and $\sigma_{N,w}$ —however, here we simply talk about A_c and A_w) and of the length L_c of the phase coherent control wires, compared to the length L of the weak link. For simplicity, we assume that the widths of the control wires are much smaller than L , allowing one to treat these wires as quasi-1D structures, connected by the rules of Nazarov's circuit theory.^{36,25} In the language of this circuit theory, the extra normal wires divert some of the spectral current to the normal reservoirs, thus decreasing the pairing correlations between the superconductors.

The spectral supercurrent as a function of energy for different cross sections A_c of the control wire is plotted in Fig. 5. Here we have taken the length $L_c = 5L \gg L$. Already a small $A_c \ll A_w$ yields a finite $\text{Im}(j_E)$ at low energies, but does not much reduce the total magnitude of the supercurrent. The resulting temperature and voltage dependencies of the total supercurrent I_s is plotted in Fig. 6. Except at the very lowest

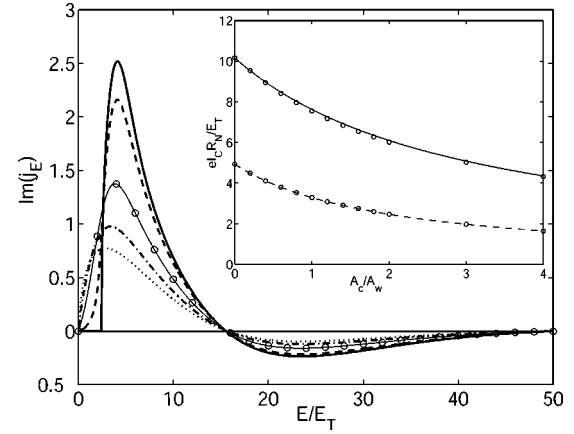


FIG. 5. Spectral supercurrent for different cross sections A_c of the control probe. From top to bottom, the cross section is $A_c = 0, 0.2, 1, 2, 4$ times the cross section of the weak link. Inset: observable supercurrent as a function of A_c for $T=V=0$ (upper set of circles) and for $k_B T = 3 E_T$ (lower set of circles). The zero-temperature result is fitted to $I_s(A_c=0)A_w/(A_w + A_c/3)$ (solid line) and the finite-temperature result to $I_s(A_c=0)A_w/(A_w + A_c/2)$ (dashed line).

voltages/temperatures of the order of the Thouless gap, the extra probes do not change the voltage/temperature dependence of I_s from the two-probe case, but only the overall magnitude is decreased. From the resulting $I_s(A_c)$ we obtain

$$I_s(A_w, A_c) = \frac{A_w}{A_w + A_c/2} I_s(A_w, A_c=0), \quad (34)$$

which holds very well for $\max(eV, k_B T) \gg E_T$.

If the length L_c of the phase-coherent control wire is larger than L , the effect of the control wires is independent of the precise value of L_c . For $L_c < L$, the spectral supercurrent is altered for $E \lesssim \hbar D/L_c^2$ such that the overall magnitude is decreased, the observable supercurrent tending towards zero as $L_c \rightarrow 0$. The spectral supercurrent and the resulting

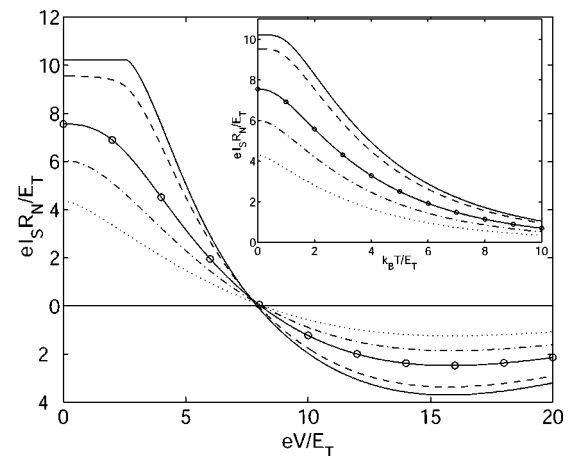


FIG. 6. Voltage dependence of supercurrent for $\phi = \pi/2$ in the presence of the control probe with different cross sections A_c . Inset: The corresponding temperature dependence of the supercurrent. The cross sections have been chosen as in Fig. 5.

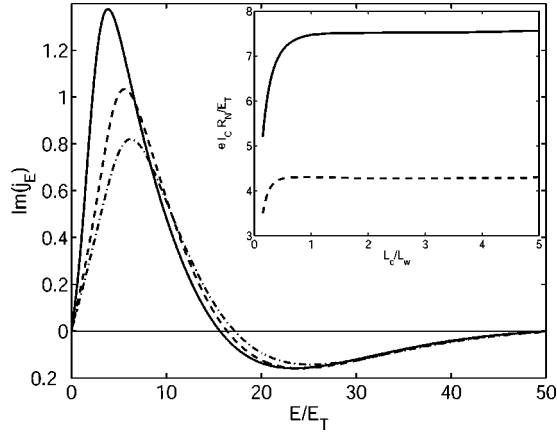


FIG. 7. Spectral supercurrent for different lengths L_c of the control probe. From top to bottom, the length is $L_c = 5, 0.25, 0.15$ times the length of the weak link. The cross section of the control probe is chosen equal to that of the weak link. Inset: Supercurrent at $T=0$ (solid line) and $T=3E_T/k_B$ (dashed) as a function of the length L_c of the control probe with respect to the length of the weak link.

temperature/voltage dependencies for $A_c = A_w$ and for three different L_c/L are plotted in Figs. 7 and 8, respectively.

VI. NONIDEAL INTERFACES

Normal-metal—superconductor interfaces with reduced transmissivity can be taken into account by specifying the transmission eigenvalues through the interface and taking them into account as in Eq. (7). Here we consider a typical case described by the distribution of eigenvalues for a “dirty” interface.

Figure 9 shows the spectral supercurrent for a long junction connected to superconductors through a dirty interface with resistance R_I (yielding a total resistance $R_N + 2R_I$ between the superconductors). Due to the additional resistance,

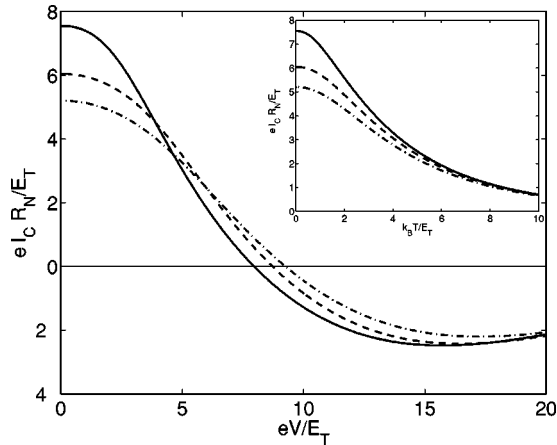


FIG. 8. Voltage dependence of supercurrent for $\phi = \pi/2$ in the presence of a control probe with length L_c and cross section equal to that of the weak link. Inset: The corresponding temperature dependence of the supercurrent. The lengths L_c have been chosen as in Fig. 7.

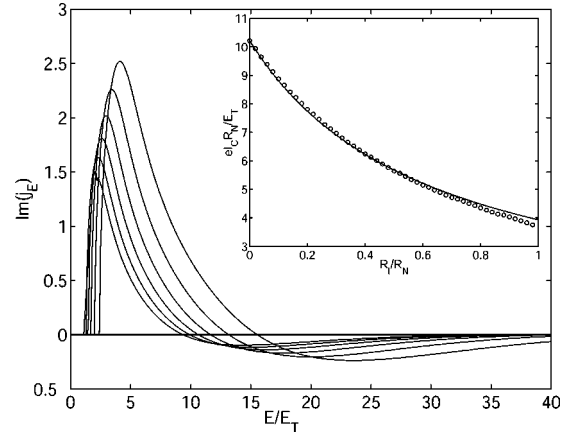


FIG. 9. Spectral supercurrent in a weak link with dirty interfaces to the superconductors, characterized by the ratio $r_b = R_I/R_N$ of the resistances. The interface resistance R_I is assumed the same for both interfaces. From top to bottom: $r_b = 0, 0.2, 0.4, 0.6, 0.8, 1.0$. Enhanced scattering at the interface reduces mostly the amplitude of the supercurrent, but also slightly the effective energy scale. Inset: zero-temperature, zero-voltage supercurrent as a function of r_b . Circles: calculated supercurrent; solid line: fit to $I_S(r_b) = I_S(r_b = 0)/(1 + 1.6r_b)$.

the amplitude of the supercurrent decays with r_b , but also the energy scales decrease since the interface barrier can to certain extent be thought as adding a barrier-equivalent length⁴³ to the path length of the quasiparticles. Observing the temperature and voltage dependencies of the resulting supercurrent, plotted in Fig. 10, shows that the amplitude of the supercurrent behaves at $T=0, V=0$ as

$$I_C(R_I, R_N) \approx \frac{I_C(R_I=0)R_N}{R_N + 1.6R_I}, \quad (35)$$

i.e., the resistances should not simply be added up but the dirty interface decreases the supercurrent less efficiently than the normal-metal resistance. Furthermore, the effective energy scale E^* found, e.g., from the voltage dependence indicates that it follows the approximate law $E^* = E_T(1$

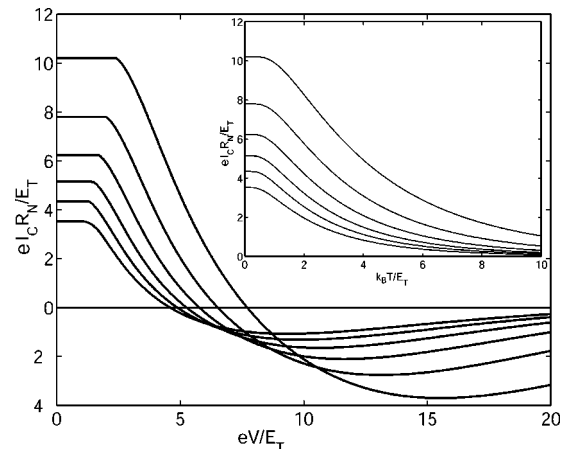


FIG. 10. Voltage dependence of the supercurrent with dirty NS interfaces at $\phi = \pi/2$. Inset: Corresponding temperature dependence. The values of R_I are the same as in Fig. 9.

+0.7 R_I/R_N). This kind of a behavior of the critical current and the spectral supercurrent is similar to those found in Ref. 24 [especially, see Eqs. (55) and (56)] and Ref. 2 in the case of a tunneling interface.

VII. CONCLUSIONS

In this paper, we have systematically investigated the spectrum of current-carrying states in a phase coherent normal-metal weak link. Taking into account the effect of extra terminals, the characteristic energy scales—the Thouless energy E_T and the BCS superconducting gap Δ —and a finite NS interface resistance makes it easier to find a quantitative agreement with the obtained experimental results on the nonequilibrium-controlled supercurrent. We have also been able to derive analytical results in a number of limits. Moreover, we have discussed the underlying microscopic phenomena leading to the π state and have explained its properties, such as its dependence on energy, and higher harmonics in the phase dependence, by invoking Andreev bound states smeared over a broad distribution of times of flight, and by multiple Andreev cycles transferring more than one Cooper pair in a single coherent process.

To obtain an optimal voltage control of the supercurrent, the interface resistances should be much smaller than the weak-link wire resistance, the control wire should be slightly

longer than the weak link (but not much longer to reduce the inelastic effects on the nonequilibrium distribution function), and as thin as possible compared to the weak link. For the observation of the π state, the ideal limit is the long-junction limit $L \gg \xi_0$, where the spectrum of the current-carrying states is not cut off by the superconducting gap.

In typical experiments, also inelastic scattering neglected here may become important. However, since equilibrium phenomena induced by the superconducting proximity effect have been quantitatively described by the quasiclassical theory without incorporating such effects (see, e.g., Refs. 10 and 44), we expect these inelastic effects to be mostly important in the kinetic equations describing the nonequilibrium distribution functions. In recent experiments,^{8,6} including these inelastic terms into the kinetic equations has led to good agreement between the theory and the experiments. Therefore our results provide an accurate and independent way of also characterizing such inelastic effects by observing how they affect the supercurrent.

ACKNOWLEDGMENTS

We thank Norman Birge, Frédéric Pierre and Jochem Baselmans for discussions. This work was supported by the Graduate School in Technical Physics at the Helsinki University of Technology.

*Author to whom correspondence should be addressed. Present address: Low Temperature Laboratory, P.O. Box 2200, FIN-02015 HUT. Finalnd. Electronic address: Tero.T.Heikkila@hut.fi

¹F. K. Wilhelm, G. Schön, and A. D. Zaikin, Phys. Rev. Lett. **81**, 1682 (1998).

²S. K. Yip, Phys. Rev. B **58**, 5803 (1998).

³A. F. Volkov, Phys. Rev. Lett. **74**, 4730 (1995); A. F. Volkov, R. Seviour, and V. V. Pavlovskii, Superlattices Microstruct. **25**, 647 (1999).

⁴A. F. Morpurgo, T. M. Klapwijk, and B. J. van Wees, Appl. Phys. Lett. **72**, 966 (1998).

⁵J. J. A. Baselmans, A. F. Morpurgo, B. J. van Wees, and T. M. Klapwijk, Nature (London) **397**, 43 (1999); J. J. A. Baselmans, B. J. van Wees, and T. M. Klapwijk, Phys. Rev. B **63**, 094504 (2001).

⁶J. Huang, F. Pierre, T. T. Heikkilä, F. K. Wilhelm, and N. O. Birge, Phys. Rev. B **66**, 020507(R) (2002).

⁷Th. Schäpers *et al.*, Appl. Phys. Lett. **73**, 2348 (1998).

⁸J. J. A. Baselmans, B. J. van Wees, and T. M. Klapwijk, Phys. Rev. B **65**, 224513 (2002).

⁹J. Kutchinsky, R. Taboryski, C. B. Sørensen, J. B. Hansen, and P. E. Lindelof, Phys. Rev. Lett. **83**, 4856 (1999).

¹⁰P. Dubos, H. Courtois, B. Pannetier, F. K. Wilhelm, A. D. Zaikin, and G. Schön, Phys. Rev. B **63**, 064502 (2001).

¹¹J. J. A. Baselmans, T. T. Heikkilä, B. J. van Wees, and T. M. Klapwijk, Phys. Rev. Lett. **89**, 207002 (2002).

¹²I. O. Kulik, Zh. Éksp. Teor. Fiz. **57**, 1745 (1969) [Sov. Phys. JETP **30**, 944 (1970)].

¹³Ch. Ishii, Prog. Theor. Phys. **44**, 1525 (1970).

¹⁴J. Bardeen and J. L. Johnson, Phys. Rev. B **5**, 72 (1972).

¹⁵M. Büttiker and T. M. Klapwijk, Phys. Rev. B **33**, 5114 (1986).

¹⁶B. J. van Wees, K.-M. H. Lenssen, and C. J. P. M. Harmans, Phys. Rev. B **44**, 470 (1991).

¹⁷C. W. J. Beenakker and H. van Houten, Phys. Rev. Lett. **66**, 3056 (1991).

¹⁸U. Günsenheimer, U. Schüssler, and R. Kümmel, Phys. Rev. B **49**, 6111 (1994).

¹⁹K.D. Usadel, Phys. Rev. Lett. **25**, 507 (1970).

²⁰For an introduction see, e.g., W. Belzig, F. K. Wilhelm, C. Bruder, G. Schön, and A. D. Zaikin, Superlattices Microstruct. **25**, 1251 (1999).

²¹J. Rammer and H. Smith, Rev. Mod. Phys. **58**, 323 (1986).

²²F. Sols and J. Ferrer, Phys. Rev. B **49**, 15 913 (1994).

²³A. V. Zaitsev, Zh. Éksp. Teor. Phys. **86**, 1742 (1984) [Sov. Phys. JETP **59**, 1015 (1984)].

²⁴M. Yu. Kupriyanov and V. F. Lukichev, Zh. Éksp. Teor. Fiz. **94**, 139 (1988) [Sov. Phys. JETP **67**, 1163 (1988)].

²⁵Yu. V. Nazarov, Superlattices Microstruct. **25**, 1221 (1999).

²⁶W. Belzig, A. Brataas, Yu. V. Nazarov, and G. E. W. Bauer, Phys. Rev. B **62**, 9726 (2000).

²⁷K. M. Schep and G. E. W. Bauer, Phys. Rev. Lett. **78**, 3015 (1997).

²⁸A. V. Zaitsev, Physica B **203**, 274 (1994).

²⁹A. A. Golubov, F. K. Wilhelm, and A. D. Zaikin, Phys. Rev. B **55**, 1123 (1997).

³⁰A. F. Andreev, Zh. Éksp. Teor. Fiz. **46**, 1823 (1964) [Sov. Phys. JETP **19**, 1228 (1969)]; **49**, 655 (1965) [**22**, 455 (1966)].

³¹A. A. Golubov and M. Yu. Kupriyanov, J. Low Temp. Phys. **70**, 83 (1988).

³²W. Belzig, C. Bruder, and G. Schön, Phys. Rev. B **54**, 9443 (1996).

³³F. Zhou, P. Charlat, and B. Pannetier, J. Low Temp. Phys. **110**, 841 (1998).

- ³⁴I. O. Kulik and A. N. Omelyan'chuk, *Fiz. Nizk. Temp.* **4**, 296 (1978) [*Sov. J. Low Temp. Phys.* **4**, 142 (1978)].
- ³⁵C. W. J. Beenakker, *Phys. Rev. Lett.* **67**, 3836 (1991); **68**, 1442(E) (1992).
- ³⁶Yu. V. Nazarov, *Phys. Rev. Lett.* **73**, 134 (1994).
- ³⁷T. T. Heikkilä, F. K. Wilhelm, and G. Schön, *Europhys. Lett.* **51**, 434 (2000).
- ³⁸A. I. Buzdin, L. N. Bulaevskii, and V. Panyukov, *Pis'ma Zh. Eksp. Teor. Fiz.* **35**, 147 (1982) [*JETP Lett.* **35**, 178 (1982)]; A. I. Buzdin and M. Yu. Kupriyanov, *ibid.* **52**, 1089 (1990) [*ibid.* **52**, 487 (1990)]; **53**, 308 (1991) [**53**, 321 (1991)]; A. I. Buzdin, B. Bujicic, and M. Yu. Kupriyanov, *Zh. Eksp. Teor. Fiz.* **101**, 231 (1992) [*Sov. Phys. JETP* **74**, 124 (1992)].
- ³⁹V. V. Ryazanov, V. A. Oboznov, A. Yu. Rusanov, A. V. Veretennikov, A. A. Golubov, and J. Aarts, *Phys. Rev. Lett.* **86**, 2427 (2001).
- ⁴⁰K. K. Likharev, *Pis'ma Zh. Tekh. Fiz.* **2**, 29 (1976) [*Sov. Tech. Phys. Lett.* **2**, 12 (1976)].
- ⁴¹A. D. Zaikin and G. F. Zharkov, *Fiz. Nizk. Temp.* **7**, 375 (1981) [*Sov. J. Low Temp. Phys.* **7**, 184 (1981)].
- ⁴²“Uncorrelated” means in this context that no microscopic correlation between the different Cooper pairs crossing the junction exist. The transport is, however, still coherent in the sense that each Cooper pair keeps its internal correlation while traveling the junction. Furthermore, the phases of the reservoirs are assumed not to fluctuate such that the Cooper pairs are transported with the same macroscopic phase and hence add up to a macroscopic steady supercurrent.
- ⁴³F. Zhou, B. Spivak, and A. Zyuzin, *Phys. Rev. B* **52**, 4467 (1995).
- ⁴⁴M. A. Sillanpää, T. T. Heikkilä, R. K. Lindell, and P. J. Hakonen, *Europhys. Lett.* **56**, 590 (2001).

Non-equilibrium supercurrent through mesoscopic ferromagnetic weak links

T. T. HEIKKILÄ^{1,2(*)}, F. K. WILHELM^{1,3} and G. SCHÖN¹

¹ *Institut für Theoretische Festkörperphysik, Universität Karlsruhe D-76128 Karlsruhe, Germany*

² *Materials Physics Laboratory, Helsinki University of Technology FIN-02015 HUT, Finland*

³ *Quantum Transport Group, TU Delft - 2600 GA Delft, The Netherlands*

(received 27 March 2000; accepted in final form 14 June 2000)

PACS. 74.50.+r – Proximity effects, weak links, tunnelling phenomena, and Josephson effects.

PACS. 71.70.Ej – Spin-orbit coupling, Zeeman and Stark splitting, Jahn-Teller effect.

PACS. 75.30.Et – Exchange and superexchange interactions.

Abstract. – We consider a mesoscopic normal metal, where the spin degeneracy is lifted by a ferromagnetic exchange field or Zeeman splitting, coupled to two superconducting reservoirs. As a function of the exchange field or the distance between the reservoirs, the supercurrent through this device oscillates with an exponentially decreasing envelope. This phenomenon is similar to the tuning of a supercurrent by a non-equilibrium quasiparticle distribution between two voltage-biased reservoirs. We propose a device combining the exchange field and non-equilibrium effects, which allows us to observe a range of novel phenomena. For instance, part of the field-suppressed supercurrent can be recovered by a voltage between the additional probes.

Externally controlled weak links in mesoscopic superconducting circuits have been at the focus of interest in recent years [1]. The possibility to control the quasiparticle distribution by external voltage probes allows tuning the supercurrent through the device (mesoscopic SNS transistors). It has been predicted that devices with tunnel junctions [2] and systems with good metallic contacts [3] can enter a peculiar mesoscopic non-equilibrium state at low temperatures, which even allows reversing the supercurrent, turning the system into a π -junction. This phenomenon has been verified experimentally [1].

Another phenomenon of high interest in superconducting mesoscopics is the combination of ferromagnetic (F) elements with superconductors (S) [4–8]. A strong exchange interaction h in the ferromagnet is expected to suppress the superconducting proximity effect, and hence also the supercurrent. (Several recent experiments [9–11] do not confirm this expectation, a fact which, at this stage, is not understood.) For weak fields, the supercurrent through a SFS weak link and the transition temperature of a SF multilayer are predicted to oscillate [12–14] as a function of the field, or of the width d of the ferromagnet. The latter defines a characteristic

(*) E-mail: Tero.T.Heikkila@hut.fi

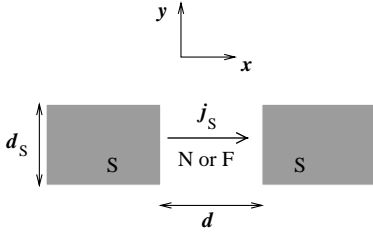


Fig. 1

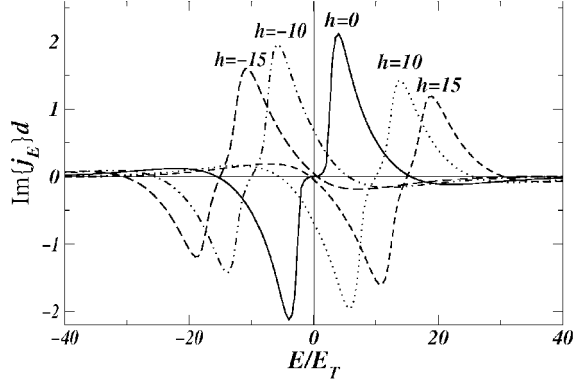


Fig. 2

Fig. 1 – Schematic picture of the studied S-F-S structure.

Fig. 2 – Spectral supercurrent for different exchange fields h at $\phi = \pi/2$ as a function of energy. The exchange fields are expressed in units of the Thouless energy E_T . The variation in the peak heights is due to a finite magnitude of the order parameter $\Delta = 50E_T$.

energy scale, the Thouless energy, which in the diffusive limit is $E_T = \hbar D/d^2$, proportional to the diffusion constant D .

In this article, we show that the non-equilibrium-controlled supercurrent in mesoscopic SNS transistors [3] and the supercurrent in SFS weak links are formally equivalent, although one is tuned by varying the distribution function, while the other is controlled by modifications of equilibrium spectral functions. Combining the two phenomena, we can recover by an applied voltage part of the supercurrent which is suppressed by the exchange field. Thereby, one can measure the exchange field in the weak link.

For definiteness we consider a quasi-one-dimensional system depicted schematically in fig. 1 assuming a three-dimensional system with structural changes only in one direction. The magnetism in the weak link, or the Zeeman splitting, is accounted for by the energy σh of a spatially homogeneous exchange field coupling to the electron spin $\sigma = \pm 1$. In the diffusive limit, the system can be described by the Usadel equation for quasiclassical Green's functions [5, 7, 15]. While the equilibrium results of the present work can also be obtained in the imaginary-time Matsubara formalism, we have chosen to use the real-time Keldysh technique in order to include also non-equilibrium processes. Then we have

$$D\partial_x^2\theta = -2i(E - \sigma h)\sinh\theta + 2\Delta\cosh\theta + \frac{D}{2}(\partial_x\chi)^2\sinh 2\theta, \quad (1)$$

$$j_E(E, h) = \sinh^2\theta\partial_x\chi, \quad \partial_x j_E = 0, \quad (2)$$

where $\theta(E, h, x)$ and $\chi(E, h, x)$ are complex variables parametrising the quasiclassical diagonal and off-diagonal Green's function $G(E, h, x) = \cosh(\theta)$ and $F(E, h, x) = \sinh(\theta)\exp[i\chi]$. For a system of length d , eq. (1) introduces a natural energy scale $E_T = D/d^2$. Hence, one way to tune the relevant energies is by varying the length d . Deep in the superconducting electrodes the exchange field or Zeeman splitting vanishes. For simplicity, we assume a bulk BCS solution up to the interfaces, $\theta_S = \arctan(\Delta/E)$, $\chi_S = \pm\phi/2$ in the superconducting electrodes with amplitudes Δ and phase difference ϕ of the order parameters of the two superconductors. Furthermore, we assume clean interfaces, and neglect the reduction of Andreev reflection

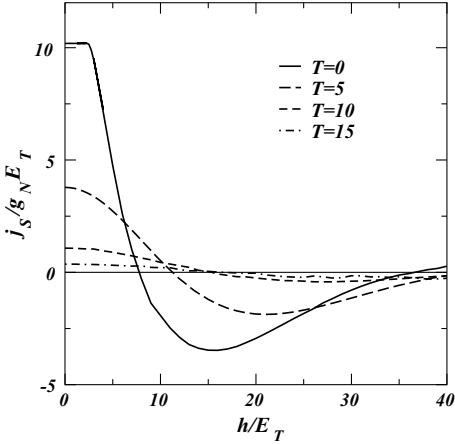


Fig. 3

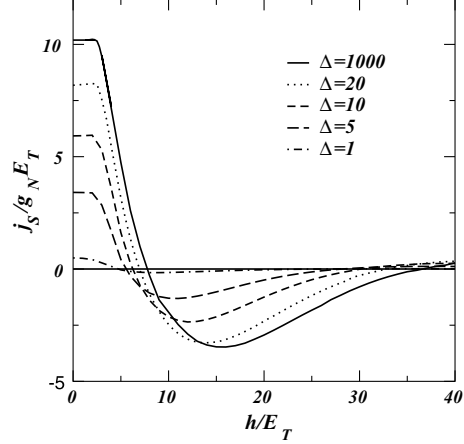


Fig. 4

Fig. 3 – Supercurrent $j_S(\phi = \pi/2)$ as a function of exchange field h/E_T through the structure depicted in fig. 1 for different temperatures T/E_T . The superconducting order parameter $\Delta = 1000E_T$.

Fig. 4 – SFS supercurrent $j_S(\phi = \pi/2)$ as a function of exchange field h/E_T for different values Δ of the superconducting order parameter at $T = 0$.

expected in spin-polarised systems [16–18]. We expect the error due to these approximations to be only quantitative (for the latter point, see the discussions below).

The imaginary part of the conserved “spectral supercurrent”, j_E , in eq. (2) enters into the observable supercurrent as

$$j_S(\phi) = \frac{d}{4} \sum_{\sigma=\pm 1} g_{N\sigma} \int_{-\infty}^{\infty} dE (1 - 2f(E)) \text{Im}\{j_E(E, \sigma h)\}. \quad (3)$$

Here $f(E)$ is the distribution function of quasiparticles in the weak link, which in the absence of applied voltages reduces to the equilibrium Fermi distribution f^{eq} . Furthermore, $g_{N\sigma} = 2e^2 N_{0\sigma} D_\sigma$ is the normal-state conductivity for spin σ , and $N_{0\sigma}$ is the corresponding normal-state density of states at the Fermi level. Our approach (eqs. (1), (2)) assumes spin-independent densities of states and diffusion constants. It is valid at low fields h , when the variation in the densities of states is small, $N_{0\uparrow} - N_{0\downarrow} \ll (N_{0\uparrow} + N_{0\downarrow})/2$. In this case we may put $g_{N\uparrow} = g_{N\downarrow} \equiv g_N$. The distribution function f in general is obtained from kinetic equations [15], but for the moment, we assume thermal equilibrium.

It is instructive to see how the spectral supercurrent $\text{Im}\{j_E\}$ depends on energy E and exchange fields h . It is plotted in fig. 2 for a phase difference $\phi = \pi/2$ between the superconducting electrodes. For $h = 0$, the function $\text{Im}\{j_E\}$ is antisymmetric around the Fermi surface. At low energies $E \lesssim E_T$, it vanishes until some phase-dependent $E_c(\phi)$. At larger energies it increases sharply, and then decreases exponentially, oscillating between positive and negative values. The exchange field shifts the position of the symmetry point from $E = 0$ to $E = \sigma h$ and for a superconducting gap Δ of the order of h , distorts the symmetry. Since Δ serves as an upper cutoff, which is not shifted, the overall magnitude of the spectral supercurrent decreases when h becomes comparable to Δ .

In equilibrium we have $1 - 2f(E) = \tanh(E/2T)$. This term and the sum of the spectral

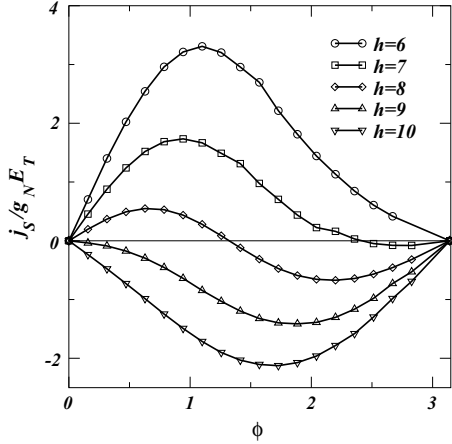


Fig. 5

Fig. 5 – Supercurrent $j_S(\phi)$ as a function of phase for different exchange fields h/E_T in the regime where the crossover from the ordinary 0-state to the π -state occurs for the first time. Here, $T = 0$ and $\Delta = 1000E_T$.

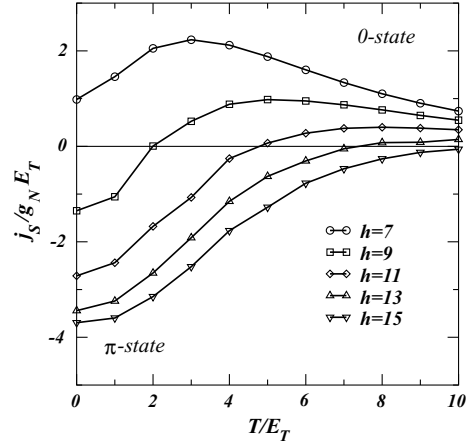


Fig. 6

Fig. 6 – Crossover from the π -state ($j_S(\phi = \pi/2) < 0$) to the 0-state ($j_S(\phi = \pi/2) > 0$) as a function of temperature T for a few values of the exchange field h/E_T .

supercurrent $\sum_{\sigma} j_E(E, \sigma h)$ are antisymmetric around $E = 0$. Hence, for the discussion of the total supercurrent j_S we can concentrate on the part $E > 0$. At low $T \lesssim E_T$ the supercurrent j_S is given by an alternating sum over the decreasing areas under the oscillating function $\text{Im}\{j_E\}$ measured from the E -axis (see fig. 2). At $h = 0$, the positive first term dominates the sum and yields a large supercurrent j_S . Increasing h shifts the negative peak from $E < 0$ to $E > 0$, hence decreasing j_S , and even reversing its sign. At finite temperature, the low-energy part, $E \lesssim T$, is effectively cut off, hence j_S decreases in amplitude. This result is illustrated in figs. 3 and 4, where $j_S(\phi = \pi/2)$ is plotted as a function of different exchange fields at different temperatures and for different bulk order parameters Δ . Analogous results can be obtained for a constant exchange field by varying the distance d of the superconducting reservoirs and through it the Thouless energy E_T .

In the regime where $j_S(\phi = \pi/2)$ is negative, the junction forms a so-called “ π -junction” [12], since the ground state of the system, with no supercurrent flowing between the two superconductors, is reached for a phase difference equal to π . The supercurrent-phase relation for different exchange fields is plotted in fig. 5, showing the crossover from an ordinary behaviour to a π -state. A closer analysis of fig. 3 shows that the precise value of h/E_T where the crossover occurs depends weakly on temperature, since higher values of T smoothen the oscillations between positive and negative contributions to j_S . At $h = 0$, $j_S(\phi = \pi/2)$ is positive for any T . It remains positive as long as the thermal energy dominates over the exchange, $T \gg h$. With increasing T the cross-over to a π -junction is shifted towards higher fields. This dependence was probably observed in ref. [19]. It is an alternative way to verify the current reversal to what has been discussed in previous proposals, where typically one requires many different samples with varying widths [4] but otherwise equal parameters. The crossover is illustrated in fig. 6 for a few values of h/E_T .

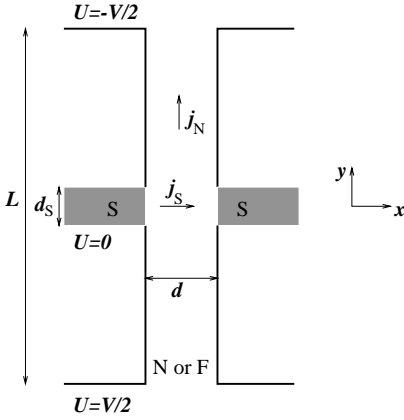


Fig. 7

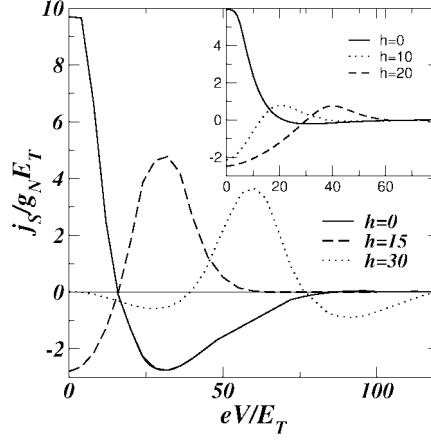


Fig. 8

Fig. 7 – Four-probe setup for studying the non-equilibrium effects on the supercurrent. It is assumed that $L \gg d_S$ and that the superconductors lie in the middle of the normal wire ($y = 0$) so that the distribution function has the two-step form between the superconductors. Furthermore, we expect that the four-probe setup does not notably alter the spectral supercurrent obtained from a quasi-one-dimensional calculation (for a more detailed discussion, see refs. [3, 23]).

Fig. 8 – Supercurrent $j_S(\phi = \pi/2)$ of the four-probe structure at different fields as a function of the voltage V between the normal probes. In the calculations for the main picture, the magnitude of the order parameter was set to $\Delta = 100E_T$, and at the inset, $\Delta = 10E_T$, thereby showing that even when Δ is of the order of h and eV , a local maximum is obtained at $eV = 2h$.

By shifting the variable of integration E in eq. (3) by σh , one finds

$$j_S(\phi) = \frac{dg_N}{2} \sum_{\sigma} \int_{-\infty}^{\infty} dE (1 - f^{\text{eq}}(E + \sigma h)) \text{Im}\{j_E(E)\}. \quad (4)$$

The shifted distribution function $f = 1/2 \sum_{\sigma} f^{\text{eq}}(E + \sigma h)$ has the same form as the two-step distribution function measured in ref. [20]. There it appeared as the solution of a kinetic equation in the centre of a diffusive metal between two normal probes with voltage $eV = \pm 2h$ in the limit where the inelastic scattering length is longer than the distance between the two normal reservoirs. The spectral supercurrent in general still depends on the exchange field via the boundary conditions. However, if the superconducting gap Δ is much larger than the exchange field, $\Delta \gg h$, this dependence can be neglected. In this limit, the supercurrent in the presence of an exchange field is the same as for a non-equilibrium distribution four-probe structure described in ref. [3] (see fig. 7 for a schematic picture).

It is interesting to note that this behaviour of the diffusive-limit supercurrent as functions of the exchange field and the external potential is very similar to the supercurrent through a multiprobe structure in the clean limit. This limit has been described by Dobrosavljević-Grujić *et al.* [21] for the ferromagnetic two-probe case and by van Wees *et al.* [22] including a voltage in a non-magnetic three-probe setup. In this case, the supercurrent is carried by the Andreev levels, whose energies are controlled by the exchange field [21], and whose occupation can be tuned by the voltage [22]. With both parameters, for example, the system can be driven into a π -state.

We can combine the effects of exchange field and non-equilibrium distribution [3, 23] by considering the structure in fig. 7, where the magnetic material is placed between superconductors and normal voltage leads. Here, the distribution function is

$$f(E, y) = \left(\frac{1}{2} - \frac{y}{L}\right) f^{\text{eq}}(E + eV/2) + \left(\frac{1}{2} + \frac{y}{L}\right) f^{\text{eq}}(E - eV/2), \quad (5)$$

exhibiting the two-step form observed by Pothier *et al.* [20]. In this case, if the superconducting reservoirs are located around $y = 0$ and provided $\Delta \gg h, eV$, the observable supercurrent can be written as a sum of four terms,

$$j_S(\phi) = \frac{dg_N}{8} \int_{-\infty}^{\infty} dE (1 - 2f^{\text{eq}}(E)) \text{Im}\{j_E(E - h - eV/2) + j_E(E - h + eV/2) + j_E(E + h - eV/2) + j_E(E + h + eV/2)\}. \quad (6)$$

For example, if the potential is exactly twice the exchange field, $eV = 2h$, due to the anti-symmetry of $\text{Im}\{j_E\}$, we have

$$j_S(\phi) = \frac{1}{2} (j_S^{\text{SFS}}(\phi, 0) + j_S^{\text{SFS}}(\phi, 2h)) \approx \frac{1}{2} j_S^{\text{SFS}}(\phi, 0). \quad (7)$$

The latter approximate equality holds if $h \gg E_T$. Here, $j_S^{\text{SFS}}(\phi, h)$ is the supercurrent through the SFS structure with the exchange field h in the weak link. Hence, one can use the external potential to recover half of the zero-field supercurrent. This is illustrated in fig. 8, where the supercurrent of the four-probe structure is plotted as a function of voltage with a few magnitudes of fields.

The results summarised by eq. (7) provide a way to measure the exchange field and at the same time to explore the applicability of the simplified model for the ferromagnet used here and previously [7, 8, 12]. When the voltage-dependent supercurrent $j_S(V)$ reaches a maximum, eV should equal $2h$. Deviations could occur as, for instance, this model neglects the band structure effects [24] important in the ferromagnets. Also, to be able to measure the actual supercurrent through a typical ferromagnet with Curie temperature $T_{\text{Cu}} \gg \Delta$, the ratio h/E_T has to be made small by fabricating very thin weak links. Moreover, our assumption of the diffusive regime requires $d \gg l_{\text{el}}$, and a quantitative agreement cannot be expected for thin structures. Finally, due to the strong electron-electron interactions in ferromagnets, producing a short inelastic relaxation length, the normal probes should be fabricated rather close to each other to obtain the two-step form for the distribution function. For conventional ferromagnets the exchange field is large, which would correspond to enormous voltages. However, we expect that our model is approximately valid for setups constructed from ferromagnetic alloys with T_{Cu} of the order of the superconducting critical temperature [19], or in situations where h can be related to the Zeeman splitting in magnetic fields much weaker than the superconducting critical field.

In summary, we have calculated the supercurrent through a ferromagnetic weak link as a function of the exchange field in the ferromagnet. In the calculations, the Keldysh technique was used to provide a description of non-equilibrium effects. We found that when $\Delta \gg h$, the problem is formally equivalent to the four-probe measurement of the supercurrent through a normal-metal weak link. Furthermore, we showed that applying a non-equilibrium potential in the transverse direction, one can recover half of the supercurrent of a ferromagnet with an exchange field $h \gg E_T$, as compared to the supercurrent in the absence of h .

* * *

We thank B. PANNETIER, M. GIROUD and M. FOGELSTRÖM for discussions. This work was supported by the Helsinki University of Technology, the DFG through SFB 195 and the EU through the EU-TMR network “Superconducting nano-circuits”. While writing this paper, we became aware of a related work by Yip [25], who introduced the exchange-field term as the Zeeman splitting of the current-carrying density of states.

REFERENCES

- [1] MORPURGO A., VAN WEES B. J. and KLAPWIJK T. M., *Appl. Phys. Lett.*, **72** (1998) 966; BASELMANS J. J. A., MORPURGO A., VAN WEES B. J. and KLAPWIJK T. M., *Nature*, **397** (1999) 43.
- [2] VOLKOV A. F., *Phys. Rev. Lett.*, **74** (1995) 4730.
- [3] WILHELM F. K., SCHÖN G. and ZAIKIN A. D., *Phys. Rev. Lett.*, **81** (1998) 1682.
- [4] JIANG J. S., DAVIDOVIĆ D., REICH D. H. and CHIEN C. L., *Phys. Rev. Lett.*, **74** (1995) 314.
- [5] DEMLER E. A., ARNOLD G. B. and BEASLEY M. R., *Phys. Rev. B*, **55** (1997) 15174.
- [6] LAZAR L., WESTERHOLT K., ZABEL H., TAGIROV L. R., GORYUNOV YU. V., GARIF'YANOV N. N. and GARIFULLIN I. A., *Phys. Rev. B*, **61** (2000) 3711.
- [7] FAZIO R. and LUCHERONI C., *Europhys. Lett.*, **45** (1999) 707.
- [8] SEVIOUR R., LAMBERT C. J. and VOLKOV A. F., *Phys. Rev. B*, **59** (1999) 6031.
- [9] PETRASHOV V. T., ANTONOV V. N., MAKSIMOV S. V., SHAIKHAIDAROV R. SH., *JETP Lett.*, **59** (1994) 551; PETRASHOV V. T., SOSNIN I. A., COX I., PARSONS A. and TROADEC C., *Phys. Rev. Lett.*, **83** (1999) 3281.
- [10] LAWRENCE M. D. and GIORDANO N., *J. Phys. Condens. Matter*, **8** (1996) L563.
- [11] GIROUD M., COURTOIS H., HASSELBACH K., MAILLY D. and PANNETIER B., *Phys. Rev. B*, **58** (1998) R11872.
- [12] BUZDIN A. I., BULAEVSKII L. N. and PANYUKOV S. V., *JETP Lett.*, **35** (1982) 178; BUZDIN A. I. and KUPRIYANOV M. YU., *JETP Lett.*, **52** (1990) 487; **53** (1991) 321; BUZDIN A. I., BUJICIC, B. and KUPRIYANOV M. YU., *Sov. Phys. JETP*, **74** (1992) 124.
- [13] RADOVIĆ Z., DOBROSAVLJEVIĆ-GRUJIĆ L., BUZDIN A. I. and CLEM J. R., *Phys. Rev. B*, **38** (1988) 2388; RADOVIĆ Z., LEDVIJ M., DOBROSAVLJEVIĆ-GRUJIĆ L., BUZDIN A. I. and CLEM J. R., *Phys. Rev. B*, **44** (1991) 759.
- [14] KHUSAINOV M. G. and PROSHIN YU. N., *Phys. Rev. B*, **56** (1997) R14283.
- [15] BELZIG W., WILHELM F. K., BRUDER C., SCHÖN G. and ZAIKIN A. D., *Superlatt. Microstruct.*, **25** (1999) 1251.
- [16] DE JONG, M. J. M. and BEENAKKER, C. W. J., *Phys. Rev. Lett.*, **74** (1995) 1657.
- [17] FAL'KO V. I., LAMBERT C. J. and VOLKOV A. F., *JETP Lett.*, **69** (1999) 532; *Phys. Rev. B*, **60** (1999) 15394.
- [18] JEDEMA, F. J., VAN WEES B. J., HOVING B. H., FILIP A. T. and KLAPWIJK T. M., *cond-mat/9901323*.
- [19] VERETENNIKOV A. V., RYAZANOV V. V., OBOZNOV V. A., RUSANOV A. YU., LARKIN V. A. and AARTS J., *Physica B*, **284-288** (2000) 495; AARTS J., private communication.
- [20] POTHIER H., GUÉRON S., BIRGE N. O., ESTEVE D. and DEVORET M. H., *Phys. Rev. Lett.*, **79** (1997) 3490.
- [21] DOBROSAVLJEVIĆ-GRUJIĆ L., ZIKIĆ R. and RADOVIĆ Z., *cond-mat/9911339*.
- [22] VAN WEES B. J., LENSSEN K.-M. H. and HARMANS C. J. P. M., *Phys. Rev. B*, **44** (1991) 470.
- [23] WILHELM F. K., SCHÖN G. and ZAIKIN A. D., *Physica B*, **280** (2000) 418.
- [24] MAZIN I. I., *Phys. Rev. Lett.*, **83** (1999) 1427.
- [25] YIP S. K., *cond-mat/0002395*.

Josephson critical current in a long mesoscopic S-N-S junction

P. Dubos,¹ H. Courtois,¹ B. Pannetier,¹ F. K. Wilhelm,^{2,3} A. D. Zaikin,⁴ and G. Schön²

¹*Centre de Recherches sur les Très Basses Températures-C.N.R.S. associated to Université Joseph Fourier, 25 Avenue des Martyrs, 38042 Grenoble, France*

²*Institut für Theoretische Festkörperphysik, Universität Karlsruhe, D-76128 Karlsruhe, Germany*

³*Quantum Transport Group, Department of Applied Physics and DIMES, TU Delft, 2600 GA Delft, The Netherlands*

⁴*Forschungszentrum Karlsruhe, Institut für Nanotechnologie, D-76021 Karlsruhe, Germany*

(Received 10 August 2000; published 18 January 2001)

We carry out an extensive experimental and theoretical study of the Josephson effect in S-N-S junctions made of a diffusive normal metal (N) embedded between two superconducting electrodes (S). Our experiments are performed on Nb-Cu-Nb junctions with highly transparent interfaces. We give the predictions of the quasiclassical theory in various regimes on a precise and quantitative level. We describe the crossover between the short- and the long-junction regimes and provide the temperature dependence of the critical current using dimensionless units $eR_N I_c / \epsilon_c$ and $k_B T / \epsilon_c$, where ϵ_c is the Thouless energy. Experimental and theoretical results are in excellent quantitative agreement.

DOI: 10.1103/PhysRevB.63.064502

PACS number(s): 73.23.-b, 74.50.+r, 74.80.Fp, 85.25.Cp

The Josephson effect is well known to exist in weak links connecting two superconducting electrodes S, e.g., a tunnel barrier I, a short constriction C or a normal metal N (S-I-S, S-C-S, and S-N-S junctions). This effect manifests itself in a nondissipative dc current flowing through the Josephson junction at zero voltage. At weak coupling, e.g., in the S-I-S case, the Josephson current can be expressed as $I_s = I_c \sin \varphi$, where φ is the phase difference between the two superconducting condensates and the maximum supercurrent I_c is called the critical current.

The Josephson effect in S-N-S junctions has been studied in a variety of configurations. The early experiments of Clarke¹ and Shepherd² were performed in Pb-Cu-Pb sandwiches. In these experiments and in the pioneering calculations by de Gennes,³ it was already realized that the presence of a supercurrent in such structures is due to the proximity effect. This can be understood as the generation of superconducting correlations in a normal metal connected to a superconductor, mediated by phase-coherent Andreev reflections at the S-N interfaces. The critical current I_c is limited by the ‘‘bottleneck’’ in the center of the N-layer, where the pair amplitude is exponentially small: $I_c \propto e^{-L/L_T}$. Here, $L_T = \sqrt{\hbar D / 2\pi k_B T}$ is the characteristic thermal length in the diffusive limit and L is the length of the junction. These calculations, as well as those by Fink,⁴ analyzed the temperature dependence of I_c within the Ginzburg-Landau theory in the vicinity of the superconducting critical temperature T_c . Later, the critical current of diffusive S-N-S microbridges^{5,6} was successfully described by Likharev⁷ with the aid of the quasiclassical Usadel equations.⁸ In this work, the emphasis was put on the high-temperature regime where the superconducting order parameter is smaller than the thermal energy $\Delta \ll k_B T$. A more general study of the Josephson effect in diffusive S-N-S junctions was made in Ref. 9.

More recently, experimental data on long Josephson junctions¹⁰ showed a surprising temperature dependence, which turned out to be in a strong disagreement with the early theory by de Gennes. These data have been discussed by some of us¹¹ within the quasiclassical approach, which we

will also use in the present work. Fink¹² attempted to analyze the data¹⁰ by means of an extrapolation of the Ginzburg-Landau theory to low temperatures.

The proximity effect in mesoscopic hybrid structures consisting of normal and superconducting metals attracted a growing interest during recent years.¹³ Here we will consider mesoscopic diffusive S-N-S junctions where the sample length is much larger than the elastic mean free path l_e but smaller than the dephasing length L_φ : $l_e < L < L_\varphi$. In N-S junctions and Andreev interferometers, we can identify—both theoretically and experimentally—the natural energy scale for the proximity effect.^{14,15} It is given by the Thouless energy $\epsilon_c = \hbar D / L^2$. Here $D = v_F l_e / 3$ is the diffusion constant of the N metal, v_F is the Fermi velocity. In contrast to the energy gap Δ that is set by the interactions in the superconducting electrodes, the energy scale ϵ_c is a single-electron quantity: ϵ_c / \hbar is merely the diffusion rate across the sample for a single electron. This energy scale remains important in nonequilibrium situations, e.g., if one drives the supercurrent across a S-N-S junction by the injection of a control current in the N metal.^{16–18}

The main purpose of the present paper is to carry out a detailed experimental investigation of the equilibrium supercurrent in relatively long diffusive S-N-S junctions with highly transparent N-S interfaces as well as a quantitative comparison of our data to the theoretical predictions. Here, a long junction means that the junction length L is much bigger than $\sqrt{\hbar D / \Delta}$. This is equivalent to $\Delta \gg \epsilon_c$. In order to perform this comparison at all relevant temperatures, we complete the previous studies by providing a rigorous expression for the Josephson critical current at $T \rightarrow 0$, which was not properly evaluated before. Our experimental results are in excellent agreement with theoretical predictions.

As before,^{9,11} our theoretical approach is based on the quasiclassical Green’s functions in imaginary time. The proximity effect is described by a finite pair amplitude F in the N metal (see Ref. 19 and references therein). We will assume N-S interfaces to be fully transparent and neglect the suppression of the pair potential Δ in the S electrodes near

the N-S interface. This is appropriate at $T \ll T_c$ or if the reservoirs are very massive as compared to the normal metal. Within those bounds, our calculation does not contain further approximations and is, e.g., valid at arbitrary temperature and sample size. We will now proceed by discussing certain limits.

In the high-temperature regime $k_B T \gg \epsilon_c$ (or, equivalently, $L \gg L_T$), the solution is well known. In this case the mutual influence of the two superconducting electrodes can be neglected and the Usadel equations can be linearized in the N metal, except in the vicinity of the N-S interfaces. One finds:⁹

$$eR_N I_c = 64 \pi k_B T \sum_{n=0}^{\infty} \frac{L}{L_{\omega_n}} \frac{\Delta^2 \exp(-L/L_{\omega_n})}{[\omega_n + \Omega_n + \sqrt{2(\Omega_n^2 + \omega_n \Omega_n)}]^2}, \quad (1)$$

where R_N is the N-metal resistance, $\omega_n = (2n+1)\pi k_B T$ is the Matsubara frequency, $\Omega_n = \sqrt{\Delta^2 + \omega_n^2}$ and $L_{\omega_n} = \sqrt{\hbar D / 2\omega_n}$. If T is close to the critical temperature: $\Delta \ll k_B T$, the gap is small as compared to the thermal energy: $\Delta \ll k_B T$. In this limit, Eq. (1) coincides with the result derived by Likharev.⁷

At lower temperatures $k_B T \lesssim \epsilon_c$ evaluation of I_c involves solutions of the Usadel equation at *all* energies.¹⁹ In order to determine the precise value²⁰ of the critical current, we performed a numerical solution of the Usadel equations for the whole range of Matsubara frequencies. In the long-junction limit ($\Delta/\epsilon_c \rightarrow \infty$), the zero temperature $eR_N I_c$ is found to be proportional to ϵ_c :

$$eR_N I_c(T=0) = 10.82 \epsilon_c. \quad (2)$$

In this case, the current phase relation is slightly different from a sine and the supercurrent maximum occurs at $\varphi = 1.27\pi/2$. As compared to previous estimates,^{11,12} the exact numerical prefactor in this formula turns out to be unexpectedly high. This observation is crucial for a quantitative comparison between theory and experiment not only in the case of conventional junctions but also for high- T_c S-N-S junctions²¹ or devices involving carbon nanotubes.²²

Let us briefly consider the short-junction regime $\Delta \ll \epsilon_c$, i.e., the case of dirty S-C-S weak links described in Refs. 23 and 24. Our numerical results reproduces quantitatively the behaviors of both the current-phase relation and the zero-temperature critical current: $eR_N I_c \approx 1.326\pi\Delta/2$ at $\varphi = 1.25\pi/2$.^{23,24} This results confirms the precision of our calculation in describing both the long-junction and the short-junction regimes. Our numerical results for $I_c(T=0)$ as a function of the Thouless energy ϵ_c are presented in Fig. 1. It confirms that it is the minimum of the gap Δ and the Thouless energy ϵ_c that limits the critical current in diffusive S-N-S junctions. At $\epsilon_c \approx \Delta$, the critical current value remains close to the short-junction case.

In the following, we will focus on long junctions $\Delta > \epsilon_c$. Figure 2 shows the temperature dependence of the $eR_N I_c$ product for various values of the superconducting gap in the long-junction regime. Both axis are given in units of the Thouless energy. The low-temperature part ($k_B T < 5\epsilon_c$)

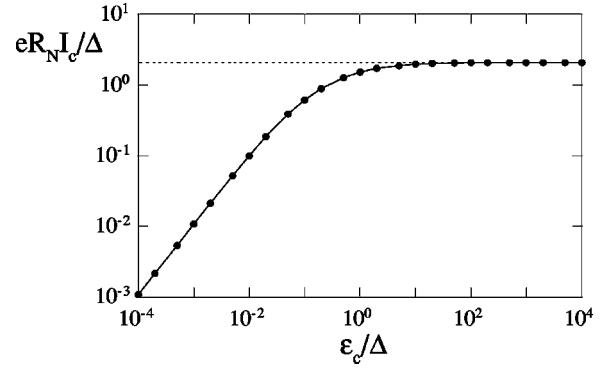


FIG. 1. Calculated dependence of the zero-temperature $eR_N I_c$ product in units of Δ as a function of the ratio ϵ_c/Δ . I_c is the Josephson critical current, R_N the normal-state resistance, ϵ_c is the Thouless energy, and Δ is the superconducting gap of S. The long-junction regime is on the left part of the graph where $\epsilon_c < \Delta$, the short-junction regime is on the right part where $\epsilon_c > \Delta$. The dashed line corresponds to the Kulik-Omel'yanchuk formula²⁵ at $T=0$.

comes from a numerical solution of the Usadel equation, while the high-temperature part comes from Eq. (1). From this figure, we can see that the characteristic decay temperature for the critical current is a few times the Thouless temperature ϵ_c/k_B . As soon as $k_B T > 5\epsilon_c$, the sum in Eq. (1) can be reduced to the first frequency term within a 3% underestimation. This term corresponds to $\omega_0 = \pi k_B T$ and $L_{\omega_0} = L_T$. Adding the second term in the summation decreases the error below 0.1% in the same temperature range.

The universal curve of Fig. 2 for $\Delta/\epsilon_c \rightarrow \infty$ is valid only in the case of a very long junction with $\Delta/\epsilon_c \gg 100$. It appears as if Δ is to be compared to the quantity $eR_N I_c(T=0) \approx 10\epsilon_c$ in the long-junction limit. In the limit of infinite Δ/ϵ_c , Eq. (1) simplifies to

$$eR_N I_c = \frac{32}{3 + 2\sqrt{2}} \epsilon_c \left[\frac{L}{L_T} \right]^3 e^{-L/L_T}. \quad (3)$$

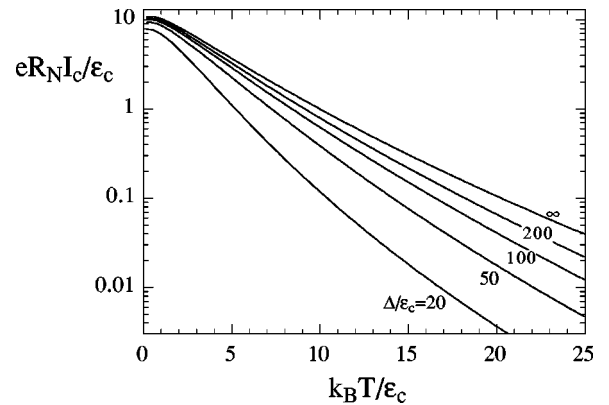


FIG. 2. Calculated temperature dependence of the $eR_N I_c$ product. The different curves correspond to various values of the ratio Δ/ϵ_c in the long-junction regime. The curve for $\Delta/\epsilon_c \rightarrow \infty$ is universal in the sense it does not depend on Δ . Note that $k_B T/\epsilon_c = L^2/2\pi L_T^2$.

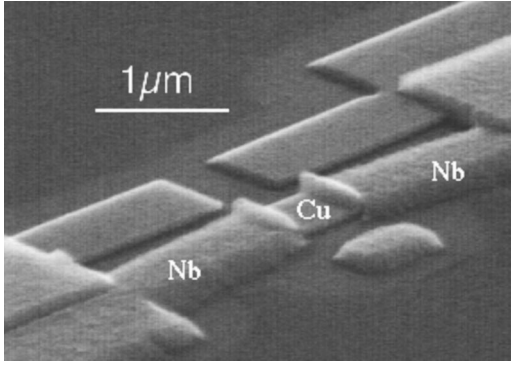


FIG. 3. Oblique micrograph of a typical S-N-S junction made of a Cu wire embedded between two Nb electrodes. The doubling of every structure due to the shadow evaporation is visible. The Nb electrodes cover the Cu strip over about 150 nm.

From Eq. (3), one can get the temperature dependence of the critical current: $I_c \propto T^{3/2} \exp(-L/L_T)$. It has been demonstrated in Ref. 11 that within a limited temperature interval this expression is *numerically* very close to a simple exponential dependence $I_c \propto \exp(-L/L_T)$ with $L_T \propto 1/T$, as one would expect in a ballistic limit.^{25,26} From Fig. 2, the quasiexponential temperature dependence of the critical current is indeed striking. This was the central result of Ref. 10, but was not understood at that time. This coincidence is purely accidental and has no special meaning.¹¹ In the low-temperature limit, the numerical solution can be approximated by $eR_N I_c / \epsilon_c = a(1 - b e^{-a\epsilon_c / 3.2k_B T})$. The coefficients a and b are 10.82 and 1.30, respectively, in the long-junction limit, i.e., at $\Delta/\epsilon_c \rightarrow \infty$.

S-N-S junctions are intrinsically shunted and have negligible internal capacitance, so they are strongly overdamped. Their current-voltage characteristics are hence intrinsically nonhysteretic. The transition from a supercurrent to a voltage state happens at the critical current, but is rounded by finite temperature.²⁷ We fabricated Nb-Cu-Nb junctions²⁸ with a large conductance so that thermal fluctuations remain small compared to the Josephson energy: $k_B T \ll \hbar I_c(T)/2e$ even at high temperature near the critical temperature of Nb. This ensures a well-defined critical current up to the critical temperature of Nb. Effects of environmental fluctuations known from mesoscopic tunnel junctions,²⁹ which are intrinsically underdamped, are absent.

We benefited from a trilayer stencil mask technology³⁰ making use of a thermostable resist that does not outgas during Nb evaporation. Thus we were able to routinely obtain a superconducting critical temperature as high as 8.1 K for the Nb electrodes. We performed successive shadow evaporations of Cu and Nb at different angles through the silicon stencil layer in an ultra-high vacuum chamber, followed by a liftoff. Figure 3 shows a typical sample. We studied a single sample (*a*) plus five different samples evaporated on the same substrate (*b*, *c*, *d*, *e*, and *f*). Table I lists the main physical parameters for these samples. The Cu metallic strips are 600 nm wide and 100 nm thick. The Nb superconducting electrodes are 800 nm wide and 200 nm thick, except for sample *a* where it is 100 nm. The length L of the metallic island was varied between 700 and 1000 nm, corresponding to a separation length d_{Nb} between Nb electrodes varying between 370 and 700 nm. For all samples, the calculated Thouless energy $\hbar D/L^2$ is therefore significantly smaller than the gap Δ .

The normal-state resistance R_N cannot be directly measured at temperature above T_c since the resistance of the Nb electrodes is measured in series. We found that the finite-bias resistance ($eV \approx \epsilon_c$) varied by about 10% between 2 K and 8 K due to the proximity effect on the conductance. We took for the normal-state resistance R_N the resistance at $T = 6$ K for a better agreement with theory. It is a relatively high temperature since $k_B T > 15\epsilon_c$ for every sample then. Using L for the Cu length, we obtain a Cu resistivity $\rho = 1.1 \times 10^{-8} \Omega \text{ m}$ for samples *b* to *f* and $\rho = 1.5 \times 10^{-8} \Omega \text{ m}$ for sample *a*.

We measured the critical current of samples *a* to *f* at temperatures down to 300 mK. Our procedure consists of sweeping the bias current while measuring the differential resistance dV/dI . We define the experimental critical current as the current where the differential resistance reaches $R_N/2$. With this criteria, the experimental uncertainty is estimated below 0.5% at $T = 2$ K, 5% around $T = 4$ K and 100% at 7 K. Figure 4 shows the data for three samples. The measured $eR_N I_c / \epsilon_c$ plotted as a function of the reduced temperature $k_B T / \epsilon_c$ show a large decrease over more than two decades. For each sample, we fitted the data to the theoretical prediction with only one fitting parameter, the Thouless energy. The zero-temperature superconducting gap Δ was calculated from the measured critical temperature of Nb using

TABLE I. Parameters of the different samples studied. L is the full length of Cu strip, while d_{Nb} is the Nb electrodes separation and w is the Cu strip width. The Thouless energy ϵ_c is derived from the fit of the experimental data to the theoretical prediction (see Fig. 4).

#	L (nm)	d_{Nb} (nm)	w (nm)	$R_{N,6 \text{ K}}$ (Ω)	D (cm^2/s)	$\hbar D/L^2$ (μeV)	ϵ_c (μeV)	Δ/ϵ_c	$\frac{eR_N I_c}{\epsilon_c}(T=0)$
<i>a</i>	1000	600	600	0.260	200	13	14.3	70	8.91
<i>b</i>	1010	680	580	0.173	300	20	18.6	70	8.99
<i>c</i>	910	570	590	0.179	260	22	21.7	60	8.83
<i>d</i>	800	470	580	0.183	230	25	25.4	51	8.64
<i>e</i>	800	476	590	0.169	250	26	26.1	50	8.62
<i>f</i>	710	370	580	0.152	250	34	33.5	39	8.32

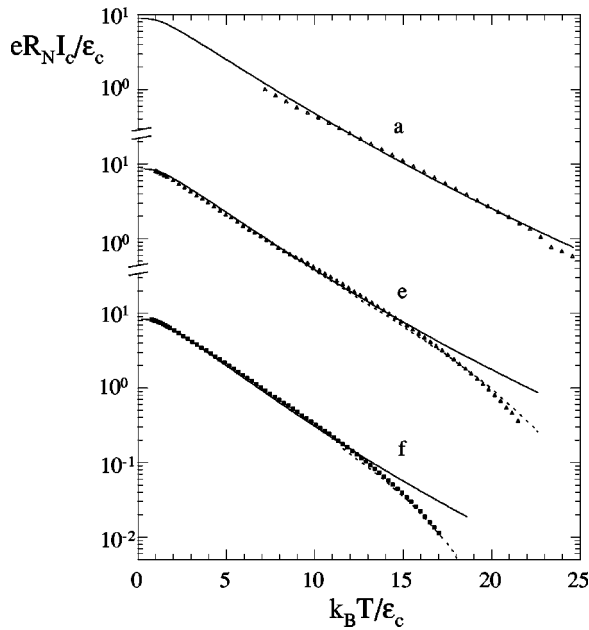


FIG. 4. Temperature dependence of the measured $eR_N I_c$ product of samples *a*, *e*, and *f* together with the theoretical fits assuming a temperature-independent gap (full line) and a gap following a BCS temperature dependence with $T_c = 7.5$ K (dashed line). The only adjustment parameter is the Thouless energy ϵ_c of each sample. For a description of the sample parameters, see Table I.

$2\Delta = 3.8 k_B T_c$.³¹ This gives $\Delta = 1.3$ meV for all samples except sample *a* for which $\Delta = 1$ meV. We used both a fixed gap equal to the zero-temperature value and a gap $\Delta(T)$ following the BCS temperature dependence, but with a slightly reduced critical temperature $T_c = 7.5$ K. For samples *e*, *f* and at high temperature, it appears necessary to take into account the temperature dependence of the gap. In this case, the agreement between theory and experiment is excellent. The fit is very sensitive to the chosen value of the Thouless energy. We would like to stress that for each sample the horizontal and vertical axis are normalized to the same Thouless energy ϵ_c . Each such value is found to be very close to the Thouless energy calculated from the full length L of the Cu strip; see Table I.

In Fig. 4, the critical current of sample *f* shows the onset of the saturation regime. At $T = 300$ mK the adjusted critical current $eR_N I_c$ reaches up to $8.2 \epsilon_c$. This number is close to the theoretical value $8.79 \epsilon_c$ for sample *f* at $T = 0$. This result discards an interpretation of our data within the Ginzburg-Landau theory of Ref. 12, which predicts a maximum $eR_N I_c / \epsilon_c$ of about 1.

In Ref. 10, an array of S-N-S junctions was made of a long N-metal wire periodically in contact with a series of superconducting islands. A good fit between the data and theory was shown in Ref. 11, but with the introduction of a strong reduction of the effective area. This may be attributed to the periodic and lateral characters of this type of samples.

Our calculation assumes perfectly transmitting interfaces with zero boundary resistance. In fact, it is sufficient that the barrier-equivalent length³² $L_t = l_e / t$ is much smaller than the sample length. As an example, this condition means an interface transparency $t > 0.1$ for sample *b*. In the case of Nb-Cu-Nb samples fabricated through a two-lithography-step process including Ar etching,³³ we found a critical current with a reduced magnitude, presumably due to a slightly degraded interface. The critical current in S-N-S junctions with partially transparent interfaces was discussed in Ref. 34. The predicted behavior features a different temperature dependence for the critical current. Nevertheless, the measured temperature dependence remained consistent with theory assuming a perfect interface. Only a reduction prefactor had to be introduced. This observation could hint at the fact that interface barriers are very inhomogeneous and the current is carried through a few highly conducting pinholes.

In summary, we discussed the Josephson critical current of diffusive S-N-S junctions. This study provides a simple and reliable formulation that enables the practical determination of the equilibrium critical current. We studied the critical current of a set of samples with different junction lengths and found excellent agreement between our data and the predictions of quasiclassical theory.

We acknowledge discussion and financial support in the EU-TMR network ‘‘Dynamics of superconducting circuits’’ as well as support from the DFG through SFB 195 and GK 284. We thank A. Golubov, T.T. Heikkilä, D. Mailly, N. Moussy, and P. Paniez for discussions.

¹J. Clarke, Proc. R. Soc. London, Ser. A **308**, 447 (1969).

²J.G. Shepherd, Proc. R. Soc. London, Ser. A **326**, 421 (1972).

³P.G. de Gennes, Rev. Mod. Phys. **36**, 225 (1964).

⁴H.J. Fink, Phys. Rev. B **14**, 1028 (1976).

⁵J. Warlaumont, J.C. Brown, and R.A. Buhrman, Appl. Phys. Lett. **34**, 415 (1979).

⁶R.B. van Dover, A. de Lozanne, and M.R. Beasley, J. Appl. Phys. **52**, 7327 (1981).

⁷K.K. Likharev, Sov. Tech. Phys. Lett. **2**, 12 (1976).

⁸K.D. Usadel, Phys. Rev. Lett. **25**, 507 (1970).

⁹A.D. Zaikin and G.F. Zharkov, Sov. J. Low Temp. Phys. **7**, 184 (1981). In Eq. 14 and 15 of that paper, the prefactor 128 refers to the case where R_N is the resistance *per spin*. It should be re-

placed by 64 if one identifies R_N with the full resistance.

¹⁰H. Courtois, Ph. Gandit, and B. Pannetier, Phys. Rev. B **52**, 1162 (1995).

¹¹F.K. Wilhelm, A.D. Zaikin, and G. Schön, J. Low Temp. Phys. **106**, 305 (1997).

¹²H.J. Fink, Phys. Rev. B **56**, 2732 (1997).

¹³See the special issue of Superlattices Microstruct. **25** (5/6), 627–1288 (1999).

¹⁴H. Courtois, Ph. Gandit, D. Mailly, and B. Pannetier, Phys. Rev. Lett. **76**, 130 (1996).

¹⁵B. Pannetier and H. Courtois, J. Low Temp. Phys. **118**, 599 (2000).

¹⁶J.J.A. Baselmans, A.F. Morpurgo, B.J. van Wees, and T.M. Klap-

- wijk, *Nature (London)* **397**, 43 (1999).
- ¹⁷F.K. Wilhelm, G. Schön, and A.D. Zaikin, *Phys. Rev. Lett.* **81**, 1682 (1998).
- ¹⁸J. Kutchinsky, R. Taboryski, C.B. Sørensen, J.B. Hansen, and P.E. Lindelof, *Phys. Rev. Lett.* **83**, 4856 (1999).
- ¹⁹W. Belzig, F. K. Wilhelm, C. Bruder, G. Schön, and A. D. Zaikin, in Ref. 13.
- ²⁰In the long-junction regime $\Delta > \epsilon_c$, the extrapolation of low-(Ref. 11) or high-(Ref. 12) energy dependencies provides a reasonable parameter dependence, but fails to predict the correct prefactor.
- ²¹K.A. Delin and A.W. Kleinsasser, *Supercond. Sci. Technol.* **9**, 227 (1996).
- ²²A.Yu. Kasumov, R. Deblock, M. Kociak, B. Reulet, H. Bouchiat, I. I. Khodos, Yu. B. Gorbatov, V. T. Volkov, C. Journet, and M. Burghard, *Science* **284**, 1508 (1999).
- ²³I.O. Kulik and A.N. Omel'yanchuk, *Sov. J. Low Temp. Phys.* **4**, 142 (1978).
- ²⁴A.D. Zaikin and S.V. Panyukov, *Zh. Éksp. Teor. Fiz.* **89**, 242 (1985) [*Sov. Phys. JETP* **62**, 137 (1985)].
- ²⁵I.O. Kulik, *Zh. Éksp. Teor. Fiz.* **57**, 1745 (1969) [*Sov. Phys. JETP* **30**, 944 (1970)].
- ²⁶C. Ishii, *Prog. Theor. Phys.* **14**, 1525 (1970).
- ²⁷V. Ambegaokar and B.I. Halperin, *Phys. Rev. Lett.* **22**, 1364 (1969).
- ²⁸F.K. Wilhelm, G. Schön, A.D. Zaikin, A.A. Golubov, P. Dubos, H. Courtois, and B. Pannetier, *Physica B* **284-288**, 1836 (2000).
- ²⁹D. Vion, M. Götze, P. Joyez, D. Estève, and M.H. Devoret, *Phys. Rev. Lett.* **77**, 3435 (1996).
- ³⁰P. Dubos, P. Charlat, Th. Crozes, P. Paniez, and B. Pannetier, *J. Vac. Sci. Technol. B* **18**, 122 (2000).
- ³¹N. Ashcroft and N. Mermin, *Solid State Physics* (Holt-Saunders, Orlando, FL, 1976).
- ³²F. Zhou, B. Spivak, and A. Zyuzin, *Phys. Rev. B* **52**, 4467 (1995).
- ³³P. Dubos and D. Mailly (unpublished).
- ³⁴M.Yu. Kuprianov and V.F. Lukichev, *Zh. Éksp. Teor. Fiz.* **94**, 139 (1988) [*Sov. Phys. JETP* **67**, 1163 (1988)].

Observation of a controllable π junction in a 3-terminal Josephson device

Jian Huang,¹ F. Pierre,¹ Tero T. Heikkilä,² Frank K. Wilhelm,³ and Norman O. Birge¹

¹*Department of Physics and Astronomy, Michigan State University, East Lansing, Michigan 48824-1116*

²*Materials Physics Laboratory, Helsinki University of Technology, FIN-02015 HUT, Finland*

³*Sektion Physik and CeNS, LMU, Theresienstrasse 37, D-80333 München, Germany*

(Received 28 February 2002; published 10 July 2002)

Recently Baselmans *et al.* [Nature, (London) **397**, 43 (1999)] showed that the direction of the supercurrent in a superconductor/normal/superconductor Josephson junction can be reversed by applying, perpendicularly to the supercurrent, a sufficiently large control current between two normal reservoirs. The unusual behavior of their 4-terminal device (called a controllable π junction) arises from the nonequilibrium electron energy distribution established in the normal wire between the two superconductors. We have observed a similar supercurrent reversal in a 3-terminal device, where the control current passes from a single normal reservoir into the two superconductors. We show theoretically that this behavior, although intuitively less obvious, arises from the same nonequilibrium physics present in the 4-terminal device. Moreover, we argue that the amplitude of the π -state critical current should be at least as large in the 3-terminal device as in a comparable 4-terminal device.

DOI: 10.1103/PhysRevB.66.020507

PACS number(s): 74.50.+r, 73.23.-b, 85.25.Am, 85.25.Cp

When a normal metal is put in contact with one or more superconductors, the properties of both materials are modified near the interface. The physical phenomena associated with superconductor (*S*)/normal (*N*) systems, namely the proximity and Josephson effects, were intensely studied in the 1960's and 1970's.¹ Interest in *S/N* systems was rekindled in the 1990's due to the ability to fabricate complex structures with submicrometer dimensions. A new, deeper understanding of the proximity effect on mesoscopic length scales has emerged,^{2,3} concentrating on equilibrium and linear-response physics.

Nonequilibrium phenomena in *S/N* systems are now taking the spotlight.⁴⁻⁶ A major discovery was made by Baselmans *et al.*,⁶ who measured a 4-terminal diffusive metal *S/N/S* Josephson device with a cross shape. Two opposing ends of the cross were connected to *S* electrodes, while the other two were connected to *N* reservoirs between which a control current was passed. Baselmans *et al.* found that, at high control current, in samples with the normal reservoirs sufficiently close together, the sign of the Josephson supercurrent between the *S* electrodes reversed direction. The current-phase relationship under such conditions becomes $I_s(\phi) = I_c \sin(\phi + \pi)$, where I_c is the (positive) critical supercurrent, rather than the usual Josephson relationship $I_s(\phi) = I_c \sin(\phi)$, hence the device is called a π junction. Such a device has been used to make a controllable π superconducting quantum interference device.⁷ The explanation of the nonequilibrium π junction consists of two parts.^{8,9} First, the supercurrent can be decomposed into an energy-dependent "spectral supercurrent" j_E , which is an equilibrium property determined by the sample geometry and resistance as well as the phase difference ϕ between the two *S* electrodes. j_E is an odd function of energy, and exhibits damped oscillations on an energy scale comparable to the Thouless energy of the sample, $E_{th} = \hbar D/L^2$, with D the diffusion constant in the wire and L the length between the superconductors. Second, the total supercurrent is determined by the occupation of the supercurrent-carrying states, given by the antisymmetric part

of the quasiparticle distribution function $f(E)$ in the normal region of the junction describing the pairs of quasiparticles ($E > E_F$) and quasiholes ($E < E_F$). Under nonequilibrium conditions, $f(E)$ can be made to have a staircase shape, with steps appearing at the voltages of the normal reservoirs.¹⁰ The staircase shape of $f(E)$ excludes the low-energy contribution of j_E from the supercurrent. When the control voltage approaches the energy where j_E changes sign, the supercurrent changes its sign relative to the equilibrium situation. In contrast to the π -junction behavior, smearing of the distribution function by electron heating or raising the sample temperature simply causes the supercurrent to decrease toward zero without ever changing sign.

The sample shown in Fig. 1 consists of a *T*-shaped Ag wire, 70 nm wide and 50 nm thick, connected to two *S* electrodes (70 nm of Al) and one *N* reservoir (230 nm of Ag).

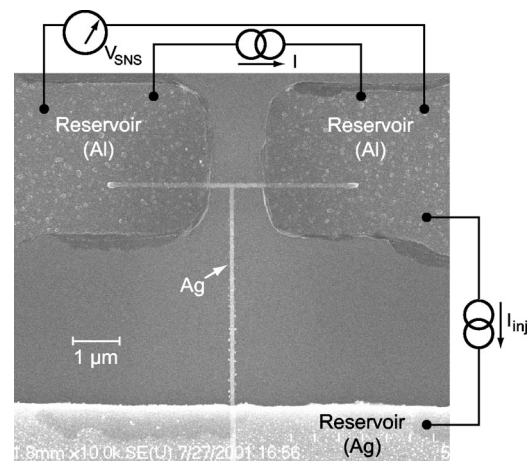


FIG. 1. Scanning electron microscope picture of the sample, with schematic drawing of the measurement circuit. The sample consists of a *T*-shaped Ag wire with lateral dimensions of 50 nm \times 70 nm, connected to two 70-nm-thick Al electrodes and one 230-nm-thick Ag electrode.

The distance between S electrodes is $1.1 \mu\text{m}$, while the distance from the top of the “ T ” to the N reservoir is $4.5 \mu\text{m}$. The phase coherence length L_ϕ in similarly prepared Ag wires is several micrometers at sub-Kelvin temperatures, hence we expect to observe a substantial Josephson effect between the two S electrodes. The sample was fabricated using one electron-beam and two optical lithography steps. The T -shaped Ag wire was fabricated first, followed by the thick Ag reservoir, and finally the Al electrodes. A gentle ion mill of the exposed ends of the Ag wire preceded the evaporation of the Al electrodes to enhance the transparency of the Ag/Al interfaces. The sample was immersed in the mixing chamber of a dilution refrigerator with filtered electrical leads.

The transport properties of the sample were determined initially by measuring the V vs I characteristics between pairs of electrodes. The V - I curve between S electrodes shows the standard Josephson-junction behavior with a critical current of $0.7 \mu\text{A}$ at 38 mK . The V - I curve between the N electrode and either of the S electrodes exhibits a change in slope at a current approximately equal to twice the critical current. This behavior is due to the superposition of opposite-flowing quasiparticle current and supercurrent in the dangling arm, as observed recently by Shaikhaidarov *et al.*¹¹ For the sample shown in Fig. 1, the left and right arms have resistances of $R_1 = 7.0 \Omega$ and $R_2 = 9.1 \Omega$, respectively, while the base of the T has a resistance of $R_0 = 36 \Omega$. From these values and the sample geometry, we deduce that about half of the 16.1Ω S - S resistance comes from the uncovered part of the Ag wire, and the other half from the Al/Ag interfaces and part of the Ag wire extending under the Al electrodes.

The measurement circuit for the nonequilibrium injection experiment is shown schematically in Fig. 1. A dc current I_{inj} is injected from the normal electrode to one of the superconducting electrodes. Simultaneously, the V - I curve between the two superconducting electrodes is measured in a four-probe configuration. Figure 2 shows a subset of V - I curves for different values of I_{inj} , and is the central result of this paper. The critical current of the $S/N/S$ junction decreases rapidly with increasing injection current. When $I_{\text{inj}} = 1.0 \mu\text{A}$, the critical current is below our measurement threshold. Upon further increase of I_{inj} , the critical current increases again, and finally disappears when $I_{\text{inj}} > 3 \mu\text{A}$. In Fig. 3, we plot I_c vs V_N at three different temperatures, where $V_N = R_N I_{\text{inj}}$ is the voltage of the normal reservoir with respect to the superconductors, and $R_N = R_0 + (R_1^{-1} + R_2^{-1})^{-1} = 40 \Omega$. In the figure we intentionally plot $I_c < 0$ after it falls to zero, to emphasize that the junction has entered the “ π ” state.¹² Our interpretation of the data is consistent with the assumption that, for fixed ϕ , I_s is a smooth function of V_N with a continuous first derivative. It is also consistent with the experiment of Baselmans *et al.*,⁶ who confirmed the existence of the “ π ” state by measuring the resistance of the normal wire as a function of the supercurrent, hence the phase difference ϕ , between the S electrodes. At zero supercurrent, their wire resistance exhibits a local minimum in the usual “0” state and a local maximum in the “ π ” state due to the proximity effect.

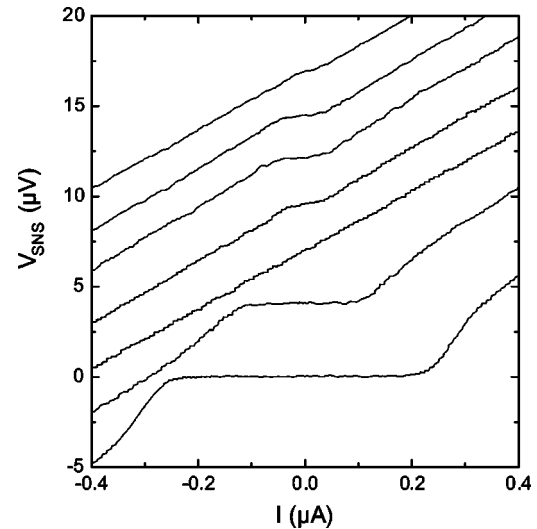


FIG. 2. A subset of $V_{S/N/S}$ vs I curves measured across the $S/N/S$ Josephson junction, for different values of the current injected from the normal reservoir. From bottom to top, the injected currents I_{inj} are in microampere: 0.53, 0.70, 1.01, 1.23, 1.89, 2.18, 3.15. The curves are offset for clarity.

The significant difference between our experiment and that of Baselmans *et al.*, aside from the reduction from 4 terminals to 3, is the presence in our sample of a dissipative quasiparticle current in the sample arms that simultaneously carry the supercurrent. In the Baselmans experiment, the control voltages of the two normal reservoirs were set to values $\pm V_N$ with respect to the superconductors, so that the electrical potential was zero everywhere along the wire connecting the two superconductors. To compare our experiment with theirs, we must understand the influence of the dissipative current on the supercurrent in our sample. We use the quasiclassical formalism in real time, which was originally

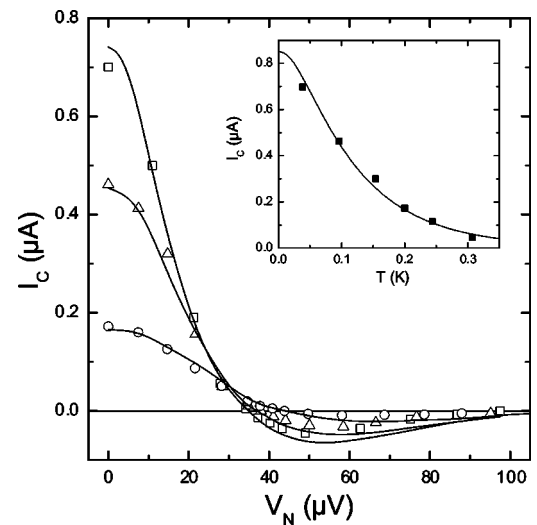


FIG. 3. Critical current of the Josephson junction vs voltage of the normal reservoir at $T = 38$ (\square), 96 (\triangle), and 200 mK (\circ). I_c is shown as negative for $V_N \geq 40 \mu\text{V}$ to symbolize the appearance of the π junction. Inset: Critical current vs temperature at $V_N = 0$. The lines are the theoretical calculations discussed in the text.

developed for nonequilibrium phenomena in massive superconductors¹³ but also adapted and successfully applied to mesoscopic proximity systems, as reviewed, e.g., in Refs. 3 and 14.

For the present paper, we are concerned primarily with the supercurrent

$$I_S = \frac{\sigma_N A}{2} \int j_E f_L(E) dE, \quad (1)$$

where σ_N and A are the conductance and cross section of the normal wire, j_E is the spectral supercurrent discussed earlier, and $f_L(E) = f(-E) - f(E)$ is the antisymmetric part of the electron energy distribution function. With the chemical potential of the superconductors taken to be zero, the symmetric distribution function $f_T(E) = 1 - f(E) - f(-E)$ describes charge imbalance, while $f_L(E)$ describes energy or heat in the conduction-electron system.

To calculate the supercurrent, first one must solve the Usadel equation for the retarded and advanced Green's functions. Those contain all information about energy-dependent properties of the sample, including the function j_E . To find $f_L(E)$, one must then solve the Keldysh component of the Usadel equation, which takes the form of conservation laws for the spectral charge and heat currents.¹⁴ When $j_E \neq 0$, the two kinetic equations are coupled, and lead to complicated spatial and energy dependences of $f_L(E)$ and $f_T(E)$ in the arms of the sample between the superconductors. A major simplification occurs in the arm of the sample connected to the normal reservoir: there $j_E = 0$ since the superconducting phase is constant along that arm. For voltages and temperatures small as compared to Δ the heat current is zero,¹⁵ hence $f_L(E)$ is constant along that arm and takes on the (equilibrium) value it has in the N reservoir: $f_L^0 = (1/2)\{\tanh[(E + eV_N)/2k_B T] + \tanh[(E - eV_N)/2k_B T]\}$. Since the total charge current is conserved along the two sample arms connecting the superconductors, we can evaluate it anywhere in those arms. At the central point, the dissipative currents diverted into the two arms cancel and we can find the supercurrent from Eq. (1) using the expression for $f_L^0(E)$ given above, without integrating the kinetic equations. We need only to evaluate j_E at the central point by solving the equilibrium Usadel equation for our sample geometry.

As an extension of previous work,⁹ we have solved the retarded Usadel equation taking into account the influence of the lead to the normal reservoir and the finite interface resistances.¹⁶ The normal reservoir induces extra decoherence into the structure, decreasing the magnitude of the observed supercurrent. We find that the full gap in the spectral supercurrent⁹ becomes a pseudogap and that the amplitude of the maximum of j_E is strongly reduced (although the total supercurrent is reduced by only 20% at 40 mK). Our fit to the equilibrium data of critical supercurrent vs temperature is shown in the inset to Fig. 3. To fit the temperature dependence, the Thouless energy was adjusted to be $E_{Th} = 3.5 \mu\text{eV}$, which corresponds to a distance $L = 1.7 \mu\text{m}$ between the superconducting electrodes—larger than the actual distance as a result of the silver wire penetration under the aluminum reservoirs and of the finite contact resistances.

Surprisingly, the magnitude of the calculated critical current had to be reduced by a factor 1.7 to match the experimental data, possibly due to the rather high S/N interface resistances in this sample.¹⁷

If we now calculate the nonequilibrium data of I_c vs V_N using the equilibrium form for f_L^0 in the normal reservoir, we find that the calculation overestimates the critical current in the “ π ” state by a large factor, and predicts too small a voltage at which the supercurrent changes sign. This failure results from neglecting inelastic collisions inside the wire and electron heating in the normal reservoir. Based on our previous measurements of $f(E)$ in nonequilibrium mesoscopic metal wires,^{10,18} we can estimate the contributions of both inelastic scattering and reservoir heating to the rounding of $f(E)$ in our sample. Inelastic scattering in similar Ag wires was well described within the framework of the Boltzmann equation using an electron-electron interaction kernel in agreement with the theoretical form $K(E) = K_{3/2} E^{-3/2}$, but with a prefactor $K_{3/2} \approx 0.5 \text{ ns}^{-1} \text{ meV}^{-1/2}$, about five times larger than predicted by theory. Heating of the normal reservoir can be estimated using the Wiedemann-Franz law and a simplified model of electron-phonon scattering in the reservoir.^{19,20} The temperature of the electrons in the reservoir is given by $T_{\text{eff}} = \sqrt{T^2 + b^2 V_N^2}$ where b^2 is proportional to the ratio of the reservoir sheet resistance to the wire resistance.¹⁹ From our sample parameters and previous measurements of similar samples,²⁰ we estimate $b \approx 1 \text{ K/mV}$. Using these values of $K_{3/2}$ and b , we have calculated $f(E)$ and thereby $I_c(V_N)$ in our sample by solving the Boltzmann equation with the correct boundary conditions at the S/N interfaces,⁵ but neglecting proximity effect in the bulk of the wire. The result of that calculation does not fit the data shown in Fig. 3. A much larger value of $K_{3/2} = 3 \text{ ns}^{-1} \text{ meV}^{-1/2}$ provides a reasonable fit, but leaves us without a plausible explanation for the enhanced electron-electron interactions. An alternative approach is to use an interaction kernel of the form $K(E) = K_2 E^{-2}$, which describes samples containing dilute magnetic impurities.^{20,21} With the value $K_2 = 0.55 \text{ ns}^{-1}$, corresponding to a magnetic impurity concentration of about 0.1 ppm, we obtain the solid curves shown in Fig. 3, which fit the data well at voltages up

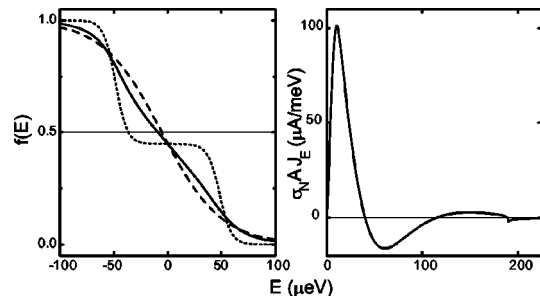


FIG. 4. Left: Solid line: distribution function $f(E)$ used to calculate the Josephson junction current in the π state at $V_N = 50 \mu\text{V}$ and $T = 38 \text{ mK}$. Dotted line: $f(E)$ taking into account only reservoir heating but not energy exchange. Dashed line: hot Fermi-Dirac distribution. Right: Numerically calculated j_E (multiplied by the prefactor $\sigma_N A$), at the central point of the sample, shown only for $E > 0$.

to the crossover to the π junction. Adding a reasonable $K_{3/2}$ term to $K(E)$ improves the fit only slightly at higher voltages. The magnetic impurity concentration of 0.1 ppm is plausible, and will limit L_ϕ to about $5 \mu\text{m}$ near the Kondo temperature—still much larger than the distance between the two superconducting electrodes.

The rather poor fit to the data at high voltages may reflect the fact that the magnitude of I_c in the π state depends on a delicate balance between the positive and negative parts of j_E , weighted by the precise shape of $f(E)$. Figure 4 shows $f(E)$ for $V_N = 50 \mu\text{V}$, near the maximum π junction I_c . By eye $f(E)$ looks nearly like a hot Fermi-Dirac function, but the dashed line in the figure shows that it is not. If the sample were shorter, so that $f(E)$ maintained the staircase structure of the dotted line in the figure, the π junction I_c would be much larger.

Figure 4 also reveals the difference between our 3-terminal experiment and the 4-terminal experiment of Baselmans *et al.* In our sample the electrical potential is non-zero at the central point, since the injection current flows into both the S electrodes. Hence $f(E=0) \neq \frac{1}{2}$ at the central point, unlike in Baselmans's sample. (The deviation from $1/2$ is

small, since the vertical arm of our sample is much longer than the horizontal arms.) Since the available phase space for quasiparticle energy exchange decreases as $f(E)$ deviates from $1/2$, the 3-terminal geometry should be favorable for maximizing I_c in the π state. A direct measurement of this subtle effect could be made in a 4-terminal sample. Biasing the two normal reservoirs at the same potential V_N , rather than at asymmetric voltages $\pm V_N$, would result in a current flow pattern and distribution functions essentially equivalent to those in our 3-terminal experiment. A comparison of the values of I_c in the π state under symmetric bias (V_N, V_N) and antisymmetric bias ($V_N, -V_N$) might reveal a subtle difference in the smearing of $f(E)$. We plan to explore this comparison experimentally.

We thank D. Esteve and H. Pothier for suggesting the “dangling arm” experiment, and I. O. Kulik for a valuable discussion concerning electron heating. This work was supported by NSF Grants Nos. DMR-9801841 and 0104178, and by the Keck Microfabrication Facility supported by NSF Grant NO. DMR-9809688.

-
- ¹G. Deutscher and P. G. deGennes, in *Superconductivity*, edited by R. D. Parks (Dekker, New York, 1969), p. 1005; K.K. Likharev, *Rev. Mod. Phys.* **51**, 101 (1979).
- ²B. Pannetier and H. Courtois, *J. Low Temp. Phys.* **118**, 599 (2000), and references therein.
- ³C.J. Lambert and R. Raimondi, *J. Phys.: Condens. Matter* **10**, 901 (1998).
- ⁴Th. Schäpers, J. Malindretos, K. Neurohr, S. Lachenmann, A. van der Hart, G. Creceius, H. Hardtdegen, H. Lüth, and A.A. Golubov, *Appl. Phys. Lett.* **73**, 2348 (1998).
- ⁵F. Pierre, A. Anthore, H. Pothier, C. Urbina, and D. Esteve, *Phys. Rev. Lett.* **86**, 1078 (2001).
- ⁶J.J.A. Baselmans, A.F. Morpurgo, B.J. van Wees, and T.M. Klapwijk, *Nature (London)* **397**, 43 (1999); J.J.A. Baselmans, B.J. van Wees, and T.M. Klapwijk, *Phys. Rev. B* **63**, 094504 (2001).
- ⁷J.J.A. Baselmans, B.J. van Wees, and T.M. Klapwijk, *Appl. Phys. Lett.* **79**, 2940 (2001).
- ⁸B.J. van Wees, K.M.H. Lenssen, and C.J.P.M. Harmans, *Phys. Rev. B* **44**, 470 (1991); G. Wendin and V.S. Shumeiko, *ibid.* **53**, R6006 (1996); L.-F. Chang and P.F. Bagwell, *ibid.* **55**, 12678 (1997).
- ⁹F.K. Wilhelm, G. Schön, and A.D. Zaikin, *Phys. Rev. Lett.* **81**, 1682 (1998); S.-K. Yip, *Phys. Rev. B* **58**, 5803 (1998).
- ¹⁰H. Pothier, S. Guéron, N.O. Birge, D. Esteve, and M.H. Devoret, *Phys. Rev. Lett.* **79**, 3490 (1997).
- ¹¹R. Shakhaidarov, A.F. Volkov, H. Takayanagi, V.T. Petrashov, and P. Delsing, *Phys. Rev. B* **62**, R14649 (2000).
- ¹²Technically it is not correct to say that I_c changes sign. What changes sign is $I_s(\phi)$ for a fixed value of ϕ , e.g., $\phi = \pi/2$. Hence I_c stays positive when V_N exceeds $40 \mu\text{V}$, while I_s changes from $I_c \sin(\phi)$ to $I_c \sin(\phi + \pi)$.
- ¹³J. Rammer and H. Smith, *Rev. Mod. Phys.* **58**, 323 (1986).
- ¹⁴W. Belzig, F.K. Wilhelm, C. Bruder, G. Schön, and A. Zaikin, *Superlattices Microstruct.* **25**, 1251 (1999). The kinetic equations are valid in a normal metal without inelastic scattering.
- ¹⁵A.F. Andreev, *Zh. Eksp. Teor. Fiz.* **46**, 1823 (1964) [*Sov. Phys. JETP* **19**, 1228 (1964)].
- ¹⁶W. Belzig, A. Brataas, Yu.V. Nazarov, and G.E.W. Bauer, *Phys. Rev. B* **62**, 9726 (2000); K.M. Schep and G.E.W. Bauer, *Phys. Rev. Lett.* **78**, 3015 (1997).
- ¹⁷In a private communication, J. J. A. Baselmans told us that similarly prepared samples can show large variations in the overall magnitude of the supercurrent while the functional dependence on the voltage remains the same.
- ¹⁸F. Pierre, H. Pothier, D. Esteve, and M.H. Devoret, *J. Low Temp. Phys.* **118**, 437 (2000).
- ¹⁹M. Henny, S. Oberholzer, C. Strunk, and C. Schönberger, *Phys. Rev. B* **59**, 2871 (1999).
- ²⁰F. Pierre, H. Pothier, D. Esteve, M.H. Devoret, A.B. Gougam, and N.O. Birge, in *Kondo Effect and Dephasing in Low-Dimensional Metallic Systems*, edited by V. Chandrasekhar, C. Van Haesendonck, and A. Zawadowski (Kluwer, Dordrecht, 2001), p. 119; F. Pierre, *Ann. Phys. Fr.* **26**, N4 (2001).
- ²¹A. Kaminski and L.I. Glazman, *Phys. Rev. Lett.* **86**, 2400 (2001).

Supercurrent-induced Peltier-like effect in superconductor/normal-metal weak links

Tero T. Heikkilä,^{1,2,*} Tommy Vänkä,¹ and Frank K. Wilhelm³

¹Materials Physics Laboratory, Helsinki University of Technology, P.O. Box 2200, FIN-02015 HUT, Finland

²Low Temperature Laboratory, Helsinki University of Technology, P.O. Box 2200, FIN-02015 HUT, Finland

³Sektion Physik and CeNS, Ludwig-Maximilians-Universität, Theresienstrasse 37, D-80333 München, Germany

(Received 30 October 2002; published 17 March 2003)

The local nonequilibrium quasiparticle distribution function in a normal-metal wire depends on the applied voltage over the wire and the type and strength of different scattering mechanisms. We show that in a setup with superconducting reservoirs, in which the supercurrent and the dissipative current flow (anti) parallel, the distribution function can also be tuned by applying a supercurrent between the contacts. Unlike the usual control by voltage or temperature, this leads to a Peltier-like effect: the supercurrent converts an externally applied voltage into a difference in the effective temperature between two parts of the system maintained at the same potential. We suggest an experimental setup for probing this phenomenon and mapping out the controlled distribution function.

DOI: 10.1103/PhysRevB.67.100502

PACS number(s): 74.25.Fy, 74.40.+k, 74.50.+r, 74.45.+c

Many of the well-understood phenomena in mesoscopic physics can be probed within the linear response of a physical system to an applied external perturbation, i.e., they are governed by equilibrium physics. Recently the attention has turned more towards the study of effects far from equilibrium. The quasiparticle distribution function $f(x;E)$ characterizing the nonequilibrium was measured in a normal-metal (N) wire between two large reservoirs^{1,2} through a superconducting (S) tunnel probe. This yielded useful information on the residual interactions between the Fermi-liquid quasiparticles. This nonequilibrium distribution was used to control the supercurrent in a normal-metal weak link.³⁻⁵ Both of these setups serve as different types of local probes for $f(x;E)$.

As a further step, we describe the control of $f(x;E)$ via the supercurrent. We show that, unlike other control parameters, it changes the profile of the effective temperature through the sample in the form of a large Peltier effect, i.e., heating the electrons in one part of the structure, and cooling them in another—even in the case of complete electron-hole symmetry. Moreover, we show how the two types of measurements for $f(x;E)$ can be combined within the same sample.

We concentrate on studying a diffusive normal-metal wire where elastic scattering is the dominant scattering mechanism. In the absence of superconductivity and for wires much shorter than the inelastic scattering length, the steady-state distribution function between two reservoirs with chemical potentials μ_1 and μ_2 has a double-step form, interpolating between the two Fermi functions in the reservoirs.¹

When the N reservoirs are replaced by superconducting ones, the leading transport mechanism at energies below the superconducting gap Δ is Andreev reflection.⁶ This leads to a penetration of superconducting correlations into the N wire (superconducting proximity effect). It modifies the charge and energy conductivities and we may introduce the corresponding diffusion coefficients $\mathcal{D}_T(x;E)$ and $\mathcal{D}_L(x;E)$ depending on space and energy.⁷ More importantly, the proximity effect allows supercurrents to flow through the N wire. To describe these effects, it is convenient to separate $f(x;E)$

into symmetric and antisymmetric parts relative to the chemical potential μ_S of the superconductor,

$$f_T(E) \equiv 1 - f(\mu_S - E) - f(\mu_S + E), \quad (1)$$

$$f_L(E) \equiv f(\mu_S - E) - f(\mu_S + E). \quad (2)$$

Below, we choose $\mu_S = 0$. These functions describe charge and energy distributions, respectively. They satisfy the kinetic equations^{7,8}

$$\frac{\partial j_T}{\partial x} = 0, \quad j_T \equiv \mathcal{D}_T(x) \frac{\partial f_T}{\partial x} + j_E f_L + \mathcal{T}(x) \partial_x f_L; \quad (3)$$

$$\frac{\partial j_L}{\partial x} = 0, \quad j_L \equiv \mathcal{D}_L(x) \frac{\partial f_L}{\partial x} + j_E f_T - \mathcal{T}(x) \partial_x f_T. \quad (4)$$

Here we assume no energy relaxation, so the kinetic equations describe the conservation of $j_T(E)$ and $E j_L$, the spectral charge and energy currents, respectively. Terms \mathcal{D}_T , \mathcal{D}_L , j_E , and \mathcal{T} can be found from quasiclassical equations for the retarded Green's function in the diffusive limit.^{9,7} All of them depend on the phase difference ϕ between the superconductors such that for $\phi = 0$, j_E and \mathcal{T} vanish. In our case, the charge diffusion coefficient \mathcal{D}_T is increased at most up to 20% from its normal-state value $\mathcal{D}_T = 1$,¹⁰ whereas for energies below Δ , \mathcal{D}_L tends towards zero near the S interface, effectively prohibiting energy transport. The term $\mathcal{T}(x;E,\phi)$ (Ref. 8) is obtained as a cross term from the retarded and advanced Green's functions. In general, it is much smaller than the other coefficients. The supercurrent is described by a spectrum $j_E(E;\phi)$ of supercurrent-carrying states,¹¹⁻¹³ which yields a contribution $j_E f_L(x)$ to the spectral charge current and, under nonequilibrium conditions involving $f_T(x) \neq 0$, a contribution to the energy current $E j_E f_T(x)$.

These kinetic equations have to be supplied with boundary conditions. At N reservoirs, electrons are simply transmitted and the distributions have to match Fermi functions with shifted chemical potentials. At the NS interface for $|E| < \Delta$, Andreev reflection prohibits the transfer of energy into S yielding $j_L = 0$. The charge distribution is continuous,

which leads to $f_T(E)=0$ at the NS interface assuming that there is no charge imbalance in the leads.

The nonequilibrium distribution function may be characterized through its moments, the local chemical potential $\mu(x)$ and the local effective temperature $T_{\text{eff}}(x)$. The previous characterizes the charge distribution function as $\mu(x) = \int_0^\infty dE f_T(x;E)$. The effective temperature describes the amount of heat in the electron system and is related to the energy distribution function via

$$\frac{e^2 \mathcal{L}_0}{2} T_{\text{eff}}^2(x) = \int_0^\infty dE E [f_{L,0}(x;E) - f_L(x;E)], \quad (5)$$

where $\mathcal{L}_0 = (\pi^2 k_B^2 / 3e^2)$ is the Lorenz number and the corresponding zero-temperature distribution has a step-function form $f_{L,0}(x;E \geq 0) = 1 - \theta[E - \mu(x)]$.

In the absence of the supercurrent, the kinetic Eqs. (3) and (4) are not coupled and, consequently, there is no thermoelectric coupling between the applied voltage and the energy currents. This results from the assumption of bands with complete electron-hole symmetry in the derivation of the formalism. Beyond the limits of the formalism, it is known that electron-hole symmetry breaking leads to small thermoelectric effects in normal metals, limited by the tiny factor $k_B T / \epsilon_F$.¹⁴

Below, we study a multiterminal setup depicted in the inset of Fig. 2: varying the voltage between the N and S reservoirs while maintaining the superconductors at equal potentials allows one to vary the distribution function in the phase-coherent wire. Such a device has already been implemented for controlling the critical current for the dc Josephson effect.⁵ It permits to study the supercurrent under nonequilibrium conditions without the complications caused by the ac Josephson effect and is, hence, an appropriate system for demonstrating the physics outlined above: As the energy flow $E j_E f_T(x)$ carried by the extra quasiparticles injected into the supercurrent-carrying states cannot pass into the superconductors, it has to be counterbalanced by another energy flow. This flow is driven by the gradient of the energy distribution function $E \mathcal{D}_L \partial_x f_L$ and hence, the applied control voltage is converted into a gradient of the effective temperature through the supercurrent.

Solving Eqs. (3) and (4) for $\phi=0$ and $E < \Delta$ is similar to a two-probe N - S case:⁷ f_L stays constant throughout the phase-coherent wire at its value in the N reservoir, $f_L^0(V) = (\tanh[(E+eV)/2k_B T] + \tanh[(E-eV)/2k_B T])/2$ and f_T is slightly modified from the linear space dependence due to the proximity effect on \mathcal{D}_T .¹⁰ Increasing the phase ϕ induces a finite supercurrent into the weak link, thereby coupling f_L and f_T . First neglecting the small coefficient \mathcal{T} , we get

$$\frac{\partial f_L}{\partial x} = -j_E \frac{f_T}{\mathcal{D}_L}, \quad \frac{\partial}{\partial x} \left(\mathcal{D}_T \frac{\partial f_T}{\partial x} \right) = j_E^2 \frac{f_T}{\mathcal{D}_L}. \quad (6)$$

Assuming that j_E is small, we observe that the major change due to the supercurrent is expected for $f_L(x;E)$; in particular, it will depend on space.

In general, a closed-form solution for $f_L(x;E)$, $f_T(x;E)$ cannot be found. Therefore, we focus on a numerical solu-

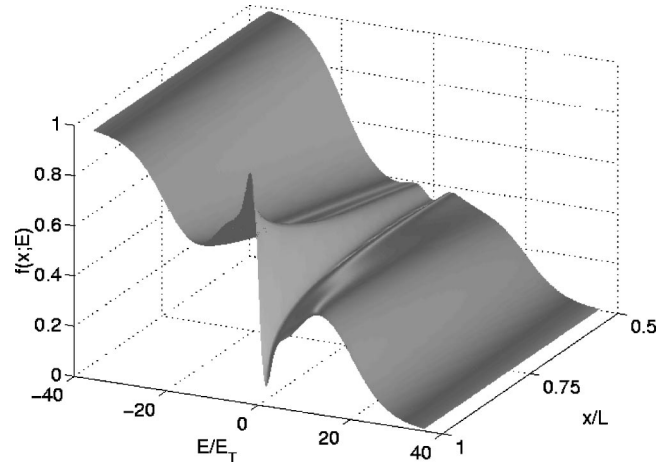


FIG. 1. Quasiparticle distribution function $f(x;E)$ in the right-horizontal arm for voltage $V=20E_T/e$, temperature $T=4E_T/k_B$, and phase difference $\phi=\pi/2$ between the superconductors. The large deviations from the rounded staircase form are created by the supercurrent flowing in the structure.

tion of both the spectral and kinetic equations. Here and below, we assume that all the energies are below Δ . The effect of the supercurrent on the distribution functions is clearest at a low temperature $k_B T \lesssim E_T$. The resulting distribution function $f(x,E)$ for the right-hand horizontal arm is plotted in Fig. 1 for $\phi=\pi/2$, yielding a supercurrent close to its maximum. As expected, the antisymmetric part of $f(x;E)$ has become space dependent, its energy dependence following that of j_E . Fixing a position in space, chosen, for example, near the NS interface in the left-hand side horizontal arm, allows us to observe how the distribution function changes as a function of phase ϕ , i.e., as it is driven by the supercurrent. This is illustrated in Fig. 2, where $f_L(E;\phi)$ is plotted for a few values of ϕ .

In the three-probe case, the chemical potential $\mu(x)$ interpolates nearly linearly between the chemical potentials of the superconductor and the normal reservoir and varies only little with the supercurrent. The changes in the effective temperature T_{eff} are much more pronounced. In the absence of the supercurrent, T_{eff} is

$$T_{\text{eff}}^0 \equiv T_{\text{eff}}(\phi=0) = \sqrt{T^2 + \{V^2 - (\mu(x)/e)^2\} / \mathcal{L}_0}. \quad (7)$$

Both $T_{\text{eff}}(x;\phi=0)$ and $\mu(x;\phi=0)$ are symmetric in the two horizontal arms. The supercurrent-induced change in $f_L(x;E)$ can be described through the change of the effective temperature compared to Eq. (7), such that $T_{\text{eff}}(x) = [T_{\text{eff}}^0(x)^2 + S(x;V) + \delta\mu(x;\phi)]^{1/2}$, where

$$S(x;V) = \frac{6}{\pi^2 k_B^2} \int_0^\infty dE E [f_L^0(E;V) - f_L(x;E)] \quad (8)$$

and $\delta\mu(x;\phi) \equiv [\mu(x;\phi)^2 - \mu(x;\phi=0)^2]/2$ describes the change in the local chemical potential due to the supercurrent, a much smaller term than $S(x)$. The kinetic equations imply that the supercurrent-induced change of the distribution function f_L is antisymmetric between the two arms, hence so is $S(x)$, i.e., T_{eff} increases in one arm and decreases

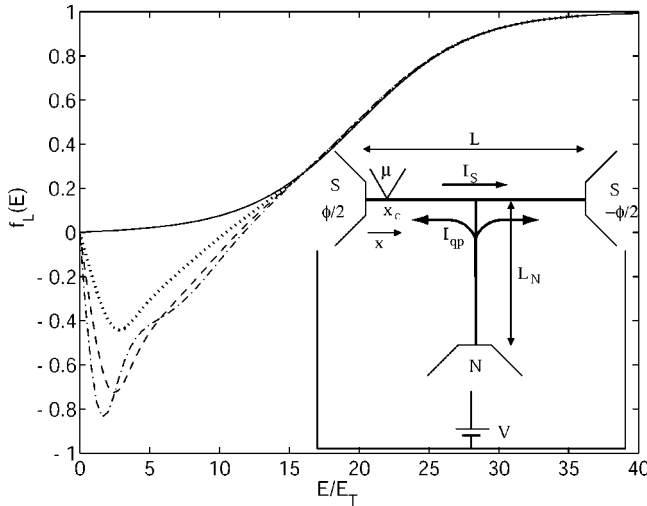


FIG. 2. Supercurrent-driven distribution function $f_L(E)$ at the left NS interface as a function of energy for $\phi=0$ (solid), $\phi=0.12\pi$ (dotted), $\phi=0.24\pi$ (dashed), and $\phi=\pi/2$ (dash dotted). The result is obtained with $T=4E_T/k_B$ and $V=20E_T/e$. The corresponding changes of f_L by the supercurrent in the right arm have the opposite sign. Inset: the system under consideration. We assume symmetric horizontal wires of length $L/2$. This length defines the Thouless energy of the weak link, $E_T \equiv \hbar D/L^2$. The resistance of the weak link is R_w and of the vertical wire R_c . Measurement of the predicted effects can be performed by placing a superconducting tunnel probe at position $x=x_c$, near the NS interface.

in the other one. Hence, the system works analogously to a Peltier device, where the control current is replaced by the supercurrent: the supercurrent “cools” one part of the system, transferring the heat to another part. The supercurrent-induced temperature change $S(x;V)$ is illustrated in Fig. 3.

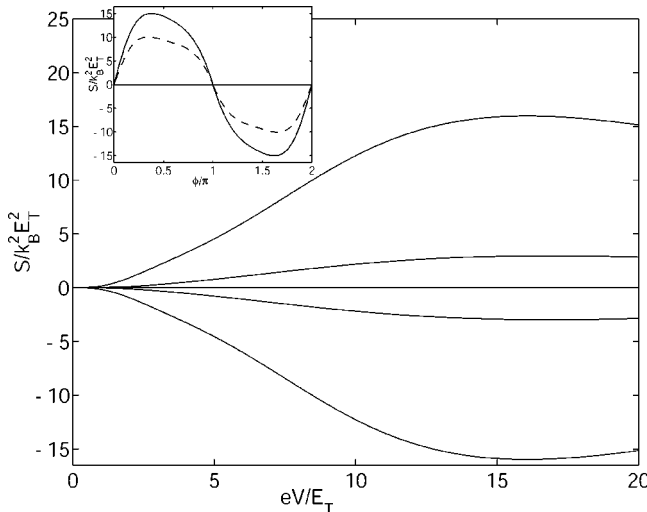


FIG. 3. Supercurrent-induced change $S(x;V)$ in the effective temperature as a function of voltage eV/E_T at different positions in the weak link with $\phi=\pi/2$. From top to bottom: $x=0$, $x=L/4$, $x=L/2$, $x=3L/4$, and $x=L$. Here $x=0$ and $x=L$ correspond to the left and right S interfaces and $x=L/2$ to the crossing point. Inset shows the phase dependence of $S(x=0)$ for $eV=12E_T$ (solid) and $eV=8E_T$ (dashed). In both curves, the bath temperature $T=0$.

To obtain an estimate for $S(x;V,\phi)$, we approximate $\mathcal{D}_T(E;x)=1$ and find

$$S = \frac{2E_T^2 R_w}{L^2(R_w + R_c)} \int_0^\infty dE E j_E(E) f_T^0(E) \int_x^{L/2} \frac{x' dx'}{\mathcal{D}_L(x';E)}. \quad (9)$$

At low temperatures $k_B T \ll eV$, f_T reduces to a step function around the potential eV in the reservoir, cutting the integration off at $E=eV$. Thus, this current-induced temperature change, which is similar to the Peltier effect, is much larger than in conventional single-metal setups.

For the measurement of the predicted effects in the distribution function, we suggest a setup shown in the inset of Fig. 2—very similar to those used in Refs. 1,2. Such a setup has also been used as a local thermometer¹⁵ of the electronic temperatures. A superconducting wire is connected to the horizontal arm via a highly resistive tunneling layer (I) at position, say, $x=x_c$. The dc current is then given by the tunneling quasiparticle current

$$I_J = \frac{1}{eR} \int_{-\infty}^{\infty} dE \rho_S(E+\mu) \rho(E) [f_0(E+\mu) - f(E)], \quad (10)$$

where $N_S \rho_S(E)$ is the BCS density of states (DOS) of the tunnel probe, $N_N \rho(E)$ is the local DOS in the mesoscopic wire at $x=x_c$, N_S and N_N are the normal-state DOS's for the two materials at $E=E_F$, $f_0(E)$ is the Fermi function, and $f(E)$ is the distribution function to be measured. When all the wires are in the normal state, the resistance through the tunnel junction is R . We can separate this expression as $I_J = I_1 + I_2$, where I_1 is the tunneling current for the equilibrium system $V=0$, probing $\rho(E)$ and

$$I_2 = \frac{1}{eR} \int_0^\infty dE \rho(E) \{ f_T(E) [\rho_S(\mu+E) + \rho_S(\mu-E)] + [f_L(E) - \tanh(E/2k_B T)] [\rho_S(\mu+E) - \rho_S(\mu-E)] \} \quad (11)$$

depends on the state of the wire, and for an equilibrium state, $V=0$, vanishes. In order to isolate I_2 , one can first determine I_1 as a function of the supercurrent by investigating the equilibrium case. Then, I_1 may be subtracted from the nonequilibrium results, leaving only currents I_2 . Moreover, $I_2(\mu) + I_2(-\mu)$ is proportional to the first part of Eq. (11), dependent on $f_T(E)$, and $I_2(\mu) - I_2(-\mu)$ to the second, dependent on $f_L(E)$.

With the above setup, the distribution functions may be characterized as a function of both the voltage V and the supercurrent driven through the weak link. The setup also makes it possible to measure the local distribution function both through the NIS contact and through the SNS critical current. These two independent probes should permit to distinguish the contributions from different inelastic scattering effects along the lines of Ref. 1.

So far we have completely neglected inelastic scattering in the wires. We can include energy relaxation due to

electron-electron scattering phenomenologically, generalizing the method of Ref. 16 to include the effect of supercurrent. In the limit $L \gg l_e$, we may describe the nonequilibrium distribution functions by Fermi functions with local chemical potential and temperature. In this case, assuming for simplicity $\mathcal{D}_T = 1$ and $T = 0$, we can integrate the two kinetic equations over energy, obtain kinetic equations for $\mu(x)$ and $T_{\text{eff}}(x)$ and find in the limit of high Δ

$$\partial_x^2 \mu(x) = -\partial_x I_S(x), \quad (12)$$

$$e^2 \mathcal{L}_0 \tilde{T}(x) \partial_x T_{\text{eff}}(x) = -\tilde{\mu}(x) \partial_x \mu(x) + Q_S. \quad (13)$$

Here $I_S(x) = [\int dE j_E(E) f_L(E, x)]/2$ is the local supercurrent, $2\mathcal{L}_0 e^2 \tilde{T} = -\int dE E \mathcal{D}_L \partial_T f_L$ and $2\tilde{\mu}(x) = -\int dE E \mathcal{D}_L \partial_\mu f_L$ describe the local temperature and chemical potential modified by \mathcal{D}_L , respectively, and $Q_S = [\int dE E j_E(E) f_T(E, x)]/2$ is the energy current carried by the nonequilibrium supercurrent. The first equation states the conservation of the total current whereas the latter describes the temperature profile. In the absence of the proximity effect, these yield the effective temperature given in Eq. (7). Similarly as above, the effective temperature can also in this case be tuned via the supercurrent, through the control of Q_S .

The predicted effect resembles a previously studied phenomenon in bulk superconductors,¹⁷ where a temperature gradient along with a supercurrent generates a charge imbalance in S . Here, the finite voltage (described through f_T) along with the supercurrent produces a temperature gradient (spatial variation of f_L).¹⁸

In Ref. 19, another thermoelectric effect, the thermopower, has been measured experimentally in a similar type of a system. The coupling of the distribution functions through the supercurrent may explain part of the observed effects. In Ref. 20, thermopower has been studied in the regime of high tunnel barriers and within linear response, leading also to an unexpectedly large effect. In that paper, all the distribution functions are, besides minor corrections, in quasiequilibrium: the transport is essentially driven by the discontinuities at the tunneling barriers. Moreover, Ref. 21 studies the Andreev interferometers through a numerical scattering approach, and predicts an oscillating thermopower as a function of the phase. However, there the quasiparticle current and supercurrent do not flow in parallel and the magnitude of the effect may be strongly affected by the very small size of the studied structure.

Summarizing, we predict that in a nonequilibrium situation created by applying a voltage between a normal metal and two superconductors, the nonequilibrium distribution functions in the normal-metal wire can be tuned by the supercurrent flowing between the superconductors. This results in a supercurrent-controlled Peltier effect. The predicted effect can be observed by the measurement of the tunneling current from an additional superconductor.

We thank N. Birge for the idea to this work and J. von Delft, D. J. van Harlingen and J. Pekola for suggestions on the manuscript. This work was supported by the Graduate School in Technical Physics at the Helsinki University of Technology.

*Email address: Tero.T.Heikkila@hut.fi

¹H. Pothier *et al.*, Phys. Rev. Lett. **79**, 3490 (1997).

²F. Pierre *et al.*, Phys. Rev. Lett. **86**, 1078 (2001).

³J.J.A. Baselmans, A.F. Morpurgo, B.J. van Wees, and T.M. Klapwijk, Nature (London) **397**, 43 (1999).

⁴J.J.A. Baselmans, B.J. van Wees, and T.M. Klapwijk, Phys. Rev. B **63**, 094504 (2001).

⁵J. Huang *et al.*, Phys. Rev. B **66**, 020507(R) (2002).

⁶A.F. Andreev, Zh. Éksp. Teor. Fiz. **46**, 1823 (1964) [JETP **19**, 1228 (1964)].

⁷W. Belzig *et al.*, Superlattices Microstruct. **25**, 1251 (1999).

⁸S.-W. Lee, A.V. Galaktionov, and C.-M. Ryu, J. Korean Phys. Soc. **34**, S193 (1999).

⁹K.D. Usadel, Phys. Rev. Lett. **25**, 507 (1970).

¹⁰P. Charlat *et al.*, Phys. Rev. Lett. **77**, 4950 (1996). This modification of \mathcal{D}_T can also be tuned by a phase between two superconductors in an Andreev interferometer [P.G.N. de Vegvar, T.A. Fulton, W.H. Mallison, and R.E. Miller, *ibid.* **73**, 1416 (1994)]. This tuning leads to the phase dependence of $\mu(x; \varphi)$.

¹¹F.K. Wilhelm, G. Schön, and A.D. Zaikin, Phys. Rev. Lett. **81**, 1682 (1998).

¹²S.K. Yip, Phys. Rev. B **58**, 5803 (1998).

¹³T.T. Heikkilä, J. Särkkä, and F.K. Wilhelm, Phys. Rev. B **66**, 184513 (2002).

¹⁴N. W. Ashcroft and N. D. Mermin, *Solid State Physics* (Saunders College, Orlando, 1976).

¹⁵J.M. Rowell and D.C. Tsui, Phys. Rev. B **14**, 2456 (1976).

¹⁶K.E. Nagaev, Phys. Rev. B **52**, 4740 (1995).

¹⁷C.J. Pethick and H. Smith, Phys. Rev. Lett. **43**, 640 (1979); J. Clarke, B.R. Fjordbøge, and P.E. Lindelof, *ibid.* **43**, 642 (1979); A. Schmid and G. Schön, *ibid.* **43**, 793 (1979); J. Clarke and M. Tinkham, *ibid.* **44**, 106 (1980).

¹⁸However, the mechanism for the coupling between the temperature gradient and charge imbalance is different in these two cases: whereas in bulk superconductors, it arises from the superconducting condensate that converts quasiparticle currents into supercurrents, the phenomenon depicted here is due to the energy current carried by the supercurrent in the nonequilibrium state.

¹⁹J. Eom, C.J. Chien, and V. Chandrasekhar, Phys. Rev. Lett. **81**, 437 (1998).

²⁰R. Seviour and A.F. Volkov, Phys. Rev. B **62**, R6116 (2000).

²¹N.R. Claughton and C.J. Lambert, Phys. Rev. B **53**, 6605 (1996).

Chapter 4

Acknowledgements

The least true piece of information in a report like this is the fact, that a single person's name is printed on the title page, whereas all the work presented results from collaborative efforts.

First credit goes to my postdoctoral advisors: Hans Mooij engaged in the true experiment of hiring me as a theorist for his experimental group and had a lot of patience on the way that my ideas and what can be implemented converged. Jan von Delft has given me huge credit by letting me supervise three of his students and create my own individual research program, still giving advice whenever it was due.

Most of the actual nuts-and-bolts research reported here was done by graduate students whom to supervise I have and had the privilege, namely Marlies Goorden, Henryk Gutmann, Udo Hartmann, and Markus Storcz. Credit also goes to Konstanze Jähne who participates in the continuation of this program. I would also like to thank my longer-term collaborators Caspar van der Wal, Kees Harmans, and Tero Heikkilä for the continuous and fruitful collaboration and friendship over the years. Bulding and maintaining a coherent research program requires agenda setting, sharing ideas, discussion and inspiration. This I picked up in particular during a number of collaboration visits, for which I would like to thank the groups of Terry Orlando, Seth Lloyd, and Leonya Levitov at MIT, the groups of John Clarke and Birgitta Whaley at Berkeley, the group of Gerd Schön at my alma mater in Karlsruhe, and the groups of Martti Salomaa and Pertti Hakonen at the Helsinki University of Technology.

Thanks also to all my co-authors and collaborators whose work con-

tributed to this report and which I did not mention yet: Norman Birge, Hervé Courtois, Donald Crankshaw, Pascal Dubos, Alex ter Haar, Jian Huang, Bill Kaminsky, Silvia Kleff, Bernard Pannetier, Frédéric Pierre, Jani Särkkä, Raymond Schouten, Tommy Vänskä, and Andrei Zaikin. I enjoyed also many other highly interesting and stimulating discussions. Milena Grifoni, Igor Goychuk, and Peter Hänggi with their immense experience with open quantum system helped me a lot when I started to learn about the field and the techniques (a process, which is certainly not complete yet). I learned many aspects of noise in Josephson circuits from Daniel Esteve, Dale van Harlingen, John Martinis, and Denis Vion.

In many pieces of this work, the importance of an appropriate environment is emphasized. For the completion of this work, the pleasant and stimulating environment at the Chair for Theoretical Condensed Matter physics, including stimulating and critical discussions at the group seminar, was of great importance. Although I did not do many numerics myself, the work of Ralph Simmler and Jens Schmalzing of keeping the network and my laptop alive is gratefully acknowledged.

Research of this kind requires appropriate funding, which means that the funding agencies trust the researcher to perform, which is not to be taken for granted for young researchers. Thus, I would like to acknowledge the advance in trust of the US Army Research Office, Contract No - P-43385-PH-QC, the European Union's Quiprocone Network, and the Deutsche Forschungsgemeinschaft with SFB 631.

Finally, none of this would have been possible without the constant personal support from my wife Bärbel.